

2010

annual progress report

Propulsion Materials

**U.S. Department of Energy
Office of Vehicle Technologies
1000 Independence Avenue S.W.
Washington, DC 20585-0121**

FY 2010

Progress Report for Propulsion Materials

Energy Efficiency and Renewable Energy
Office of Vehicle Technologies
Advanced Materials Technologies

Patrick B. Davis	Program Manager, OVT
Carol L. Schutte	Team Leader, Advanced Materials Technologies
Jerry L. Gibbs	Technology Manager

January 2011

CONTENTS

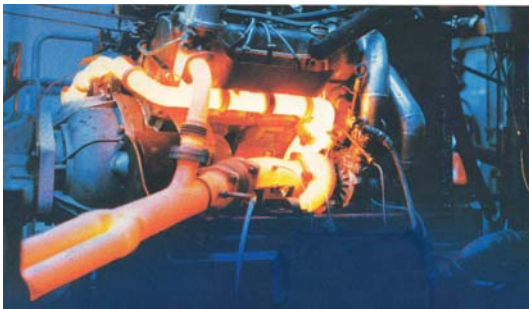
INTRODUCTION.....	1
PROJECT 18516 - MATERIALS FOR ELECTRIC AND HYBRID DRIVE SYSTEMS.....	13
Agreement 16307 - Modeling/Testing of Environmental Effects on Automotive PE Devices...	13
Agreement 16305 - Solder Joint of High Performance Power Electronics: Materials by Design	25
Agreement 16306 - Power Electronics Materials Compatibility.....	33
Agreement 19201 - Non-rare Earth Magnetic Materials.....	37
Agreement 17955 - Lithium Battery Recycling Issues.....	43
Agreement 13257 - High Performance Embedded Capacitors.....	47
Agreement 13295 - Permanent Magnet Development for Automotive Traction Motors.....	55
PROJECT 18517 – COMBUSTION SYSTEM MATERIALS.....	75
Agreement 11752 - Materials for HCCI Engines.....	75
Agreement 8697 - NO _x Sensor Development	81
Agreement 9440 - Surface Texturing for Friction Control.....	89
Agreement 11754 - Hydrogen Materials Compatibility.....	95
PROJECT 18518 - MATERIALS FOR HIGH EFFICIENCY ENGINES.....	105
Agreement 16304 - High Performance Valve Materials.....	105
Agreement 13329 - Design Optimization of Piezoceramic Multilayer Actuators for Heavy Duty Diesel Engine Components.....	109
Agreement 17058 - Compact NO _x Sensor with Built-in Reference.....	121
Agreement 19202 - Surface Titanium Friction and Wear: Surface Engineering of Connecting Rods and Other Bearing Components.....	127
Agreement 15050 - Materials Testing with ACERT Engine.....	133
Agreement 15054 - Fatigue Enhancements by Shock Peening.....	137
Agreement 15055 - Tailored Materials for High Efficiency CIDI Engines.....	143
Agreement 16303 - Materials for High Pressure Fuel Injection Systems.....	155
Agreement 17257 - Materials for Advanced Turbocharger Designs.....	161
Agreement 17894 - NDE Development for ACERT Engine Components.....	167
Agreement 18570 - Engine Materials Compatibility with Alternate Fuels.....	175
Agreement 18571 - Materials Issues Associated with EGR Systems.....	179
Agreement 19192 - Titanium for Vehicle Propulsion Applications.....	185
Agreement 19215 - Surface Texturing for Friction Control (BLL).....	191
Agreement 19217 - Ultra-fast Chemical Conversion Surfaces.....	197
Agreement 19216 - Friction Modeling for Lubricated Engine and Drive-train Components....	207
PROJECT 18519 – MATERIALS FOR CONTROL OF EXHAUST GASES AND ENERGY RECOVERY SYSTEMS.....	211
Agreement 9130 - Materials Analysis Tools for Studying NO _x Adsorber Catalysts (CRADA with Cummins, Inc.).....	211
Agreement 10461 - Durability of Diesel Particulate Filters (CRADA with Cummins, Inc.)	221
Agreement 10635 - Catalysis by First Principles.....	231
Agreement 19214 - Effects of Biodiesel Fuel on Diesel Particulate Filter Materials.....	243
Agreement 20091 – Electrically Assisted Diesel Particulate Filter Regeneration.....	253

PROJECT 18865 - MATERIALS BY DESIGN.....	265
Agreement 13723 - Residual Stresses in Thin Films.....	265
Agreement 9105 - Ultra-High Resolution Electron Microscopy for Characterization of Catalyst Microstructures and Deactivation Mechanisms	271
Agreement 17895 - Durability of ACERT Engine Components.....	285
Agreement 14957 - Modeling of Thermoelectrics.....	293
Agreement 15529 – Utilization of Nanofluid Coolants.....	303
Agreement 16308 - Thermoelectric Theory and Structure	309
Agreement 16309 - Carbon-based Thermoelectrics.....	313
Agreement 18340 - Thermoelectric Materials for Advanced Vehicle Energy Recovery.....	317
Agreement 13721 - Low-friction Hard Coatings.....	333
Agreement 20370 - Life Cycle Modeling of Propulsion Materials.....	342
Agreement 16226 - Integrated Surface Engineering Technology Development for Improving Energy Efficiency of Engine Components.....	347

INTRODUCTION

Propulsion Materials R&D: Enabling Technologies to Meet Vehicle Technologies Program Goals

The Department of Energy's (DOE's) Office of Vehicle Technologies (OVT) is pleased to introduce the *FY 2010 Annual Progress Report for the Propulsion Materials Research and Development Program*. Together with DOE national laboratories and in partnership with private industry and universities across the United States, the program continues to engage in research and development (R&D) that provides enabling materials technology for fuel-efficient and environmentally friendly commercial and passenger vehicles.



This introduction summarizes the objectives, progress, and highlights of the program in FY 2010. The Propulsion Materials Technology actively supports the energy security and reduction of greenhouse emissions goals of the Vehicle Technologies Program by developing advanced materials that enable development of higher efficiency powertrains for ground transportation. Propulsion Materials works closely with the other disciplines within the VT Program to identify the materials properties essential for the

development of cost-effective, highly efficient, and environmentally friendly next-generation heavy and light duty powertrains. The technical approaches available to enhance propulsion systems focus on improvements in both vehicle efficiency and fuel substitution, both of which must overcome performance limitations of materials currently in use. The Propulsion Materials Technology activity works with National Laboratories, industry experts, and VT Program teams on strategies to overcome materials limitations in powertrain performance. The technical maturity of projects funded range from basic science to subsystem prototype validation.

The Propulsion Materials activity is a partner and supporter of the VT Program Hybrid and Vehicle Systems, Energy Storage, Power Electronics and Electrical Machines, Advanced Combustion Engines, and Fuels and Lubricants R&D activities. Projects within the Propulsion Materials activity address materials concerns that directly impact the critical technical barriers in each of these programs—barriers such as fuel efficiency, thermal management, emissions reduction, waste-heat recovery and reduced manufacturing costs. The program engages only the barriers that involve fundamental, high-risk materials issues.

Enabling Technologies

The Propulsion Materials Technology activity focuses on key technical deficiencies in materials performance that limit expanded capabilities of advanced combustion engines, electric-drive systems, and fuels and lubricants. It provides materials R&D expertise and enabling advanced materials that support the goals of combustion, hybrid, and power electronics development. The program provides enabling materials support for combustion, hybrid, and power electronics development, including the following:

- Materials for high-efficiency combustion technologies, for example, homogenous-charge compression-ignition
- Materials for 55% thermal efficiency heavy-duty diesel engines

- Materials for waste-heat recovery via thermoelectric modules, with potential 10% increase in fuel efficiency
- Materials technologies for efficient and effective reduction of tailpipe emissions, including diesel particulate filters, catalyst characterization and testing, and exhaust-gas recirculation (EGR) coolers
- Materials technologies for electric and hybrid-electric vehicles, including advanced power electronics materials and electric motors
- Materials for alternate-fuels vehicles, including materials compatibility and corrosion
- Alternatives to rare and costly materials, for example, rare-earth elements, and technologies to improve overall materials availability, for example, recycling.

The program supports these core technology areas by providing materials expertise, testing capabilities, and technical solutions for materials problems. The component development, materials processing, and characterization that the program provides are enablers of the successful development of efficient and emissions-compliant engines.

Program Organization

The Propulsion Materials Program consists of five R&D projects that support the VTP propulsion technologies. Each project consists of several related R&D agreements.

- Materials for Electric and Hybrid Drive Systems
 - Develop materials appropriate for power electronics, electric motors and other hybrid system applications
- Combustion System Materials
 - Develop materials for HECT engines and fuel injection systems
- Materials for High Efficiency Engines
 - Develop materials for efficient engine components, such as valvetrain components, fuel injectors, and turbochargers
- Materials for Control of Exhaust Gases and Energy Recovery Systems
 - Develop materials for exhaust aftertreatment and waste heat recovery applications
- Materials by Design (Application Specific Materials Simulation, Characterization and Synthesis)
 - Adopt a computational materials – atomic-scale characterization protocol to develop advanced materials for NO_x catalysts, lithium-ion batteries, thermoelectric generators, and electric motors

R&D Projects and Agreements are evaluated annually using strategic objectives. Agreements are evaluated on relevance to Vehicle Technology Program objectives and supported team's priorities, strength of industrial support for the activity, and perceived value of the R&D activity to the Vehicle Technologies Program. In order to keep the program fresh and up-to-date, over 10% of agreements are retired annually. New projects are selected in accordance with identified Office of Vehicle Technologies needs, for example:

- Advanced Combustion Team
 - Internal combustion engine materials
 - Thermoelectric materials

- Catalysts and aftertreatment materials
- Materials for engine sensors
- Hybrid Electric Systems Team
 - Power electronics materials
 - Materials for energy storage
 - Materials for electric motors
- Fuels Team
 - Alternative fuels materials compatibility

Selected Highlights:

Materials for Electric and Hybrid Drive Systems

The goal of the Automotive Power Electronic and Electric Machines (APEEM) Program is to reduce the size, weight, and volume of the power electronics without increasing the cost or reducing the reliability. Many, if not most, technical barriers are directly linked to the contemporary material limitations of sub-components found within devices that comprise inverters, converters, and motors. The material limitations include:

- Insufficient temperature capability
- Excessive thermal insulations
- Excessive electrical insulation
- Insufficient power density in permanent magnets
- Insufficient bandgap

The role of Propulsion Materials is to provide materials support for the components and systems under development by the Power Electronics and Electric Machines sub-program. Research activities will develop improved materials and processes for development of improved thermal management systems, capacitors, motors, and power electronics.

In an R&D agreement completed in FY2010 researchers at ORNL evaluated the complex relationship between environment (e.g., temperature, stress, etc.) and automotive power electronic device performance through materials characterization and modeling, and identified alternative material constituents and architectures that will improve devices reliability and enable their operation at higher temperatures without compromise to electronic function. The mechanical evaluation of silicon and silicon carbide semiconductors was completed, using brittle-materials testing, characterization, and modeling techniques to evaluate the role of bulk, surface, and edge flaws and the effects of chip finishing on the mechanical reliability of the chip. Fig 1 illustrates the evaluation of stress profiles along the edges of a chip, using the testing technique of anticlastically bending.

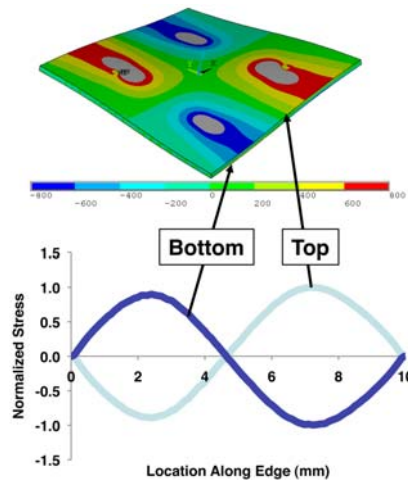


Figure 1. Stress profile along the edges of an anticlassically bent chip.

The use of vehicles with electric drive, which could reduce our oil dependence, will depend on lithium-ion batteries. But there are questions about the supply of lithium. The maximum demand for lithium and other materials was estimated by Argonne National Laboratory (ANL) assuming electric-drive vehicles expand their market share rapidly, estimating material demand per vehicle for four battery chemistries. This R&D effort was co-funded with the Energy Storage Program. Total demand for the United States is based on market shares from an Argonne scenario that reflects high demand for electric-drive vehicles, and total demand for the rest of the world is based on a similar International Energy Agency scenario. Total material demand is then compared to estimates of production and reserves, and the quantity that could be recovered by recycling, to evaluate the adequacy of supply. In the case of materials for lithium-ion batteries, it appears that even an aggressive program of vehicles with electric drive can be supported for decades with known supplies, if recycling is instituted. However, reliance on pure electrics could eventually strain supplies of lithium and cobalt.

Combustion System Materials

The purpose of the Combustion System Materials project is to develop materials and materials processing technology that support the Advanced Combustion Engine R&D Program. The focus is on technologies that have application across the range of engine types and combustion systems being considered within the Vehicle Technologies Program including diesel, advanced combustion, HCCI, and hydrogen ICE.

Researchers at the Lawrence Livermore National Laboratory (LLNL) are continuing to develop an inexpensive, rapid-response, high-sensitivity and selective electrochemical sensor for oxides of nitrogen (NO_x) for compression-ignition, direct-injection (CIDI) exhaust gas monitoring. Because the need for a NO_x sensor is fairly recent and the performance requirements are extremely challenging, most are still in the development phase. Currently, there is only one type of NO_x sensor that is sold commercially, and it seems unlikely to meet more stringent future emission requirements. Work in FY2010 included improving sensor robustness to allow testing of prototypes directly mounted onto the exhaust manifold. Previous attempts had required exhaust gases to be routed into a separate furnace for testing due to mechanical failure from engine vibrations. Real engine conditions caused either the Au wire or dense LSM to detach from the substrate. The modification of sensor prototypes by adding a ceramic adhesive successfully improved mechanical stability and robustness while simultaneously retaining the sensing performance.

Researchers at the Pacific Northwest National Laboratory (PNNL) and Ford Motor Co. are continuing the characterization and development of piezoelectric materials for service in fuel injectors for hydrogen gas. PNNL's approach includes evaluation of failure modes for piezoelectric actuators in hydrogen gas,

development of a model for hydrogen diffusion, absorption and damage in piezoelectric ceramics, and development of methods for controlling or remediating the hydrogen damage to prolong actuator life, measurement of the friction and wear characteristics of injector materials in hydrogen environments, measuring the performance of piezoelectric actuators and actuator materials in hydrogen environments, and development of a design approach to hydrogen injectors based on material behavior and performance in hydrogen. Results in 2010 led to the following conclusions: (1) Significant hydrogen-induced blistering occurs in lead-zirconium titanate, but less in barium titanate. These findings indicate that barium titanate may be preferential for hydrogen environments. (2) Electrode mixing between Pd and Pb occurs during hydrogen charging, but does not occur for Ba and Pd in barium titanate/Pd systems. Further investigation is warranted, but this may indicate BTO systems are better suited to hydrogen. (3) Through Gauge repeatability testing and statistical design-of-experiments testing, we were able to conclude that the two primary factors impacting the durability of nanolaminates are 1) ion-assisted deposition and 2) the nitrogen:argon ratio.

In a new R&D agreement at ANL, the beneficial effects of surface texturing for friction control are being evaluated. Within the first year of this program significant advancements were made toward better understanding of the influence that surface texture has on tribological performance. More importantly, the groundwork for developing a systematic method of evaluating and optimizing surface texture application and design for friction and wear reduction was achieved.

First, to better understand the mechanism by which surface dimples influence hydrodynamic lubrication action, an optical profilometry technique was employed. (Figure 2 illustrates a laser-dimpled surface) For this non-conformal contact configuration no enhancement to the lubricant film thickness was observed. Second, to assess the effect of surface dimples on friction performance, application specific testing was conducted on a conformal block-on-ring setup to simulated journal bearing applications. These results demonstrated a significant friction reduction across a range of operating conditions, up to 50% reduction. Further texture design optimization is needed to realize the full potential benefits of this treatment for this application. Third, surface texture was tested for scuffing performance, in order to test behavior of this surface treatment at severe contact conditions. In comparison to smooth samples, dimpled surface demonstrated a threefold increase in scuffing resistance, measured by contact severity index. Last, a novel surface texturing method, vibro-mechanical texturing, was assessed in coordination with Northwestern University to develop a cost effective and accessible texturing technique.

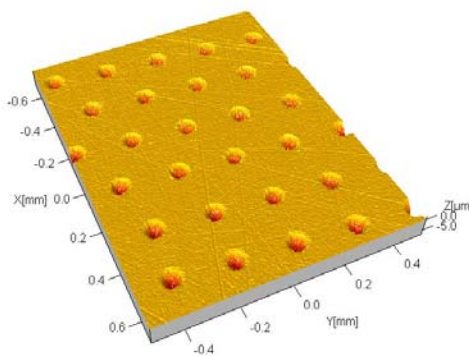


Figure 2. Three-dimensional profile of a typical laser dimpled surface.

The use of HCCI combustion will subject engine components to significantly higher temperatures and pressures. The temperatures for diesel engines will reach over 1600°F, and pressure may reach >2000 psi. Such severe engine operating conditions will require a significant improvement in materials performance in order to take advantage of the HCCI engine concept. An R&D project at ORNL deals with identifying materials requirements for HCCI engines for automotive and truck applications and the

development of advanced, yet cost-effective, materials through computational design. The approach is described in Table 1.

Table 1. ORNL materials-by-design toolbox

Modeling	Experimentation	Characterization
Thermodynamic modeling of material properties vs. alloy composition	Ultra-high-gauss magnetic stabilization of alloy steels	Advanced microscopy techniques
Neural-network modeling of diverse, nonlinear materials properties and process variations	Low-temperature gas carburization of finished components	X- ray and neutron scattering
Detailed microstructure based empirical modeling	Ability to produce small quantities of materials and fabricate them into test bars for property measurements and production of prototype components by a variety of methods, including sand and die casting, extrusion, forging and rolling	Surface and bulk property measuring techniques
Non-equilibrium modeling of solidified structures		
Extrapolation of properties from simple alloy systems to complex systems using interaction parameters		

In 2010 rotating beam tests confirm the high temperature fatigue properties of several commercial Ni-based alloys; computational thermodynamics models were used to identify promising alloy compositions with the potential to have desirable fatigue performance at higher temperatures and small heats were cast; and one larger batch of alloy was prepared for fatigue testing in FY 2011.

Materials for High Efficiency Engines

In support of the Vehicle Technology Program goal of developing a heavy-duty engine with 55% thermal efficiency by 2013, the materials for high efficiency engines project develops materials, material treatments, coatings, and surface treatments necessary to overcome the technical hurdles to these objectives. This project focuses on key material related technical issues identified by the Advanced Combustion Engine (ACE) group and industrial partners.

R&D agreements for high-efficiency engines are either driven by industry needs for specific classes of components, or by the invention of new methods of processing materials or new alloys, which can be exploited to respond to the needs of industry for new materials for high-efficiency engines. The R&D efforts in this Project involve materials development for valvetrain materials, turbochargers, exhaust-gas recirculation (EGR) systems and fuel systems. In addition, processing-driven efforts include those that exploit new technologies in joining, shock peening, friction-stir processing, and processing specifically of titanium alloys. An engine test cell and dedicated diesel engine have been made available for testing advanced materials and components. Highlights from those efforts are shown below:

An R&D agreement by PNNL and Caterpillar proposes to experimentally develop friction-stir processing (FSP) to engineer the surface of propulsion materials for improved properties. The application focus is to tailor the mechanical properties and thermal conductivity of engine materials, both ferrous and non-ferrous materials, by using FSP techniques. This microstructural modification is expected to lead to a set of materials with enhanced surface properties that can handle increased combustion pressure and exhaust

temperatures, resulting in improved engine efficiency. In 2010, the primary focus of project work was on FSP of aluminum piston materials used for light-duty and medium-duty CIDI engines. The work is intended to improve the thermal fatigue performance of typical piston alloys to allow them to be used in higher peak stress environments without suffering premature bowl rim failure. The concept is illustrated in Figure 3.

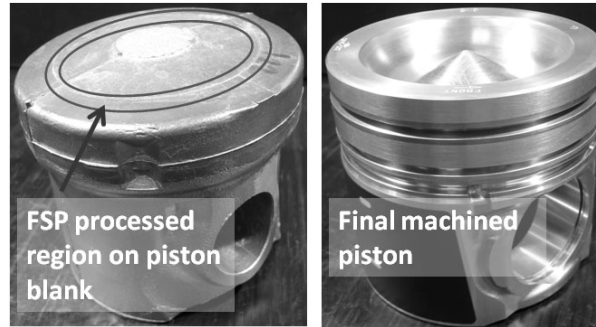


Figure 3. Cast piston blank. (The area in the bowl rim after machining will be friction stir processed for improved microstructure.)

A cooperative research and development agreement (CRADA) between Caterpillar, Inc. and ORNL has addressed the wear and failure modes of current on-highway heavy-duty diesel exhaust valves and seats, and then evaluated changes in seat-insert processing and advanced exhaust-valve alloys that will enable higher temperature capability, as well as better performance and durability. The need for such upgraded valve-seat alloys is driven by the demands to meet new emissions and fuel economy requirements, which then continue to push diesel exhaust component temperatures higher. In 2010 ORNL and Caterpillar identified several commercial Ni-based superalloy upgrade candidates, and worked with the valve supplier to obtain new materials for critical mechanical testing and valve prototyping. Wear testing in Caterpillar's valve testing rig demonstrated a 200% reduction in wear rate relative to the reference 31V alloy (see Figure 4).

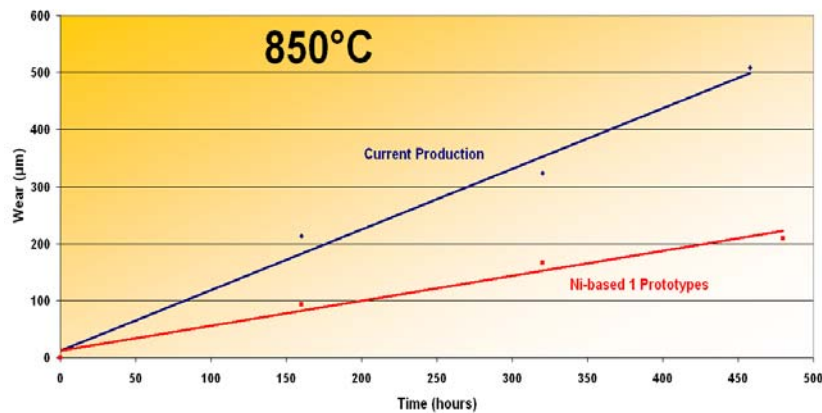


Figure 4. Caterpillar wear-rig testing of cumulative wear (valve and seat-insert) for standard 31V alloy exhaust valves and new Ni-based 1 superalloy prototype valves at 850°C in air.

An energy benefits study of CF8C-Plus cast stainless steel conducted by ORNL indicates that cast stainless steel has the potential to save 143 trillion BTUs by 2020 for turbocharger and gas/steam turbine applications, with about 66% of that coming from automotive vehicle turbochargers (Figure 5). Far more energy savings are realized by life cycle, end-use calculations rather than the initial material/component considerations. Energy savings for CF8C-Plus cast stainless steel was evaluated relative to HK30 cast stainless steel, and the Ni-based superalloy 625.

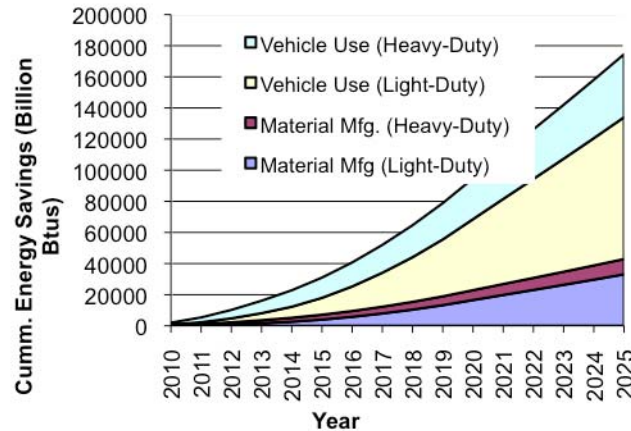


Figure 5. Estimated total cumulative life-cycle energy savings for use of CF8C-Plus steel for turbocharger housings in the automotive market.

Argonne National Lab investigated synchrotron X-ray CT for NDE characterization of friction-welded joint between a TiAl turbocharger wheel and Ti-alloy shaft. From a preliminary test for calibration weld samples, the CT results showed detailed resolution of crack networks and structural variations in the weld plane (Figure 6). This technology will be further evaluated for joint samples made with different processing parameters. The results can be used to optimize processing parameters to manufacture reliable weld components.

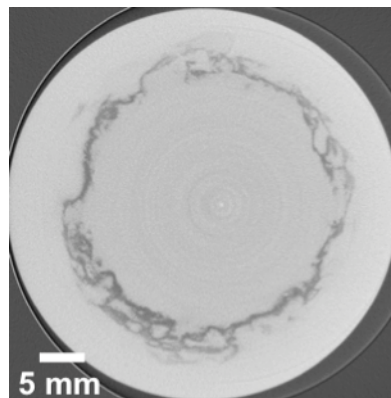


Figure 6. A typical X-ray CT slice within the weld plane of a turbocharger rotor-to-shaft joint.

In order to conduct a systematic assessment of potential engine materials corrosion in ethanol fuel blends, a Cooperative Research and Development Agreement (CRADA) has been established between participants at Oak Ridge National Laboratory and domestic automobile manufacturers (USCAR, LLC). The overall effort is composed of several tasks to be performed primarily in parallel: (1) Evaluation of corrosion and surface films on engine components, (2) in-situ extraction and analysis of gas/fluid from valve seat crevice (Figure 7), and (3) development of laboratory corrosion testing.

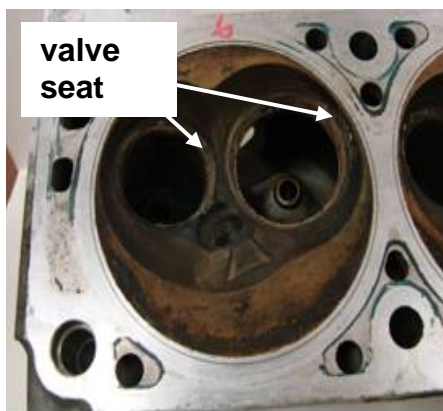


Figure 7. Portion of an aluminum head received for evaluation of corrosion in the valve seat crevice location.

Materials for Control of Exhaust Gases and Energy Recovery Systems

Roughly 30% of the chemical energy stored in the fuel consumed by an internal combustion engine is contained within the flow of engine exhaust gases. This project focuses on development of materials necessary to efficiently control the flow these exhaust gases while extracting the maximum amount of usable energy from them with minimal negative impact on engine efficiency. The evolving combustion regimes and fuels that high efficiency engines may need to utilize in the future complicate the objectives of this project. Materials developed under this project will be used for high performance components including: high temperature exhaust manifolds, exhaust gas recirculation devices, advanced turbochargers, direct energy conversion devices, exhaust gas sensors, and low restriction exhaust aftertreatment devices.

Ammonia containing compounds may be added to diesel exhaust to reduce NO_x to N_2 , as in selective catalytic reduction (SCR). The reductant reduces NO_x to H_2O and N_2 . Excess ammonia is often needed resulting in NH_3 escaping or “slip”. This slip is a concern for sociability and environmental reasons. Although not regulated, proactive steps are taken to mitigate even small amounts of ammonia slip by employing a selective oxidation catalyst. Oxidation catalysts are usually present in aftertreatment systems to oxidize ammonia that is not being oxidized upstream by the SCR catalysts. These oxidation catalysts ensure that ammonia slip to ambient is minimal and are referred to several names: ammonia oxidation (AMOX) catalysts, selective catalytic oxidation (SCO) catalysts or ammonia slip catalysts (ASC). Candidate catalysts are typically zeolite-based, alumina-supported metal or alumina-supported metal oxide catalysts. Hydrothermal conditions, temperature and water content, strongly influence the functioning of these catalysts by changing or “aging” the catalytic materials. These changes and their impact on performance are not well understood. Cummins, Inc. and the Oak Ridge National Laboratory are collaborating in an R&D CRADA to make use of transmission electron microscopy (TEM), X-ray diffraction (XRD), photoelectron spectroscopy (XPS), and Raman spectroscopy tools available in the ORNL High-Temperature Materials Laboratory to develop a detailed understanding of the catalyst aging. Figure 8 illustrates the use of high-resolution TEM for elemental analysis of the washcoat of an ammonia oxidation catalyst.

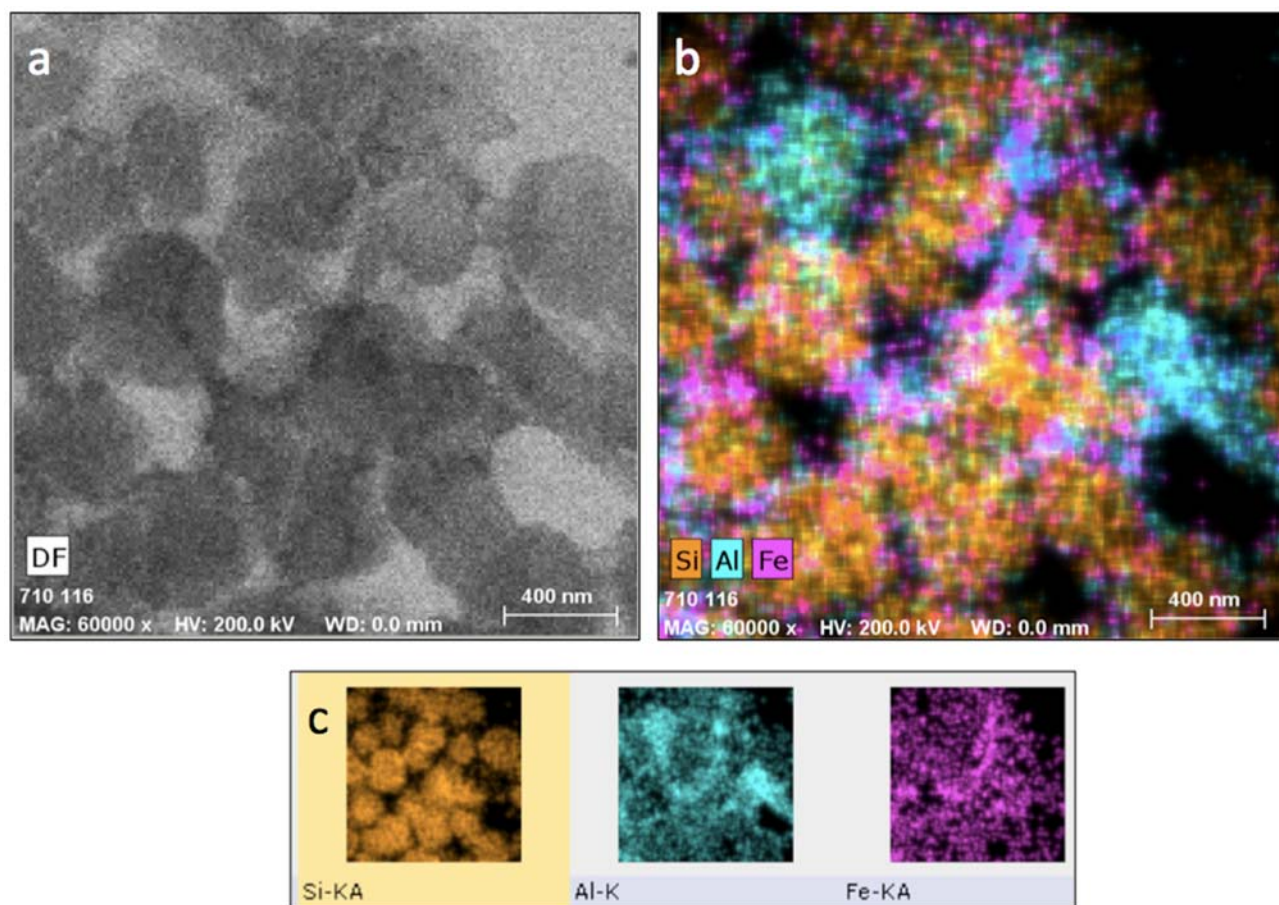


Figure 8. Elemental mapping data acquired using the Bruker-Nano SDD system on the ACEM. (a) the ADF image shown with Si, Al and Fe distributions overlaid in (b). This overlay shows that the blocky particles are either Si-rich or Al-rich, and the Fe distribution correlates primarily to some of the Al-rich areas. Individual maps of the Si, Al and Fe distributions are shown in (c).

The development of new emission-treatment catalytic systems is still largely dominated by trial and error, which is often slow and expensive. A knowledge gap between theory and experiment has been a major contributing factor: traditional computational approaches have been significantly simplified in comparison to real materials, and experimental studies, especially on emission treatment catalysts, have primarily focused on fully formulated systems that can treat engine-out emissions in vehicles. Researchers at the Oak Ridge National Laboratory are developing a protocol that combines the power of theory and experiment for atomistic design of catalytically active sites that can contribute directly to complete catalyst system suitable for technical deployment. The protocol includes theoretical modeling of catalyst systems via density functional theory (DFT), synthesis of experimental catalyst systems, exposure of catalysts under simulated operating conditions (including an ex-situ reactor which permits duplication of the reaction conditions in a bench-top reactor and facilitates high-resolution scanning transmission electron microscopy), and characterization of the catalyst performance and changes that occur in the catalysts during operation. Recent theoretical studies on single atoms show that the bonding of platinum with θ -alumina is different from that reported for α - or γ -alumina. Pt on θ -alumina is in zero oxidation state while it is $d9s1$ on either α - or γ -alumina. Nickel and palladium atoms also show similar bonding patterns. Interestingly, the agglomeration of single atoms can also be modeled on 010 θ -alumina surfaces and our studies show that there is no significant barrier that prevents independent platinum atoms to bond and form large particles.

Materials by Design (Application Specific Materials Simulation, Characterization and Synthesis)

Application Specific Materials Simulation, Characterization, and Synthesis: is a materials discovery and development approach consisting of computational modeling and materials characterization, often at the nanoscale (i.e. at length scales down to and including atomic and sub-atomic) to elucidate and enable the prediction of structure-function relationships of materials to be developed for specific applications. Propulsion materials research uses "materials by design" to ensure the success of emerging technologies such as new power electronics, advanced internal combustion engines, hybrid systems, and emission reduction technologies. This approach will be used, combined with advanced materials characterization instrumentation and synthesis techniques to postulate new materials, compositions, and structures to greatly enhance the materials properties necessary for advanced high performance propulsion systems.

Marlow Industries and ORNL are collaborating in research to enhance the durability of thermoelectric modules used for automotive waste heat recovery. These devices will experience daily thermal cycling with temperature difference of several hundred degrees. Residual stresses exist after the metallization and bonding to the ceramic substrate. The best tool to study the residual stress is X-ray or neutron diffraction. Since X-ray is a surface technique and could not penetrate deep into/through materials, they conducted preliminary study of residual stress mapping at the High Flux Isotope Reaction (HFIR) at ORNL using neutron diffraction. On the HFIR beam line HB-2, a prototype PbTe module, shown in Figure 9, was used for strain mapping. Preliminary results are shown in Figure 10, illustrating the utility of the technique.

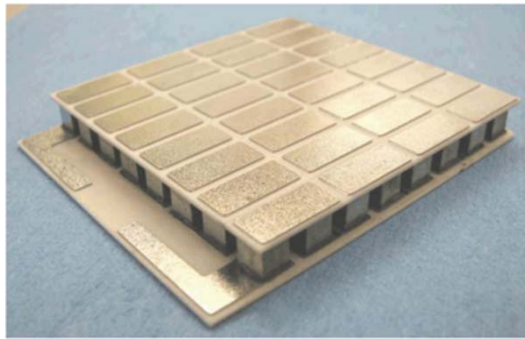


Figure 9. Photo of a prototype PbTe module.

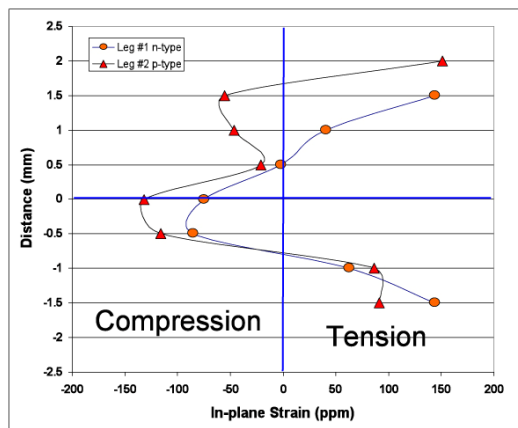


Figure 10. Preliminary neutron strain mapping of a pair of p-type and n-type legs in a PbTe module.

One class of thermoelectric materials that shows great promise is the filled-skutterudites. The first such material was $\text{La}(\text{Fe},\text{Co})_4\text{Sb}_{12}$. More recently, higher performance was obtained via replacement of La by mixtures of rare earth elements, or rare earth elements plus Ba, particularly in n-type material. These materials derive their performance from the combination of low lattice thermal conductivity due to the rare earth filler and a favorable electronic structure that has multiple heavy conduction bands. Researchers at ORNL performed electronic structure calculations that indicated that the chemical range where high performance can be achieved is larger than previously thought and identified alkaline earth filled skutterudites containing Ni and Fe instead of Co as promising. Transport calculations verified this is in fact the case and made quantitative predictions for the thermopower, which were favorable for both n and p types. ORNL also performed first principles calculations of the vibrational densities of states for these materials in order to assess the prospects for obtaining low thermal conductivity. Figure 11 shows the result for Sr.

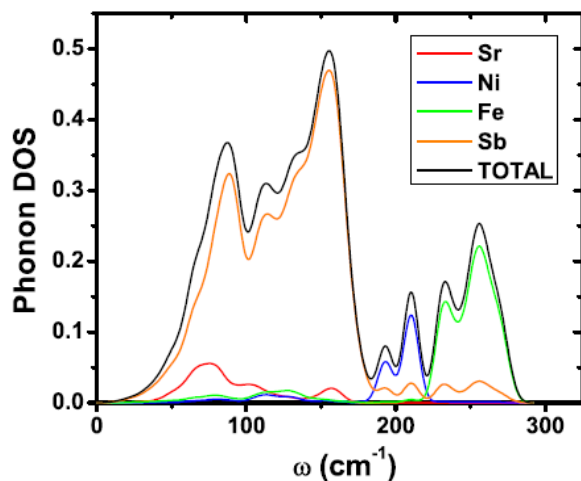


Figure 11: Vibrational density of states for $\text{SrFe}_3\text{NiSb}_{12}$ from first principles calculations.

Carol L. Schutte
 Team Leader, Advanced Materials Technologies
 Office of Vehicle Technologies
 Energy Efficiency and Renewable Energy

Jerry L. Gibbs
 Technology Manager
 Office of Vehicle Technologies
 Energy Efficiency and Renewable Energy

Project 18516 - Materials for Electric and Hybrid Drive Systems

Agreement 16307 - Modeling/Testing of Environmental Effects on Automotive PE Devices

A. A. Wereszczak, H. -T. Lin, and P. J. Ritt

Ceramic Science and Technology Group

Oak Ridge National Laboratory

P.O. Box 2008, MS 6068, Bldg. 4515

Oak Ridge, TN 37831-6068

(865) 576-1169; fax: (865) 574-6098; e-mail: wereszczakaa@ornl.gov

DOE Technology Manager: Jerry L. Gibbs

(202) 586-1182; fax: (202) 586-1600; e-mail: jerry.gibbs@ee.doe.gov

ORNL Technical Advisor: D. Ray Johnson

(865) 576-6832; fax: (865) 574-6098; e-mail: johnsondr@ornl.gov

Contractor: Oak Ridge National Laboratory, Oak Ridge, Tennessee

Prime Contract No.: DE-AC05-00OR22725

Objectives

- Understand the complex relationship between environment (e.g., temperature, stress, etc.) and the performance and reliability of the material constituents within automotive power electronic devices (PEDs)
- Provide supportive systems through materials characterization and modeling.

Approach

- Complete evaluation of the strength of (brittle) semiconductor chips and apply Weibull distribution statistics.
- Complete apparent thermal diffusivity and apparent thermal expansion evaluations of copper bonded substrates.

Accomplishments

- Completed mechanical evaluation of silicon and silicon carbide semiconductor chips with respect to failure initiation occurring at edges and Weibull effective lengths.
- Completed evaluation of apparent thermal diffusivity and apparent thermal expansion of copper bonded aluminum oxide and aluminum nitride substrates.

Future Direction

- Project ended at the end of FY10

Introduction

Research performed under the FreedomCAR and Vehicle Technologies Program's Vehicle Systems subprogram seeks to lessen technical and cost barriers and enable development that will benefit advanced vehicles such hybrid electric vehicles. Weight, volume, and cost targets for the power electronics and electrical machines subsystems of the traction drive system in those

vehicles must be attained to achieve success. Research areas include more powerful novel traction motor designs, more efficient and higher temperature-capable inverter technologies, reduced footprint and weight of converters, more effective thermal control and packaging technologies, and motor/inverter concepts.

Many, if not most, technical barriers are directly linked to the contemporary material limitations of

subcomponents found within devices that comprise inverters, converters, and motors. For automotive power electronic devices (PEDs), contemporary material limitations include insufficient temperature capability, excessive thermal insulation, and excessive electrical insulation (i.e., generates excessive heat).

This project's objectives are to understand the complex relationship between environment (e.g., temperature, stress, etc.) and automotive power electronic PED performance through materials characterization and modeling, and identify alternative material constituents and architectures that will improve their reliability and enable their operation at higher temperatures without compromise to electronic function.

Results

The description of this year's progress is divided into two sections and also includes the conclusion of this project. They are completion of the mechanical evaluation of silicon and silicon carbide semiconductors, and the evaluations of the thermal diffusivity and expansion behaviors of copper bonded substrates used in electronic components. Both of these efforts directly or indirectly support this project's primary two objectives of understanding reliability as a function of environment (e.g., temperature, stress) and the search for improved PED architectures that will improve thermal management.

Mechanical Evaluations of Semiconductor Chips

Silicon (Si) and silicon carbide (SiC) chips in power electronic devices are subjected to thermal gradients, have coefficient of thermal expansion mismatches with the constituents they are attached to, and therefore are subjected to consequential thermomechanical tensile stresses during operation that can initiate their fracture.

Being they are brittle like glasses and ceramics, it stands to reason that their tensile failure strength is statistical in nature. Several studies have pursued the mechanical testing of silicon chips and interpreted the measured failure stress in this manner.

Wereszczak *et al.* [1] conducted 4-pt bend tests using different test specimen dimensions and statistically examined the strength of etched and polished surfaces. They found that edge-slicing quality could be quite limiting of the overall failure stress but that surface-type flaws, and hybrids of edge- and sur-

face-type flaws could be operative too. A convenient manner to portray their competition is shown in Fig. 1. Extrinsic flaws (e.g., surface pitting, scratches, edge-chipping) tend to limit the mechanical strength of chips whereas intrinsic flaws (volume- or bulk-based) are very rare. Another class of brittle materials that is like semiconductor chips is glass.

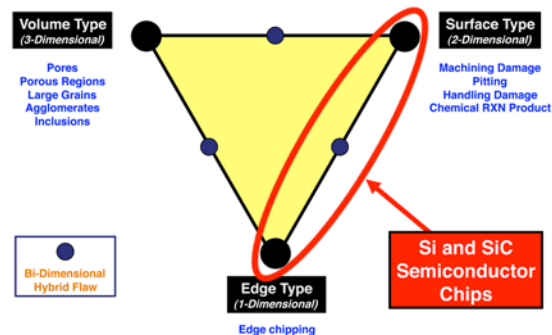


Figure 1. Potential strength-limiting flaw types in semiconductor chips.

Cotterell *et al.* [2] examined the statistical failure stress using 4-pt-bend and ring-on-ring (i.e., axisymmetric 4-pt-bend) testing. While Cotterell's work was systematic, concern over those results arises from the relatively large spans that were used relative to the chip thickness, and the belief that nonlinear elastic effects were likely introduced as a consequence. These were not accounted for and inaccuracy in the results was likely caused. Such issues need to be considered in flexure testing and indeed are considered in standardized tests for uniaxial and biaxial flexure testing [3-4].

Colleti *et al.* [5] considered the competition of edge- and surface-based strength limiting but used ring-on-ring testing to focus study on the latter.

Zhao *et al.* [6] used 3-pt-bending and ball-on-ring (i.e., axisymmetric 3-pt bending) to study the convolution of edge- and surface-type flaws that limit failure stress. A problem with ball-on-ring testing is its generated effective area (i.e., sampled area under tension) is quite small and uncertainty can therefore be produced when comparing the failure strength of different surface conditions. Additionally, Zhao *et al.* used a 3-parameter Weibull distribution to fit the failure stress data; while a "good" fit was perhaps produced, disadvantages of using the 3-parameter fit are it can mask the presence (and

problems) of exclusive flaw populations (an indicator of inhomogeneously distributed flaw populations) [7-8], and it does not lend itself easily to strength-size-scaling analysis [9] that is routinely used with 2-parameter Weibull distributions [10] when designing brittle material components and estimating their mechanical reliability.

The present study had several objectives. First, it sought to measure and compare failure stresses in Si and SiC semiconductor chips that had the same physical size and mechanically tested in the same manner. Second, owing to the author's past experience with edges limiting strength in sliced Si semiconductors [1], we sought to use mechanical test methods that would promote failure initiation at the edges. Third, the authors have performed an extensive amount of mechanical testing involving edge characterization of glass tiles [11]. Owing to the fact that glass tiles have similarity to semiconductor chips (i.e., very smooth surfaces with cut, chamfered, or sliced edges or the same flaw types of interest in Fig. 1), and that the authors have found anticlasic bend testing to be an effective method to measure failure stresses with glass tiles, anticlasic bending of Si and SiC chips was pursued to judge its applicability.

Silicon {111} and silicon carbide (n-type 4H {0001}) chips were acquired from commercial sources. Dimensions were 10 x 10 x 0.25 mm. One side of the Si chips was lapped and the other was polished. Both sides of the SiC chips were polished. None of the chips of either material had metallization on them. Neither specific slicing method nor procedure was prescribed for either material. Record of the orientation of all chips (or specimens) was kept through the testing history. The primary flat of the silicon wafer was parallel to <112> and that for the silicon carbide was parallel to <112̄0>.

Flexure testing of the entire (square) chips was conducted using uniaxial flexure (three-point-bending) and biaxial flexure (anticlastic bending).

For 3-pt bending, a 5.0-mm span was chosen to sustain classical Eulerian beam bending with respect to the 0.25-mm thick chips. A schematic of the test configuration is shown in Fig. 2. 4-pt bending typically has an advantage over 3-pt-bending in that more of a specimen is desirably subjected to a uniform tensile stress; however, if test specimen geometries and fixtures are small (such as they are in this study), then it can be experimentally difficult to promote, sustain, and validate alignment with the 4-

pt configuration. Because of that, the authors pursued 3-pt-bending because maintaining alignment is experimentally easy to achieve, and that advantage was deemed to be more important than the disadvantage of it sampling less material to a tensile stress.

The failure stress (S_{3pt}) for 3-pt-bending is represented by

$$S_{3pt} = \phi \frac{3PL}{2bt^2} \tag{1}$$

where P is failure load, L is the fixture span (5.0 mm), b is the base (10.0 mm), and t is thickness (0.25 mm), and ϕ (=1.02) is a correction factor that takes into account the relatively large base to thickness ratio for the chip to distinguish it from a beam [12]. The outer-fiber tensile stress profile across the span is shown in Fig. 3.

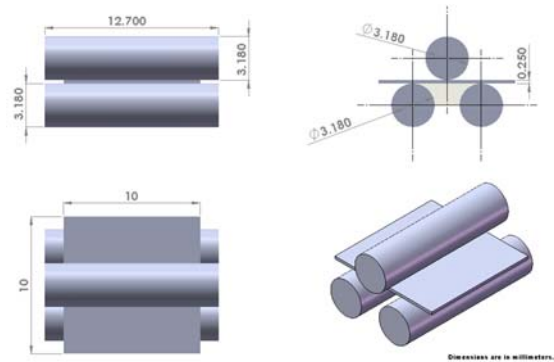


Figure 2. Schematic diagram of the 3-pt-bend test setup. The support span was 5.0 mm.

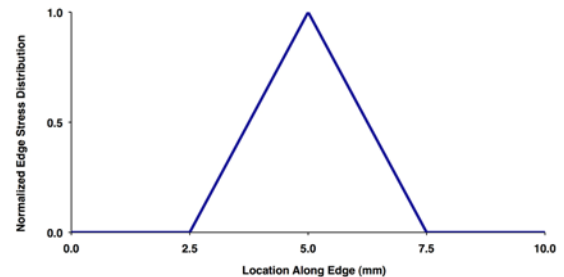


Figure 3. Outer-fiber tensile stress distribution for the 3-pt-bend fixture.

The anticlastic (AC) biaxial flexure specimen was first used by Zamrik *et al.* [13-14] to study crack growth behavior under biaxial fatigue conditions.

The advantage of the anticlastic bend test is all eight edges are subjected to identical sinusoidal stress distribution so the tensile failure stress will be sensitive to the chip's edge-state quality, crystallographic orientation, and surface condition too. Four balls, two on each side of the chip or plate, aligned along counter-opposing diagonals are compressed to produce the anticlastic bending state. This is an example where a schematic (see Fig. 4) is much more effective to describe the manner of loading than a narrative is.

A finite element analysis (FEA) model was constructed to examine the stress state of the 10 x 10 x 0.25 mm chips subjected to anticlastic bending. The first principal (equivalent) stress profile is shown in Fig. 5 for an applied compressive load of 100 N. High radial tensile stresses around the four Hertzian loading positions are not the source of failure initiation if the surface condition of the plate is of high surface finish or has minimally sized flaws and if there are edge-located flaws of relatively large size or severity. This scenario is why AC bending works well with glass and also why it was considered for use in this study with semiconductor chips.

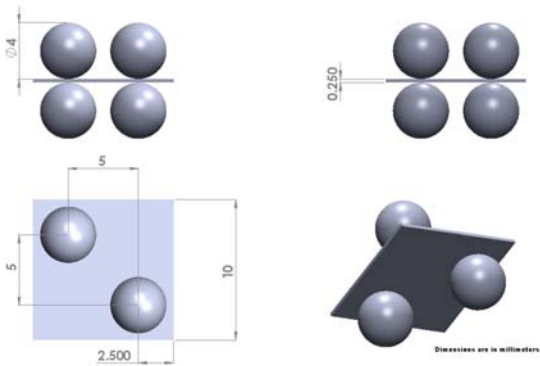


Figure 4. Schematic diagram of the anticlastic bend test setup.

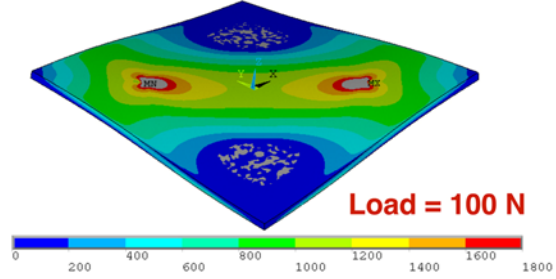


Figure 5. First principal (or equivalent) stress profile of an anticlastically bent silicon chip.

The stress profiles along two of the edges of an anticlastically bent specimen are shown in Fig. 6, and the relationship between compressive force and maximum tensile stress, as determined by FEA, is shown in Fig. 7. The relationship shown in Fig. 7 was used to determine failure stress in the anticlastic bend tests. The sinusoidally produced stress profile along each edge is apparent, and all 8 of the primary edges are subjected to this. If the stress-limiting flaws at an edge are larger in size than those flaws on the surface of the plate, then failure initiation will commence from an edge. This is accomplished within a single specimen. Additionally, this AC bend method is sensitive to the chip's edge-state quality, crystallographic orientation, and surface condition too. Many specimens would be needed for a uniaxial flexure (i.e., 3-pt or 4-pt bending) test matrix to equivalently examine all these effects, and "surface-based" test methods, such as ball-on-ring and ring-on-ring would not be effective at concurrently sampling edge-effects like the AC bend method.

To examine strength-size-scaling or tensile-failure-size-scaling based on Weibull effective length, the probability of failure (P_f) can be represented by

$$P_f = 1 - \exp \left[- \left(\frac{\sigma_{max}}{\sigma_{0L}} \right)^m L_e \right] \quad (2)$$

where σ_{max} is the maximum applied tensile stress along the edges, σ_{0L} is the scale parameter due to edge-type flaws, m is the Weibull modulus, and L_e is the effective length. The effective length is described as

$$L_e = \int \left(\frac{\sigma(x)}{\sigma_{\max}} \right)^m dx \quad (3)$$

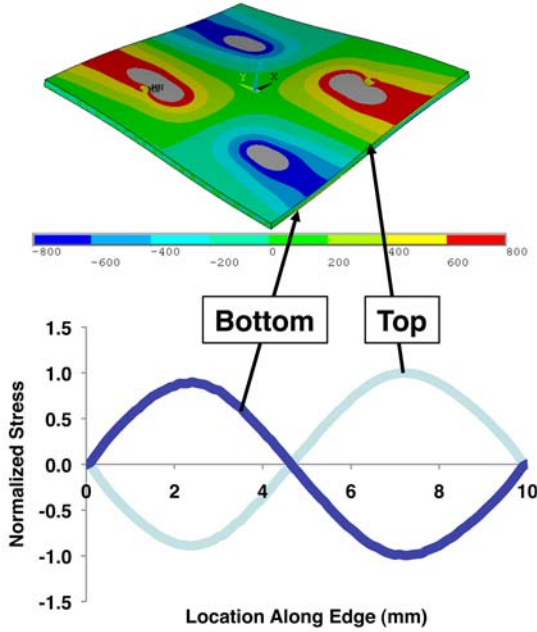


Figure 6. Stress profile along the edges of an anticlastically bent chip.

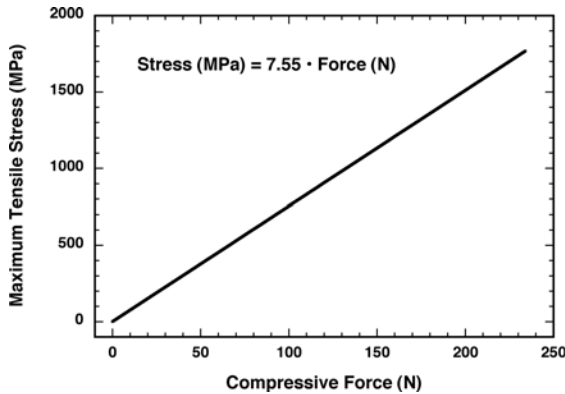


Figure 7. Maximum tensile stress as a function of compressive for the anticlastic bend specimen whose loading is shown in Fig. 4.

The effective length can be used for strength scaling whereby the strength of one component (or specimen in this case) can be predicted from that of

another with different stress distribution and edge length by equating their probabilities of failure according to

$$\left(\frac{\sigma_{f1}}{\sigma_{f2}} \right) = \left(\frac{L_{e2}}{L_{e1}} \right)^{\frac{1}{m}} \quad (4)$$

In order to evaluate the effective length using Eq. 3 for the AC bent chip, the stress distributions along the edges of the chip must be described as a function of position, x . This stress profile is illustrated in Fig. 6. Hence, Eq. 3 for the AC flexure specimen simplifies to

$$L_{e,AC} = \frac{4}{\sigma_{\max}^m} \left[\int_0^{x1} \sigma_{top_edge}^m(x) dx \right] + \frac{4}{\sigma_{\max}^m} \left[\int_0^{x2} \sigma_{bottom_edge}^m(x) dx \right] \quad (5)$$

Unlike the AC flexure specimen, the 3-point bend test induces tensile stresses along only two edges. The effective length formula for a 3-point bend specimen is associated with the stress profile in Fig. 3 is given by

$$L_{e,3pt} = \frac{2L}{m+1} \quad (6)$$

The effective lengths are a function of Weibull modulus and the profiles for the anticlastic and 3-pt bend specimens that are shown in Fig. 8. This figure shows that, for a given Weibull modulus, the anticlastic bend specimen subjects much more edge length to a tensile stress than the 3-pt bend specimen does.

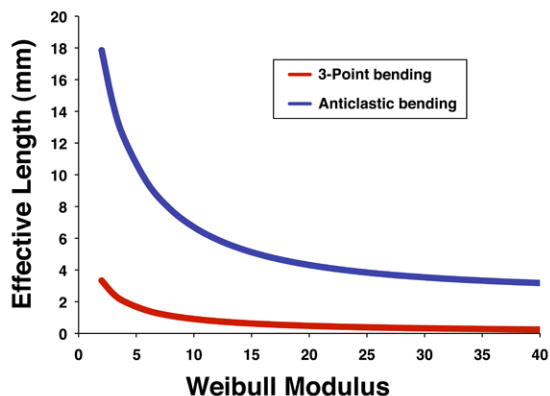


Figure 8. Weibull effective length as a function of Weibull modulus for the two bend test configurations used in this study.

All 3-pt and anticlastic bend tests were done using an electromechanical test frame and a crosshead displacement rate of 0.5 mm/min. At least 14 specimens were tested for each condition and their Weibull failure stress distributions were determined using commercial statistical software which uses maximum likelihood estimation to determine the (2-parameter) Weibull modulus and characteristic strength of each set. 95% confidence ratio rings were determined for each set and were used to compare data sets.

Optical microscopy was used to identify the failure locations of all the specimens. Scanning electron microscopy was used with a select few specimens to examine the edge and surface qualities of the chips.

The 3-pt strength distributions for the Si chips are shown in Fig. 9. There were two surface conditions for the Si (lapped and polished) and two crystallographically aligned orientations with the chip's edges ($\langle 112 \rangle$ and $\langle 110 \rangle$ directions), so there were four combinations tested with the 3-pt bending. The $\langle 112 \rangle$ lapped set had the lowest characteristic strength among the four while the $\langle 112 \rangle$ polished set exhibited the least amount of scatter (as represented by a higher Weibull modulus). The characteristic strengths of both polished orientations were equivalent.

Optical microscopy showed that failure initiation with the 3-pt bend specimens occurred on the surfaces (and not the edges) of the lapped Si chips but that initiation occurred at edges of the polished Si chips.

Examples of chipping along edges on the lapped and polished surfaces are illustrated in Figs. 10-11. Edge chipping on the two crystallographic directions (Fig. 10) was not noticeably different and that is probably why their characteristic strengths were equivalent. However, the edge chipping on the edges bordering the lapped surface was much more severe (Fig. 11); however, the surface-located flaws inherent to the lapped surface were still more dominant in limiting strength than these severe edge-type flaws.

When a component is mechanically confined and concurrently subjected to a thermal gradient through its thickness (i.e., such as these chips during service), then higher tensile stresses will occur on the colder side. For an attached chip subjected to cooling, the lapped side of the chip will be that colder side. How may the results in Fig. 8 be interpreted in context with this? If an attached chip is subjected to a uniform biaxial tensile stress, then (Mode I) failure initiation is more likely to occur perpendicular to the weakest direction $\langle 112 \rangle$ and away from the edge. From a design perspective, if a rectangular chip could be used instead of a square chip (but with the same area or edge length), then a rectangular chip whose longer axis is parallel to $\langle 110 \rangle$ will have a higher probability of survival (all other things being equal).

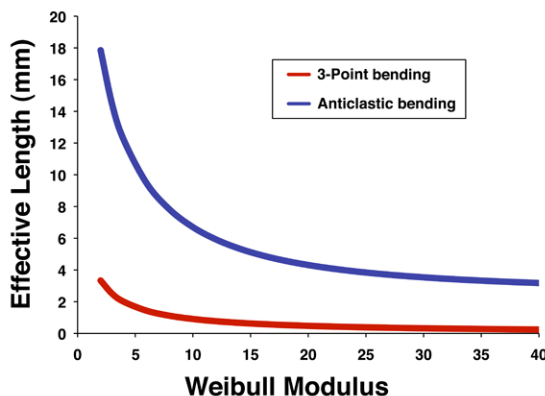


Figure 9. A Weibull strength distribution for the four combinations of 3-pt-bend test sets on the Si chips. 95% confidence ratio rings shown.

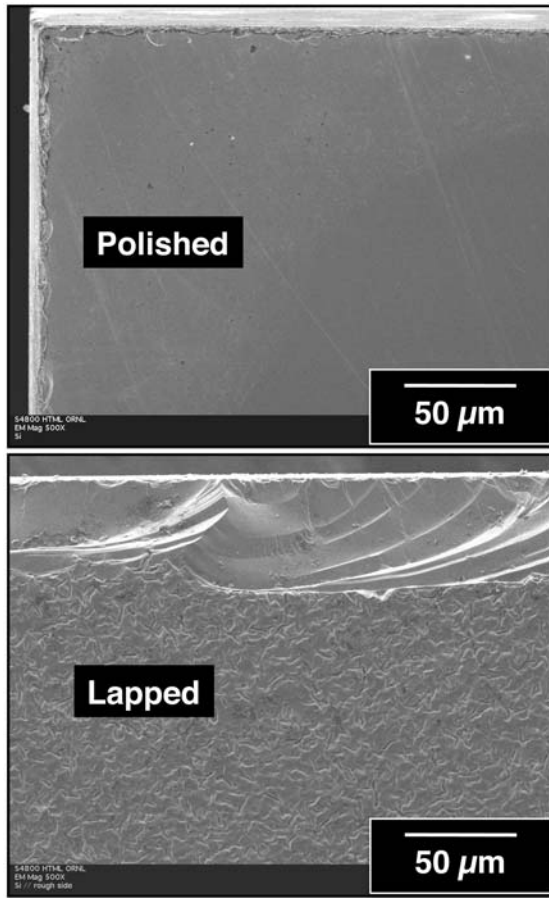


Figure 10. Representative edge chipping and comparison of polished and lapped surfaces on a Si chip.

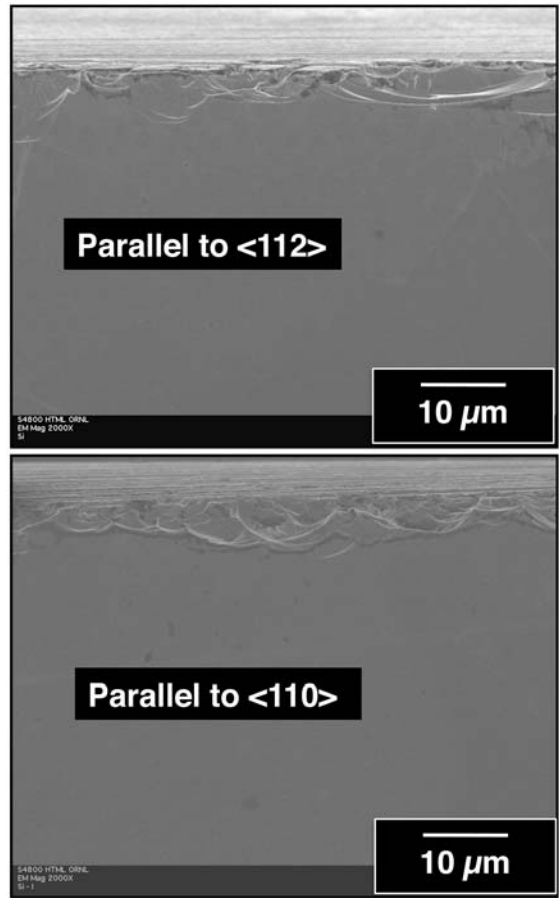


Figure 11. Representative edge chipping and comparison of polished surfaces on edges parallel to $\langle 112 \rangle$ and $\langle 110 \rangle$ directions on a Si chip.

The 3-pt failure stress distributions for the two SiC chips are shown in Fig. 12. The two surfaces of the SiC chips were both polished so only crystallographic orientation effects were examined. While the characteristic strengths of all the SiC chips were approximately an order of magnitude larger than those for the Si chips, the characteristic strength of the SiC chips tensile stressed perpendicular to $\langle 112 \rangle$ were stronger than those stressed parallel to that direction. Additionally, the failure initiation of all SiC chips occurred at their edges. This shows that surface polishing removes (or minimizes the effects of) surface-type strength-limiting flaws and that translates into failure initiation at the edges.

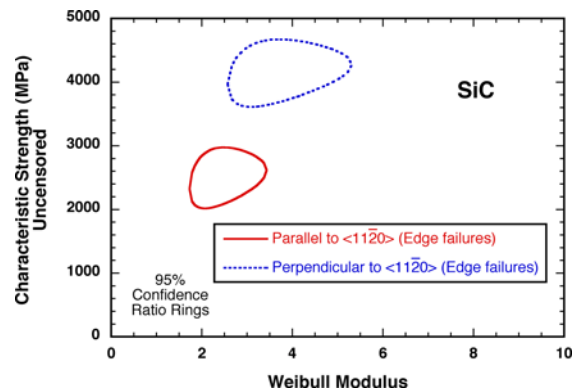


Figure 12. A Weibull strength distribution for the two combinations of 3-pt-bend test sets on the SiC chips (both sides were polished). 95% confidence ratio rings shown.

The significantly higher characteristic strength of the SiC chips compared to the Si chips is likely a consequence of the difference in the quality of the edge slicing. Examples of edge chipping on the SiC chips are shown in Fig. 13. The chipping is much smaller in stature than the chipping in the Si chips (compare with Figs 10-11). Given these differences in edge quality, one could conclude that the differences in characteristic strength are due to differences in these extrinsic type of strength-limiting flaws and not differences in intrinsic or bulk material differences.

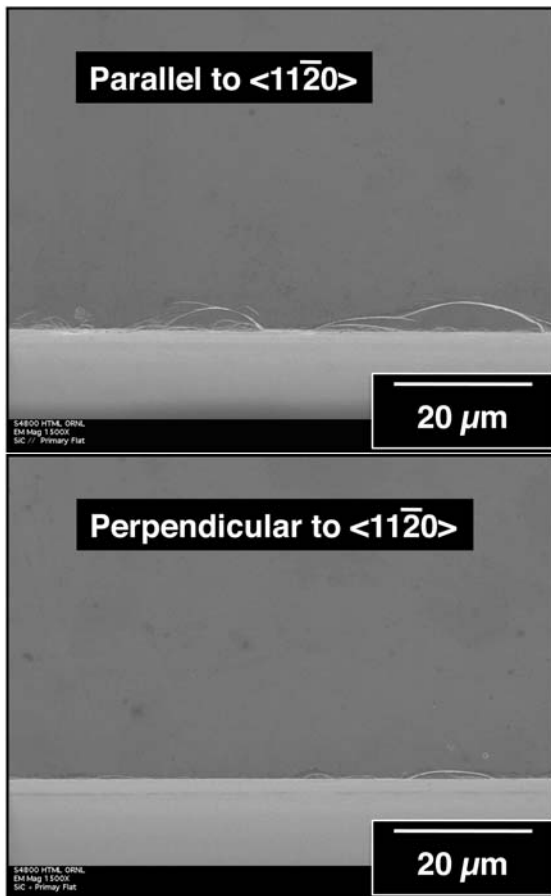


Figure 13. Representative edge chipping and comparison of polished surfaces on edges parallel and perpendicular to $\langle 11\bar{2}0 \rangle$ direction on a SiC chip.

The anticlastic bending characteristic strength of the SiC chips was almost an order of magnitude larger than that for the Si chips as shown in Fig. 14. Failure initiation with the SiC chips occurred at an edge whereas failure initiation with the Si chips oc-

curred away from the edge. In fact, optical fractography showed that failure initiation with the Si chips routinely occurred on the lapped surface directly opposite (or under) where one of the two balls was making contact with the polished surface.

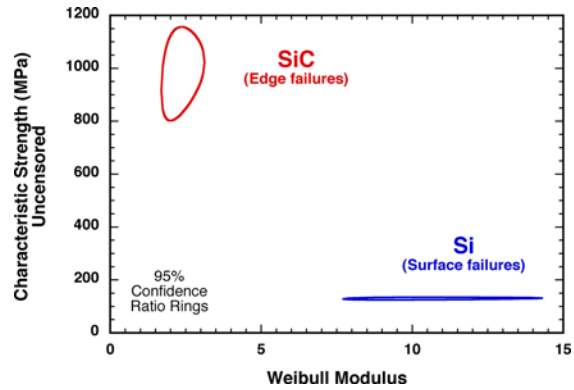


Figure 14. Weibull strength distributions for anticlastic bend test sets. 95% confidence ratio rings shown.

Anticlastic bending tensile stresses operate over greater total lengths of chip edges than 3-point bending does, and because of that, its specimens fail at lower failure stresses when surface type-flaws are not operative (i.e., in the case of the SiC chips). The anticlastic failure stress for SiC chips was approximately one-third that of the 3-pt bend characteristic stresses. For more confident design and mechanical reliability analysis, it is always advantageous to have failure stress data from test coupons that sample (or tensile stress) as much material as possible. Therefore, anticlastic bending can be an effective test method for evaluating edge failure stress in semiconductor chips if surface-type strength-limiting flaws are not dominant.

Apparent Thermal Diffusivity and Expansions

Direct copper bonded (DCB) ceramic substrates from Curamik were evaluated. Apparent thermal diffusivity was studied as a function of copper cladding and the ceramic thicknesses. An illustration of the DCB cross-section is shown in Fig. 15. The ceramic was either aluminum oxide (Al_2O_3) or aluminum nitride (AlN). Six DCB substrates are considered and their basic characteristics are shown in Table. I.



Figure 15. Polished cross-section of a DBC with 1.02-mm thick Al_2O_3 sandwiched by 0.30-mm thick copper cladding.

Table I. Dimensions of evaluated DBCs.

	Manuf Reported Ceramic Thickness (in)	Manuf Reported Copper Thickness (in)	Manuf Reported Total Thickness (in)	Manuf Reported Ceramic Thickness (mm)	Manuf Reported Copper Thickness (mm)	Manuf Reported Total Thickness (mm)
DBC Ceramic						
Al_2O_3	0.015	0.008	0.031	0.38	0.20	0.79
Al_2O_3	0.040	0.008	0.056	1.02	0.20	1.42
Al_2O_3	0.040	0.012	0.064	1.02	0.30	1.63
AlN	0.025	0.008	0.041	0.64	0.20	1.04
AlN	0.025	0.012	0.049	0.64	0.30	1.24
AlN	0.040	0.012	0.064	1.02	0.30	1.63

Thermal diffusivity samples with a 12.7-mm diameter were core-drilled from each of the six substrates shown in Table 1. To counteract the reflective nature of the copper, a graphite coating was applied to the underside of each sample, or the side that would be subjected to the xenon energy source. The graphite coating was a spray coating and applied in a fumigated hood. The six samples were loaded consecutively into a 24-capacity, aluminized sample holder from Anter. Three laser pulse shots were taken on each sample at 20 and 200°C. An illustration of the repeatability of the thermal diffusivity responses is shown in Fig. 16. Spring-loaded detector pins on the top of the sample determined the change in voltage through the sample during the shot. Once three shots have been fired on a sample, the sample holder rotated automatically to the next sample.

Thermal diffusivity differences were observed among the six DBCs. A comparison of the tempera-

ture transients for each at 20 and 200°C are shown in Figs. 17-18, respectively. The longer the time it takes to get to maximum temperature at 200°C the lower the apparent thermal diffusivity.

The transient temperature data were analyzed using the classical Parker thermal diffusivity (α) equation

$$\alpha = \frac{0.1388d^2}{t_{1/2}} \tag{7}$$

where d is the sample thickness, and $t_{1/2}$ is the one-half time for the sample to reach a maximum voltage after the laser shot. The average thermal diffusivities for each of the six DBCs are summarized in Table II. An increase in temperature from 20 to 200°C causes the thermal diffusivity in all to go down in temperature.

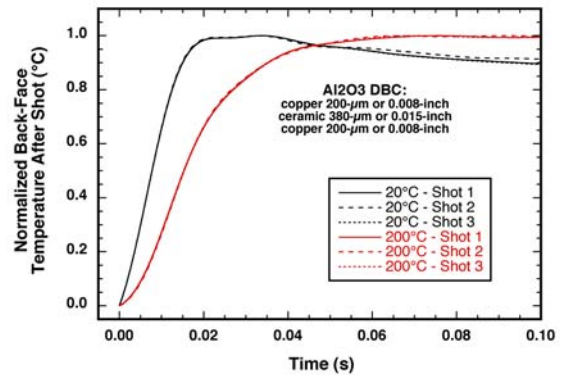


Figure 16. The thermal diffusivity responses in all six samples were repeatable. An example of this is shown for one of the six samples at 20 and 200°C.

The thermal diffusivity can significantly decrease in aluminum oxide and aluminum nitride DBCs between 20 and 200°C. The use of a temperature-independent value of thermal diffusivity will produce a predicted thermal transfer that is non-conservative. Therefore, a temperature-dependent thermal diffusivity of DBCs should be used in modeling when considering thermal management of power electronic devices containing them.

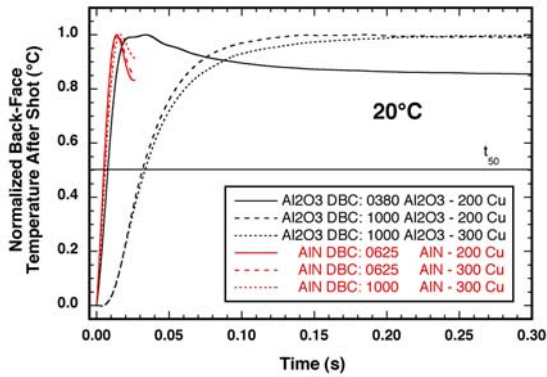


Figure 17. Thermal diffusivity response of DBCs at 20°C.

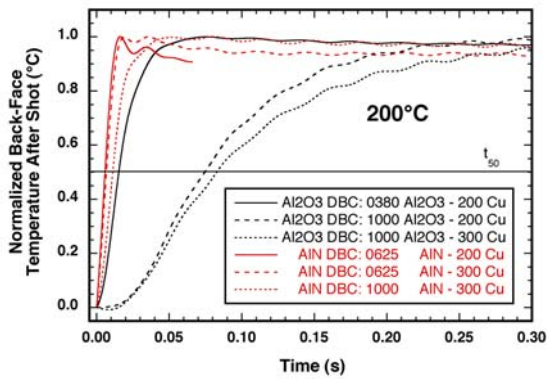


Figure 18. Thermal diffusivity response of DBCs at 200°C.

Table II. Thermal diffusivity results of evaluated DBCs.

DBC Ceramic	Manuf Reported Ceramic Thickness (mm)	Manuf Reported Copper Thickness (mm)	Manuf Reported Total Thickness (mm)	Temperature (°C)	Measured Total Thickness (mm)	Thermal Diffusivity Average (cm ² /s)
Al ₂ O ₃	0.38	0.20	0.79	20	0.779	0.1089
				200		0.0549
Al ₂ O ₃	1.02	0.20	1.42	20	1.591	0.1113
				200		0.0469
Al ₂ O ₃	1.02	0.30	1.63	20	1.551	0.0998
				200		0.0403
AlN	0.64	0.20	1.04	20	1.012	0.2843
				200		0.2442
AlN	0.64	0.30	1.24	20	1.209	0.3852
				200		0.2974
AlN	1.02	0.30	1.63	20	1.564	0.5680
				200		0.3050

The CTE of the DBCs listed in Table I was measured. 12.7x3.0mm strips were harvested from

each of the six DBCs and heated in a dual-rod dilatometry up to 350°C. A sapphire standard was used. The measured responses are shown in Fig. 19.

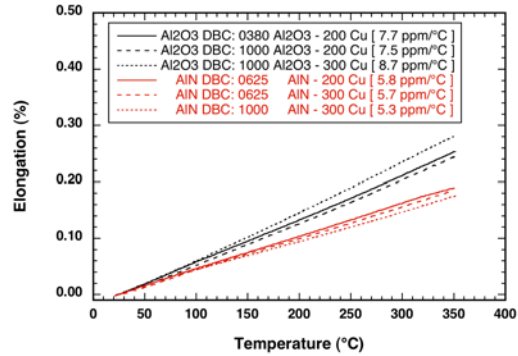


Figure 19. Elongations and average coefficients of thermal expansions of the investigated DBCs. ppm/°C = 10⁻⁶/°C.

The CTEs shown in the legend of Fig. 19 for the DBCs are equivalent to those of monolithic aluminum oxide and aluminum nitride. This means that the presence of the attached copper, with its higher CTE (~ 17 ppm/°C), contributes little, if anything, the elongation response of the entire DBC.

Conclusions

Extrinsic strength-limiting flaws located at their edges and on lapped surfaces limit tensile stress tolerance of Si and SiC chips. And that tensile stress tolerance exhibits size scaling. Namely, failure stress is lower with longer (effective) edge lengths and with larger (effective) areas. This is consistent with the established utilization of censored Weibull tensile strength distributions for the design and mechanical reliability estimation of brittle material components.

Anticlastic bending tensile stresses much greater lengths of chip edges than 3-point bending does, and because of that, this specimens fails at lower failure stress when surface type-flaws are not operative. For more confident design and mechanical reliability analysis, it is always advantageous to have failure stress data from test coupons that sample (or tensile stress) as much material as possible. Therefore, anticlastic bending can be an effective test method for evaluating edge failure stress in semiconductor chips if surface-type strength-limiting flaws are not dominant.

Edge-strength anisotropy was observed with both the Si and SiC. This suggests that if non-square chips are used (e.g., rectangular chips) that there is an advantage to having the longer axis being parallel with the stronger direction.

Surface-strength anisotropy was observed with the Si because one side was lapped and the other polished. The lapped side is weaker. Others have described this effect too. For conservative design or mechanical reliability estimation, the use of the strength distribution measured with the (weaker) lapped should be used.

The SiC chips failed at higher tensile stresses than Si chips; however, that difference may be a ramification of edge slicing differences and not intrinsic material differences.

The thermal diffusivity can significantly decrease in aluminum oxide and aluminum nitride DBCs between 20 and 200°C. The use of a temperature-independent value of thermal diffusivity will produce a predict thermal transfer that is non-conservative.

The coefficient of thermal expansion for a DBC is equivalent to that of monolithic aluminum oxide and aluminum nitride. This means that the presence of the attached copper contributes little, if anything, the elongation response of the entire DBC. Therefore, it is apparent that the thermal expansion of a DBC can be predicted by just using the coefficient of thermal expansion of the ceramic that is part of the DBC itself.

References

- [1] A. A. Wereszczak, A. S. Barnes, and K. Breder, "Probabilistic Strength of {111} n-Type Silicon," *Journal of Materials Science: Materials in Electronics*, Vol. 11, pp. 291-303, 2000.
- [2] B. Cotterell, Z. Chen, J. -B. Han, and N. -X. Tan, "The Strength of the Silicon Die in Flip-Chip Assemblies," *Journal of Electronic Packaging*, Vol. 125, pp. 114-119, March, 2003.
- [3] Standard Test Method for Flexural Strength of Advanced Ceramics at Ambient Temperatures, ASTM C1161, Vol. 15.01, ASTM International, West Conshohocken, PA, 2008.
- [4] Standard Test Method for Monotonic Equibiaxial Flexure Strength of Advanced Ceramics at Ambient Temperature, ASTM C1499, Vol. 15.01, ASTM International, West Conshohocken, PA, 2008.
- [5] G. Coletti, C. J. J. Tool, and L. J. Geerligs, "Mechanical Strength of Silicon Wafers and Its Modeling," Presented at the 15th Workshop on Crystalline Silicon Solar Cells & Modules: Materials and Processes, Vail, CO, Aug. 7-12, 2005.
- [6] J. -H. Zhao, J. Tellkamp, V. Gupta, and D. Edwards, "Experimental Evaluations of the Strength of Silicon Die by 3-Point-Bend Versus Ball-on-Ring Tests," 2008 11th IEEE Intersociety Conference on Thermal and Thermomechanical Phenomena in Electronic Systems, I-THERM, pp. 687-694, 2008.
- [7] C. A. Johnson, "Fracture Statistics in Design and Application," GE Report No. 79CRD212, General Electric, Schenectady, NY, 1979.
- [8] A. A. Wereszczak and T. P. Kirkland, "Exclusivity of Strength-Limiting Extrinsic Surface and Hybrid Flaws," *Ceramic Engineering Science Proceedings*, Vol. 27, No. 2, pp. 593-601, 2006.
- [9] Standard Practice for Size Scaling of Tensile Strengths Using Weibull Statistics for Advanced Ceramics, ASTM C1683, Vol. 15.01, ASTM International, West Conshohocken, PA, 2008.
- [10] Standard Practice for Reporting Uniaxial Strength Data and Estimating Weibull Distribution Parameters for Advanced Ceramics, ASTM C1239, Vol. 15.01, ASTM International, West Conshohocken, PA, 2008.
- [11] A. A. Wereszczak, T. P. Kirkland, K. T. Strong, Jr., and T. J. Holmquist ORNL/TM-2009/234 Report: "ORNL Quasi-Static Mechanical Characterization and Analysis: FY09 Annual Report to TARDEC," December, 2009.
- [12] F. I. Baratta, "When is a Beam a Plate?" *Journal of the American Ceramic Society*, Vol. 65, No. 5, p. C86, 1981.
- [13] S. Y. Zamrik, and M. Shabara, "The Effect of Stress Ratio on Fatigue Crack Growth in a Biaxial stress Field," *ASME Transactions, Journal of Pressure Vessel Technology*, Vol 99, Series J, No. 1, p. 137-143 (1977).
- [14] S. Y. Zamrik, and D. C. Davis, "A Novel Test Method and Apparatus for Multiaxial Fatigue Studies," *Advances in Multiaxial Fatigue*, ASTM STP 1191, D. L. McDowell and R. Ellis, Eds., American Society for Testing and Materials, pp. 204-219, 1993.

Publications

A. A. Wereszczak, O. M. Jadaan, and T. P. Kirkland, "Edges and Failure Stress of Si and SiC Semiconductor Chips," in press, proceedings of High Temperature Electronics (HiTEC 2010), May 11-13, 2010, Albuquerque, NM.

Agreement 16305 - Solder Joint of High Performance Power Electronics: Materials-by-Design

G. Muralidharan and Andrew Kercher
Materials Science and Technology Division
(865)574-428; fax: (865) 574-4357; e-mail: muralidhargn@ornl.gov

Burak Ozpineci
Engineering Science and Technology Division
(865) 241-4329; fax: (865) 574-9329; e-mail: ozpinecib@ornl.gov

Scott Leslie
Powerex Inc
(724) 925-4482; fax: (724) 925-4468; email: sleslie@pwr.com

DOE Technology Manager: Jerry L. Gibbs
(202) 586-1182; fax: (202) 586-1600; e-mail: jerry.gibbs@ee.doe.gov
ORNL Technical Advisor: D. Ray Johnson
(865) 574-4556; fax: (865) 241-0411; e-mail: stintondp@ornl.gov

Contractor: Oak Ridge National Laboratory, Oak Ridge, Tennessee
Prime Contract No.: DE-AC05-00OR22725

Objectives

- Evaluate the reliability of high temperature solders for use in power electronic packages subject to thermal cycling
- Identify material property characteristics that would impact long-term reliability of solder joints to enable materials-by-design approach

Approach

- Evaluate the degradation in solder joint properties due to thermal cycling and steady state aging
- Evaluate the effect of solder joint compositions and hence the mechanical and physical properties on solder joint property degradation.

Accomplishments

- Solder joints consisting of one Au-Sn and one Sn-Ag solder capable of 200°C operation were fabricated between Si dies or SiC dies and DBC substrates
- Thermal cycling between 200°C and 5°C have been carried out in representative joints of Au-Sn and Sn-Ag up to about 3000 cycles and damage evolution has been followed using high resolution X-ray radiography
- Finite element models have been developed to study stress evolution within solder joints
- Data analysis procedures are being developed to understand thermal measurements on solder joints.

Future Direction

- Correlations will be made between damage development and finite element models
 - Use of thermal properties as damage accumulation models will be evaluated
-

Introduction

Development of next generation hybrid and electric propulsion vehicles depend on the availability of high efficiency, lower cost, lower weight and lower volume, power electronic components and subsystems. These future power electronic systems need to operate reliably for 15 years at junction temperatures of 200°C in contrast to current maximum junction temperatures of about 125°C for such packages. Thus, there is a significant need to understand the effect of higher temperatures on power electronic components and subsystems.

Electronic packaging is a multidisciplinary technology which takes additional complications in power electronics due to the advanced thermal management that is required for packaging of such devices. Functions of an electronic package can be classified into a few categories:

1. Electrical interconnection (providing electrical path for power and signals)
2. Thermal interconnections (providing thermal path for the heat dissipated by the parts)
3. Electrical insulation (providing integrity of the electrical signals)
4. Environmental protection (providing protection of the parts and assembly from damage during handling and from the environment, especially moisture)
5. Mechanical support (providing mechanical support, rigidity, and ductility)

Typical packages used for devices consist of multiple elements. In designing a package for electronic devices to operate at high temperatures in harsh environmental conditions, a few important factors have to be considered:

1. Heat dissipation to keep the temperatures at safe operating levels.
2. Materials used must be stable at the higher temperatures and be able to maintain their properties during prolonged exposure to these temperatures and harsh environments
3. Thermal stresses caused by thermal expansion mismatches between the devices and various package elements including the substrate must be mitigated
4. Thermal shock resistance will be needed to withstand thermal cycling during service

Elements of a typical high-temperature package:

Figure 1 shows a cross-section of a typical state-of-the-art packaging technology used for packaging SiC devices. Functions of several key elements are outlined below along with the materials requirements.

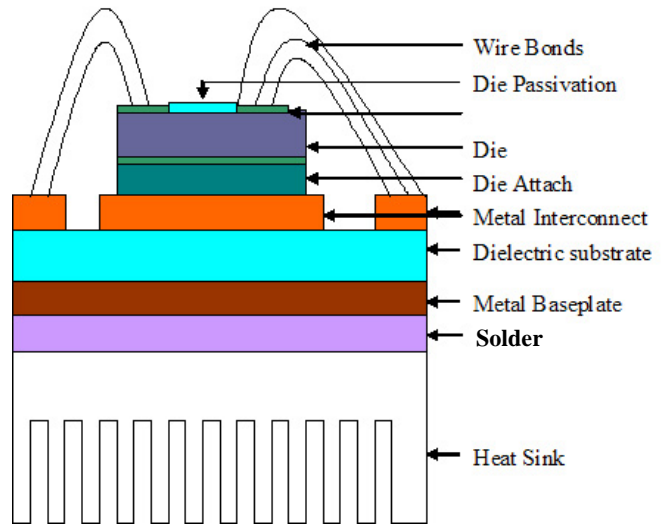


Figure 1. Schematic of a typical high temperature package

Substrate: The key part of the package is the insulating dielectric substrate which has an electrically conductive metallization bonded to it on one surface. The insulating substrate can be either Al₂O₃ or AlN with the metallization layer being copper (as in Direct Bonded Copper (DBC)) or Au. Since SiC devices are designed to operate at high temperatures and high voltages, it is critical that the substrates remain thermally and mechanically stable, while retaining their dielectric properties to desired temperatures.

The metallization layer provides an electrical path between the multiple active and passive devices that may be bonded to the same substrate, and between the packaged devices and the external circuit. It is important that the metallization layer has good bonding with the substrate, retains its good electrical conductivity at high temperatures along with minimum tendency for the formation of intermetallic compounds. In addition, it is desirable that the metallization layer possesses good environmental resistance, and resistance to electromigration. As a rule of thumb, the melting temperature must at least be 1.5 times the operating temperature (in Kelvin) to

prevent any diffusion related problems such as creep and electromigration.

Although the substrate is electrically insulating, it is desirable that its thermal conductivity be high to enable efficient dissipation of heat away from the SiC die. Hence AlN which has a higher thermal conductivity than Al₂O₃ is preferred from a thermal management perspective. Another important factor is the difference in the coefficient of thermal expansion between the device and the substrate. Larger differences in the coefficient of thermal expansions cause larger thermal stresses. Both Al₂O₃ and AlN have a thermal expansion coefficient that compares well with that of SiC.

Wire bonds: Electrical path from the device to the package is achieved through the use of one or more wire-bonds. These are typically aluminum wire bonds that are thermo-sonically bonded to the bond-pads on the device and to the metallization layer. Multiple wires are used for high current applications and to reduce stray inductance. It is known that wire-bonds are one of the weakest links within all the packaging elements.

Die-attach: The device or die is mechanically bonded to the metallization layer through the use of a die attach. A die attach material should have the following properties:

1. Good adhesion with both the die and the substrate to that no debonding or delamination occurs
2. Self-resilience to provide good stress relaxation behavior so that the internal stresses are reduced to low levels
3. High thermal conductivity so that the heat dissipated from the power chip and the thermal expansion difference between the die and the substrate can be minimized
4. An appropriate processing temperature and good thermal stability to fit the typical process hierarchy
5. Good corrosion resistance
6. Good reworkability

Although organic materials have been used as die-attaches for packaging Si-based devices, these materials have limited applications in packages designed for temperatures of 200°C. Many different kinds of materials have been explored for potential use in die-attach applications. High melting point solders, such as gold-tin, gold-germanium; gold-indium, as well as Au-Ag-Si

transient liquid phase bonding, gold thermo-compression bonding and thick-film materials have been considered in previous work. Thus, the choice of appropriate die-attach materials is critical in achieving desired operating temperatures and performance, including the reliability. Another important issue with the use of increased operating temperature is that devices will have to tolerate deeper thermal cycles. The stresses from mismatched coefficients of thermal expansion (CTE) increase with larger thermal cycles and so the potential for fatigue failure is greater with high-power devices. Since metallic brazes have a relatively large thermal expansion, there is a large expansion mismatch with the SiC device and the substrate (such as AlN, Al₂O₃, or Si₃N₄), thus generating large thermal stresses and hence resulting in premature failure during thermal cycling.

Since solder joints and wire bonds serve as pathways for electrical connection to and from electronic devices used in hybrid and electric vehicles, failure of these solder joints and wire bonds will result in catastrophic failures of critical electronic components and hence systems used in these automobiles. Thus, there is a significant need to study the failures of electronic packages induced by metallurgical changes of solder joints and wire bonds. The focus of this work is to understand factors related to the reliability of a die attach solder joint used in power packages and to help understand factors that affect the selection of the appropriate solder material for reliable high temperature operation.

Task 1. Evaluate the reliability of selected commercially available packages. This task will be accomplished through interactions with industrial partners actively involved in the fabrication of power packages. It should be noted that there are no power packages currently available commercially for use at temperatures of 200°C. Hence this part of the work will be performed on commercially available packages that can operate at the highest temperature currently feasible. The key concept behind this task is to understand the reliability of packages that are currently commercially available for high temperature use. This would establish a baseline to help compare the performance of alternate higher temperature solders in terms of expected lifetime. Since failures are induced in solder joints and other components by combination of temperatures, and stresses it is anticipated that reliability will be evaluated using steady state exposures to high temperatures and thermal cycling between temperature extremes as specified by JEDEC standards. Electrical properties will be measured as a function of

thermal cycles to understand the impact of thermal cycling on electrical properties.

Task 2. Evaluate the reliability of joints prepared from selected high temperature solders. In this task, in collaboration with industrial partners, we will identify compositions of solders that have the potential to be used in a package capable of operating at a temperature of 200°C. Single solder joints will be fabricated and will be representative of die attach region in power packages. These joint will be subjected to steady state high temperature exposure and thermal cycling as in Task 1 to understand the evolution of microstructure and defects. The effect of solder melting temperature, and solder physical and mechanical properties on the lifetime observed during thermal cycling will be evaluated. This will eventually result in the identification of solder joint compositions and properties that will result in reliable high temperature packages. It should be noted that current reliability testing of plastic packages using JEDEC standards is limited to a high temperature of about 150°C. Standards to evaluate accelerated testing using thermal cycling representative of exposure to 200°C have not been established at this time. It is anticipated that knowledge gained from this work will assist in the establishment of such standards.

Task 3. Characterize microstructural evolution in solder joints subject to thermal cycling: Microstructural evolution occurs in solder joints during high temperature exposure. Coarsening of solder joint microstructures takes place during high temperature due to accelerated diffusion, and interdiffusion results in the formation of intermetallic compounds. Furthermore, combination of stresses and high temperatures results in creep deformation and combined creep/fatigue of solder joints resulting in the formation of voids. Characterization of microstructure of joints will be carried out using a combination of optical microscopy, x-ray radiography, ultrasonics and other techniques. Emphasis in this task is to understand the effect of high temperature exposure and thermal cycling on the evolution of defects and ultimately the failure of the functionality of the solder joint.

Extensive interaction with industrial partners will occur during all three tasks. Discussion with industrial partners is expected to help in the selection and fabrication of solder joints relevant to the industry. Results obtained in this work on the reliability data can be effectively transferred to industrial partners. It is anticipated

that this work will ultimately help in the identification of appropriate solder joint compositions and fabrication of packages with optimum reliability.

Results

Solder Joint Fabrication

In collaboration with Powerex Inc., two solder joint compositions – 80Au-20Sn ($T_m=280^\circ\text{C}$) and Sn-3.5Ag ($T_m=221^\circ\text{C}$) were downselected for reliability evaluation in FY2009. Initial reliability testing of solder joints were carried out with solder joints prepared between silicon dies and DBC substrates. 2.5 mm x 2.5 mm silicon dies with Ti/Ni/Au metallization were mounted on a metallized AlN DBC substrate with the metallization consisting of a medium phosphorus (6-12%) Nickel layer followed by a flash Au layer on the surface. To understand the void content in the solder joint, high resolution x-ray radiography was carried out on selected specimens in the as-received condition. Figure 2 shows a typical Au-Sn solder joint prepared in collaboration with Powerex Inc. and a corresponding high resolution x-ray image of the joint showing voids present within the solder joint.

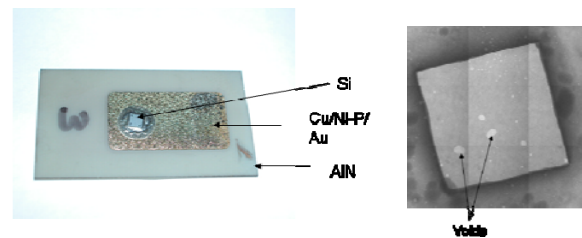


Figure 2. Typical Image and High Resolution X-ray Radiograph of Processed Au-Sn Solder Joint.

Reliability of solder joints were evaluated using thermal cycling between 200°C and 5°C with hold times of 30 minutes at 200°C and 5 minutes at 5°C. This thermal profile was selected since it represented exposure to the maximum proposed operating temperatures of 200°C on the higher end for prolonged periods of time as would be typical of uninterrupted operation at these temperatures. Figure 3 shows a typical thermal profile used in these experiments. The effect of thermal cycling on damage evolution within the solder joints was followed using high resolution X-ray radiography. Effect of steady state exposure on the microstructure of the solders is also

being evaluated using steady-state aging at 200°C for times up to 3000 hours.

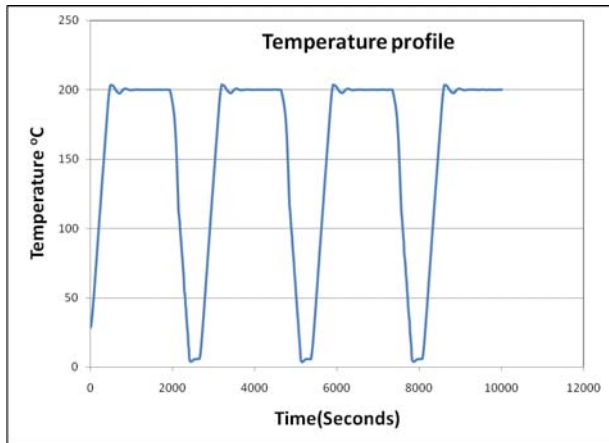
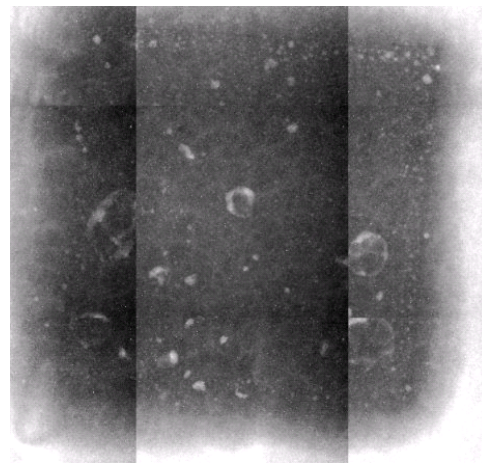


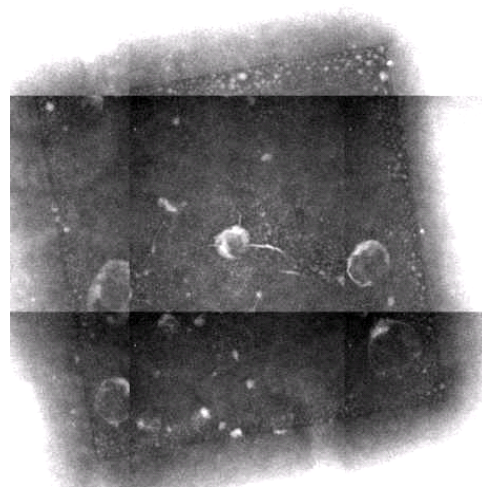
Figure 3. Typical thermal cycling profile used in the reliability testing of solder joints.

Thermal cycling of Au-Sn solder joints between DBC and SiC

Initial results show that when Au-Sn joints between silicon die and DBC are thermally cycled, cracks are formed in the silicon die very early in the thermal cycling process. However, there was a need to understand the behavior of joints between SiC and DBC substrates subject to similar thermal cycling conditions. 2.0 mm x 2.0 mm SiC dies were mounted on a metallized AlN DBC substrate with the metallization consisting of a medium phosphorus (6-12%) Nickel layer followed by a flash Au layer on the surface. Thermal cycling of these joints show that SiC is generally more tolerant to the use of Au-Sn and can sustain a greater number of thermal cycles without cracking of the SiC die as shown in Figure 4.



(a)



(b)

Figure 4 (a) High resolution X-ray radiography from a Au-Sn solder joint between SiC and DBC in the as-processed condition. Note the presence of voids within the solder joint. (b) High resolution X-ray radiography from the same Au-Sn solder joint after thermal cycling. Note the presence of cracks that have been formed due to the cyclic stresses in the thermal cycling process.

Thermal Cycling of Sn-Ag solder joints

2.5 mm x 2.5 mm silicon dies with Ti/Ni/Au metallization were mounted on a metallized AlN DBC substrate with the metallization consisting of a medium phosphorus (6-12%) Nickel layer followed by a flash Au layer on the surface using Sn-Ag solder joints. Figure 5 shows the results of thermal cycling on the high resolution X-ray radiograph obtained from the samples. Note that significant damage has been introduced due to thermal cycling but the joint has not failed mechanically

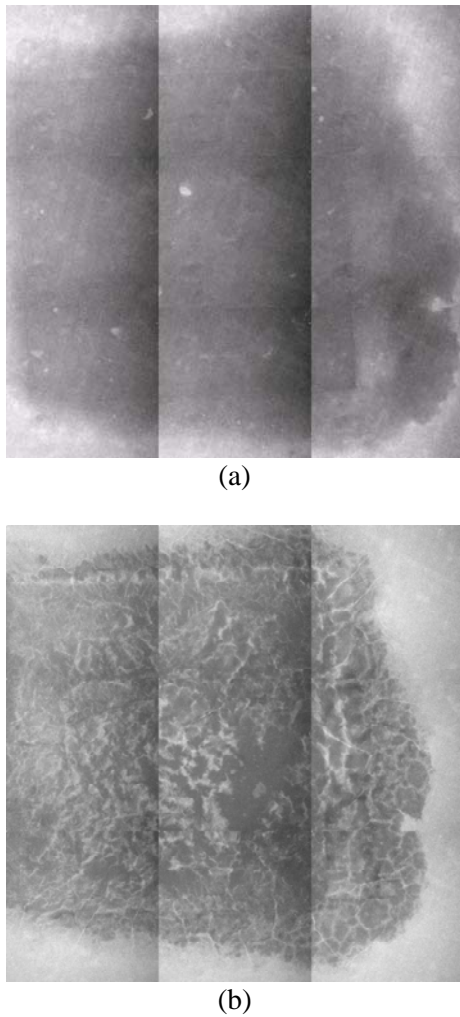


Figure 5 (a) High resolution X-ray radiography from a Sn-Ag solder joint in the as-processed condition. Note the presence of voids within the solder joint. (b) High resolution X-ray radiography from the same Sn-Ag solder joint after 3000 thermal cycles. Note the significant damage that has been introduced within the solder joint due to thermal cycling.

even after 3000 thermal cycles. Future work will evaluate the strengths of these joints as a function of thermal cycling.

Finite Element Modeling of Sn-Ag Solder Joints

Finite element models have been developed to understand the effect of thermal cycling on stresses within the solder joints. Figure 6 shows the 3-D finite element mesh used in the model along with results on total plastic work observed after two thermal cycles. Results are being compared with experimental observations on damage accumulation.

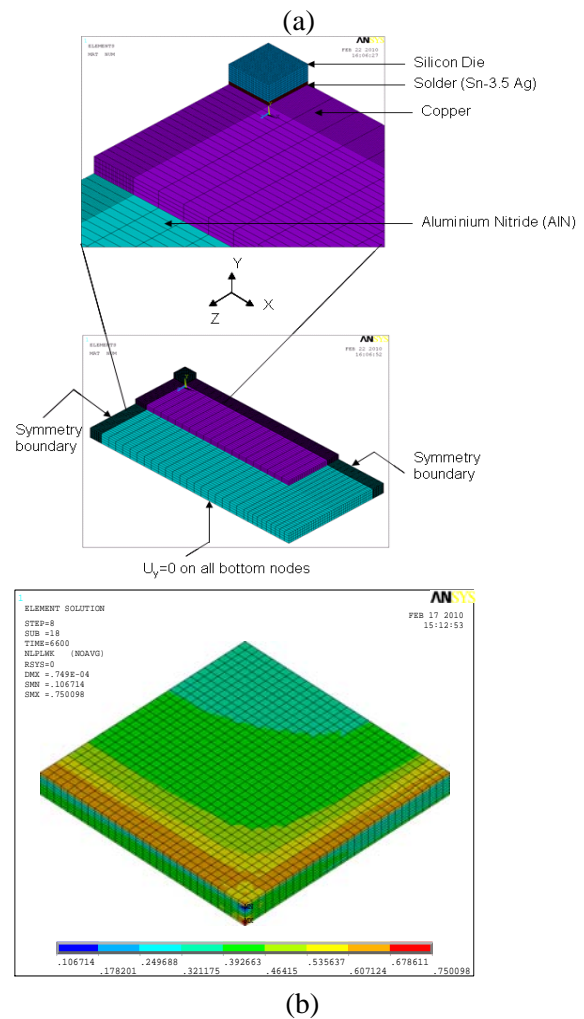


Figure 6. Finite Element of Sn-Ag solder Joint, and (b) Plastic Work Accumulated After Two Thermal Cycles

In addition, infrared techniques are being evaluated to see if these can be used to assess joint degradation. Computational models are being used to fit the thermal diffusivity data to evaluate thermal diffusivity variations in the solder joint.

Conclusions

- Thermal cycling of Sn- Ag and Au-Sn solder joints have been completed to about 3000 thermal cycles
- Damage accumulation has been followed in both types of joints
- Finite element models have been developed to understand evolution of thermal stresses in solder joints.
- Further evaluation of techniques to monitor damage evolution is required.
- Sn-Ag joints show progressive degradation during thermal cycling but do not show complete mechanical failure when subject to as many as 3000 thermal cycles.

Publications/Presentations

Publications:

- 1. "Reliability of Sn-3.5Ag solder joints in high temperature packaging applications," Muralidharan, Govindarajan; Kurumaddali, Kanth; Kercher, Andrew K.; Leslie, Scott G., *Electronic Components and Technology Conference (ECTC), 2010 Proceedings 60th , vol., no., pp.1823-1829, 1-4 June 2010*

Presentations:

- Poster presentation entitled "Reliability of Sn-3.5Ag solder joints in high temperature packaging applications," at the *Electronic Components and Technology Conference (ECTC), 2010, Las Vegas, NV, 1-4 June 2010*
- *Invited presentation* at the 2010 Electronics Packaging Symposium, GE/SUNY Binghamton, entitled "Materials Issues in High Temperature Packaging." September 9-10, 2010

Agreement 16306 - Power Electronics Materials Compatibility

D. F. Wilson, B.L Armstrong, C.W. Ayers, S.L. Campbell, and S.J. Pawel

Oak Ridge National Laboratory

P.O. Box 2008, MS 6063, Bldg. 4515

Oak Ridge, TN 37831-6068

(865)241-5862; fax: (865) 574-4913; e-mail: armstrongbl@ornl.gov

DOE Technology Manager: Jerry L. Gibbs

(202) 586-1182; fax: (202) 586-1600; e-mail: Jerry.gibbs@ee.doe.gov

ORNL Technical Advisor: D. Ray Johnson

(865) 576-6832; fax: (865) 574-6098; e-mail: johnsondr@ornl.gov

Contractor: Oak Ridge National Laboratory, Oak Ridge, Tennessee

Prime Contract No.: DE-AC05-00OR22725

Objectives

- Develop the methodology to map the materials compatibility space of power electronic materials in their operating environment.
- Validate the methodology for accelerated evaluation of power electronic devices.
- Populate a materials-coolant performance database.

Approach

- Establish methodology and build a test apparatus based on power pulsing an electronic component while it is immersed in coolant.
- Evaluate degradation mechanisms using analytical tools.

Accomplishments

- Built a test apparatus based on power pulsing an electronic component while immersed in coolant.
- Developed a flexible accelerated testing methodology.
- Methodology allows for expression of failure modes.
- Reproduced failure mode on different cross-sectional geometry.

Future Direction

- Refine methodology for accelerated testing.
- Evaluate additional coolant effects and begin development of a database indicating performance boundaries.

Introduction

The use of evaporative cooling for power electronics (PE) has grown significantly in recent years as power levels and related performance criteria have increased. As service temperature and pressure requirements are expanded, there is concern among the Original Equipment Manufacturers (OEMs) that

the reliability of electrical devices will decrease due to degradation of the electronic materials that contact the liquid refrigerants. Potential forms of degradation are expected to include corrosion of thin metallic conductors as well as physical/chemical deterioration of thin polymer materials and/or the

interface properties at the junction between dissimilar materials in the assembled components.

Barriers to the deployment of new power electronic components in automotive applications include weight, size, reliability and cost. One approach to reduce the weight of the PE system is to use direct cooling from existing air conditioning systems using R134a refrigerant. This would reduce the weight of the power electronics system by eliminating the need for a separate cooling system. However, direct contact 2-phase cooling necessitates the evaluation of the PE compatibility with and reliability in the coolant. This project will develop the laboratory methodology to evaluate the degradation of power electronics materials by evaporative liquids. In addition, a database indicating performance boundaries for standard materials and for several candidate coolants will be established.

Results

Test Methodology

A laboratory test system, shown in Fig. 1, which was designed and built in FY 2008, allows for high current flow and shaping of the wave form. Testing has been performed using a square wave of one or two seconds on and one or two seconds off to drive 10 to 40 amperes through 0.4 mm (400 microns) diameter aluminum wire shown in Fig. 2. The apparatus allows for condensation and recycle of the evaporated liquid, data recording and visual observation of the boards during testing.

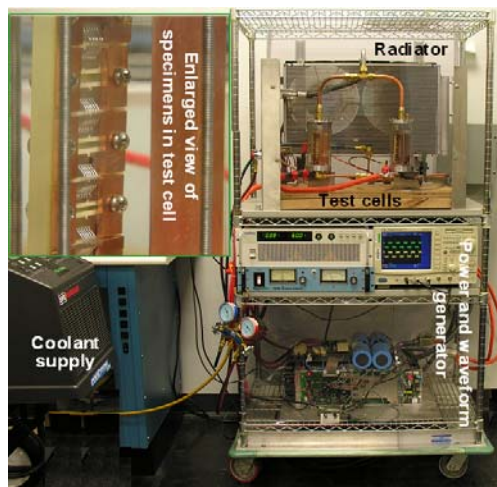


Figure 1. Two circuit boards are shown within their glass enclosures, which are in front of the condensing cooling radiator. Below this is shown the wave form shaping system and the high current power supply.

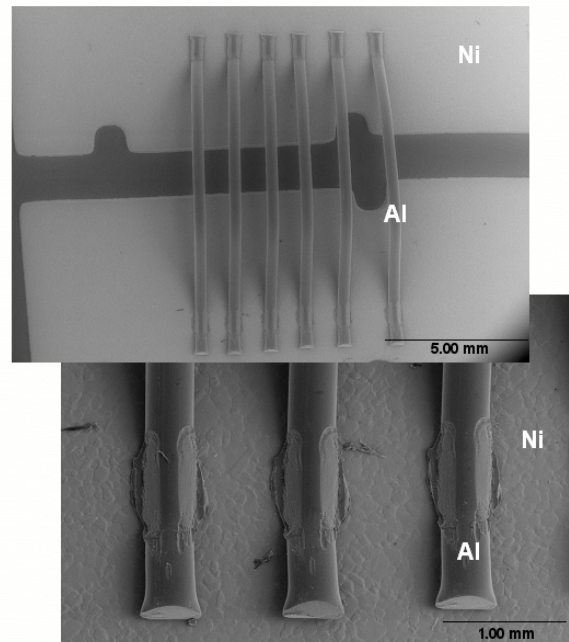


Figure 2. Scanning electron (SE) images of the typical appearance of six-wire test circuit. The bond regions show uniform contact area and deformation associated with the bonding process.

The test methodology that involves pulsing of the PE circuit at appropriate power levels and exaggerated cycle times allows for changes in power-on and power-off times. As such, it facilitates accelerated testing without changes in the failure mode(s) that would be observed in service. Further, the methodology allows for an evaluation of the effect of nucleate boiling on the failure mechanism(s).

Evaluations

As previously reported, pulsing at 240 amps (40 amps through each 400 micron diameter wire) with 2 seconds on and 2 seconds off cycles, produced marked changes at the crown of wires. Deformation (Fig. 3) and pore formation (Fig. 4) was demonstrated. Optical microscopy (Fig. 5) revealed a significant change in grain size and structure from the bond region to the crown of the wire as a result of this testing. Near the bond region, the structure consists of small diameter, elongated grains that is consistent with wire drawing. Moving along the wire toward its crown, increasing grain size is observed until at the crown, very large equiaxed grains that are consistent with recrystallization and grain growth from high temperature excursions present themselves. This recrystallization and grain growth

results in few grains across the diameter of the aluminum wire at the crown, as shown in Fig. 5.

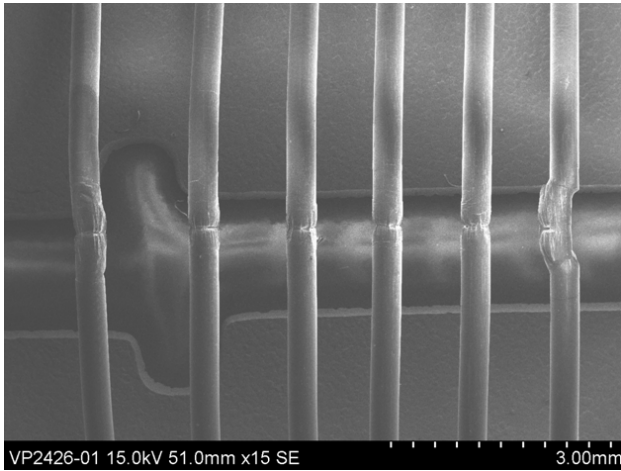


Figure 3. SEM image showing deformation and large pores on the aluminum wires.

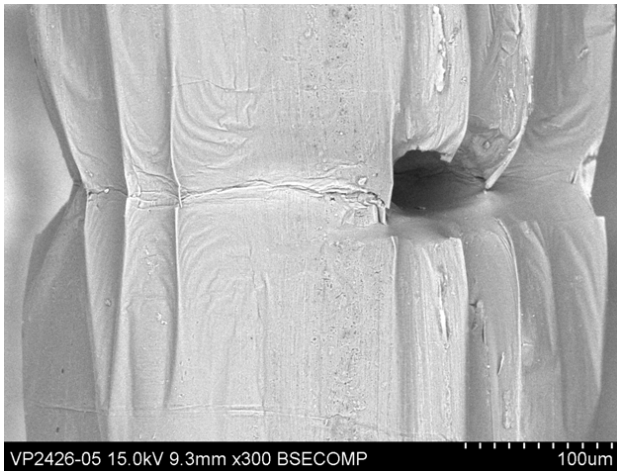


Figure 4. SEM image showing details of the typical deformation and large pore observed on the aluminum wire.

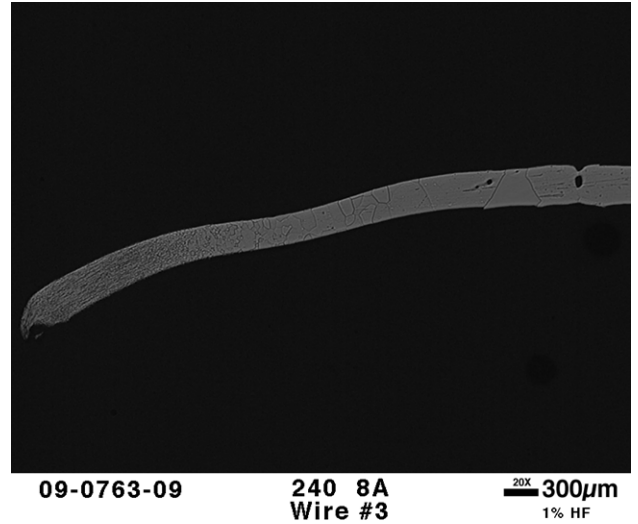


Figure 5. Polished cross section of aluminum wire showing the change in grain size and structure from the bond point (left) to the crown (right).

The behavior of the circular cross-sectional wire was compared to that of a rectangular cross-sectional wire. Rectangular cross-section wires were evaluated with pulsing of 39 amperes per ribbon with 2 seconds on and 2 seconds off cycle. Figure 6 shows that the microstructure of the as-received wire consisted of fine grains aligned along the length of the wire. In contrast, after cyclic testing, the microstructure displays grains of increasing size on moving from the bond region toward the crown of the ribbon (Fig. 7). This behavior is very similar to that for circular cross-section wires. Cyclic pulsing of the ribbons and microstructural evaluation of cross sections are continuing.

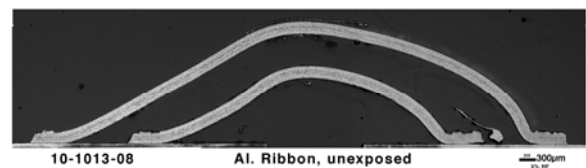


Figure 6. Cross-section of unexposed aluminum ribbon showing similar grain structure throughout its length.

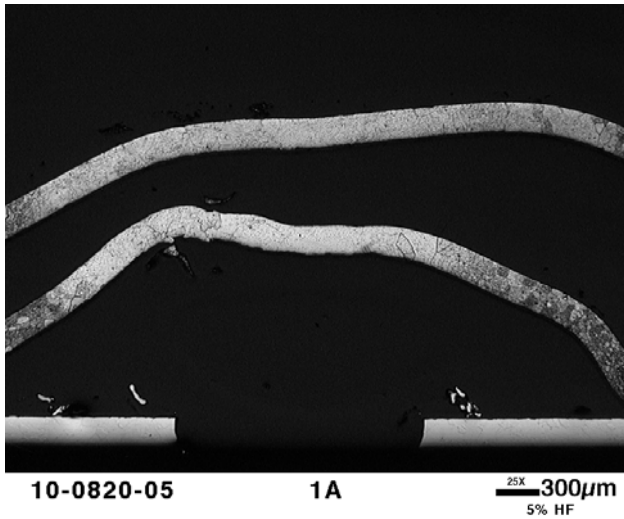


Figure 7. Cross-section of cycled aluminum ribbon showing increasing grain sizes from the bond end to the crown of the ribbon.

Conclusions

The adopted testing methodology is allowing for an expression of failure modes that would be observed in service. Further, it is facilitating accelerated testing.

Agreement 19201 – Non-Rare Earth Magnetic Materials

*M. A. McGuire, D. J. Singh, N. J. Ghimire**

Materials Science and Technology Division

Oak Ridge National Laboratory

P.O. Box 2008, MS 6056, Bldg. 3150

Oak Ridge, TN 37831-6056

(865) 574-5496; fax: (865) 574-4814; e-mail: mcguirema@ornl.gov

** University of Tennessee, Knoxville, TN*

DOE Technology Manager: Jerry L. Gibbs

(202) 586-1182; fax: (202) 586-1600; e-mail: jerry.gibbs@ee.doe.gov

ORNL Technical Advisor: D. Ray Johnson

(865) 576-6832; fax: (865) 574-6098; e-mail: johnsondr@ornl.gov

Contractor: Oak Ridge National Laboratory, Oak Ridge, Tennessee

Prime Contract No.: DE-AC05-00OR22725

Objectives

- Discover new, strong, permanent magnet materials which do not contain rare-earth elements.
- Develop an understanding of the magnetic properties of discovered materials using properties measurements and first-principles calculations to direct work towards improved permanent magnet properties.

Approach

- Investigate understudied known materials and search for new materials in rare earth free chemical systems which hold promise for the discovery of new high-temperature ferromagnets with the large magnetic moments and strong anisotropies required for technologically useful permanent magnet materials.
- Target materials which contain a relatively high concentration of magnetic 3d elements (e.g. Cr, Mn, Fe, Co) and heavier 4d or 5d transition metals (e.g. Zr, Hf, Nb, Ta, Mo, W) which have strong spin orbit coupling.
- Focus on anisotropic crystal structures to allow strong magneto-crystalline anisotropy.

Accomplishments

- Identified specific chemical systems which are most likely to produce good permanent magnet properties without rare-earth elements.
- Synthesized and characterized melt-spun and annealed samples of ferromagnetic Zr_2Co_{11} and Hf_2Co_{11} . Examined effects of chemical substitutions and interstitial additions.
- Initiated an investigation of W_6Fe_7 -type μ -phases to determine potential for ferromagnetism and strong anisotropy.

Future Direction

- Finalize analysis and assessment of permanent magnet potential of FY2010 materials.
 - Focus on discovery of new multinary materials in candidate chemical systems combining Cr/Mn/Fe with heavy transition metals and light p-block elements. Develop an understanding of magnetic properties of these new materials which can guide synthesis efforts in the most promising directions.
-

Introduction

The strategic importance of rare earth elements (REEs) and the associated potential problems are receiving increased attention due to their use in permanent magnets (PMs) for electric motors. There are currently no alternative PM materials competitive with Nd₂Fe₁₄B which do not contain REEs. The development of such materials would allow progress toward lowering the cost of electrical propulsion systems toward the performance goals of \$12 /kW by 2015 and \$8 /kW by 2020 for the Hybrid and Electric Propulsion subprogram set forth by the FreedomCAR and Vehicles Technologies Program.

The technical barrier that must be overcome in this research area is related to the role that the REE plays in current state-of-the-art PMs. Realizing good PM behavior (large remnant magnetization and high coercivity) requires strong magnetic anisotropy. This anisotropy gives preference to a particular orientation of the magnetic moment, and presents an energetic barrier to the reorientation of the net moment required to demagnetize the material. There are two sources of magnetic anisotropy: shape and magnetocrystalline. Shape anisotropy results from the difference in demagnetization factors along different directions in non-spherical magnetic particles. Magnetocrystalline anisotropy arises from the interactions between the magnetic moments and the crystal lattice, giving an intrinsic preferred direction for the magnetization. Directional bonding determines the orientation of orbitals with respect to the crystal structure. Spin-orbit coupling then produces a correlation between magnetic moment (spin) and specific directions relative to the crystal lattice. In RE magnets, the strong spin-orbit coupling and large magnetic moment of the REE is crucial to providing strong magnetic anisotropy. The primary barrier to the development of better non-RE PMs is achieving strong magnetocrystalline anisotropy in the absence of REEs.

Strong spin-orbit coupling is not unique to REEs. Its strength is proportional to the atomic number, and is thus high in all heavy elements. PtCo has strong magnetocrystalline anisotropy due to the large spin-orbit coupling of Pt and its interaction with the 3d Co moments. Despite the high cost of Pt, this material has seen commercial use in magnetic recording applications. This example demonstrates the potential of using heavy *d*-block transition metals to play the role of REEs.

We believe that the most promising chemical systems for discovery and development of new PM materials are those that include the 3d transition metals Cr, Mn, Fe, and Co with heavy 4d or 5d metals like Zr, Hf, Nb, Ta, Mo, W. Many complex binary intermetallic phases are known to form between these sets of elements, some of which are relatively understudied, particularly in regard to how their magnetic behaviors respond to chemical manipulations. Identifying and analyzing promising candidates among these known structure-types is one path toward new hard ferromagnets. However, the discovery of entirely new materials is likely to have the largest impact on technology. This requires examining ternary (or higher) systems, as binary compositional phase diagrams are generally well characterized. We note that moving beyond binary compounds was important in the development of RE magnets as well. Better PM properties are realized in ternary Nd₂Fe₁₄B-based materials than the in the best binary compounds based on SmCo₅. We believe that the addition of nitrogen as the third component in systems containing 3d and heavy transition metals may prove beneficial to magnetic properties, but the combination of synthetic challenges and air and temperature stability issues of products (both related to the high stability of the molecule N₂) may limit the payoff of this strategy. Other light elements near N on the periodic table may prove more beneficial.

This project's objective is to use the ideas outlined above to target new and known materials with the aim of identifying rare-earth free chemical systems which contain permanent magnets with potential for use in electric motors. Replacing Nd₂Fe₁₄B is a serious and important materials challenge which likely will require long term research efforts, and which must begin with advancements in performance and understanding of non-RE magnets, and perhaps most importantly, the discovery and development of new materials.

Results

In FY2010 (the project's first year), work has focused on compiling information on current PM materials, examination of crystal structure and phase diagram databases for promising materials among known compounds and structure types, and the experimental investigation of several of the resulting candidates. The results of these studies to date are summarized below, and analysis of these materials will continue into FY2011.

The usefulness of a PM material can be characterized by the maximum energy product $(BH)_{\max}$ in the second quadrant of the magnetization loop (the demagnetization curve) as these are the conditions under which the magnet is used. The best RE magnets have energy products of about 50 MG·Oe near room temperature. The most competitive non-RE material is AlNiCo, which has an energy product near 10 MG·Oe. The other most commonly used permanent magnets are ferrites, with energy products limited to about 5 MG·Oe. Bearing in mind that AlNiCo and ferrites have been studied and optimized for many decades, these numbers suggest that incremental advances in current non-RE PM materials will not result in the significant improvements required to compete with $\text{Nd}_2\text{Fe}_{14}\text{B}$. Thus, new families of ferromagnetic materials are needed.

Among known compounds, two classes were identified for study during FY2010: (1) Co-based materials with compositions near $M_2\text{Co}_{11}$ with $M = \text{Zr}$ or Hf , and (2) so-called μ -phases, with composition near AB with $A = \text{Nb, Ta, Mo, W}$ and $B = \text{Fe, Co, and Ni}$, which adopt a surprisingly complex crystal structure typified by W_6Fe_7 .

$\text{Zr}_2\text{Co}_{11}$ and $\text{Hf}_2\text{Co}_{11}$

$\text{Zr}_2\text{Co}_{11}$ is the most cobalt-rich compound in the Zr-Co binary phase diagram. It is a known ferromagnet with a Curie temperature near 500 °C. The crystal structure is not well characterized but appears to be highly anisotropic with one long unit cell axis, and is perhaps a modulated structure. We were particularly interested in the 5d analogue $\text{Hf}_2\text{Co}_{11}$ for which magnetic properties have not been reported to our knowledge. We have confirmed that $\text{Hf}_2\text{Co}_{11}$ is also ferromagnetic and high temperature magnetization measurements (Figure 1) shows the Curie temperature to be near 750 K (~ 477 °C), similar to $\text{Zr}_2\text{Co}_{11}$.

Many samples in this family were synthesized by arc-melting, annealing, and melt-spinning. We have investigated the effects of the addition of boron to the alloys, as well as the partial replacement of Co with other 3d transition metals. The results of magnetic properties measurements at room temperature on $\text{Zr}_2\text{Co}_{11}$ - and $\text{Hf}_2\text{Co}_{11}$ -based materials are summarized in Table 1. Narrow, thin ribbons of melt-spun samples were measured with the field along the long axis of the ribbons.

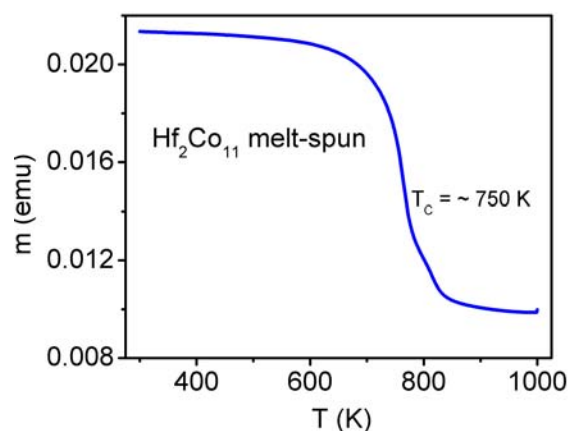


Figure 1. Magnetization vs. temperature for melt-spun $\text{Hf}_2\text{Co}_{11}$ in an applied field of 1 kOe.

Table 1. Measured magnetic properties (saturation magnetization M_s , remnant magnetization B_r , and coercive field H_c) of $\text{Zr}_2\text{Co}_{11}$ - and $\text{Hf}_2\text{Co}_{11}$ -based materials at room temperature. Uncertainties are estimated to be about 10 % on all numbers.

material	M_s (emu/g)	B_r (G)	H_c (Oe)
$\text{Hf}_2\text{Co}_{11}$ arc-melt	70	390	< 500
$\text{Zr}_2\text{Co}_{11}$ arc-melt	86	270	< 500
$\text{Hf}_2\text{Co}_{11}$ anneal	71	280	< 500
$\text{Zr}_2\text{Co}_{11}$ anneal	90	250	< 500
$\text{Hf}_2\text{Co}_{11}$ melt-spin	86	4600	1400
$\text{Zr}_2\text{Co}_{11}$ melt-spin	103	4400	1200
$\text{Hf}_2\text{Co}_{11}\text{B}$ melt-spin	66	4500	2000
$\text{Zr}_2\text{Co}_{11}\text{B}$ melt-spin	81	5100	1300
$\text{Hf}_2\text{Co}_{10}\text{Fe}$ melt-spin	78	3700	450
$\text{Hf}_2\text{Co}_{10}\text{Mn}$ melt-spin	72	3700	< 200

The large magnetization above 750 K for the $\text{Hf}_2\text{Co}_{11}$ sample shown in Figure 1 suggests that some free Co ($T_C = 1394$ K) exists in the material. Thus, microstructure analysis will likely be important in understanding the magnetic behavior of these materials.

Inspection of the results presented in Table 1 show the effects of preparation conditions and chemical manipulations. Arcmelted and annealed samples do not show hard magnetic behavior, having little remanent magnetization and small coercive fields. The properties are significantly enhanced by melt-spinning, which increases both the remanence and the coercivity. Boron addition was observed to decrease the saturation magnetization, but improve the coercivity in the Hf material and the remanence in the Zr material. Attempts to replace some of the Co with Fe and Mn seriously degraded the coercivity of both materials.

In the samples studied to date in this family, the highest energy product observed at room temperature is near 3 MG·Oe. According to powder X-ray diffraction analysis, all of the samples in Table 1 are poorly crystallized. Better properties may be expected in more crystalline material. Annealing melt-spun ribbons has improved the crystallinity, but degraded hard magnetic properties. This is likely due to loss of important fine structure formed during rapid quenching. To improve the crystallinity while retaining anisotropy, high magnetic field annealing experiments are currently underway.

μ -phases

The μ -phases adopt the complex, anisotropic, rhombohedral crystal structure shown in Figure 2. Many of these materials are binary compounds. Binary μ -phases have a range of compositions typically including A_7B_6 , AB (equivalently $A_{6.5}B_{6.5}$), and A_6B_7 , where A is an early 4d or 5d transition metal and B is a 3d metal. They are known in the following binary systems (A-B): W-Fe, Mo-Fe, Ta-Fe, Nb-Fe, W-Co, Mo-Co, Ta-Co, Nb-Co, Ta-Ni, Nb-Ni. Some ternary compositions are also known. In fact, in some chemical systems, μ -phases seem to be stable only when the third component is present. Ternary phase can be stabilized by the addition of P, Si, Al, or Ga and allow the incorporation of other metals like V, Cr, Mn, Zr and Re. Stoichiometric differences between systems and homogeneity ranges within a system show that partial mixing of the light and heavy transition metals occurs on some crystallographic sites.

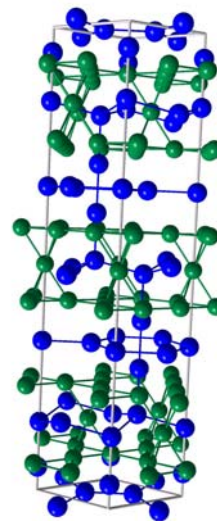


Figure 2. The μ -phase crystal structure. In the prototype W_6Fe_7 , green spheres represent Fe atoms and blue spheres represent W.

From the description above, it is clear that these materials may hold promise for hard ferromagnetism. They combine the targeted groups of elements (light and heavy transition metals), can incorporate “interstitials” like Si and Al, and adopt an anisotropic, complex crystal structure. In addition, the chemical flexibility of this structure type, known to form with binary and ternary combination of at least 17 different elements, should allow some chemical control over the properties through alloying.

In FY 2010 we have initiated an investigation of this family as potential PM materials. Many samples have been synthesized by arc melting and subsequent annealing in the binary systems listed above. We have observed antiferromagnetic ordering near and above room temperature in our Nb-Fe and Ta-Fe samples, and have discovered a new magnetic ordering in the Mo-Fe system which is still under study. The exact nature of this phase transition, which occurs near 115 K, is not yet clear, but appears also to be antiferromagnetic. We have observed preliminary evidence of weak ferromagnetism in a ternary system, although the source of this behavior has not been definitively identified. First principles electronic structure calculations are underway to help understand the magnetic properties of these materials, and may indicate where strong ferromagnetic interactions are likely to be found in these systems.

Conclusions

In FY 2010 we began our investigation of RE-free chemical systems for new strong ferromagnets in an effort to identify materials with potential applications in PM motors. Some understudied known materials have been investigated and their analysis is ongoing. Assessment of currently used PM materials indicates that the most likely path toward advanced non-RE permanent magnets is through the investigation of new materials. We believe that the most promising chemical systems will combine light ($3d$) and heavy ($4d$ or $5d$) transition metals in ternary compounds which adopt anisotropic crystal structures.

Among known materials, the $(Zr/Hf)_2Co_{11}$ -based alloys may hold some promise. However, systematic improvement of properties must await a better understanding of the true composition, crystal structure, and microstructure. In the end, the cost of Co may limit the utility of these materials.

The μ -phases combine several of the targeted attributes (heavy transition metals, light transitions metals, anisotropic structure). The chemical versatility of the structure type suggest that a wide range of behaviors may be expected. To date, only antiferromagnetism has been clearly identified, although hints of weak ferromagnetism have been observed in one ternary system. Further experimentation and theoretical calculations are underway to determine whether good PM properties are likely to be found in these materials.

The ideas and experience developed in FY2010 will continue to guide the experimental and theoretical work as the project progresses. The investigation of materials discussed here will continue, as well as the identification of other promising known materials, and the search for entirely new RE-free compounds with interesting PM properties.

Agreement 17955 - Lithium Battery Recycling Issues

(This project is co-funded by the Energy Storage R&D Program)

Linda Gaines

Center for Transportation Research

Argonne National Laboratory

9700 S. Cass Ave.

Argonne, IL 60439

630/252-4919, Fax: 630/252-3443; E-mail: lgaines@anl.gov

DOE Technology Manager: Jerry L. Gibbs

(202) 586-1182; fax: (202) 586-1600; e-mail: jerry.gibbs@ee.doe.gov

Contractor: Argonne National Laboratory, Argonne, Illinois

Contract No.: DE-AC02-06CH11357

Objectives

- Estimate material demands for Li-ion batteries
 - Identify any potential scarcities
- Calculate theoretical potential for material recovery
- Evaluate real potential for recovery using current recycling processes
- Determine potential for recovery via process development
- Characterize ideal recycling process
- Develop improved process to maximize material recovery

Barriers

- Scarcity could increase costs for battery materials
 - Recycling could increase effective material supply and keep costs down
 - Current processes recover cobalt, use of which will decline
 - Recycling economics in doubt because of low prices for lithium and other materials
- Process data are not published

Technical Goals

- Characterize current battery recycling processes
- Determine current production methods for other materials
- Estimate impacts of current recycling processes
- Estimate energy use/emissions for current material processes
- Estimate energy use/emissions for current battery processes
- Evaluate alternative strategies for additional material recovery
- Develop improved recycling processes

Accomplishments

- Selected promising battery chemistries
 - Designed battery packs for each chemistry and vehicle type
 - Estimated materials use for optimistic EV demand scenario Compared US and world lithium demand to reserves and determined sufficiency past 2050
 - Presented demand estimates and technology comparison at battery and plug-in vehicle conferences
 - Determined current production methods for lithium and batteries
 - Characterized current and developing methods for recycling Li-ion batteries
 - Began production and recycling lifecycle analysis to compare impacts and identify ideal recycling processes
-

Introduction

Recycling of material from spent batteries will be a key factor in alleviating potential material supply problems. We are examining battery recycling processes that are available commercially now or have been proposed. The processes are being compared on the basis of energy saved and emissions reductions, suitability for different types of feedstock, and potential advantages. We are comparing the potential of several recycling processes to displace virgin materials at different process stages (Figure 1), thereby reducing energy and scarce resource use, as well as

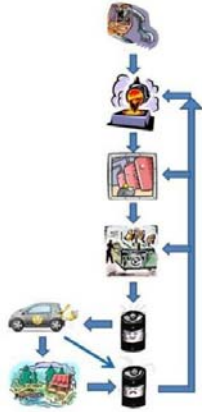


Figure 1 Recycled Materials Enter Varying Production Stages

potentially harmful emissions from battery production. Although few automotive batteries have been produced to date, work is under way to develop the best processes to recycle these batteries when they are no longer usable in vehicles. Secondary use of the batteries could delay return of material for recycling, thus increasing the demand for virgin materials and the resultant life-cycle impacts (see Figure 2).

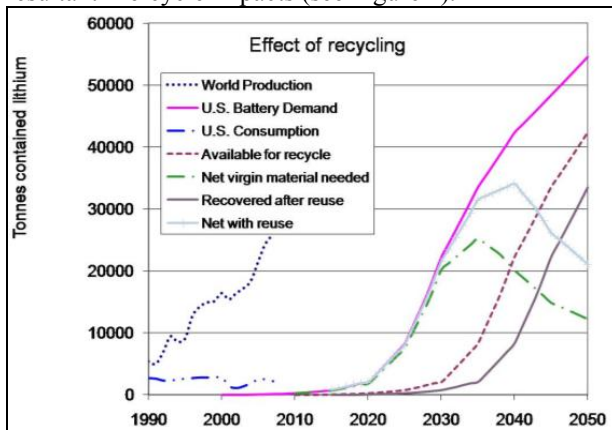


Figure 2 The Impact of Recycling and Reuse on Future US Lithium Demand

Approach

We answered these questions to address material supply issues.

- How many electric vehicles will be sold in the U.S. and world-wide?
- What kind of batteries might they use?

- How much lithium would each use?
- How much lithium would be needed annually?
- How does the demand compare to the available resources?
- How much difference can recycling make?
- What recycling processes are available?
- Could other materials become scarce?

Now, lifecycle analysis, based on detailed process data, will be used to compare energy savings and emissions reductions enabled by different types of recycling processes.

Results

Battery Production-- Roughly half of battery mass consists of materials (copper, steel, plastics, aluminum) that have been extensively documented in previous analyses. Therefore, we focus on the active battery materials that are not as well-characterized. Production steps are shown schematically in Figure 3.

The cathode (positive electrode) material is a metal oxide, with lithium ions inserted into the crystal structure. Commercial electronics batteries generally use cobalt, but oxides containing nickel, manganese, and other elements are being developed for vehicle batteries. Both cobalt and nickel are smelted from sulfide ores, leading to significant sulfur dioxide emissions, even from plants with extensive controls. Lithium carbonate is produced from salars (large brine lakes), mostly in Chile. Brines are concentrated in

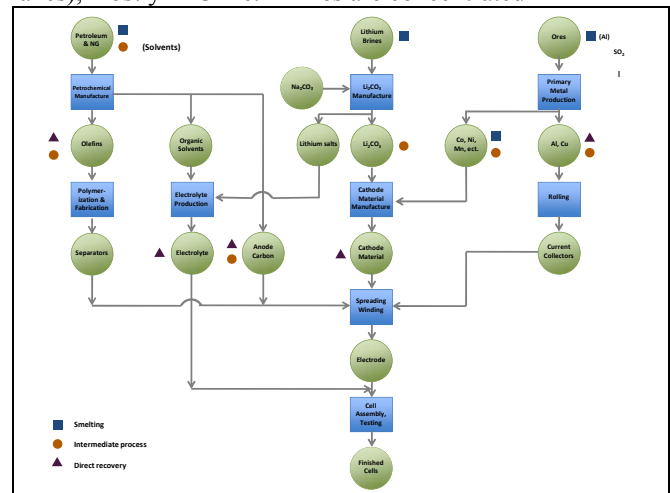


Figure 3 Where Recycled Materials Could Enter Battery Production

ponds for over a year, then treated with soda ash. The carbonate precipitates, and is filtered out and dried. Active cathode compounds are made from lithium

carbonate and metal salts by chemical replacement reactions in solution. High temperature treatment may be required to produce the desired configurations.

The anode (negative electrode) is generally made of graphite. To eliminate detrimental oxygen-containing species on the surface, it is baked at 2,000F (1,100C) in a reducing or inert atmosphere. Additives are mixed in to make the anode paste. The electrode materials are spread onto thin metallic foil substrates, which also serve as the current collectors. For the cathode, aluminum foil (about 20 μm thick) is used, and for the anode, copper (about 14 μm thick).

Separators for Li-ion batteries are typically made from polyolefins using 3- to 8-μm layers (PP/PE/PP or else just PE). The porous film keeps the electrodes apart, and if the cell becomes too hot, melts and closes off the pores, thereby shutting off the cell current. The electrodes and separator are rolled up together and placed in cans before addition of the electrolyte, which is usually a dilute solution of a fluorine-containing lithium salt in an organic solvent. Assembled cells are conditioned and tested.

Recycling Processes-- Recycling can recover materials at different production stages, from basic building blocks to battery-grade materials. The chart in Figure 2 is marked with symbols to show where 3 current recycling processes can actually recover materials. Impacts from all process steps above the symbols are avoided.

At one extreme are smelting processes that recover basic elements or salts. These are operational now on a large scale and can take just about any input, including different battery chemistries (including various Li-ion, Ni-MH, etc.), or mixed feed. Smelting takes place at high temperature, and organics, including the electrolyte and carbon anodes, are burned as fuel or reductant. The valuable metals (Co and Ni) are recovered and sent to refining so that the product is suitable for any use. The other materials, including lithium, are contained in the slag, which is now used as an additive in concrete. The lithium could be recovered by using a hydrometallurgical process, if justified by price or regulations.

At the other extreme, recovery of battery-grade material has been demonstrated. Such processes require as uniform feed as possible, because impurities jeopardize product quality. The components are separated by a variety of physical and chemical processes, and all active materials and metals can be recovered. It may be necessary to purify or reactivate some components to make them suitable for reuse in

new batteries. Only the separator is unlikely to be usable, because its form cannot be retained. This is a low-temperature process with a minimal energy requirement. Almost all of the original energy and processing required to produce battery-grade material from raw materials is saved.

The third type of process is between the 2 extremes. It does not require as uniform a feed as direct recovery, but recovers materials further along the process chain than does smelting.

Comparison of Recycling to Primary Production--

In Figure 4, we see that a large percentage of the battery production energy is consumed during assembly and testing and cannot be recovered by recycling. If the battery can be used again, however, the energy use and emissions

per use are divided among service lives. Once the battery is no longer usable, it can still be recycled, although some of the materials may be more degraded after two uses and therefore

require more processing.

Metals illustrate the benefits of recycling, as the percent reduction in energy consumption ranges from about 25% for steel to 75% for aluminum and nickel. Advanced batteries will likely require high grade materials for their components, so it will be important to understand the quality of the output from recycling processes. A closed-loop battery recycling process would produce materials that could be used in the production of new batteries, while an open-loop recycling process would produce materials that would be used in another product.

Enablers of Recycling and Reuse-- Material separation is often a stumbling block for recovery of high-value materials. Therefore, design for disassembly or recycling would be beneficial. Similarly, standardization of materials would reduce the need for

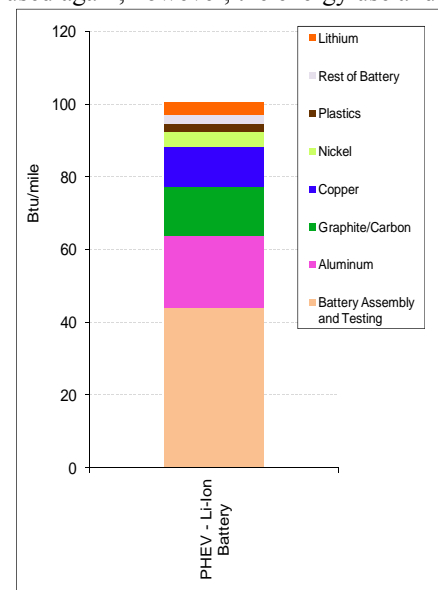


Figure 4 Energy Use for Battery Production Steps

separation. In the absence of material standardization, labeling of cells would enable recyclers to sort before recycling. Standardization of cell design, at least in size and shape, would foster design of automated recycling equipment. Standardization would also be beneficial to reuse schemes, where cells from various sources would be tested and repackaged in compatible groups for use by utilities or remote locations.

Presentations and Publications FY2010

Presentations--

Lithium Ion Batteries: Examining Material Demand and Recycling Issues, TMS 2010 Annual Meeting & Exhibition, Seattle, WA, February 14-18, 2010.

Recycling Processes for Lithium Ion Batteries, 27th International Battery Seminar & Exhibit, Ft. Lauderdale, FL, March 15 - 18, 2010.

Battery Materials Availability and Recycling, Building a US Battery Industry for Electric Drive Vehicles: Progress, Challenges, and Opportunities (NAS Review), Livonia, MI, July 26-27, 2010 (invited).

Lifecycle Analysis for Lithium-Ion Batteries, Plug-In 2010, San Jose, CA, July 26-29, 2010, and US China Battery Meeting, Argonne National Laboratory, August 30-31, 2010 (invited)

Papers--

Lithium Ion Batteries: Examining Material Demand and Recycling Issues, TMS 2010 Annual Meeting & Exhibition, Seattle, WA, February 14-18, 2010.

A Review of Battery LCAs: State of Knowledge and Critical Needs, Argonne National Laboratory Draft Report August 2010.

Agreement 13257 - High Performance Embedded Capacitors

(co-funded by Project 19025 – Advanced Power Electronics)

U. (Balu) Balachandran, Beihai Ma, Sheng Tong, Manoj Narayanan, and Stephen Dorris
Argonne National Laboratory
9700 S. Cass Avenue
Argonne, IL 60439-4838
(630) 252-4250; fax: (630) 252-3604; e-mail: balu@anl.gov

DOE Technology Manager: Jerry L. Gibbs
(202) 586-1182; fax: (202) 586-1600; e-mail: jerry.gibbs@ee.doe.gov
ANL Technical Advisor: U. (Balu) Balachandran
(630) 252-4250; fax: (630) 252-3604; e-mail: balu@anl.gov

Contractor: Argonne National Laboratory, Argonne, Illinois
Contract No.: DE-AC02-06CH11357

Objective

- The purpose of this effort is to develop ceramic capacitors that have excellent high temperature performance and meet the Vehicle Technologies Program specifications for power electronic systems in electric drive vehicles. **This project is jointly funded by the Propulsion Materials and Advanced Power Electronics programs.**

Approach

- Fabricate a high permittivity ferroelectric material, $(\text{Pb,L a})(\text{Zr,Ti})\text{O}_3$ (abbreviated as PLZT), on base-metal and Si foils in controlled environment.

Accomplishments

- Fabricated high dielectric constant (>1300) PLZT films with self-clearing electrodes.
- Fabricated and measured capacitance $\approx 6 \mu\text{F}$ on a 20-mm-diameter PLZT film-on-foil capacitor; this is a factor of 2 increase in capacitor film area and 6 times increase in capacitance value compared to the FY09 results.
- Deposited PLZT film-on-foil capacitors via acetic acid route (2-MOE free) which has better compatibility with factory production environment.
- Measured temperature dependent dielectric properties and breakdown strength of PLZT film-on-foil fabricated by acetic acid method.

Future Direction

- Continue to fabricate high quality PLZT on larger area substrates. Using small area top electrodes, the R&D effort has demonstrated that the properties of PLZT film-on-foils are suitable for power electronics operating at under-the-hood temperatures. The next step is to optimize the processing and fabrication conditions to make large area capacitors with the desired dielectric properties. Important processing issues such as substrate polishing, defects in the films, humidity level, clean room processing, pyrolysis and crystallization temperatures have been identified.
 - Our preliminary results showed that acetic acid method is promising. We will optimize synthesis conditions and fabricate and characterize the dielectric properties of PLZT film-on-foils with larger area top electrodes.
 - Develop fabrication technique for adaptation by capacitor industry.
-

Introduction

Power inverter modules are a critical subsystem within electric drive vehicles (EDVs) and their performance directly affects fuel efficiency and battery life. Capacitors occupy $\approx 35\%$ of the inverter volume and account for $\approx 25\%$ of the weight in current designs. Thus, even if all other components in the inverter are reduced significantly, the capacitor requirement is a serious impediment to achieving the required volume and weight reduction. In addition, the use of high-temperature coolants further exacerbates the situation because existing film capacitors lose their capability to absorb ripple currents at elevated temperature, necessitating the addition of extra capacitors. Increasing the volumetric performance (capacitance per unit volume) of DC bus capacitors is required, and their maximum operating temperature also must be increased to assure reliability requirements. Theoretically, ceramic capacitors have the greatest potential for volume reduction; they could be as small as 20% of the volume of an aluminum electrolytic capacitor. Ceramics offer high dielectric constants and breakdown fields and, therefore, high energy densities. They also can tolerate high temperatures with a low equivalent series resistance (ESR), enabling them to carry high ripple currents even at elevated temperatures, although the capacitance may vary strongly with temperature.

The objective of this R&D program is to utilize ceramic dielectric films with high capacitance density in developing capacitors that meet, if not surpass, DOE's OVT goals for higher operating temperatures, improved packaging and reliability, and reduced size, weight, and cost. Our approach uses ferroelectric thin films (PLZT) on base-metal foils (film-on-foils) that are either stacked on or embedded into printed wire boards (PWBs). Embedded film-on-foil capacitors reduce the component footprint area, shorten interconnect lengths, and reduce parasitic inductive losses and electromagnetic interference. Reliability is improved because the number and size of interconnects are reduced. Solder joints that are most susceptible to failure are no longer needed. Our R&D efforts focus on examining the underpinning issues of film-on-foil capacitor performance and reliability, developing low cost capacitor designs, making multilayer film-on-foil

capacitors, fabricating high-voltage-capable film-on-foil capacitors defined by the inverter application requirements, establishing robust fabrication protocols that are commercially and economically viable, and transferring the technology to industry for manufacturing. This R&D effort is funded jointly by the Advanced Power Electronics and Propulsion Materials Technology programs. The goal of the activity funded by the Propulsion Materials Technology program is to explore fabrication processes to make large-area capacitors for application in electric drive vehicles. The acetic acid synthesis method is compatible with factory production environment. It has greater potential for production of large area film-on-foil sheets for stacking and/or embedding to produce large capacitors for the power electronic applications. As a first step, we fabricated film-on-foil capacitors with up to 5-mm-diameter top electrodes. Next, we will fabricate larger area capacitors through (1) use of high quality substrates, (2) optimization of deposition conditions, and (3) tight control of processing environment.

Approach

Nickel substrates (25 mm \times 25 mm, 0.5 mm thickness, 99.8% pure, ESPI Metals) were polished to 1- μm finish (~ 0.4 mm final thickness) and ultrasonically cleaned in acetone and methanol prior to coating. Last year we used 2MOE process and the detailed procedure for preparation of precursor solutions by 2MOE route were reported elsewhere [1-4]. This year we have used the 2MOE-free acetic acid synthesis route for preparation of LNO and PLZT precursor solutions. 0.3M LNO precursor solution was prepared by dissolving appropriate amount of $\text{La}(\text{NO}_3)_3 \cdot 6\text{H}_2\text{O}$ and $\text{Ni}(\text{OAc})_2 \cdot 4\text{H}_2\text{O}$ into acetic acid at 105°C and aged over 24 h. LNO layers were deposited by spin-coating the stock solution on polished nickel substrate at 3000 rpm for 30 s. Each layer was pyrolyzed at 325°C for 10 min, crystallized at 650°C for 5 min with a final annealing at 650°C for 20 min. 0.5M PLZT precursor solution with 20 mol% excess lead content was prepared by the sol-gel route based on acetic acid chemistry. The starting precursors were 99% lead acetate trihydrate, 97% titanium isopropoxide, 70% zirconium n-propoxide in 1-propanol and 99.9% lanthanum acetate hydrate (all from Sigma-Aldrich Co.).

Zirconium n-propoxide and titanium isopropoxide were first mixed and chelated with acetic acid. Lead acetate and lanthanum acetate were mixed in sequence in acetic acid and dissolved by heating to 105°C. Appropriate amounts of n-propanol and de-ionized water were added to obtain a volume ratio of acetic acid, n-propanol and water of 15:15:2 to achieve a final concentration of 0.5M. The solution was aged for 24 h before thin film deposition. PLZT films were prepared by spin-coating the stock solution on LNO buffered nickel substrates at 3000 rpm for 30 s. Each layer was pyrolyzed at 325°C for 10 min and crystallized at 650°C for 5 min. The films were crystallized for extra 5 min after every three layers. This process was repeated to achieve films of desired thickness and the films were exposed to a final crystallization at 650°C for 15 min. Platinum top electrodes (100 nm thickness) were deposited through a shadow mask by electron-beam evaporation. Phase identification was carried out using a Bruker D8 AXS diffractometer with General Area Detector Diffraction System while thickness was characterized using Hitachi S4700 field-emission scanning electron microscope. An Agilent E4980A Precision LCR Meter was used to measure the capacitance and dissipation factor under applied bias field. A Radiant Technologies' Precision Premier II tester was used to measure the hysteresis loop. The samples were immersed in Fluka silicone oil (Sigma-Aldrich) during high-field hysteresis loop and dielectric breakdown measurements. A Keithley 237 high-voltage source meter was used to measure the current-voltage characteristics. The leakage current density was determined by fitting the current density relaxation data to the Curie-von Schweidler equation [5].

Results

Figure 1 shows the dielectric constant and loss measured as a function of bias voltage at different temperatures on a $\approx 1\text{-}\mu\text{m}$ -thick PLZT deposited on a $0.4\text{-}\mu\text{m}$ -thick LNO buffered Ni substrate coated with $250\text{-}\mu\text{m}$ -diameter Pt top electrodes. Typical ferroelectric behavior, butterfly shaped curves, were observed at all measured temperatures from -50°C to 150°C . The double-peak separation decreases with increasing temperature. We measured dielectric constant, k , ≈ 600 , $\text{DF} \approx 0.06$ at -50°C ; $k \approx 900$, $\text{DF} \approx 0.06$ at room temperature; and $k \approx 1300$, $\text{DF} \approx 0.05$ at 150°C , respectively. Figure 2 shows the dielectric

constant and dielectric loss measured under applied bias voltage as a function of temperature from -50°C to 250°C . The sample is a $\approx 1\text{-}\mu\text{m}$ -thick PLZT deposited on a $0.4\text{-}\mu\text{m}$ -thick LNO buffered Ni substrate coated with $250\text{-}\mu\text{m}$ -diameter Pt top electrodes. Dielectric constant (hence the capacitance) increases and dielectric loss decreases with increase in temperature up to 200°C . Increase in capacitance lowers the ESR and the ripple current capability of the capacitor improves with increase in temperature. This improvement in performance is desired for DC bus capacitors in high temperature inverters for electric drive vehicles.

Figure 3 shows the time relaxation for the current density measured on a $\approx 1\text{-}\mu\text{m}$ -thick PLZT/LNO/Ni sample at room temperature with a constant bias potential of 10 V across the top and bottom electrodes. The time relaxation curve shows strong initial time dependence, indicating depolarization process. The decay in dielectric relaxation current obeys the Curie-von Schweidler law [5],

$$J = J_s + J_0 \cdot t^{-n}$$

where J_s is the steady-state current density, J_0 is a fitting constant, t is the relaxation time in seconds, and n is the slope of the log-log plot. A steady state leakage current density of $3.8 \times 10^{-8} \text{ A/cm}^2$ was measured.

Figure 4 shows hysteresis loop measured on a $250\text{-}\mu\text{m}$ diameter, $\approx 2.7\text{-}\mu\text{m}$ -thick PLZT deposited on LNO buffered nickel substrate at 25°C and 150°C . External electric field of 600 V and 500 V were applied at room temperature and at 150°C , respectively for the hysteresis loop measurement. We observed a slim loop, which is desirable for energy storage/conversion applications. Based on our data, energy conversion efficiency of 79% and 75% can theoretically be achieved at room temperature and at 150°C , respectively.

Figure 5 shows a Weibull plot of breakdown field strength obtained from 20 measurements with Pt/PLZT/LNO/Ni film-on-foil capacitors (with $\approx 1\text{-}\mu\text{m}$ -thick PLZT). The solid straight line is a fitting to the two-parameter distribution function resulting in mean breakdown field strength of 1.7 MV/cm.

Figure 6 shows the dielectric constant and dielectric loss measured at room temperature on two PLZT/LNO/Ni film-on-foil samples. On the PLZT

film of $\approx 1\ \mu\text{m}$ -thickness a bias voltage of 120 V was applied (corresponding to 1.2 MV/cm). On the PLZT film of $\approx 2.7\ \mu\text{m}$ -thickness a bias voltage of 190 V was applied. Dielectric constant and dielectric loss both decrease with increasing bias field. Dielectric constant of ≈ 120 and dielectric loss ≈ 0.02 were measured at 1 MV/cm bias field.

Figure 7 shows hysteresis loop measured at room temperature on two PLZT/LNO/Ni film-on-foil samples of 1 μm and 2.7 μm in thicknesses respectively. Measurements were conducted using 5-mm-diameter Pt top electrodes. Again, we observed slim loops, which are desirable for energy storage/conversion applications.

Figure 8 shows capacitance and dielectric loss as a function of bias field measured at room temperature on a $\approx 0.7\text{-}\mu\text{m}$ -thick PLZT deposited on platinum-coated silicon (Pt/Si) substrate. This sample was fabricated using 2MOE precursor solution with a top electrode of 20-mm-diameter. We measured capacitance of $\approx 6.2\ \mu\text{F}$ on this large area film-on-foil capacitor at room temperature under zero-bias field; this corresponds to a capacitance density $\approx 2\ \mu\text{F}/\text{cm}^2$. Compared to the FY09 result, capacitor area has been increased by a factor of two, and the capacitance value increased ≈ 6 times. Capacitance of $\approx 5\ \mu\text{F}$ was measured on a $\approx 0.7\text{-}\mu\text{m}$ -thick PLZT film deposited on LNO buffered Ni foil.

Summary

In summary, we fabricated PLZT film-on-foils by 2MOE-free acetic acid process which is easier for adaptation by capacitor industry. We measured dielectric constant, k , ≈ 600 , DF ≈ 0.06 at -50°C ; $k \approx 900$, DF ≈ 0.06 at room temperature; and $k \approx 1300$, DF ≈ 0.05 at 150°C , respectively. Leakage current density $\approx 3.8 \times 10^{-8}\ \text{A}/\text{cm}^2$ and breakdown field strength $\approx 1.7\ \text{MV}/\text{cm}$ was measured at room temperature. Based on high field P-E hysteresis measurement, energy conversion efficiency of 79% and 75% can theoretically be achieved at room temperature and at 150°C , respectively. Using 2MOE synthesis route, we fabricated a $\approx 0.7\text{-}\mu\text{m}$ -thick PLZT film-on-foil capacitor with 20-mm diameter top electrode. Capacitance of $\approx 6.2\ \mu\text{F}$ on this large area film-on-foil capacitor was measured at room temperature under zero-bias field. Compared to FY09 results, capacitor film area has

been increased by a factor of two, and the capacitance value increased by ≈ 6 times.

References

- [1] B. Ma, D.-K. Kwon, M. Narayanan, and U. Balachandran, *J. Electroceram.* 22, 383, (2009).
- [2] D.Y. Kaufman, S. Saha, and K. Uprety, Proc. 12th US-Japan Seminar on Dielectric and Piezoelectric Ceramics, Annapolis, MD, 305-308 (2005).
- [3] B. Ma, D.-K. Kwon, M. Narayanan, and U. Balachandran, *Mater. Lett.* 62, 3573 (2008).
- [4] Q. Zou, H. E. Ruda, and B. G. Yacobi, *Appl. Phys. Lett.* 78, 1282 (2001).
- [5] K. Jonscher, *Dielectric Relaxation in Solids*, Chelsea Dielectrics Press, London (1983).

Publications and Presentations

- [1] B. Ma, M. Narayanan, S. Tong, U. Balachandran, *Fabrication and Characterization of Ferroelectric PLZT Film Capacitors on Metallic Substrates*, *J. Mater. Sci.*, 45, 152, 2010.
- [2] U. Balachandran, D. K. Kwon, M. Narayanan, B. Ma, *Development of PLZT Dielectrics on Base-Metal Foils for Embedded Capacitors*, *J. European Cer. Soc.*, 30, 365, 2010.
- [3] M. Narayanan, B. Ma, and U. Balachandran, *Improved Dielectric Properties of Lead Lanthanum Zirconate Titanate Thin Films on Copper Substrates*, *Mater. Lett.*, 64, 22, 2010.
- [4] M. Narayanan, B. Ma, U. Balachandran, and W. Li, *Dielectric Spectroscopy of $\text{Pb}_{0.92}\text{La}_{0.08}\text{Zr}_{0.52}\text{Ti}_{0.48}\text{O}_3$ Films on Hastelloy Substrates with and without LaNiO_3 Buffer Layers*, *J. Appl. Phys. Lett.*, 107, 024103, 2010.
- [5] B. Ma, D. K. Kwon, M. Narayanan, U. Balachandran, *Dielectric Properties and Energy Storage Capability of Antiferroelectric $\text{Pb}_{0.92}\text{La}_{0.08}\text{Zr}_{0.95}\text{Ti}_{0.05}\text{O}_3$ Film-on-Foil Capacitors*, *J. Mater. Res.*, 24, 2993, 2009.

Acronyms

2MOE	2-methoxyethanol
DF	Dissipation factor
EDV	Electric drive vehicle
ESR	Equivalent series resistance
LNO	Lanthanum nickel oxide
PLZT	Lead lanthanum zirconium titanate
PWB	Printed wire board

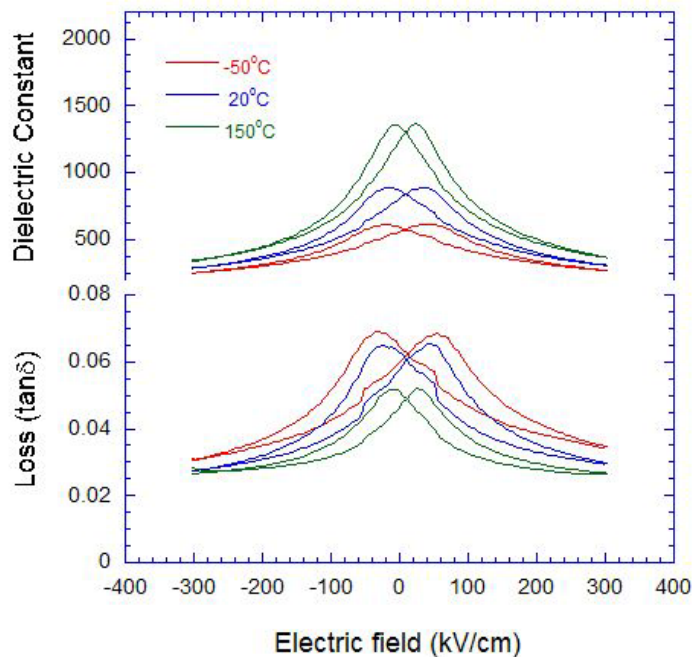


Figure 1. Dielectric constant and loss versus bias voltage measured at various temperatures on $\approx 1 \mu\text{m}$ thick PLZT/LNO/Ni film-on-foil capacitors with $250 \mu\text{m}$ diameter Pt electrodes.

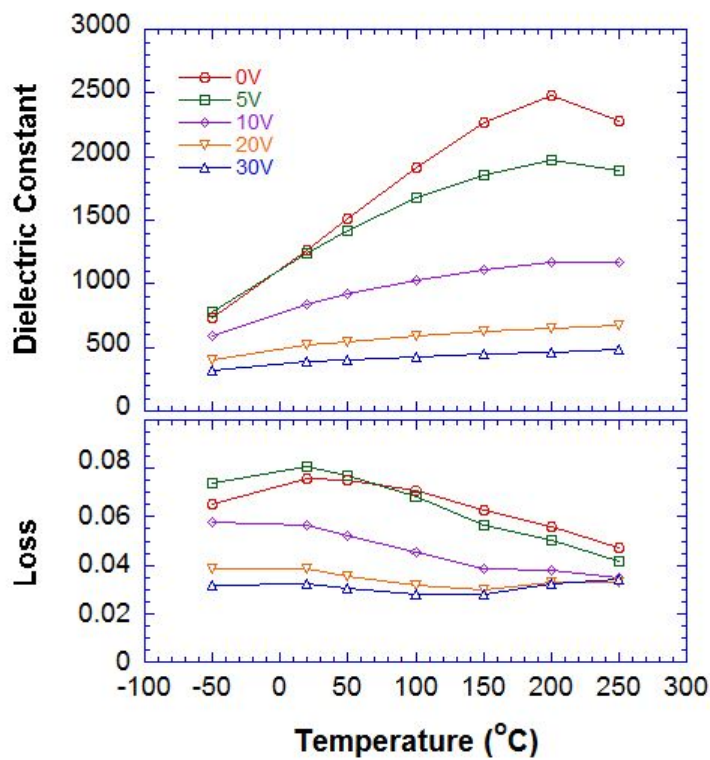


Figure 2. Dielectric constant and loss as a function of temperature measured under applied bias voltages.

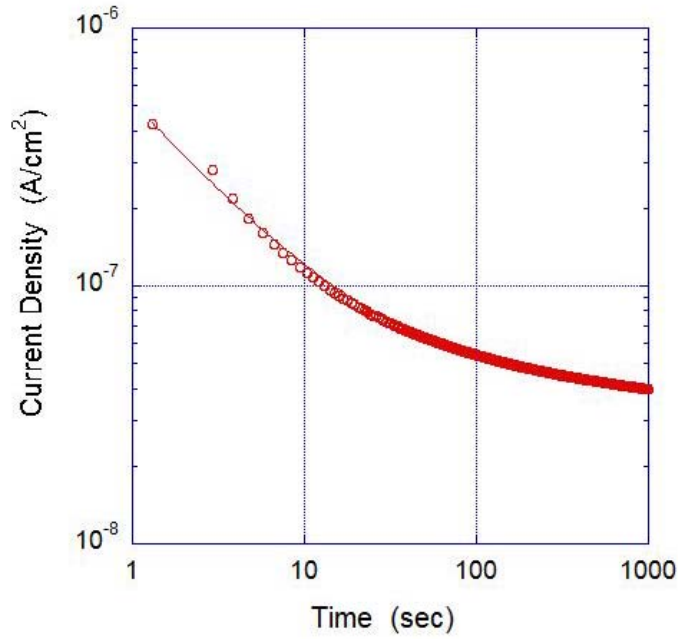


Figure 3. Time relaxation data measured at room temperature on a $\approx 1 \mu\text{m}$ thick PLZT/LNO/Ni film-on-foil capacitor. Leakage current density of $3.8 \times 10^{-8} \text{ A/cm}^2$ was measured.

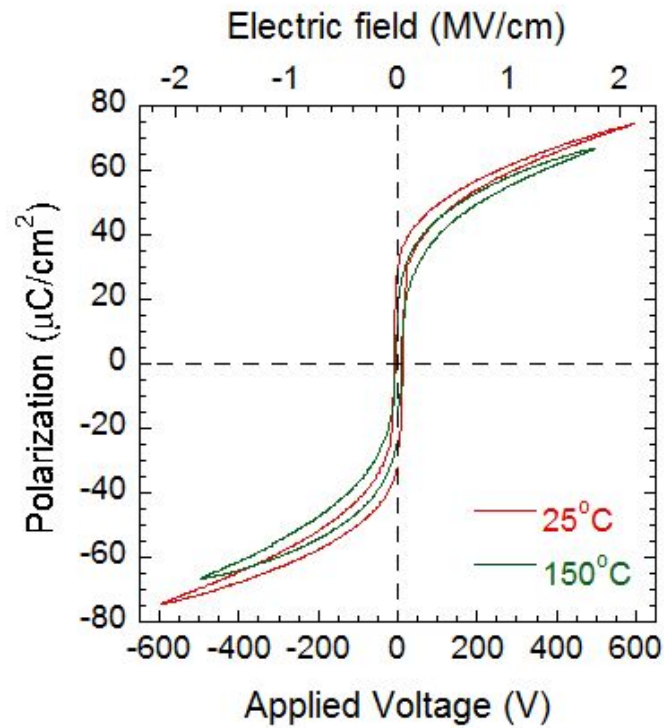


Figure 4. P-E hysteresis loops measured at 25°C and 150°C on a $\approx 2.7 \mu\text{m}$ thick PLZT/LNO/Ni film-on-foil capacitor with $250 \mu\text{m}$ diameter Pt electrodes.

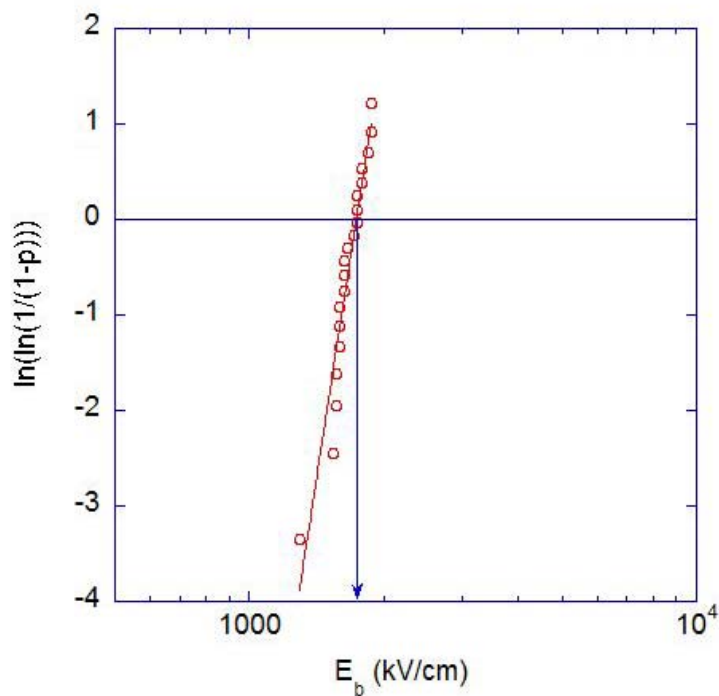


Figure 5. Weibull plot of breakdown field strength measured at room temperature on samples of $\approx 1 \mu\text{m}$ thick PLZT/LNO/Ni film-on-foils. Mean breakdown field strength of 1.7 MV/cm was determined.

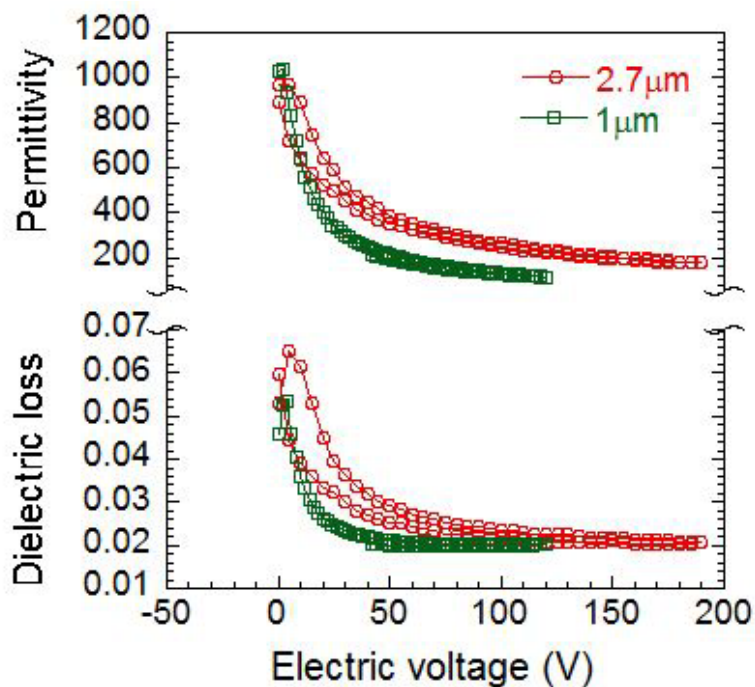


Figure 6. High bias field dielectric properties measured at room temperature on two samples of $\approx 1 \mu\text{m}$ and $\approx 2.7 \mu\text{m}$ thick PLZT/LNO/Ni film-on-foils.

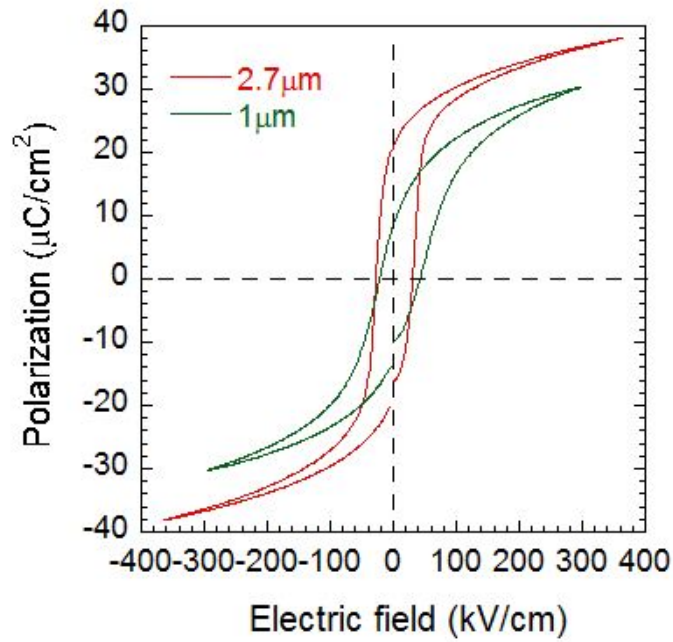


Figure 7. P-E hysteresis loops measured at room temperature on two samples of $\approx 1 \mu\text{m}$ and $\approx 2.7 \mu\text{m}$ thick PLZT/LNO/Ni film-on-foils with 5-mm diameter Pt top electrodes.

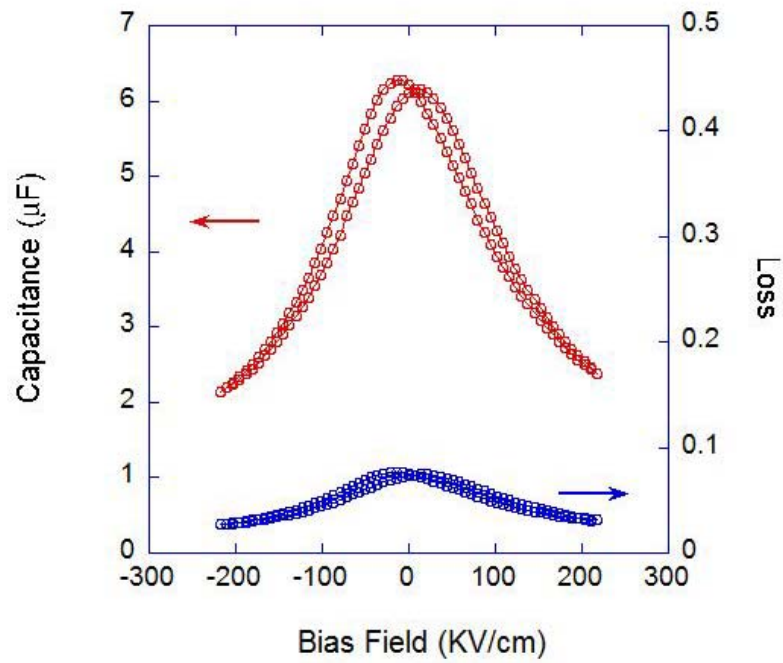


Figure 8. Dielectric properties of a $\approx 0.7\text{-}\mu\text{m}$ -thick PLZT on Pt/Si substrate measured at room temperature on a $\approx 20\text{-mm}$ -diameter top electrode.

Agreement 13295 - Permanent Magnet Development for Automotive Traction Motors (co-funded by Project 19026 – Electric Motors)

Principal Investigator: Iver E. Anderson

Division of Materials Sciences and Engineering

Ames Laboratory, Iowa State University

Ames, IA 50011

Voice: 515- 294-9791; Fax: (515) 294-8727; E-mail: andersoni@ameslab.gov

DOE Technology Development Manager: Susan A. Rogers

Voice: 202-586-8997; Fax: 202-586-1600; E-mail: Susan.Rogers@ee.doe.gov

DOE Technology Manager (Propulsion Materials): Jerry L. Gibbs

(202) 586-1182; fax: (202) 586-1600; e-mail: jerry.gibbs@ee.doe.gov

Contractor: Ames Laboratory, Ames, IA 50011

Prime Contract No.:

Objectives

- Develop the materials and processes needed to fabricate high performance permanent magnets (PM) that can be used for advanced traction drive motors with an internal PM rotor design to meet APEEM goals for enhanced performance at elevated temperature (180-200°C) and reduced cost.
- Anisotropic magnets should be developed to satisfy the need for magnets with maximum magnetic energy density and minimum content of valuable materials. If possible, improved magnet forming processes and mechanical properties also should be developed to further reduce manufacturing costs and extend lifetime in service.
- While magnet materials meeting the technical specifications are most readily achieved using rare earth (RE) permanent magnets, the market factors of rising RE demand/cost and near total foreign control of RE supplies dictate that in the long term, alternative non-RE magnets must be developed.

Approach

This program consists of two major thrust areas.

- Continue investigation of ***RE anisotropic*** permanent magnets, as recommended in an industry expert study, placing effort on generating anisotropic particulate for bonded magnets and on novel processing of sintered RE permanent magnets, exploiting the improved high temperature tolerance of the Ames mixed rare earth (MRE)-Fe-B alloys.
- Develop aligned nano-structures in MRE-Fe-B magnet alloy particulate by enhanced control of crystal nucleation and growth or by controlled rapid solidification as a low cost route to make large gains in bonded magnet strength for simplified motor manufacturing.
- Further develop anisotropic sintered permanent magnets from micron-sized single crystal particles of MRE-Fe-B alloys using pressure-driven liquid phase sintering with intrinsic or extrinsic sintering additives for fully dense magnets of the highest magnetic strength, aiming for reduced Dy content.
 - This research thrust will be phased out as milestones are met and technology transfer is accomplished. It should also be noted that techniques being developed to produce anisotropic RE magnets probably can be used in the second thrust area, as well.

- New high strength ***non-RE anisotropic*** permanent magnets will be developed that meet the requirements for advanced interior PM electric traction motors. The investigation will involve theory and modeling efforts, as well as experimental synthesis of magnet compounds and prototype magnet fabrication and characterization.
- Development of non-RE anisotropic permanent magnets will include attempts to improve on known systems, by gaining enhanced knowledge of coercivity mechanisms with more sensitive characterization techniques and by innovative processing with greater control of microstructure.
- Non-RE anisotropic permanent magnets also will be pursued with help from theory and modeling, seeking to discover new phases with beneficial intrinsic properties, i.e., high Curie temperature, magnetization and magnetic anisotropy.
- If the new non-RE permanent magnet phases have insufficient magnetic properties as single-phase magnets, increased properties will be sought with further extrinsic manipulation, including use a soft magnetic second phase to produce enhanced exchange coupling.
 - It should be noted that this task area is extremely high risk, but if successful it will revolutionize the cost structure of permanent magnet motors and reduce the reliance on foreign controlled commodities for hybrid and electric vehicle production.

Major Accomplishments

- Solved problem with degraded high temperature performance of the segregated type of “core-shell” 2-14-1 phase structure (with Nd-enriched/Y-depleted shell or rim on each grain) in intrinsic (unmodified) sintered MRE-Fe-B magnet samples by adding uni-axial pressure assistance to the sintering process to permit reduced sintering temperature (<850°C) for full density magnets.
- Demonstrated that a devitrification method with uni-axial applied pressure during annealing of glassy ribbon samples (as-spun) was successful at producing directional growth of aligned 2-14-1 nano-crystals with the a-axis (higher elastic modulus) perpendicular to the pressure vector direction, but with an unusual grain boundary disorder that appears to degrade magnetic anisotropy on this particulate for bonded anisotropic magnets.
- Performed preliminary electronic structure calculations of the Fe-Co system to determine the composition dependence of the magnetic moments, magnetic anisotropy and Curie temperature, where the original linear response scheme was modified and adjusted for this project. Results indicate that the maximum of each property occurs at a significantly different Fe-Co concentration.
- Used combinatorial synthesis on an appropriate model ternary alloy (Fe-Co-W) to search for single-phase magnetic compounds with anisotropic crystal structure and a minimum of Co content. Synchrotron micro-diffraction indicates that the main diffraction peak across the full spread corresponds to that of the (110) bcc phase. From MH (hysteresis) loop characterization of the lower W concentration region (~2%), we found several compositions where the out-of-plane (OOP) MH loop displays significant (promising) coercive field.
- Embarked on an extensive analysis of Alnico 5-7 samples by initial microstructural analysis in the SEM. Because the SEM samples were prepared to a high surface quality, orientation imaging microscopy (OIM) analysis could be performed. This verified that good alignment of the [001] direction was achieved in the growth direction of the grains, but that the grains were randomly oriented in the transverse plane of the casting. The SEM micrographs also determined grain size in the commercial samples, which will be important for TEM analysis during the coming year.

Future Directions

- Perform more focused work on improved processing of ***RE anisotropic*** permanent magnets, continuing to work on novel processing of sintered RE permanent magnets and on generating anisotropic particulate for bonded magnets, exploiting the improved high temperature tolerance of the Ames mixed rare earth (MRE)-Fe-B alloys.
 - Focus on development of anisotropic sintered magnets using pressure assisted intrinsic sintering at reduced temperature, exploring extrinsic additives to diminish Dy use.
 - Thoroughly develop pressure-driven anisotropic crystallization of amorphous magnet alloy ribbon to accentuate anisotropy in precursor particulate for bonded magnets.
- Accelerate effort to develop new high strength ***non-RE anisotropic*** permanent magnets that meet the requirements for advanced interior PM electric traction motors. It is critical that the investigation maintains close collaboration of theory and modeling efforts, of experimental magnet material synthesis work, and of detailed characterization studies on the new materials.
 - Develop theoretical tools for the investigation of potential new phases
 - Complete analysis of commercial Alnico
 - Understand texture development and develop control strategies in Alnico
 - Develop improved spinodal decomposition methods in Alnico
 - Complete combinatorial investigation of the Fe-Co-W system
 - Complete analysis of clusters in the Co-W system
 - Perform chemical synthesis of hard magnet particles for nano-composite magnets
 - Conduct Annual Workshop (Nov. 2010--completed) and Spring Workshop (May 2011)

Technical Discussion

Accomplishments in Rare Earth Anisotropic ($R_2Fe_{14}B$ -type) Magnet Research

Anisotropic bonded or sintered magnets are the most cost effective for traction motor because they can obtain the highest maximum energy product $(BH)_{max}$ compared to isotropic magnets. This work builds on our earlier accomplishments in high temperature mixed rare earth (MRE) magnets of the isotropic type. There are several techniques to make anisotropic magnets, including aligned sintered magnets with micron-sized grains and melt-spun ribbons with nanocrystalline grain size and textures induced by controlling the solidification process or by hot-deforming glassy ribbons. Because the technical processes of anisotropic magnets are different from those of isotropic ones, new compositions, processes, and resulting microstructure need to be systematically studied and well understood in order to achieve good magnetic properties. In the past year, we mainly focused on four different aspects to approach our targets of anisotropic rare earth magnets. In addition, a 3-D reconstruction method for enhancing TEM

results was applied to study the microstructure of melt-spun $MRE_2Fe_{14}B$ ribbons.

1. Optimization of composition and processes of sintered magnets made from $Nd_{0.45}(Y_rDy_1)_{1/r+1*0.55}]_xFe_{14}Co_{0.3}B_{1.1}$ ($r=1-5$, $x=2.4-2.6$)

In our previous work, we have prepared aligned sintered magnets $Nd_{0.45}(Y_3Dy_1)_{1/4*0.55}]_xFe_{14}B_{1.1}$ with improved magnet properties by adjusting alloy composition to introduce a liquid phase and using hydrogen decrepitation and conventional ball milling techniques. The $(BH)_{max}$ of new developed magnets with $x=2.8$ (WT220) reached to 25 MGOe. However, the magnet exhibits a strong temperature dependence for coercivity, similar to Nd-based magnets. Microstructural studies showed that the 2-14-1 grains form a core-shell structure with Nd segregation to the outer shell, negating the addition of Dy for bolstering the higher temperature magnetic properties after sintering at 1000-1100°C. In order to understand the complex partitioning behavior in the mixed rare earth system, the

effects of composition and post annealing conditions on magnetic properties are systematically studied. In addition, the powder preparation and handling process have been greatly improved so as to control the Oxygen content to a level as low as possible. These improved processes make it possible to reduce the total RE content. Table 1 lists the changes of magnetic properties of

$[\text{Nd}_{0.45}(\text{Y}_3\text{Dy}_1)_{1/4*0.55}]_x\text{Fe}_{14}\text{B}_{1.1}$ when x decreases from 2.8 to 2.6. It is seen that the $(\text{BH})_{\text{max}}$ increases from 25.4 to 29.3 MGOe with decreasing x=2.8 to 2.6. Unfortunately, the $(\text{BH})_{\text{max}}$ drops dramatically at 400k due to a larger temperature coefficient of coercivity in those magnets. The temperature compensation effect which exists in the mixed RE melt-spun ribbons is not observed in the sintered magnets.

Table 1. Effect of RE ratio x and DyF₃ on magnetic properties of $[\text{Nd}_{0.45}(\text{Y}_3\text{Dy}_1)_{1/4*0.55}]_x\text{Fe}_{14}\text{B}_{1.1}$

Ratio	2.8	2.6	2.6
DyF ₃ (wt%)	0	0	5
Mr (kGs)	10.8	11.4	10.7
Hc (kOe)	8.7	8.6	17.8
(BH)m (MGOe)@300k	25.4	29.3	26.0
(BH)m (MGOe)@400k	10.2	14.0	19.1
α (%/°C)	0.15	0.11	0.10
β (%/°C)	0.63	0.58	0.48

In order to improve temperature stability of sintered magnets, one of the most effective methods is to improve the coercivity by adding heavy rare earth elements, such as Dy or DyF₃. It is obvious that using DyF₃ is more economical. It is seen from Table 1 that the coercivity greatly increases from 8.6 to 17.8 kOe by adding 5% DyF₃. Although the $(\text{BH})_{\text{max}}$ at room temperature decreases from 29 to 26 MGOe due to the addition of 5% DyF₃, the

$(\text{BH})_{\text{max}}$ at 400K increases from 14 to 19.1 MGOe. Therefore, the temperature stability and coercivity of magnets is obviously improved by adding DyF₃.

Since 2009, the improvement of magnetic properties of $[\text{Nd}_{0.45}(\text{Y}_3\text{Dy}_1)_{1/4*0.55}]_x\text{Fe}_{14}\text{B}_{1.1}$ magnets is listed in Table 2. The best magnet obtains a $(\text{BH})_{\text{max}}$ of 26 MGOe at 300K and 20 MGOe at 400K, respectively

Table 2. Development status of magnetic properties of high temperature magnet $[\text{Nd}_{0.45}(\text{Y}_3\text{Dy}_1)_{1/4*0.55}]_x\text{Fe}_{14}\text{B}_{1.1}$

Year	09	09-10	10
Mr (kGs)	10.8	10.4	10.6
Hc (kOe)	8.7	14.5	16.7
(BH)m (MGOe)@300k	25.4	24.4	26.0
(BH)m (MGOe)@400k	10.2	17.4	20.0
α (%/°C)	0.15	0.13	0.09
β (%/°C)	0.63	0.58	0.49

For comparison, the $(BH)_{\max}$ values as a function of temperature for the experimental magnets and a commercial magnet are shown in Fig.1. The temperature coefficients of the experimental magnets are equal to or even better than that of the commercial magnet. However, their $(BH)_{\max}$ values are still lower than that of the commercial magnet over the entire

temperature range. In summary, if further processing improvements and composition adjustments can optimize the extrinsic parameters for $[\text{Nd}_{0.45}(\text{Y}_r\text{Dy}_1)_{1/(r+1)*0.55}]_x\text{Fe}_{14}\text{B}_{1.1}$ and make the ambient temperature $(BH)_{\max}$ match the commercial magnet, the experimental magnets will be superior above 100°C .

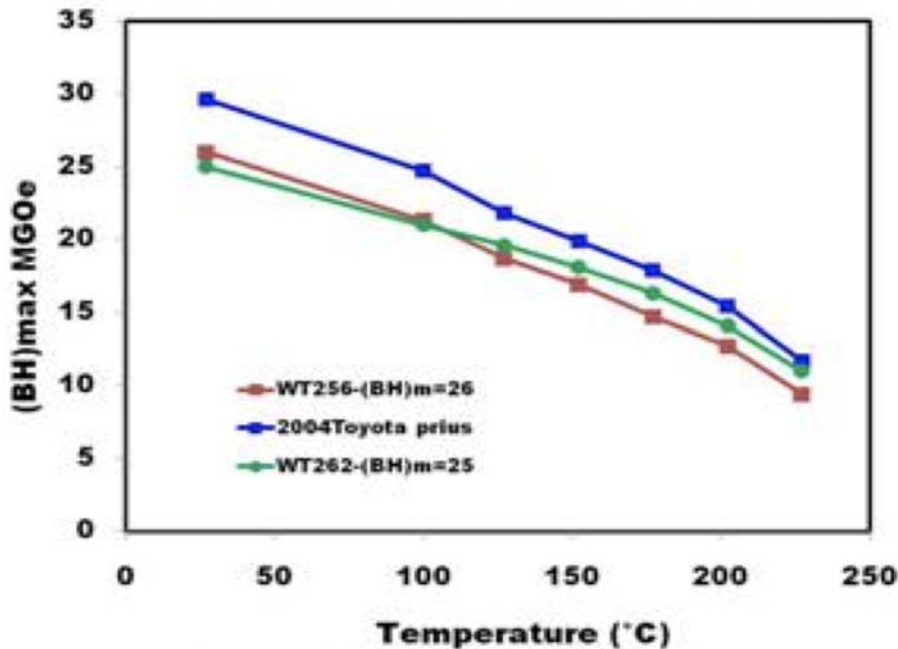


Figure 1. $(BH)_{\max}$ as a function of temperature for experimental and commercial magnets.

2. Study of microstructure and magnetic properties of sintered

$[\text{Nd}_{0.45}(\text{La}_r\text{Dy}_1)_{1/(r+1)*0.55}]_{2.6}\text{Fe}_{14}\text{B}$ magnets ($r=1-3$)

In this work, Y was replaced with La. La and Y are magnetically equivalent so that the magnetic properties of the alloy should be largely unchanged. On the other hand, since La is a light rare earth, the solidification behavior of the alloy should be similar to those of Nd-Fe-B alloys. Therefore, the replacement of Y with La should remove the driving force for partitioning and help to obtain a uniform microstructure, which is expected to promote sintered magnets with better temperature stability.

The microstructures and the composition profiles across grains of the magnet sample were studied as presented in Fig. 2a and b. The results of electron microprobe composition profiles across the second phase and grains (Fig.2b) show that the grain boundaries are rich in La and Nd but depleted in Dy while the La, Nd and Dy contents are constant across the 2:14:1 grains. Therefore, the core-shell grain structure observed in that of $(\text{Nd-Y-Dy})_{2.6}\text{Fe}_{14}\text{B}$ alloy was eliminated. In addition, the areas at triple junction and grain boundaries are a RE-rich phase, and highly rich in La and moderately rich in Nd but depleted in Dy, which results in a lower coercivity. In order to strengthen these regions, to improve the coercivity, DyF_3 is added in the magnets.

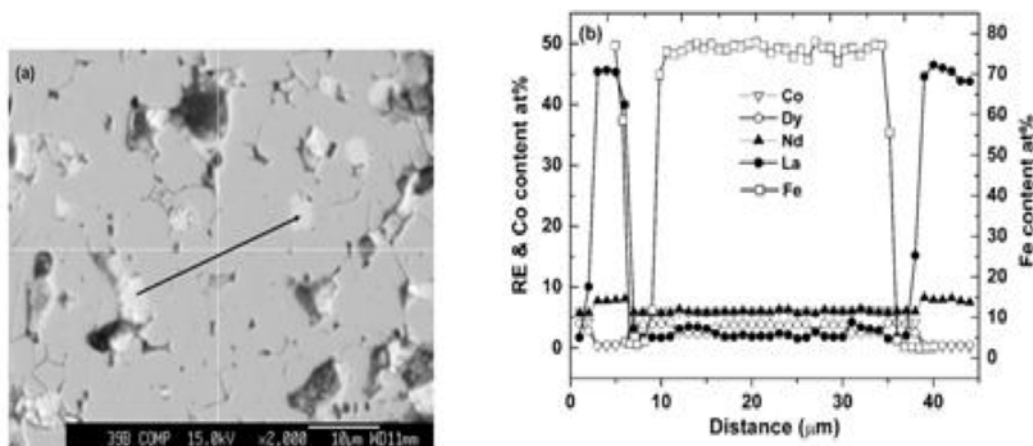


Figure 2. Microstructure and electron microprobe composition profiles with La substituted for Y.

Table 3 lists the magnetic properties of magnets with the addition of 5%wt DyF₃ and different r (ratio of La:Dy). It is seen that the coercivity of the magnet with r=3 is greatly increased from 2.1 to 8.7 kOe after the addition of 5%wt DyF₃. In addition, the temperature coefficient of coercivity is significantly improved with increasing coercivity. At 100°C,

the temperature coefficient α and β are as low as -0.06 and -0.48%/°C, respectively, while the typical values for the best high temperature Nd-based magnets are -0.10 and -0.48%/°C, respectively. The temperature coefficient values for the studied magnet are comparable to those of Nd-based magnets. However, the (BH)_{max} of the studied magnet needs to be further improved.

Table 3. Magnetic properties of sintered [Nd_{0.45}(La_rDy₁)_{1/(r+1)+0.55}]_{2.6}Fe₁₃Co₁B magnets with 5% DyF₃ addition and different r

r	3	2	1
M _r (kGs)	9.4	9	9
H _c (kOe)	8.7	9.7	15.1
(BH) _{max} (MGoe)	20.2	19.0	21.1
α (%/°C)	0.084	0.080	0.060
β (%/°C)	0.632	0.608	0.470

3. Study of anisotropic melt spun ribbons devitrified during vacuum hot pressing

In pursuit of anisotropic powders for bonded magnets, studies applying uni-axial pressure during crystallization of Nd₂Fe₁₄B are being performed. For uni-axial pressure crystallization, a Nd₂Fe₁₄B + 3 wt % TiC alloy was arc melted and melt-spun. Melt spinning was done at 25 m/s in order to form a mostly amorphous microstructure. The ribbons were hot pressed at

106 MPa in a graphite die while being heated to 640°C under vacuum. Fig. 3 shows an XRD pattern of the sample. The x-ray diffraction and SQUID measurements (not shown) both indicate that significant texturing was achieved through the application of uni-axial pressure during crystallization (ref.3). However, the annealing parameters need to be adjusted since the coercivity of the samples was much lower than expected. It was suspected that the grains had grown too large to effectively pin domain walls.

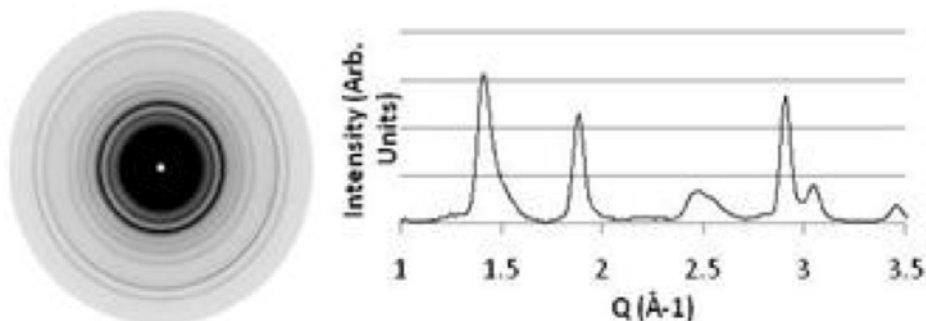


Figure 3. XRD pattern of an amorphous ribbon that was crystallized during vacuum hot pressing.

A series of samples from the hot pressing experiments were also investigated using TEM in order to understand the crystallization behavior under applied pressure. The samples' nominal composition is $\text{Nd}_{0.8}\text{Y}_{0.8}\text{Dy}_{0.4}\text{Fe}_{14}\text{B} + 3\% \text{TiC}$, coded as NO-121-B (as-spun), NO-121-B-2 (580 °C/60 min, 110MPa) and NO-121-B-3 (580 °C/60 min, no applied pressure). Figure 4 gives the typical microstructures of the three alloys. The as-spun sample is almost fully amorphous with very few nuclei found in the matrix. EDS analysis didn't find any segregation/enrichment of TiC in the sample.

The annealed sample without applied pressure shows a similar microstructure as other TiC added MRE samples (WT series). The average grain size of hard phase (2-14-1) is about 60 nm and many TiC particles (5–10 nm) formed along grain boundaries and triple junctions (Fig. 4 (right)). The sample annealed with applied pressure exhibits a quite unusual microstructure; see Fig. 4 (middle). The corresponding EDP can be indexed to either strong textured 2-14-1 or α -Fe, or both. A new series of the pressure-applied samples are under preparation for further verification/investigation for this effect.

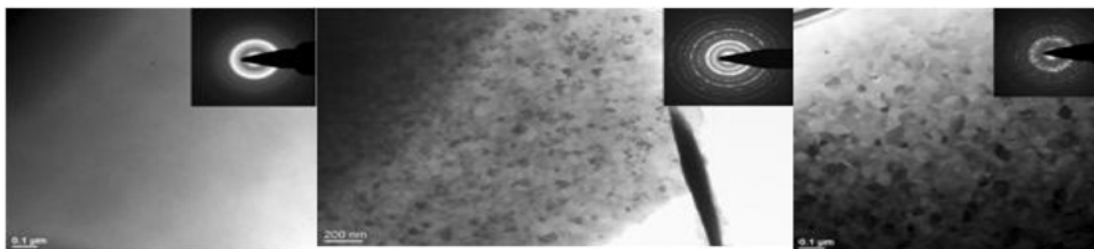


Figure 4. TEM bright field images with corresponding electron diffraction patterns of (left) NO-121-B (as-spun), (middle) NO-121-B-2 (580°C/60min., 110MPa), and (right) NO-121-B-3 (580°C/60min., no applied pressure).

4. Study of new sintering technique on $[\text{Nd}_{0.45}(\text{Y}_3\text{Dy}_1)_{1/4*0.55}]_{2.6}\text{Fe}_{\text{bal}}\text{B}_{1.1}$ magnets

It is known that the microstructure of $[\text{Nd}_{0.45}(\text{Y}_3\text{Dy}_1)_{1/4*0.55}]_{2.6}\text{Fe}_{\text{bal}}\text{B}_{1.1}$ magnets after sintering at 1000°C or above shows a core-shell segregation structure in the 2-14-1 grains, which might be responsible for a strong temperature dependence. In a new sintering technique, the samples were sintered at 800-850°C for 1h with a uni-axial applied pressure up to 110MPa. Figure 5 shows a micrograph and electron microprobe composition profiles of the sintered sample. It is seen that the distribution of Nd, Y

and Dy are basically uniform in the 2:14:1 grains. No obvious shell-core structure was observed. Sintered at 825°C for 1h under a 110MPa pressure, the sample has a density less than 7.0 cm³/g, and its magnetic properties have not been fully developed, indicating that the processing parameters still need to be modified or optimized. However, the new sintering technique is very promising to develop high performance magnets with a composition much closer to that in Table 2. These investigations are ongoing.

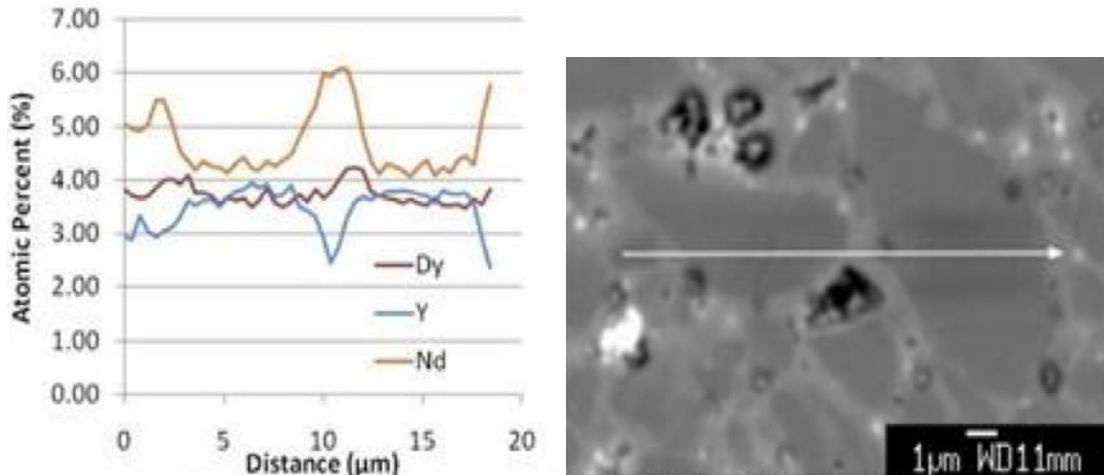


Figure 5. Microstructure and electron microprobe composition profiles of sample sintered at 825°C/1h with 110MPa applied pressure in vacuum hot press.

5. Study of reconstructed 3-D TEM images of $MRE_2Fe_{14}B$ ribbons

We successfully applied the STEM tomography technique to a ribbon sample

(WT165) using the Tecnai G² F20 STEM. Figure 6 gives the STEM HAADF (Z-contrast) image and corresponding 3-D reconstruction results.

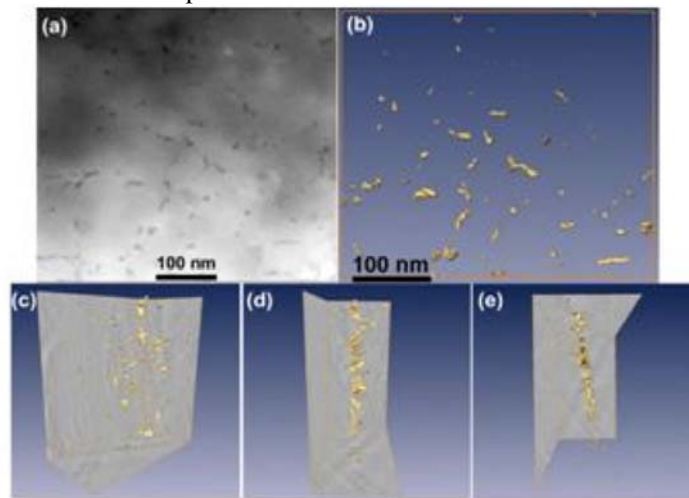


Figure 6. (a) STEM HAADF image of the alloy (TiC particles in darker contrast) and corresponding ET 3-D reconstructed volume shown in (b) z-axis, (c) random, (d) x-axis, and (e) y-axis. The shape and morphology of the TiC particles are illustrated in yellow by using the iso-surface method.

Figure 7 gives the details at the center region of the reconstructed area. The majority of the TiC particles are oval or short rod-like in appearance and in a range of 5–10nm. During annealing procedure, excess Ti and C atoms are expelled from the formation of RE2-14-1 phase and then form TiC phase. The TiC grains inhibit

the hard phase to grow larger, therefore control microstructure. In this study, the 3D reconstructed sampled volume contains more than 20 grains of the RE2-14-1 phase and more than 70 TiC nano-particles. Therefore, there are $\sim 1.7 \times 10^8$ TiC particles within a 1 mm³ volume in the alloy, accounting for the strong pinning

effect of the carbide addition. In summary, the STEM Tomography technique is a useful tool to

explore and understand the details of magnet alloy microstructures.

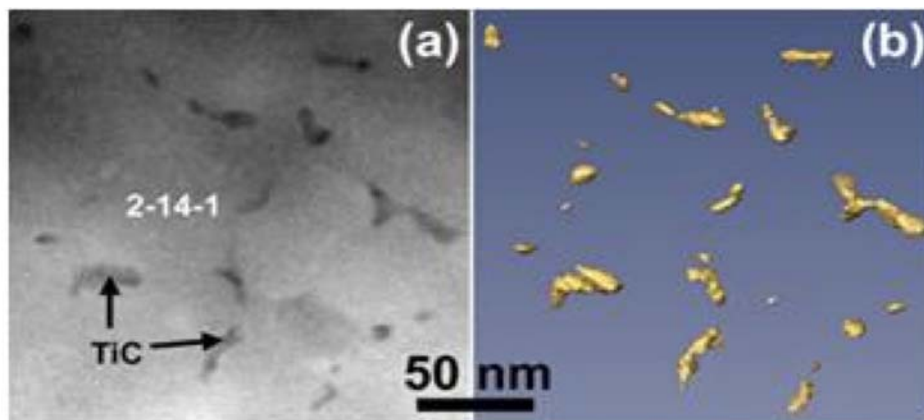


Figure 7. (a) STEM HAADF image and (b) corresponding ET 3-D reconstructed volume, where the TiC particles are represented by the iso-surface.

Accomplishments in Beyond Rare Earth Magnets (BREM) Research

Accelerating rare earth cost pressure (resulting in a doubling of the cost of RE magnets in one year) and a recent glimpse of Chinese power (source for 97% of the world's RE supply) to impose RE supply limits outside of China have motivated a major augmentation of the original RE permanent magnet research project to include non-RE magnets. The new research thrust is an effort to elevate non-RE permanent magnet alloy designs to the realm of magnetic strength necessary for high torque PM motors. More specifically, this thrust will seek to develop permanent magnets based on Fe and Co with greatly increased coercivity and energy product, as well as a high Curie temperature, for advanced IPM traction motors. The investigation team includes first principles theory and modeling efforts (Theory Group), innovative synthesis of magnet compounds and prototype magnet fabrication (Synthesis Group), and highly detailed characterization with state-of-the-art instrumentation (Characterization Group). Drawing from US universities (Univ. Nebraska-Lincoln, Univ. Maryland, Brown Univ.), National Laboratories (Oak Ridge Nat. Lab., Ames Lab.), and commercial magnet producers (Arnold Magnetic Technologies), experts in magnetic materials from each area were formed into the team. Many team members belong to multiple groups as a natural

coordination arrangement and the Ames Lab leadership core has structured numerous ways (including a team website, regular internet presentation/conference calls, and semi-annual face-to-face meetings) to ensure operation of the research team in a tight feedback loop.

After two workshop meetings the team developed and refined a plan that was followed in FY2010 and the accomplishments for the first partial year of work are summarized below, organized according to the task structure. The initial general plan is to explore two parallel research tracks, i.e., improvement of the best existing non-RE magnet system, Alnico, and discovery of new non-RE magnetic phases, focused on Fe, Co, and Fe-Co systems. The Alnico work will seek enhanced knowledge of coercivity mechanisms, increased control of microstructure and magnetic alignment, and beneficial composition modifications. New magnetic phase discovery will involve theory and modeling to guide the choices of base compositions and selection of minor additives to accentuate magneto-crystalline anisotropy, searching for maxima in intrinsic magnetization, magnetic anisotropy, and Curie temperature. Micromagnetics modeling will help specify extrinsic parameters for the new phases that optimize anisotropy, maximizing shape, stress, surface, and exchange contributions to coercivity. As the experimental results from magnet synthesis work indicate promising directions, bulk magnet fabrication work will

proceed to produce scale-size magnet samples for IPM motor testing and for development of magnet processing methods that can be scaled to industrial magnet production techniques.

Progress on the 4 tasks in the Theory Group studies:

Task 1. Literature Analysis for Assembly of Known and Promising Compounds

We have successfully initiated an effort in collaboration with Synthesis Partners (separately funded by VT) to identify appropriate search algorithms for assembling a database of non-rare earth (primarily) magnet compounds. Refined tests on a set of 5 papers selected from the literature showed that the computer algorithms can identify targeted data such as crystal structures and intrinsic magnetic properties (Curie temperature, magnetic moment, and magnetic anisotropy). Some preliminary investigation of “machine reading” of literature for maximum efficiency and coverage of early work on non-RE permanent magnets is in progress. In the next stage, we will expand the scope of the database to encompass as many English language publications as possible, and add new publications to the database from all surveyed sources and further explore “machine reading” of literature. The beginning minimal database is now open for use by the entire project team members. Suggestions for improvement and changes will be coordinated for the team by the database oversight committee (Skomski, McCallum, and Antropov), but all team members are expected to contribute literature copies for analysis. Rehbein will perform the technical effort required to create and maintain database. We will also pursue the implementation of searchable annotations of literature to create an “expert” database.

Task 2. Theoretical Phase Diagram Exploration and Materials Structure Optimization

We have initiated the development of efficient computational algorithms to explore the crystal structure configuration space for a given set of

compounds within a range of compositions of interest. To effectively search complex systems with multi-element (binary, ternary and beyond) compositions and a large number of atoms per unit cell (e.g. 50-100), it is necessary to search phase space with the use of fast empirical inter-atomic potentials. Since developing such potentials can be very time consuming, we adopted a strategy of developing algorithms that can provide a feedback mechanism to modify the accuracy of the inter-atomic potentials at the same time that the search is being performed. Candidate structures from such a search strategy will be further refined and validated by ab initio calculations. The success of such on-the-fly algorithms will enable the efficient and timely use of computational resources for materials discovery. One postdoctoral fellow will start in October 2010 to begin work on this project.

Task 3. Magnetic Properties Calculations

Initial studies of intrinsic properties of specific materials have been performed for several systems:

- a. Fe-Co systems of ordered intermetallics and disordered alloys were studied. The magnetic moments, magnetic anisotropy and Curie temperature have been calculated using electronic structure methods and the original linear response scheme was modified and adjusted for this project. Preliminary results that we obtained indicate that the maximum of each property occurs at a different Fe-Co concentration (see Fig. 8). The ordered intermetallics demonstrated better magnetic anisotropy compared to disordered alloys at the same concentration. An experimentally unknown bcc phase of Co was found to have a very high Curie temperature. Such a Co crystal structure may exist in this films and clusters. Studies of Fe-Co alloys will be continued due to the importance of this prototype system for our project. We will consider the inclusion of the effects of different distortions, substitutions, defects and impurities.

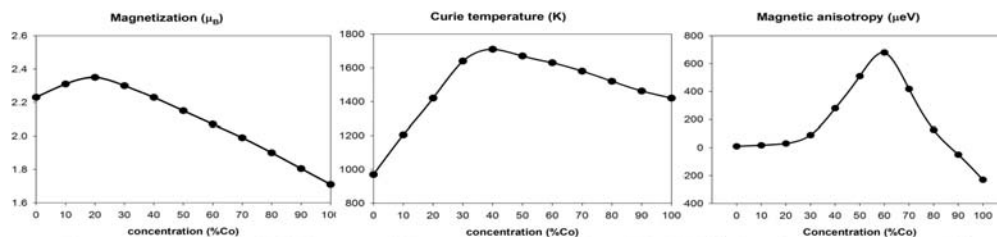


Figure 8. Electronic structure calculation results for intrinsic magnetic properties of Fe-Co system.

b. The $Fe_{16}N_2$ system was studied, where the record magnetization has been reported. Our initial studies indicated no significant increase of magnetization with a moderate Curie temperature and significant magnetic anisotropy only in film geometry. These studies also will be continued to provide better argumentation about whether or not this material is suitable for our project.

c. We have studied the magneto-crystalline anisotropy energy of Fe atoms situated in the highly anisotropic environment of a single layer on a metal surface to establish the limit of how a strongly anisotropic environment can be used to enhance the magnetic anisotropy of a material.

d. We have investigated how interstitial C and N modify the magnetic anisotropy of iron. The effect has long been exploited in steel

magnets, and there are many studies on the corresponding structural and mechanical properties and, to lesser extent, on magnetic properties such as magnetization. However, very little is known about the origin of the systems magnetic anisotropy. In cooperation with Arti Kashyap and her group, we have used a full-potential linear augmented plane wave (FP-LAPW) method with a generalized gradient approximation (GGA) for exchange and correlations. The carbon and nitrogen atoms, which occupy one set of octahedral interstitial sites in the tetragonally distorted bcc structure (see example of C in Fe in Fig. 9), yield a pronounced chemical contribution to the anisotropy, in addition to the well-known strain effect caused by long-range elastic interactions and martensitic ordering.

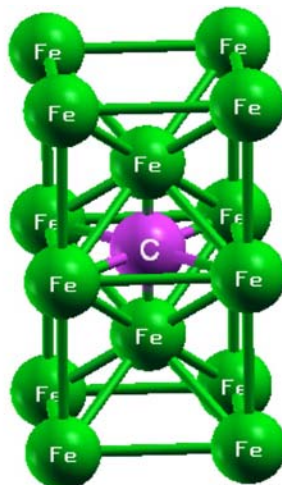


Figure 9. Illustration of C in interstitial site of bcc-Fe lattice.

The magnetic moments of the Fe atoms are slightly reduced due to hybridization, but the system exhibits an appreciable magnetic anisotropy. Extrapolated to 100% C and N, respectively, the predicted anisotropies are 7.7

MJ/m³ and 3.9 MJ/m³, which is promising and consistent with available experimental data. The calculated magnetic properties also are consistent with available experimental anisotropies, such as 0.40 meV and 0.32 meV

per atom for C and N in martensitic Fe, respectively. Carbon contents in many steels are typically of the order of 0.9 wt %, or 4 at % (Fe_{96}C_4), which translates into an anisotropy constant of 0.21 MJ/m³.

Task 4. Micromagnetics modeling

At this early stage, we are still in the process of identifying suitable magnetic systems for our micromagnetics modeling study.

Progress on the 3 tasks in the Synthesis Group studies in FY2010:

Task 1. Synthesis of Model Magnet System Samples

Compilation of an inventory of thin film and nano-scale magnet material synthesis capabilities at each partner institution was begun for the project data library.

In concert with theoretical analysis, combinatorial synthesis experiments were performed on an appropriate binary alloy (Fe-Co) that is modified by a third element (W), searching for single-phase magnetic compounds with anisotropic crystal structure and a minimum of Co content. As Fig. 10 indicates, 3 separate sputtering targets were used to deposit several 500 nm thick films at room temperature with variable composition on a pre-oxidized Si substrate. Individual tiles that capture a limited composition sector were sliced from the deposited film and were prepared for characterization by annealing under vacuum at several temperatures. One set of samples that was annealed at 600°C was subject to detailed characterization. A large composition region covering most of the ternary phase diagram was mapped (Fig. 10), and regions of lower W concentration (%W less than 40%) were studied in detail.

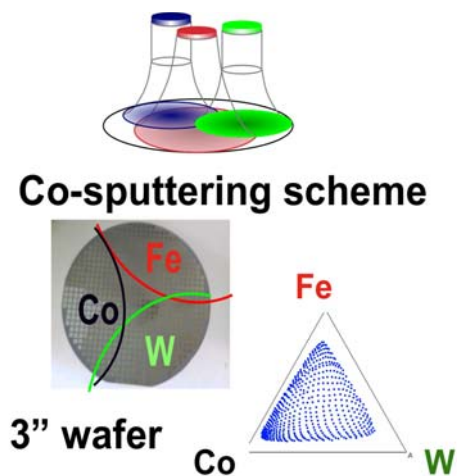


Figure 10. Schematic of combinatorial synthesis experiment to generate composition field of Co-Fe-W.

In coordination with theoretical efforts, experiments on nano-particulate cluster deposition were started. We have measured the magnetic anisotropy constant (K_1) for cluster-deposited YCo_5 and $\text{Co}_{1-x}\text{Pt}_x$ ($x \sim 0.1$) nano-particles from the magnetic measurements carried out using a SQUID magnetometer. YCo_5 nano-particles were observed to be ferromagnetic with $H_c \sim 6$ kOe at 300 K and M vs. H curves reveal that the magnetization does not reach the saturation even at an applied field of 70 kOe. We estimated the value of K_1 to be $\sim 2.0 \cdot 10^7$ ergs/cm³ for YCo_5 nano-particles by

fitting the experimental magnetization curves using the method "law of approach to saturation." $\text{Co}_{0.9}\text{Pt}_{0.1}$ nano-particles exhibit super-paramagnetic behavior with $H_c = 0$ and $M_r/M_s = 0$ at $T_{\text{meas}} \geq 50$ K and show non-zero coercivities at $T_{\text{meas}} \sim 30$ K. FC and ZFC magnetization curves also reveal the super-paramagnetic behavior of these nano-particles by showing a blocking at $T_b = 50$ K. We estimated the value of the magnetic anisotropy constant (K_1) of $\text{Co}_{0.9}\text{Pt}_{0.1}$ nano-particles using T_b to be $1.2 \cdot 10^7$ ergs/cm³. Co-W nano-clusters also were produced by inert gas condensation. A

composite target was used, with relative areas of Co and W designed to produce a composition of

Co-25 atomic percent W, based on relative sputtering yields.

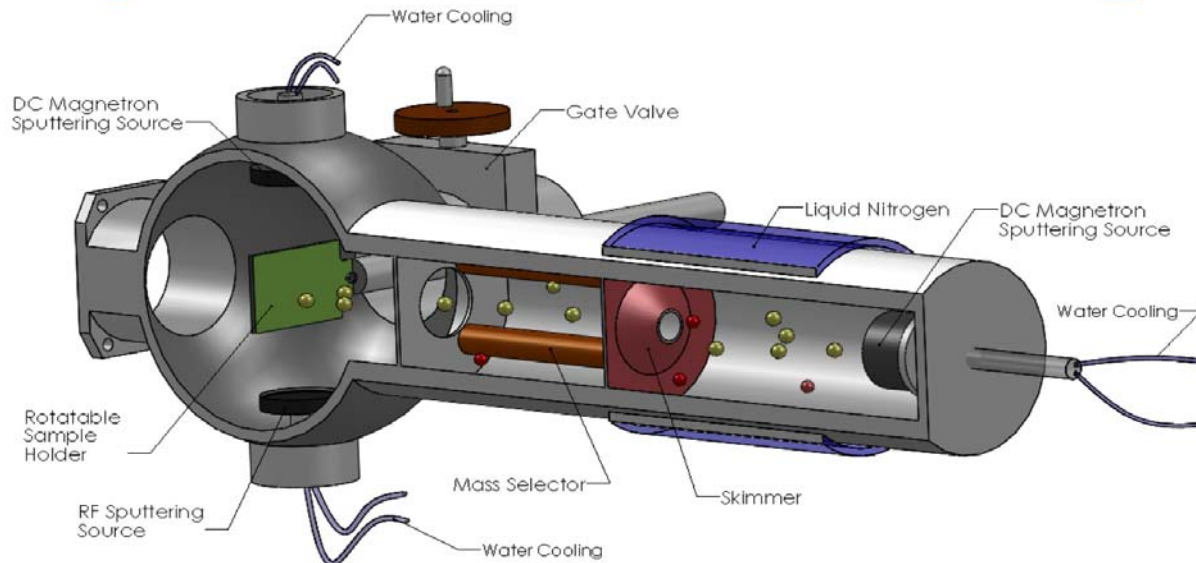


Figure 11. Schematic of cluster deposition system for producing nano-particulate of magnet alloys.

In the past year, focus was placed on synthesis and self-assembly of ferromagnetic FePt and Fe nano-particles to demonstrate that self-assembly is a future approach to high performance dual phase exchange-spring nano-composite magnets containing non-rare earth nano-particles. Previously (Nature 2002), we have reported that self-assembly of FePt and Fe₃O₄ nano-particles followed by reductive annealing led to the formation of an exchange-spring FePt-Fe₃Pt nano-composite magnet with its (BH)_{max} enhanced by 37% compared with the single component FePt nano-materials. However, the high temperature annealing step caused serious nano-particles aggregation/sintering and inter-particle Fe/Pt diffusion. As a result, it is difficult to control size and composition of both hard and soft phases. In the current efforts, we plan to make ferromagnetic FePt and Fe nano-particles first, then assemble them into nano-composites without the high temperature thermal annealing process. If it is successful, we will be able to make exchange-spring FePt-Fe nano-composite magnets with both size and composition controlled and (BH)_{max} optimized. Figure 12 outlines the general method we used for preparing ferromagnetic face-centered

tetragonal (fct) FePt nano-particles. We first made super-paramagnetic face-centered cubic (fcc) FePt nano-particles via thermal decomposition of iron pentacarbonyl, Fe(CO)₅, and reduction of platinum acetylacetonate, Pt(acac)₂, with oleic acid and oleylamine as surfactant and diphyether as solvent. After the synthesis, we further coated fcc-FePt nano-particles with MgO by decomposing Mg(acac)₂ on the fcc-FePt nano-particle surface. With the robust MgO coating, the FePt/MgO nano-particles could be annealed at high temperature and the fcc to fct structure transformation was achieved within the MgO coating shell that was removed by washing with dilute HCl solution. Figure 12 A illustrates the synthesis. Figure 12 B and C are the TEM images of the 7 nm fcc-Fe₆₀Pt₄₀ and fct-FePt nano-particles, respectively. Although sintering was not excluded in these earlier tests, the fct-FePt nano-particles indeed were made by removing the MgO coating and they do show ferromagnetic properties (Figure 12 D). Work to improve the quality of the fct-FePt nano-particles is underway.

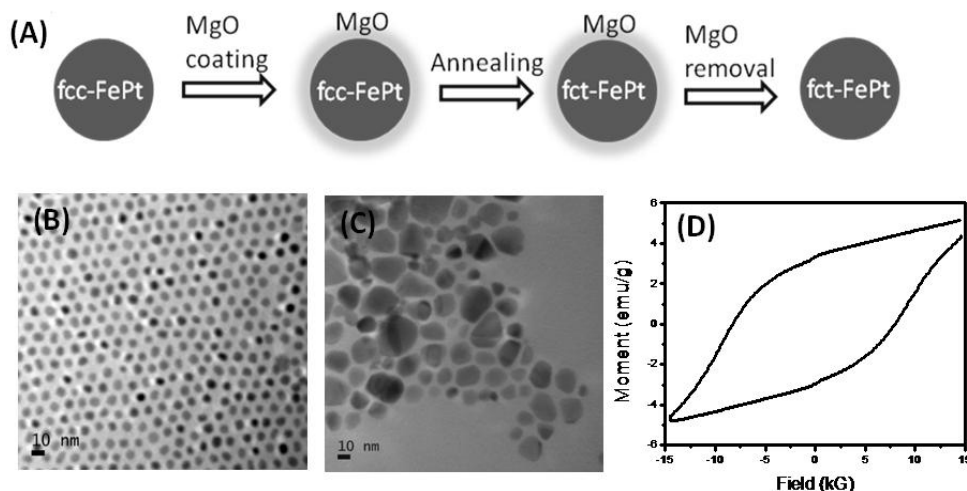


Figure 12. (A) Schematic illustration of the synthesis of fct-FePt nano-particles; (B) TEM image of the 7 nm fcc-Fe₆₀Pt₄₀ nano-particles; (C) TEM image of the fct-FePt nano-particles after MgO removal; (D) room temperature hysteresis loop of the fct-FePt nano-particles.

To make high moment Fe nano-particles, we have developed a method via thermal decomposition of Fe(CO)₅ with oleylamine and hexadecylamine-hydrochloric acid as surfactants and 1-octadecene as solvent.

The decomposition at 180°C yielded single crystalline monodisperse Fe nano-particles as proved by observation in the TEM (Figure 13 A) and XRD (Figure 13 B).

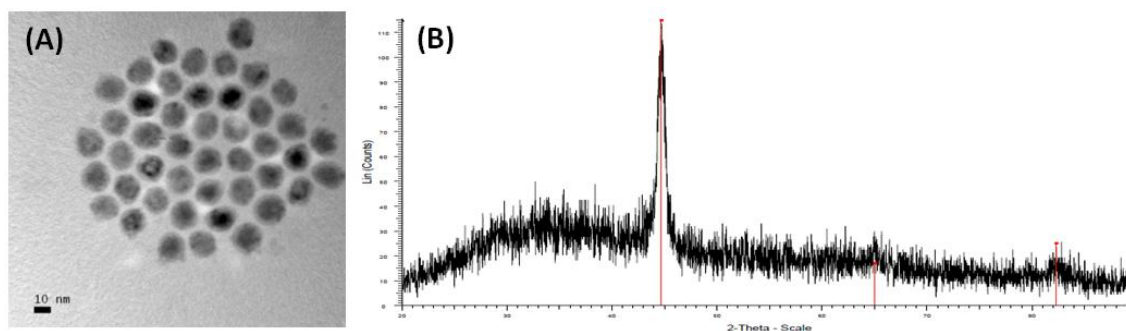


Figure 13. TEM image of the 14 nm Fe nano-particles; (B) XRD of the 14 nm FePt nano-particles showing typical body centered cubic (bcc) structure.

Task 2. Experimental Magnetic Materials Fabrication

Compilation of inventory of material processing capabilities for bulk magnet fabrication at each partner institution was begun for the project data library.

Investigation of the coercivity contributions in Alnico (dual phase spinodal Fe-Co/Ni-Al alloys) was started with a literature review on the contributions of various alloying additions, microstructure evolution, and processing. From

this review and discussions with Arnold Magnetic Technologies, the Alnico 5-7 alloy was selected for further analysis, since it has the highest energy product and a columnar microstructure. Alnico 5-7 samples were supplied by Arnold Magnetic Technologies at various stages of the heat treatment and thermal magnetization process and were sectioned and mounted for SEM characterization. A special sample of a finished magnet also was prepared from a section perpendicular to the columnar growth axis for orientation imaging microscopy

(OIM). The process of preparing TEM samples is ongoing, where a problem with demagnetization was recently solved, but determination of a suitable chemical etchant remains ahead. Full alloy sputtering targets also were prepared from larger arc-melted ingots for synthesizing experimental thin films of analogous Alnico compositions in an apparatus similar to that in Fig. 10. All samples have been distributed to the Characterization Group for collaborative microstructure and magnetic analysis.

A directional decomposition experiment is currently being developed, involving rods cut from finished Alnico 5-7 magnets. The intent of the experiment is to determine the effect of a thermal gradient on the microstructure of the magnet. The commercial production uses a magnetic field during the heat treatment to align the precipitates, improving the magnetic properties of the finished magnet. The experiment will examine if a thermal gradient can supplement or replace the magnetic field during the heat treatment.

The Theory Group was consulted on selection of a limited set of promising binary or ternary magnetic systems that are known to form anisotropic intermetallic phases or have other general interest for theoretical analysis.

Task 3. Analysis of Critical Magnet Material Constituents

A listing of potential magnet material constituents was compiled and representative commercial pricing and supply information was obtained for the purpose of preparing a position paper on the cost analysis and availability of several magnet constituents, starting with Co.

Progress on the 3 tasks in the Characterization Group studies in FY2010:

Task 1. Development of Data Sharing Mechanism for Characterization Results

Web-based data sharing methods and protocols were brought to the final stages of development to enable active comparison of results by all

partners for the same materials that are characterized by a full spectrum of characterization tools.

Task 2. Advanced Characterization Methods

Collaborations have been initiated at synchrotron sources (SLAC and APS) to develop the capabilities for a variety of high-throughput materials characterizations studies. Team members have contributed jointly to an NSLS-II beamline proposal entitled: "Multiscale XRD," which was approved for NSLS-II at Brookhaven. Preliminary experiments have been performed on combinatorial libraries of Fe-Co-W at beamline 11-3 at SLAC in collaboration with A. Mehta (see below). Contacts have been made at port 8-2 at SLAC for the possibility of doing X-ray magnetic circular dichroism (XMCD) on selected samples.

Task 3. Structural and Magnetic Characterization

Compilation of a complete inventory of magnet material characterization capabilities at each partner institution was begun to add to the project data library.

Bulk structural and microstructural analysis and magnetic measurements on preliminary samples from the Synthesis Group have been performed and shared with the team members for analysis of potential magnetic material candidates. In the case of the Co-Fe-W thin film tiles that resulted from combinatorial synthesis, synchrotron micro-diffraction (see Fig. 14) of tile regions from the spread indicates that the main diffraction peak corresponds to that of the (110) bcc phase across the spread. Near the Fe-Co binary line, the lattice constant of the bcc phase changes in an expected manner, namely that the lattice constant increases as Fe concentration is increased. As the W concentration is increased beyond ~10%, the diffraction peak width increases substantially consistent with the fact that W has a much higher crystallization temperature (Fig. 14).

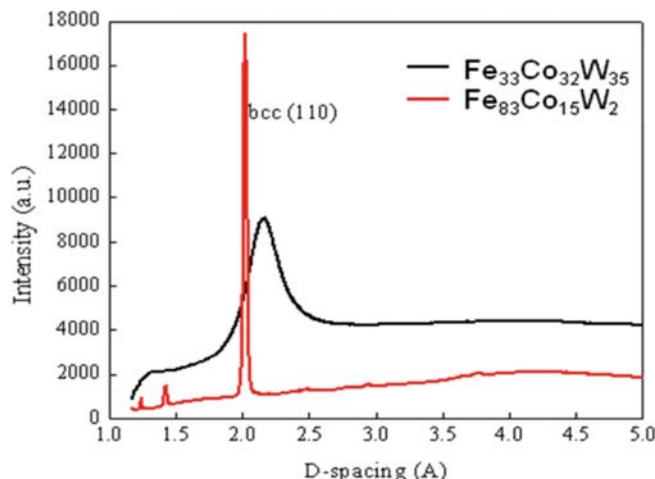


Figure 14. Synchrotron diffraction results of selected compositions. Peak broadening at higher W concentration indicates that the material has not fully crystallized at the annealing temperature of 600 °C.

From MH (hysteresis) loop characterization of the lower W concentration region (~2%), we found several compositions where the out-of-plane (OOP) MH loop displays significant coercive field (see Fig. 15). In particular, Fe₈₃Co₁₅W₂ shows a coercive field higher than 3 kOe. By carrying out angular dependent hysteresis loops on selected compositions, we found that the magnetization reversal

mechanism changes with changing W composition. We plan to repeat this experiment with new spreads where the composition region is focused to the lower W concentration and to study detailed composition dependent magnetic properties in order to confirm if there is indeed a promising high coercive field phase in this region.

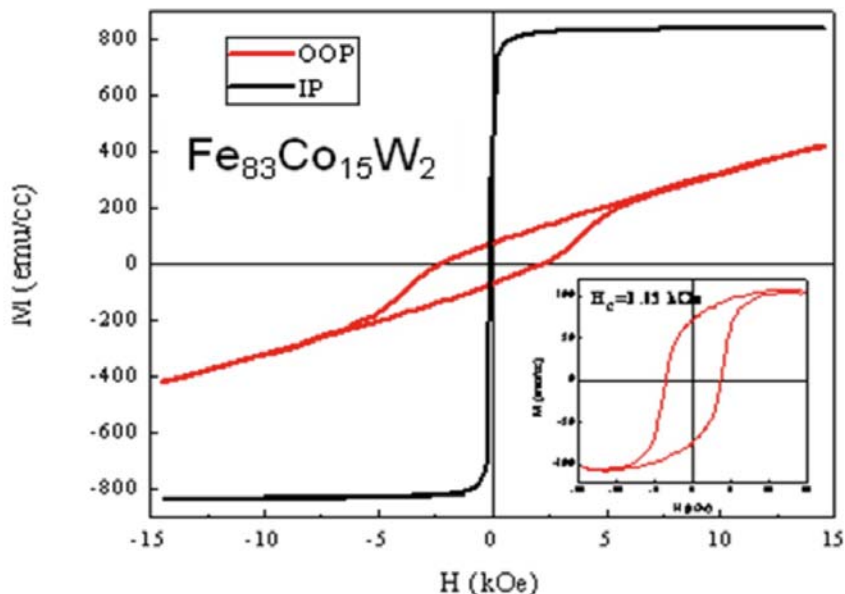


Figure 15. MH loops of one of the compositions that displays a large coercive field in the out of plane (OOP) direction. The inset is the out-of-plane loop with the “linear” background subtracted.

A proof of concept experiment (with Co-W initially) was performed using advanced electron microscopy to connect (correlate) cluster synthesis experiments and large-scale modeling.

Samples of the initial as-condensed Co-W particulate from the cluster deposition experiments were characterized by STEM, with an example shown in Fig. 16. From EDS

measurements in the STEM, the average composition of all of the nano-particulate appeared to be Co-21 at %W (near the intended composition), but significant composition segregation also was evident. The finest particulate (about 1 nm) appeared to be Co-75W and the larger clusters (3-5 nm) appeared to be Co-15W and amorphous. STEM images also suggested that the ~ 5 nm clusters were agglomerations of several clusters,

indicated by inhomogeneous contrast within the larger clusters. This is the first case that we have seen where two different cluster types precipitated from the gas phase. Modifications to the evaporation target and deposition parameters were made to address this issue, as well as a suitable annealing procedure to promote particulate homogenization and crystallization. The new clusters have yet to be analyzed.

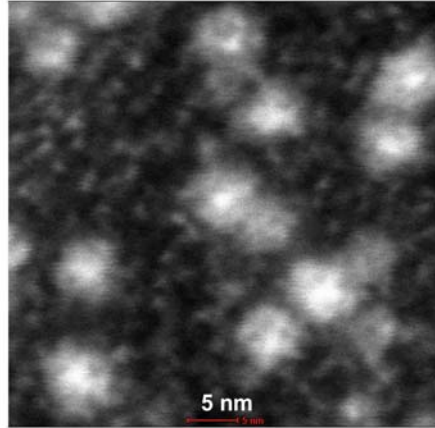


Figure 16. High resolution STEM micrograph of as-deposited Co-W nano-particulate from cluster deposition experiments.

Alnico 5-7 samples were imaged in the SEM (see Fig. 17). The micrographs were used to determine if significant grain growth occurred during the heat treatment process, as well as to determine the extent of columnar growth in the casting. OIM analysis (Fig. 17) was performed

on a wafer of finished Alnico 5-7. The results showed good alignment of the [001] with the growth direction of the grains, but random orientation of the grains in the transverse plane of the casting.

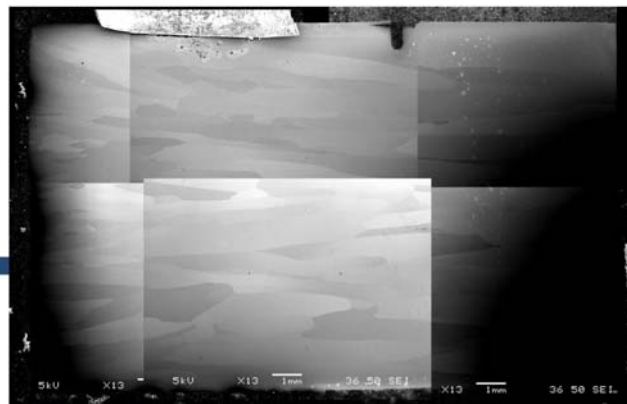
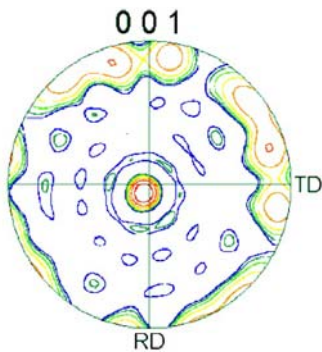


Figure 17. OIM pole figure (left) from transverse section of Alnico 5-7 that shows excellent grain alignment along the magnetization direction, but random orthogonal alignment. Also, a composite SEM micrograph of the transverse section is shown (right), where very large aligned grains are visible.

Conclusion

To enable anisotropic sintered MRE magnet development, refinement continued of the processing steps needed to make particulate with an average particle size of $\sim 3\mu\text{m}$, with lower oxygen contamination, and with a reduced Dy content, along with progress toward significant reduction of excess rare earth in the MRE alloy to reduce alloy cost and to help enhance final energy product. In subsequent progress, a new pressure-enhanced sintering process was developed specifically for MRE magnet alloys that enabled reduced temperature ($<850^\circ\text{C}$) sintering to eliminate the deleterious “core-shell” segregation pattern in the 2-14-1 phase grains (with Y-enrichment around the rim of each grain) in the finished magnets and to restore high temperature stability by returning to the preferred Y addition to the MRE. To enable anisotropic bonded MRE magnet development, application of a uni-axial pressure gradient on ribbon samples during crystallization proved promising and will be pursued further. In response to a request to initiate a new research thrust that goes beyond rare earth permanent magnets, a large new thrust was started within the project. As described in the progress elements above, a detailed plan was developed in two planned workshop sessions and the full team of research partners began a highly collaborative research program in April of 2010. The initial general plan to explore two parallel research tracks was followed, i.e., seeking improvement of the best existing non-RE magnet system, Alnico, and discovery of new non-RE magnetic phases, focused on Fe, Co, and Fe-Co systems. The first Alnico efforts are still focused on enhanced knowledge of coercivity mechanisms, but we will begin studies of increased control of microstructure and magnetic alignment next year. Initial work on new magnetic phase discovery involved theory and modeling of Fe, Co, and Fe-Co base compositions and started into selection of minor additives to accentuate magneto-crystalline anisotropy, searching for maxima in intrinsic magnetization, magnetic anisotropy, and Curie temperature. Micromagnetics modeling will probably commence next year. Several of the experimental magnet synthesis efforts generated

promising results and more detailed efforts will proceed next year. The suite of characterization tools for magnetic properties, microstructural analysis, and crystal structure determination proved very useful for feedback on the synthesis experiments and for general guidance to the theory and modeling efforts. Much more progress is anticipated in FY2011 since a full year of effort can be expended. It should be noted also that we have added a new industrial partner to our team, Arnold Magnetic Technologies, which should help to preserve our focus on eventual manufacturing and application of the non-RE permanent magnets that we develop.

Publications

W. Tang, Y. Q. Wu, K. W. Dennis, N. T. Oster, M. J. Kramer, I. E. Anderson, R. W. McCallum, *Magnetic properties and microstructure of gas atomized $\text{MRE}_2(\text{Fe, Co})_{14}\text{B}$ powder with ZrC addition ($\text{MRE} = \text{Nd} + \text{Y} + \text{Dy}$)*, Journal of Applied Physics (2009), 105(7, Pt. 2), 07A728/1-07A728/3.

Y. Q. Wu, W. Tang, M. J. Kramer, K. W. Dennis, N. T. Oster, R. W. McCallum, I. E. Anderson, *Correlation of the energy product with evolution of the nanostructure in the Y,Dy,Nd-(Fe, Co)-B magnetic alloy*, Journal of Applied Physics (2009), 105(7, Pt. 2), 07A720/1-07A720/3.

References

1. D. Dadon, Y. Gefen, and M. Dariel, "The texture of melt spun $\text{Fe}_{76}\text{Nd}_{16}\text{B}_8$ ribbons," *Magnetics, IEEE Transactions on*, vol. 23, pp. 3605-3606, 1987.
2. M. J. Kramer, N. Yang, R. W. McCallum, K. W. Dennis, and L. H. Lewis, "In situ determination of Nd-Fe-B crystallization pathways," *J. Appl. Physics*, vol. 91, pp. 8156-8158, 2002.
3. W. B. Kamb, "Theory of Preferred Crystal Orientation Developed by Crystallization under Stress," *The Journal of Geology*, vol. 67, pp. 153-170, 1959.

Patents

1. R. W. McCallum, Y-W. Xu, I. E. Anderson, K. W. Dennis, and M. J. Kramer, U.S. Patent Application (PCT) filed November 18, 2002, "Permanent Magnet Alloy with Improved High Temperature Performance," under examination.

Project 18517 – Combustion System Materials

Agreement 11752 – Materials for HCCI Engines

G. (Murali) Muralidharan, and Rick Battiste

(865)574-4281; fax: (865) 574-4357; e-mail: muralidhargn@ornl.gov

Bruce G. Bunting

Engineering Science and Technology Division

(865) 946-1512; fax: (865) 946-354; e-mail: buntingbg@ornl.gov

DOE Technology Manager: Jerry L. Gibbs

(202) 586-1182; fax: (202) 586-1600; e-mail: jerry.gibbs@ee.doe.gov

ORNL Technical Advisor: D. Ray Johnson

(865) 574-4556; fax: (865) 241-0411; e-mail: johnsondr@ornl.gov

Contractor: Oak Ridge National Laboratory, Oak Ridge, Tennessee
Prime Contract No.: DE-AC05-00OR22725

Objectives

- Identify and catalog the materials operating conditions in homogeneous charge compression-ignition (HCCI) engines and use computational design concepts to develop advanced materials for such applications.
- Interact with designers of HCCI engines and manufacturers of components in order to identify the components that will be affected by the harsh operating conditions resulting from the HCCI design.

Approach

- Identify engine components, currently used materials, and current operating conditions and compare them with the expected component operating conditions for HCCI engines.
- Demonstrate the feasibility of the “materials-by-design” approach for the highest-priority item. Improve material performance for HCCI applications through computational modeling and experimental validation.

Accomplishments

- Rotating beam tests confirm fatigue performance of down-selected commercial alloys
- Additional compositions have been prepared in small heats, their high temperature tensile properties have been evaluated, promising alloys have been identified, and microstructural characterization has been performed
- One larger batch of alloy has been prepared and fatigue tests will be performed in FY 2011

Future Direction

- Continue to communicate with automotive companies, valve manufacturers, and other teams on the progress made through computational design.
- Fatigue properties of new ORNL alloys will be evaluated using rotating beam tests and/or fully-reversed fatigue tests
- Additional alloys will be prepared in larger heats to enable fatigue testing

Introduction

There has been an increasing interest in HCCI combustion in recent years because of its potential to increase engine combustion efficiency and reduce

emissions. However, the use of HCCI combustion will subject the engine components to significantly higher temperatures and pressures. The temperatures for diesel engines will reach over 1600°F, and pressure may reach > 2000 psi, which is approximately

four times that of the normal combustion engine. Such severe engine operating conditions will require a significant improvement in materials performance in order to take advantage of the HCCI engine concept. This project deals with identifying materials requirements for HCCI engines for automotive and truck applications and the development of advanced, yet cost-effective, materials through computational design.

“Materials-by-design” is an Oak Ridge National Laboratory (ORNL) concept that encompasses a collection of materials-related techniques including modeling, correlation, and materials modification. The premise behind materials-by-design is that mechanical properties are correlated to microstructure and phase chemistry. The phase composition and microstructure can be achieved through thermodynamic equilibrium or through non-equilibrium techniques such as quenching, rapid casting solidification, or mechanical working. These characteristics can then be correlated to desired mechanical properties through equilibrium thermodynamics or through a variety of correlation techniques. The correlations allow untested compositions or treatments to be modeled so that desired trends can be rapidly established. Small heats of targeted materials can then be processed to confirm the modeled properties and to broaden the correlation data base.

Finally, there are several techniques, such as magnetic processing or low-temperature carburizing, that can be applied to allow further modification and optimization of desired properties. Materials-by-design is ideally suited to cast materials and heavily thermally processed materials (e.g., stainless steels, Ni alloys, cast irons, alloy steels, and brazed wrought aluminum alloys), and the concept has been successfully applied in such diverse areas as high-temperature furnace components, exhaust valves, exhaust manifolds, and tube fittings. Figure 1 and Table 1 provide an outline of the materials-by-design approach and a summary of the techniques that can be applied.

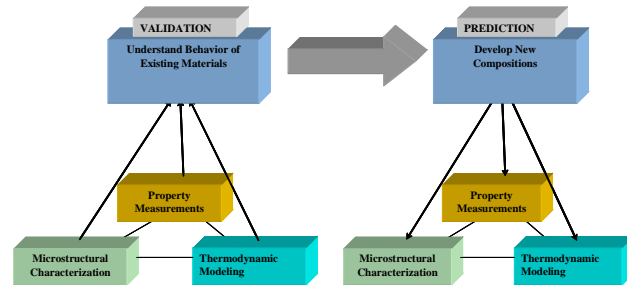


Figure 1. Overall approach for materials-by-design.

In our approach, we examined critical heavy-duty diesel engine materials and identified means to reduce their cost for acceptance in HCCI applications. This was accomplished through the following tasks:

Task 1. Identify critical material requirements for HCCI engines based on their operating conditions. This task will be accomplished through interactions with advanced engine and component designers. The interactions will include personal visits to six companies: Caterpillar, Cummins Engine, Deer, International Truck, Eaton Corp., and General Motors. Visits will be supplemented by a literature search, a review of advanced engine design studies, and follow-up discussions afterward. The key outcomes from this task will include (1) identifying operating conditions for advanced engine concepts, with a focus on the HCCI concept; (2) identifying components most affected by these operating conditions; (3) identifying currently used materials, new requirements, and performance targets; and (4) ranking the highest-priority items for study by the materials by design approach.

Task 2. Demonstrate the feasibility of materials-by-design approach for the highest-priority item. In this task, we will identify the details of the currently used material for the highest-priority item. Specifically, we will examine material compositions, processing methods, mechanical properties, corrosion properties, and cost. Based on the available mechanical properties data, microstructural analysis, and thermodynamic phase stability calculations, we will identify the underlying mechanism that delivers the current properties.

Table 1. ORNL materials-by-design toolbox

Modeling	Experimentation	Characterization
Thermodynamic modeling of material properties vs alloy composition	Ultra-high-gauss magnetic stabilization of alloy steels	Advanced microscopy techniques
Neural-network modeling of diverse, nonlinear materials properties and process variations	Low-temperature gas carburization of finished components Ability to produce small quantities of materials and fabricate them into test bars for property measurements and production of prototype components by a variety of methods, including sand and die casting, extrusion, forging and rolling	X- ray and neutron scattering Surface and bulk property measuring techniques
Detailed microstructure based empirical modeling		
Non-equilibrium modeling of solidified structures		
Extrapolation of properties from simple alloy systems to complex systems using interaction parameters		

Task 3. Improve materials performance for HCCI application through computational modeling and experimental validation.

In this task, we will use computational modeling (key basis for the material-by-design concept) to identify compositions that will deliver the desired phases for two purposes: (1) improving property performance and (2) finding alternatives to reduce cost for both current and improved performance. The outcome of the analysis will be validated through experimentation. The validation will be carried out in the following steps:

1. Prepare compositions identified based on computational design in 1-lb heats for microstructural analysis and very limited property determination; compare the results with output based on computational analysis for validation.
2. Scale up the validated composition into 20-lb to 100-lb heats and cast them into ingots for processing trials. In most cases, the material is expected to be used in the wrought condition. However, if it is to be used in the cast condition, we will save part of the ingots for analysis of as-cast properties.
3. Subject cast ingots to processing steps that are currently used by industry. Develop optimum processing and heat-treatment conditions to obtain the desired microstructure.

4. Carry out microstructural analysis and mechanical properties analysis on the material processed and heat-treated with optimum conditions.
5. Prepare prototype components for HCCI engine tests.

Extensive interaction with industrial partners will occur during all three tasks. This collaboration is expected to result in the rapid transfer of materials improvement from this project to industry for use in HCCI and other advanced engine concepts.

Results

Materials Development through Computational Design

Ni-based alloys have been identified as potential candidates for improved valve materials. There is particular interest in increasing the operating temperature of exhaust valves to about 1600°F (870°C). High temperature fatigue strength has been identified as a critical factor in determining the performance of these alloys in the valve application. An evaluation of the microstructure of various Ni-based alloys and correlation with limited information on the fatigue properties that are available show that the volume fraction of the γ' phase is likely to be a dominant factor in determining the performance of these alloys at high temperatures.

Since the size of the strengthening precipitates is also critical, it is anticipated that the kinetics of coarsening this phase would also be influential in the long-term performance of the alloys in this application. Based upon discussions with various users and suppliers, a range of Ni-based alloys with potentially varying weight fractions (or volume fractions) of γ' have been identified in efforts to correlate the fatigue properties with the microstructure of the alloys. To obtain initial information on the microstructures of these alloys at equilibrium, thermodynamic calculations have been carried out using JMatPro V4. Comparison of the results of the calculations showed that all alloys have a matrix of γ with the major strengthening phase as γ' . One or more carbide phases such as $M_{23}C_6$, MC, and M_7C_3 may also be present in different alloys. The primary difference between the microstructures of the various alloys is in the weight percent of the γ' phase at a given temperature and the highest temperature at which the γ' phase is stable in the different alloys.

Fatigue Property Measurement

In order to develop relationships between the microstructures of the alloys and their mechanical properties, high-temperature fatigue property data were obtained on all down-selected alloys as a part of the project. Load-controlled, fully-reversed fatigue tests were conducted *in-situ* at a temperature of 870°C. Stresses of 21.8 (150) Ksi (MPa), 29 (200 MPa), 39.9 (275 MPa), 43.5(300 MPa), 50.8(350 MPa), and 54.4(375 MPa) were used to investigate the fatigue performance of the alloy. Since rotating beam tests are commonly used to specify required materials properties for applications in valves, a new rotating beam testing equipment was installed at ORNL. Correlations were obtained between results from rotating beam tests and uniaxial fatigue tests. Using the approximate correlation, several alloys were identified as candidates for high temperature valve applications. This year further rotating beam tests were performed on these alloys to confirm their fatigue lives as measured using the rotating beam tests. These results are shown in Figure 2.

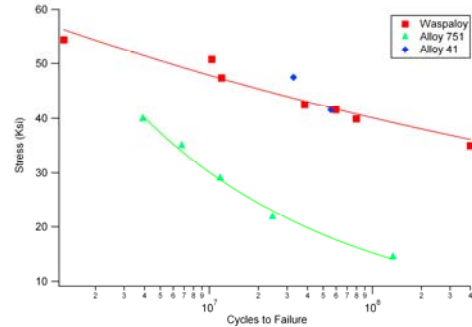


Figure 2. Results from rotating beam tests on several commercial alloys confirm conclusions on the potential for commercial alloys with data obtained from uniaxial fully-reversed fatigue tests.

Development of Improved Alloys through Computational Modeling

Using the microstructures of these alloys as a guide, computational thermodynamics was used to identify additional alloys with microstructure similar to the commercial alloys with desirable properties. In contrast to the commercially available alloys with Ni-contents in the range of 50 wt.% to 60 wt. %, the Ni-content in these alloys ranges from about 30 wt. % to 45 wt. % with the potential to achieve comparable properties. This implies that the alloys will be of lower cost but comparable mechanical properties.

Based upon the results of alloy design, small batches of alloys were cast. Subsequent to casting, these alloys were homogenized, and rolled at high temperatures. Small tensile specimens were machined from these alloys and tensile tests were conducted *in-situ* at 870°C. Several new alloys were cast in FY 2010 and tensile tests were conducted on the alloys at 870°C in the aged condition. Alloys were characterized using optical microscopy. Selected alloys were also characterized using scanning electron microscopy. Figure 3 shows the results of some of the microscopy and tensile tests performed on the alloys at 870°C. One of the alloys from the newly developed alloys was also downselected for the preparation of a larger sized heat. It was cast under inert gas cover and then mechanically processed into a plate for further machining. Figure 4 shows an optical image of the processed plate. Fatigue specimens have been machined and will be tested in the following year. Additional alloys are also being prepared in small heats to continue the

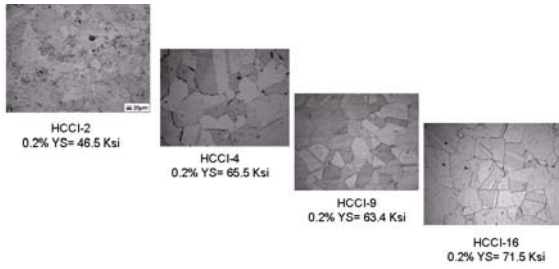


Figure 3. Results from optical microscopy and high temperature tensile tests show several promising alloys.

development of improved alloys. Tensile tests on these alloys will be completed in FY 2011.

Conclusions

- Rotating beam tests confirm the high temperature fatigue properties of several commercial Ni-based alloys
- Computational thermodynamics models have been used to identify several promising alloy compositions with the potential to have desirable fatigue performance at higher temperatures and small heats have been cast
- One larger batch of alloy has been prepared and fatigue tests will be performed in FY 2011

Agreement 8697 - NO_x Sensor Development

Leta Y. Woo and Robert S. Glass

Lawrence Livermore National Laboratory

P.O. Box 808, L-103

Livermore, CA 94551-9900

(925) 423-7140; fax: (925) (422-5844); e-mail: glass3@llnl.gov

DOE Technology Manager: Jerry L. Gibbs

(202) 586-1182; fax: (202) 586-1600; e-mail: jerry.gibbs@ee.doe.gov

Contractor: Lawrence Livermore National Laboratory, Livermore, California

Prime Contract No.: W-7405-Eng-48; LLNL-TR-418835

Objectives

- Develop an inexpensive, rapid-response, high-sensitivity and selective electrochemical sensor for oxides of nitrogen (NO_x) for compression-ignition, direct-injection (CIDI) exhaust gas monitoring
- Explore and characterize novel, effective sensing methodologies based on impedance measurements and designs and manufacturing methods that could be compatible with mass fabrication
- Collaborate with industry in order to (ultimately) transfer the technology to a supplier for commercialization

Approach

- Use an ionic (O²⁻) conducting ceramic as a solid electrolyte and metal or metal-oxide electrodes
- Correlate NO_x concentration with changes in impedance by measuring the cell response to an ac signal
- Evaluate sensing mechanisms and aging effects on long-term performance using electrochemical techniques
- Collaborate with Ford Research Center to optimize sensor performance and perform dynamometer testing

Accomplishments

- Modified sensor designs to successfully improve mechanical robustness for withstanding engine vibrations and prevent failure during engine/vehicle dynamometer testing
- Developed a preliminary strategy to mitigate major noise factors and improve accuracy by quantifying effects of temperature, water, and oxygen to generate a numerical algorithm
- Publications/Presentations:
 - L.Y. Woo, et al. "Effect of electrode material and design on sensitivity and selectivity for high temperature impedancemetric NO_x sensors." *J. Electrochem. Soc.*, 157(3):J81-87, 2010
 - Oral presentations at the American Ceramic Society 34th International Conference and Exposition on Advanced Ceramics and Composites; the 217th Electrochemical Society Meeting; and the 2010 DOE Vehicle Technologies and Hydrogen Programs Annual Merit Review and Peer Evaluation Meeting

Future Directions

- Continue developing more advanced prototypes suitable for cost-effective, mass manufacturing
 - Continue evaluating performance of prototypes, including long-term stability and cross-sensitivity, in laboratory, dynamometer, and on-vehicle tests
 - Continue efforts to initiate the technology transfer process to a commercial entity
-

Introduction

NO_x compounds, specifically NO and NO₂, are pollutants and potent greenhouse gases. Compact and inexpensive NO_x sensors are necessary in the next generation of diesel (CIDI) automobiles to meet government emission requirements and enable the more rapid introduction of more efficient, higher fuel economy CIDI vehicles.¹⁻³

Because the need for a NO_x sensor is recent and the performance requirements are extremely challenging, most are still in the development phase.⁴⁻⁶ Currently, there is only one type of NO_x sensor that is sold commercially, and it seems unlikely to meet more stringent future emission requirements.

Automotive exhaust sensor development has focused on solid-state electrochemical technology, which has proven to be robust for in-situ operation in harsh, high-temperature environments (e.g., the oxygen stoichiometric sensor). Solid-state sensors typically rely on yttria-stabilized zirconia (YSZ) as the oxygen-ion conducting electrolyte and then target different types of metal or metal-oxide electrodes to optimize the response.²⁻⁶

Electrochemical sensors can be operated in different modes, including amperometric (a current is measured) and potentiometric (a voltage is measured), both of which employ direct current (dc) measurements. Amperometric operation is costly due to the electronics necessary to measure the small sensor signal (nanoampere current at ppm NO_x levels), and cannot be easily improved to meet the future technical performance requirements. Potentiometric operation has not demonstrated enough promise in meeting long-term stability requirements, where the voltage signal drift is thought to be due to aging effects associated with electrically driven changes, both morphological and compositional, in the sensor.⁷

Our approach involves impedancemetric operation, which uses alternating current (ac) measurements at a specified frequency. The approach is described in detail in previous reports and several publications (See Ref. 8-11). Briefly, impedancemetric operation has shown the potential to overcome the drawbacks of other approaches, including higher sensitivity towards NO_x, better long-term stability, potential for subtracting out background interferences, total NO_x measurement, and lower cost materials and operation.⁸⁻¹¹

Past LLNL research and development efforts have focused on characterizing different sensor

materials and understanding complex sensing mechanisms.⁸⁻¹¹ Continued effort has led to improved prototypes with better performance, including increased sensitivity (to less than 5 ppm) and long-term stability, with more appropriate designs for mass fabrication, including incorporation of an alumina substrate with an imbedded heater.

Efforts in the last year to further improve sensor robustness have led to successful engine dynamometer testing with prototypes mounted directly in the engine manifold. Previous attempts had required exhaust gases to be routed into a separate furnace for testing due to mechanical failure of the sensor from engine vibrations. A more extensive cross-sensitivity study was also undertaken this last year to examine major noise factors including fluctuations in water, oxygen, and temperature. The quantitative data were then used to develop a strategy using numerical algorithms to improve sensor accuracy.

The ultimate goal is the transfer of this technology to a supplier for commercialization. Due to the recent economic downturn, suppliers are demanding more comprehensive data and increased performance analysis before committing their resources to take the technology to market. Therefore, our NO_x sensor work requires a level of technology development more thorough and extensive than ever before.

Background

For an electrochemical cell with two electrodes, impedancemetric sensing requires that at least one of the electrodes act as the “sensing” electrode with preferable response to NO_x over other gas phase components. This contrasts to the case in potentiometric sensing, which relies on differential measurements between the two electrodes. Therefore, the impedancemetric sensor design is more flexible and can either contain one sensing electrode and one counter (i.e., non-sensing) electrode, or two sensing electrodes. It opens up the opportunity to use a greater variety of materials.

Both electrode composition and microstructure influence sensitivity, which relies on limiting the oxygen reaction on the electrode so that the NO_x reaction can be resolved.⁹⁻¹¹ Impedancemetric sensing is possible with a variety of electrode materials, both metal and metal oxides, that meet general sensor criteria, which include a dense microstructure and appropriate composition to limit the catalytic activity towards oxygen.¹⁰⁻¹¹

Impedance is defined as the measured response to an alternating current and is a complex quantity with both magnitude and phase angle information. The phase angle has been found to provide a more stable response at higher operating frequencies and is chosen as the sensor signal.⁸⁻¹¹

In previous work, impedancemetric sensing of either gold or strontium-doped lanthanum manganite (LSM), an electronically conducting metal oxide, electrodes was investigated in laboratory and engine testing. Preliminary results indicated that gold electrodes have good stability and the potential for low water cross-sensitivity, but also have a higher thermal expansion coefficient and lower melting temperature than the YSZ electrolyte, which limit processing flexibility. LSM electrodes have high melting temperatures and better thermal expansion match with YSZ, but have shown more water cross-sensitivity than gold.

Previous work also evaluated more advanced prototypes incorporating alumina substrates with imbedded heaters, provided by Ford Motor Company. Figure 1a shows the substrate with the sensor located at one end with leads located on the opposite end designed for packaging into a protective sensor housing (Fig. 1b) suitable for directly mounting into the exhaust manifold.

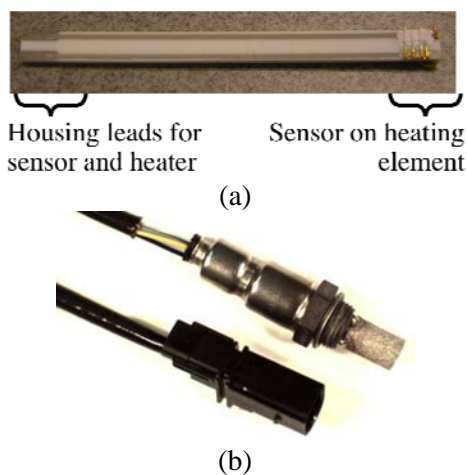


Figure 1. Picture of (a) alumina substrate with imbedded heater, provided by Ford Motor Company, suitable for packaging into (b) protective sensor housing.

Experimental

Two different sensing materials, Au and LSM, were investigated. Figure 2a shows a schematic of a prototype using Au wire as the sensing electrode and alumina with an imbedded Pt resistive heater as the

substrate (70 mm × 4 mm × 1 mm, see Fig. 1a). The substrate has a total of four leads, two leads for the Pt resistive heater located on one side, and two leads for the sensor located on the opposite side.

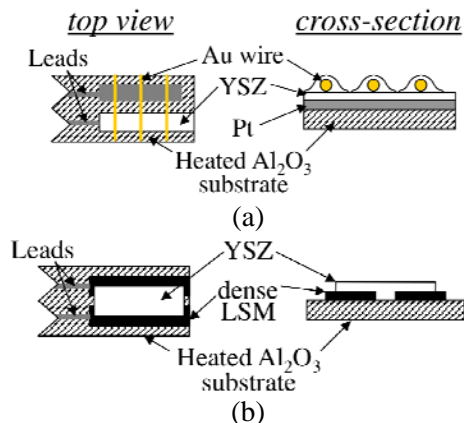


Figure 2. Schematic of NO_x prototype sensors using either (a) Au wire or (b) dense LSM as the sensing electrode.

One of the substrate leads contacted the Pt counter electrode. Ytria-stabilized zirconia (YSZ, 8 mol % yttria doping) slurry was then applied on top of the Pt. Au wires were then added and additional YSZ slurry was applied on top of the wires with the entire assembly fired at 1000°C to produce the porous YSZ electrolyte. The second substrate lead for the sensor housing contacted the Au wire.

Figure 2b shows a schematic of the prototype using LSM as the sensing electrode. A dense pellet was prepared with commercial (La_{0.85}Sr_{0.15})_{0.98}Mn oxide powder (Praxair) by pressing in a uniaxial die and sintering at 1250°C. Two pieces of LSM (6 mm × 2 mm × 1 mm) were machined and attached to the top of the substrate using Pt paste and fired to 1200°C. YSZ slurry was applied on top of the dense LSM pieces and the assembly fired at 1000°C.

Heater voltage was set between 9-9.5 V, which corresponded to approximately 600 to 650°C. The exact temperature corresponding to the heater voltage was not known, but was correlated with the behavior of similar prototypes that underwent furnace testing. Future prototypes may incorporate resistive temperature detectors to more accurately determine temperature.

A more extensive laboratory study of the Au wire prototype was performed using an alumina substrate (10 mm × 10 mm × 0.5 mm) without imbedded heaters. The alternative substrate was more suitable for controlled temperature testing in a tube

furnace. The sensor geometry was similar to that shown in Fig. 2a.

Gas composition was controlled in laboratory testing by mixing air, N_2 , NO, and ammonia (NH_3) using a standard gas handling system equipped with thermal mass flow controllers. Humidity was controlled using a water injection system monitored with a humidity sensor.

Dynamometer testing of real diesel exhaust was performed at Ford Research Center using an engine test cell fitted with a urea-based selective catalytic reduction (SCR) system for reducing NO_x emissions. The exhaust gas composition was analyzed with Fourier Transform Infrared (FTIR) spectroscopy. The test setup also included a commercially available NO_x sensor located alongside the prototype. Electrochemical measurements were performed using a Solartron 1260 Impedance Analyzer where the phase angle response at 5 Hz and 100 mV excitation amplitude was chosen as the sensor signal.

Results and Discussion

Engine dynamometer testing

Previous prototype designs lacked the necessary mechanical robustness for mounting directly to the exhaust manifold during engine dynamometer testing. Instead, exhaust gases had to be routed into a separate test setup. Real engine conditions, including vibrations, caused either the Au wire or dense LSM to detach from the substrate. To improve adhesion, an additional ceramic adhesive was used to anchor the Au wire and dense LSM to the substrate.

Testing was performed on a laboratory test stand at Ford Motor Company both prior to and after the prototypes being directly mounted into the exhaust manifold and operated for several hours under real-world engine conditions. Figure 3 shows results for the Au wire and LSM prototypes on the Ford laboratory test stand in 4% O_2 and 4% H_2O with 30 sec. pulses of 20 ppm NO.

The results in Fig. 3 show reproducible responses before and after several hours of diesel engine dynamometer testing. The higher sensitivity of the Au wire prototype compared to the LSM can be explained by previous results indicating that LSM has larger oxygen catalytic activity and therefore lower sensitivity when operated at similar temperatures as the Au wire prototype.¹¹ The modification of sensor prototypes with the addition of the ceramic

adhesive successfully improved mechanical stability and robustness.

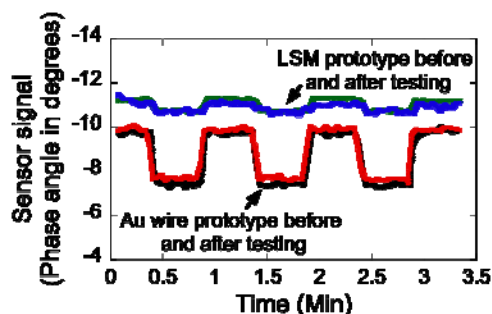


Figure 3. Sensing behavior of Au wire and LSM prototypes in 4% O_2 and 4% H_2O with 30 sec. pulses of 20 ppm NO prior to (black and green curves) and after (red and blue curves) being operated directly mounted into the exhaust manifold.

Evaluation on the Ford laboratory test stand after engine testing not only indicated improved sensor robustness, but was also used to investigate NH_3 cross-sensitivity. Figure 4 shows results of testing NH_3 cross-sensitivity in 10.5% O_2 and 4% H_2O with 30 sec. pulses of 50 ppm NO, 50 ppm NH_3 , or 50 ppm of both NO and NH_3 . The gas flow profile sequence is identified in Fig. 4a. In Fig. 4b, the response of the Au wire prototype (shown by the black curve) had higher sensitivity to NH_3 than NO, where only NH_3 was measured when both NO and NH_3 were added. In Fig. 4b, and in more detail in Fig. 4c, the response of the LSM prototype (shown by the green curve) had higher sensitivity to NO than NH_3 , with more selectivity to NO when both were added.

The results on the Ford laboratory test stand were used to explain the results from the dynamometer engine testing. In all cases, engine testing resulted in the generation of less than a few ppm of NO_2 ; therefore, only NO concentrations are shown. Figure 5a and 5b show engine test results for the LSM and Au wire prototypes, respectively, where the red curve indicates the sensor response and corresponds to values on the left axis. The blue curve indicates the commercial NO_x sensor tested alongside in the manifold and corresponds to values on the right axis. The green curve indicates the NO concentration from gas analysis (FTIR) and also corresponds to values on the right axis.

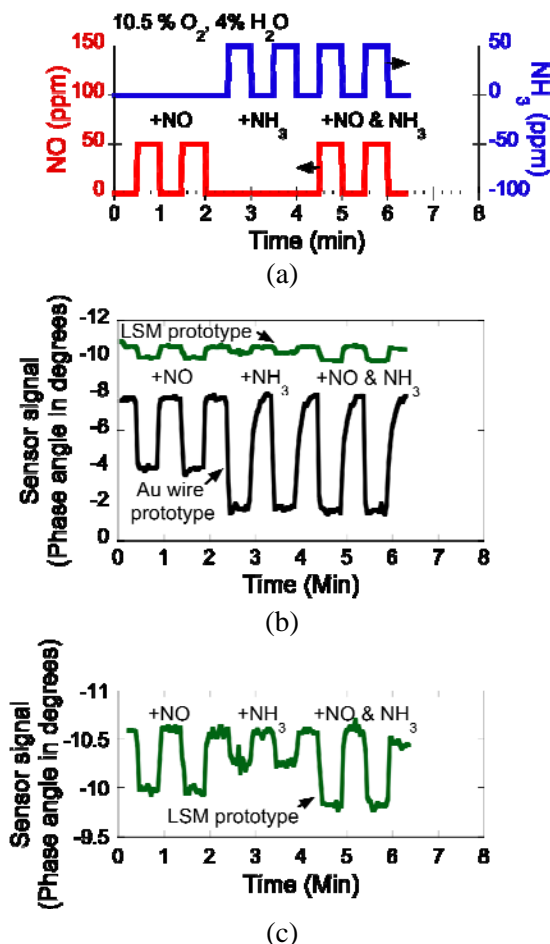


Figure 4. (a) Gas flow profile used for testing NH₃ cross-sensitivity with 30 sec. pulses of 50 ppm NO, 50 ppm NH₃, or 50 ppm of both NO and NH₃. (b) Measured response of Au wire and LSM prototypes and (c) expanded data for LSM prototype showing more detail.

The response of the LSM prototype in Fig. 5a had good correlation with both the commercial sensor and the gas analysis. The bottom of Fig. 5a also shows the measurement of NH₃ concentration from the gas analysis (the green curve corresponding to values on the right axis). In the bottom of Fig. 5a, from about 23 to 30 min., the NH₃ concentration increases from about 10 to 30 ppm with no change in the NO concentration. The commercial sensor, shown by the blue curve at the top of Fig. 5a, also increased from 23 to 30 min and indicated cross-sensitivity to NH₃. In contrast, the LSM prototype did not seem affected by changes in NH₃, with the response remaining flat from 23 to 30 min.

The response of the Au wire prototype in Fig. 5b did not correlate as well as the LSM prototype did with the commercial sensor and the gas analysis. Furthermore, the commercial sensor in the top of

Fig. 5b (blue curve) also did not correlate well with the gas analysis (green curve). The behavior can be explained by the measured NH₃ concentration shown in the bottom of Fig. 5b by the green curve. High levels of NH₃, from 20 to 75 ppm, were measured. In Fig. 5b, both the Au wire prototype and commercial sensor detected changes in NH₃ concentration, including the spike in concentration at 20 to 23 min. Additionally, the Au wire prototype showed more selectivity to NH₃ than to NO, with the sensor response (red curve in bottom of Fig. 5b) correlating with the NH₃ concentration from gas analysis (green curve) instead of changes in the NO concentration (green curve in top of Fig. 5b).

The composition of real diesel exhaust was influenced by the history and age of the engine and exhaust after-treatment system. Testing revealed that the dynamometer engine test stand had significant “slip” where the exhaust after-treatment was unable to catalyze the NO_x reactions resulting in larger amounts of unreacted NH₃. Vehicle testing with better quality exhaust systems are planned that should yield lower levels of both NO and NH₃.

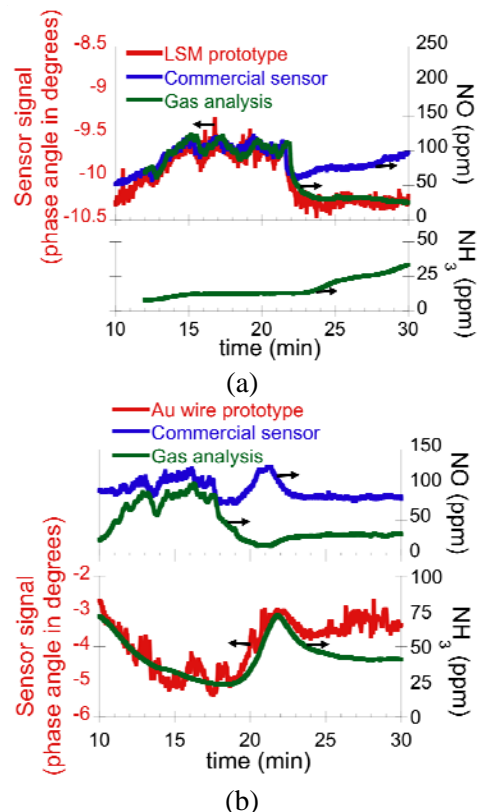


Figure 5. Engine dynamometer testing of (a) LSM and (b) Au wire prototypes mounted directly into exhaust manifold.

Au wire prototype: Strategy for improving accuracy using numerical algorithms

A more extensive study of the cross-sensitivity of the Au wire prototype was performed using a sensor fabricated on an alumina substrate (10 mm × 10 mm × 0.5 mm) without imbedded heaters. The alternative sensor design was more suitable for controlled temperature testing in a tube furnace. The sensor geometry was similar to that shown in Fig. 2a. The major noise factors were investigated which included temperature, water, and oxygen.

Before beginning the cross-sensitivity evaluation, the Au wire prototype was initially aged at 650°C for 720 hrs under dry conditions and demonstrated stable and reproducible response. The prototype was then aged at 650°C for 96 hrs in about 2% H₂O before beginning the evaluation.

Figure 6 shows the sensing behavior of the Au wire prototype design (top red curve) while the bottom blue curve shows the corresponding changes in the water concentration measured during testing. The response of the prototype for different oxygen and ppm NO concentrations was not influenced by spikes in the water concentration of about 2 to 4% indicating low water cross-sensitivity. Gas flow profiles stepped through 2, 10.5 and 18.9% O₂, with changes in NO concentration at each oxygen level (100, 50, 20, 10 ppm). The gas flow profile was used at three water concentrations (2, 4 and 6%) and three temperatures (625, 650, and 675°C). Measurements indicated water cross-sensitivity was minimized for operation at the intermediate temperature of 650°C.

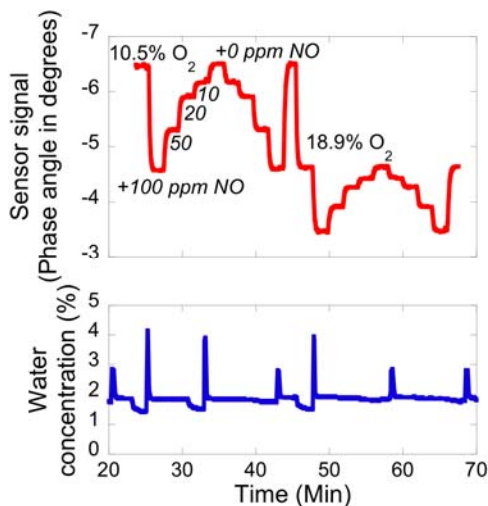


Figure 6. Sensing behavior of Au wire prototype (red curve) on an alumina substrate at 625°C in varying O₂ and NO concentrations, with corresponding changes in H₂O concentration (blue curve).

The data collected for the cross-sensitivity evaluation was used to develop a mathematical procedure for minimizing interferences, which can be summarized in three general steps. The first step is choosing an operating temperature to minimize water interference, which was found to be 650°C. The temperature can be assumed to be controlled to approximately ±5°C, and measurable to within 1°C.

The oxygen signal can be obtained using a separate measurement at a different frequency, as described in more detail in last year’s report as well as in a previous publication.⁸ At 1 kHz and T = 650°C, the prototype does not respond to NO and only responds to oxygen, allowing an independent measurement of the oxygen concentration. Figure 7 shows how the sensor signal at 1 kHz (θ_{1kHz}) varies with oxygen concentration (%O₂). In Fig. 7, a linear curve fit (dotted line) is shown and given by the following equation:

$$\%O_2 = \frac{\theta_{1kHz} + 6.08}{0.0305} \quad (1)$$

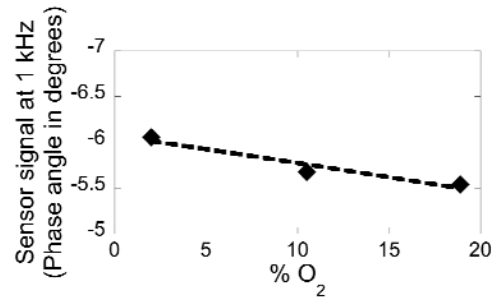


Figure 7. Measured sensor signal at 1 kHz (θ_{1kHz}) for different O₂ concentrations, with linear curve fit (dotted line).

Using both the measured temperature and oxygen, the second step then involves using additional numerical relationships, derived from fitting the data collected in the cross-sensitivity evaluation, to calculate the expected sensor signal for zero NO_x, or when NO_x is not present at the known temperature and oxygen level.

Figure 8a shows how the sensor signal (θ_{O_2}) changes with oxygen concentration at 650°C when NO_x is not present, and the corresponding polynomial fit (dotted line) is given by the following equation:

$$\theta_{O_2} = -14 + 1.2(\%O_2) - 0.035(\%O_2)^2 \quad (2)$$

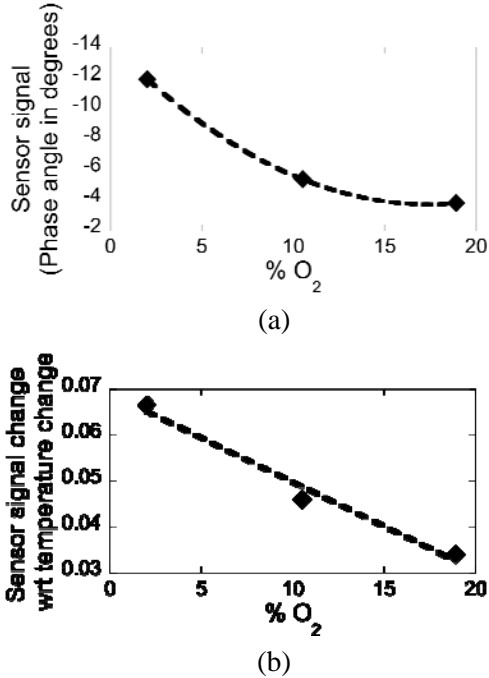


Figure 8. Influence of %O₂ at 650°C when NO_x is not present on the (a) sensor signal (θ_{O_2}), and on the (b) sensor signal with respect to (wrt) changes in temperature ($\Delta\theta/\Delta T$). Curve fits are shown as dotted lines.

Figure 8b shows how changes in the sensor signal with respect to changes in temperature ($\Delta\theta/\Delta T$) are influenced by oxygen concentration at 650°C when NO_x is not present, and the corresponding linear fit (dotted line) is given by the following equation:

$$\left(\frac{\Delta\theta}{\Delta T}\right)_{O_2} = 0.069 - 0.0019(\%O_2) \quad (3)$$

The two values calculated by the relationships in Fig. 8a and 8b (Eqs. 2 and 3) and the measured temperature ($T_{measured}$) are then used to calculate the zero NO_x (θ_{ONOX}) using the following equations:

$$\theta_{ONOX} = \theta_{O_2} + \left(\frac{\Delta\theta}{\Delta T}\right)_{O_2} \Delta T \quad (4)$$

$$\Delta T = T_{measured} - 650 \quad (5)$$

Finally, in the third step, the difference between the calculated zero NO_x signal (θ_{ONOX}) and the actual measured NO_x signal ($\theta_{measured}$) is used to provide a measurement of the amount of NO_x that minimizes the influence of oxygen, water, and temperature.

Figure 9 shows how changes in the sensor signal with respect to changes in ppm NO ($\Delta\theta/\Delta NO$) are influenced by oxygen concentration at 650°C, and the corresponding polynomial fit (dotted line) is given by the following equation:

$$\left(\frac{\Delta\theta}{\Delta NO}\right)_{O_2} = 0.055 - 0.0050(\%O_2) + 0.00014(\%O_2)^2 \quad (6)$$

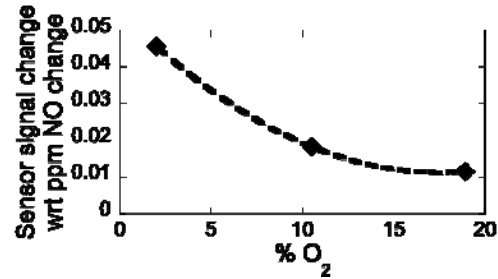


Figure 9. Influence of %O₂ at 650°C on the sensor signal with respect to (wrt) changes in ppm NO ($\Delta\theta/\Delta NO$) and the corresponding best fit (dotted line).

The value calculated by the relationship in Fig. 9 (Eq. 6) is then used to determine the amount of measured NO_x (ΔNO), where the influence of fluctuations in oxygen, water, and temperature are now minimized, using the following equations:

$$\Delta NO = \frac{\Delta\theta}{\left(\frac{\Delta\theta}{\Delta NO}\right)_{O_2}} \quad (7)$$

$$\Delta\theta = \theta_{ONOX} - \theta_{measured} \quad (8)$$

The cross-sensitivity relationships were also used to provide a rough estimate of sensor accuracy in terms of error or noise introduced by either temperature or water fluctuations. Since the measured sensor signal had a linear dependence on changes in both temperature and water concentration, changes in the sensor signal with respect to changes in ppm NO could be determined for changes in either temperature or water. The noise introduced varied with oxygen concentration, where the minimum noise occurred at 2% O₂. For oxygen concentrations ranging from 2 to 18.9%, noise from $\pm 1^\circ C$ temperature fluctuations decreased NO accuracy by ~ 1.5 to 3 ppm NO, and noise from $\pm 1\%$ H₂O fluctuations de-

creased NO accuracy by ~1.2 to 2.2 ppm NO. The noise values need further improvement to meet the desired ± 1 ppm, but are beginning to approach the accuracy required to meet emission limits.

Conclusions

Work in FY2010 included improving sensor robustness to allow testing of prototypes directly mounted onto the exhaust manifold. Previous attempts had required exhaust gases to be routed into a separate furnace for testing due to mechanical failure from engine vibrations. Real engine conditions caused either the Au wire or dense LSM to detach from the substrate. The modification of sensor prototypes by adding a ceramic adhesive successfully improved mechanical stability and robustness while simultaneously retaining the sensing performance.

Laboratory ammonia (NH₃) testing and engine dynamometer testing in real diesel exhaust were consistent with each other and found different behavior for the Au wire and LSM prototypes. The LSM prototype was found to be more selective than the Au wire prototype for NO when both NH₃ and NO were present.

Finally, a more extensive cross-sensitivity study was undertaken to examine major noise factors including fluctuations in water, oxygen, and temperature. The quantitative data were then used to develop a strategy using numerical algorithms to improve sensor accuracy. For oxygen concentrations ranging from 2 to 18.9%, noise from $\pm 1^\circ\text{C}$ temperature fluctuations decreased NO accuracy by ~1.5 to 3 ppm NO, and noise from $\pm 1\%$ H₂O fluctuations decreased NO accuracy by ~1.2 to 2.2 ppm NO.

References

1. N. Yamazoe, *Sens. Actuators, B*, **108**, 2 (2005).
2. R. Moos, *Int. J. Appl. Ceram. Technol.*, **2**, 401 (2005).
3. S. Akbar, P. Dutta, and C. Lee, *Int. J. Appl. Ceram. Technol.*, **3**, 302 (2006).
4. F. Menil, V. Coillard, and C. Lucat, *Sensors and Actuators B*, **67**, 1 (2000).
5. S. Zhuiykov and N. Miura, *Sens. Actuators, B*, **121**, 639 (2007).
6. J. W. Fergus, *Sens. Actuators, B*, **121**, 652 (2007).
7. S. -W. Song, L. P. Martin, R. S. Glass, E. P. Murray, J. H. Visser, R. E. Soltis, R. F. Novak, and D. J. Kubinski, *J. Electrochem. Soc.*, **153**, H171 (2006).
8. L. P. Martin, L. Y. Woo, and R. S. Glass, *J. Electrochem. Soc.*, **154**, J97 (2007).
9. L. Y. Woo, L. P. Martin, R. S. Glass, and R. J. Gorte *J. Electrochem. Soc.*, **154**, J129 (2007).
10. L. Y. Woo, L. P. Martin, R. S. Glass, W. Wang, S. Jung, R. J. Gorte, E. P. Murray, R. F. Novak, and J. H. Visser. *J. Electrochem. Soc.*, **155**, J32 (2008).
11. L.Y. Woo, R.S. Glass, R.F. Novak, and J.H. Visser. *J. Electrochem. Soc.*, **157**, J81 (2010).

Publications/Presentations

L.Y. Woo, R.S. Glass, R.F. Novak, and J.H. Visser. "Effect of electrode material and design on sensitivity and selectivity for high temperature impedancemetric NO_x sensors." *J. Electrochem. Soc.*, 157(3):J81-87, 2010.

Oral presentation entitled "Impedancemetric NO_x Gas Sensors Based on Porous YSZ for Diesel Exhaust: O₂ and Water Cross-Sensitivity" at The American Ceramic Society 34th International Conference and Exposition on Advanced Ceramics and Composites, in Daytona Beach, Florida, January 24-29, 2010.

Oral presentation entitled "Long-Term and Temperature Cycling Stability of Impedancemetric NO_x Gas Sensors Based On Porous Yttria-Stabilized Zirconia (YSZ)" at the 217th Meeting of the Electrochemical Society, in Vancouver, British Columbia, Canada, April 26-30, 2010.

Oral project presentation at the 2010 DOE Vehicle Technologies and Hydrogen Programs Annual Merit Review and Peer Evaluation Meeting, June 7-11, 2010 in Washington, D.C.

Agreement 9440 - Surface Texturing for Friction Control

Oyelayo Ajayi, Aaron Greco, Robert Erck, and George Fenske

Argonne National Laboratory

9700 South Cass Avenue

Argonne, IL 60439

(630)252-9021; fax (630)252-5568; e-mail: ajayi@anl.gov

DOE Technology Manager: Jerry Gibbs

(202) 586-1182; fax: (202) 586-1600; e-mail: jerry.gibbs@ee.doe.gov

Contractor: Argonne National Laboratory, Argonne, Illinois

Prime Contract No.: DE-AC02-06CH11357

Objectives

- Develop mechanistic understanding of the effect of surface texturing on friction behavior in various lubrication regimes
- Develop application specific performance evaluation methodology for textured surfaces
- Develop methods for the optimization of surface texture design for different applications
- Determine the impact of surface texturing on mitigating tribological failure mechanisms (i.e. scuffing)

Approach

- In lubricated contacts, the effect of surface topography and texture will be more pronounced on the lubricant fluid film. Consequently, mechanistic study of the impact of surface texture (dimples for a start) will be studied by measuring lubricant fluid film thickness and friction under different lubrication regimes.
- Application specific evaluation will be evaluated initially with appropriate bench top test rig. Eventually, component testing will be conducted on optimized textured surfaces.
- The impact of surface texturing on basic tribological failure mechanisms will be evaluated using appropriate testing, surface and subsurface analysis and characterization.

Accomplishments

- Initial testing of surface texturing effect on lubricant film thickness in non-conformal contact showed that dimples do not necessarily increase film thickness
- Friction reduction (up to 50%) through surface texturing was observed for conformal contact applications (journal bearings) over a range of operating conditions, from mixed to full film lubrication regimes
- Significant improvement in contact severity index (3 fold increase) was achieved through surface texturing in applications where scuffing failure is assessed
- Identified texturing methods which would allow for a cost effective treatment method for friction and wear reduction

Future Direction

- Continue application specific tribological performance testing of textured surfaces to facilitate texture design for optimized friction and wear reduction
 - Expand evaluation of the impact of surface texturing on the various tribological failure mechanisms – Scuffing, wear, contact fatigue, etc
 - Evaluate the impact and potential enhancements of surface texturing on the actions of lubricant additives in formation of tribochemical boundary films
 - Explore various methods and forms of surface texturing for tribological performance enhancement
-

Introduction

Surface texturing, in the form of micro-scale dimples, has been shown to potentially improve tribological performance of lubricated surfaces in the form of friction reduction [1]. However, for certain applications, especially under non-conformal contact conditions, texturing has shown mixed results on its benefits [2]. Although, texturing is currently being used in some applications and its impact on frictional and wear behavior being actively investigated, the mechanisms associated with the effect of texturing on tribological performance is not fully understood yet. The commonality between most current investigations is that the performance is shown to be highly influenced by the subtleties of the texture design. Small variations in texture dimensions (i.e. depth, diameter, and coverage density) typically result in significant difference in friction behavior; therefore, a systematic approach to optimizing texture design for specific applications is necessary to realize the full potential benefits of this treatment technique. Furthermore, there are other forms of surface texturing or micro-geometrical designs other than dimples that can significantly improve the friction and wear behavior of lubricated components.

Approach

In order to better understand the impact of surface texturing (ST) on friction and wear behavior, and to further enhance the usefulness of other DOE sponsored effort in the area of texturing, we plan a two phase effort: (1) Mechanistic study of the impact of ST on fluid film and boundary regime lubrication, and (2) Application specific evaluation of ST including various engine and vehicle components. The effect of ST on lubrication mechanisms is studied by the simultaneous measurement of lubricant fluid film thickness and friction coefficient using an advanced elastohydrodynamic lubrication test rig Figure 1, which uses optical interferometry principle to measure the

lubricant film thickness profile within the contact. Film thickness for different texture and un-textured surfaces can be thoroughly characterized under different frictional behavior.

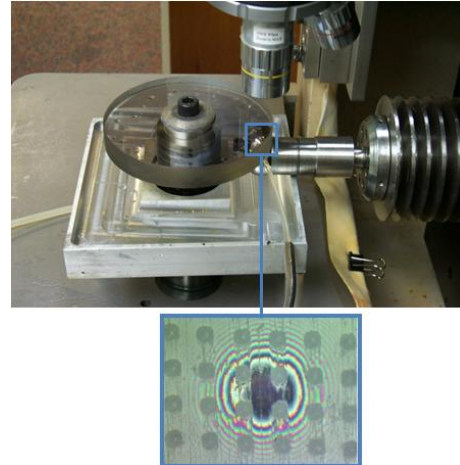


Figure 1. Elastohydrodynamic test rig for measuring lubricant film separation showing contact spot of dimpled ball on glass disk

The effect of ST on the frictional behavior of conformally contacting surfaces is also performed to simulate the application of journal bearing components. This will be evaluated using a conformal block-on-ring test rig, Figure 2, where friction can be monitored across various operating conditions. The test results presented in this report are performed off-site. At the time that this report was written this test rig was being installed on-site, which would allow for more in depth future investigation.



Figure 2. Conformal block-on-ring test rig for simulating journal bearing application

Lastly, to study the influence of surface texture at severe operating conditions,

testing is performed to analyze the scuffing resistance. More specifically, textured surfaces are compared with similar non-textured surfaces in reciprocating sliding contact under controlled step loading until the scuffing failure is induced. This performance is compared in relation to the contact severity index (CSI).

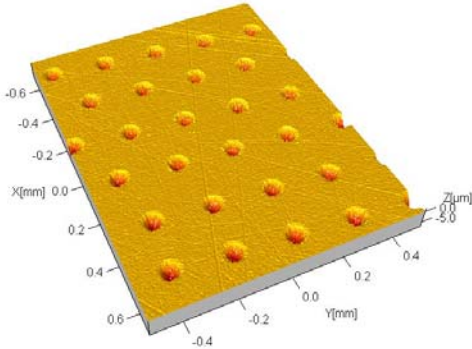


Figure 3. Three dimensional profile of a typical laser dimpled surface

Currently the texturing is achieved through a laser surface texturing (LST) method which is capable of producing well defined and controlled dimple features. For the current work all textures are in the form of micro-scale dimples with depths in the

mechanical texturing, which is also explored in this work.

Results

The results presented here summarize the achievements from this first year of this project. This progress has established the ground work for developing a systematic method of evaluating and optimizing surface texture application and design for friction and wear reduction.

The first objective of this work was to investigate the mechanism by which ST influences the lubrication behavior across a range of operating conditions, and subsequently lubrication regimes: full film separation to boundary. This was achieved using the equipment described in Figure 1, which utilizes optical interferometry to measure the fluid film separation between a ball and disc surface.

The optical images presented in Figure 3 show lubrication thickness profiles within the contact spot at various entrainment velocities. The thickness of the fluid film corresponds to the color of the profile, increasing film thickness with higher

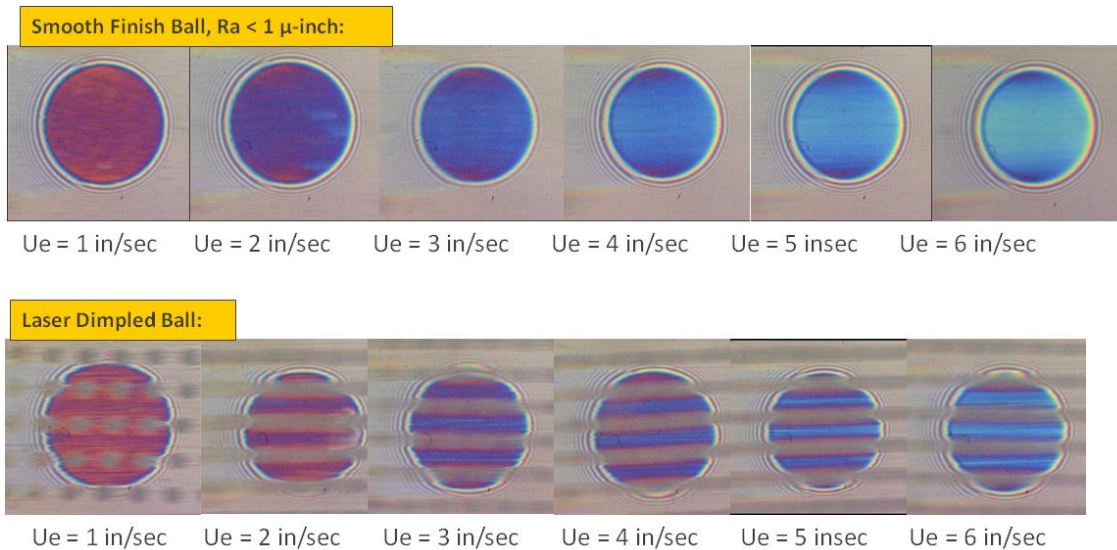


Figure 4. Optical profilometry images of lubricant film thickness, Top- smooth ball, Bottom- dimpled ball entrainment velocity.

range of 5-10 μm and diameters in the range of 50-150 μm . These features can be achieved using other surface texturing methods that may present a more cost effective treatment process, namely vibro-

Two types of balls were tested: one with a smooth finish, the other with laser generated dimples. The corresponding profile for the dimple ball shows streaking

along the row of dimples since the measurement system capture rate is too slow to resolve the profile between dimples at higher velocities. However, in the rows with no dimples the film thickness can be measured. To more accurately compare the difference in film thickness between the two types of surfaces the plot is presented in Figure 4 which shows the average centerline film thickness at each corresponding entrainment velocity. The film thickness for the dimpled ball is lower than that for the smooth for all speeds, but only by 10 nm or less for the entrainment velocity of 100 mm/sec and slower. This result indicates that surface dimples do not enhance the film separation for this current non-conformal contact configuration, and in most cases causes a slight reduction in film thickness. Further investigation is necessary to determine if dimples do not offer any enhancement to the hydrodynamic film separation for other types of contact configurations.

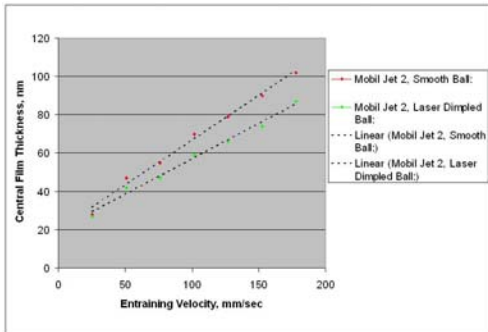


Figure 5. Film thickness plot comparing dimpled and smooth ball in non-conformal contact

The friction performance of dimpled surfaces in conformal contact is evaluated using the test equipment described in Figure 2, to simulate a journal bearing type of application. Here a ring is in lubricated contact with a curved block where again two types of rings are compared: one with a smooth surface, the other with laser generated dimples. The friction is measured over a range of rotation speeds and plotted in Figure 5. The low friction at high speed operation indicates a near hydrodynamic condition. As the speed decreases the

friction enters into a mixed condition. The friction curve for the dimpled ring is consistently lower than that of the smooth/plain ring, by more than 50% at around 200 RPM. This preliminary result indicates that significant friction reduction is achievable for applications of conformal contact and further improvement may be possible through optimization of the dimple design.

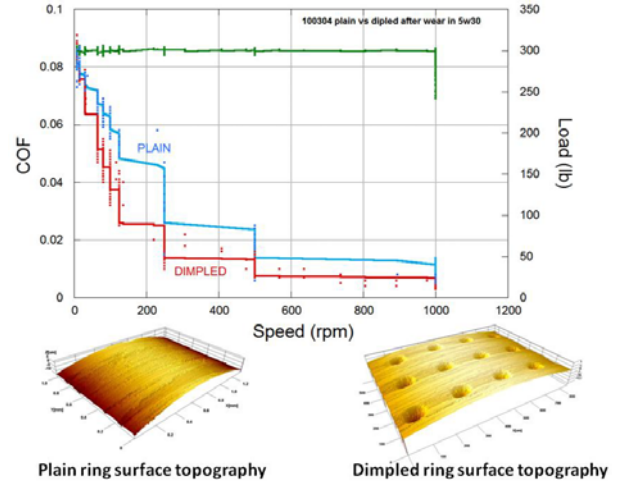


Figure 6. Friction plot comparing smooth and dimpled ring in conformal contact (journal bearing)

The final type of performance evaluation that was conducted is scuffing failure analysis. This type of failure mechanism is characterized by a sudden/sharp increase in friction with increasing contact severity. This event coincides with catastrophic surface failure and wear; in application this can result in total system failure. Contact severity is defined by the operating parameters of contact load and sliding speed in addition to the sliding friction coefficient. The scuffing performance was evaluated using a linear reciprocating sliding contact of a ball and flat with base synthetic oil lubrication. Again a textured flat surface with laser generated dimples is compared with a similar smooth sample. Tests are conducted at a constant sliding speed with increasing contact load. The plot shown in Figure 6 shows the friction profile for both the smooth and textured flat under the same

loading condition. The non-textured smooth sample experiences a scuffing limit at around 550 N load while the textured flat does not scuff until 1700 N, representing a nearly threefold increase in contact severity index with the textured surface. Contact severity index for the tests of textured surfaces was calculated to be 7 on average, which is a level that is generally only achievable through the use of certain high performance surface coatings. Post mortem examination of the flat sample shows that the dimples are still largely intact prior to the scuffing event which indicates that these surface features are contributing to the scuffing performance. More extensive testing is necessary to determine the underlying mechanisms responsible for this increase in scuffing resistance; however, these results give an indication that surface dimpling may offer a viable treatment method for significantly improving performance at severe operating conditions.

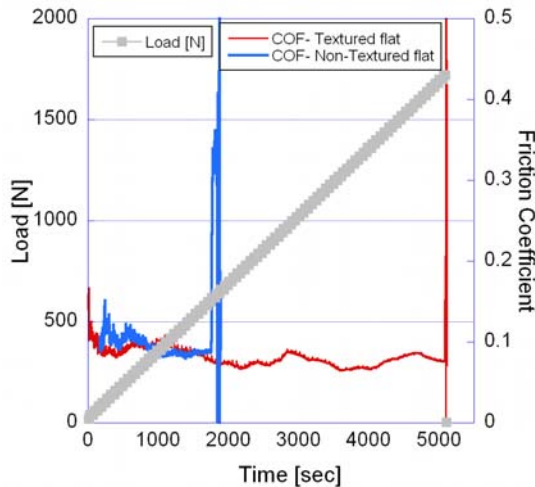


Figure 7. Scuffing performance plot comparing smooth flat with textured

Finally, in order to develop a cost effective and accessible surface texturing method a partnership with Northwestern University was formed to explore Vibro-Mechanical Texturing (VMT). This method utilizes more standard machining techniques to form surface textures. VMT is based on a lathe method where the standard static tool mount is replaced with a piezo-electric actuated tool stage. The tool initially

developed by Prof. Ehmann’s group at NU has been optimized to form precision controlled dimple features on a variety of materials [3]. Figure 8 shows a schematic of the tool stage in relation to a texturing workpiece. The frequency and amplitude of tool oscillation is used to precisely control the dimple design.

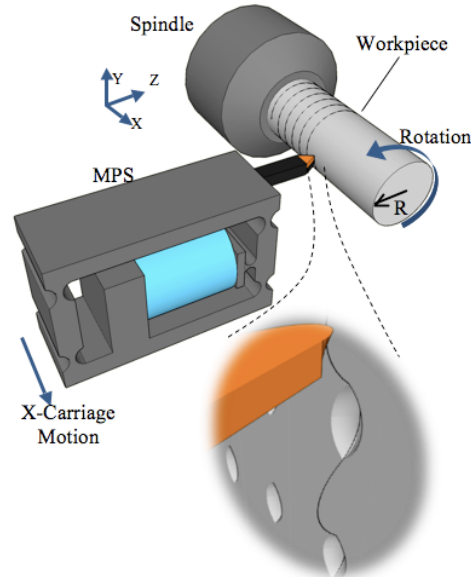


Figure 8. Vibro-Mechanical Texturing schematic

Since this method is based on a standard lathe operation and only requires a simple retrofit to incorporate the advanced micro-positioning stage (MPS) it is more readily accessible than other more complex texturing methods. VMT also has the potential to be a cost effective method of surface treatment in industrial production settings.

Conclusions

Within the first year of this program significant advancements have been made toward better understanding of the influence that surface texture has on tribological performance. More importantly, the ground work for developing a systematic method of evaluating and optimizing surface texture application and design for friction and wear reduction has been achieved.

First, to better understand the mechanism by which surface dimples influence hydrodynamic lubrication action,

an optical profilometry technique was employed. For this non-conformal contact configuration no enhancement to the lubricant film thickness was observed. Second, to assess the effect of surface dimples on friction performance, application specific testing was conducted on a conformal block-on-ring setup to simulated journal bearing applications. These results demonstrated a significant friction reduction across a range of operating conditions, up to 50% reduction. Further texture design optimization is needed to realize the full potential benefits of this treatment for this application. Third, surface texture was tested for scuffing performance, in order to test behavior of this surface treatment at severe contact conditions. In comparison to smooth samples, dimpled surface demonstrated a threefold increase in scuffing resistance, measured by contact severity index. Last, a novel surface texturing method, vibro-mechanical texturing, was assessed in coordination with Northwestern University to develop a cost effective and accessible texturing technique.

These current results demonstrate the potential benefits of surface texturing treatment in terms of friction and wear behavior. Further testing is necessary to realize the full potential benefits and to determine the fundamental mechanisms that

would allow for more appropriate design and application of surface texturing.

References

- [1] A. Kovalchenko, O. Ajayi, A. Erdemir, G. Fenske, and I. Etsion, "The effect of laser surface texturing on transitions in lubrication regimes during unidirectional sliding contact," *Tribology International*, vol. 38, no. 3, pp. 219-225, Mar. 2005.
- [2] A. Greco, A. Martini, Y. Liu, C. Lin, and Q. J. Wang, "Rolling Contact Fatigue Performance of Vibro-Mechanical Textured Surfaces," *Tribology Transactions*, vol. 53, no. 4, p. 610, 2010.
- [3] A. Greco, S. Raphaelson, K. Ehmann, Q. J. Wang, and C. Lin, "Surface Texturing of Tribological Interfaces Using the Vibromechanical Texturing Method," *Journal of Manufacturing Science and Engineering*, vol. 131, no. 6, pp. 061005-8, Dec. 2009.

Publications and Presentations

A. Greco, O. Ajayi, R. Erck. *Micro-Scale Texture Design for Improved Performance at Severe Contact Conditions*, 2010 International Joint Tribology Conference, San Francisco CA, Oct. 201

Agreement 11754 - Hydrogen Materials Compatibility

Principal Investigator: Stan Pitman

Kyle Alvine, Joe Ryan, Dan Skorski

Pacific Northwest National Laboratory

P.O. Box 999

Richland, Washington 99354

(509) 376-0356; fax: (509) 376-0418; e-mail: stan.pitman@pnl.gov

Alan Welch

Westport Innovations; email awelch@westport.co

Brad Boyer

Ford Motor Company; email bboyer1@ford.co

DOE Technology Manager: Jerry L. Gibbs

(202) 586-1182; fax: (202) 586-1600; e-mail: jerry.gibbs@ee.doe.gov

Field Technical Manager: Dean Paxton

(509) 375-2620; fax: (509) 375-2186; e-mail: dean.paxton@pnl.gov

Contractor: Pacific Northwest National Laboratory

Contract No.: DE- AC05- 76RL01830

Objectives

- Develop an understanding of the levels of hydrogen absorption and diffusion and damage in piezoelectric materials for the ultimate goal of mitigating absorption or removal of hydrogen.
- Measure the friction and wear characteristics of injector materials in hydrogen environments, including *in situ* and *ex situ* materials characterization.
- Qualify nanolaminate (NL) coatings and identify impactful deposition factors for optimization.
- Develop a design approach to hydrogen injectors based on material behavior and performance in hydrogen based on experimental data.

Approach, including partner/collaborator and path to technology transfer and commercialization

- Working with our industrial partners, the overall approach is to improve the performance and endurance of piezoelectric actuators. These actuators are used in an internal combustion hydrogen test engine to improve output, efficiency, and endurance. A major milestone was achieved in engine efficiency (45% Brake Thermal Efficiency) by the Ford Motor Company team, using actuators designed by Westport. These efficiencies are comparable to those that may ultimately be achieved by fuel cell technologies, at significantly lower cost.
- Further advances in efficiency and reliability require prolonged actuator lifetime. This requires the development of piezoelectric actuators that are robust in the required service conditions and meet the stringent requirements for actuator speed and accuracy.
- Hydrogen diffusion in the piezoelectric materials and associated hydrogen damage are the limiting factors for actuator life. These issues are being addressed using experimental methods.
- Using advanced ion scattering techniques at Pacific Northwest National Laboratory (PNNL), we are able to measure the hydrogen uptake in the piezoelectric materials over a range of temperatures.

- Using advanced neutron scattering techniques at the NIST Center for Neutron Research (NCNR) within the National Institute of Standards and Technology (NIST), we were able to measure the hydrogen diffusion over a range of temperatures in both lead zirconium titanate (PZT) and barium titanate (BTO).

Milestones, Metrics and Accomplishments

- Completed a study of hydrogen absorption from ion scattering in bare piezoelectric materials.
- Partially completed hydrogen diffusion studies in piezoelectrics. Awaiting additional neutron beamtime for further studies to confirm. Demonstrated hydrogen surface blistering and degradation in piezoelectrics.
- Demonstrated that 1) ion-assisted deposition and 2) the nitrogen:argon ratios are the most impactful parameters to optimizing NL response in terms of low friction and improved wear resistance.
- Made three presentations at national/international conferences, including one invited presentation at the CAARI conference, Dallas, Texas, and one paper on our hydrogen/piezoelectric work accepted to *Applied Physics Letters*.
- Held workshop with Westport and University of British Columbia about Hydrogen in Piezoelectrics to discuss progress to date and future directions. Workshop was hosted at PNNL.

Future Directions

- Hydrogen absorption as a function of electrode material
- Hydrogen absorption & desorption as a function of temperature
- Evaluation of hydrogen barriers such as paralyne
- Further optimize tribological properties of NL films by control of deposition parameters.

Introduction

For the transportation sector, hydrogen internal combustion engines using direct injection can be viewed as a high-efficiency/low-emission technology for bridging the transition process to the hydrogen economy based upon fuel cell technology. It has been estimated that a hydrogen direct injection (DI) engine can be integrated into a hybrid vehicle system that would demonstrate fuel consumption (fuel energy used per unit distance) only about 15% to 20% greater than a hybridized fuel cell vehicle of similar mass. Significantly lower hardware cost (as compared to present fuel cell systems) and use of existing manufacturing facilities for conventional reciprocating engines makes this an attractive consideration. Some engine manufacturers have identified robust fuel injection technology as one of the key enablers for commercialization of advanced hydrogen DI engines.

Originally, the basic hydrogen injector architecture was designed and developed for

earlier natural gas DI engine programs. Fundamental issues limiting injector durability were expected, and potential engineering solutions have been evaluated by PNNL researchers and their partners, Westport Innovations and Ford Motor Company. Overall, the injectors used in the research have been useful tools for developing engine combustion strategies and assessing fuel system technology. If there were a significant level of interest in this type of engine technology, the long-range intention is to advance the injector technology to the point at which it could enter limited production.

Compared to liquid hydrocarbon fuels, hydrogen is a challenging fluid to use in precision injectors because it has very low viscosity and low density, and it can alter material properties through atomic diffusion or chemical reduction. The goal of this work is to understand the basic mechanisms that limit injector life and identify promising

strategies to significantly improve the technology for the next phase of research and development.

Technical Challenges

The following two issues are critical to the success of the hydrogen DI technology (Figure 1):

1. Hydrogen diffusion into piezoelectric actuator and subsequent degradation
2. Impact and sliding wear between the needle and the jacket.

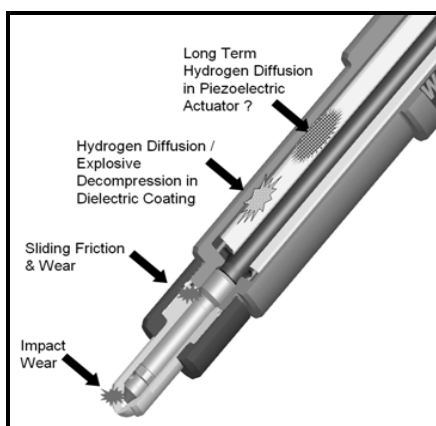


Figure 1. Hydrogen materials compatibility challenges for the HICE injector

Hydrogen Diffusion and Damage in Piezoelectrics Background: Previous experiments in this project and OEM studies have shown that piezoelectric actuators that inject hydrogen tend to fail prematurely in a high-pressure hydrogen environment. This severely limits the reliability and lifetime of the direct injection hydrogen injection combustion engine (HICE) and makes the option less attractive to industry. By developing an understanding of the failure mechanisms of the piezoelectric in hydrogen, we can then develop the tools to address the issues and bring the direct injection HICE closer to the marketplace.

It is known from the literature that even low-pressure hydrogen can damage piezoelectric materials from studies of ferroelectric random access memory or FERAM [1-3].

However, studies on the effects of high-pressure hydrogen on piezoelectric materials are lacking. The PNNL studies are designed to fill this knowledge gap by addressing the following three main areas: hydrogen diffusion within piezoelectrics; hydrogen absorption in piezoelectrics; and hydrogen induced damage in piezoelectrics. We have begun to address these three issues over the past two years with a combination of microscopy and advanced ion and neutron scattering techniques that are uniquely suited to studying hydrogen and its effects.

Technical Approach:

Hydrogen Compatibility of Piezoelectrics:

Thin films of piezoelectric material, and in some cases piezoelectric powders, were used in place of complete actuators or sections of actuators. Initially, we attempted to use sectioned actuators; however, hydrogen contamination from the epoxy surrounding the actuator rendered the results inconclusive. Instead, we opted to study piezoelectric thin films fabricated by magnetron sputtering. This approach has many benefits. The first is that the results are then more easily comparable to the low-pressure hydrogen results in the literature, which used sputtered piezoelectric films. The second is that the films are of very high quality and low roughness, thus ensuring that surface damage is more easily observed and that roughness does not affect the surface scattering results. A schematic of the thin film system is shown in Figure 2. In some systems, a metal electrode also was deposited. For diffusion measurements with neutron scattering, neat powders of the piezoelectric material were used instead. This will be discussed in a later section.

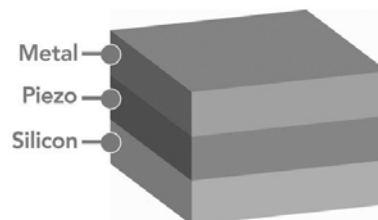


Figure 2. Schematic of thin film samples.

Piezoelectric samples (powder and thin films) were exposed to high pressure hydrogen (2500 psi) and 100°C for at least 24 hours prior to measurements to charge them with hydrogen. High-pressure hydrogen autoclaves at PNNL (Figure 3) were used to accomplish this.



Figure 3. High-pressure hydrogen autoclaves used to charge piezoelectric samples

Hydrogen Absorption and Surface Damage:

PNNL used advanced ion scattering techniques to investigate the hydrogen absorption in piezoelectric materials, specifically BTO and PZT, with advanced-ion scattering. Understanding hydrogen absorption is important to determining ways to mitigate or remove the hydrogen through thermal cycling or vacuum application. Also, by comparing BTO and PZT, we are able to look at materials effects. Ion scattering, specifically elastic recoil detection analysis (ERDA), is one of only a handful of techniques that is well suited to hydrogen studies. We also have used the more standard Rutherford backscattering spectrometry (RBS) to look at surface degradation of the piezo/electrode interface. This is particularly important because even minimal damage at the electrode interface can cause device failure.

In ERDA, high-energy helium ions cause the forward recoil of absorbed hydrogen, which is collected by an energy dispersive detector. Nuclear resonance analysis (NRA) is a similar technique in which high-energy fluorine ions combine with absorbed hydrogen to form an excited state and then decay, emitting gamma rays that are detected. Both methods are extremely

sensitive to hydrogen and can offer concentration depth profiles. In FY 2009, and FY 2010, PNNL carried out ERDA and NRA studies that show hydrogen absorption in the bare PZT and BTO films on the order of 5 atomic % with a higher hydrogen background for BTO. For films with a Pd electrode, the H levels absorbed after 24 hours at 2400 psi and 100°C increase to nearly 20 to 30 atomic % of hydrogen. Details will be published in an upcoming journal article (see publications).

RBS data also involves the scatter of high energy (MeV) He ions from the sample in the back-scattering geometry (Figure 4). RBS was measured on these films to determine the heavy element concentrations as a function of depth. For most films, there was little or no change between those charged in hydrogen and the control samples. One notable exception was the PZT/Pd system. This system showed considerable surface mixing between the Pd and Pb in the system. The RBS data from this system is shown in Figure 5.

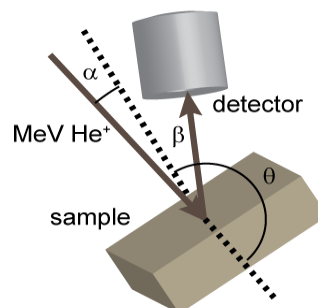


Figure 4. Ion scattering geometry

Surface Degradation – Blistering:

In addition to some cases of surface mixing at the electrode we have also seen evidence of surface blistering on the piezoelectric materials. Blistering is fairly common in metals that have been exposed to large amounts of hydrogen. Hydrogen within the system can recombine into hydrogen at cracks or voids within the system. When the external hydrogen pressure is removed rapidly, the hydrogen within the system can rapidly expand causing a void to form. If

this occurs on the surface, it is called a blister. Blistering is shown for a PZT film along with a schematic of blistering in Figure 6.

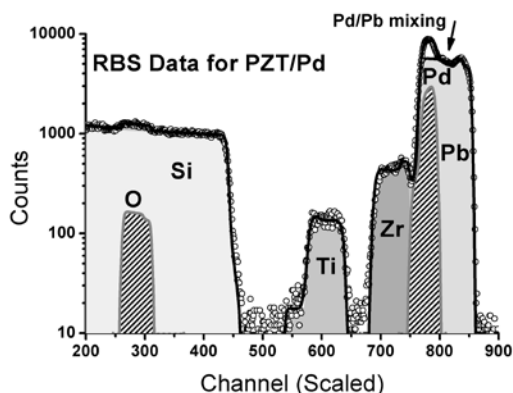


Figure 5. RBS data showing the different elemental spectra. Overlapping Pb and Pd spectra indicate elemental mixing at the piezo/electrode interface.

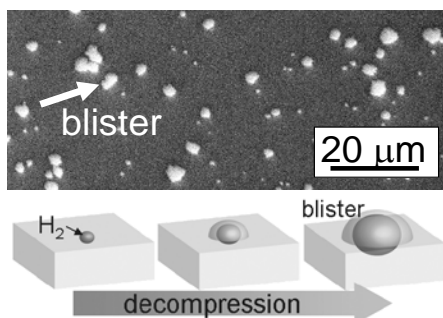


Figure 6. Hydrogen blistering in PZT and a schematic of the blistering process

Hydrogen Diffusion in Piezoelectrics (Experiments – Neutron Scattering):

In FY 2010, we continued to investigate hydrogen diffusion in piezoelectrics. Thus far, we have obtained preliminary results from neutron scattering techniques discussed in previous reports and are awaiting confirmation of further beamtime for additional neutron studies. We also are exploring the option of purchasing an apparatus to measure bulk permeation for complementary measurements to the neutron results. We hope to complete this analysis in mid FY 2011.

Further Piezoelectric/Hydrogen Studies:

In FY 2010, we prepared a series of piezoelectric thin films of PZT and BTO with various different metal electrode films to study hydrogen absorption as a function of the catalytic properties of the metal. We also plan to study hydrogen absorption as a function of temperature.

Technical Approach: Impact Wear and Sliding Friction on Nanolaminates (NL):

This section discusses the tribological studies of wear and coefficient of friction on BN/CrN NLs performed in FY 2010. The NLs were designed to be a durable low friction coating in hydrogen environments for use in DI HICES. The films were deposited in alternating BN and CrN layers, each on the order of 5nm in thickness (Figure 7).

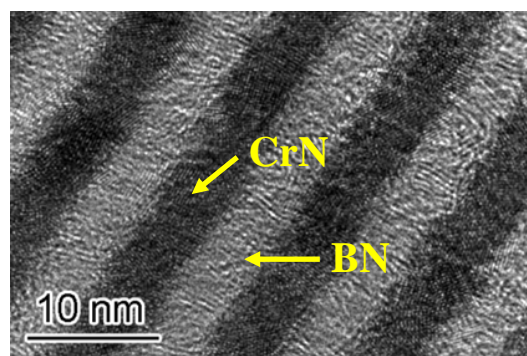


Figure 7. Transmission electron microscope (TEM) micrograph of the alternating CrN and BN layers in the NL

A total of 40 pairs were deposited in each film to achieve a final coating thickness of approximately 0.4 μm. Testing of the films included both structural investigations by TEM, scanning electron microscope (SEM), and x-ray diffraction (XRD) as well as tribological tests to determine wear performance (Figure 8, 9).

In FY 2010, we 1) standardized our current tribometer unit for use in a hydrogen environment, 2) purchased a new standard tribometer from CSM Instruments to bolster testing validity and provide rapid testing capabilities, 3) qualified our testing methods

through an ANOVA Gage Repeatability and Reproducibility study (Gage R&R), and 4) determined the primary drivers of successful coatings through a statistical design of experiments.

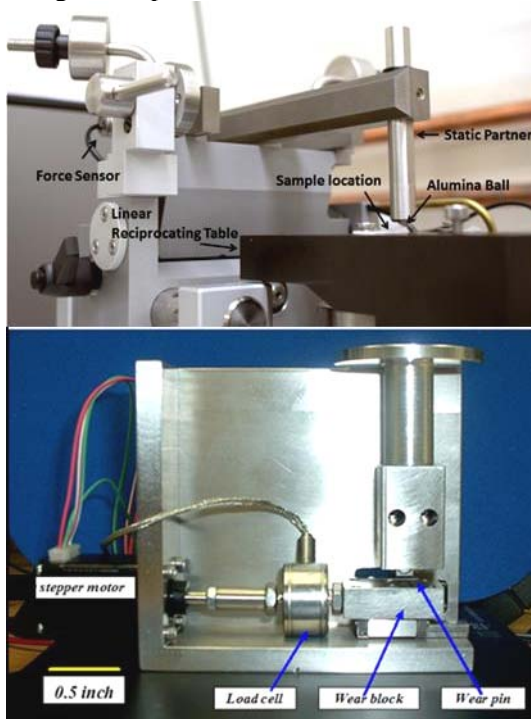


Figure 8. (Top) Tribometer from CSM Instruments conforming to ASTM G133 and ASTM G99 standards. (Bottom) Home-built tribometer conforming to the ASTM G133 standard.

Our results have shown increased quality of coatings with ion-assisted deposition and/or an increase in the nitrogen in the deposition chamber. Quality is defined by the metrics defined later in Table 3. While both of these factors decreased the amount of wear induced on the coating during subsequent testing, improvement was not additive. Further investigation in FY 2011 is warranted to optimize these fabrication parameters for improved tribological properties. Details of the complete tests of the different deposition parameters follow.

A series of BN/CrN NLs were deposited using on both Silicon and M2 tool steel. These samples were used to determine the reproducibility and quality of the testing and depositions as well as the driving factors

behind the NL wear. The coatings on the tool steel samples were used primarily for tribological testing, while the coatings on the silicon wafers were used for TEM, SEM, and XRD characterization. Ion-assisted deposition (a combination of bombardment with argon or nitrogen ions and sputter deposition) was used to determine the potential for increases in the bond strength, orientation, and crystallinity within the specific sample layers. Regular small lattice mismatch between the layers can result in alternating tensile and compressive stressed areas that dramatically increase the intrinsic strength of the film. A total of four sample series were created in FY 2010 with details shown in Table 1.

Table 1. Four primary sample series

Batch	Ion-Assisted Deposition	Environment	Deposited Thickness (nm)
1	Yes	2:1 N ₂ :Ar	352
2	No	2:1 N ₂ :Ar	424
3	Yes	5:1 N ₂ :Ar	366
4	No	5:1 N ₂ :Ar	421

All samples of a given series were coated simultaneously in an attempt to reduce the variation between samples. Tribological testing was performed using the ASTM G99 (pin-on-disk) or ASTM G133 (linear reciprocating) standard with a 6-mm alumina ball, and the coating was deposited onto the M2 steel substrate.

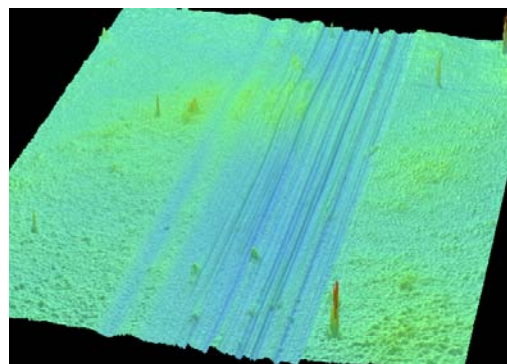


Figure 9. A typical OP image of a wear track in a NL film from tribological testing. The depth and width of these tracks are used as metrics for film quality evaluation. The spikes are dust particles.

The morphological structure of the NLs on the silicon substrate was examined using TEM, which showed the correct morphology with excellent spacing and layer uniformity (Figure 7). Further examination of the layer crystallinity with electron diffraction (TEM) indicated that the CrN layers were polycrystalline, while the BN layers exhibited a more amorphous structure.

Tribological testing during FY 2010 was performed using a standard linear reciprocating motion tribometer (CSM instruments, see Figure 8, top) and a home-built tribometer (see Figure 8, bottom) designed for *in situ* tribological testing in a hydrogen environment. Both systems used the same static partner (6-mm alumina ball), contact stress, and calibration technique.

Tribological testing consists of reciprocating the sample under a ball or pin that is held under a constant normal force, similar to a record player stylus. This oscillatory motion produces a wear track in the film with dimensions related to the film hardness and resistance to wear. The wear track dimensions were measured in three dimensions using optical profilometry (OP) techniques. A typical OP measured topography of a NL wear track is shown in Figure 9. In addition, force sensors allow real-time calculation of the friction coefficient between the pin and the sample surface. The next sections go into more detail about experiment design and testing procedures that we used in FY 2010 to evaluate reproducibility of our tests and different deposition parameters.

An ANOVA Gage R&R was performed on samples from the four coating series defined previously to determine the reproducibility of the results between samples, machine operators, and different locations on the substrates. The experiment was completed using two machine operators, four samples, and four different areas on each sample. All samples were tested using the standard calibrated tribometer under ASTM G133. Tests were completed in an argon

atmosphere with 0.5 N of force and a maximum speed of 1 cm/s. Results showed good statistical repeatability for all samples with increased repeatability on the ion-assisted samples.

With reproducibility confirmed, we set up a Statistical Design of Experiment (SDoE) to investigate the effects of different deposition and testing parameters in a statistically meaningful and efficient way. This approach allowed us to understand the primary causes of variation within a reasonable number of tests. The seven parameters/factors that were varied are listed in Table 2.

Table 2. Factors for the design of experiments

Design of Experiment Factors	Option 1	Option 2
Testing Environment	Argon	Hydrogen or Air
Ion Assisted Deposition	Yes	No
Deposition Environment (N ₂ :Ar)	2:1	5:1
Hydrogen Charging (Hours)	0	300
Contact Stress During Testing (MPa)	382	638
Testing Speed (cm/s)	0.5	2
Machine	CSM Instruments	Home-built

To evaluate the results of the SDoE testing, we chose six different metrics to describe the quality of the films based on tribological performance (Table 3).

Table 3. Description and units for each of the measured metrics

Name	Description	Units
OP Width	Average wear track width from optical profilometer across 30µm of the wear track.	µm
OP Depth	Average wear track depth from optical profilometer across 30µm of the wear track	µm
Optical Rating	A 1-9 grading scale on the quality of the film after testing. 1= Least worn 9 = completely worn	NA
Cycles until Failure	Number of cycles before friction reached 0.8 or a significant change in the friction was observed and the film was confirmed to be worn through via optical microscopy.	Cycles
Steady State	Steady state friction achieved after break-in but before failure.	Unitless
Minimum Friction	The minimum friction observed on the sample for more than 2 points after the test was started.	Unitless

Based on our evaluation of the different metrics, the optical rating, wear track width, and minimum coefficient of friction were most affected by variation of the deposition parameters. Details of deposition parameter variation and the strength of the effect on the different metrics are given in Tables 4 and 5.

Table 4. General effects of each of the Controlled Factors. “+” is an increase in quality, “-“ is a decrease in quality, “*” is no observable effect, “s” indicates it was a statistically significant single factor.

	Width	Depth	Optical Characterization
Statistically Significant Prediction %	15%	3%	23%
Deposition Environment 2:1 -> 5:1	+ _s	+ _s	+ _s
Ion Assist Off -> On	+ _s	+	+ _s
Hydrogen Charging 0h -> 408hr	*	*	*
Testing Machine CSM -> Home	*	*	*
Testing Environment Argon -> H ₂ or air	*	*	*
Contact Stress Low -> High	*	+	*
Speed 0.5cms -> 2cms	+	+	+

Table 5. General effects of each of the Controlled Factors. “+” is an increase in quality, “-“ is a decrease in quality, “*” is no observable effect, “s” indicates it was a statistically significant single factor.

	Cycles Until Failure	Steady State	Minimum Friction
Statistically Significant Prediction %	4%	11%	15%
Deposition Environment 2:1 -> 5:1	+	+	+
Ion Assist On -> Off	+	+ _s	+
Hydrogen Charging 0h -> 408hr	*	-	-
Testing Machine CSM -> Home	*	*	*
Testing Environment Argon -> H ₂ or air	+ _s	*	+
Contact Stress Low -> High	*	-	-
Speed 0.5cms -> >2cms	+	+	+

We note that given the number of tests that were performed, these results only allow for prediction of general trends and not for specific values. For example (see Table 4), the +s value for changing the deposition environment from 2:1 (nitrogen:argon) indicates that a statistically significant within a 90% confidence interval, positive quality effect on the wear track width (i.e., a narrower track width).

General trends that were not statistically significant (i.e., very minor) are indicated without the “s” subscript. The total correlation values are listed at the top of Tables 4 and 5. A value of 100% would indicate that all of the expected variation was predicted within a 90% confidence

interval based upon the input factors. In nearly all samples tested, the deposition environment was the most important influencer on overall durability, and increasing from a 2:1 to a 5:1 nitrogen:argon ratio produced more favorable coatings based on wear track width, optical rating, and minimum coefficient of friction. We also observed a decrease in the wear properties and coating uniformity across the substrate without the ion-assisted deposition. We also performed a multifactor interaction analysis to determine if there were any significant correlations between factors and the changes in the metrics (i.e., looking for effects that are additive or subtractive). Based on our analysis, we did not observe any significant positive or negative interactions between the drivers, but we did note that specific drivers increased quality, such as ion-assisted deposition and increased nitrogen in the deposition chamber, were not cumulative.

Conclusions

The behaviors of hydrogen in piezoelectric materials and in NLs were evaluated using advanced experimental techniques. The following conclusions were obtained:

- Significant hydrogen-induced blistering occurs in PZT, but less in BTO. These findings indicate that BTO may be preferential for hydrogen environments.
- Electrode mixing between Pd and Pb occurs during hydrogen charging, but does not occur for Ba and Pd in BTO/Pd systems. Further investigation is warranted, but this may indicate BTO systems are better suited to hydrogen.
- Through Gauge RR testing and SDoE testing, we were able to conclude that the two primary factors impacting the durability of NLs are 1) ion-assisted deposition and 2) the nitrogen:argon ratio.

Presentations/Publications/Patents

- Alvine et al, “Hydrogen Materials Compatibility”, CAARI conference, Dallas, TX (invited speaker)
- Alvine et al, “Hydrogen Materials Compatibility”, APS March Meeting, Portland, OR (speaker)
- Alvine et al, “Hydrogen Materials Compatibility”, DOE Annual Merit Review, Washington, DC.
- Alvine et al, “High Pressure Hydrogen Materials Compatibility of Piezoelectric Films”, Applied Physics Letters (accepted, in press, October 2010)

References

- [1] Huang HY, WY Chu, YJ Su, KW Gao, J X Li, and LJ Qiao. 2007. *J. Am. Ceram. Soc.* 90, 2062.
- [2] KushidaAbdelghafar K, H Miki, K Torii, and Y Fujisaki. 1996. *Appl. Phys. Lett.* 69, 3188.
- [3] Aggarwal S, SR Perusse, CW Tipton, R Ramesh, HD Drew, T Venkatesan, DB Romero, VB Podobedov, and A Weber. 1998. *Appl. Phys. Lett.* 73, 1973.
- [4] Wu M, HY Huang, B Jiang, WY Chu, YJ Su, JX Li, and LJ Qiao. 2009. *J. Mater. Sci.* 44, 5768.
- [5] Aimi M, M Arik, J Bray, T Gorczyca, D Michael, and S Weaver. 2007. Medium: ED.
- [6] Shimamoto Y, K KushidaAbdelghafar, H Miki, and Y Fujisaki. 1997. *Appl. Phys. Lett.* 70, 3096.
- [7] Peng X, YJ Su, KW Gao, LJ Qiao, and WY Chu. 2004. *Mater. Lett.* 58, 2073.
- [8] Avasthi DK. 1996. *Bull. Mat. Sci.* 19, 3.
- [9] Kramer EJ. 1991. *Physica B* 173, 189.
- [10] Ishikawa A, H Maekawa, T Yamamura, Y Kawakita, K Shibata, and M Kawai. 2008. *Solid State Ion.* 179, 2345.
- [11] Park CH and DJ Chadi. 2000. *Phys.*

Rev. Lett. 84, 4717.

[12] Meyer A, RM Dimeo, PM Gehring, and DA Neumann. 2003. *Rev. Sci. Instrum.* 74, 2759.

[13] Pivovarov AM, MD Ward, T Yildirim, and DA Neumann. 2001. *J. Chem. Phys.* 115, 1909.

[14] Perdew JP, K Burke, and M Ernzerhof. 1996. *Phys. Rev. Lett.* 77, 3865.

[15] Bellaiche L and D Vanderbilt. 2000. *Phys. Rev. B* 61, 7877.

[16] Henkelman G, BP Uberuaga, and H Jonsson. 2000. *J. Chem. Phys.* 113, 9901.

Acronyms

PZT: Lead Zirconate Titanate

BaTiO₃: Barium Titanate

NL: nanolaminates

QENS :Neutron, Quasi-elastic Neutron Scattering

RBS: Rutherford Back-scattering Spectrometry

ERDA: Elastic Recoil Detection Analysis

NRA: Neutron Resonance Analysis

FWHM: Full-Width at Half Maximum

HFBS: High-Flux Back Scattering

FANS: Filter Analyzed Neutron Spectrometer

PNNL: Pacific Northwest National Laboratory

NIST: National Institute of Standards and Technology

NCNR: NIST Center for Neutron Research

ANOVA: ANalysis Of VAriance between groups

Gage R&R: Gage Repeatability and Reproducibility study

SDoE: Statistical Design of Experiment

OP: Optical Profilometry

SEM – Scanning Electron Microscopy

TEM – Transmission Electron Microscopy

XRD - X-ray Diffraction

Project 18518 – Materials for High Efficiency Engines

Agreement 16304 – High Performance Valve Materials (HPVM)

P. J. Maziasz and N. D. Evans

Materials Science and Technology Division

Oak Ridge National Laboratory

P.O. Box 2008, MS-6115

Oak Ridge, TN 37831-6115

(865) 574-5082; fax: (865) 576-6298; e-mail: maziaszpj@ornl.gov

M.D. Veliz

Advanced Materials Technology

Caterpillar Technical Center

14009 Old Galena Rd.

Mossville, IL 61552

(309) 578-2700; fax: (309) 578-2953; e-mail: veliz_mark_d@cat.com

DOE Technology Manager: Jerry L. Gibbs

(202) 586-1182; fax: (202) 586-1600; e-mail: jerry.gibbs@ee.doe.gov

ORNL Technical Advisor: D. Ray Johnson

(865) 576-6832; fax: (865) 574-6098; e-mail: johnsondr@ornl.gov

Contractor: Oak Ridge National Laboratory, Oak Ridge, Tennessee

Contract No.: DE-AC05-00OR22725

Objectives

- Characterize current engine exhaust seats and valves to define and understand temperature, performance and durability limitations
- Use understanding of the behavior of current valves and seats to enable advanced designs and/or selection of advanced materials and processing to upgrade temperature capability and performance/durability limitations.

Approach

- Team with Caterpillar (CAT) diesel engine valve and seat suppliers to define temperature/performance limitations of current technology, and provide upgraded seat and valve options that are commercially viable, so that prototype modified components can be supplied for testing and evaluation.
- Microanalysis at ORNL of the various seat and valve components from simulation-rig or engine testing to define the nature and causes of wear/degradation of exhaust valve/seat pairs relative to fresh components.
- ORNL perform critical mechanical properties testing to define the benefits of Ni-based superalloys for exhaust valves with more temperature capability and performance than standard Pyromet 31V.
- Use detailed data and analyses to guide component manufacturers in producing prototype valves and seats with upgraded performance and capability.

Accomplishments

- ORNL and Caterpillar identified processing modifications for the Co-based superalloy seats to mitigate lower temperature wear, and confirmed reduced wear rates with testing at Caterpillar.

- ORNL and Caterpillar identified several commercial Ni-based superalloys with upgraded capabilities, and obtained both mechanical properties specimens for testing at ORNL and prototype valves for wear-rig testing at Caterpillar.
- ORNL completed tensile testing and continued creep-testing at 816-871°C that defined the benefits of Ni-based alloy 1 relative to 31V.
- Caterpillar completed the initial wear-rig testing at 850°C that defined significant benefits of Ni-based alloy 1 relative to 31V alloy.

Future Direction

- Complete long-term creep testing and aging experiments on Ni-based superalloys with upgraded valve performance and capability to define benefits and durability relative to 31V alloy (ORNL).
 - Perform longer-term rig-testing of upgraded exhaust valves and oxidation testing to define durability limits of Ni-based superalloys with upgraded capabilities (CAT).
 - Extend CRADA Project for 24 more months due to technical success and expanded/extended workscope.
-

Introduction

This is a continuing ORNL CRADA project with Caterpillar, NFE-07-00995 and DOE, OVT Agreement 16304, which began in 2007, and was scheduled to last for about 2.5 years. This CRADA was extended for 12 more months last year, and this year, due to technical success with identifying and testing new upgraded valve alloys, was extended for an additional 24 months, with extended and expanded workscope. This CRADA project has addressed the wear and failure modes of current on-highway heavy-duty diesel exhaust valves and seats, and then changed seat-insert processing and selected advanced exhaust-valve Ni-based superalloys with higher temperature capability. The need for such upgraded valve-seat alloys is driven by the demands to meet new emissions and fuel economy requirements, which then continue to push diesel exhaust component temperature higher. Requests for more detailed information on this project should be directed to Caterpillar, Inc.

Approach

Caterpillar provides and analyzes the baseline wear and mechanical behavior characteristics of engine-exposed valves and seats, and similar exposure of those components to laboratory simulation-rig testing at Caterpillar. ORNL completes more in-depth characterization and microanalysis of those valves and seats. These data established the root-cause analyses which then provided the basis for modifying seat

processing, and for selecting Ni-based superalloys with upgraded performance relative to standard Pyromet 31V last year. This year, Caterpillar and ORNL teamed with Caterpillar's component suppliers to implement these solutions and obtain prototype components for wear-rig testing at Caterpillar, and specimens for testing and characterization at ORNL.

Upgrading the temperature capability of the various critical exhaust components will enable the increased engine temperatures needed to allow a 3% decrease in fuel consumption for on-highway trucks.

Technical Progress

Caterpillar

Previously, Caterpillar provided exhaust valve and seat materials of standard materials that had been wear-tested at various temperatures on the Caterpillar "Buettner" Rig. Seats were a J3 Co-based superalloy. Exhaust valves are standard 31V Ni-based superalloy. ORNL and Caterpillar identified modified seat-insert processing designed to mitigate low-temperature wear. Caterpillar verified benefits of trial seats with modified processing wear-rig testing.

This year, a valve supplier provided prototype valves of two Ni-based superalloys that Caterpillar and ORNL identified last year as having more performance and temperature capability than the standard 31V alloy. Caterpillar began testing the new prototype valves (Ni-based 1 and 2 alloys) in the wear-rig facility. Results for 480 h testing of

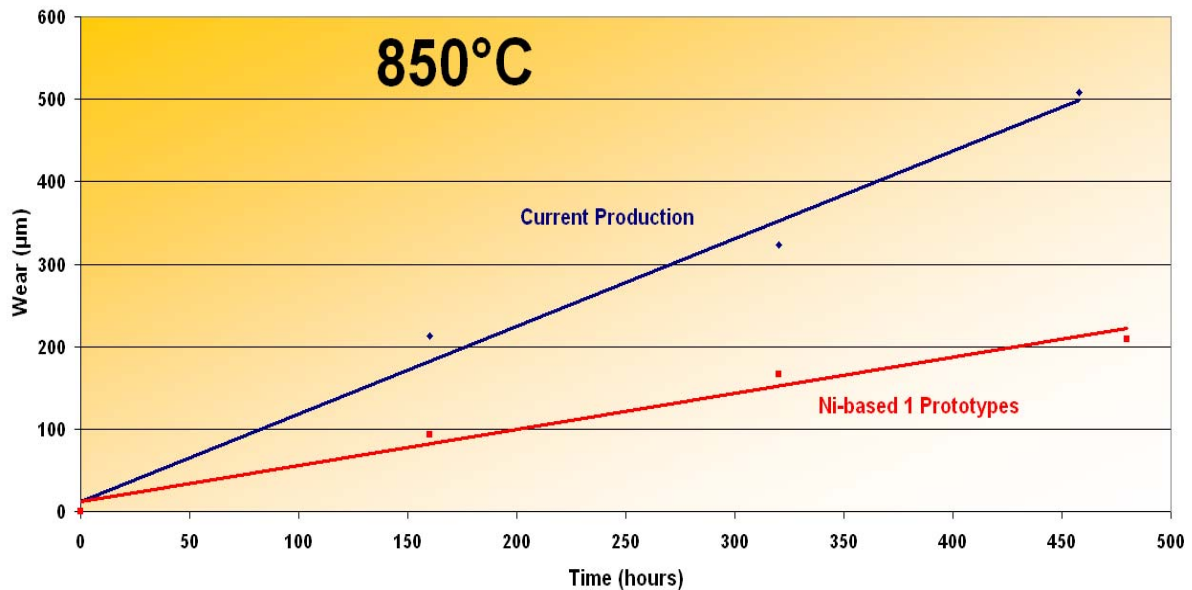


Figure 1. Caterpillar wear-rig testing of cumulative wear (valve and seat-insert) for standard 31V alloy exhaust valves and new Ni-based 1 superalloy prototype valves at 850°C in air. The Ni-based 1 alloy showed a 200% reduction in wear relative to the 31V alloy.

Ni-based alloy 1 and standard 31V valves tested against the standard seat-inserts at 850°C in air is shown in Figure 1. After 480 h of testing, the upgraded Ni-based 1 alloy valves show a 200% reduction in cumulative wear (valve + seat) relative to the standard 31V alloy. Testing of Ni-based 2 alloy valves at 850°C is in progress, and similar tests of both alloys will be made at lower temperatures, and for longer times at 850°C.

ORNL

ORNL completed thorough microstructural and microcompositional characterization studies of the standard valve and seat components last year, which defined the detailed changes occurring at the oxidation-surfaces. Analysis included surface oxides as well as the underlying metal interface and bulk regions (including fresh and aged, non-wear control specimens). Root-cause analysis of the 31V alloy at 760-850°C showed that there was dissolution of gamma-prime and the formation of internal oxidation (of Al and Ti), which weaken the subsurface region relative to the underlying base metal. This information indicated Ni-based alloys with more temperature capability

(better oxidation resistance and more gamma-prime) than 31V were needed, and ORNL and Caterpillar identified several commercial Ni-based superalloys as upgrade materials. Caterpillar's valve supplier provided prototype valves to Caterpillar, and mechanical properties specimens (tensile and creep) from the rod-stock used to forge valves to ORNL for mechanical properties testing.

ORNL tensile testing at 700-900°C indicated that Ni-based alloys 1 and 2 and the 31V alloy were all quite strong at 700°C, as measured by yield-strength, with all being close to 100 ksi. However, the YS of the 31V alloy drops precipitously with increasing temperature above 700°C, while the Ni-based 1 and 2 alloys still have YS values of 95-100 ksi at 816°C (Fig. 2). At 816°C, the YS of the 31V alloy is slightly less than 70 ksi. ORNL also conducted creep-rupture testing at 816 and 871°C of these 3 alloys at stress of 15-30 ksi. Despite Ni-based 2 alloy having slightly higher YS at 816°C, the Ni-based 1 alloy clearly has much been creep-rupture resistance, as shown for creep in air

at 816°C and 30 ksi in Figure 3. Creep-testing is still in progress now, and will continue next year. Aging of specimens of these alloys at 800-850°C also began this year, and will continue to 5000 h next year.

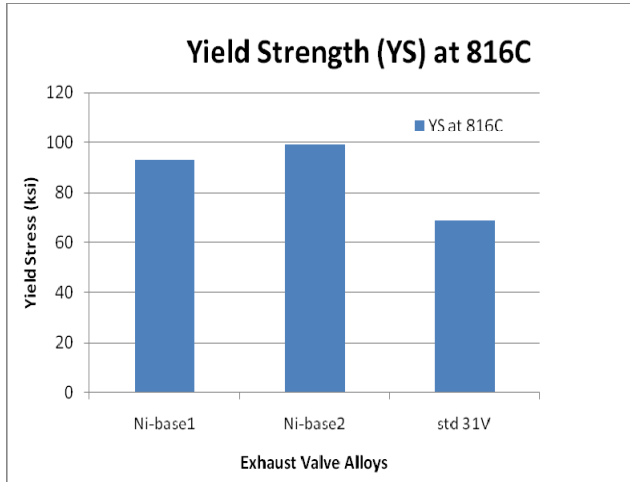


Figure 2 –Yield strength (YS) of exhaust-valve alloys at 816°C, determined from tensile testing of Ni-based 1 and 2 alloys and 31V alloy at 700-900°C in air.

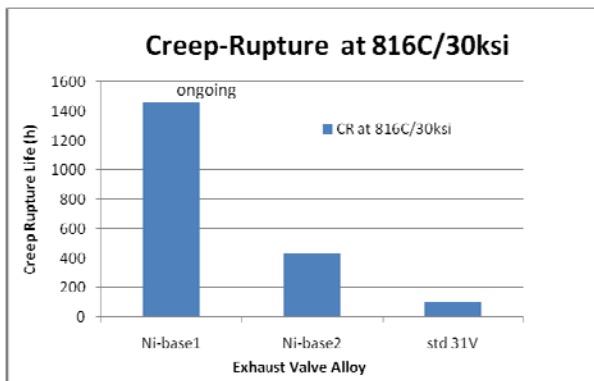


Figure 3 – Creep-rupture life of exhaust valve alloys, as determined for creep-testing in air at 816°C and 30 ksi. The Ni-based 1 alloy clearly has more creep-rupture resistance than the other two alloys, and that test is ongoing.

Conclusions

Caterpillar completed longer-term wear-rig testing of seat-inserts with modified processing and determined increased wear-resistance benefits. Caterpillar received prototype valves of 2 commercial Ni-based alloys with more performance and temperature capability than the standard 31V alloy. Wear-rig testing to about 500h at 850°C shows considerably less cumulative wear for the Ni-based 1 alloy relative to the standard 31V alloy. Similar testing of Ni-based 2 alloy valves is in progress.

ORNL received tensile and creep specimens made from the rod-stock used to forge valves of Ni-based 1 and 2 alloys and the standard 31V alloy. Tensile testing at 700-900°C showed that YS remained close to 100 ksi at 800°C for both Ni-based 1 and 2 alloys, whereas the YS of the 31V declined above 700°C, and was slightly below 70 ksi at 800°C. Initial creep-rupture testing at 816 and 871°C at stresses on 15-30 ksi shows that the Ni-based 1 alloy has much more creep-rupture resistant than 31V or Ni-based alloy 2. Creep-testing and long-term aging of specimens of these alloys will continue next year.

Publications/Presentations

None

Special Recognitions and Awards/Patents Issued

None

Agreement 13329 - Design Optimization of Piezoceramic Multilayer Actuators for Heavy Duty Diesel Engine Fuel Injectors

Hua-Tay Lin, Hong Wang, and Andrew A. Wereszczak

Ceramic Science and Technology Group

Oak Ridge National Laboratory, P.O. Box 2008, MS 6068

Oak Ridge, TN 37831-6068

(865) 576-1169; fax: (865) 574-6098; e-mail: linh@ornl.gov

DOE Technology Manager: Jerry L. Gibbs

(202) 586-1182; fax: (202) 586-1600; e-mail: Jerry.gibbs@ee.doe.gov

ORNL Technical Advisor: D. Ray Johnson

(865) 576-6832; fax: (865) 574-6098; e-mail: johnsondr@ornl.gov

Contractor: Oak Ridge National Laboratory, Oak Ridge, Tennessee

Contract No.: DE-AC05-00OR22725

Objectives

- Apply established structural ceramic probabilistic design and reliability analysis to piezoelectric multilayer actuators (PMLAs).
- Generate required micromechanical property data on lead zirconate titanate (PZT) piezoceramics and macromechanical property data on PMLAs for input into the design and reliability analysis of the latter.
- Identify minimum mechanical performance requirements for fuel injector PMLAs.
- Adapt these strategies to improve reliability of PMLAs under candidacy for use in diesel engine fuel injectors.

Approach

- Evaluate PMLA reliability under representative service conditions.
- Link constituent piezoceramic micro-mechanical and PMLA macro-mechanical responses.

Accomplishments

- Calibrated the piezodilatometer and developed the methodology to characterize the candidate poled PZT ceramics under cyclic fatigue. Studied piezoelectric and dielectric behavior of KCI PZT ceramics under unipolar and bipolar cycling.
- Characterized the mechanical strength of KCI PZT ceramic using various test configurations and identified the strength-limiting flaw. Investigated the temperature effect on the strength of PZT ceramic.
- Developed experimental approach to characterizing mechanical properties of PZT ceramic of EPCOS stack. Studied the mechanical strength of multilayer PZT ceramic and evaluated the temperature effect.
- Explored experimental method to study the dielectric strength of EPCOS encapsulating materials.

Future Direction

- Develop database for candidate piezoceramics and PMLAs of Cummins under the simulated application environments.
 - Measure and evaluate piezoelectric and mechanical reliabilities of tape-cast and pressed PZT piezoceramics.
 - Fabricate additional PMLA fatigue test frames with controlled environmental capability.
-

Introduction

The use of piezoelectric multilayer actuators (PLMAs) as diesel fuel injectors has the potential to reduce injector response time, provide greater precision and control of the fuel injection event, and lessen energy consumption. Compared to conventional solenoid operation of an injector, the alternative use of a PMLA can enable precise rate shaping of the entire injection cycle that accurately controls injection timing and fuel quantity. Piezoelectric multilayer actuators (or piezo-stacks) fuel injectors contain a solid-state ceramic actuator (or “piezostack”) that converts electric energy into linear motion precisely controlling the needle’s opening and closing. This capability results in an engine with outstanding performance, improved fuel economy, low noise, and low emissions. Though their use is very attractive for the reasons mentioned above, uncertainty continues to exist over how reliable piezo-actuated fuel injectors will be in the challenging environment of a heavy-duty diesel engine. Though piezoelectric function is the obvious primary function of lead zirconate titanate (PZT) ceramic PMLAs for fuel injectors, their reliability can be a performance and life limiter because the PZT ceramic within them is brittle, lacks high strength, and may exhibit fatigue susceptibility. That brittleness and relatively low strength can be overcome with proper probabilistic component design methodology.

This project undertakes the reliability characterization of candidate PMLAs used in these fuel injectors and the piezoceramics used in the PMLAs. Technical communications via teleconferences and onsite visits have been maintained with Cummins within the CRADA in the FY2010. Extensive test and characterization on the comprising components of PZT stacks have been conducted based on recommendations from Cummins, Inc. This includes mechanical, piezoelectric and dielectric properties and relevant temperature effect. The products from Kinetic Ceramics, Inc. (KCI) and EPCOS have been focused during FY2010.

Approaches

1. Mechanical Testing and Characterization

Single-Layer PZT

Characterization on the mechanical strength of KCI PZT ceramic has been conducted. The data

generated in this task will serve as the input for the subsequent reliability design study on the multilayer actuator. Both the as-extracted and as-received single-layer PZT materials were examined in this period. For the former, the specimens were obtained from a supplied KCI PZT stack by dissolving bond epoxy using a recommended chemical solution. Each PZT specimen was a circular plate with two opposite cuts or flats in the same size. Its nominal diameter was 15.00 mm, flat-to-flat distance 12.26 mm, and thickness 0.500 mm.

The ball-on-ring (BoR) and four-point bend tests were used to study mechanical strength of as-extracted PZT, strength-limiting flaw, and size-scaling of the strength. For this group of tests, all were done at room temperature (RT, 22°C) by using an indentation system in a displacement-controlled mode with a rate of 0.01 mm/s. The BoR was a steel-steel pair consisting of a 9.5 mm steel ring and 6.35 mm steel ball. Test data were processed with a method described in reference.^{1,2,3} For the four-point bending, a semi-articulated 4-point bend fixture was used. The loading and supporting spans were 3.175 mm and 6.35 mm, respectively. All data were processed using bending plate theory.⁴

High temperature tests were carried out on INSTRON testing machine (Norwood, MA) by using the same four-point bend fixture as on the indentation system. An environment furnace (INSTRON furnace SFL) was used. Its controller can ramp the temperature to 200°C in 10 minutes. For the stabilization of system, a 20 minute soak-time was generally provided before the mechanical loading. The cross head rate was set at 0.01 mm/s, and a 1-kN load cell was used.

Multilayer PZT

Testing on EPCOS PZT ceramic resorted to a different configuration because the stand-alone single-layer PZT specimen was not available; particularly, 10-layer plate specimens were used. These multilayer plates were sized 6.8 x 6.8 x 0.76 mm³ and extracted from commercial PZT stacks (6.8 x 6.8 x 30 mm³) by chemical dissolving plus heating temperature.

The BoR setup was employed in tests. Some of plates from stack 1 were tested at room temperature using ϕ 6.35 mm Si₃N₄ ball and ϕ 5.12 mm polymer ring. This was conducted in the in-house indentation system with the high precision alignment control in a displacement control mode, 0.01 mm/s. A 100-lb

load cell was used in tests for measuring the mechanical force. Tests at high temperature were carried out on INSTRON testing machine again (Norwood, MA). A self-alignment fixture was modified for the BoR loading. This was achieved by using an alumina double-tube structure whose protruded inner tube served as the support ring. The end edge of the inner tube was carefully machined to provide the required contour, and the obtained ring was sized with $\phi 4.88$ mm. A $\phi 12.7$ mm alumina sphere was used as the loading ball. The temperature environment was provided by INSTRON furnace SFL. The temperature was raised to 200°C in 10 minutes, and maintained additional 20 minute prior to the onset of mechanical loading. The cross head rate was set at 0.01 mm/s, and a 1-kN load cell was used.

PZT Stack Bars

The field tests on piezoelectric stacks in fuel injection system revealed the stack failure quite often in delamination on the interfaces either between the PZT layer and internal electrode or between the end face of PZT plate (composed of multilayer PZT) and bonding layer. Though it is considered as a strategy to deflect the fracture, delamination and its response in relevant interfaces is of interest in terms of design and service of stacks. A test, or a semi-articulate four-point bending setup, was designed to test and characterize the response of stack with a special attention given on the properties of interfaces.

EPCOS stacks were studied for this purpose. Bar specimens sized with $3 \times 2.5 \times 30\text{mm}^3$ were prepared from the supplied uncapsulated PZT stacks ($6.8 \times 6.8 \times 30\text{mm}^3$) by splitting them longitudinally and following the recommended procedure in standard.⁵ The four-point bending fixture had a load span of 6.35mm and a support span of 25.4mm, and the tests were performed in room temperature using the indentation system at a displacement rate of 0.001 mm/s.

2. Piezoelectric and Dielectric Testing and Characterization

Single-Layer PZT

Piezoelectric and dielectric responses are the backbone of PZT as an actuator and a sensor, and their long-term durability needs to be carefully evaluated. Meanwhile, a thorough understanding on

the fatigue mechanism of PZT is also critical to fabricate a robust piezoelectric ceramic and to achieve a reliable performance of stack through an effectively-controlled operation.

Piezodilatometer⁶ developed in this project has been enabled in this fiscal year to conduct the comprehensive fatigue test of targeted PZT ceramics under electric cycling. All data were processed by partially refer to reference.⁷ Major achievements include the adaption of mechanical and electric contact and developments of test procedure, data processing, and characterization approach. The fatigue has been centered on unipolar and bipolar cycling and unipolar and bipolar measurement. Cross measurements (unipolar measurement on bipolar cycling and bipolar measurement on unipolar cycling) have been proven to be quite necessary to reveal the phenomena of interest that otherwise cannot be disclosed.

As-received KCI PZT ceramic has been tested extensively under electric cycling in this fiscal year. This testing and characterization development, at the same time, established a sound base for further testing other candidate piezoelectric ceramics and other coupling conditions.

Encapsulating Polyester

Dielectric breakdown of encapsulating materials has been demonstrated to be related to most of the stack failures in field tests. The ability of insulators against the dielectric breakdown under controlled electric loading is therefore needed to be tested and characterized effectively before they are integrated into stack.

The polyester as associated to EPCOS stacks was focused in this study. The specimens were prepared from four end sectors of a stack encapsulating tube. These sectors were 12 mm long, 3 mm wide and 1 mm thick. The thickness was reduced to 30 to 50 μm by grinding and polishing. Thereafter, the polyester films were transferred into carbon tape and mounted into a Cu substrate.

The tests were conducted on the piezodilatometer with the specimens submerged in electronic liquid (FC-40). A 60 Hz ac electric sine wave was used with a ramping rate of about 390 V/s.

Microstructure Study

Optical and scanning electronic microscopes (SEM) were used extensively during the project to investigate the failure and fatigue mechanisms

associated with the mechanical, piezoelectric, and dielectric processes of stack components and comprising materials including PZT, internal electrode, and encapsulating.

Results

Mechanical Strength of Single-Layer PZT and Temperature Effect

Flexure strength and temperature effect of KCI PZT in as-received and as-extracted states can be seen from Fig. 1. These results are based on the tests

specimen extraction process. The heating to more than 200°C (but lower than its Curie temperature) during the extraction may result in partially-reoriented polarization that was frozen by the cooling to room temperature. Testing of as-extracted PZT ceramic thus reflected the status of PZT in heating, and their strength eventually was equivalent to that of the as-received PZT under corresponding temperature range.

Extensive fractographical studies have been conducted using optical and scanning electron

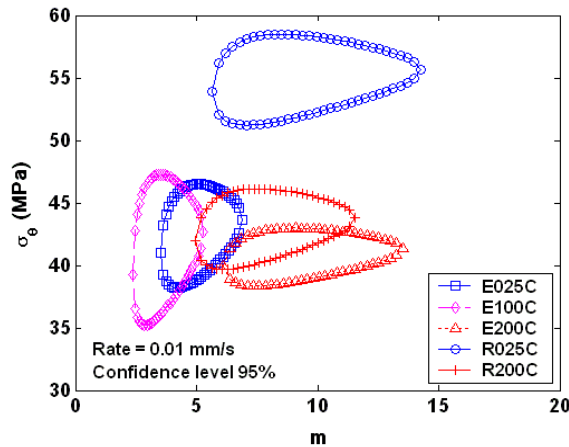


Fig. 1. Confidence ratio rings (95% level) of flexure strength for as-extracted PZT at 25°C (E025C), 100°C (E100C), 200°C (E200C), as-received PZT at 25°C (R025C), and at 200°C (R200C); 4-point bend with 3.175 mm of loading span and 6.35 mm of supporting span was used.

with semi-articulated four-point flexure. For the as-extracted PZT, it appeared that the strengths subjected to various temperatures actually had a similar range of variation. The Weibull moduli of as-extracted PZT changed a little. The position of 100°C confidence ring is seen to be separated from other two. This may manifest the relative role of different strength-limiting flaw types that were activated under a sampling condition. It is interesting to see that, for the as-received PZT, the strength at 25°C was significantly higher than that at 200°C, while the latter exhibited a confidence ring largely overlapping with those of the as-extracted PZT. There are at least two points that can be made with regard to the observation: 1) the temperature indeed had a significant effect on the mechanical strength of this PZT material; 2) the strength insensitivity of as-extracted PZT to temperatures may be attributed to the heating-induced depolarization during the

microscopes. Surface-located volume pore, porous region, agglomerate, and surface void were revealed to occur at identified failure origins. Several representative origins are given in Fig. 2.

Mechanical Strength of Multilayer PZT and Temperature Effect

Three commercial EPCOS stacks were selected from those tested in previous stage of the project for extracting individual multilayer plates. All the stacks have been broken dielectrically; among them, stack No. 1 actually experienced more cycling in earlier trials before the breakdown. Fifteen of multilayer plates from stack No.1 were tested in BoR at RT with the polymer support ring, nine in BoR at RT with alumina support ring, and three at 200°C with alumina support ring. As shown in Fig. 3(a), results are comparable in the case of RT for both support rings. Therefore, given the parent stack from which

plates were extracted, flexure strengths obtained with polymer and alumina support rings were statistically same. The double-tube structure has been demonstrated to be robust and its protruded edge worked effectively as a support ring as designed. It is interesting to see that the multilayer

plates exhibited a quasi-plastic deformation in the case of alumina support ring. Specifically, their loading curves were mostly with a yielding point and some of them had a strain hardening. The yielding was pronounced also at 200°C. This quasi-plasticity is perhaps related to the contact condition

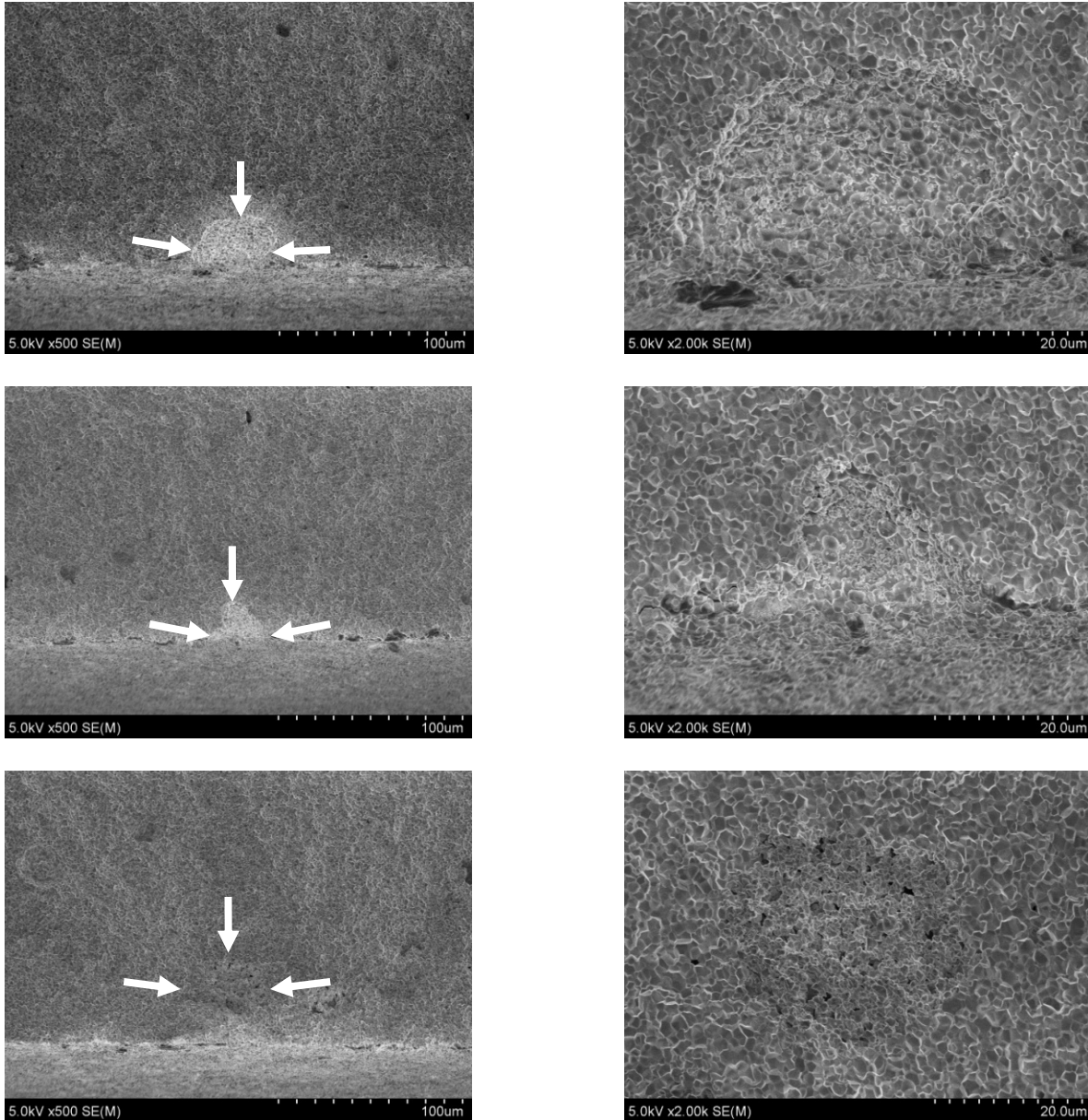


Fig. 2 Failure origins featuring (a) & (b) volume pore, $\sigma_f = 58.8$ MPa, (c) & (d) surface void, $\sigma_f = 50.1$ MPa, and (e) & (f) porous region, $\sigma_f = 60.0$ MPa. Data were based on the as-received PZT and semi-articulated four-point flexure setup was used with loading span 3.175 mm and supporting span 6.35 mm; the crosshead rate was 0.01 mm/s.

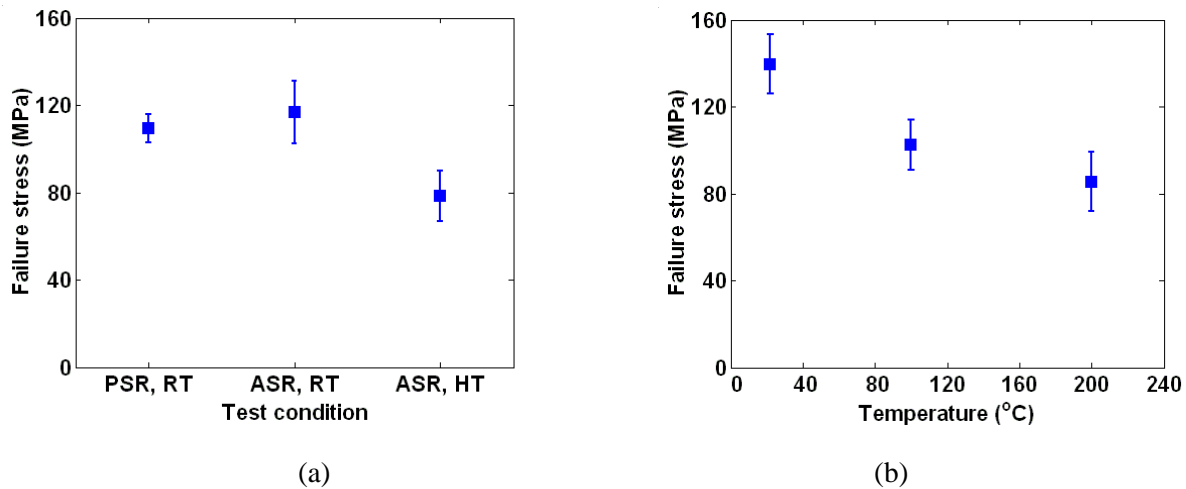


Fig. 3 (a) Flexure strength of multilayer PZT plates from stack 1 with polymer support ring (PSR) and alumina support ring (ASR) in ball-on-ring setup; RT= 22°C, HT= 200°C. (b) Flexure strength of plates from stacks 2 and 3 with ASR under various temperature conditions. The cross head was set at a rate of 0.01 mm/s.

because it was not seen with polymer supporting ring. However, the failure load can be identified readily based on the yielding point on loading curves.

Plates from stacks No.2 and 3 were tested in three temperature conditions: 22°C, 100°C, and 200°C. Each included twenty-two specimens. It was observed that mechanical strength of plates decreased with increasing temperature within the tested range as shown in Fig. 3(b). A comparison of RT results from stack 1 with those of stacks 2 and 3 also revealed that the flexure strength was related to the degree of damage of parent stacks introduced by pre-fatigue tests. Authors realized that the effect of transverse shear was not considered in estimating the flexure strength; the analysis and data processing are expected to be elaborated in the next step.

SEM fractographical studies illustrated that failure origins are actually located in the outer PZT layer as shown in Fig. 4. Though there were a few cases in which the failure origins were developed on the interfaces with Cu electrode layer involved, the failure of multilayer PZT structure has been demonstrated to be largely controlled by the PZT layer. This observation agrees with the relative thickness of metal electrodes to PZT layers (4 μm versus 80 μm). Therefore, the experimental approach proposed here indeed characterized the

strength property of PZT and further justified the experimental approach.

Mechanical Failure of PZT Stack Bars

Bar specimens sized with 3 x 2.5 x 30 mm³ were used in four-point bending tests, and six of them delivered useful data. A mean value of 35 MPa was obtained for the flexure strength. The failure usually took place on plate-to-bonding layer interface. This was confirmed because the half PZT layer could be recognizable as the bottom of an individual plate segment when the SEM beam was directed on the side of segment that was taken from a broken bar specimen. No failure origin could be identified since there was no fracture ledge developed on the failed surface. The failure is thus considered to be a result of delamination and the obtained strength characterizes the interface resistance against de-bonding. On the other hand, PZT-layer-to-internal electrode interface had a higher mechanical strength with no delamination observed nearby.

Piezoelectric and Dielectric Responses of Poled PZT under Electric Cycling

Unipolar and bipolar cycling modes were used in fatigue tests on poled KCI PZT ceramic specimens. Both unipolar and bipolar measurements were conducted to characterize the responses. The

detailed experimental results were reported elsewhere. The following will focus on the unipolar measurement as it provides design with the essential

the target specimens varied among themselves, but the trend with the number of cycles was quite appreciable. As a result of that, the measured

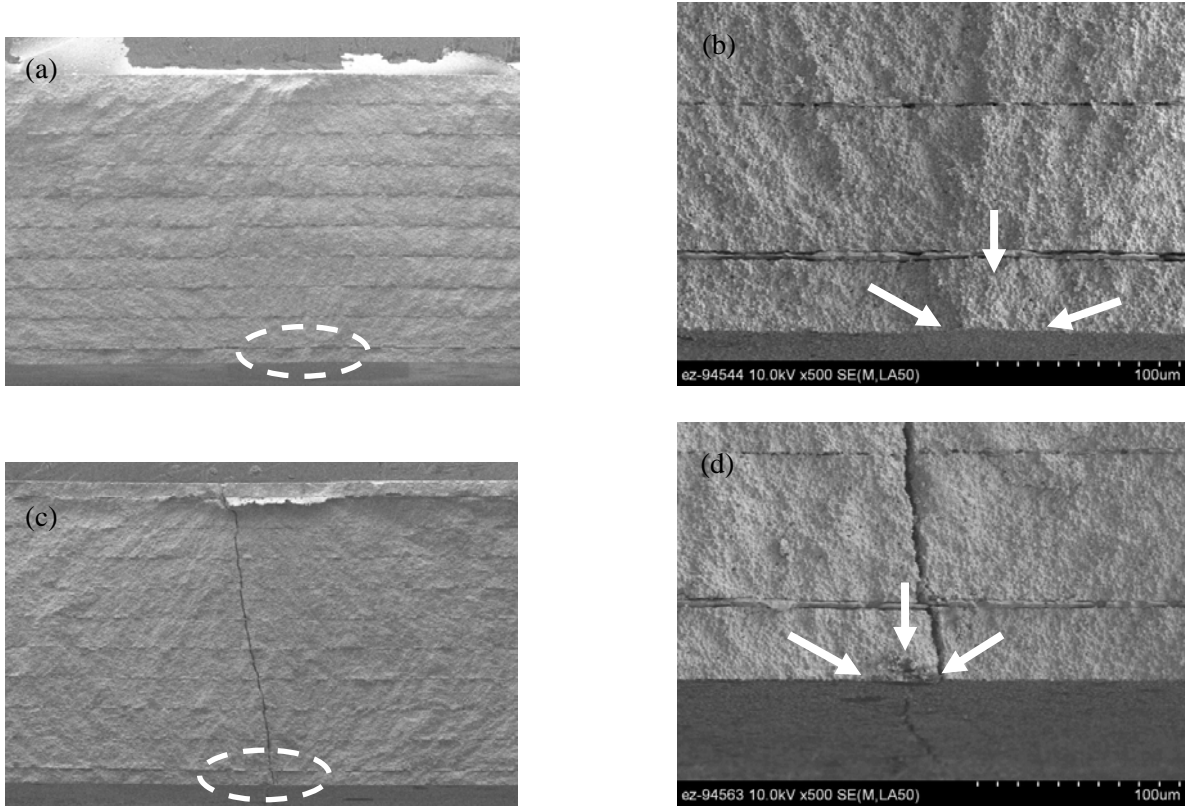


Fig. 4. Failure origins of multilayer PZT generated by ball-on-ring loading for (a) and (b) #6 in room temperature, (c) and (d) #21, 100°C. Alumina loading ball of 12.7 mm diameter with alumina support ring of 4.88 mm diameter was used with the cross head rate was 0.01 mm/s.

data; the loading mode used in this measurement is same as in a typical application for driving stacks.

It is of great interest to examine how the amplitudes and hystereses of responses change during the cyclic process. These quantities were, therefore, extracted from all the measurements including mechanical strain loop amplitude ΔS , piezoelectric hysteresis U_d , charge density loop amplitude ΔD , and dielectric hysteresis U_H .

As shown in Fig. 5, these quantities exhibited various changes with the cycling in target specimens. In the case of reference specimens, they fluctuated but without any defined trend. Because of observation on the insensitivity of quantities of interest to the electric cycling, the following discussion will focus on the results of target specimens. The degree of variation involved with

responses were normalized with respect to their pre-fatigue values and averaged. The processed strain amplitude ($\Delta S/\Delta S_0$) and piezoelectric hysteresis (U_d/U_{d0}) are given in Fig. 5(a) and (b). If focusing on unipolar cycling case, one can see that only a marginal decrease occurred in mechanical strain near 10^8 cycles, but the decrease amounted to 30% in piezoelectric hysteresis. The processed strain amplitude ($\Delta D/\Delta D_0$) and piezoelectric hysteresis (U_H/U_{H0}) are given in Fig. 5(c) and (d). A consistent decrease took place in both charge density and dielectric hysteresis during cycling, which was approximately 30% at the end of cycling.

A different scenario occurred in the case of bipolar cycling for both mechanical strain and charge density as shown in Fig. 5. It can be seen that both the mechanical strain and piezoelectric

hysteresis varied in a pattern of rise-and-fall. This corresponded to less than 10% increase in strain and

Dielectric Breakdown of Polyester

The testing was carried out for four polyester

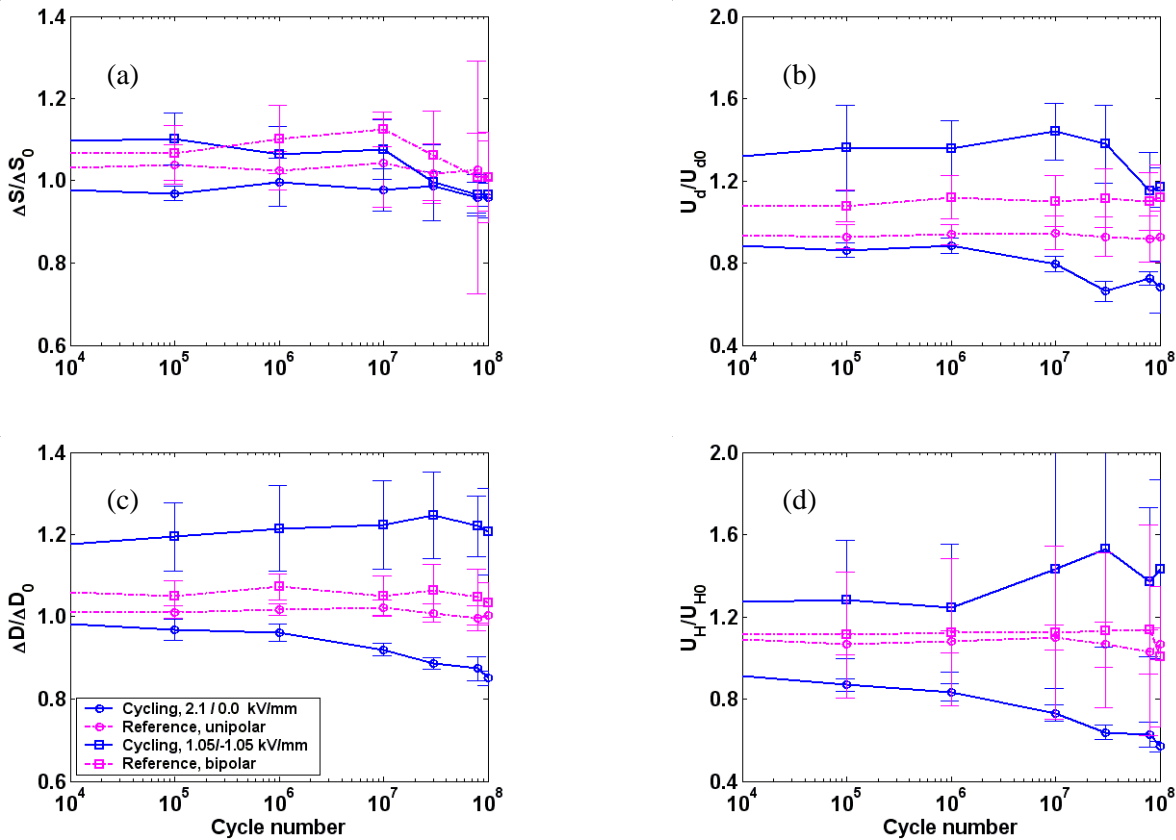


Fig. 5. Variation as a function of cycle number for (a) mechanical strain, (b) piezoelectric hysteresis, (c) charge density, and (d) dielectric hysteresis. Results are based on unipolar measurements, normalized with respect to prefatigue values. Results are averaged among 4 to 5 specimens, and error-bars correspond to one standard deviation. Tests were conducted on KCI poled PZT using piezodilatometer

around 40% increase in piezoelectric hysteresis, even though both of them exhibited an impressive drop towards the end of cycling. At the same time, the measurement on charge density and dielectric hysteresis revealed even more significant increases. As is discussed in various applications, the bipolar cycling in within the coercive field range from -1.05 to +1.05 kV/mm was found to have induced a certain amount of depolarization, which contributed to the observed increases.

film specimens. The electric field at dielectric breakdown was found to be from 38 to 54 kV/mm. The breakdown field was relatively higher compared with that of regular PZT materials that is (11 kV/mm). These tested polyester specimens were potted by using epoxy. Cross sections were then prepared by cutting and polishing. SEM and EDS were carried out for these prepared sections. One of them was shown in Fig. 6. The polyester was observed to have a large volume fraction of reinforcement oxide particles. These particles contained a certain amount of Si, Ca, Al and Mg (and probably C also).

Sizable gap can be seen usually between the polyester film and the adhesive layer of Cu disk. The gap may pre-exist attributed to poor bonding between the Cu sheet and polyester or result from the local dielectric breakdown. For the large cavity as seen in Fig. 6, the contribution of local dielectric breakdown cannot be ignored as the plastic flow is

significance of results obtained here is two folds: 1) the data can be used for the input for reliability analysis; 2) the developed experimental approach can be used in testing and characterizing the candidate PZTs in more representative working conditions.

With the nowadays' advance in fabrication

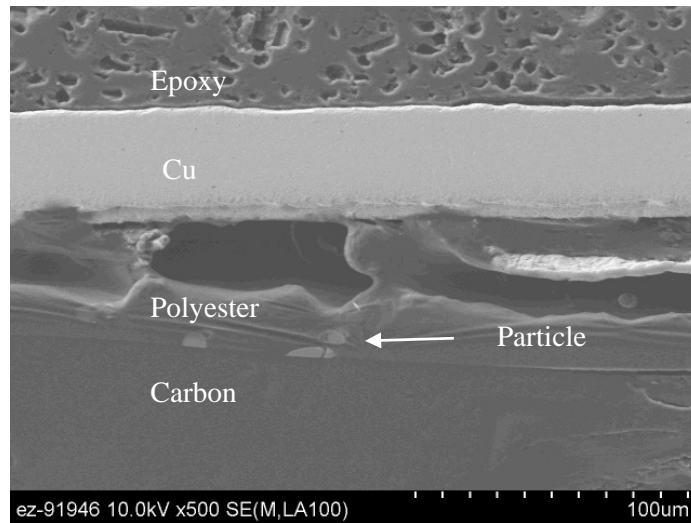


Fig. 6. Cross section of an epoxy-potted polyester-film specimen (copper substrate is not shown).

quite impressive. The localized breakdown can induce substantial heat that further softens and even melts the neighboring area whenever the heat cannot give off promptly.

Conclusion and Future Work

Extensive mechanical testing and characterization on comprising materials of PZT stacks have been conducted in this past fiscal year.

Mechanical strength of PZT ceramics and temperature effect have been tested and evaluated. This includes two candidate PZT ceramics that have different fabrication routes, namely, pressing for KCI and tape casting for EPCOS. Single layer PZT of KCI and multilayer PZT of EPCOS were studied. Four-point bending and ball-on-ring setups were used in the respective studies due to the different geometrical dimensions of specimens. The difference obtained in the four-point bending and ball-on-ring tests for two PZT ceramics reflected the important effects of size-scaling and strength-limiting flaws.³ Their influences on the Weibull parameters have been effectively observed. The

technology, the quality of PZT ceramic has a much more control than even before, and that results in more homogeneous PZT ceramic. This means the variance of strength-limiting flaws from batch to batch has been minimized. Therefore, the response of PZT ceramic to any external factors depends on the behavior of these flaws to a larger degree. Observation on these flaws and their responses enables the understanding of polarization status within the stresses body, especially of the piezoelectric materials. Just as the study on the effect of electric field on the flexure strength of poled PZT allows us to describe the status of polarization, the temperature also provides the opportunity to characterize the role of polarization from different point of view. The statistical difference in the mechanical strengths of different temperature levels has just validated the hypothesis. The humidity or vapor content will be brought into the test matrix to study how the strength of PZT reacts under a defined environmental condition. The test data obtained in this study together with those

from other series of tests would provide us a clear picture of strength performance of candidate PZTs.

The piezoelectric phenomenon stems from the remnant polarization, status of which is related to the degree of poling. However, the polarization can be consumed and its amount can be reduced due to the electric cycling fatigue. This has a significant impact on the performance of stack because the piezoelectric response is decreased also. Therefore, it is critical to test the fatigue of PZT ceramic under an equivalent cycling condition. During FY2010, an engineered test system, piezodilatometer, has been enabled to test and characterize the electric fatigue response of PZT ceramics. The testing on the KCI indicated the results of this piezoelectric ceramic are very typical of soft PZT ceramic under the given cycling condition as expected. Moreover, the cycling of poled PZT ceramic using a unipolar loading mode indeed revealed a significant degradation of PZT ceramic near 10^8 cycles in terms of piezoelectric and dielectric coefficients as well as their loss tangents. These data have not only advanced our understanding on the performance of PZT ceramic under high field loading, but also provided the important input for screening candidate PZT ceramics and the sound basis for testing these materials under other equivalent working condition such as mechanical and/or thermal couplings.

In the coming year, the complementary tests will be conducted on both KCI and EPCOS PZT ceramics. These tests are the part of tasks in mechanical testing and characterization of PZT ceramic. The effect of humidity will be focused. In addition, the alternative approach to testing and characterization of the mechanical strength and electric field effect will be explored with respect to EPCOS PZT ceramic for which the single layer PZT specimen is not available now.

The fatigue test will be pursued as inspired by the results obtained in FY2010. The performance of single layer PZT specimen (i.e. KCI) will be inspected beyond 10^8 cycles, and the experimental approach to testing and characterizing the electric fatigue on EPCOS PZT ceramic will be also explored. The latter is raised also because of the unavailability of stand-alone single layer PZT for EPCOS.

Testing EPCOS stacks will be pursued using the current stack fatigue facility with necessary modifications. This includes the effects of mechanical preloading, temperature, and humidity

under the controlled condition. At the same time, the microstructure analysis will be performed on the failed (supplied by Cummins after engine test) and fatigued stacks.

Finally, the simulation will be explored to incorporate the generated data into the probabilistic design for the recommended stack configuration and work conditions.

References

- [1] Wang, H. and Wereszczak, A. A., Effects of electric field on the biaxial strength of poled PZT, *Proc. 31st Int. Conf. on Adv. Ceramics and Composites*, Jan. 21-26, 2007, Daytona Beach, FL; also on *Advances in Electronic Ceramics, Ceram. Eng. Sci. Proc.*, 28 (8), 2007, 57-67.
- [2] Wang, H. and Wereszczak, A. A., Effects of electric field and biaxial flexure on the failure of poled lead zirconate titanate, *IEEE Trans. Ultrasonic, Ferroelectrics, and Frequency Control*, 55 (12), 2008, 2559-2570.
- [3] Wang, H., Matsunaga, T., and Lin, H.-T., Characterization of poled single-layer PZT for piezo stack in fuel injection system, to be submitted to *Proc. 34th Int. Conf. on Adv. Ceramics and Composites*, Jan. 24-29, 2010, Daytona Beach, FL.
- [4] Timoshenko, S. P. and Goodier, J. N., *Theory of Elasticity*, McGraw-Hill Int. Editions, 1970. p. 288-290.
- [5] ASTM Standard C1161-94, *Standard Test Method for Flexure Strength of Advanced Ceramics at Ambient Temperature*, Vol. 15.01, Mar. 2002.
- [6] Wang, H., Wereszczak, A. A., and Lin, H.-T., Dual-rod piezodilatometer and method for testing a piezoceramic plate, *ORNL Invention Disclosure*, 200802179, DOE S-115, 208, 11/21/2008.
- [7] Wang, H., Wereszczak, A. A., and Lin, H.-T., Fatigue response of a PZT multilayer actuator under high-field electric cycling with mechanical preload, *J. Appl. Phys.*, 105 (1), 2009, 014112.

Presentations and Publications

Presentations

1. Wang, H., Characterization on piezoelectric ceramics and actuators for engine system, Sept. 29, 2010, *ORNL*, Oak Ridge, TN.

2. Wang, H., Matsunaga, T., and Lin, H.-T., Characterization of poled single-layer PZT for piezo stack in fuel injection system, *34th Int. Conf. on Adv. Ceramics and Composites*, Jan. 24-29, 2010, Daytona Beach, FL.
3. Lin, H.-T., Wang, H., Wereszczak, A. A., Memering, D., Carmona-Valdes, J., and Stafford, R., Design optimization of piezoceramic multilayer actuators for heavy duty diesel engine fuel injectors, *2nd Meeting on ORNL-Cummins CRADA*, Dec. 1, 2009, Columbus, IN.

Publications

1. Wang, H., Matsunaga, T., Lin, H.-T., Mottern, A. M., and Wereszczak, A. A., Piezoelectric and dielectric performance of poled lead zirconate titanate subjected to electric cyclic fatigue, 2010, to be submitted for reviewing.
2. Wang, H., Matsunaga, T., and Lin, H.-T., Temperature effect on flexure strength of lead zirconate titanate, 2010, in preparation.
3. Wang, H., Cooper, T. A., Lin, H.-T., and Wereszczak, A. A., Fatigue responses of PZT stacks under semi-bipolar electric cycling with mechanical preload, *J. Appl. Phys.* 108, 084107 (2010)
4. Wang, H., Lin, H.-T., and Wereszczak, A. A., Strength properties of poled PZT subjected to biaxial flexural loading in high electric field, *J. Am. Ceram. Soc.*, 93 (9), 2010, 2843-2849.
5. Wang, H., Matsunaga, T., and Lin, H.-T., Characterization of poled single-layer PZT for piezo stack in fuel injection system, *Proc. 34th Int. Conf. on Adv. Ceramics and Composites*, Jan. 24-29, 2010, Daytona Beach, FL, also on Mechanical Properties and Performance of Engineering Ceramics and Composites V, *Ceram. Eng. Sci. Proc.*, 31 (2), 2010, 127-136.

Agreement 17058 – Compact NO_x Sensor with Built in Reference

Principal Investigators: J. L. Routbort, D. Singh (co-worker: Kristen Pappacena)

Argonne National Laboratory

9700 S. Cass Avenue

Argonne, IL 60439-4838

(630) 252-5065; fax: (630) 252-5568; e-mail: routbort@anl.gov

DOE Technology Manager: Jerry L. Gibbs

(202) 586-1182; fax: (202) 586-1600; e-mail: jerry.gibbs@ee.doe.gov

Contractor: UChicago Argonne LLC

Contract No.: DE AC03 06CH11357

Objective

- Use joining technique to produce compact oxygen and NO_x sensors with internal reference
- Develop electronic conducting ceramic to replace the Pt electrodes in the sensor
- Develop technique to directly join the conducting ceramic to the YTZP body of the sensor

Approach

- Vary the composition of LaSrAlMnO (LSAM) such that the electrical conductivity is maximum at the operating temperature of the sensor
- Assure that there is no reaction between the YTZP and the LSAM
- Modify the composition such that the LSAM can be plastically deformed at the same temperature and strain rates as the YTZP

Accomplishments

- Strong, pore-free joints have been made with various ceramics, cermets, intermetallics, composites, and biomaterials, with and without various interlayers, fracture occurs away from interface at the region of maximum residual stress
- Demonstrated that grains in SrTiO₃ rotate during deformation
- Published 25 journal papers, 3 patents issued for plastic joining process, patent applications filed for oxygen and NO_x sensor, negotiations for licensing of oxygen sensor started
- R&D 100 Award for oxygen sensor
- Developed initial NO_x sensor
- Developed one composition of electrically conducting ceramic to replace Pt connections that will bond directly to sensor removing need for glass seal and providing a more robust, higher temperature sensor

Future Direction

- Continue to develop conducting ceramics to replace expensive Pt interconnects
 - Improve sensitivity of NO_x sensor
-

Introduction

Monitoring gas composition, like O₂, NO_x, CO, CO₂, in the combustion environment with good accuracy has been of great importance since the advance of combustion heat engines in the last century. For instance, controlling the oxygen level in boilers carefully can maximize energy output and minimize pollutant emissions. It is estimated that yearly savings of \$409 million from coal-fired power plants could be saved through combustion optimization. NO_x (NO + NO₂) sensing has also been considered as one of the key elements of next generation internal combustion engines. A reliable and accurate NO_x sensor is needed to monitor NO_x and trigger the regeneration of NO_x adsorption catalysts, or control the injection of reductants for continuous NO_x reduction.

Previously we have demonstrated that it is possible to form pore-free, high-strength joints in yttria-stabilized zirconia (YTZP) by applying a small stress at elevated temperatures ($T/T_m \approx 0.5$, where T_m is the melting temperature in K [1,2]). This technique has been used to produce oxygen sensors by encapsulating a metal/metal oxide powder in a container consisting of a lower YTZP disk, joined to an YTZP cylinder [3]. A metal/metal oxide powder is placed in the cavity that is then sealed by plastic joining to another YTZP disk to which is attached a thin Pt electrode top and bottom side. When placed in a combustion environment, the metal/metal oxide powder decomposes to produce oxygen. The difference between the internal oxygen activity (the reference) and that of the activity of the gas to be measured produces an emf that is proportional to $\ln(a_O/a_{Oref})$ where a_o is the oxygen activity of the gas to be measured and a_{Oref} is the activity of the reference gas.

This technique has been applied to produce NO_x sensors [4] that could enable simultaneous measurements of NO_x and O₂ in a combustion environment. The Pd/PdO-containing reference chamber was sealed within the stabilized zirconia superstructure

by a high pressure/temperature bonding method that initiated grain boundary sliding between the ceramic components. NO_x sensing was conducted in both amperometric and potentiometric modes. Pt-loaded zeolite Y was used to obtain total NO_x capacity and to cover Pt electrodes for detecting oxygen in the presence of NO_x. Both amperometric and potentiometric type sensors will eventually be tested for signal stability, total NO_x response, and NO_x-O₂ cross interference.

The glass that was used to seal the internal Pt wire limited the operating temperature of the O₂ and the NO_x sensor. Last FY we developed an electrically conducting ceramic La_{0.77}Sr_{0.20}Al_{0.9}Mn_{0.1}O₃ (LSAM) that can be directly joined to the YTZP by plastic flow without any special preparation of the mating surfaces, eliminating the need for the internal Pt wire, and producing a much more robust sensor with higher temperature capabilities. The effort in FY10 continued this work, concentrating on developing more compounds with high electrical conductivity that could be joined to the body of the sensors, thereby replacing the expensive and leak prone Pt electrodes.

Experimental Details and Results

Details of the preparation of the LSAM can be found in ref. [5] and hence only the characterization will be summarized in this annual report. La_{0.8}Sr_{0.2}Al_xMn_{1-x}O₃ materials of four compositions (x=0, 0.3, 0.5, 0.7) were prepared. Each of these compositions were analyzed using X-ray diffraction to look at the lattice structure, scanning electron microscopy (SEM) and energy-dispersive X-ray spectroscopy (EDS) to look at the microstructure and chemical composition, and Archimedes' density measurements to determine the quantity of open porosity in the sintered pellets. Electrical conductivity was measured as a function of temperature for each composition. Deformation testing was also done for compositions Al=0, 0.3, 0.5 at

1270°C at three strain rates (5×10^{-5} /s, 1×10^{-5} /s, 5×10^{-6} /s) to optimize conditions for joining with YTZP.

X-ray diffraction was performed on both calcined powders (calcined to 1200°C for 50 hours) and crushed sintered pellets (sintered to 1450°C for 50 hours for all except $x=0.7$, which was sintered for 12 hours). Silicon powder was added as a standard to normalize the 2theta axis and to ensure that any peak shift observed was a result of varying compositions. The X-ray diffraction patterns for the sintered ceramic are shown overlaid in figure 1(a). From this plot, it is clear that the peaks shift slightly to the right with increasing alumina content. An example of a calcined powder paired with its respective sintered pellet is shown in Figure 1(b) to illustrate that the composition does not change as a result of sintering.

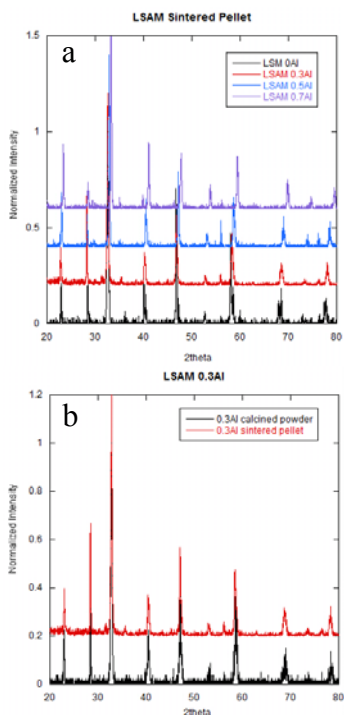


Figure 1: X-ray diffraction patterns of (a) LSAM $x=0, 0.3, 0.5, 0.7$ crushed sintered pellets and (b) LSAM $x=0.3$ calcined powder and crushed sintered pellet.

Porosity was determined by Archimedes' density measurements, and for each sintered ceramic of $x=0, 0.3, 0.5$, the porosity was under 3%. For $x=0.7$, the porosity was

about 8%. This higher porosity is correlated to the shorter sintering time, indicating that the longer time is necessary for more complete densification.

SEM images with EDS analysis were taken of compositions $x=0, 0.3, 0.5$ to learn more about the microstructure and composition. Examples of each composition are shown in Figure 2(a)-(c).

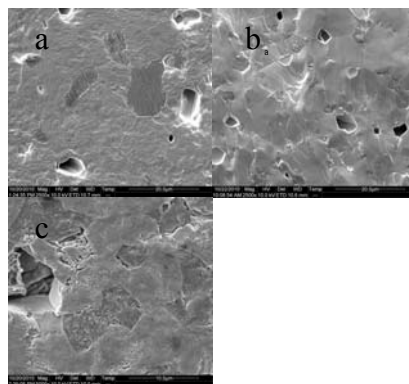


Figure 2: SEM images of (a) LSM (b) LSAM 0.3Al and (c) LSAM 0.5Al.

In each of the three compositions, EDS indicated phase separation in the darker grains. In LSM, these darker grains were Mn rich, while the lighter regions were La and Sr rich. In the $x=0.3$ and 0.5 compositions, the phase separation involved Al. In 0.3Al, the Al and Mn were segregating in the darker regions, and La and Sr were rich in the light regions. However, in the 0.5Al composition, the dark grains were Al and Sr rich, while the lighter regions had high concentrations of La and Mn. It is evident that in the presence of aluminum, phase segregation occurs, but the reason for different compounds in each case is unclear at this point.

High electrical conductivity is crucial for the LSAM ceramic to successfully replace the Pt electrodes in the gas sensor housing. Electrical conductivity was measured by applying a 10mA current to the sample and measuring the corresponding voltage. The electrical conductivity of 3 compositions is shown in Figure 3. The conductivity clearly increases with decreasing aluminum content. The 0.7Al resulted in an extremely low conductivity,

and will not be useful in this application. For the 0.3Al and 0.5Al compositions, the electrical conductivity increases as a function of temperature, and slowly levels off at higher temperatures. For the LSM, with no Al, the conductivity initially decreases with increasing temperature, but after about 300°C, follows a similar trend to the other compositions. Literature values for electrical conductivity of $La_{(1-y)}Sr_yMnO_3$ where $y=0.2-0.4$, were also shown to have a discontinuity around the magnetic transition temperature, near 100°C [6]. The resulting electrical conductivity values tested here for $x=0.3$ and 0.5 are significantly higher than those reported in the literature for similar compositions [7]. This is likely due to the higher success in densification for the current samples as compared with Holc et al.[7].

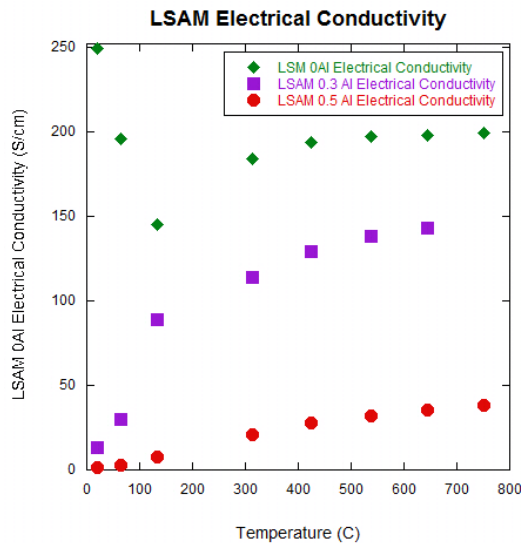


Figure 3: Electrical conductivity of LSAM ceramics of compositions $x=0, 0.3, 0.5$ as a function of temperature.

Deformation testing was performed on LSAM samples with compositions of $x=0, 0.3, 0.5$ Al. All tests were performed at 1270°C. Three strain rates, $5 \times 10^{-6}/s, 1 \times 10^{-5}/s$ and $5 \times 10^{-5}/s$ were tested for 1-2 samples at each composition. Each stress versus strain curve exhibited an initial linear region followed by an area where the curve begins to flatten out, and eventually decrease, indicating the onset and progression of plastic deformation. The equilibrium stress

that is achieved during this plastic regime is the flow stress, and is pertinent for joining with YTZP. Figure 4 shows a plot of the flow stress at each strain rate for the three different compositions tested. The flow stress increases with increasing strain rate.

The strain rate-stress relationship follows equation 1:

$$\dot{\epsilon} \propto \sigma^n \quad (1)$$

where $\dot{\epsilon}$ is the strain rate, σ is the flow stress and n is the stress exponent [8]. The stress exponents can be calculated from a fit of the data shown in Figure 4. For the $x=0.3$ and 0.5 Al samples, the stress exponents were 2.2 and 2.4, respectively. These agree well with each other, and correspond fairly well to a diffusion mechanism for deformation [8]. For LSM with no Al, the stress exponent is a lot higher: 4.9. Cook et al. studied deformation behavior of various compositions of $La_ySr_{(1-y)}MnO_3$, and for $y=0.8$, the composition tested here, measured a stress exponent of around 1 [9]. This difference in exponent value can be attributed to the grain sizes seen in the current work that are almost 10x larger than those in Cook's work [9].

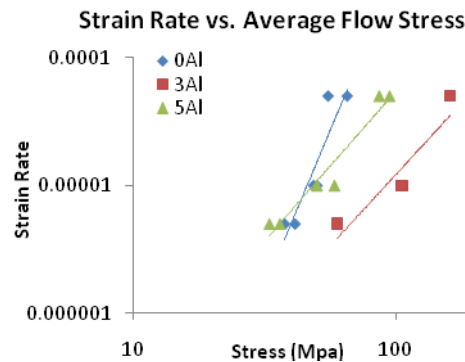


Figure 4: Flow stress at different strain rates for different compositions of LSAM.

Conclusion

$\text{La}_{0.8}\text{Sr}_{0.2}\text{Al}_x\text{Mn}_{(1-x)}\text{O}_3$ samples of compositions of $x=0, 0.3, 0.5, 0.7$ were fabricated and analyzed to begin to determine the optimal composition for use in the gas sensor housing. Compositions of $x=0, 0.3$ and 0.5 exhibited electrical conductivities that could potentially be used in this application. Initial deformation testing was performed.

Future Directions

The work here demonstrates introductory steps towards replacing the Pt electrode in the oxygen/ NO_x sensors. One key future step is to determine the origin of the segregating phases occurring in each of the compositions. It is important to prevent these extra phases from forming.

In addition, the deformation testing has only been completed at one temperature. In order to complete the deformation study, more temperatures will be investigated. After the optimized composition is selected, joining experiments will be performed with the optimized LSAM composition and YTZP. Then, the degree of potential reaction between the two materials will be studied, and the resulting electrical conductivity change (if any) will be measured. After these investigations are completed, the optimized LSAM can replace the Pt electrode in the sensor packaging, which will simplify the sensor construction in that the external wires can be placed on the outside of the sensor eliminating the glass seal.

In addition to the completion of the LSAM study, the other directions of interest are adding additional gas sensing capabilities, including CO and CO_2 to the sensor. The materials for this sensing need to be determined and investigated for cross sensitivity with O_2 and/or NO_x sensing.

References

1. F. Gutierrez-Mora, A. Dominguez-Rodriguez, J. L. Routbort, R. Chaim, and F. Guiberteau, "Joining of Ytria-tetragonal Stabilized Zirconia Polycrystals using Nanocrystals," *Scripta Mater.* **41** 455-60 (1999).
2. F. Gutierrez-Mora, K. C. Goretta, S. Majumdar, J. L. Routbort, M. Grimdisch, and A. Dominguez-Rodriguez, "Influence of Internal Residual Stresses in Superplastic Joining of Zirconia Toughened Alumina," *Acta Mater.* **50** 3475-3486 (2002).
3. J. V. Spirig, R. Ramamoorthy, S. Akbar, J. L. Routbort, D. Singh, and P. K. Dutta, "High-temperature Zirconia Oxygen Sensor with Sealed Metal/Metal Oxide Internal Reference", *Sensors and Actuators B* **124**, 192-201 (2007).
4. J. C. Yang, J.V. Spirig, D. Karweik, J. L. Routbort, D. Singh, and P. K. Dutta, "Compact electrochemical bifunctional NO_x/O_2 sensors with metal/metal oxide internal reference for high-temperature applications" *Sensors and Actuators, B* **131**(2), 448-454 (2008) *Patent application pending*
5. J. V. Spirig, J. L. Routbort, D. Singh, G. King, P. M. Woodward and P. K. Dutta, "Joining of highly aluminum-doped lanthanum strontium manganese oxide with tetragonal zirconia by plastic deformation, *Solid State Ionics* **179**, 550-557 (2008) *Patent application pending*.
6. H. Kamata, Y. Yonemura, J. Mizusaki, H. Tagawa, K. Naraya, and T. Sasamoto. "High temperature electrical properties of the perovskite-type oxide $\text{La}_{1-x}\text{Sr}_x\text{MnO}_{3-d}$. *J. Phys. Chem. Solids* **56**(7), 943-950 (1995).
7. J. Holc, D. Kuscer, M. Hrovat, S. Bernik, and D. Kolar. Electrical and microstructural characterization of $(\text{La}_{0.8}\text{Sr}_{0.2})(\text{Fe}_{1-x}\text{Al}_x)\text{O}_3$ and $(\text{La}_{0.8}\text{Sr}_{0.2})(\text{Mn}_{1-x}\text{Al}_x)\text{O}_3$ as possible SOFC cathode materials. *Solid State Ionics* **95**, 259-268 (1997).

8. T.G. Langdon. The characteristics of superplastic-like flow in ceramics. In *Plastic Deformation of Ceramics*, ed. R.C. Bradt, C. A. Brookes and J. L. Routbort. Plenum Press, New York 1995 pp.251-268.
9. R. E. Cook, K. C. Goretta, J. Wolfenstine, P. Nash, and J.L. Routbort. High-temperature deformation and defect chemistry of $(La_{1-x}Sr_x)_{1-y}MnO_{3+\delta}$. *Acta mater.* **47** (10), 2969-2980 (1999).

Agreement 19202 – Surface Titanium Friction and Wear: Surface Engineering of Connecting Rods and Other Bearing Components

Peter J. Blau and Dinesh Bansal*

Oak Ridge National Laboratory, P. O. Box 2008, Mail Stop 6063

Oak Ridge, TN 37831-6063

**(865) 574-5377; fax: (865) 574-4913; e-mail: blaupj@ornl.gov*

DOE Technology Manager: Jerry L. Gibbs

(202) 586-1182; fax: (202) 586-1600; e-mail: Jerry.gibbs@ee.doe.gov

ORNL Technical Advisor: D. Ray Johnson

(865) 576-6832; fax: (865) 574-6098; e-mail: johnsondr@ornl.gov

*Contractor: Oak Ridge National Laboratory, Oak Ridge, TN
Prime DOE Contract Number DE-AC05-00OR22725*

Objectives

- To help to achieve a 50% increase in vehicle freight efficiency through the use of lightweight titanium (Ti) alloy moving parts and bearing surfaces.
- To identify and develop novel surface engineering approaches that reduce the friction and wear of Ti bearing surfaces in engine components like connecting rods.
- To design, construct, and use a variable-load connecting rod bearing simulator to enable the cost-effective screening of candidate surface engineering approaches for Ti alloys.
- To demonstrate the potential for surface engineering Ti-based bearing surfaces on full-sized, prototype connecting rods.

Approach

- A three-phase effort is planned: (Phase I) Conduct bench-scale friction and wear experiments on candidate surface treatments using established methods (ASTM); (Phase II) Design and construct a variable-loading simulator and use it to screening candidate surface engineering approaches down-selected during Phase I; and (Phase III) In conjunction with a diesel industry partner, demonstrate the performance of surface engineered Ti bearing surfaces on full-sized, prototype connecting rods.
- Compare existing commercialized surface engineering processes with more novel pre-commercialization approaches like oxygen diffusion treatments, infrared synthesized surface layers, nanocomposite coatings, and various combinations of treatments.
- Work with an engine maker to develop useful bench-scale simulations of crankshaft bearing operating conditions.

- Work with an engine maker to fabricate and test a prototype Ti-based a connecting rod with integral, surface-engineered bearings.

Accomplishments

- Selected 20 candidate surface engineering treatments (single treatments and combinations) and several reference materials for investigation. The reference materials included a bronze bearing alloy typically used in connecting rod bearings and a non-treated Ti alloy Ti-6Al-4V that will also serve as the substrate for experimental surface treatments.
- Obtained candidate surface treatments from various suppliers including Eaton Corporation Innovation Center, Phygen Corporation, Metal Improvement Company, and Argonne National Laboratory. Some treatments were purchased, others were contributed for study, and some materials were prepared at ORNL using techniques ranging from vacuum melting and casting to high-intensity infrared surface treatment to form composites in situ.
- Completed bench-scale tests of 20 surface treatment variants using a standardized diesel engine drain oil (T-11 test) as the lubricant. Down-selected promising surface treatments for study during Phase II of the effort. Submitted a paper, co-authored with Argonne National Laboratory, for the 18th International Conference on Wear of Materials.
- Completed the design and began construction of a variable-load apparatus to conduct friction and wear tests on candidate surface-engineered materials for use in the large-end bearing of a lightweight connecting rod.

Future Directions

- Complete construction of a variable-load test apparatus and validate its performance on baseline materials. Test parameters will be selected based on discussions with a diesel engine maker.
- Using the variable-load testing apparatus, conduct tests on the most promising surface treatment options for Ti alloys, primarily based on the results of research conducted during FY 2010.
- Finalize a prototype design for a full-sized Ti connecting rod with engineered bearing surfaces. The prototype will be tested in a dynamometer or a fired diesel engine.

Introduction

The Department of Energy's heavy vehicle research and development plan has targeted a 50% increase in freight efficiency (measured in ton miles per gallon). A combination of approaches is being used to achieve this goal. This includes a reduction in parasitic losses (e.g., friction, aerodynamic drag, etc.), more efficient designs, and the use of lightweight materials.

Titanium (Ti) alloys are strong, corrosion-resistant, and lighter-weight than similarly-sized steel or cast iron parts. Once used mainly in aerospace, Ti's applications have expanded into areas like human joint replacements, dental implants, sports equipment, and industrial machinery. Recent developments in processing Ti raw materials by non-traditional routes promise to make its alloys more affordable for use in fuel-efficient heavy vehicles.

Despite the aforementioned advantages, Ti alloys also have drawbacks that limit their use in heavy vehicle engine components subjected to rubbing contact. These drawbacks include a propensity for scuffing, galling, and adhesive wear. Lubricant formulations that were designed for ferrous alloys do not work for Ti surfaces as-machined. If, however, the friction and wear of Ti could be improved by surface engineering, new opportunities to use these alloys for pistons, cam shafts, crank shafts, tappet shims, fuel injector needles, and connecting rods with integral bearing surfaces, would be enabled.

Approach

A three-phased approach is planned, culminating in the demonstration of a Ti alloy connecting rod that contains integral, surface-engineered bearing bores. The three phases of the project are as follows:

Phase I: Selection and bench-testing of candidate surface engineering treatments and coatings

Phase II: Design and use of a simulator to impart variable loads, as would be seen by a connecting rod bearing.

Phase III: Preparation and testing of a full-scale, prototype Ti connecting rod with engineered bearing surfaces.

Progress in FY 2010

Candidate surface treatments and coatings. After a comprehensive literature review and discussions with suppliers during FY 2010, more than two dozen candidate surface treatment and coating approaches were considered. Ti-6Al-4V alloy was obtained and machined test coupons. This alloy was used both as the non-treated reference and as a substrate for various surface treatments, or coatings. As shown in Table 1, some processes were used singly, and others were applied in combination.

Table 1. Materials, Treatments, and Coatings

Bulk Materials	
1	Baseline, non-treated Ti64
2	Baseline, CDA 932 (bearing bronze)
3	60Ni-40Ti (NASA developed bearing alloy)
Mechanical Treatments	
4	Shot peening
Thermal and Chemical Treatments	
6	Oxygen diffusion treatment (ORNL)
7	Carburized surface
8	Nitrided surface
9	Oxidation/surface hardening
10	Anodizing
Hard and Soft Coatings	
11	TiN hard coating (commercial)
12	CrN hard coating (commercial)
13	DLC hard coating (Argonne National Lab)
14	Nanocomposite AlMgB (DOE/EERE/ITP project)
15	In situ IR-produced Ti MMC (ORNL)
16	Metallic soft coating of Cu-Ni-In on Ti-6Al-4V
17	Metallic soft coating of Cu-Ni-In on CDA 932 bronze
Hybrid Treatments	
18	Shot peening after oxygen diffusion treatment
19	Shot peening after carburizing
20	Shot peening after nitriding

Selection of the Phase I test method.

Owing to the experimental nature of some of the candidate coatings and surface treatments, it was decided to use small 25 x 25 x 6.35 mm test coupons for initial experiments. A standardized reciprocating sphere-on-flat friction and wear test (ASTM G133), which developed by ORNL with DOE support in the mid-1990s, was used. Bearing steel AISI 52100 was selected as the slider (fixed ball) since hardened chrome-steel is commonly used for bearing shafts, rollers, and fuel injector bodies.

Two test variants of ASTM G133 were used: dry sliding at low load, and sliding at higher load in a drain oil from a standard diesel engine test (T-11 test). In fact, the same oil was used for a recent international inter-laboratory program to validate ASTM standard test G181 for piston ring and cylinder liner friction, also developed at ORNL with support from DOE. Both Procedure A and B were performed at room temperature for these screening experiments.

Table 2. ASTM G133 Test Procedures.

Test Variable	Procedure A (dry)	Procedure B (lubricated)*
Applied load (N)	25	200
Stroke length (mm)	10	10
Oscillation rate (Hz)	5	10
Test duration (s)	1000	2000
Sliding distance (m)	100	400
Lubrication method	not applicable	immersion
Lubricant	none	used 15W-40 (T-11 engine test sequence)

* Run at room temperature rather than 150 °C per the standard. Hence, referred to here as Procedure B (mod.).

Except for cases of premature failure (excessive friction or vibration), most material combinations (that is, AISI 52100 steel pins reciprocating against the materials in Table 1) were tested three times to establish data repeatability. In all, 64 experiments were performed.

The details of this work, including studies of cross-sectioned surfaces, are included in a paper submitted to the *International Conference on Wear of Materials* (see **Publications**, below). Examples of Phase I test results follow.

Friction coefficient versus sliding distance. Baseline tests were performed on non-coated Ti alloy and bearing bronze. Under dry conditions, the non-treated Ti alloy had a friction coefficient of about 0.4-0.5. Figure 1 exemplifies friction traces for five different material combinations tested under ASTM G133 Procedure B (mod.). While all materials tended to have friction levels within the regime called ‘boundary lubrication,’ the friction coefficients for DLC, TiN and CrN coatings are about 35% lower than those of the CuNiIn-coated Ti alloy. The as-received roughness of the sprayed CuNiIn is likely to be the cause for its higher friction.

Materials whose average three-test friction coefficients (lubricated) were less than 0.15, and which also survived the full 400 m sliding distance were designated as ‘passed.’ Thus, seven materials passed: (i) oxidized NiTi alloy, (ii) DLC coating, (iii)

bearing bronze, (iv) TiN hard coating, (v) CrN hard coating, (vi) oxygen diffused Ti-6Al-4V, and (vii) nitrided Ti-6Al-4V.

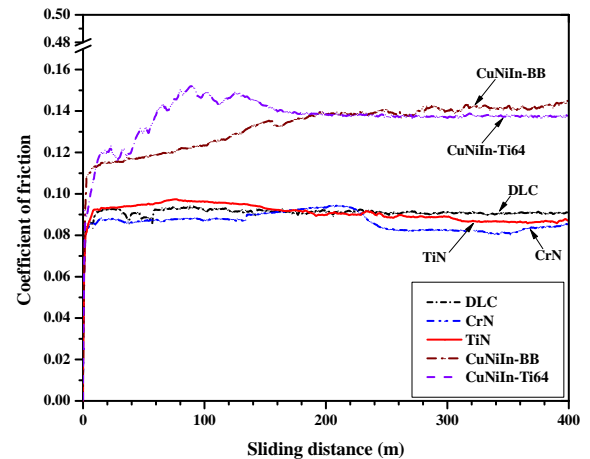


Figure 1. Friction coefficient versus sliding distance for Ti-based test coupons. Labels refer to the following line numbers used in Table 1: CuNiIn-BB (line 17); CuNiIn-Ti64 (line 16); DLC (line 13), TiN (line 11); CrN (line 12)

Wear results. Wear measurements for the steel slider were based on microscope measurements of the wear scar diameter, and the wear of the flat coupons was measured using vertical scanning interferometry (VSI) of the grooves (see Figure 2). Only couples that passed the friction criteria and which lasted the full test length were measured for wear.

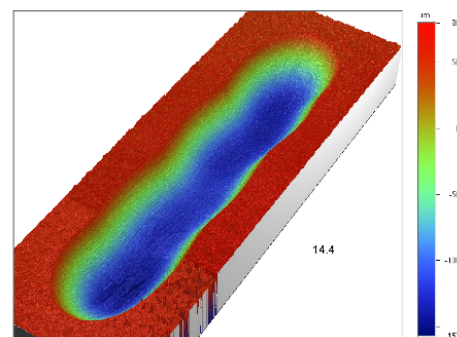


Figure 2. VSI image of a wear groove in a flat specimen. Depth is color-coded from +90 µm (bright red to - 157 µm (dark blue).

Figure 3 compares the ball and flat wear volumes for the four best treatments to those for the reference bronze alloy (CDA 932). The three tests for each material are shown separately. The DLC and CrN treatments had the lowest total wear of ball and flat specimens, and all four treatments on Ti alloys had more than ten times lower wear than that of the bronze specimens.

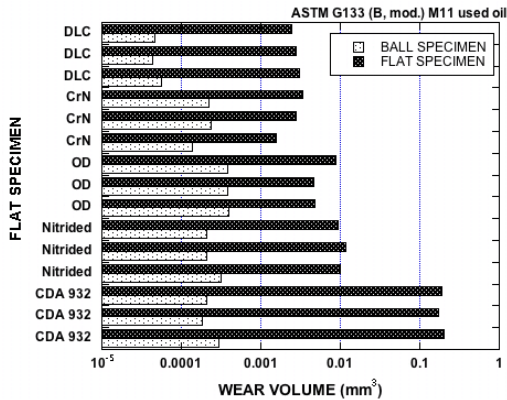


Figure 3. Wear volumes of the 52100 balls (dotted) and selected flat specimens (solid). Note that the horizontal axis is logarithmic.

Design of a variable-load apparatus for simulating connecting rod bearing conditions. Connecting rods, such as the one shown schematically in Figure 4, contain a big end and small end bearing. The dynamics of the crankshaft generates different systems of forces and accelerations on the surfaces these bearings. The shaft in the small end bearing oscillates as the piston moves up and down, but the big end bearing rotates in the same direction.

Due to inertial forces, engine dynamics, and power pulses during fuel ignition, the forces on the bearing surfaces are in a continual state of change. That affects the lubricant film thickness in the interface and in turn, the friction and wear. While analyses of these forces have been published in the automotive engineering literature, ORNL is also working with a U.S. diesel engine manufacturer to define realistic load-time spectra for use in Phase II testing.

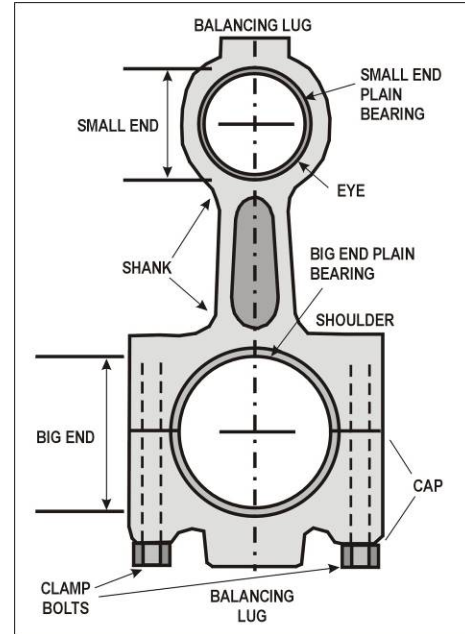


Figure 4. Schematic diagram of a typical connecting rod.

The computer rendering of the Variable-Load Bearing Tester (VLBT) in Figure 5 shows its basic components. At the upper left is a 3-phase variable-speed motor, coupled through a torque cell and a pillow-block bearing to a pair of chucks that hold the rod specimen that simulates the crankshaft. A computer-controlled servo-actuator applies force to a bearing test specimen from underneath to load it against the rotating specimen. The VLBT was under construction at the end of FY 2010.

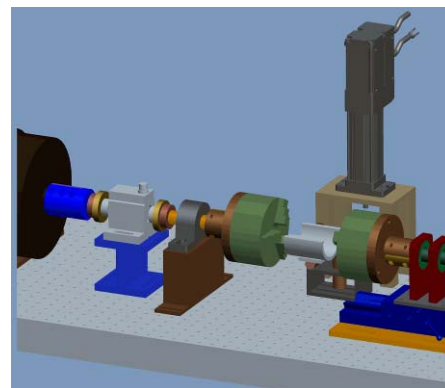


Figure 5. Component layout for the VLBT.

Summary and Conclusions

- Based on a literature review and information from commercial sources and research laboratories, 20 candidate materials were selected, obtained, and evaluated using the ASTM G133 friction and wear test method. A diesel engine drain oil was used as the lubricant.
- The most promising treatments for Ti-6Al-4V were a nitriding treatment, an oxygen-diffusion treatment, a chromium nitride coating, and a low-friction diamond film. Certain combinations of treatments, such as nitriding plus shot-peening did not offer advantages in friction or wear performance, but smoother surface finishes remain to be investigated as a means to overcome some of these shortfalls in performance.
- The design of a variable-load, friction and wear tester to simulate the interfacial conditions in bearings for connecting rods has been completed, and construction is proceeding. In FY 2011, the apparatus will be used to down-select surface-engineering approaches for a prototype Ti-based connecting rod.

Publications/Presentations

- 1) P. J. Blau and D. Bansal (2011) "Surface engineering to improve the durability and lubricity of Ti-6Al-4V alloy," submitted to the 18th International Conference on Wear of Materials, Philadelphia, PA, April 3-7, 2011.

Agreement 15050 – Materials Testing with ACERT Engine (CRADA with Caterpillar)

M. D. Kass, T. J. Theiss, R. Wagner, and N. Domingo

Fuels, Engines and Emissions Group

Oak Ridge National Laboratory

NTRC Building

2360 Cherahala Blvd.

Knoxville, TN 37932

(865) 946-1241; fax: (865) 946-1354; e-mail: kassmd@ornl.gov

H. T. Lin

Ceramic Science and Technology Group

Oak Ridge National Laboratory

P.O. Box 2008, MS 6068, Bldg. 4515

Oak Ridge, TN 37831-6068

DOE Technology Manager: Jerry L. Gibbs

(202) 586-1182; fax: (202) 586-1600; e-mail: Jerry.gibbs@ee.doe.gov

ORNL Technical Advisor: D. Ray Johnson

(865) 576-6832; fax: (865) 574-6098; e-mail: johnsondr@ornl.gov

Contractor: Oak Ridge National Laboratory, Oak Ridge, Tennessee
Prime Contract No.: DE-AC05-00OR22725

Objectives

- Improved diesel engine performance, efficiency, and emissions through the applications of materials enabled technologies.
- Evaluate material/component performance on a heavy-duty diesel engine platform.

Approach

- Evaluate components and materials for improved efficiency in a 2004 Caterpillar C-15 ACERT instrumented for thermal and combustion analysis.

Accomplishments

- Installed and commissioned power-factor correction system
- Performed engine baseline experimentation to confirm operating parameters
- Evaluated novel turbo concept for improved performance and efficiency

Future Direction

- Install and evaluate performance of new valve alloy for improved durability
 - Install and evaluate new exhaust manifold alloy for improved thermal performance
 - Install Tier IV engine for aftertreatment studies
-

Introduction

The purpose of this Cooperative Research and Development Agreement between UT-Battelle Inc. and Caterpillar, Inc. is to improve diesel engine performance, efficiency, and emissions through the application of materials-enabled technologies. The demands of meeting new emissions and fuel economy goals are continuing to push heavy-duty diesel engine components to higher temperatures and pressures and improved durability. Engine manufacturers have recognized several key needs that need to be addressed in order for heavy duty diesel engines to achieve a national efficiency goal of 55% by the year 2012. These include 1) improved structural materials to accommodate higher cylinder pressures and temperatures (associated with advanced combustion methodologies), 2) improved thermal management and waste heat recovery technologies, 3) improved durability, 4) improved transient performance, and 5) better aftertreatment performance. These needs address barriers associated with high parasitic losses, high-efficiency clean combustion and thermal management of the cylinder and exhaust.

This CRADA brings together expertise and facilities from the ORNL Materials Science & Technology and Engineering & Transportation Science Divisions. Similarly, materials and engine research staff at Caterpillar are also working together. In anticipation of this CRADA, Caterpillar provided ORNL with two 600 hp motoring dynamometers and C15 ACERT engine. Caterpillar (working with ORNL) will develop and provide components to be evaluated on the engine platform. ORNL engine research staff will evaluate the engine performance with emphasis on combustion diagnostics, optimization and modeling. Materials scientists at ORNL will examine material performance and provide guidance to materials development.

Results

The infrastructure necessary for heavy-duty engine experimentation was completed and successfully commissioned. The engine was broken-in using Caterpillar protocol and baselined successfully. A photograph showing the installed engine is shown in Figure 1. The engine and exhaust system were instrumented for temperature and pressure measurement. This instrumentation is necessary to

perform the detailed thermodynamic analysis necessary to identify areas of potential efficiency gains. A diagram detailing the type and location of instrumentation is shown in Figure 2.



Figure 1. Photograph showing mounted engine and dynamometer. Engine has been instrumented for 2nd Law Analysis.

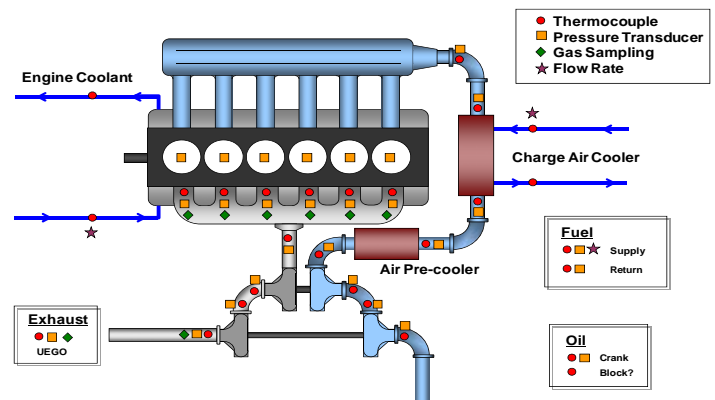


Figure 2. Schematic diagram showing location of instrumentation

The engine was successfully baselined and the results were compared to factory measurements and a model developed to predict thermal performance of the engine. These results are shown in Figure 3 and indicate that the engine results matched the factory-tested engine closely except for the intake manifold pressure. Also the predicted model results did match the experimental performance, which indicated that some adjustment to the model is necessary.

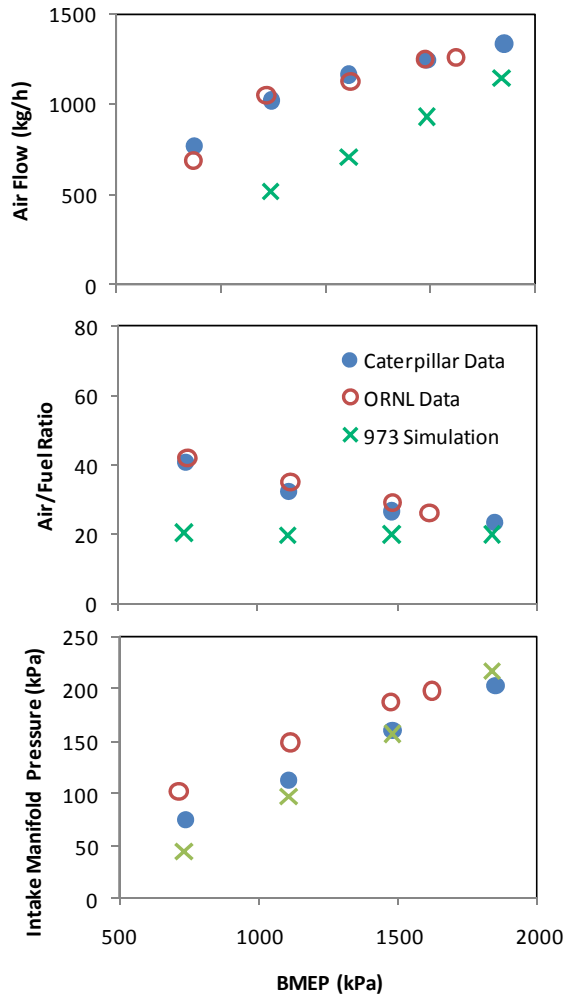


Figure 3. Baseline comparison of ORNL engine with a factory-tested engine and a thermodynamic model.

Conclusions

The engine was successfully baselined and the results were comparable to a factory-tested engine. The thermodynamic model results did not match engine performance and need correction to better reflect engine operation performance. Future efforts will revolve around testing actual components and assess their impact on overall engine efficiency.

Agreement 15054 - Fatigue Enhancements by Shock Peening

Principal Investigators: Curt A. Lavender and Elizabeth V. Stephens

Energy Materials Group

Pacific Northwest National Laboratory

PO Box 999, MS K2-44

Richland, WA 99352

(509) 372-6770; fax: (509) 375-2186; e-mail: curt.lavender@pnl.gov

(509) 375-6836; fax: (509) 375-4448; e-mail: elizabeth.stephens@pnl.gov

Yong-Ching Chen

Cummins Inc.

(812) 377-8349; e-mail: yong-ching.c.chen@cummins.com

DOE Technology Manager: Jerry L. Gibbs

(202) 586-1182; fax: (202) 586-1600; e-mail: jerry.gibbs@ee.doe.gov

Field Technical Manager: Dean Paxton

(509) 375-2620; fax: (509) 375-2186; e-mail: dean.paxton@pnl.gov

Contractor: Pacific Northwest National Laboratory

Contract Number: DE-AC05-76RL01830

OBJECTIVES

- Evaluate the capability for surface modification techniques such as laser shock peening (LSP), water jet peening (WJP), and friction stir processing (FSP) to improve the fatigue performance of steel, aluminum, and cast iron engine components.
- Evaluate the fatigue performance impact offered by these surface treatments to induce compressive residual stresses and to modify microstructure in the surface of aluminum, steel, and cast iron engine components.
- Compare fatigue performance and thermal stability of these novel surface treatment approaches to traditional shot peening methods.

ACCOMPLISHMENTS

- Waterjet peening produced surface compressive residual stresses in A354 while maintaining the surface finish.
- WJP cast aluminum alloy A354 specimens showed a significant improvement in fatigue life in comparison to the control.
- Plasticization of cast iron was observed with the use of cover plates and no pre-heating when friction stir welding cast iron.

FUTURE DIRECTIONS

- Complete waterjet peening evaluations of A356-T6 aluminum specimens.
- Identify component to be processed by WJP for full-scale test evaluations.
- Continue development of surface treatment techniques of cast iron material via friction stir processing/joining.

- Evaluate emerging surface enhancement technologies such as cavitation peening and initiate preliminary studies on 52100 steel.
-

Introduction

The primary objective of this project is to evaluate the impact of LSP, WJP, and FSP on the fatigue performance of aluminum, cast iron, and steels. Fatigue performance is an important factor in propulsion materials, especially for fuel system components, cylinder heads and blocks, etc. With the advent of faster injector response and higher pressures for better control of combustion events, cam stresses are significantly increased leading to reduced contact and flexural fatigue life. Cyclic fatigue improvements of forming dies made from tool steels have been achieved by selectively applying compressive residual stresses at the surface. Methods to apply these stresses vary, but among them, LSP has been used successfully. LSP not only induces compressive residual stresses at the surface, improving cyclic fatigue life more than five times, but it has also been shown to decrease the susceptibility of steels to stress corrosion cracking. However, there are some uncertainties with the application of the LSP process for engine components: 1) knowing exactly where to optimally apply the process based on part starting condition and ultimate performance requirements, and 2) the parameters required to effectively improve performance based on failure modes encountered.

For softer metals like aluminum, a lower-energy option that operates similarly to LSP is high-pressure WJP. This process is still in its infancy, but it has shown promise for improving fatigue performance in aluminum castings and wrought products with better control of residual stress distribution. Like that of LSP of high strength steels, the fatigue life enhancement mechanisms of WJP and optimum processing parameters are not yet well defined. Further understanding of the effects of LSP on aluminum alloys is also needed.

A cost and energy-efficient way of localized processing of metals to improve their fatigue life and wear resistance is by using FSP. This

process is known to increase fatigue life by refining the grain structure and homogenizing the microstructure of the metal, thereby eliminating defects, if any, within the processed area. Porosity is inherent to a cast metal, and its strength is always lower than that of a forged metal. By friction stir processing the area of interest, forged properties can be attained in a cast component and low cost, high-strength castings still can be produced. This is ideal for applications like cylinder heads and engine blocks, where high strength and wear properties are desired in localized areas such as the combustion chamber, bolt hole bosses, etc. This process can deliver high strength in aluminum, cast iron, and steel. Significant challenges exist in understanding the effect of FSP process parameters on mechanical properties of high-temperature materials like steel and cast iron.

This project is a three-year development and demonstration effort and will include active participation by Cummins, Inc. In October 2007 (FY2008), a formal Cooperative Research and Development Agreement (CRADA) was established with Cummins.

Approach

In this research, two approaches are being implemented to meet the objectives and deliverables of the project: technology development and technology transfer and commercialization. Technology development includes 1) demonstrating that surface treatments can induce deep subsurface compressive residual stresses in test specimens; 2) characterizing the stress distributions in test specimens as well as the surface roughness after treatments and comparing results to control specimens; 3) evaluating the mechanical properties of surface-treated bar specimens using rolling contact fatigue and rotating beam fatigue tests methods; 4) performing thermal stability tests of surface-modified specimens; 5) demonstrating FSP technique for processing of cast iron; and 6) developing a cost model for process deployment. Technology transfer and

commercialization includes Cummins demonstrating LSP and WJP surface modification approaches on a full-scale steel and/or aluminum component using engine systems qualification tests; Cummins/PNNL developing and demonstrating a cost effective process sequence for LSP/WJP of a relative high-volume production; and Cummins disseminating technology benefits to product design and development groups.

Results and Discussion

Experimental Characterization of A354-T6 Cast Aluminum

During this reporting period, characterization focused on the WJP evaluations where waterjet technology was used for peening the A354 cast alloy to enhance its fatigue life. Task 2 was completed and work is progressing in Task 3.

In Task 2, a quadratic model design of experiments (DOE) was applied where the supply pressure, air pressure, stand-off distance, and traverse rate was varied to determine the optimum processing parameters from the promising methodologies determined in Task 1. The goal of Task 2 was to achieve the highest level of residual stress while minimizing the surface roughness so no secondary machining would be needed. Twenty-six runs were conducted, and residual stress measurements and three dimensional surface profilometry were performed on each specimen processed. These measurements verified that waterjet peening can produce surface compressive residual stresses in A354 while maintaining the surface finish. The maximum compressive stresses observed among the specimens ranged from 75 MPa to 275 MPa with depths at max stress ranging from 0 to 0.070 mm, and the average R_a surface roughness measurements observed ranging from 0.8 μm to 7 μm .

From the Task 2 results (focusing on the residual stress and surface roughness relationship), three processing conditions were selected for Task 3: WJP methods A, B, and C. Figure 1 compares the residual stress profile between specimens fabricated from methods A and C and illustrates

a representative surface image from a method C specimen.

In addition, a Pareto Analysis of the DOE results was performed to evaluate the parametric contributions. The analysis determined that the supply pressure and traverse rate were key contributors on the resulting max residual stress and surface roughness observed on the specimens, while the stand-off distance and air flow rate had a minimal role.

In Task 3, three sets/populations of rotating beam fatigue specimens were fabricated and processed with the WJP parameters determined from Task 2, Set A, B, and C. No secondary machining was performed. Fatigue tests are currently in progress with the current results plotted in Figure 2. The WJP A354 specimens show significant improvement in fatigue life in comparison to the control. A statistical analysis of the fatigue results will be performed to quantify the results observed.

Experimental Characterization of 52100 Steel

In late FY 2009, Cummins identified a component to be processed via LSP for full-scale test evaluations. Cummins identified overstressed regions of engine components that would benefit from residual compressive stress and where LSP could improve the component's fatigue performance. In FY 2010, the prototype parts were fabricated, and test evaluations were initiated.

Friction Stir Processing Development of Cast Iron

The overall goal of the development is to demonstrate enhancements achieved by FSP for Grade 40 cast iron. However, we must first be able to weld the material before identifying processing parameters that can produce successful, thermally stable, defect-free welds. This year, development focused on achieving plasticization of the material. The use of cover plates (304L stainless steel, 1018 steel, and copper) were investigated to aid in the development of FSP for cast iron without pre-heating the material and to prevent the extrusion of cast iron material during friction stir welding.

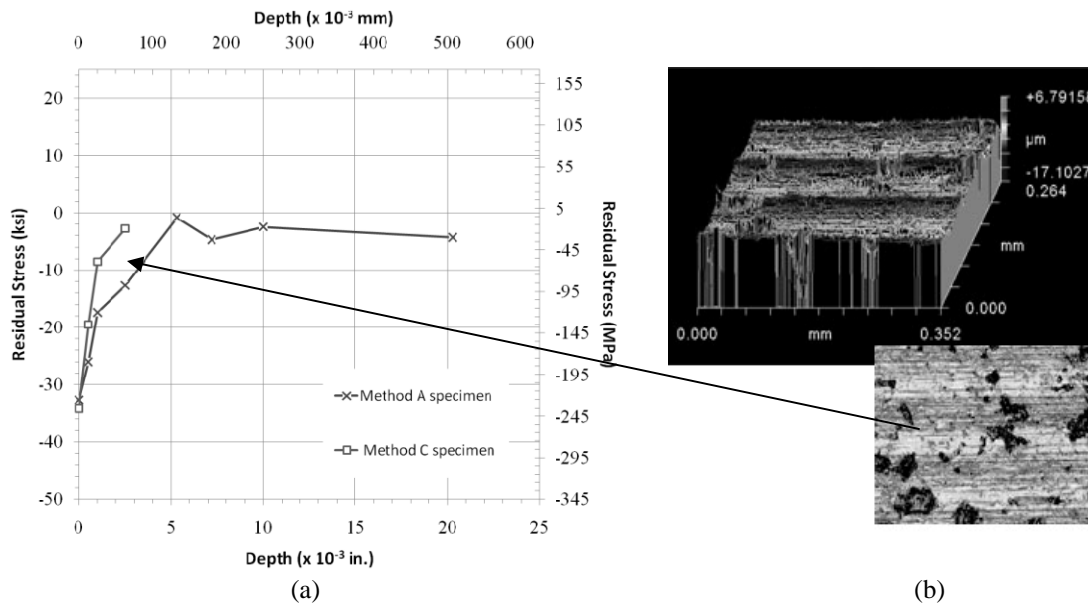


Figure 1. Comparison of residual stress profiles between WJP methods A and C (a) and a representative image of the surface roughness profile image for a specimen processed by method C (b).

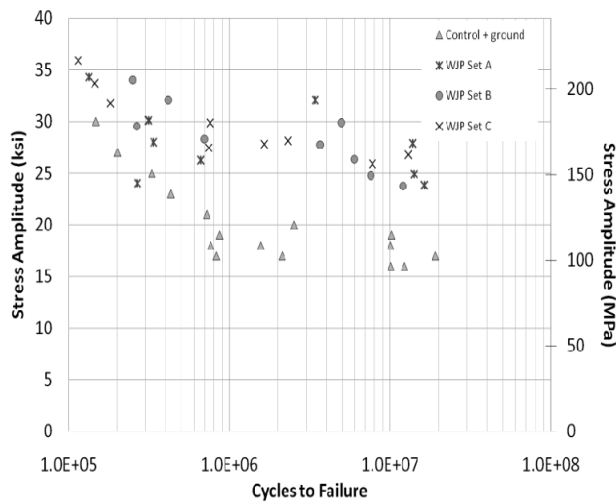


Figure 2. Comparison of the rotating beam fatigue tests results of the WJP specimens and control.

Plasticization of the cast iron was observed between a 304L cover plate and cast iron and between a 304L shim/copper cover plate and cast iron. In the evaluations, the use of copper appeared to enhance the ductility of the cast iron and decrease tool wear. However, using a copper cover plate alone did not generate enough heat for welding. Figure 3 shows a

cross-section of a consolidated joint between the cast iron and the 304L shim/copper cover plate. No gross defects were observed but realignment of the graphite flakes was observed between the copper and cast iron on both the advancing side and retreating side of the weld nugget. In addition, the weld was only a 1-inch translation.

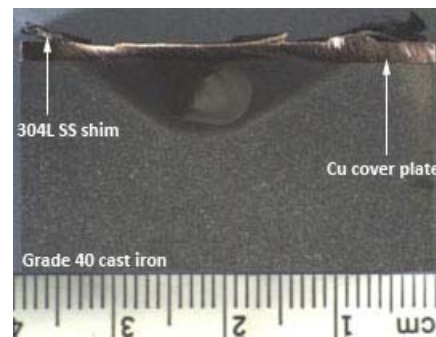


Figure 3. Cross-section of the copper cover plate on cast iron showing a consolidated joint.

Although processing parameters may not have been optimum for the consolidated joints observed, the results are promising and research is focusing on longer translations of the weld and better defining the processing parameters.

Conclusions

During this reporting period, the following conclusions were reached:

- WJP of A354 aluminum can produce surface compressive residual stresses while maintaining a required surface finish.
- WJP cast aluminum alloy A354 specimens showed a significant improvement in fatigue life in comparison to the control.
- Plasticization of cast iron was observed with the use of cover plates and no pre-heating when friction stir welding cast iron.

PRESENTATIONS/PUBLICATIONS/PATENTS

Cummins Internal Project Review, October 2009 and December 2009.

DOE Hydrogen Program and Vehicle Technologies Program Annual Merit Review, June 2010.

Cummins/PNNL CRADA Project Review, July 2010.

ACRONYMS

CRADA: Cooperative Research and Development Agreement

DOE: Design of Experiments

FSP: Friction Stir Processing

LSP: Laser Shock Peening

mm: Millimeter

μm: Micrometer

MPa: Megapascal

WJP: Water Jet Peening

Agreement 15055 – Tailored Materials for High Efficiency CIDI Engines (CAT)

Principal Investigator: Glenn J. Grant

Energy Materials

Pacific Northwest National Laboratory

902 Battelle Blvd., K2-03

Richland, Washington 99356

(509) 375-6890; fax: (509) 375-4448; email: glenn.grant@pnl.gov

Nate Phillips

T&SD AMT–High Temp Materials

M. Brad Beardsley

Technology Leader–Surface Engineering

Caterpillar, Inc.

Technical Center Bldg. C-13, PO Box 1875

Peoria, Illinois 61656-1875

(309) 578-5788; cell: (309) 361-8309; email: Phillips_Nate@cat.com

DOE Technology Manager: Jerry L. Gibbs

(202) 586-1182; fax: (202) 586-1600; email: Jerry.gibbs@ee.doe.gov

Field Technical Manager: Dean Paxton

(509) 375-2620; fax (509) 375-2186; email: dean.paxton@pnl.gov

Contractor: Pacific Northwest National Laboratory

Contract No.: DE-AC05-76RL01830

Objective

- To develop friction stir processing (FSP) to tailor the properties of conventional, low-cost engine materials (cast iron, alloy steels, and aluminum alloys) with the goal of increasing their high-temperature performance, durability, and thermal properties.
- To deploy friction stir processed components that can enable energy-efficient combustion strategies, especially those that will require higher peak combustion pressure or higher temperature operation.

Approach including partner/collaborator and path to technology transfer and commercialization

- This project will develop surface modification techniques, modified materials, and components. The project is a Cooperative Research and Development Agreement (CRADA) with Caterpillar, Inc., but also involves input from piston suppliers for diesel engines.
- The project is primarily investigating FSP, a new technology that can produce functionally graded surfaces with unique and tailored properties that will allow propulsion materials to withstand higher temperatures and pressures without appreciably losing strength, hot hardness, or wear resistance, and exhibit improved resistance to thermal fatigue.
- FSP treated components will be evaluated and tested by the industry collaborators to demonstrate efficiency benefits and potential commercial applications

Milestones, Metrics and Accomplishments

- **Milestone:** Demonstrate property improvements from FSP that can reach the following metrics established by the project team: minimum twofold improvement in fatigue life, significant reduction in thermal fatigue crack initiation and growth rate, 20% improvement in average failure stress level at N cycles. (Completed)
 - FSP was found to produce significant improvement in fatigue performance when compared to as-cast aluminum alloy 356. Depending on the stress ratio and the stress level, the FSP-processed materials showed from 5 to 15 times improvement in fatigue life over as-cast material. In addition, FSP-processed materials showed up to 80% improvement in fatigue strength across a wide range of maximum stress levels.
- FSP also was used to modify the surface of an aluminum alloy analog to a production piston alloy. Tooling was developed, and process parameters were explored that allow for processed regions showing very fine-grained, homogeneous microstructure.
- FSP was used to physically “stir-in” multi-wall carbon nanotubes and several different carbon nanofiber compositions into aluminum surfaces to a depth of 5.8 mm.
- **Milestone:** Demonstrate consolidated FSP regions in a ferrous piston alloy, and establish process window to successfully stir particulate into the surface of steel.
 - The tooling and process parameter space for accomplishing thick section (up to 13 mm thick) FSP of steel materials was investigated. Fully consolidated process zones were demonstrated, but tool survivability must be improved.
- **Milestone (June 2010):** Demonstrate a friction stir processed zone in a circular configuration appropriate to a piston bowl rim modification in an aluminum piston alloy. (Completed)

Future Direction

- In preparation for prototype part testing, develop the process and equipment needed to create two-dimensional curved FSP regions on piston blanks.

Introduction

The overall goal of the project is to enable the implementation of new combustion strategies, such as homogeneous charge compression ignition (HCCI), that have the opportunity to significantly increase the energy efficiency of current diesel engines and decrease fuel consumption and environmental emissions. These strategies, however, are increasing demands on conventional engine materials, either from increases in peak cylinder pressure (PCP) or from increases in the temperature of operation. The specific objective of this project is to investigate the application of a new material processing technology, friction stir processing (FSP), to improve the thermal and mechanical properties of engine components. The concept is to modify the surface of conventional, low-cost engine materials. The approach is to produce components with functionally graded surfaces that are optimized for thermal properties and better in-service performance without suffering the cost penalty of using exotic or expensive materials. Low-cost, higher-performance materials will allow new combustion strategies to be implemented that can improve

energy efficiency. This project is a Cooperative Research and Development Agreement (CRADA) in partnership with Caterpillar, Inc.

Background

Almost since the inception of internal combustion engines, there has been a steady rise in specific power (SP) output, or the power per liter of engine displacement. SP is correlated with efficiency and is the combined effect of better optimization of combustion, fuels, engine materials and design, reduction in parasitic losses, and improved heat management. Figure 1 shows that, from 1970 to 2001, there has been a steady increase in SP. After 2001, the SP levels dropped due to emission and after-treatment devices and controls mandated by federal legislation (primarily increased exhaust gas recirculation [EGR] rates and particulate filters). The drop in SP from 2001 to about 2003 would have been even greater were it not for significant advances in engine management, computer control, higher injection pressures, etc., made during this period to compensate for the power losses. However, around 2003, a different restriction on the optimization of the combustion

process was beginning to force diminishing returns. The restriction is illustrated in Figure 1 as the plot of the PCP. As the peak pressure increases, more work can be done by the piston as it is forced downward in the bore, resulting in a higher SP.

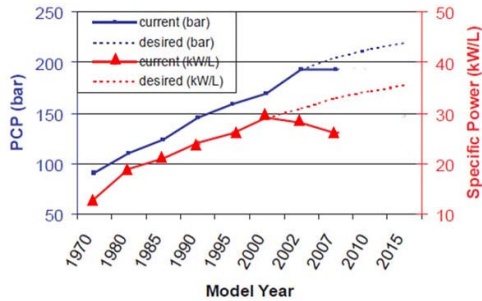


Figure 1. Plot showing the increase in SP and PCP for typical heavy-duty diesel engines over the last 38 years. (Figure modified from the Southwest Research Institute website at www.swri.org.)

Since 2003, PCP has leveled at around 190 bar to 200 bar, because above this level, conventional engine materials in pistons, cylinder liners, and cylinder heads will be beyond strength and fatigue limits¹. To increase efficiency further, either unconventional, expensive materials (i.e., nickel alloys, titanium, compacted graphite iron, nodular iron, or micro-alloyed steels) must be used or conventional materials must be modified in a way that increases their durability. New energy-efficient combustion strategies, especially HCCI, will increase PCP potentially above 220 bar. Accordingly, materials must be improved to enable this process.

One of the major challenges for conventional materials under increasing peak pressure environments is resistance to thermal fatigue failure. Pistons and cylinder heads are particularly vulnerable to this failure mode because of the cyclic nature of the loading and temperature changes in the combustion chamber.

¹ Figure 1 represents data primarily from medium-duty to heavy-duty diesel engines. Production automotive diesel engines (light-duty, high-speed) now achieve SP levels up to 75kW/L in turbocharged and intercooled configurations.

Figure 2 shows failures of pistons in the bowl rim area when subjected to high PCP over time.

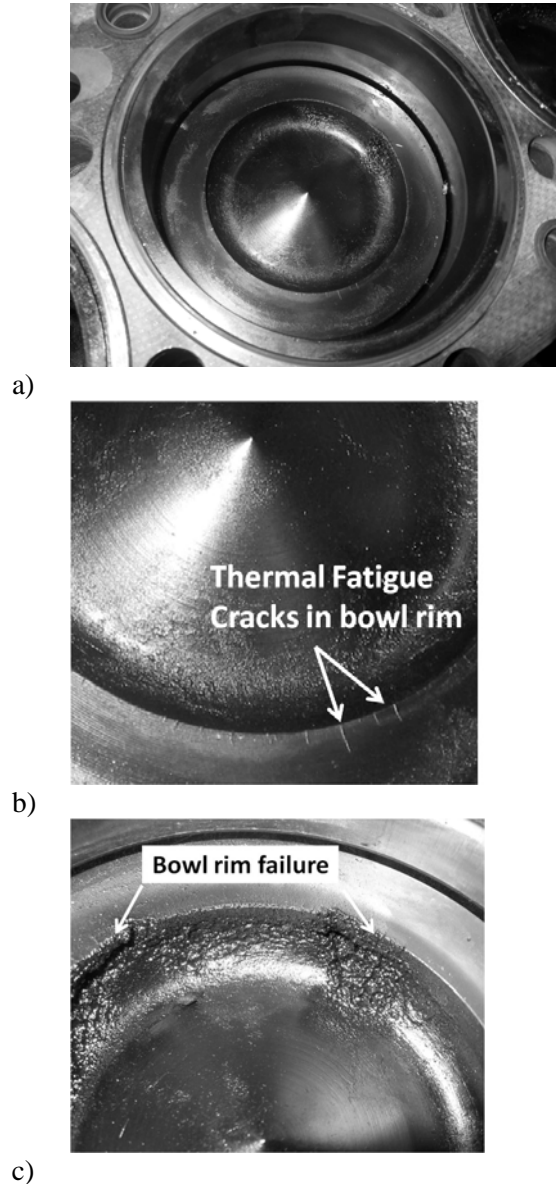


Figure 2. a) Piston in bore; b) cracks on inside edges of bowl rim; c) bowl rim failure

Rather than substitute a potentially high-cost, high-temperature, monolithic material, one low-cost strategy to enable higher PCP involves using techniques to improve the thermal fatigue performance of current materials. In the case of thermal fatigue in the bowl rim area, the technique need only be applied to the narrow area around the bowl rim itself because failures of this area drive the overall material selection.

FSP is a new technology that can be used to create engineered regions on selective areas of a part. In recent years, PNNL has developed techniques and tools that allow FSP to be accomplished in steel, cast iron, and aluminum.

FSP is an outgrowth of friction stir welding (FSW), which was invented 18 years ago by TWI, Ltd. (Figure 3). It has been recognized that the same techniques and processes used to make a friction stir weld could be used to process a material for enhanced properties. The process can be selectively applied to the surface of a material, and it alters the microstructure by the severe plastic deformation that occurs in the processed zone. FSP can create a robust and graded structure with fundamentally different properties than the underlying surface, and it has been shown to produce surface regions with improved fatigue life, ductility, and strength.

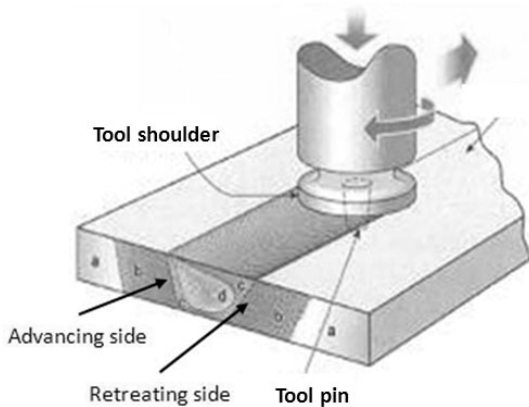


Figure 3. FSP illustration (top) and typical friction stir tools

FSP produces a surface modified region that is different from a coating. Commonly, surface treatments designed to enhance wear or thermal

performance include various coating methods or fusion-welded hard facings. Most of these processes are liquid state and often involve detrimental temperature effects on the base material. Heat-affected zones in the base metal and various deleterious high-temperature reactions can create a coated part with less-than-desirable properties.

Also, traditional thin coatings can suffer from issues involving the nature of the interface between the coating and the base material (spalling, debonding, and cracking on the interface), especially under high-stress, gouging wear conditions or under cyclic-thermal conditions where coefficient of thermal expansion (CTE) mismatch is an issue. Also, failure of a coating under high-loading conditions can occur when the substrate below a thin, hard coating fails by plastic deformation. Regions treated with FSP can be significantly more robust than traditional coatings for two reasons: 1) FSP produces a modified region that transitions to the base material without a sharp interface (Figure 4), and 2) the modified region is generally thicker and the transition region wider than traditional coating because the plasticized region depth is related to the tool geometry, specifically the depth and size of the pin.

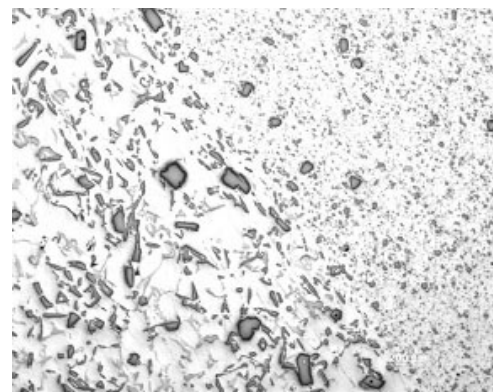


Figure 4. Micrograph of the edge of a stirred zone showing particle refinement in the processed region. (FSP can close porosity in castings and decrease both size and aspect ratio of particles, thus producing better fatigue performance.)

It also is possible to use FSP to “stir” insoluble particles from the surface into the substrate to depths limited only by the FSP tool geometry

(Figure 5). This engineered metal matrix composite layer can create unique surface properties, including increased hardness, wear resistance, and thermal characteristics. To date, the addition of up to 20% ceramic to aluminum has been demonstrated and approximately 10% addition to steel has been achieved.

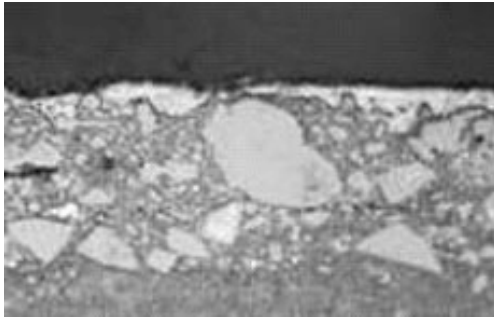


Figure 5. Ceramic particulate also can be stirred into the surface to produce functionally graded surfaces and near-surface metal matrix composites.

FSP can be used to alter the original microstructure, create surface composites and new alloys, and has the potential to produce selective areas of improved material performance. This project will investigate several opportunities for FSP to improve engine materials to enable increases in engine efficiency.

Approach

This project proposes to experimentally develop the FSP processes and technologies required to engineer the surface of propulsion materials for improved properties. The application focus is to tailor the mechanical properties and thermal conductivity of engine materials, both ferrous and non-ferrous materials, by using FSP techniques. This microstructural modification is expected to lead to a set of materials with enhanced surface properties that can handle increased combustion pressure and exhaust temperatures, resulting in improved engine efficiency.

The project scope will involve developing the FSP manufacturing parameters, and selecting and evaluating proper tool materials and techniques to produce defect-free FSP regions. Coupon-level testing and evaluation of the thermal and mechanical properties will be conducted. These

efforts will focus on specific performance targets identified by project partners. If performance metrics are met for sample materials enhanced by FSP, additional research will include developing and demonstrating the appropriate method to apply this process to two-dimensional and three-dimensional geometry. If successfully developed, this class of engineered materials can significantly impact the efficiency and durability of compression ignition direct injection (CIDI) and potentially address some of the technical barriers to implementing HCCI engines.

In 2010, the primary focus of project work was on FSP of aluminum piston materials used for light-duty and medium-duty CIDI engines. The work is intended to improve the thermal fatigue performance of typical piston alloys to allow them to be used in higher peak stress environments without suffering premature bowl rim failure. The concept is illustrated in Figure 6. If FSP were applied to the area of a piston blank (prior to final machining) that will be the bowl rim area, then, after final machining, the bowl rim will be composed entirely of fine-grained FSP “nugget” material that will possess improved fatigue performance. Adjacent areas of the piston will remain unmodified.

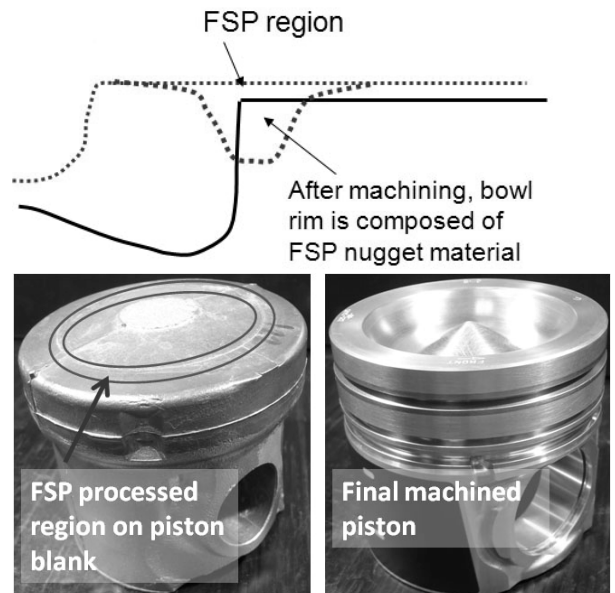


Figure 6. Cast piston blank. (The area in the bowl rim after machining will be friction stir processed for improved microstructure.)

The project approach is to first develop the techniques (i.e., process parameters, friction stir tools, and methods) needed to create robust process zones, then physically perform the FSP process on full-sized piston blanks, machine them to shape, and test them in actual operating conditions on test cell engine dynamometers or single-cylinder test engines.

Results

During FY 2010, the project focused primarily on FSP in aluminum materials that are compositional analogs to the typical piston and head alloys seen in small- to mid-sized CIDI engines.

Investigations focused primarily in the following two areas: 1) FSP of cast hypo-eutectic aluminum (Alloy 356/357) with no introduction of any new component materials (with a demonstration of a circular processed zone for a prototype piston top) and 2) FSP of aluminum alloys involving physically “stirring-in” various quantities of carbon nanotubes, nanofibers, and large-scale carbon fiber ribbons. Summary discussions of the two investigations follow.

FSP of Alloy 356

FSP significantly refines microstructure, closes casting porosity, and reduces the aspect ratio of the Si particles in cast Al-Si alloys. These three features produce a dramatic improvement in fatigue life. Figure 7 shows the S/N curves for both tensile and bending fatigue performance comparing the as-cast to the FSP-processed material. A 90% improvement in maximum tensile stress at the fatigue limit and improvements in bending fatigue lifetime up to an order of magnitude can be shown for this alloy.

In current applications of these alloys, especially for pistons and cylinder heads, fatigue, particularly thermal fatigue, is the primary limiting condition on part life. As CIDI engines evolve to lean-burn technologies and potentially more HCCI-like conditions (i.e., maximum stress in bowl rim edges, ring landings, bridge areas between valves, etc.), much higher stress levels than current designs will exist. The improvements offered by selective FSP of these regions may enable these energy-efficient combustion strategies.

Work during FY 2010 demonstrated the techniques necessary for the practical application of FSP by demonstrating a circular “two-dimensional” processed region on a simulated piston top. Figure 8a shows the circular weld region and Figure 8b shows the machined final piston top with the processed region on the bowl rim.

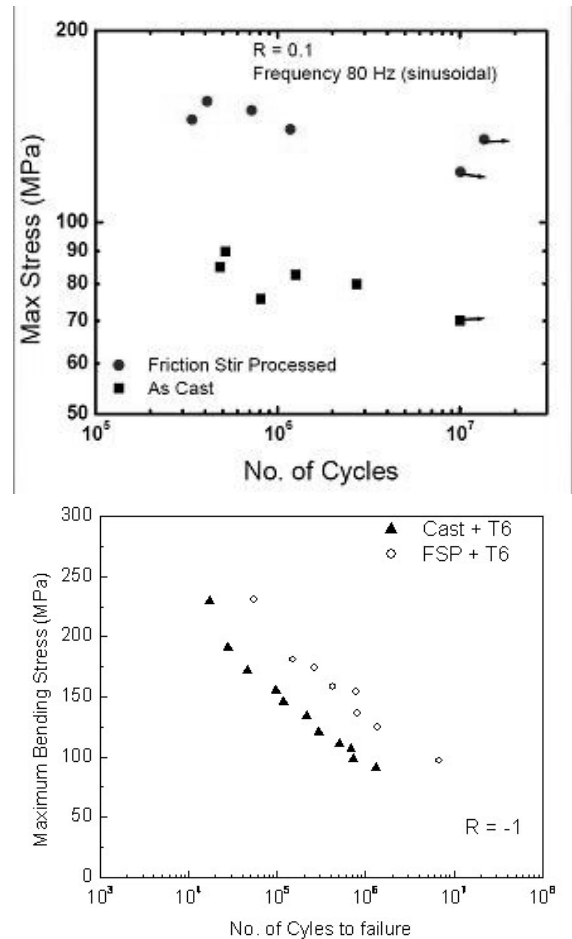


Figure 7. S/N curve for tensile loading (top) at R=0.1 (showing as-cast 356 versus FSP-processed 356) and SN Curve for bending (bottom) at R=-1 (showing as-cast 356 versus FSP-processed 356 [1,2,3]).

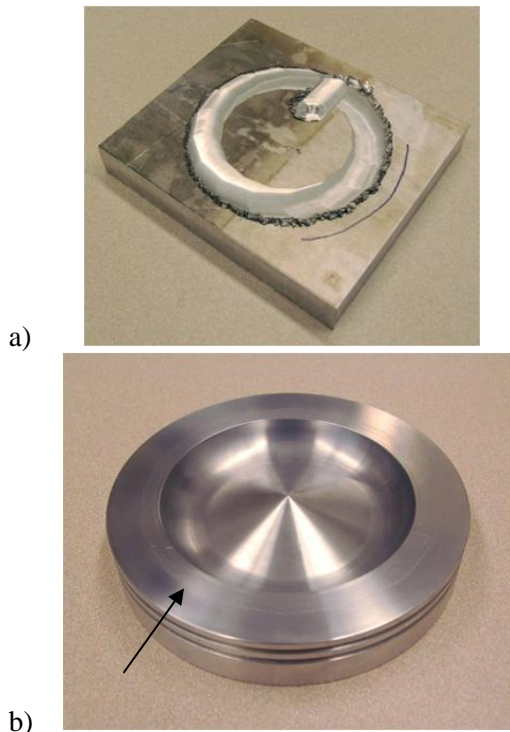


Figure 8. a) Circular process region created by “welding” in a counterclockwise direction then turning to center and exiting where the piston bowl will be located. b) The arrow points toward a faint line demarking the edge of the FSP processed zone on the bowl rim after machining. The processed region is fully consolidated and composed of material with a highly refined microstructure to resist thermal fatigue cracking.

FSP—“Stirring-in” Carbon Nanotubes and Nanofibers

The primary failure at high PCP in service is fatigue and thermal fatigue at several locations on the piston and head. Our goal is to use FSP to improve the microstructural and mechanical properties that most influence thermal fatigue (i.e., CTE, conductivity, and, to a lesser extent, high temperature strength). Primarily, the goal is to reduce CTE and increase conductivity. Table 1 shows candidate materials that could be stirred into the base metal to selectively modify mechanical properties.

Table 1. Potential additions to the base material

Material	Modulus	CTE	Conductivity
Aluminum	80 GPa	25 $\mu\text{m}/\text{m}^\circ\text{C}$	180 W/m-K
SiC	410 GPa	4.4 $\mu\text{m}/\text{m}^\circ\text{C}$	150 W/m-K
Al ₂ O ₃	370 GPa	8.5 $\mu\text{m}/\text{m}^\circ\text{C}$	13 W/m-K
Carbon Nanotubes	>600 GPa	Low or Can be negative !	> 1000 W/m-K

Of these, carbon nanotubes and fibers offer the best potential to improve thermal fatigue because of their very low CTE and high conductivity. The bulk of the experimental effort in FY 2010 was devoted to developing the methods, procedures, FSP tools, and process parameters needed to create processed regions with even distributions of particulate. This work continues efforts undertaken in FY 2009 to find the best methods of stirring in particulate into the aluminum substrate while producing the most homogeneous and highest particulate loading possible.

During FY 2010, two different carbon fibers, polyacrylonitrile (PAN) and graphite (GRPH), were used as reinforcements added into 6061 aluminum plates by FSP. Work in FY 2009 showed that the use of carbon nanotubes as reinforcements led to some agglomeration inside the processed region. Therefore, carbon fibers were selected for this study. Two different carbon fibers were chosen in order to study their effect on the thermal conductivity and the mechanical properties of the processed region. In general graphite fibers show significantly higher conductivity values compared to PAN fibers. On the other hand, PAN fibers are known for their better mechanical properties. The carbon fibers were added into the 6061 aluminum matrix by first cutting a number of grooves (1.0-in. long, 0.25-in. wide, and 0.20-in. deep) along the length of the aluminum plate, with a 0.10-in. spacing between adjacent grooves. This is shown schematically in Figure 9. After filling the grooves with continuous 1-in.-long carbon fiber woven strips, metal plugs made of 6061 aluminum were press fitted into these grooves. Finally, the aluminum plate was subjected to FSP along the length of the grooves. Because the grooves were wider than the

friction stir tool pin diameter; multiple passes were employed to create the processed zone. The aluminum plate was finally cross-sectioned perpendicular to the FSP run direction to study the distribution of the carbon fibers inside the process zone.

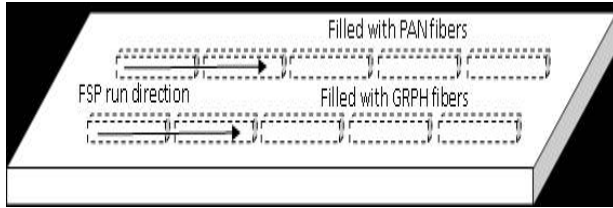


Figure 9. Schematic drawing of the technique used for reinforcing aluminum plate with carbon fiber

Cross-section images of both the PAN-filled and GRPH-filled grooves indicated the presence of large cavities inside the processed region. Figures 10a and 10b show typical examples of PAN and GRPH fiber-filled processed regions, respectively. Cavities marked by arrows are visible on both the images.

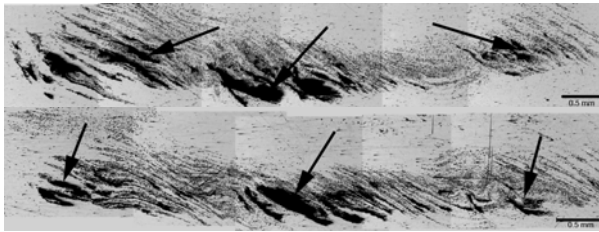


Figure 10. Cross-section images of the process region: (a) PAN-filled and (b) GRPH-filled.

Also, a single pass raster pattern of friction stir passes did not, in these studies, produce uniformly distributed carbon fibers at areas away from the large cavities. It can further be noted that the carbon fibers inside the processed region are distributed in a layered manner, which is indicative of the complex material flow during FSP. However, very limited mixing of carbon fibers is noted along the vertical direction. Because the initial trials left large cavities, some regions were reprocessed to fill those cavities. This was done by positioning the friction stir tool pin in the center of those cavities and then running along the entire length of the aluminum plate. Figures 11a and 11b show cross-section images obtained from two separate locations along the

PAN-filled reprocessed region. It is evident from both the images that the reprocessing technique led to a significant reduction of cavities inside the processed zone. However, as shown by the arrow in Figure 11b, some porosity still remained even after the reprocessing runs. Moreover, after comparing Figures 11a and 11b, it is noted that there is variability in carbon fiber distribution inside the process region along the length of the aluminum plate.

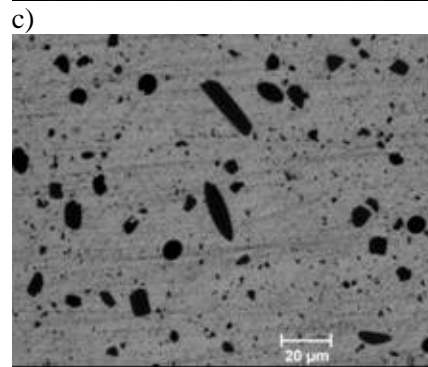
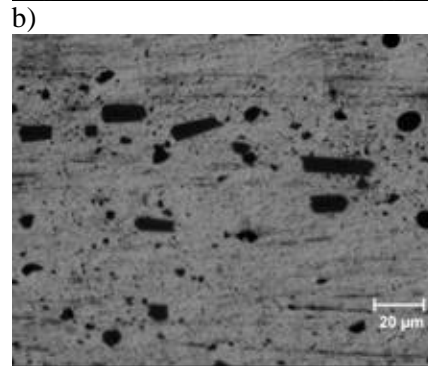
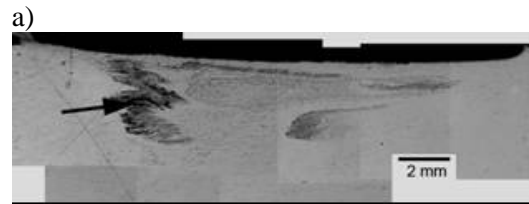
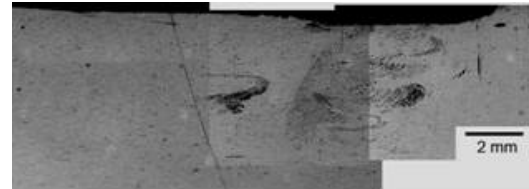


Figure 11. Cross-section images from the PAN-filled process zone. (a, b) Low-magnification overview of the process zone at two locations. (c, d) Morphology of the individual carbon fibers after FSP.

Higher magnification images from the reprocessed region showed that, in fine detail, the carbon fibers were broken and distributed in the aluminum matrix (Figures 11c and 11d). The FSP process was able to chop the continuous carbon fibers into smaller sections. FSP resulted in random orientation of the carbon fibers inside the process zone. The size of most of the carbon fibers was found to be ~10 μm, although a small fraction of carbon fiber fragments were noted to have significantly smaller or larger sizes than the average. Chopping of carbon fibers inside the process zone was confirmed by scanning electron microscope (SEM) images as well. Figure 12a shows a typical SEM image of the process zone after initial processing. Fragmentation of carbon fibers is evident in this image.

The technical literature on aluminum-carbon fiber composites often reports presence of an aluminum-carbide reaction layer during manufacturing of carbon-fiber reinforced aluminum by melt processes. However, no such reaction layer was found in our work. Figure 12b shows a single carbon fiber embedded inside the aluminum matrix. The aluminum-carbon fiber interface in this image does not show any signs of the presence of a third phase.

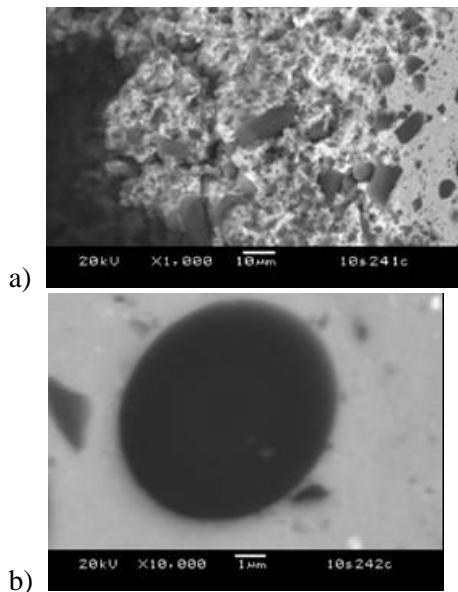


Figure 12. (a): SEM image showing fragmentation of carbon fibers inside the process zone, and (b): aluminum-carbon fiber interface without aluminum-carbide reaction zone.

To determine the effects of carbon-fiber reinforcements on the mechanical properties of the 6061 aluminum plate, hardness profile maps were generated. Microstructural examination of the process zone revealed a homogeneous distribution of carbon fibers at a few locations inside the aluminum matrix. Therefore, a hardness profile map should be able to indicate if incorporation of carbon fibers resulted in the strength enhancement of the aluminum matrix, at least in those areas.

A hardness profile map of a PAN-filled reprocessed section is shown in Figure 13. Considerable softening of the aluminum matrix can be observed inside the process zone. The 6061 aluminum is a heat-treatable alloy; therefore, significant softening of the matrix occurred during FSP because of the associated multiple heating events. However, the presence of carbon fiber particles inside the process zone does not appear to have enhanced the hardness values.

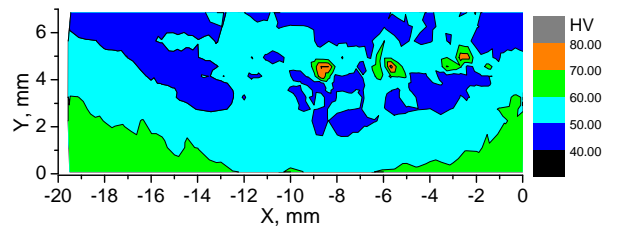


Figure 13. Hardness profile map of the PAN-filled reprocessed section

To eliminate the softening effects from repeated heating and cooling during FSP on the 6061 aluminum matrix, sections from both the PAN-filled and the GRPH-filled reprocessed material were given a T6 heat treatment. Hardness profile maps were then determined on the T6 temper sections. Figures 14a and 14b show a hardness profile map and a macrograph of the profiled area from a PAN-filled cross section after T6 treatment, respectively. The hardness profile map has been superimposed on the macrograph for a better understanding the effects of carbon fiber on hardness. Significant strengthening of the aluminum matrix after the T6 treatment is evident from the hardness profile plot. However, areas of the cross-section that were carbon-fiber rich showed a lower hardness compared to the rest of the aluminum matrix. Because the average size of the chopped carbon fibers was ~10 μm, significant

strengthening of the aluminum matrix is not expected from their presence. We speculate that the lower hardness in the carbon-fiber-rich areas may be the result of the presence of subsurface porosity in and around the carbon-fiber-rich areas.

The hardness profile plot from the GRPH-filled section is shown in Figure 15a, while Figure 15b shows the macrograph of the profiled section. Similar to the previous observation, lower hardness in carbon-fiber-rich areas is noted in the GRPH-filled section as well.

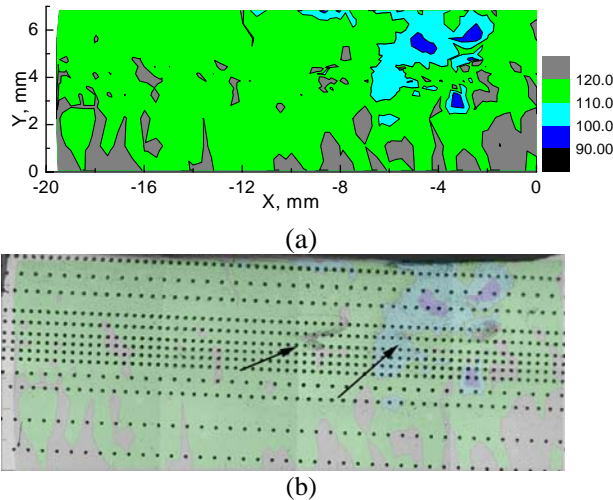


Figure 14. (a) Hardness profile plot for T6 treated PAN-filled section. (b) Macrograph of the profiled section. Hardness map has been superimposed. Arrows indicate carbon-fiber-rich locations. It appears that incorporation of PAN carbon fiber did not result in any appreciable matrix strengthening.

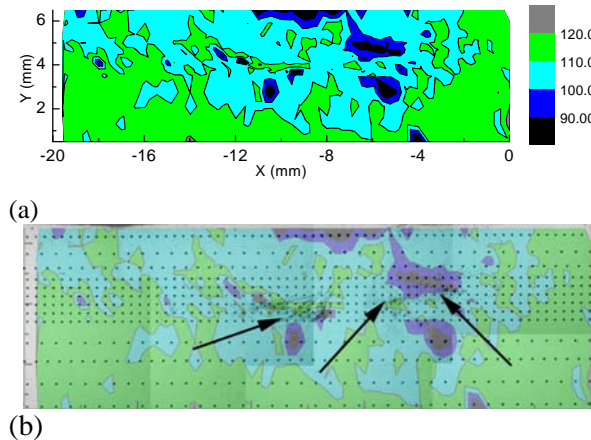


Figure 15. (a) Hardness profile of T6 treated GRPH-filled section. (b) Macrograph of the profiled section. Hardness map has been superimposed. Arrows indicate carbon-fiber-rich locations.

It appears that incorporation of carbon fiber did not result in any appreciable matrix strengthening. The current FSP technique was able to chop the individual carbon fibers; however, the size of the chopped carbon-fiber particles is probably too large to offer any matrix strengthening effect. The effect of carbon-fiber particles on fatigue and toughness, however, may be different, but has not been tested yet.

The current study showed the presence of softer zones around C fiber rich areas. This is possibly related to the presence of porosity around the carbon-fiber-rich areas. The reprocessing technique used in the current study was able to close most of the large cavities. However, an appreciable amount of small porosity still remained in the process zone, which affected the mechanical properties considerably.

Samples from the process zone also were tested for thermal conductivity. For the thermal conductivity test, three aluminum samples from parent metal, seven PAN-filled samples, and seven GRPH-filled samples were tested. Thermal diffusivity was determined first from room temperature to 400°C using a laser flash technique specified in ASTM E1461. Bulk density of the samples was then determined from the sample’s geometry and mass. Finally, specific heat, C_p , was measured using differential scanning calorimetry. Thermal conductivity values were calculated as a product of these quantities (i.e. $\text{Conductivity} = \text{Diffusivity} \times C_p \times \text{density}$). The average bulk density of the various samples used in this study is summarized in Table 2. Bulk density of both the PAN and GRPH samples are noted to be less than the parent. Moreover, scatter in the density data also is high. Presence of porosity around carbon-fiber-rich areas inside the process zone might be the reason for the lower density of PAN or GRPH samples. Figure 16a shows the average measured thermal diffusivity data as a function of temperature. Thermal diffusivities for both the PAN and the GRPH samples are found to be considerably lower than the parent. Moreover, the scatter in the data for PAN or GRPH samples is quite high. It is believed that the presence of porosity resulted in poor thermal diffusivity for both the carbon-fiber samples. Calculated thermal

conductivity values as a function of temperature are shown in Figure 16b.

Table 2. Bulk density (g/cc) of samples in this study

Parent Aluminum	PAN-Filled Samples	GRPH-Filled Samples
2.69 ± 0.003	2.60 ± 0.008	2.61 ± 0.026

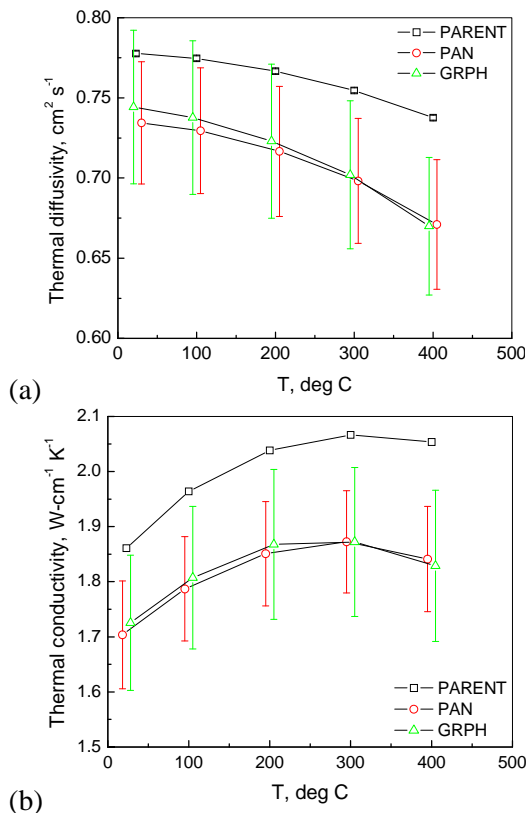


Figure 16. (a) Thermal diffusivity vs. temperature, and (b) thermal conductivity vs. temperature

Summary of Carbon Fiber Work

- Carbon-fiber reinforcement of the aluminum matrix is possible by the current FSP technique. However, two major problems associated with the current technique are porosity around the carbon fibers and non-uniform distribution of chopped carbon fibers inside the process zone. It is believed that the size of the grooves used in this study may be too large to be closed effectively. Use of smaller grooves or a different/larger friction stir tool may lead to better carbon-fiber distribution.
- Use of carbon fiber as a reinforcement did not result in hardness enhancement of the matrix.

This is an expected result, given the size of the chopped carbon fibers. However, lower hardness in carbon-fiber-rich areas may indicate the presence of porosity. It is highly possible that the “true” effect of carbon fibers on hardness might have been masked by porosity.

- Finally, incorporation of carbon fibers also did not improve the thermal properties. This is a surprising result, at least, for the graphite carbon-fiber-filled samples. Once again, the bulk density of the carbon-fiber-filled samples suggested the presence of voids inside. This factor might have overshadowed the beneficial aspect of the carbon fiber on thermal properties, if any.

Conclusions

The goal of this project is to deploy friction stir processed components that can enable energy-efficient combustion strategies, especially strategies that will require higher PCP or higher temperature operation. FSP produces selected, graded structures that have shown increased strength and durability in fatigue. Surface modification through FSP may address some emerging material problems seen in very high combustion pressure systems such as HCCI engines. In addition, the process enables the incorporation of particulate into the surface, potentially selectively modifying the properties of materials to alter the thermal environment for increased thermal efficiency.

Experimental work to date on aluminum systems has shown significant increases in fatigue lifetime and stress-level performance in aluminum-silicon alloys using friction processing alone, but work to demonstrate the addition of carbon nanotubes and fibers into aluminum substrates has shown mixed results due primarily to the difficulty in achieving porosity-free, homogeneous distributions of the particulate.

Work in the final year of this project will concentrate on FSP processes (without particle reinforcement) that have been shown to produce fatigue resistant surface regions on fatigue-failure prone CIDI engine components. Future work includes quantifying property improvements

further and fabricating prototype parts for engine durability testing.

Presentations/Publications/Patents

Jana S, RS Mishra, JB Baumann, and G Grant. 2009. "Effect of stress ratio on the fatigue behavior of a friction stir processed cast Al-Si-Mg alloy." *Scripta Materialia* 61(10):992-995.

Jana S, RS Mishra, JB Baumann, and G Grant. "Effect of friction stir processing on fatigue behavior of an investment cast Al-7Si-0.6 Mg alloy." *Acta Materialia* (2009), doi:10.1016/j.actamat.2009.10.015

Jana S, RS Mishra, JB Baumann, and GJ Grant. 2010. "Effect of Friction Stir Processing on Microstructure and Tensile Properties of an Investment Cast Al-7Si-0.6Mg Alloy." *Metallurgical and Materials Transactions. A, Physical Metallurgy and Materials Science* 41A (10):2507-2521. doi:10.1007/s11661-010-0324-1

Agreement 16303 – Materials for High Pressure Fuel Injection Systems

Peter J. Blau, Camden Hubbard, and Amit Shyam
Oak Ridge National Laboratory, P. O. Box 2008, Mail Stop 6063
Oak Ridge, TN 37831-6063
(865) 574-5377; fax: (865) 574-4913; e-mail: blaupj@ornl.gov

and

Michael J. Pollard and Nan Yang
Caterpillar Inc.
Technical Center Bldg. E-854
P.O. Box 1875
Peoria, IL 61656-1875

DOE Technology Manager: Jerry L. Gibbs
(202) 586-1182; fax: (202) 586-1600; e-mail: Jerry.gibbs@ee.doe.gov
ORNL Technical Advisor: D. Ray Johnson
(865) 576-6832; fax: (865) 574-6098; e-mail: johnsondr@ornl.gov

Contractor: Oak Ridge National Laboratory, Oak Ridge, TN
Prime DOE Contract Number DE-AC05-00OR22725

Objectives

- To critically evaluate current and future material choices for high pressure fuel injector nozzles indented for energy-efficient, low-emissions diesel engines.
- To provide metallurgical analysis, fatigue test data, hole metrology information, and residual stress measurements that will aid in the selection of alternative high-performance alloys for advanced, high-pressure diesel engine fuel injection systems.

Approach

- Working through a Cooperative Research and Development Agreement (CRADA) between ORNL and Caterpillar, characterize the metallurgical structure, hardness, and fatigue behavior of current and candidate high-pressure fuel injector nozzle alloys.
- Develop methods to characterize injector spray hole shapes, sizes, and bore morphology.
- Using unique facilities at ORNL and other national laboratories, evaluate the ability of alternative x-ray and neutron-based methods to determine the residual stress states of materials in the ‘sack’ (nozzle tip) of fuel injectors.
- Develop and use appropriate methods to determine the fatigue life and reliability of ferrous alloys for fuel injectors in the presence of spray-hole-like features and in fuel environments.

Accomplishments

- In FY 2009, a means to cross-section fuel injector holes and measure the interior surface features, and roughness, of 200 μm -diameter fuel spray holes was demonstrated.
- In FY 2009, X-ray and neutron-based experiments were conducted at four different DOE facilities to determine which method might be suitable to measure residual stress on fuel injector nozzle tips. No significant levels of residual stress were detected, and that result was consistent with independent X-ray studies conducted at Caterpillar facilities. It was decided to defer further residual stress studies in this project.
- In FY 2009, a series of baseline tests were completed on smooth specimens of the current fuel injector steel with specimens provided by Caterpillar. Depending on the applied stress, two regimes of fatigue crack initiation and propagation were revealed. This work resulted in a conference publication submitted during FY 2010.
- This FY a new, high-resolution optical (tele-microscope) system was installed to observe the propagation of small fatigue cracks from the edges of EDM holes during fatigue testing. This allowed the determination not only of fatigue life, but also crack propagation rates and how cracks meander through the microstructure of the steel.
- Advanced specimen preparation techniques, using a focused ion beam, were used to prepare transmission electron microscope (TEM) cross-sections of the interior wall of a fuel injector spray hole. *To our knowledge, this is the first time TEM has ever been used to reveal the nanostructure of EDM spray holes in fuel injector nozzles.*
- Caterpillar continued in-house testing of candidate next generation fuel injector steels using a rotating bend method. The effects of post-shot peening heat treatments on fatigue were investigated. Materials included new alloys from Carpenter Technology Corporation.
- A methodology was developed to determine the fatigue initiation and propagation behavior of cracks that emanated from artificial EDM holes fabricated on test specimens

Future Directions

- Continue to characterize of current and potential fuel injector alloys using metallurgical studies, fractography, and residual stress methods applied to fatigue test specimens.
- Continue research on fatigue crack initiation and propagation in current and candidate fuel injector alloys, especially focusing on the effects of fuel environments on fatigue cracks initiated from synthetic flaws that are the size of spray holes.

Introduction

In order to improve fuel efficiency while controlling emissions, diesel engine designers have raised the pressures imposed on the fuel injectors. Repetitive pressurization exceeding 25,000 psi could stress the walls of the tips of the fuel injector

nozzles above the endurance limit, leading to fatigue cracking and fracture. The consequences of these events will significantly affect engine performance, and the ability of nozzle materials to resist these effects becomes extremely important.

As the diesel engine operates, physical processes begin to affect the ability of spray

holes to deliver the desired quantity and pattern of fuel spray. These processes include hole erosion and the formation of deposits. Figures 1 and 2 compare a new nozzle with one returned from service, showing holes that are fouled by carbonaceous deposits.

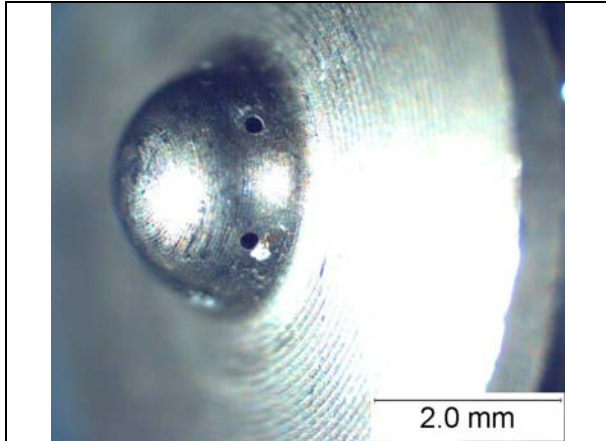


Figure 1. Unused fuel injector nozzle tip (also called the ‘sack’) showing the spray holes.

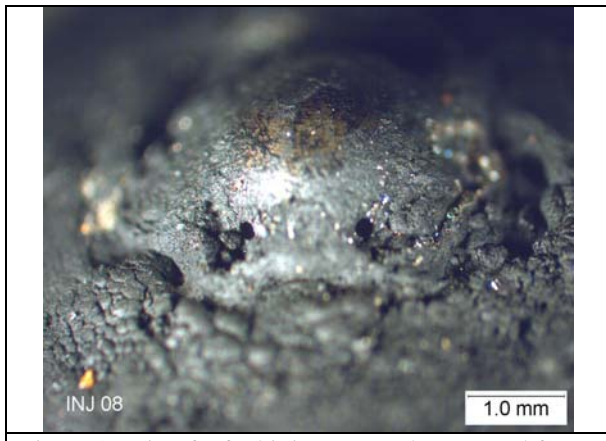


Figure 2. Tip of a fuel injector nozzle removed from service showing deposits clogging the spray holes.

The objective of this work is to investigate the ability of current and next-generation alloys to withstand the high pressures and fatigue environments experienced by advanced diesel engine fuel injector tips. Meeting this challenge involves a multi-disciplinary approach.

Approach

A three-pronged approach is being used: (1) metallurgical characterization and hole metrology, (2) characterization of residual stress, and (3) fatigue testing of smooth and notched specimens, both dry and in the presence of fuel.

Progress

During FY 2009, metallurgical studies of cross-sectioned tips revealed the structure of the alloys and the interior of the spray holes. The electro-discharge machining (EDM) hole making process results in the formation of recast layers on the hole walls (see for example, Figure 3). In FY 2010, a focused ion beam (FIB) apparatus was used by Dorothy Coffey and Jane Howe, both at ORNL, to remove a thin section of the hole wall in a fuel injector and examine it at high resolution in a transmission electron microscope. *To the best of our knowledge this is the first study of its kind.*

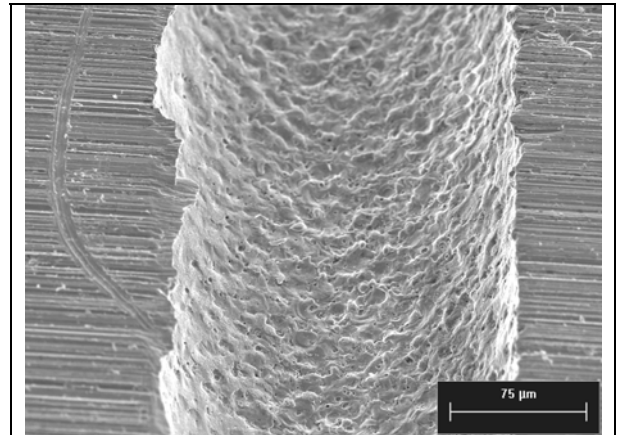


Figure 3. Re-cast structure inside a spray hole.

Figure 4 reveals a cross-sectional TEM view of a ‘splat’ peeling from the wall of a spray hole. The presence of highly-defected structures, showing tangles of dislocations, and a distinct discontinuity between the underlying material (right of center). Networks of sharp microcracks underlying splats could be facilitate fatigue crack initiation.

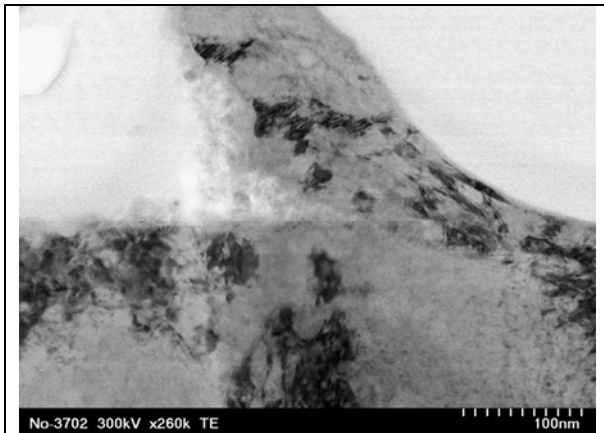


Figure 4. Nanostructures in the re-cast layer of a spray hole.

Residual stress studies. Caterpillar investigated the effects of aging time at 250 and 290° C on the residual stress levels in five alloy steels that had been shot-peened. In all cases, the largest stress reduction was seen in the first 10 hours, and the magnitude of reduction was slightly greater at the higher aging temperature.

Fatigue testing. Fatigue tests were performed both at the Caterpillar Technical Center and at ORNL. Caterpillar used rotating bend tests, and ORNL used smooth bars with reduced cross sections, both with and without controlled flaws (see Figure 5).

ORNL axial fatigue tests were performed using an MTS 810 servo-hydraulic machine at a frequency of 20 Hz. The tests were performed under load control at a load ratio (R), defined as minimum load/maximum load, equal to -1. The maximum stress in the cycle was varied to obtain the stress-life (S-N) response of the material.

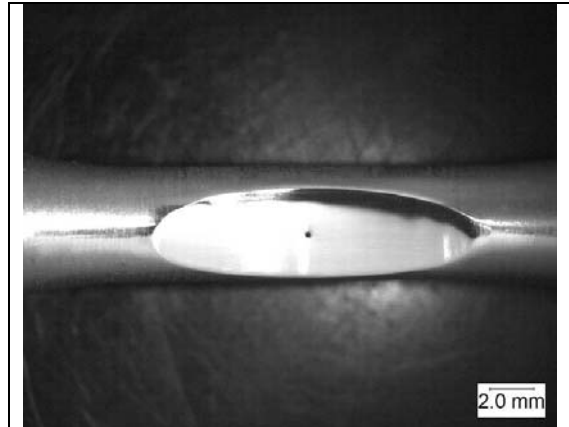


Figure 5. Polished side of an axial fatigue specimen showing an elongated EDM notch to simulate the stress concentration due to a spray hole. The loading direction in this view is horizontal.

The fracture surface of a specimen showing its origins at the artificial notch is shown in Figure 6. Crack length is plotted as a function of number of cycles in Figure 7. Such information can be used to determine the initiation behavior of defects emanating from spray holes.

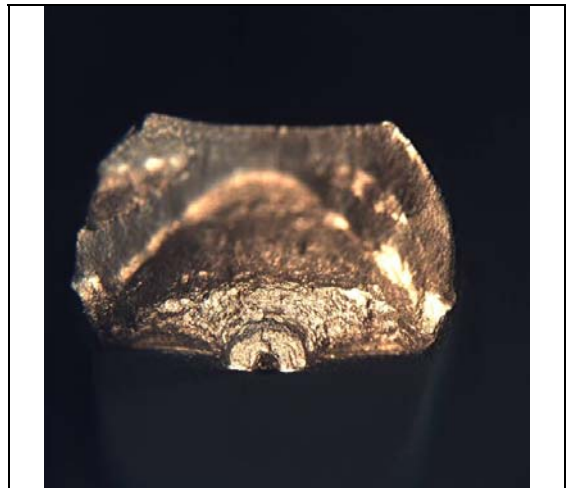


Figure 6. Low-cycle fatigue fracture surface on a specimen similar to that in Fig. 5, showing the origins at an EDM flaw (at the bottom).

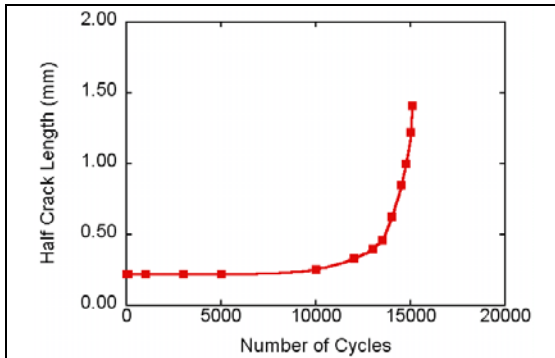


Figure 7. Crack length values as a function of the number of cycles for a fatigue test performed at $\sigma_{\max} = 800$ MPa and $R=-1$.

FY 2011 plans include studying the effects of diesel fuel that will be introduced into ORNL's notched fatigue test system. This is key to determining the effects of a diesel fuel environment on crack initiation and fatigue life under high applied stress.

Summary and Conclusions

- Studies of the microstructure of diesel engine fuel injector nozzle hole walls continued with ground-breaking TEM studies.
- Fatigue testing continued at Caterpillar Technical Center to investigate the effects of residual stress and heat treatment on fatigue life of alloy steels.
- Fatigue tests at ORNL studied the initiation and propagation of fatigue cracks as a function of applied stress on smooth and notched specimens.

Publications/Presentations

1) A. Shyam, P. J. Blau, and M. J. Pollard "The very high cycle fatigue behavior of tool steel materials for diesel fuel injectors," submitted to the 5th International Conference on Very High Cycle Fatigue, Berlin, Germany, June 28-July 1, 2011.

Agreement 17257 – Materials for Advanced Turbocharger Designs

P. J. Maziasz, A. Shyam, and S. Das
Materials Science and Technology Division
Oak Ridge National Laboratory
P.O. Box 2008, MS-6115
Oak Ridge, TN 37831-6115
(865) 574-5082; fax: (865) 754-7659; e-mail: maziaszpj@ornl.gov

K. Pattabiraman
Global Materials Engineering Manager
Honeywell – Turbo Technologies
3201 W. Lomita Blvd.
Torrance, CA 90505
(310) 571-1616; fax: (310) 539-7061; e-mail: kalathur.pattabiraman@honeywell.com

DOE Technology Manager: *Jerry L. Gibbs*
(202) 586-1182; fax: (202) 586-1600; e-mail: jerry.gibbs@ee.doe.gov
ORNL Technical Advisor: *D. Ray Johnson*
(865) 576-6832; fax: (865) 574-6098; e-mail: johnsondr@ornl.gov

Contractor: Oak Ridge National Laboratory, Oak Ridge, Tennessee
Contract No.: DE-AC05-00OR22725

Objectives

- CRADA NFE-08-01671 – Provide the critical test data for new, improved materials, which in turn will enable the design of advanced turbocharger systems with upgraded performance, durability and reliability relative to conventional systems.
- CF8C-Plus Energy Benefits Study – Materials component casting and component finishing processes, and component end-use temperature capability are evaluated to determine the energy benefits of CF8C-Plus cast stainless steel relative to HK30 and Ni-based superalloy 625 for diesel and automotive turbocharger and larger gas-turbine casing/end-cover applications.

Approach

- CRADA NFE-08-01671 – This is a 3 year project designed to consider both for the turbine and compression sections, and to consider turbochargers for both passenger/gasoline and commercial/diesel engines. Honeywell assesses and prioritizes the components that benefit most from materials upgrades or alloy development. ORNL works with Honeywell materials/component suppliers to obtain new materials for testing and evaluation.
- CF8C-Plus Economics Study – Data and information from component makers and end-users were evaluated to provide the energy benefits of CF8C-Plus cast stainless steel diesel and automotive turbocharger or gas-turbine casing/cover applications.

Accomplishments

- CRADA NFE-08-0171 started at the beginning of FY2010 with a kick-off meeting at Honeywell in Torrance, CA. ORNL and Honeywell defined neutron-scattering residual stress measurements, first for turbine wheel/shaft components, and then for turbine housings. Long-term creep and oxidation evaluation of CF8C-Plus cast stainless steel continued for diesel and automotive turbine housings.
- A draft report on the energy benefits of CF8C-Plus stainless steel in automotive and diesel turbocharger applications was completed, and such deployment of CF8C-Plus steel could save 143 trillion BTUs by 2020.

Future Direction

- CRADA – Upgrade materials for wheel, shaft and housing of the turbine portion of the turbocharger will continue to be assessed. The benefits for making turbocharger systems lighter weight, and capable of higher temperatures for gasoline engine passenger vehicles will be a priority.
- CF8C-Plus Benefit Studies – The benefits of CF8C-Plus stainless steel relative to more expensive heat-resistant alloys will continue to be assessed, particularly for automotive applications.

Introduction

A new ORNL CRADA project with Honeywell, NFE-08-01671 (DOE/EERE/OVT Agreement 17257) began in September, 2009, and will last for 3 years. This CRADA project addresses the limitations of lifetime or use-temperature for the various components (casing, wheel, shaft, bearings) of both the turbine and compressor parts of the turbocharger system. Requests for more detailed information on this CRADA project should be directed to Honeywell, Inc.

Agreement 17257 also included an economic assessment of CF8C-Plus for automotive applications last year, and an energy benefits assessment this year. More information can be obtained from Sujit Das at the National Transportation Research Center (NTRC) at ORNL.

Approach

CRADA Project

The new CRADA project, which began in September, 2009, will extend for 3 years, and cover several different tasks. The first task assesses and prioritizes the various components that need or would most benefit from materials upgrades to increase temperature capability and performance, as well as durability and reliability. The next tasks examine current performance and degradation modes of wheel/shaft assemblies for turbines and compressors, and turbine housings, particularly for automotive applications. New materials will then be obtained and tested to verify upgraded performance and benefits.

CF8C-Plus Energy Benefits Analysis

Energy benefits analysis was based on gathering extensive information on commercial turbocharger housing manufacturing, and

evaluating the impact of higher temperatures and longer life-cycle on automotive and diesel engines. Similar information was also obtained for using the new stainless steel for gas turbine and steam turbine casings and end-covers. Energy benefits in manufacturing components and in life-cycle for the end-use were projected to 2020-2025.

Technical Progress

CRADA Project

This new CRADA project began in September, 2009, and is comprised of six tasks, which will span the 3y duration of this project. ORNL and Honeywell discussed the priority of the various tasks and turbocharger components for materials upgrades at a kick-off meeting held in Torrance, CA in October, 2009.

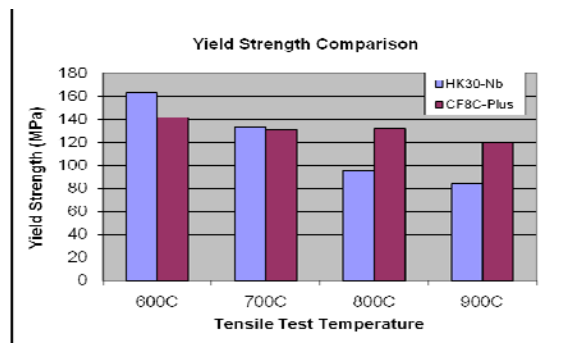


Figure 1 – Comparison of yield strength (YS) measured by elevated temperature tensile testing of both cast CF8C-Plus and cast HK30-Nb austenitic stainless steels. While the HK30-Nb has slightly higher YS at 600°C, the CF8C-Plus steel is stronger at 800 and 900°C.

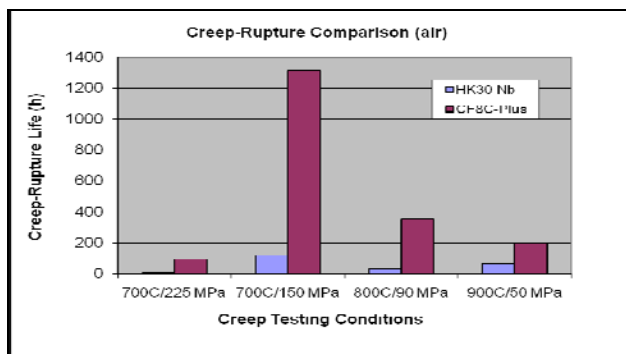


Figure 2 – Creep-rupture life comparison of the new CF8C-Plus cast stainless steel to commercial HK30-Nb cast stainless alloy. Initial comparison suggests CF8C-Plus steel has much better creep-resistance at 700-900°C than HK30-Nb.

The turbine wheel-shaft assembly was chosen as the first component for analysis of residual stresses near the weld-joint of the Ni-based superalloy wheel to the steel shaft, using neutron-scattering at the HFIR reactor at ORNL. Residual stress analysis with neutron-scattering will also be done on certain critical locations of turbine housings currently made of SiMo cast-iron. Similar residual-stress measurements are planned at similar locations for new turbine housings made from CF8C-Plus steel sometime next year.

Additional testing was done to extend previous work by ORNL and Honeywell comparing the new CF8C-Plus steel to HK30-Nb, a standard commercially available upgrade material for turbochargers for heavy-duty truck diesel engines when temperatures exceed the limitations of SiMo cast iron. Figure 1 shows the comparison of yield-strength (YS) for CF8C-Plus and HK30-Nb steels tensile tested at 600-900°C. Clearly CF8C-Plus has more strength at 800 and 900°C. Additional creep-testing was done at 600 and 700°C this year, and creep-tests of CF8C-Plus at 600°C are still going without rupture. Figure 2 shows creep-rupture life after creep-testing at several different conditions at 700-900°C, and clearly, CF8C-Plus steel has better creep-resistance than the HK30-Nb alloy. Materials comparisons and additional testing will be included to enable CF8C-Plus steel to be evaluated for turbine housings for passenger vehicle gasoline engines.

CF8C-Plus Energy Benefit Analysis

A detailed energy benefit analysis for automotive exhaust manifolds and turbocharger housings was conducted for the new CF8C-Plus cast stainless steel compared to HK30 steel and SiMo cast iron by S. Das at the NTRC. SimaPro LCA software was used, and data for energy and mass differences for manufacturing exhaust components from different alloys was taken from a similar study of cost analysis done by S. Das last year. CF8C-Plus has benefits in the primary energy used to manufacture cast automotive or diesel exhaust components due a 7-8% mass savings compared to HK30 and other considerations related to alloy composition, as shown in Figure 3. Both steels require less energy compared to the Ni-based superalloy 625.

Annual projected sales data for light- and heavy-duty vehicles for the period 2010 – 2025 were used from the latest EIA estimates (EIA 2010a). Figure 4 shows the energy savings related to using CF8C-Plus steel, considering the 7-8% mass savings noted above, considering materials manufacturing alone. Clearly automotive use for turbochargers produces significant energy savings by the year 2020. The total cumulative life cycle energy savings include fuel economy improvements (2% for light-duty vehicles and 0.66% for heavy-duty vehicles) due to turbocharging, as well as average miles traveled per vehicle, and other factors, and those results are shown in Figure 5. Again, the total life cycle energy benefits are larger than the materials manufacturing benefits, and at 2020, the energy savings benefits for light-vehicle use are much larger than those for heavy vehicle use. If all the total cumulative life-cycle energy savings values for transportation applications of CF8C-Plus steel are added up from Figure 5 in 2020, they come to 94 trillion BTUs. Similar calculations for energy savings were done for steam-turbine and gas-turbine applications of CF8C-Plus steel, using similar assumptions to those done for cost-savings last year, and in 2020, the total cumulative life-cycle energy savings values are 49 trillion BTUs. The combined total cumulative energy savings for both the transportation and turbine applications of CF8C-Plus steel in 2020 is 143 trillion BTUs, with the transportation application of turbochargers accounting for 66% of that total. More details on

the assumptions and the details of these calculations can be found in the full report.

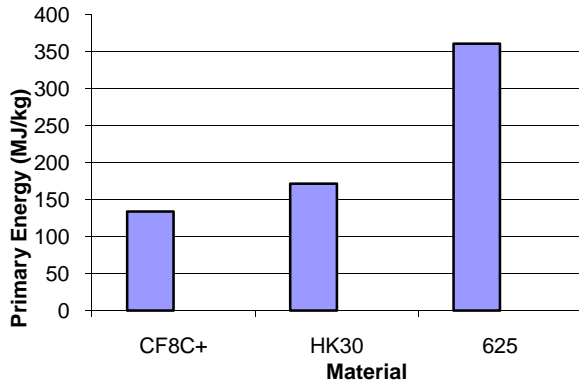


Figure – 3 – Estimated competing energy required to manufacture the material, the part and the material use, on a life-cycle basis, for CF8C-Plus steel, HK30 steel and Ni-based superalloy 625.

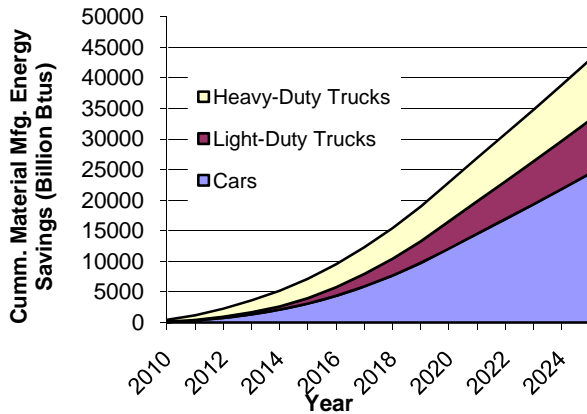


Figure – 4 – Estimated cumulative materials manufacturing energy savings due to using CF8C-Plus stainless steel for turbocharger housings in the automotive market.

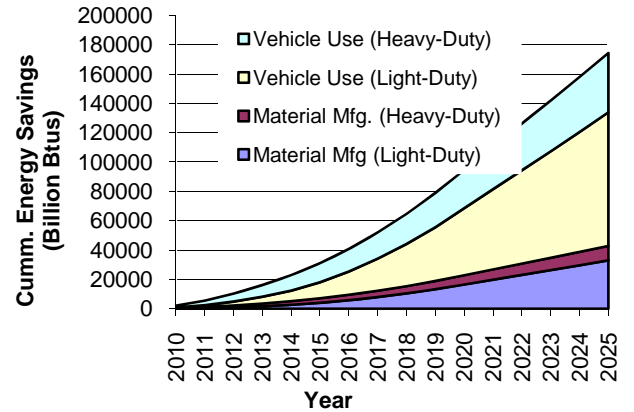


Figure – 5 – Estimated total cumulative life-cycle energy savings for use of CF8C-Plus steel for turbocharger housings in the automotive market.

Conclusions

CRADA – The benefits of CF8C-Plus steel relative to HK-30Nb steel at 700-900°C were defined for diesel turbocharger housing applications, and long-term creep-testing of CF8C-Plus at 600-700°C continued. Neutron-scattering residual stress experiments were defined for the welded region of turbine wheel/shaft assemblies for passenger vehicle turbochargers.

CF8C-Plus Energy Benefits Study – CF8C-Plus cast stainless steel has to potential to save 143 trillion BTUs by 2020 for turbocharger and gas/steam turbine applications, with about 66% of that coming from automotive vehicle turbochargers. Far more energy savings are realized by life-cycle, end-use calculations rather than the initial material/component considerations. Energy savings for CF8C-Plus cast stainless steel was evaluated relative to HK30 cast stainless steel, and the Ni-based superalloy 625.

Publications/Presentations

A draft of an ORNL Report on Potential Energy Benefits of CF8C-Plus Cast Austenitic Stainless Steel was prepared for DOE/EERE/OVT by Sujit Das in September, 2010.

Special Recognitions and Awards/Patents

Issued

None

Agreement 17894 - NDE Development for ACERT Engine Components

Jiangang Sun

Argonne National Laboratory

9700 South Cass Avenue

Argonne, IL 60439

630-252-5169; fax: 630-252-2785; e-mail: sun@anl.gov

DOE Technology Manager: Jerry L. Gibbs

(202) 586-1182; fax: (202) 586-1600; e-mail: Jerry.gibbs@ee.doe.gov

ORNL Technical Advisor: D. Ray Johnson

(865) 576-6832; fax: (865) 574-6098; e-mail: johnsondr@ornl.gov

Contractor: Oak Ridge National Laboratory, Oak Ridge, Tennessee

Contract No.: DE-AC05-00OR22725

Subcontractor: Argonne National Laboratory, Argonne, Illinois

Objectives

- Develop rapid, reliable, and repeatable nondestructive evaluation (NDE) methods for inspection of advanced materials and processing technologies to support the material-enabled high-efficiency diesels program.
- Establish NDE methods and test procedures for characterization of advanced materials and components being tested in an ACERT experimental engine at ORNL.

Approach

- Develop infrared thermal imaging methods for quantitative measurement of thermal barrier coating (TBC) properties and 3D imaging of TBC structures to determine TBC degradation and detect delamination.
- Evaluate optical imaging methods for detection of TBC delaminations and for characterization of subsurface crack geometry in advance ceramics.
- Investigate synchrotron x-ray CT for NDE characterization of material flaws and welding quality of light-weight metallic components for diesel engines.

Accomplishments

- Optimized processing parameters and enhanced lateral resolution for thermal tomography NDE characterization of TBCs.
- Correlated NDE results from optical and thermal imaging technologies for detection of delaminations in TBCs.
- Evaluated high-energy synchrotron x-ray CT for NDE characterization of metallic joint components for diesel engines.

Future Direction

- Continue development of optical and thermal imaging NDE technologies for characterization of TBCs applied on diesel engine components.
 - Develop/utilize x-ray and ultrasonic imaging NDE technologies for inspection of joint components for diesel engine.
 - Investigate vibro-thermography NDE technology for detection of fatigue cracks in turbine components.
-

Introduction

Application of advanced materials in diesel engines may enhance combustion and reduce parasitic and thermal losses, thereby improving fuel efficiency while meeting the emission standard. Engine components developed from advanced materials and processing technologies, however, require rigorous assessment to assure their reliability and durability in higher temperature and pressure operating conditions associated with advanced engine systems. To address these materials challenges, selected materials/components are being prepared and tested in a Caterpillar heavy-duty C15 ACERT experimental diesel engine located at ORNL. The engine tests will provide crucial information on material performance/durability and effect to engine efficiency and parasitic losses in combustion and thermal management systems¹. In collaboration with materials scientists and engine engineers from Caterpillar and ORNL, these engine materials and components are being characterized by nondestructive evaluation (NDE) technologies at ANL to determine their reliability and durability for engine applications. The objective of this work is to develop and assess various NDE methods for characterization of advanced materials and components for ACERT engine systems. NDE technologies established at ANL, including optical scanning, infrared thermal imaging, vibro-thermography, ultrasonic imaging, and x-ray computed tomography (CT), are being further developed for detection of volumetric, planar, and other types of flaws that may limit the performance of these components. NDE development is focused on achieving higher spatial resolution and detection sensitivity.

The primary effort in FY 2010 was focused on developing infrared thermal and optical imaging technologies and correlating their results for thermal barrier coatings (TBCs) considered for application in engine exhaust systems. Another effort was directed on developing and evaluating high-energy synchrotron x-ray CT for NDE characterization of joint components made from advanced light-weight metallic materials. This research is collaborated with Caterpillar Inc. and ORNL.

Approach

Advanced TBC is a key enabling material technology to allow for diesel engines to achieve

higher fuel efficiency and reduce cost. A TBC material typically has lower thermal conductivity and superior oxidation resistance, which may reduce heat losses and at the same time prevent corrosion and facilitate utilization of cost-effective metals in engine systems because of the decreased component temperature. In the gas turbine industry, ceramic TBCs have become an integral part of high-temperature components in hot-gas paths. TBCs have also been developed for diesel-engine components such as pistons and exhaust systems. These TBCs have wide variations in composition and thickness, ranging from tens of microns to a few millimeters. Characterization of these TBCs is very challenging and requires development of NDE methods that can (1) accurately measure TBC properties to allow for quantitative determination of TBC quality and degradation and (2) detect TBC cracks and delaminations that cause TBC spallation. NDE technologies mostly used for TBCs are pulsed thermal imaging and optical methods. ANL has been active in developing both technologies. The thermal tomography method developed at ANL, which is based on pulsed thermal imaging, has been demonstrated to be capable of detecting flaws and delaminations at various depths of multilayer TBC material systems². Optical methods, including laser backscatter and optical coherence tomography (OCT), have higher spatial resolution and are suitable to detect cracks and delaminations in thin translucent TBCs. Under this project, these NDE methods are utilized to characterize TBCs developed for diesel exhaust components. The results are correlated between the methods and with visual observations to validate detection accuracy and sensitivity.

Titanium aluminide (TiAl) has been identified as a promising material for rotating and oscillating components in gasoline and diesel engines. TiAl is an intermetallic material and has unique combination of favorable properties such as low density and high-temperature strength. One of the most promising TiAl engine components is the turbocharger wheel. A challenge in this application is the joining of the TiAl wheel to the Ti-alloy shaft. Friction welding is the most suitable method for such task and has been investigated by Caterpillar³. However, friction welding is very difficult to join dissimilar materials and may produce cracks at the joint plane that can be difficult to detect by conventional NDE methods. High-energy

synchrotron x-ray CT, developed at the advanced photon source (APS) at ANL, was found to be suitable for NDE characterization of the joint quality. The synchrotron x-ray source has a high peak energy (>250keV) to penetrate the metallic material, and the detector (imager) has a high spatial resolution (~40μm) to resolve small flaws. This system has been evaluated for inspection of TiAl joint samples.

Results

Optimization of Processing Parameters for Thermal Tomography Analysis of TBCs

Thermal tomography is a data-processing method that reconstructs 3D thermal effusivity distribution from the raw data acquired from a pulsed thermal imaging test. Because thermal effusivity is a material physical property, which is unique to each material, material compositional as well as structural variation within the internal of the sample can be determined simultaneously. Thermal tomography has been successfully used to characterize as-processed and thermally-cycled TBC samples in FY2009². However, several processing and experimental parameters were found to affect the tomography results. Optimization of these parameters was therefore carried out.

Figure 1 shows a schematic of the thermal imaging test setup. The parameters that affect the tomography reconstruction include the flash duration of the flash lamps, the amount and depth of heat absorbed on TBC surface, and the data acquisition speed. The flash duration, typically in the range of 1-2ms, affects only the early transient time period that corresponds to the top few slices (within the coating layer) in the tomography result. Therefore, it is necessary to correctly account for the flash duration effect in order to generate accurate NDE results for the coating layer.

The parameter optimization is illustrated using the as-processed TBC specimen #10 shown in Fig. 2a. From the experimental data acquired at a speed of 1068Hz for a duration of ~3s, the reconstructed coating layer (~100μm thick) consisted 5 plane slices (each of ~20μm thick). A 2ms flash duration was used in previous data processing², and a 0.8ms was used in new processing. Figure 3 compares the coating slices #1, #3, and #5 derived based on old (Fig. 3a) and new parameter (Fig. 3b); it is evident

that the new parameter considerably improved image quality (lower noise) in the first three slices. More importantly, the coating layer becomes more uniform and distinct from the substrate in the new data (Fig. 4b), as seen from the cross-sectional slices in Fig. 4.

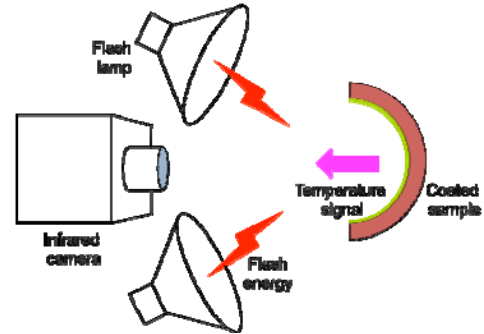


Figure 1. Schematic top view of thermal imaging setup.



Figure 2. Photographs of TBC specimen #10 with (a) as-received and (b) a black-painted surface.

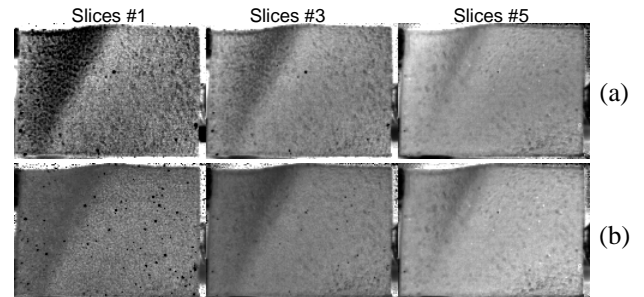


Figure 3. Plane slices of the coating layer for TBC specimen #10 obtained with (a) 2.0ms and (b) 0.8ms flash duration parameter.

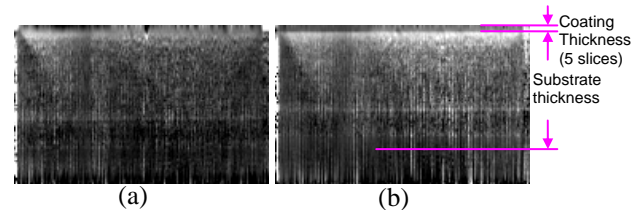


Figure 4. Cross-section slices for TBC specimen #10 obtained with (a) 2.0ms and (b) 0.8ms flash duration parameter.

The new flash-duration parameter was also used to construct tomography images of other TBC samples based on previously acquired thermal-imaging data. Because of the reduced noise level in shallow coating depths, the new images are particularly useful to identify shallow delaminations in thermal-cycled coatings. Figure 5 shows the plane slices of the coating layer in thermal-cycled TBC specimen #9. As indicated, shallow flaws are observed at the top-right corner in slice #1 (which is on surface); they disappear at slices deeper than #2. Within a large rectangular area at the left side, many individual delamination spots emerge at deeper depths (in slices >#3). At the lower-right corner of the sample, no apparent flaws are detected. This area shows a darker brownish color on surface (see Fig. 8), which corresponds to a surface where the coating has already been spalled. The results in Fig. 5 clearly demonstrate that thermal tomography can easily detect flaws and delaminations and resolve their size and depth distributions.

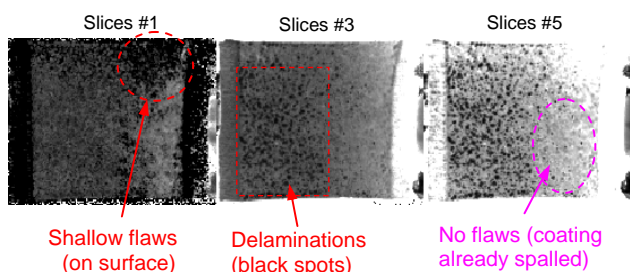


Figure 5. Characterization of delamination depth and distribution in thermal-cycled TBC #9.

Another parameter affecting image quality is the high optical reflection of as-processed TBC surface, which causes low heat absorption during thermal imaging test. For as-processed TBC #10, for example, the maximum surface temperature during the flashing time was found to be <math><5^{\circ}\text{C}</math>, which is significantly lower than an adequate heating level. As a result, the noise in the tomography results (Figs. 3-4) is higher especially in deeper substrate layer. A solution to improve surface heat absorption is to apply a graphite-based black paint on the coating surface. The black paint is typically 1-2 μm thick and can be easily burn off at $\sim 700^{\circ}\text{C}$ within a short time. To assess the effectiveness of the black paint, and also to verify the result obtained without the paint, half of the TBC #10 surface was painted as shown in Fig. 2b. The experiment was conducted

at a higher data-acquisition speed of 1905Hz for the painted area. With the black paint, the maximum surface temperature during the flashing period was found to be $>32^{\circ}\text{C}$, a significant improvement in heat absorption efficiency.

Figure 6 shows plane and cross-sectional slices in the painted area of TBC #10. From the cross-section image (Fig. 6b), the coating layer has a distinct lower thermal effusivity and a thickness consisted of 7 plane slices. Accordingly, Fig. 6a shows several plane slices within the coating. By comparing the images acquired with (Fig. 6) and without paint (Figs. 3-4) in the same sample area, the surface paint resulted in a higher image quality (especially in the substrate) and a sharp resolution of the interface.

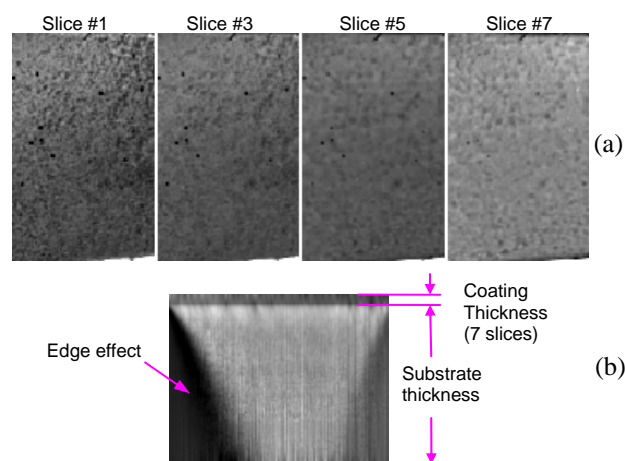


Figure 6. (a) Plane slices within the coating layer and (b) a cross-section slice for as-processed TBC #10 with a black paint on surface.

Although a black paint may improve the result, it is normally undesirable to paint the TBC surface. Under such conditions, thermal imaging must be performed on natural TBC surface, and the accuracy of the acquired data has to be assured. To address this issue, the plane slices near the interface from unpainted and painted data are compared in Fig. 7 to determine if the same result is obtained. Because TBC #10 is a “good” sample, the only features to be compared are the darker spots corresponding to the surface bumps. From Fig. 7, it is evident that the number and distribution of the darker spots are essentially the same in both images. The slight difference in spot sizes and grayscales is due to focusing and data-acquisition speed. Therefore, it is concluded that thermal imaging can reliably

examine coating and interface conditions for natural TBCs that may have high surface reflections.

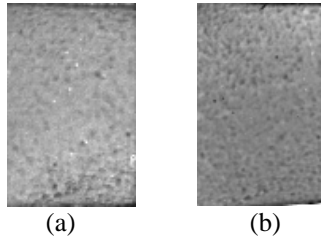
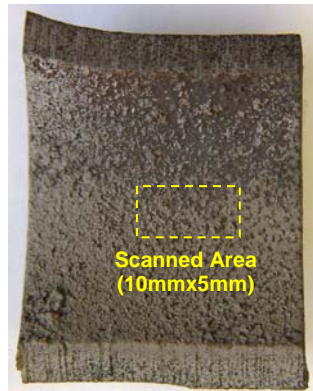


Figure 7. Comparison of plane slices at interface obtained (a) without and (b) with black paint on as-processed TBC #10.



Laser backscatter scan image

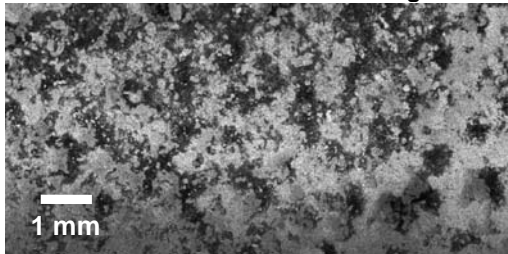
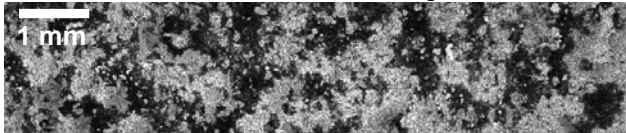


Figure 8. Photograph and laser backscatter scan image of thermal-cycled TBC #9 surface.

Laser backscatter scan image



Optical micrograph

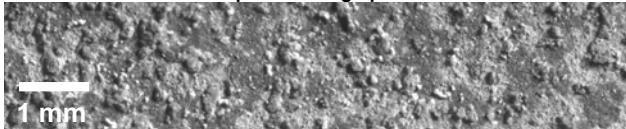


Figure 9. Comparison of laser-scatter scan image with surface micrograph for thermal-cycled TBC specimen #9.

Optical Imaging Analysis of Thermal-Cycled TBC

Optical imaging methods have higher spatial resolution, in the order of ten microns, so are suitable to detect small flaws that are abundant in these TBCs. However, optical methods have limited detection depth because these coatings are partially translucent. To establish detection sensitivity, the laser backscatter method was used to scan a thermally-cycled TBC surface and the result is correlated with optical micrograph and thermal imaging data. This correlation is served as a means to validate and calibrate the NDE technologies for reliable inspection and prediction of TBC conditions.

Figure 8 shows a laser backscatter scan image on the surface of thermal-cycled TBC specimen #9. The scan image has a dimension of 10 mm x 5 mm, with a pixel size of 10 μm. In general, the TBC surface exhibits either high or low laser-scatter intensities. The intensity pattern in the scan image matches well with that observed in the photograph. The regions with high-scattering intensities correspond to the gray surface where TBC is cracked or delaminated but still remains on surface, and the regions with low scattering intensities to the dark-brown surface where TBC has already been spalled off². A detailed comparison of the laser-scatter NDE data with a photomicrograph of the TBC surface is shown in Fig. 9.

Thermal Imaging Analysis of TBCs with High Lateral Resolution

In standard thermal imaging test, the entire TBC surface is imaged by the detector array that has limited number of pixels (e.g., 160x128 pixels). The lateral resolution is therefore limited by the pixel size which is ~0.2mm when testing 1"-squared specimens. Because flaws in these TBCs are generally smaller than this size (see Fig. 9), it has been difficult to directly correlate thermal imaging data with optical data. A higher lateral resolution can be obtained by placing the infrared camera closer to the sample as illustrated in Fig. 10. However, because of the small space between the camera lens and sample surface, only one flash lamp can be used with a large incident angle to the sample surface. As a result, heating efficiency was lower.

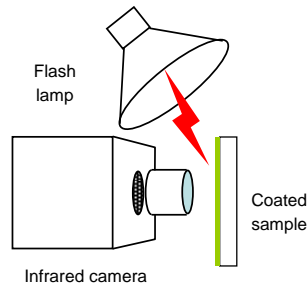


Figure 10. Schematic top view of experimental setup.

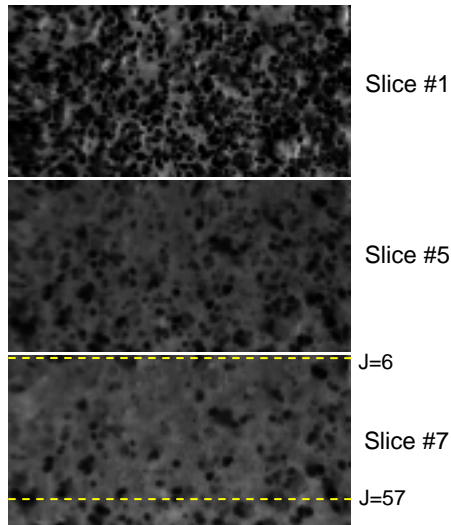


Figure 11. Plane slices #1, #5, and #7 within the coating layer for thermal-cycled TBC specimen #9.

Thermal imaging tests using the modified setup were conducted for thermal-cycled TBC specimen #9. Of particular interest is the 10-mm x 5-mm region scanned by the laser backscatter method as shown in Fig. 8. By proper close-up adjustment and with a detector array of 128x80 pixels (imaging speed at 1905 Hz), the pixel size is ~78µm. Typical thermal tomography plane slices from this test are shown in Fig. 11. Under this test condition, the first 7 plane slices are located within the coating layer (when coating exists). In plane slice #1 (on surface), all regions with low grayscale (low effusivity) represent the coated areas that are either damaged (with increased porosity) or cracked/delaminated, and the regions with brighter grayscale correspond to coating-spalled areas. The delaminated regions can be better identified in deeper depths, as seen in Slices #5 and #7 (the darker spots).

The thermal tomography results are correlated with optical micrograph to validate the detection of

delaminations, as shown in Fig. 12. From the micrograph, cracked/delaminated coatings can be easily identified because they are raised above surface as surface bumps. In the tomography images, all cracked/delaminated coatings are shown with lower grayscale (low effusivity), and their sizes and shapes match well with those in the micrograph. This correlation clearly demonstrates that the detected coating damages by thermal tomography are indeed coating cracks and delaminations. In addition, thermal tomography detected other coating damages that are not visible on surface. Two of these are circled in Fig. 12; they should be delaminations at deeper depths.

The improved lateral resolution also helps to reveal other features that were not observed with coarse resolutions. Figure 13 shows two cross-section slices for TBC specimen #9. Three inclined darker features were detected; they run from the surface to the right side into the depths. These features are different from those of typical delaminations, which are aligned in the vertical direction as seen for some in Slice J=57. It is unclear if these are due to the shadowing effect of flash lighting because the flash lamp is located at the left side with a very low incident angle. The exact nature of these features is unknown and may need further investigation.

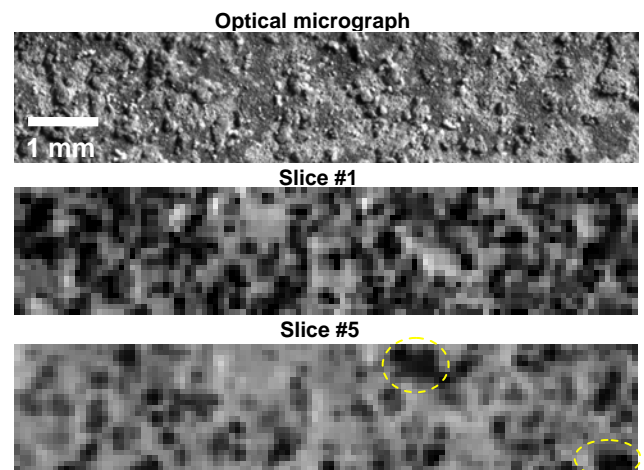


Figure 12. Detailed comparison of surface micrograph and thermal tomography images for thermal-cycled TBC specimen #9.

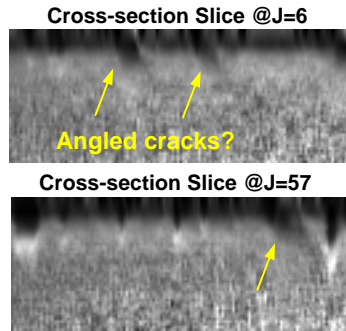


Figure 13. Cross-section slices at locations indicated J=6 & J=57 in Fig. 11 for thermal-cycled TBC specimen #9.



Figure 14. Friction welded turbine wheels³.

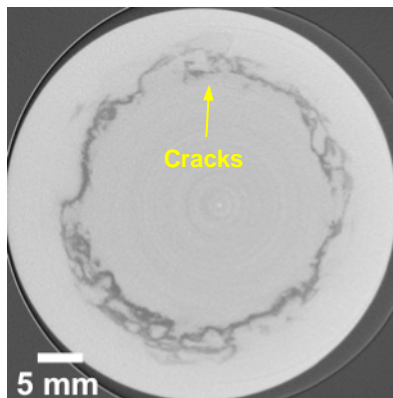


Figure 15. A typical x-ray CT slice within weld plane.

X-Ray CT Characterization of Joint

Synchrotron x-ray CT was investigated for characterization of friction-welded joints between TiAl turbine wheel and Ti-6Al-4V shaft (see Fig. 14). A preliminary test was conducted for calibration joint samples that contain weld cracks. Figure 15 is a typical cross-section CT slice, which shows, for the first time, the complex crack networks within the

weld plane. These images may be further processed to reveal more detailed structural variations. With 3D volume rendering, the 3D crack geometry in the volume may be visualized. This result therefore demonstrated that synchrotron x-ray CT is the most suitable NDE technology to characterize 3D flaw distribution within the weld plane. The result may also help to understand the effect of various processing parameters to the resultant weld quality. This information may be used to optimize processing parameters to manufacture reliable components for industrial applications.

Conclusions

Thermal imaging and optical scanning methods were developed for NDE inspection of TBCs consisting of a top ceramic coat and a cast Fe-steel substrate. The FY2010 effort was focused on optimization and validation of thermal tomography method for detection of flaws such as cracks and delaminations in TBCs. With an optimized flash duration parameter, the resultant tomography images showed considerable improvement, with reduced noise in shallow depths and sharper resolution of the coating/substrate interface. This improvement allowed for better detection of shallow defects in thermal-cycled TBCs. Another parameter that may affect detection sensitivity was the high surface reflection on as-processed TBC surfaces. This effect was evaluated by painting the surface black, a condition considered ideal for thermal imaging. The results showed significant improvement in image quality, especially in the substrate depths. However, it does not affect the sensitivity for detection of flaws within the coating layer.

Thermal imaging data were validated based on their correlation with optical imaging data because the damages (cracks and delaminations) in these TBCs are visible as surface bumps. Because of the small sizes of the damages (typically <0.2mm), the thermal imaging system was reconfigured to obtain a pixel size of ~78µm, which is the highest lateral resolution obtained so far. At this resolution, thermal imaging data correlated well with optical data, thus confirming the detected flaws. These results demonstrated that thermal tomography can be used reliably to detect flaws in TBCs.

Synchrotron x-ray CT was investigated for NDE characterization of friction-welded joint between TiAl turbine wheel and Ti-alloy shaft. From a

preliminary test for calibration weld samples, the CT results showed detailed resolution of crack networks and structural variations in the weld plane. This technology will be further evaluated for joint samples made with different processing parameters. The results can be used to optimize processing parameters to manufacture reliable weld components.

References

1. M.D. Kass, et al., "Materials Testing with ACERT Engine," *Annual Report for FY2008, Heavy Vehicle Propulsion Materials Program*.
2. J.G. Sun, "NDE Development for ACERT Engine Components," *Annual Report for FY2009, Heavy Vehicle Propulsion Materials Program*.
3. Nan Yang, et al., "Development of Titanium Alloys for Heavy-Duty Diesel Engines," *Quarterly Progress Report for April through June 2005, Heavy Vehicle Propulsion Materials Program*.

Presentations and Publications

J.G. Sun, "Thermal Property Measurement for Thermal Barrier Coatings by Thermal Imaging Method," in *Ceramic Eng. Sci. Proc.*, eds. S. Mathur and T. Ohji, Vol. 31, no. 3, pp. 87-94, 2010.

J.G. Sun, "Thermal Tomographic Imaging for Nondestructive Evaluation of Ceramic Composite Materials," in *Ceramic Eng. Sci. Proc.*, eds. S. Mathur and T. Ohji, Vol. 31, no. 2, pp. 137-144, 2010.

J.G. Sun, "Quantitative Three-Dimensional Imaging by Thermal Tomography Method," paper presented at the 37th Annual Review of Progress in Quantitative Nondestructive Evaluation, San Diego, CA, July 18-23, 2010.

J.G. Sun, "Method for Analyzing Multi-Layer Materials from One-Sided Thermal Imaging," U.S. Patent No. 7,769,201, issued Aug. 3, 2010.

Agreement 18570 – Engine Materials Compatibility with Alternate Fuels

S. J. Pawel, D. F. Wilson, H. M. Meyer, and M. D. Kass*

** Corrosion Science and Technology Group*

Oak Ridge National Laboratory

1 Bethel Valley Road, Bldg. 4500-S, MS-6156

Oak Ridge, TN 37831-6156

(865) 574-5138; fax: (865) 214-0215; e-mail: pawelsj@ornl.gov

DOE Technology Manager: Jerry L. Gibbs

(202) 586-1182; fax: (202) 586-1600; e-mail: jerry.gibbs@ee.doe.gov

ORNL Technical Advisor: D. Ray Johnson

(865) 576-6832; fax: (865) 574-6098; e-mail: johnsondr@ornl.gov

Contractor: Oak Ridge National Laboratory, Oak Ridge, Tennessee

Prime Contract No.: DE-AC05-00OR22725

Objectives

- Conduct a systematic assessment of engine materials corrosion in ethanol fuel blends to develop a mechanistic understanding of performance boundaries and material selection requirements.
- Seek to relate forensic analysis of materials returned from field exposures (samples created from actual engine operation) with laboratory corrosion test results to develop a rapid corrosion assessment technique.

Approach

- Evaluate corrosion and surface films on components returned from vehicles (engines tests, actual service) via forensic analysis and compare with similar results generated in laboratory testing.
- Investigate possibilities for in-situ extraction and analysis of liquid/gas constituents from the valve seat crevice.
- Gather corrosion information and test data to enable development of relatively rapid electrochemical test protocols to assess potential for susceptibility to corrosion of engine materials.

Accomplishments

- Cylinder heads for evaluation of structure and corrosion products have been received and prepared for analysis at ORNL. Microprobe and Auger examination is underway but; unfortunately, very little evidence of valve seat crevice corrosion is apparent among these components.
- A proof-of-principle technique for evaluation of the valve seat crevice environment has been demonstrated. Cylinder heads for testing are being machined to incorporate the required capillary tube inserts.
- Autoclave test chambers were specified and procured for use in evaluation of corrosion as a function of ethanol-blend composition material composition variables. Laboratory safety protocols for high temperature fuels testing have been designed and approved, and testing initiated.
- Surveys of available information via library literature search and assessment of publically available information from the Partners research libraries yielded very little useful information regarding performance of aluminum and aluminum alloys in ethanol fuel blends.

Future Direction

- Develop baseline structure and surface analysis results representing valve seat pocket corrosion for the initially identified candidate cylinder heads. Use this information to support interpretation of static immersion test results and identification of relevant corrosion mechanisms.
- Complete machining of heads with capillary tubes inserted for analysis of gas/liquid accumulations in the valve seat crevice. Use this information to support interpretation of static corrosion test results and identification of relevant corrosion mechanisms.
- Perform battery of static immersion corrosion tests of aluminum and aluminum alloys in ethanol fuel blends of variable composition and environmental conditions. Initiate exploratory electrochemical testing.

Introduction

With the experience in the past ten years in Brazil with fuel blends up to E100 and more recent experience in the US and Europe with extensive production of flex-fuel vehicles to run on fuel blends up to E85, observations of corrosion problems not previously observed with ethanol-free gasoline have begun to accumulate. Like water, ethanol is a proton-bearing medium capable of sustaining electron transfer such that it is potentially corrosive. Absolutely pure ethanol is not generally corrosive toward many metallic engineering materials, but depending on the carbohydrate source and processing variables used in the production and handling of ethanol, contaminants such as water, oxygen, organic acids, and salts can accumulate and lead to general or localized corrosion of a variety of common engine materials. This has been observed, in particular, in corrosion initiating in the crevice between the aluminum cylinder head and the ferrous alloy valve seat of some engines. In addition, corrosion of fuel pump and fuel injector components and issues with hot corrosion has been reported.

From a potential corrosion perspective, the addition of ethanol to traditional gasoline changes two important fuel properties. Firstly, ethanol is several orders of magnitude more electrically conductive than gasoline, so that even small additions of ethanol can substantially increase conductivity and the potential for corrosion problems (including galvanic attack). In addition, the affinity of ethanol for water (and its associated solubility) is many orders of magnitude greater than the affinity/solubility of gasoline for water, and thus various “aqueous” corrosion issues may be expected in ethanol fuel blends that are not observed in traditional gasoline.

In order to conduct a systematic assessment of engine materials corrosion in ethanol fuel blends, a Cooperative Research and Development Agreement (CRADA) has been established between participants at Oak Ridge National Laboratory and domestic automobile manufacturers (USCAR, LLC). The overall effort is composed of several tasks to be performed primarily in parallel, with each briefly described herein.

Results

Evaluation of corrosion and surface films on engine components

Cylinder heads for evaluation of surface structure and corrosion products have been identified by the USCAR Partners from among several engines subjected to dynamometer testing under a variety of conditions. An example of a portion of an as-received head is shown in Fig. 1.

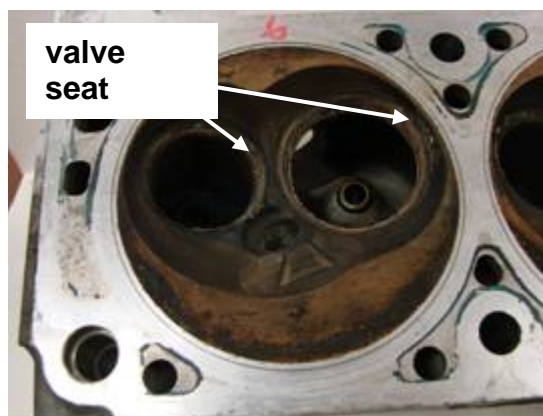


Figure 1. Portion of an aluminum head received for evaluation of corrosion in the valve seat crevice location.

After receipt and initial inspection, the components were machined to a reduced size suitable for insertion into the analytical microscopes. This was accomplished via electro-discharge machining and special handling to minimize additional contamination or distress to the existing surfaces of interest. The purpose of these analyses is to elucidate corrosion products and their distribution to potentially gain insight into the composition of corrosive species and environmental conditions within the valve seat crevice leading to degradation. In this manner, bench-top tests can be manipulated to mimic the same environment (that is, generate the same material features and corrosion product formation) assuring that corrosion mechanisms and potential solutions derived from lab testing are relevant. Initial indications are that the components provided exhibit relatively little valve seat crevice corrosion of the type of interest, but additional components are being sought, and others will no doubt be developed as part of this Program.

In-situ extraction and analysis of gas/fluid from valve seat crevice

Initial efforts have been made to demonstrate a proof-of-principle device for sampling of gas/fluids in the valve seat crevice.

A cylinder head provided by the USCAR Partners was sectioned and a small diameter hole (to accommodate a 320 μm diameter tube) drilled from behind the intake to the gap between the head and valve seat. Initial tests to withdraw water from this area were successful (see Fig. 2).

Six additional heads are presently being modified by one of the USCAR Partners that include machined holes for placement of the extraction tube. Once the tubes are inserted and valve seats pressed into place, dynamometer testing will commence using E85 and related fuel blends. Analysis of any gas/liquid collected in the valve seat crevice during engine operation as a function of fuel type, valve seat material, and other variables will be used to identify key components of the actual environment at this location responsible for the observed corrosion. Further, this information is expected to guide formulation of test environments for accelerated corrosion testing to identify superior materials or engineering solutions to mitigate corrosion.

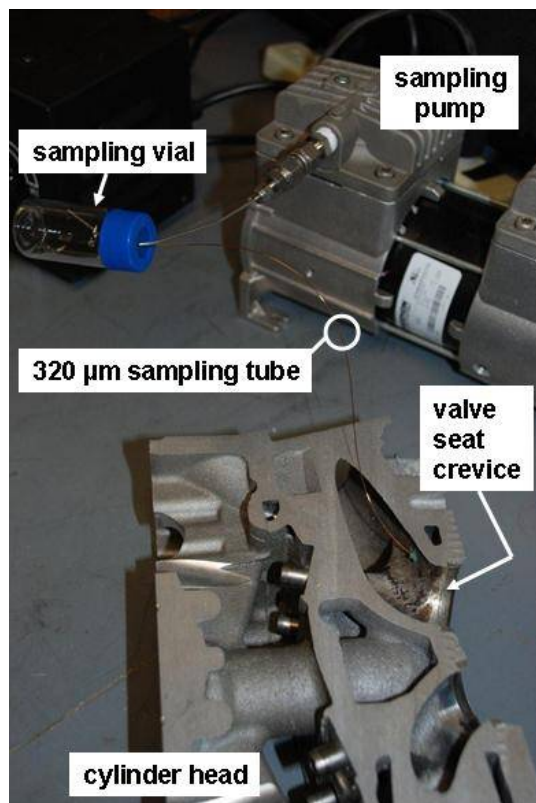


Figure 2. Proof-of-principle device for sampling gas/liquid from the valve seat crevice region.

Development of laboratory corrosion testing

Laboratory bench-top testing capability to assess corrosion of various materials in alternative fuel blends has been established. This activity included design and approval of safety protocols for containment of fuels at elevated temperature and pressure, and procurement of a dedicated glove box (for handling ethanol fuel mixtures and excluding unintended water additions during preparation/storage of test solutions) and autoclaves (for use in elevated temperature/pressure testing of metal coupons in fuels). In particular, the autoclaves were designed with a small working volume yet with multiple feed-through fittings on the lid to permit inclusion of multiple electrodes (working, counter, and reference) as well as manipulation of head space gas composition and monitoring of temperature and other environmental variables. Figure 3 represents one of the Teflon-lined autoclaves that was procured for this Program.

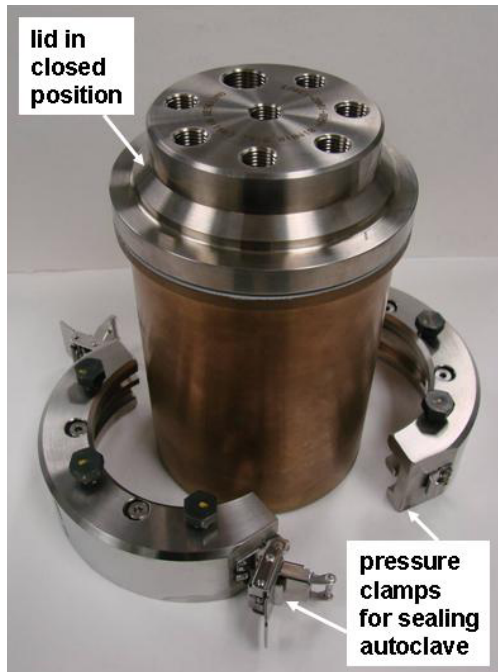


Figure 3. One of the autoclaves to be used for electrochemical testing. Interior of autoclave vessel, about 4" diameter and 6" deep, is Teflon-lined with a compression seal.

Surveys of available information via library literature search and assessment of publically available information from the Partners research libraries yielded very little useful information regarding performance of aluminum and aluminum alloys in ethanol fuel blends. As a result, static immersion testing of a variety of aluminum alloys representing engine alloy development will be initiated immediately to address this shortcoming. Coupons for use have been procured from a specimen shop; in that regard, they represent a wide range of cast alloy compositions (for example, types 319, 333, and 356) without necessarily having the same structure or structure gradients present within actual engines for which variable solidification rate and segregation may be substantial factors for corrosion resistance. To date, attempts to procure suitable specimens of cast alloys from the Partner's suppliers have been unsuccessful. Test coupons have been machined from a cylinder head, but these are sufficiently small that they have utility only for limited electrochemical testing later in the Program, and represent only a single composition/structure in any case.

To date, efforts to procure appropriately-sized coupons representing the powder metallurgy ferrous insert components through the Partner's suppliers have also been unsuccessful. For the interim, actual valve seat ring components of various materials will be procured for static immersion testing as a function of fuel blend composition, temperature, and galvanic contact with aluminum alloys, but these ring-shaped specimens are unsuitable for electrochemical testing. A long term solution to limited availability of valve seat insert test materials remains to be indentified.

Static immersion test results as a function of important environmental and material variables will be used to establish the basis for development of relatively rapid electrochemical testing to identify combinations of materials and fuels susceptible to corrosion. Based on findings suggesting that leaking reference electrodes (resulting in test solutions unnaturally contaminated with high chloride concentrations, for example) dominate corrosion behavior in some fuel/materials combinations, substantial effort to overcome this obstacle using only metallic reference electrodes or other creative testing options will be explored.

Conclusions

Documented corrosion data for the material/environment combinations of interest are substantially lacking, yet necessary to establish a corrosion test protocol, so the Project will adapt and create systematically-derived information to begin mechanistic assessment of the valve seat corrosion issues.

Agreement 18571 – Materials Issues Associated with Exhaust Gas Recirculation Systems

M. J. Lance, C. S. Sluder, and J. M. E. Storey**

Ceramic Science and Technology Group

Oak Ridge National Laboratory

P.O. Box 2008, MS 6068, Bldg. 4515

Oak Ridge, TN 37831-6068

(865) 241-4536; fax: (865) 574-6098; e-mail: lancem@ornl.gov

** Fuels, Engines and Emissions Research Center, ORNL*

DOE Technology Manager: Jerry L. Gibbs

(202) 586-1182; fax: (202) 586-1600; e-mail: Jerry.gibbs@ee.doe.gov

ORNL Technical Advisor: D. Ray Johnson

(865) 576-6832; fax: (865) 574-6098; e-mail: johnsondr@ornl.gov

Contractor: Oak Ridge National Laboratory, Oak Ridge, Tennessee

Prime Contract No.: DE-AC05-00OR22725

Objectives

- Provide information to industry specialists about fouling deposit properties so as to enable improved models and potential design improvements to reduce fouling and its impact on the performance of EGR (exhaust gas recirculation) coolers.

Approach

- Assemble EGR engineers from member companies of the Diesel Crosscut Team to serve as an advisory board for this project.
- Purchase and set up a diesel engine as an exhaust generator with a sampler system that will allow for the formation of controlled particulate matter (PM) deposits on model cooler tubes.
- Obtain and evaluate representative (half-useful-life) EGR coolers from industry members.

Accomplishments

- An EGR Team consisting of nine diesel engine OEMS was assembled and survey as to what the greatest materials issues are facing EGR systems. The main problem was high pressure EGR cooler fouling.
- An EGR tube sampling system was designed and tested with a GM 1.9 L engine.
- A bench-flow tube reactor was designed and set-up which will allow for aging of deposits under controlled conditions.
- Eight companies have provided twelve real-world coolers for analysis. Deposits have been analyzed using a variety of experimental techniques to identify common features that will help to guide future research.

Future Direction

- Use exhaust sampler system to generate PM deposits that will be aged in controlled conditions using a bench-flow reactor so as to evaluate the effect of water, hydrocarbon and cycling on deposit properties.
 - Characterize industry-provided deposits using neutron tomography.
 - Establish deposit mechanical properties measurement techniques.
-

Introduction

High-pressure exhaust gas recirculation (HP-EGR) is the dominant NO_x -reduction technology used by the diesel engine community today. High-pressure EGR systems extract a portion of the exhaust gases upstream of the exhaust turbine, pass the gases through a compact heat exchanger (EGR cooler) and then introduce them to the intake downstream of the compressor and charge-air cooler (inter-cooler). As the exhaust gas flows through the EGR cooler, particulate matter (PM) will migrate from the hot exhaust gas to the cooled heat exchanger surface forming a porous deposit that has a thermal conductivity comparable to Styrofoam making it a nearly ideal thermal insulator. As the thickness of the deposit increases, the effectiveness of the EGR system goes down due to the inability to cool the exhaust gas. This is known as cooler fouling. Despite its importance for (HP) EGR, there do not appear to be many investigations of the effect of fouling from diesel particulate matter on the performance of EGR cooling devices or heat exchangers.

In February of 2009, a team consisting of engineers responsible for EGR systems was assembled from nine diesel engine manufacturers: Caterpillar, Cummins, Detroit Diesel, Ford, GM, John Deere, Navistar, PACCAR (now DAF Trucks) Volvo/Mack and one heat exchanger supplier, Modine. They were surveyed to identify the biggest problem facing EGR systems. The clear winner was EGR cooler fouling. The EGR Team then recommended the purchasing of a traditional engine-on-dynamometer to generate fouling deposits on model tubes. They also agreed to send a real-world cooler from an actual engine that had seen enough operation to categorize it as 'half-useful-life'. Of the 10 team members, the 8 companies that currently use HP-EGR all sent at least one cooler for analysis with the data obtained to be shared with the entire team. The results of this survey will be discussed below.

Experimental Approach

Figure 1 shows the GM 1.9 L engine on a Driven controller, operational in standard and PCCI modes that will be used as a pollution generator. The EGR team recommended this set-up as opposed to the proposed genset as an exhaust generator. Figure shows the model tube assembly that will be attached to the exhaust of the engine to generate deposits. This system is based on a previous sampling system designed at ORNL that directs exhaust gas through square tubes that are externally cooled to temperatures similar to those existing in actual EGR coolers. Additionally, a bench flow reactor is being built for accelerated aging of deposits at controlled temperatures and gas composition. This will allow for the characterization of microstructural changes that occur in the deposits due to engine transients.

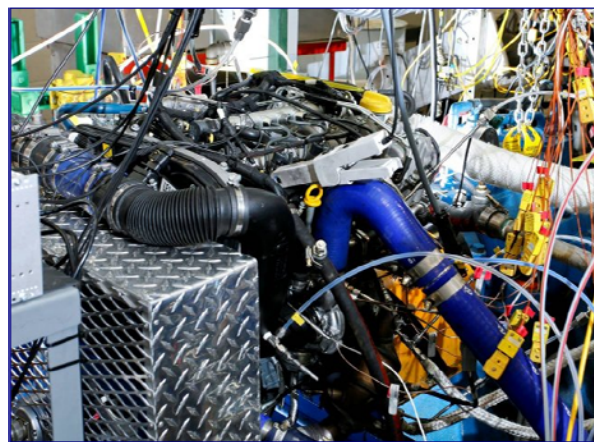


Figure 1: GM 1.9L engine.



Figure 2: Two views of the tube reactor that will be used to generate deposit samples.

A tube reactor system (Figure 3) was designed to flow humid or hydrocarbon-laden exhaust-type gases over particulate deposits in a single EGR tube. The system consists of a gas manifold supplied by two (can be expanded to four) digital mass flow controllers flowing air or bottled gases, a water vapor introduction system, a gas heater and a water jacket to cool or heat the sample tube. Additionally, the water jacket can be left empty for an insulated system. It is equipped with multiple thermocouples to monitor gas temperature before and after the sample and the cooling water entry and exit temperatures. This tube reactor will be used to age engine-produced deposits under different exhaust gas conditions and coolant temperatures.

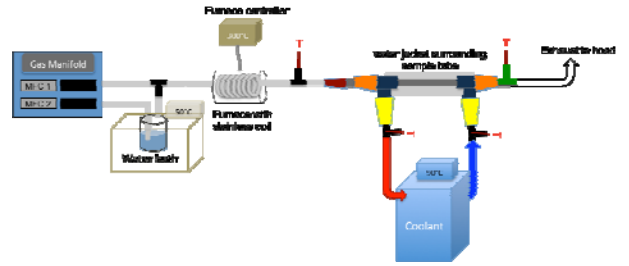


Figure 3. Tube Reactor system schematic.

Results

Samples are currently being imaged with neutron tomography. Figure 4 shows a plugged EGR tube section that was harvested from an industry-provided cooler. Steel is transparent to neutrons whereas hydrogen is a strong neutron attenuator which makes neutron tomography a powerful non-destructive method of collecting images hydrocarbon/soot deposits in EGR coolers. Figure 4 shows that neutron imaging can be used to observe microstructural features such as hydrocarbon-rich bands, mudcracks and channels that are still open for exhaust gas flow.

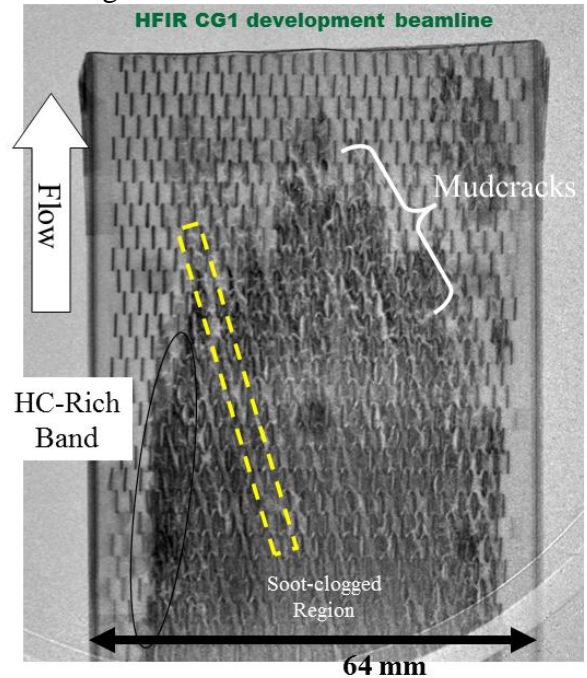


Figure 4. Neutron images of a plugged EGR tube. The yellow box highlights a diagonal channel that is still open for exhaust gas to flow through the plug.

Chemical characterization of industry provided coolers has continued with recent GC-MS measurements conducted at FEERC. X-ray Photoelectron Spectroscopy (XPS) was carried out on all deposit samples and the carbon 1s spectra are presented in Figure 5. All samples exhibited the C-C bonding peak at 285 eV, and with the exception of cooler deposit #5, all showed the C-O bonding peak at 289 eV.

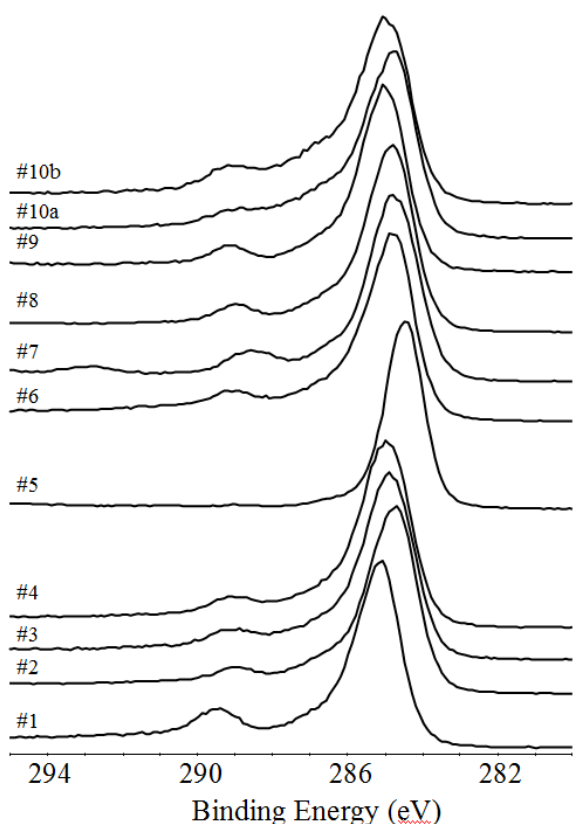


Figure 5. Carbon 1s spectra measured by X-ray Photoelectron Spectroscopy (XPS). The peak positions are uncorrected for sample charging. The large peak around 285 eV is from C-C bonding and the smaller peak around 289 eV is from C-O bonding.

Hydrocarbon profiles were measured with gas chromatography-mass spectrometry (GC-MS). Four species that indicate different hydrocarbon origins (fuel, oil and oxidized fuel) are listed in Table 1. Most samples had concentrations of individual hydrocarbon species be-

low 1 ng per μg of deposit. Cooler #3 had high amounts of fuel hydrocarbons and partially-oxidized fuel but no heavy hydrocarbons from oil. Cooler #5 had large amounts of both fuel and oil hydrocarbon but no oxidized fuel which compares well to the XPS results which also showed no C-O bonding in this deposit.

Table 1. Estimated mass (in ng/ μg) of four common hydrocarbon species in the cooler deposits measured by GC-MS. Naphthalene and nonadecane correspond to aromatic and alkane species in diesel fuel, respectively. Pentacosane is a heavier hydrocarbon species more common in oil. Naphthalenic anhydride indicates partially oxidized fuel.

Cooler #	naphthalene	nonadecane	pentacosane	naphthalenic anhydride
1	0.0	0.3	0.0	0.2
2	0.6	0.2	0.5	0.0
3	18.0	8.4	0.0	5.4
4	0.4	1.5	0.6	0.6
5	11.0	87.8	49.6	0.0
6	0.5	1.6	1.1	0.4
7	0.0	3.9	0.0	0.2
8	0.1	0.3	2.7	0.1
9	0.9	0.1	0.0	0.3
10a	0.0	1.7	0.0	1.0
10b	0.0	0.0	0.0	0.0

Thermogravimetric analysis (TGA) and differential thermal analysis (DTA) were conducted in argon to determine the volatile mass fraction of all the deposits. Samples were first heated to 600°C in argon at a rate of 5°C/min and held for 1 hour. The remaining nonvolatile deposit was then heated to 700°C in air to determine the mass fraction of the elemental carbon and the non-combustible residue. Table 2 shows the mass percent of three regions of the volatile component; water (25 - 120°C), light hydrocarbon (120 - 350°C) and heavy hydrocarbon (350 - 600°C), and the nonvolatile components; elemental carbon and residue.

Table 2. Mass percentage of volatile and non-volatile components of the deposit measured by TGA. EC = elemental carbon.

Cooler#	Volatile			Nonvolatile	
	25-120°C	120-350°C	350-600°C	EC	Residue
1	7.7	16.5	29.8	34.2	11.8
2	1.4	2.7	20.7	71.1	4.1
3	1.1	17.9	20.9	55.0	5.0
4	1.4	9.5	19.4	70.3	0.0
5	0.7	10.9	1.5	4.0	83.0
6	0.8	4.3	8.2	34.0	52.7
7	17.2	6.5	14.0	4.6	57.6
8	2.3	6.3	13.6	57.1	20.7
9	6.1	10.7	32.2	31.3	19.7
10a	2.3	19.6	14.9	54.7	8.5
10b	2.1	19.8	14.3	53.8	9.9

With three exceptions, the water content of all the deposits was less than 2.5% and most of this mass loss occurred below 80°C peaking around 45°C. Coolers #1 and #9 had high water loss likely due to the presence of hydrated metal sulfates which will dehydrate during heating. The high water content of cooler #7 was probably caused by water adsorbed on to silicates in the deposit. Above 120°C, coolers #2, #4, and #6 - #8 had at least twice the mass loss in the heavy hydrocarbon region than the light hydrocarbon region which indicates that little unburned or partially burned fuel was present in these deposits. Above 350°C, volatilization is due mostly to partially oxygenated hydrocarbons, heavy hydrocarbons typical of lubricant, and polycyclic aromatic hydrocarbons (PAHs) present in all diesel particulate matter. For coolers #1 and #9, volatile mass percentage above 120°C was mostly governed by the decomposition of Fe₂(SO₃) to Fe₂O₃ and so does not accurately reflect the nature of the carbonaceous portion of the deposit. Coolers #3, #5, #10a and #10b had significant hydrocarbon devolatilization between 120 and 350°C which suggest the presence of fuel components in these deposits. Of particular note is cooler #5 which devolatilized almost entirely in the light hydrocarbon temperature range.

Figure 6 compares the derivative weight change in argon of the lightest deposit from (#2) to the heaviest deposit (#3). The highest

mass loss rate for cooler deposit #2 occurred above 500°C, much higher than cooler deposit #3 which had its highest mass loss rate at 216°C. This suggests that most of the mass of cooler deposit #3 is from unburned fuel.

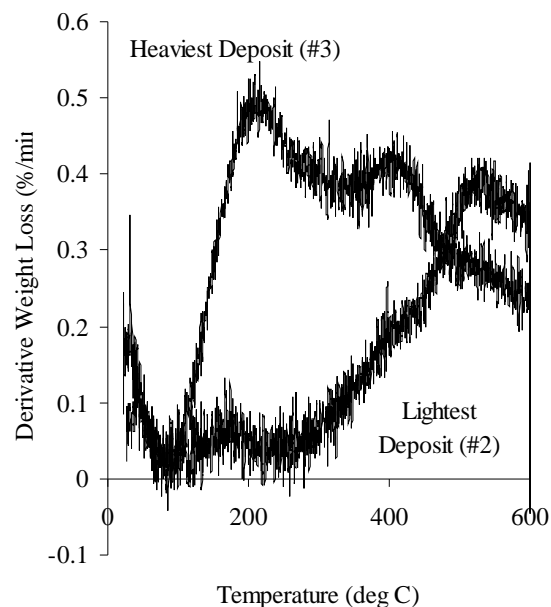


Figure 6. Derivative weight loss in percent per minute versus temperature (°C) while heating in argon for the lightest (#2) and the heaviest (#3) cooler deposits.

In addition, mechanical properties measurements have been attempted by indenting a laboratory-generated deposit with a 2 mm diameter punch. Using a high resolution load cell, a load could be measured on the deposit prior to compressing it. Future measurements will be conducted as a function of temperature in order to see if the mechanical properties of the deposit change during EGR operation.

Three removal mechanisms were identified in the coolers that, to the authors' knowledge, have not heretofore been described in the literature on EGR cooler fouling. Figure 7 shows all three of these phenomena in one image from cooler deposit #8. Longitudinal grooves form on the leading edge of the turbulence structure (here a sinusoidal wave down

the length of the cooler). These grooves could be formed by debris hitting and eroding the deposit propelled by the exhaust gas. This debris may then roll along the deposit, collecting more deposit forming a groove. A second feature in Figure 7 is mudcracking which will form as the deposit shrinks in the plane of the metal substrate presumably due to hydrocarbon and water condensation. Conversely, mudcracks may also form during drying of the deposit after the engine is turned off.

A third feature from Figure 7 is spallation which seems to be linked to mudcracking. Once mudcracks have encircled a region of the deposit, and if shrinkage of the deposit continues, it will begin to buckle and will eventually spall. The fracture plane for the spalled region in Figure 7 was within the coarse region of the deposit, and not at the metal-deposit interface. This was also the case for coolers #1 and #2 which also exhibited spallation. This suggests that hydrocarbon and water condensation will promote spallation both by shrinking the deposit and by providing a brittle fracture plane for a crack to propagate. This may be the origin of spontaneous regeneration that has been reported by many EGR consortium members.

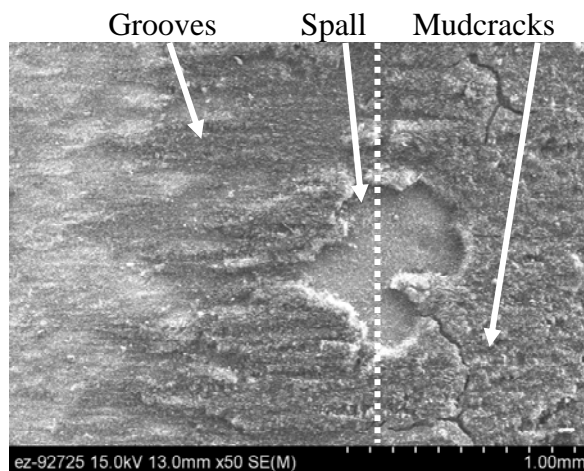


Figure 7. SEM image of the surface of cooler deposit #8. The dashed white line indicates the peak of the sinusoidal wave of the turbulence structure.

Conclusions

A team of industry advisors has been assembled that will help guide future research directions of this pre-competitive research.

An engine and a sampler tube system for laying down controlled PM deposits has been designed, purchased and tested. A portable gas manifold for controlled post-deposition aging has been built.

Hydrocarbon condensation plays a pivotal role in EGR fouling and will affect clogging, densification, heat transfer, mud-cracking and adhesion.

Neutron tomography has been used to characterize deposit microstructures on the industry-provided coolers. Microstructures observed compared well to those seen on epoxy-mounted cross-sections.

Publications and Presentations

- Michael Lance, Charles Scott Sluder, John M.E. Storey, and Samuel A. Lewis “Characterization of Field-Aged EGR Cooler Deposits,” SAE 2010-01-2091.
- Michael J. Lance, C. Scott Sluder, Hassina Bilheux, Keely Willis, Andrea Strzelec, John M.E. Storey, and Samuel A. Lewis Jr., “Characterization of Field-Aged Exhaust Gas Recirculation Cooler Deposits” presented at 2010 DEER conference.
- Michael J. Lance, Hassina Bilheux, Keely Willis, Andrea Strzelec, C. Scott Sluder, “Characterization of Field-Aged Exhaust Gas Recirculation Cooler Deposits using Neutron Tomography,” presented at the Global Powertrain Conference, Troy, MI, 2010.
- Diesel Crosscut Team Meetings: November 12, 2009; March 11th, 2010; July 15th, 2010; September 22nd, 2010.

Agreement 19192 - Titanium for Vehicle Propulsion Applications

Principal Investigators: Curt A. Lavender, K. Scott Weil and Eric N. Nyberg

Energy Materials Group

Pacific Northwest National Laboratory

PO Box 999, MS K2-44

Richland, WA 99352

(509) 372-6770; fax: (509) 375-2186; e-mail: curt.lavender@pnl.gov

(509)375-2103; fax: (509)375-2186; e-mail: eric.nyberg@pnl.gov

(509)375-6796; fax: (509)375-2186; e-mail: scott.weil@pnl.gov

Yong-Ching Chen

Cummins Inc.

(812) 377-8349; e-mail: yong-ching.c.chen@cummins.com

PK Mallick

University of Michigan at Dearborn

(313)593-5119; e-mail: pkm@umich.edu

Vladimir Moxson

ADMA Products Inc.

(330)650-4000; e-mail: moxson@admaproducts.com

DOE Technology Manager: Jerry L. Gibbs

(202) 586-1182; fax: (202) 586-1600; e-mail: jerry.gibbs@ee.doe.gov

Field Technical Manager: Dean Paxton

(509) 375-2620; fax: (509) 375-2186; e-mail: dean.paxton@pnl.gov

Contractor: Pacific Northwest National Laboratory

Contract No.: DE-AC05-76RL01830

Objective

- Increase the efficiency of vehicle engines by reducing the mass of rotating and reciprocating components through the use of titanium and titanium alloys.
- Increase the efficiency of vehicle engines by increasing the operating temperature of selected components through the use of titanium and titanium alloys.
- Predict the engine efficiency improvements made possible through the use of titanium.

Approach including industrial partner/collaborator and path to technology transfer and commercialization

- Develop, prototype, and evaluate the performance of components at Cummins Inc. to ensure that components developed produce the predicted performance improvements in actual engine systems.
- Use suppliers to fabricate most titanium components to ensure that processing used is prototypic of a full-scale production process.

Milestone, Metrics and Accomplishments

- Initial mass analysis of a gasoline engine has been initiated and a diesel engine has been identified and will be provided to University of Michigan at Dearborn. (Milestone)
- The lower than expected mechanical properties observed in the Ti6Al4V pressed and sintered material were related to porosity and resolved by hot isostatic pressing (HIP).
- The HIPed Ti6Al4V materials were fatigue tested and exhibited properties like those of wrought Ti6Al4V, indicating that substantial cost savings can be realized by the TiH₂ powder processing approach. (Milestone)
- Two engine components have been identified for further development and ultimately systems testing at Cummins Inc.

Future Direction

- Complete fatigue studies on low cost Ti6Al4V from titanium hydride for rotating component applications.
- Complete fatigue studies on the low cost beta alloy bar stock suitable for spring applications.
- Perform a modeling study on the effect of titanium on the fuel economy of a vehicle through substitution of materials used in propulsion applications.
- Complete cost analysis of the ADMA Products Inc. process for Ti6Al4V production.

Introduction

This project is a collaborative effort between Cummins Inc., ADMA Products Inc., and Pacific Northwest National Laboratory (PNNL) focused on the development and evaluation of low-cost titanium components produced by emerging production technologies.

Over the past 30 years, many original equipment manufacturers, researchers, and titanium companies have demonstrated titanium's ability to increase internal combustion engine efficiency. However, titanium has only been used in a limited number a production applications and sometimes only over limited production periods. Even though performance benefits resulting in engine efficiency improvements of as much as 20% have been demonstrated, the high cost of producing titanium components using current technologies has been a limiting factor.

In recent years, the Department of Defense (DOD) and the commercial aerospace industry (the largest consumers of titanium) have become increasingly reliant on titanium to meet performance needs. A study commissioned by the Defense Logistics Agency revealed that not

only was the titanium raw material costly, but the manufacturing processes used to produce titanium components often had production yields of 5%, meaning that the DOD was buying as much as much as 20 times the titanium as was used in the final application. To address this cost, the Defense Advanced Projects Agency (DARPA) began an activity to reduce titanium component cost. The DARPA project started many activities, new low-cost-titanium development projects, and stimulated titanium production activity throughout the world—with as many as 20 methods under development.

In prior reporting periods, this project was focused on assessing “emerging” low-cost development activities by using technical evaluation and cost modeling to analyze the products for suitability in vehicle and engine applications. It was determined that two of the processes, developed by International Titanium Powder and ADMA Products Inc., could produce titanium raw materials at costs that approach those needed to achieve widespread titanium usage and have an impact on the overall fuel economy in the United States.

The next step for these emerging processes is to identify applications and create a demand for the

titanium in order to move them from development to full-scale production, thus meeting the cost projections associated with high-volume production.

The purpose of this project is to identify and demonstrate applications within the vehicle propulsion system which, when titanium is used, would produce an increase in engine and vehicle efficiency. The project will be performed in three topical areas: the first is focused on vehicle propulsion system modeling, the second is focused on technical development of the titanium semi-finished products, and the third is focused on technical demonstration of the components in systems level tests.

The goal of the project is to use titanium, where appropriate, to increase the efficiency of vehicle propulsion systems. This report summarizes progress toward that goal.

Approach

This project will increase vehicle efficiency through use of titanium by 1) identifying, through vehicle system models, critical components to be made from titanium that will impact efficiency, 2) demonstrating that those titanium components can be made from emerging low-cost processing, and 3) demonstrating efficiency improvements through systems level tests at Cummins Inc.

Vehicle system modeling will be performed at the University of Michigan at Dearborn (UMD) by disassembling two engines; one fueled by diesel and the second by gasoline. Each component will be weighed and measured, then analyzed and redesigned for titanium to determine the impact of the component on efficiency. A component by component analysis will then take place to determine the overall vehicle efficiency impact. Components will be manufactured by a combination of suppliers and PNNL to ensure that the components developed can be produced in commercial settings. Systems level component testing will be carried out by Cummins Inc. using the appropriate engine test system.

Results and Discussion

Vehicle System Modeling

This task started later than expected and to-date UMD has completed the disassembly and measurement of the gasoline powered engine. The diesel engine to be disassembled will be a 5.9 liter Cummins engine to be provided by PNNL or Cummins by the end of the calendar year 2010.

The gasoline engine chosen for the evaluation was a Toyota Echo engine (Figure 1). The engine is a modern, multi-valve 80kW engine with variable valve timing and multi-point electronic fuel injection, and is representative of a high-efficiency modern internal combustion engine.



(a)



(b)

Figure 1: Toyota 1.5L VVT-I engine, (a) shown in the vehicle (b) outside the vehicle, before dismantling into components.

The mass analysis of the engine components was completed and is shown in Table 1. The redesign and analysis of the titanium components has been initiated.

Table 1. Mass analysis of the Toyota Echo engine to be used for the basis to evaluate the impact of titanium on engine efficiency.

Engine Component	Weight per part (gm)	Number of parts in engine	Total Weight (gm)
Inlet Valve	34	8	272
Exhaust Valve	27	8	216
Valve Spring Retainer	8	16	128
Valve Spring	20	16	320
Valve Lifter	29	16	464
Inlet & Exhaust Common Bearing Cap	165	1	165
Piston(w rings)	236	4	944
Con-Rod	215	4	860
Wrist Pin	64	4	256
Con-Rod Bolt	18	8	144
Conrod-Cap	90	4	360
Conrod Cap Bearing (Each 8 gm)	16	4	64
Exhaust Camshaft	1664	1	1664
Intake Camshaft	2664.85	1	2664.85
Crankshaft	10177.5	1	10177.5
Timing Chain	371	1	371
Flywheel	6633.8	1	6633.8
Crankshaft Bearing Cap	344	4	1376
Crankshaft Bearing Cap (Center)	390	1	390
Crankshaft Bearing	18	8	144

Component Fabrication

During this reporting period, component fabrication focused on two semi-finished products that would be used for titanium part fabrication. The first was a large, blocky, pressed and sintered part from the Ti6Al4V alloy and the second was a bar stock from a beta alloy.

The Ti6Al4V was pressed and sintered into a right cylinder that could be used for components that require forging and machining to produce the final shape. The challenge with a producing a forged part from a pressed and sintered block is achieving adequate fatigue strength. During the previous reporting period it was determined that the interstitial level for the Ti6Al4V would be established by the tensile strength levels and rotating beam fatigue (RBF) life. Tensile samples that were tested previously exhibited low strengths and ductility and little or no correlation between interstitial content, which was attributed to porosity. During this period additional sintered blocks were produced and subjected to hot isostatic pressing, using a typical cycle at greater than 700°C at a pressure greater than 70 MPa, to close the porosity. RBF and tensile samples were machined from the blocks and tested to produce tensile strengths and stress versus number of cycle (S-N) curves, respectively.

The tensile strengths for HIPed samples tested were in excess of the 800 MPa minimum and ductilities were in excess of 18%, as would be expected for alloys with their level of interstitial content and the observed microstructure. The S-N curves for the materials were identical for each interstitial and the selection of the composition for further development will be based on the minimum interstitial content that ADMA Products Inc. can confidently produce in high volume production. This result indicates that the Ti6Al4V alloy processed by the press and sinter method with HIP will meet the requirements of wrought Ti6Al4V. The pressed and sintered materials can be produced for less than 50% of the cost of the wrought alloy. The next step for the Ti6Al4V development will be to determine the minimum amount of forging

required to transform the spaghetti structure to a more equiaxed alpha and produce even higher fatigue life.

The beta alloy bar production was repeated at two additional levels of oxygen and samples have been heat treated and are undergoing tension and RBF testing.

Component Testing

Cummins Inc. has identified components of interest and property targets. Future work will be focused on producing the semi-finished products required for the Cummins components.

Conclusions

During this reporting period, the following conclusions were reached:

- Lower than expected mechanical properties observed in the Ti6Al4V sinter bars were attributed to porosity and resolved by HIPing.
- RBF testing of the HIPed Ti6Al4V pressed and sintered bars produced fatigue life expected for Ti6Al4V in a wrought condition with the same microstructure and interstitial content. This result demonstrates that the TiH₂ powder processed by press-sinter and HIP will meet the wrought property requirements and reduce the cost to produce Ti6Al4V components by more than 50%.

Also during this period, development activities were initiated at UMD to determine the maximum impact that titanium can have for vehicle efficiency and components were identified by Cummins Inc. for vehicle system testing during the next fiscal year.

Low Cost Titanium-Propulsion Applications

Lavender CA, YC Chen, and VS Moxson. 2010. "Low Cost Titanium – Propulsion Applications." Presented by Curt Lavender (Invited Speaker) at DOE-VTP Merit Review, Washington, DC, on June 10, 2010. PNNL-SA-72900.

Development of High Strength Titanium Alloy Bar Stock from TiH₂ Powder

Curt Lavender (Invited Speaker); Elizabeth Stephens, Eric Nyberg; Vladimir Moxson; Volodymr Duz Presented at TMS annual Meeting Seattle WA, February 2010.

Evaluation of Titanium for Vehicle Fuel Economy and Performance Improvement

PK Mallick, Curt Lavender and Scott Weil. Presented at TMS annual Meeting Seattle WA, February 2010.

Opportunities for Titanium Alloy Development - Solid State Processing. Presented by Curt Lavender (Invited Speaker) at 47th Sagamore Army Materials Research Conference on June 15, 2010. PNNL-SA-72883.

Keywords

Titanium, titanium alloys, solid state consolidation, rod-rolling, beta titanium alloys, cold isostatic press and sinter, titanium alloy, and heat treatment.

Brief Description of Report

This report describes progress in the development of low-cost titanium for vehicle and propulsion system applications.

Agreement 19215 - Surface Texturing for Friction Control (BLL)

Oyelayo Ajayi, Aaron Greco, Robert Erck, and George Fenske

Argonne National Laboratory

9700 South Cass Avenue

Argonne, IL 60439

(630)252-9021; fax (630)252-5568; e-mail: ajayi@anl.gov

DOE Technology Manager: Jerry Gibbs

(202) 586-1182; fax: (202) 586-1600; e-mail: jerry.gibbs@ee.doe.gov

Contractor: Argonne National Laboratory, Argonne, Illinois

Prime Contract No.: DE-AC02-06CH11357

Objectives

- Develop mechanistic understanding of the effect of surface texturing on friction behavior in various lubrication regimes
- Develop application specific performance evaluation methodology for textured surfaces
- Develop methods for the optimization of surface texture design for different applications
- Determine the impact of surface texturing on mitigating tribological failure mechanisms (i.e. scuffing)

Approach

- In lubricated contacts, the effect of surface topography and texture will be more pronounced on the lubricant fluid film. Consequently, mechanistic study of the impact of surface texture (dimples for a start) will be studied by measuring lubricant fluid film thickness and friction under different lubrication regimes.
- Application specific evaluation will be evaluated initially with appropriate bench top test rig. Eventually, component testing will be conducted on optimized textured surfaces.
- The impact of surface texturing on basic tribological failure mechanisms will be evaluated using appropriate testing, surface and subsurface analysis and characterization.

Accomplishments

- Initial testing of surface texturing effect on lubricant film thickness in non-conformal contact showed that dimples do not necessarily increase film thickness
- Friction reduction (up to 50%) through surface texturing was observed for conformal contact applications (journal bearings) over a range of operating conditions, from mixed to full film lubrication regimes
- Significant improvement in contact severity index (3 fold increase) was achieved through surface texturing in applications where scuffing failure is assessed
- Identified texturing methods which would allow for a cost effective treatment method for friction and wear reduction

Future Direction

- Continue application specific tribological performance testing of textured surfaces to facilitate texture design for optimized friction and wear reduction
 - Expand evaluation of the impact of surface texturing on the various tribological failure mechanisms – Scuffing, wear, contact fatigue, etc
 - Evaluate the impact and potential enhancements of surface texturing on the actions of lubricant additives in formation of tribochemical boundary films
 - Explore various methods and forms of surface texturing for tribological performance enhancement
-

Introduction

Surface texturing, in the form of micro-scale dimples, has been shown to potentially improve tribological performance of lubricated surfaces in the form of friction reduction [1]. However, for certain applications, especially under non-conformal contact conditions, texturing has shown mixed results on its benefits [2]. Although, texturing is currently being used in some applications and its impact on frictional and wear behavior being actively investigated, the mechanisms associated with the effect of texturing on tribological performance is not fully understood yet. The commonality between most current investigations is that the performance is shown to be highly influenced by the subtleties of the texture design. Small variations in texture dimensions (i.e. depth, diameter, and coverage density) typically result in significant difference in friction behavior; therefore, a systematic approach to optimizing texture design for specific applications is necessary to realize the full potential benefits of this treatment technique. Furthermore, there are other forms of surface texturing or micro-geometrical designs other than dimples that can significantly improve the friction and wear behavior of lubricated components.

Approach

In order to better understand the impact of surface texturing (ST) on friction and wear behavior, and to further enhance the usefulness of other DOE sponsored effort in the area of texturing, we plan a two phase effort: (1) Mechanistic study of the impact of ST on fluid film and boundary regime lubrication, and (2) Application specific evaluation of ST including various engine and vehicle components. The effect of ST on lubrication mechanisms is studied by the simultaneous measurement of lubricant fluid film thickness and friction coefficient using an advanced elastohydrodynamic lubrication test rig Figure 1, which uses optical interferometry principle to measure the

lubricant film thickness profile within the contact. Film thickness for different texture and un-textured surfaces can be thoroughly characterized under different frictional behavior.

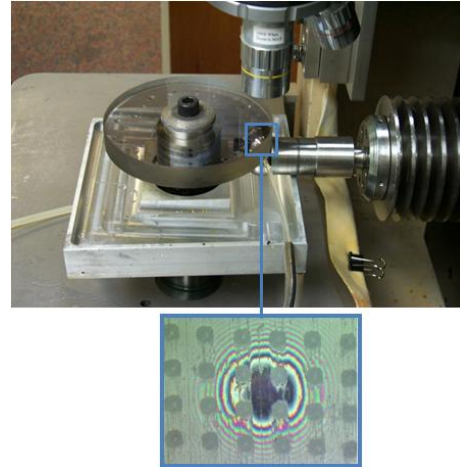


Figure 1. Elastohydrodynamic test rig for measuring lubricant film separation showing contact spot of dimpled ball on glass disk

The effect of ST on the frictional behavior of conformally contacting surfaces is also performed to simulate the application of journal bearing components. This will be evaluated using a conformal block-on-ring test rig, Figure 2, where friction can be monitored across various operating conditions. The test results presented in this report are performed off-site. At the time that this report was written this test rig was being installed on-site, which would allow for more in depth future investigation.



Figure 2. Conformal block-on-ring test rig for simulating journal bearing application

Lastly, to study the influence of surface texture at severe operating conditions,

testing is performed to analyze the scuffing resistance. More specifically, textured surfaces are compared with similar non-textured surfaces in reciprocating sliding contact under controlled step loading until the scuffing failure is induced. This performance is compared in relation to the contact severity index (CSI).

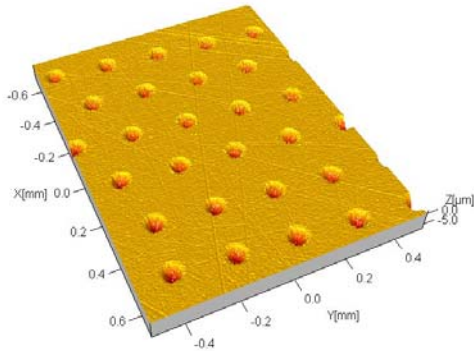


Figure 3. Three dimensional profile of a typical laser dimpled surface

Currently the texturing is achieved through a laser surface texturing (LST) method which is capable of producing well defined and controlled dimple features. For the current work all textures are in the form of micro-scale dimples with depths in the

mechanical texturing, which is also explored in this work.

Results

The results presented here summarize the achievements from this first year of this project. This progress has established the ground work for developing a systematic method of evaluating and optimizing surface texture application and design for friction and wear reduction.

The first objective of this work was to investigate the mechanism by which ST influences the lubrication behavior across a range of operating conditions, and subsequently lubrication regimes: full film separation to boundary. This was achieved using the equipment described in Figure 1, which utilizes optical interferometry to measure the fluid film separation between a ball and disc surface.

The optical images presented in Figure 3 show lubrication thickness profiles within the contact spot at various entrainment velocities. The thickness of the fluid film corresponds to the color of the profile, increasing film thickness with higher entrainment velocity.

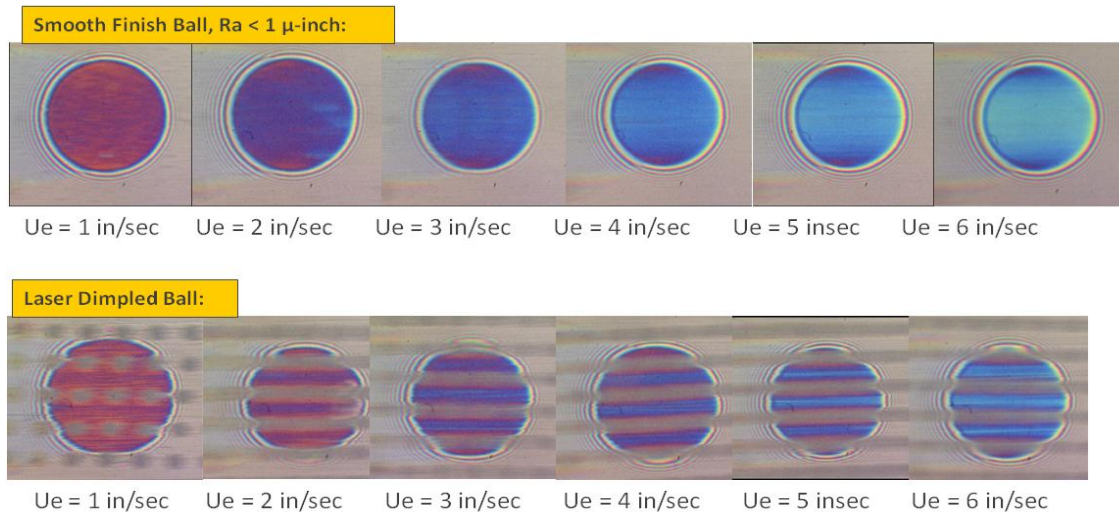


Figure 4. Optical profilometry images of lubricant film thickness, Top- smooth ball, Bottom- dimpled ball range of 5-10 µm and diameters in the range of 50-150 µm. These features can be achieved using other surface texturing methods that may present a more cost effective treatment process, namely vibro-

Two types of balls were tested: one with a smooth finish, the other with laser generated dimples. The corresponding profile for the dimple ball shows streaking along the row of dimples since the measurement system capture rate is too slow

to resolve the profile between dimples at higher velocities. However, in the rows with no dimples the film thickness can be measured. To more accurately compare the difference in film thickness between the two types of surfaces the plot is presented in Figure 4 which shows the average centerline film thickness at each corresponding entrainment velocity. The film thickness for the dimpled ball is lower than that for the smooth for all speeds, but only by 10 nm or less for the entrainment velocity of 100 mm/sec and slower. This result indicates that surface dimples do not enhance the film separation for this current non-conformal contact configuration, and in most cases causes a slight reduction in film thickness. Further investigation is necessary to determine if dimples do not offer any enhancement to the hydrodynamic film separation for other types of contact configurations.

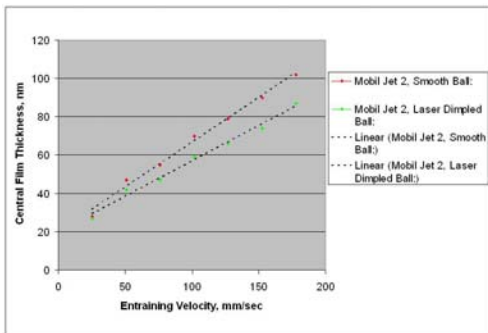


Figure 5. Film thickness plot comparing dimpled and smooth ball in non-conformal contact

The friction performance of dimpled surfaces in conformal contact is evaluated using the test equipment described in Figure 2, to simulate a journal bearing type of application. Here a ring is in lubricated contact with a curved block where again two types of rings are compared: one with a smooth surface, the other with laser generated dimples. The friction is measured over a range of rotation speeds and plotted in Figure 5. The low friction at high speed operation indicates a near hydrodynamic condition. As the speed decreases the friction enters into a mixed condition. The friction curve for the dimpled ring is

consistently lower than that of the smooth/plain ring, by more than 50% at around 200 RPM. This preliminary result indicates that significant friction reduction is achievable for applications of conformal contact and further improvement maybe possible through optimization of the dimple design.

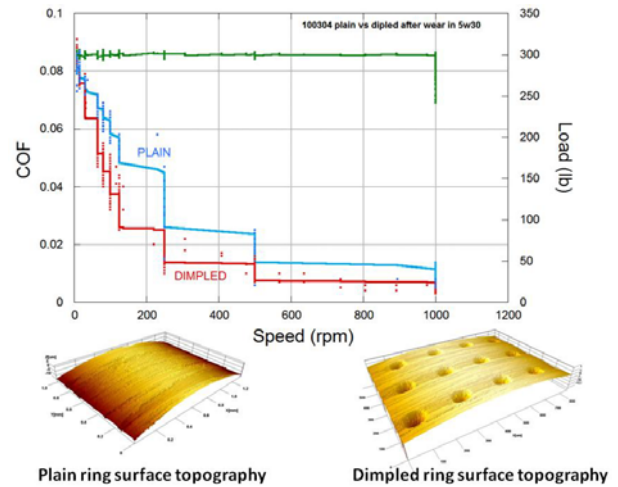


Figure 6. Friction plot comparing smooth and dimpled ring in conformal contact (journal bearing)

The final type of performance evaluation that was conducted is scuffing failure analysis. This type of failure mechanism is characterized by a sudden/sharp increase in friction with increasing contact severity. This event coincides with catastrophic surface failure and wear; in application this can result in total system failure. Contact severity is defined by the operating parameters of contact load and sliding speed in addition to the sliding friction coefficient. The scuffing performance was evaluated using a linear reciprocating sliding contact of a ball and flat with base synthetic oil lubrication. Again a textured flat surface with laser generated dimples is compared with a similar smooth sample. Tests are conducted at a constant sliding speed with increasing contact load. The plot shown in Figure 6 shows the friction profile for both the smooth and textured flat under the same loading condition. The non-textured smooth sample experiences a scuffing limit at

around 550 N load while the textured flat does not scuff until 1700 N, representing a nearly threefold increase in contact severity index with the textured surface. Contact severity index for the tests of textured surfaces was calculated to be 7 on average, which is a level that is generally only achievable through the use of certain high performance surface coatings. Post mortem examination of the flat sample shows that the dimples are still largely intact prior to the scuffing event which indicates that these surface features are contributing to the scuffing performance. More extensive testing is necessary to determine the underlying mechanisms responsible for this increase in scuffing resistance; however, these results give an indication that surface dimpling may offer a viable treatment method for significantly improving performance at severe operating conditions.

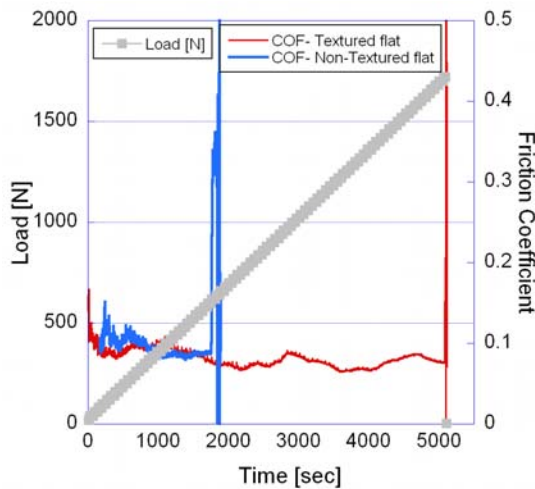


Figure 7. Scuffing performance plot comparing smooth flat with textured

Finally, in order to develop a cost effective and accessible surface texturing method a partnership with Northwestern University was formed to explore Vibro-Mechanical Texturing (VMT). This method utilizes more standard machining techniques to form surface textures. VMT is based on a lathe method where the standard static tool mount is replaced with a piezo-electric actuated tool stage. The tool initially developed by Prof. Ehmann’s group at NU has been optimized to form precision

controlled dimple features on a variety of materials [3]. Figure 8 shows a schematic of the tool stage in relation to a texturing workpiece. The frequency and amplitude of tool oscillation is used to precisely control the dimple design.

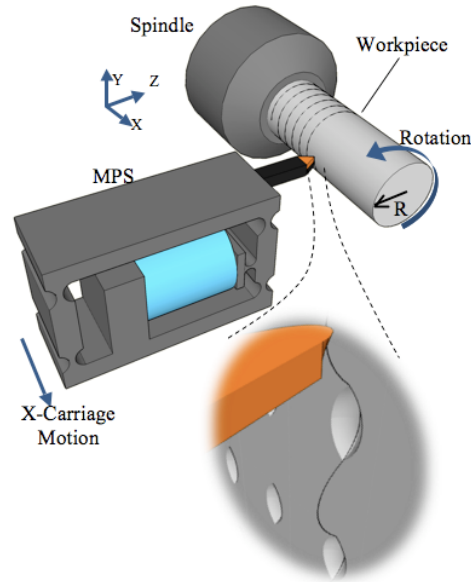


Figure 8. Vibro-Mechanical Texturing schematic

Since this method is based on a standard lathe operation and only requires a simple retrofit to incorporate the advanced micro-positioning stage (MPS) it is more readily accessible than other more complex texturing methods. VMT also has the potential to be a cost effective method of surface treatment in industrial production settings.

Conclusions

Within the first year of this program significant advancements have been made toward better understanding of the influence that surface texture has on tribological performance. More importantly, the ground work for developing a systematic method of evaluating and optimizing surface texture application and design for friction and wear reduction has been achieved.

First, to better understand the mechanism by which surface dimples influence hydrodynamic lubrication action, an optical profilometry technique was employed. For this non-conformal contact

configuration no enhancement to the lubricant film thickness was observed. Second, to assess the effect of surface dimples on friction performance, application specific testing was conducted on a conformal block-on-ring setup to simulated journal bearing applications. These results demonstrated a significant friction reduction across a range of operating conditions, up to 50% reduction. Further texture design optimization is needed to realize the full potential benefits of this treatment for this application. Third, surface texture was tested for scuffing performance, in order to test behavior of this surface treatment at severe contact conditions. In comparison to smooth samples, dimpled surface demonstrated a threefold increase in scuffing resistance, measured by contact severity index. Last, a novel surface texturing method, vibro-mechanical texturing, was assessed in coordination with Northwestern University to develop a cost effective and accessible texturing technique.

These current results demonstrate the potential benefits of surface texturing treatment in terms of friction and wear behavior. Further testing is necessary to realize the full potential benefits and to determine the fundamental mechanisms that

would allow for more appropriate design and application of surface texturing.

References

- [1] A. Kovalchenko, O. Ajayi, A. Erdemir, G. Fenske, and I. Etsion, "The effect of laser surface texturing on transitions in lubrication regimes during unidirectional sliding contact," *Tribology International*, vol. 38, no. 3, pp. 219-225, Mar. 2005.
- [2] A. Greco, A. Martini, Y. Liu, C. Lin, and Q. J. Wang, "Rolling Contact Fatigue Performance of Vibro-Mechanical Textured Surfaces," *Tribology Transactions*, vol. 53, no. 4, p. 610, 2010.
- [3] A. Greco, S. Raphaelson, K. Ehmann, Q. J. Wang, and C. Lin, "Surface Texturing of Tribological Interfaces Using the Vibromechanical Texturing Method," *Journal of Manufacturing Science and Engineering*, vol. 131, no. 6, pp. 061005-8, Dec. 2009.

Publications and Presentations

A. Greco, O. Ajayi, R. Erck. *Micro-Scale Texture Design for Improved Performance at Severe Contact Conditions*, 2010 International Joint Tribology Conference, San Francisco CA, Oct. 201

Agreement 19217 – Ultra-fast Chemical Conversion Surfaces

Principal Investigators: A. Erdemir and O. L. Eryilmaz

Argonne National Laboratory

9700 S. Cass Avenue, Argonne, IL 60439-4838

(630) 252-6571; fax: (630) 252-5568; e-mail: Erdemir@anl.gov ; Eryilmaz@anl.gov

DOE Technology Manager: Jerry L. Gibbs

(202) 586-1182; fax: (202) 586-1600; e-mail: jerry.gibbs@ee.doe.gov

Contractor: UChicago Argonne LLC

Contract No.: DE AC03 06CH11357

Objective

- Develop and optimize an ultra-fast chemical conversion (or boriding) process for improving the durability and tribological performance of engine components.
- Demonstrate scalability, reliability, and cost-competitiveness of process.
- Transfer optimized process to automotive and heat treatment industries to reduce energy and carbon intensity of engines and high-temperature treatment processes.

Approach

- Produce hard and thick chemically converted boride layers on representative steel substrates and characterize their structural, chemical, and mechanical properties.
- Perform systematic friction and wear studies to confirm their superior properties and performance characteristics of the test samples as compared to conventionally carburized and borided surfaces.
- Demonstrate applicability of optimized process to appropriate engine parts, like piston pins, rings, transmission parts, etc., and confirm their superior mechanical and tribological properties.
- Using advanced surface analytical tools, identify fundamental tribological mechanisms that are responsible for superior friction, wear, and scuffing properties of the borided test samples and actual components under boundary, mixed, and hydrodynamic lubrication regimes.
- Demonstrate scalability of optimized process for large-scale applications in engines.
- Verify higher energy efficiency and lower carbon intensity of the test samples.

Accomplishments

- Successfully treated a large number of test samples made out of the same grades of steels as those used for actual engine components.

- Performed extensive bench tests to compare the mechanical and tribological properties of ultra-fast borided surfaces with those of the carburized surfaces.
- Optimized process conditions and developed reliable/repeatable treatment protocols for a variety of steel and non-ferrous alloys.
- Initiated friction and wear tests using a ring-on-liner test machine and correlated these results with structural, chemical, and mechanical properties of the borided surfaces.
- Initiated fundamental surface analytical studies to understand friction and wear mechanisms of borided surfaces.
- Initiated feasibility studies for the treatment of large batches of several engine parts.
- Verified superior mechanical and tribological properties for borided parts using bench-top friction and wear test machines.
- Initiated licensing talks with a major heat-treatment company. A term sheet has been developed and is currently being reviewed by Argonne's Technology Transfer Office.

Future Direction

- Perform long-duration performance and durability studies on a large number of test samples and actual engine components and characterize their surface mechanical and tribological properties using bench-top and component-level test systems.
 - Develop repeatable/reliable process conditions and more effective quality control protocols for large-scale manufacturing.
 - Prepare actual engine parts for field evaluation.
 - Continue licensing talks with industrial partners.
-

Introduction

Among the many thermal treatment and chemical conversion processes for component surfaces, nitriding, carburizing, boriding (or boronizing), etc., represent some of the most popular, and they are used extensively by all kinds of industrial sectors to achieve superior surface chemical, mechanical, and tribological properties in numerous applications. Unfortunately, these traditional processes are very slow, energy and carbon intensive, and environmentally unsafe (i.e., they produce large amounts of gaseous emissions and liquid and solid wastes).

In this project, we propose to develop and optimize a breakthrough chemical conversion process that can electrochemically deposit boron on the surfaces of suitable metallic parts and subsequently diffuse into the subsurface and convert the near-surface chemistry of such parts to a very hard and thick boride layer. The process is ultra-fast, cheap, and environmentally safe. Due to its transformational features, this process has the potential to revolutionize the high-temperature material processing and heat-treatment field.

The new process is capable of producing nearly 100- μm -thick borided case depths in 30 min as opposed to more than 10 hr in the case of conventional boriding and other thermal treatment processes. The chemically converted boride layers consist of FeB and Fe₂B phases and achieve hardness values ranging from 16 to 20 GPa, depending on the type of steel. Figure 1 shows a typical cross-section image of a borided steel surface and the indentation marks of hardness tests from the top to the interior. Beneath the thick boride layer, there is a very

thick (much thicker than the boride layer itself) boron diffusion layer that provides good mechanical support to the top boride layer.

Undoubtedly, further understanding of the growth mechanism of such chemically converted boride layers and further optimization and scaling-up of the process for widespread industrial uses will have a huge positive impact on transportation and manufacturing industries. The new boriding process uses a simple electrochemical cell with high current density and low voltage as the processing medium. The main ingredients of the molten electrolyte are

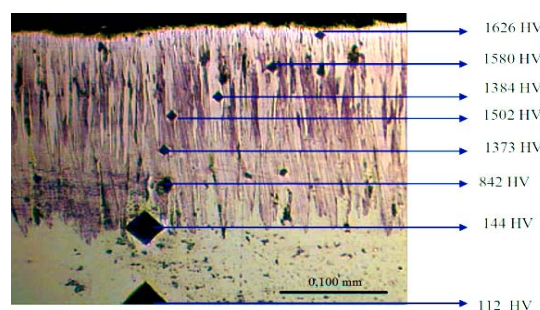


Figure 1. Cross-sectional SEM photomicrograph of a borided low carbon steel sample. The indentation marks with actual hardness values are also provided in the cross-sectional image.

made of borax (Na₂B₄O₇) and a range of inorganic sodium compounds, like sodium carbonate. These are very cheap, non-toxic, natural minerals and, hence, are not expected to pose any type of hazards and toxic emissions or wastes. However, many unknowns in the process remain (especially the understanding of the fundamental growth and process control mechanisms), and with further scientific insight (to be gained under this project), we should be able to further optimize and tailor this new process for

large-scale applications in transportation and other key industries.

Accordingly, the main objective of this project is to develop and optimize an ultra-fast boriding process for improved durability in all kinds of moving mechanical assemblies of light and heavy duty engines. We will also demonstrate the cost-competitiveness, superior performance, and durability characteristics of borided engine parts in various transportation applications (including gears, bearings, piston pins, rings, fuel injector components, crankshafts, tappets, and other moving parts and components that require higher wear resistance and lower friction) and finally transfer the optimized technology to industry for large-scale applications.

We have already demonstrated the ultra-fast nature of our method for the treatment of all kinds of ferrous and non-ferrous materials. We have also successfully borided piston rings and pins with great success. Based on these positive developments, our process should be equally effective in the boriding of other critical engine parts and components. Very thick and hard boride layers produced on these parts by our method can have a significant positive impact on the performance and durability of these parts under severe sliding conditions of light and heavy duty engines involving sliding wear, scuffing damage, corrosion and oxidation, fatigue, and abrasion. Due to continuous changes in oil and fuel chemistry, the operating conditions of sliding, rolling, and rotating engine components are becoming more and more severe; hence, there is an urgent need for novel materials, coatings, and surface treatments that can increase

durability. Because our process is able to produce very thick and hard boride layers, it has a very good chance to meet the more stringent application conditions of future engines.

Again, compared to existing and/or competing technologies (like carburizing, nitriding, traditional pack-boriding, etc.), our method is very fast, clean, efficient, and low cost. Hence, it is an ideal alternative to the existing methods for high-temperature thermal treatment.

During FY10, we achieved all of our project milestones for the year by successfully processing a large variety of steel parts and test samples. Using laboratory-scale test capabilities, we also confirmed their superior tribological performance and initiated discussions on technology transfer and licensing with a large thermal treatment company. Several engine and part-supplier companies are also impressed by our technology and provided some parts for boron treatment. We successfully treated their parts for mechanical and tribological evaluation.

Experimental

Most of our experimental activities in FY10 were focused on the boriding of various grades of steels that are typical of most engine parts and components. We also concentrated on building a larger boriding unit that can treat numerous test samples or bigger engine components. While pursuing these activities, we had to consider many parameters and further optimize them to achieve very thick, uniform, and defect-free boride layers on steel samples.

During the scale-up effort from a small (4 in.) boriding unit to medium-size (22 in.) unit, we had to overcome several obstacles, including selection of a large power source, new fixture and cap designs for electrodes, crucible material, bath composition, and reliable process control and safety systems. In the end, we successfully constructed a 22 in. unit and developed reliable boriding protocols that provided consistent boride layers one batch after another. Figure 2 shows a photo of the 22 in. boriding unit as some parts are being immersed into the molten electrolyte.



Figure 2. View of 22 in. boriding unit. Some industrial parts ready to be immersed into the molten electrolyte.

In this new system, we performed a series of studies on process optimization, reliability, and boride layer repeatability to make sure that the resultant boride layers would be at a desired thickness for most end applications. Some of these studies involved detailed microscopic

studies of cross sections and mechanical testing using a microhardness test machine.

A typical boriding treatment includes the following steps: (1) attachment of test samples to a holder or fixture, (2) their connection to the cathode, (3) immersion of fixture with samples into the molten electrolyte (made of borax and sodium carbonate), and (4) electrolysis for about 15 min, then recovery and cooling down of the samples. In some cases, we hold the borided samples in molten electrolyte for an additional 45 min and then recovered and cooled them down. As part of our quality control procedures, we routinely checked samples for boride layer uniformity (especially on sharper corners or thinner edges), surface defects, and chemical and structural integrity. These and other quality control studies were important for achieving good performance and durability on the treated parts. After these studies, we also conducted a series of mechanical and tribological tests on borided samples.

During our boriding experiments, we also assessed the relationship between mechanical property and the structural and chemical nature of boride layers. In our boriding units, we could achieve thick boride layers with FeB and Fe₂B phases or just Fe₂B. The mixed phase was much harder, but from a fracture toughness point of view, it was not strong enough. Upon Rockwell C indentation, occasionally, the top FeB layer tended to spall or severely crack. However, for a pure Fe₂B layer, the toughness was much better, and we could not see any evidence of spallation or cracking after Rockwell C indentation.

Results

Figure 3 shows the cross-sectional microstructure of a borided steel sample that was subjected to a boriding experiment for 15 min. As is clear, it consists of two distinct phases. Near the top, there is a layer of FeB phase (darker contrasting); right beneath it, the Fe₂B layer (lighter contrasting) exists. As mentioned earlier, the FeB layer on top is hard and brittle (due to poor fracture toughness). As shown in Fig. 4, upon indentation by a Rockwell C diamond indenter, the FeB phase on top generates extensive cracks around the edges of the indented spot, further confirming the brittleness.

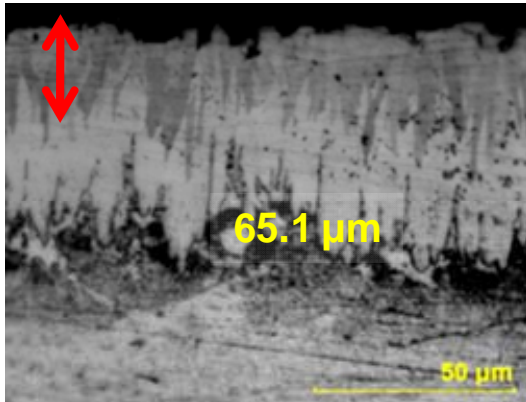


Figure 3. Typical cross-sectional image of a borided steel sample. The darker phase near the top is FeB, while the lighter phase right beneath is Fe₂B.

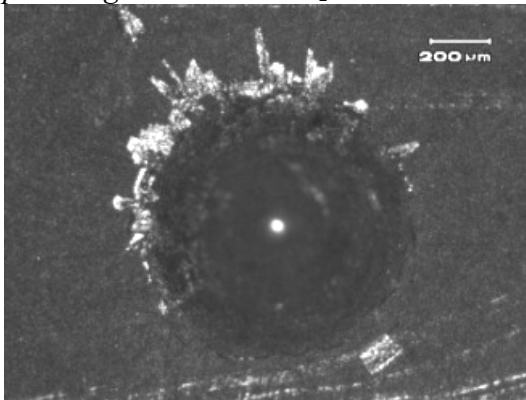


Figure 4. Condition of boride layer showing significant fracture and delamination around the rim of indent, suggesting poor fracture toughness.

The FeB phase was always present near the top surface after most boriding experiments. Due to its very brittle nature, this phase is undesirable for most mechanical and tribological applications. Specifically, due to its very poor fracture toughness, it could easily fracture upon impact or cyclic loading/unloading. By leaving the borided samples in the molten electrolyte for an additional 30 to 45 min, we could totally eliminate the FeB phase, and at the same time, increase the layer thickness by an additional 25%. In short, such a sequential treatment seems to be effective in the elimination of the FeB phase on the top, as shown in Fig. 5. Glancing angle x-ray diffraction (XRD) studies also confirmed that after 45 min of additional holding time in molten electrolyte, the only phase remaining was Fe₂B phase, as shown in Fig. 6.

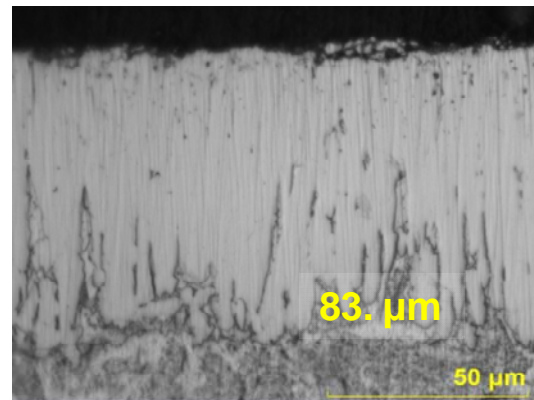


Figure 5. Cross-sectioned image of steel sample after 15 min boriding and then immersion in molten electrolyte (without polarization) for 45 min. The whole boride layer was turned into Fe₂B phase.

When similar Rockwell C indentation tests were run on the boride layer consisting of only Fe₂B phase, the indentation was clean, and no major microcracks or delamination was evident, as shown in Fig. 7. Again, without

holding the sample in electrolyte, the borided layer undergoes severe fracture and chipping around the edges, as shown in Fig. 4.

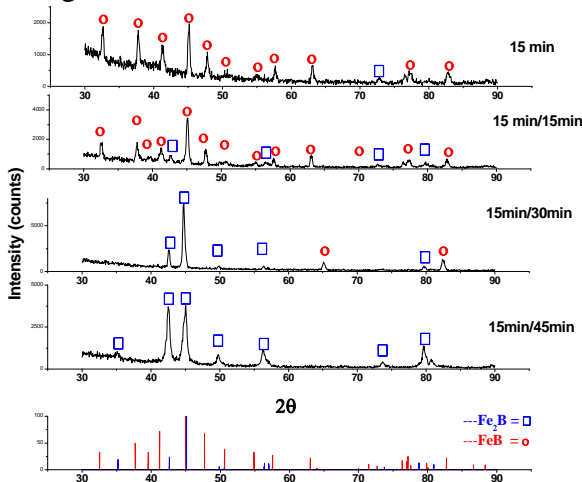


Figure 6. Glancing angle XRD (1 degree, CuK α , 45 V, 40 A) spectra of 15 min electrochemically borided steel, with various holding times (i.e., 0, 15, 30, 45 min) in the molten electrolyte. They confirm that after 45 min holding time, the whole boride layer was turned into Fe₂B.

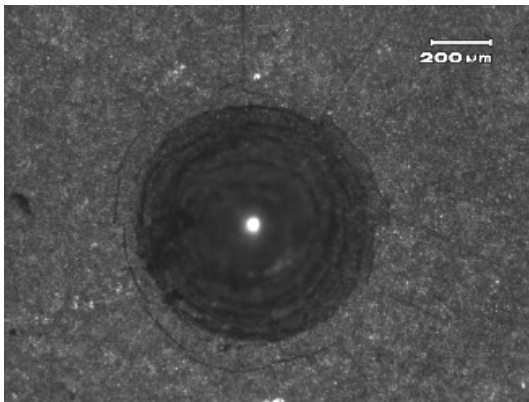


Figure 7. Optical micrograph of Rockwell C indentation on a borided layer consisting of Fe₂B.

Borided layers were subjected to extensive mechanical and tribological tests in our laboratory to verify their superior properties. In Fig. 8, we provide an optical image and hardness profile of a borided steel sample. As shown in Fig. 8a,

the borided layer resists indentation due to high mechanical hardness until the unborided steel substrate is reached. As shown in Fig. 8b, the hardness near the top is around 1600 Vickers and decreases gradually with depth into the substrate. But even up to 60 μm into the substrate, the hardness remains above 1000 Vickers.

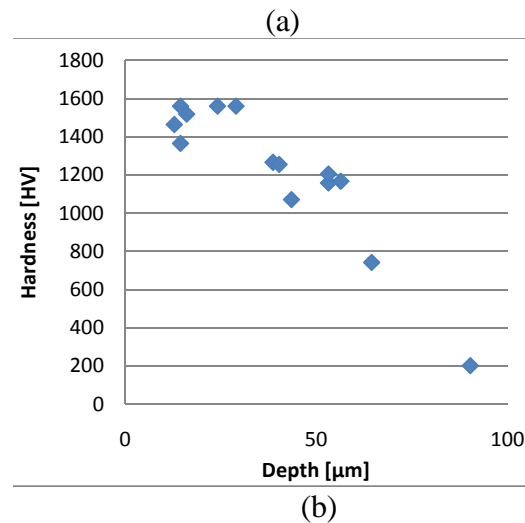
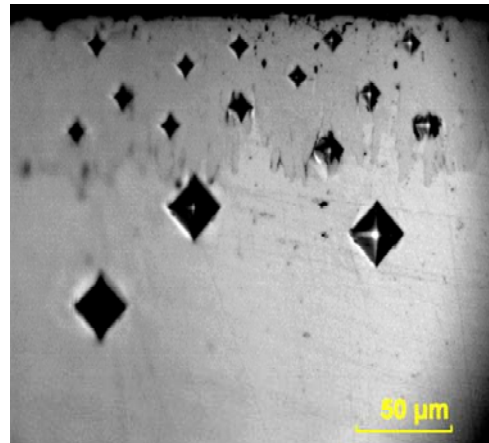


Figure 8. (a) Microscopic image of the hardness tested boride layer and (b) variation of hardness of the same borided steel from top to well into the unborided steel substrate. The boride layer was pure Fe₂B, and the load used in microhardness measurements was 100 g.

Tribological characterization of unborided, conventionally carburized, and ultra-fast borided test samples was

carried out in a pin-on-disk machine, and the results are summarized in Fig. 9. As is clear from the curves, the samples treated by our method provided the best performance despite the dryness (unlubricated) of these tests. Carburized and un-borided test samples suffered significant wear losses, and their friction coefficients were also much higher.

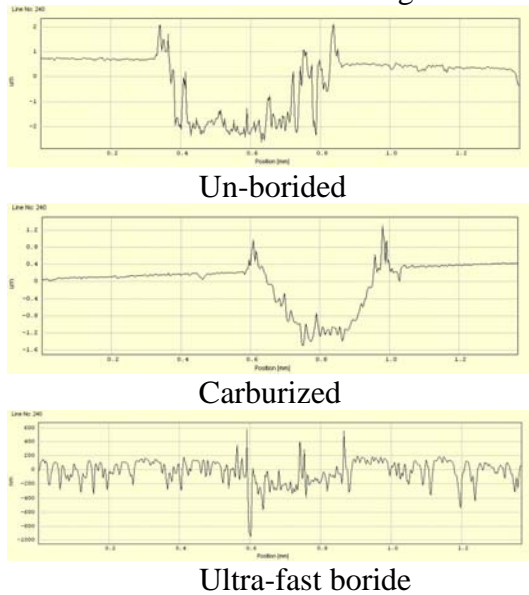


Figure 9. Comparison of wear performance of borided steel with that of untreated and carburized steel (test conditions: 5-N load, 6.5-cm/s sliding velocity, 1-km sliding distance).

Systematic friction and wear studies under lubricated test conditions with borided and other tests samples are underway. Figure 10 shows initial results from carburized steel samples with and without boriding in tests using a common gear oil. As is clear, the borided sample provided the best protection against wear, while carburizing alone is not sufficient for good wear resistance.

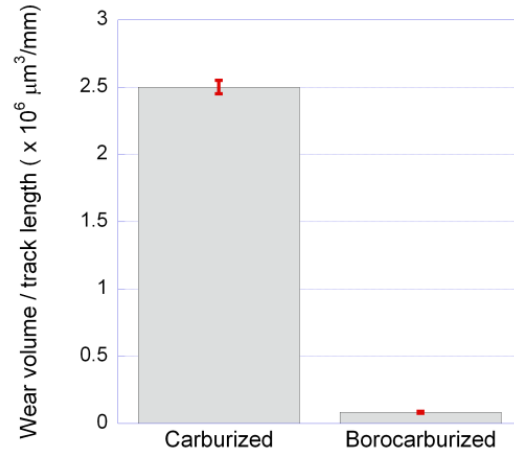


Figure 10. Wear performance of carburized steel samples with and without boriding in common gear oil.

Conclusions

Despite being the first year in the project, we made significant progress toward meeting our goals in FY10. Using small- and medium-scale boriding units, we performed numerous boriding experiments and optimized the boriding conditions to achieve a thick and hard boride layer on various steel samples. Using these samples, we conducted systematic mechanical and tribological studies and verified much superior mechanical and tribological properties of borided samples. The hardness of borided layers was on the order of 1600 Vickers, while the wear of such boride layers was difficult to measure, but the un-borided or carburized surfaces suffered severe wear damage.

During FY10, we also attempted to scale up the boriding process to treat large batches and big engine parts and components. In the end, we succeeded in the building of a 22 in. boriding unit that can easily treat several engine parts in one run or large numbers of test samples. Our industrial partner in this project is excited over the prospect of this

technology being scalable to the levels of large production runs. They have already initiated licensing talks with Argonne's Intellectual Property Department. During FY10, we also performed numerous boriding trials on some engine components furnished by our industrial partners and confirmed that we can successfully treat these components without any problems. In the near future, we will be focusing more on industrial applications and will further scale-up of the technology so that it can meet the large production needs of our industrial partners.

Publications and Presentations

During FY10, we published and/or presented several papers on the work that was performed under this project as listed below.

1. "Electrochemical Boriding of Titanium for Improved Mechanical Properties," G. Kartal, S. Timur, M. Urgan, and A. Erdemir, *Surface and Coatings Technology*, 204 (2010) 3935-3939.
2. "Influence of Process Duration on Structure and Chemistry of Borided Low Carbon Steel," G. Kartal, S. Timur, O. L. Eryilmaz, and A. Erdemir, accepted for publication in *Surface and Coatings Technology*.
3. "An Investigation of Electrochemical Boriding Kinetics of Low Alloy Steels," G. Kartal, O. L. Eryilmaz, G. Krumdick, A. Erdemir, and S. Timur, submitted to *Surface and Coatings Technology*.
4. "Comparison of Abrasive Wear Resistance of Low Carbon Steels Subjected to Carburizing, Nitriding, Nitrocarburizing, and Boriding Treatments," V. Sista, G. Kartal, A. Erdemir, O. Eryilmaz, G. Krumdick, and S. Timur, submitted to *Surface and Coatings Technology*.
5. "Ultra-fast and Thick Boriding as a Novel Surface Treatment for Demanding Tribological Applications," A. Erdemir, presented at the International Conference on Metallurgical Coatings and Thin Films, April 26-30, 2010, San Diego, CA.
6. "Comparison of Abrasive Wear Resistance of Low Carbon Steels Subjected to Carburizing, Nitriding, Nitrocarburizing, and Boriding Treatments," V. Sista, G. Kartal, A. Erdemir, O. Eryilmaz, G. Krumdick, and S. Timur, presented at the International Conference on Metallurgical Coatings and Thin Films, April 26-30, 2010, San Diego, CA.
7. "Effect of Process Duration on Structure, Chemistry, and Mechanical Properties of Borided Low Carbon Steels," G. Kartal, O. L. Eryilmaz, A. Erdemir, G. Krumdick, and S. Timur, presented at the International Conference on Metallurgical Coatings and Thin Films, April 26-30, 2010, San Diego, CA.
8. "The Effect of Boron Based Surface Treatment and Nano-particle Lubricant Additives on Friction and Wear Behavior for Wind Energy Applications," A. Greco, K. Mistry, V. Sista, and A. Erdemir, to be presented at the 18th International Conference on Wear of Materials, Philadelphia, PA, April 3-7, 2011.
9. "Structural and Mechanical Characterization of Electrochemically-Borided ICONEL 600," V. Sista, G. Kartal, Q. Zeng, A. Erdemir, O. Eryilmaz, G. Krumdick, S. Timur, presented at the Materials Science & Technology Conference & Exhibition, Houston, TX, October 17-21, 2010.

Agreement 19216 - Friction Modeling for Lubricated Engine and Drive-train Components

Oyelayo Ajayi, Cinta Lorenzo-Martin, George R. Fenske
Argonne National Laboratory
9700 South Cass Avenue
Argonne, IL 60439
(630)252-9021; fax (630)252-4798; e-mail: ajayi@anl.gov

DOE Technology Manager: Jerry Gibbs
(202) 586-1182; fax: (202) 586-1600; e-mail: jerry.gibbs@ee.doe.gov

Contractor: Argonne National Laboratory, Argonne, Illinois
Prime Contract No.: DE-AC02-06CH11357

Objectives

- Develop a methodology and simulation tools for prediction of friction in lubricated systems under various lubrication regimes.
- Use the new tool to develop sustainable low-friction interface technologies for vehicle systems.

Approach

- Model friction by simultaneous shearing of the three structural components of the lubricated interface, namely, lubricant fluid film, boundary films, and near-surface material (asperity).
- Develop constitutive equation for shear behavior of each component of lubrication.
- Integrate the shearing of each frictional component over the entire contact area, taking into account the surface topography, for prediction of total friction.

Accomplishments

- Based on available information on fluid film lubrication, developed equations for determining lubricant fluid film thickness and shear behavior.
- Initiated measurement of nano-mechanical properties of tribochemical boundary films to determine their shear properties and use in development of constitutive equation.
- Completed initial analysis of asperity contact and shear behavior for constitutive equation regarding near-surface materials.

Future Direction

- Continue measurement of nano-mechanical properties for boundary films in both indentation and scratching modes.
 - Formulate constitutive equation for shear behavior of boundary films.
 - Integrate shear equations for the three components of surface lubrication for total friction predictive model.
 - Working with Argonne Leadership Computing Facility (ALCF), develop codes and tool to predict friction of lubricated sliding interface.
-

Introduction

Several components in vehicles systems (engine and driveline) are either oil or grease lubricated. Significant energy losses occur in these components as a result of friction. The ability to predict friction in the components and systems will facilitate design and development of efficient components and systems. The friction at the lubricated contact interface is due to the shearing of one or more of three structural elements, namely, lubricant fluid film, boundary films, and the near-surface materials. Under the hydrodynamic and elastohydrodynamic (EHD) regime, the friction is determined primarily by the shearing of the fluid film. However, under the boundary lubrication regime (in which most engine components operate) friction is determined by the shearing of the three structural elements. This shearing is further complicated by the effect of surface roughness. Consequently, friction under boundary lubrication is usually assumed or measured. This approach is inadequate for conducting a thorough or complete system analysis. With recent advances in the ability to determine the structures and pertinent properties of the boundary films and near-surface materials, coupled with the advanced computational capabilities available at the national laboratories (e.g., the Leadership Computing Facility at Argonne), the stage is set for development of a method to predict the frictional behavior of severely loaded lubricated contacts. This new proposed effort is to embark on such a task. The approach will involve development of constitutive equations for the shear behavior of boundary films and near-surface materials. These equations will then be used to develop a computer simulation and predictive tool for friction in lubricated systems.

The main objective of the project is to develop a methodology and simulation tools that predict the friction behavior in lubricated systems under various lubrication regimes. This objective will be met by integrating the contribution of fluid,

boundary film, and near-surface material into an analysis of the interfacial shearing process in sliding contacts. Such a tool will be very useful, indeed critical to the development of sustainable low-friction interface technologies for vehicle systems. The ability to accurately predict the friction behavior of severely loaded contacts will facilitate the design and development of reliable and durable high-power-density systems for transportation applications. Results of this project can also be integrated into simulation and analysis tools for other vehicle systems to make them more robust. The project will provide a valuable tool for surface finish and treatment, lubricant formulation, and materials optimization and integration for high-power-density systems.

Approach

The approach for the proposed effort will be based on modeling of simultaneous shearing of the three structural elements shown in Figure 1 [1], i.e., fluid film, tribochemical boundary films, and the near-surface material at the contact interface.

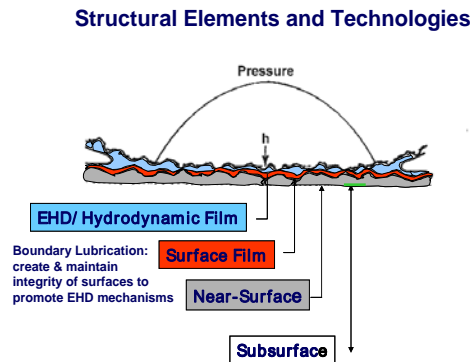


Figure 1: Elements of surface lubrication.

The friction coefficient at the contact interface can thus be calculated as

$$\mu = \frac{F_{sf} + F_{sb} + F_{sa}}{F_N}$$

where F_{sf} is the shear force of the fluid film, F_{sb} is the shear force of the boundary film, and F_{sa} is the solid asperity shear force of the near-surface, and F_N is the normal force

The total friction of the sliding and/or rolling interface can be calculated by integrating the shear forces of the three elements over the entire contact area as a function of time, taking into account the contact parameters and surface roughness. Changes in surface roughness and tribochemical film formation and properties as a function of time can be taken into account in the friction calculations.

Progress

This is a new project that started in FY10. During the year, the constitutive equation for the shear behavior of the lubricant fluid film was developed on the basis of the large body of work available in the literature. Indeed, analysis of the mechanical and shear behavior of lubricant fluid films is relatively mature and adequately developed through hydrodynamic and elastohydrodynamic theories and experiments.

Assuming a Newtonian behavior for the lubricant fluid film, the shear stress in the film (τ_f) can be calculated by the equation:

$$\tau_f = \mu_0 e^{\alpha P} \frac{S}{h_m}$$

where μ_0 is the viscosity at atmospheric pressure, α is the pressure–viscosity coefficient, P is the contact pressure, S is the sliding velocity, and h_m is the lubricant fluid film thickness (which can be calculated from an appropriate EHD equation). For instance, in a ball-on-flat contact configuration, the lubricant fluid film thickness is given by the equation:

$$h_m = 3.07 \frac{(\mu_0 U_c)^{0.71} \alpha^{0.87} R^{0.49}}{E'^{0.08} W^{0.11}}$$

where U_c is the entraining velocity, R is the combined radius of curvature, E' is the combined elastic modulus, and W is the applied load.

The shear force (F_{sf}) in the fluid film can be calculated by multiplying the shear stress and the contact area (A_f):

$$F_{sf} = \tau_f A_f$$

Measurements of the nano-mechanical properties for the tribochemical boundary films were also started during FY10. Of the three structural elements of lubrication, the tribochemical film is the most challenging in terms of the formulation of the constitutive equation. At present, there is little or no information on the mechanical behavior of these films in the open literature. Consequently, the properties and mechanical behavior of these films have to be experimentally determined by an instrumented nano-mechanical probe. Some preliminary measurements were conducted with the Hysitron Nano probe shown in Figure 2.

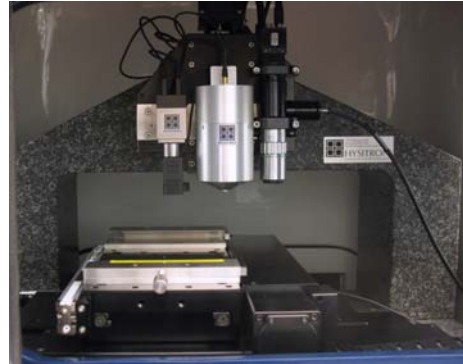


Figure 2: Hysitron nano probe system

From the force-displacement curves (shown in Figure 3) during load-and-unloading nano indentation, some basic mechanical properties of the films can be measured. The mechanical behavior of the boundary films and, hence, the constitutive shear equations can also be formulated with the appropriate test by the nano indentation and nano scratching technique.

Project 18519 - Materials for Control of Exhaust Gases and Energy Recovery Systems

Agreement 9130 - Development of Materials Analysis Tools for Studying NO_x Adsorber Catalysts (CRADA No. ORNL-02-0659 with Cummins Inc.)

Thomas Watkins, Larry Allard, Michael Lance, Harry Meyer and Larry Walker
Oak Ridge National Laboratory
P.O. Box 2008
Oak Ridge, TN 37831-6064
(865) 574-2046; fax: (865) 574-4913; e-mail: watkinstr@ornl.gov

Krishna Kamasamudram and Aleksey Yezerets
Cummins Inc.
1900 McKinley Av., MC 50197
Columbus, IN 47201
(812) 377-4935; fax: (812) 377-7226; e-mail: Krishna.Kamasamudram@Cummins.com

DOE Technology Manager: Jerry L. Gibbs
(202) 586-1182; fax: (202) 586-1600; e-mail: jerry.gibbs@ee.doe.gov
ORNL Technical Advisor: D. Ray Johnson
(865) 576-6832; fax: (865) 574-6098; e-mail: johnsondr@ornl.gov

Contractor: Oak Ridge National Laboratory, Oak Ridge, Tennessee
Contract No.: DE-AC05-00OR22725

Objective

- The objective of this effort is to produce a quantitative understanding of the process/product interdependence leading to catalyst systems with improved final product quality, resulting in diesel emission levels that meet the prevailing emission requirements.

Approach

- Characterize lab-engine tested samples with X-ray diffraction, spectroscopy, and microscopy. Correlate findings with Cummins data and experience.

Accomplishments

- Initiate evaluation of feasibility of the advanced tools available at ORNL for quantitative analysis of the materials changes underlying the ammonia oxidation catalyst performance degradation with age.
- Redesigned and improved portable gas manifold system. This system will provide varied atmospheres for in-situ studies using diffraction, spectroscopy, and microscopy.

Future Direction

- Continue evaluation of feasibility of the advanced tools available at ORNL for quantitative analysis of the materials changes underlying the AMOx catalyst performance degradation with age.
 - Assist Cummins to competitively produce engines which attain the required emission levels while maintaining the advantage of the diesel's inherent energy efficiency.
-

Introduction

In order to meet the 2010 US Environmental Protection Agency (EPA) emission requirements for diesel exhaust, aftertreatment in diesel engines may be necessary. The technology necessary for 2010 will need to integrate aftertreatment with engine control systems. Currently, no commercial off-the-shelf technologies are available to meet these standards. Consequently, Cummins Inc. is working to understand the basic science necessary to effectively utilize these catalyst systems. ORNL is assisting with the materials characterization effort. This report will focus on the study of materials used in ammonia oxidation.

Ammonia containing compounds may be added to diesel exhaust to reduce NO_x to N_2 , as in selective catalytic reduction (SCR). The reductant reduces NO_x to H_2O and N_2 . [1] Excess ammonia is often needed resulting in NH_3 escaping or “slip”. This slip is a concern for sociability and environmental reasons. Although not regulated, proactive steps are taken to mitigate even small amounts of ammonia slip by employing a selective oxidation catalyst.

Oxidation catalysts are usually present in after treatment systems to oxidize ammonia that is not being oxidized upstream by the SCR catalysts. These oxidation catalysts ensure that ammonia slip to ambient is minimal and are referred to several names: ammonia oxidation (AMOX) catalysts, selective catalytic oxidation (SCO) catalysts or ammonia slip catalysts (ASC). Candidate catalysts are typically zeolite-based, alumina-supported metal or alumina-supported metal oxide catalysts. Hydrothermal conditions, temperature and water content, strongly influence the functioning of these catalysts by changing or “aging” the catalytic materials. These changes and their impact on performance are not well understood.

Goals, Barriers, Relevance & Integration

In the study area of OVT's Advanced Combustion Engine research, the *goals* are to (1) improved commercial vehicle engine efficiency by at least 20% and (2) to achieve engine system cost, durability and emissions targets. This project addresses the three *barriers* related to the Emission Control System in this study area: Improving durability, numerous components and costly precious metal content. This project is *relevant* to these goals as the understanding of materials

changes underlying the AMOX catalyst performance degradation with aging increases, efficient and durable AMOX with higher NO_x conversion efficiencies can be attained. This minimizes constraints on engine-out NO_x emissions and allowing engines to be tuned for optimal fuel efficiency, cost and durability. This project supports clean diesel, which increases acceptance by the public. Larger acceptance, in turn, results in larger percentages of conversion to diesel, with the resulting reduction in petroleum usage/dependency upon foreign oil. This project is *integrated* within Vehicle Technologies program as it utilizes characterization tools acquired and maintained by the High Temperature Materials Laboratory (HTML) Program.

Samples and Approach

Through 2009, progress had been slowed considerably due to sample unavailability because of Cummins' 2010 product launch focus. Commercial ammonia oxidation samples were received in January 2010. Initial analysis at Cummins, visual and performance, suggested these commercial ammonia oxidation catalysts were constructed with platinum group metals (PGM) and ammonia storage catalysts such as transition metal zeolite.

In the prior work, both ORNL and Cummins personnel have participated in the work to understand zeolite based SCR catalyst degradation. A commercial Fe zeolite powder was being examined with diagnostic tools developed under this CRADA. The crystal structure, morphology, phase distribution, particle size, and surface species of catalytically active materials supplied by Cummins were characterized using transmission electron microscopy (TEM), X-ray diffraction (XRD), X-ray photoelectron spectroscopy (XPS), and Raman Spectroscopy. Several of the above tools were expected to be more suited for characterization of the less understood PGM containing catalysts such as ammonia oxidation catalysts.

Initial plan was to qualitatively (and if possible quantitatively) understand how the oxidation and SCR functions were integrated in to the AMOX catalyst with the help of the above advanced tools and the current report presents these initial results. It is expected that ammonia oxidation catalysts can come from all stages of the catalyst's life cycle: as received, calcined, aged etc. and in the second stage

of the project will diagnose such field returned or simulated catalysts.

Results

XRD and XPS

The x-ray diffraction (XRD) pattern analysis of the as-received zeolite-based AMOx catalyst revealed two potential zeolite structures and cordierite from the honeycomb support (see Figure 1). The X-ray Photoelectron Spectroscopy (XPS) was conducted in three locations of a honeycomb core, which was cut in half. Figure 2 shows the composition (see inset Table) at these three locations. The reported Al:Si:Fe ratio assumes Al₂O₃, SiO₂, and Fe₂O₃ are present. The Si 2P, Al 2p and O 1s core level spectra were identical for all three sample regions which is consistent with literature for zeolites. Similarly, the Fe 2P core level spectra are identical for all three locations and indicate Fe³⁺. Further, the adsorbed water O 1s signal was ignored. The metal/oxygen ratio was found to be 0.68 and it is typically 0.59, indicating a slight oxygen deficiency in the near surface region. This AMOx zeolite shows significantly higher Fe concentrations than prior SCR samples, which facilitated detection and characterization of the Fe species by microscopy.

Microscopy

Baseline microstructural data on cross-sections of the AMOx monolith were obtained using scanning transmission electron microscopy ((S)TEM). The initial (S)TEM results presented here were obtained using the HTML's Hitachi HF-3300, a new 300kV cold-field-emission instrument that provides conventional bright-field (BF) TEM images via a 2k x 2k pixel CCD camera system, and BF and annular dark-field (ADF) images in scanning transmission mode. Energy-dispersive spectra were acquired using a Tracor-Noran Si(Li) detector system on the microscope.

Samples for TEM analysis were prepared by grinding and polishing the thin cross-sectional slice first cut from the polished metallographic mount to a thickness of about 0.2 mm, and sections of "crosses" of the cordierite monolith about 2mm square were cut and mounted on 3 mm diameter graphite support rings. These sections were dimple-ground and finally ion-beam milled using 6kV Ar ions at 15° incidence angles (from top and bottom

simultaneously) until the middle of the cross was perforated, providing electron-transparent regions intersecting the cordierite/washcoat interfaces. Figure 3 shows a low-magnification secondary electron image of an entire cross recorded on a Hitachi S-3400 SEM in the HTML. It should be noted that the nature of the phases in this sample makes such TEM cross sections extremely fragile, and it is not uncommon to lose some of the initial thin regions while handling the samples and loading them into the TEM holder.

Figure 4 shows a thin region of cordierite/washcoat interface, and the associated energy-dispersive spectra (EDS) from different regions are shown. The cordierite is the expected to have Mg aluminosilicate phase, and the washcoat at the interface shows both Pt and Fe peaks, in addition to other washcoat components. The EDS spectra from the TEM were correlated to EDS analysis results on two different ion-milled TEM specimens prepared in a similar fashion. These spectra were acquired using the Hitachi S-3400 SEM, which allows a much more intense electron beam, and runs at much lower voltage (e.g. 15kV) which is better for generation of EDS spectra in the 0-10keV range than the 300kV beam in used in the HF-3300. EDS spectra of washcoat active materials are shown in Figure 5, acquired from areas similar to those shown in Fig. 4. Fe peaks are seen in the cordierite and washcoat phases, similar to those shown from the HF-3300 data. It is likely that these peaks do not result from instrumental artifacts, but that Fe is an artifact of the ion milling process. A semi quantitative analysis procedure from the high-count data of these spectra showed a Pt concentration in the washcoat of 1.83 (nominally 2) percent by weight, and an Fe concentration of about 8 percent by weight.

Figure 6b shows a higher magnification region of the area of Figure 6a (same as Figure 4), in BF. A number of dark particles in the 2-3 nm size range are seen (e.g. arrows), and presumed to be Pt. These particles should show in bright contrast if imaged in ADF mode (see Figure 7b). The bright contrast of the nanoparticles is consistent with the higher atomic number of Pt relative to the average atomic number of the washcoat. Figure 7 shows an adjacent region of the washcoat in BF TEM (Figure 7a) and a higher magnification nearby region in ADF STEM mode (Figure 7b).

Some preliminary details on the structure of the zeolite washcoat were obtained using the imaging and elemental analysis capabilities of the ACEM. Figure 8 shows an annular dark-field image of a typical area of the zeolite washcoat; two general morphologies are seen, a very fine-grained, large aggregate (A), and a 'matrix' of blocky, equiaxed grains (B). EDS spectra showed very similar compositions from both regions (Figures 8b and c). Figure 9 is a higher magnification ADF image of the blocky phase, which shows bright contrast regions coating edges of the particles. Figure 10 shows EDS mapping of a similar area of the blocky phase. The bright regions are Fe-rich, and the blocky particles are not uniform in composition; particles are either Si-rich or Al-rich. The Fe appears to be associated primarily with the Al-rich component. Further results will be reported in the next quarterly.

Redesigned Portable Gas Manifold

Andrea Strzelec, a postdoc from NTRC, redesigned and improved the portable manifold system for in-situ studies using XRD, TEM and Raman. Six new mass flow controllers and a power supply have been ordered and received and will replace the existing ones, which are oversized. The total flow of the revised system will be 50 to 400 standard cubic centimeters per minute (SCCM) and will have heated lines for the component gases: NO in N₂, O₂/N₂, CO₂, H₂O in N₂, NH₃ in N₂, and N₂. The water bubbler on the cart will be replaced with a water bath system (to go on the bottom of cart). The mass flow controllers will be calibrated with a Gilibrator using N₂ with a corresponding user-friendly calibration spreadsheet. Before collecting in-situ data, the safety paperwork will be generated, followed by preliminary testing.

Summary

The as-received AMOx catalyst has been characterized using XRD, TEM and XPS. The

effect of hydrothermal conditions on the AMOx catalyst will be characterized next to continue the evaluation of feasibility of the advanced tools available at ORNL for quantitative analysis of the materials changes underlying the AMOx catalyst performance degradation with age.

Reference

[1] I. Chorkendorff and J. W. Niemantsverdriet, Concepts of Modern Catalysis and Kinetics, Wiley-VCH Verlag GmbH & Co. KGaA, Weinheim, 2003, pp. 395-400.

Presentations

T. R. Watkins, L. Allard, M. Lance, H. Meyer, K. Kamasamudram, A. Yezerets, "Catalyst Characterization," presented at the DOE 2010 Vehicle Technologies Annual Merit Review and Peer Evaluation Meeting, Washington, D.C., June 10, 2010.

Acronyms

ACEM	aberration-corrected electron microscope
AMOx	ammonia oxidation
ASC	ammonia slip catalysts
BF	bright-field
BSE	back-scattered electron
EDS	Energy dispersive spectroscopy
EPA	Environmental Protection Agency
HA-ADF	high-angle annular dark-field
HTML	High Temperature Materials Laboratory
NOx	Nitrogen and Oxygen containing compounds
ORNL	Oak Ridge National Laboratory
SCO	selective catalytic oxidation
SCR	selective catalytic reduction
(S)TEM	scanning transmission electron microscopy
XPS	X-ray photoelectron spectroscopy
XRD	X-Ray Diffraction

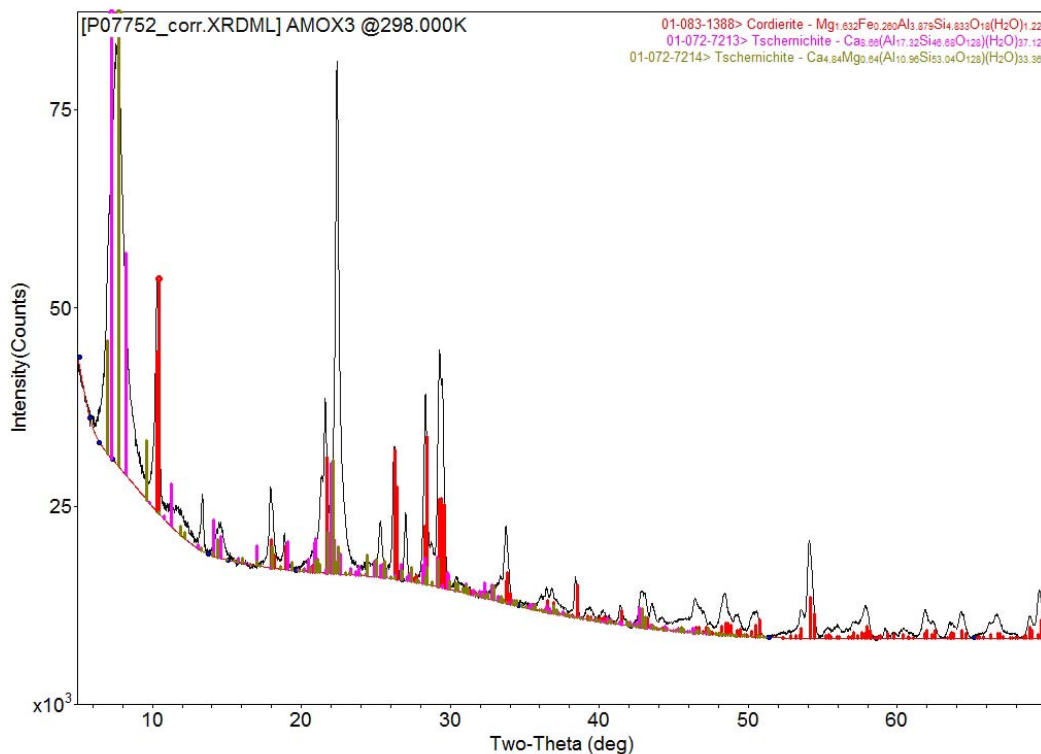


Figure 1. The x-ray diffraction pattern of an AMOx catalyst.

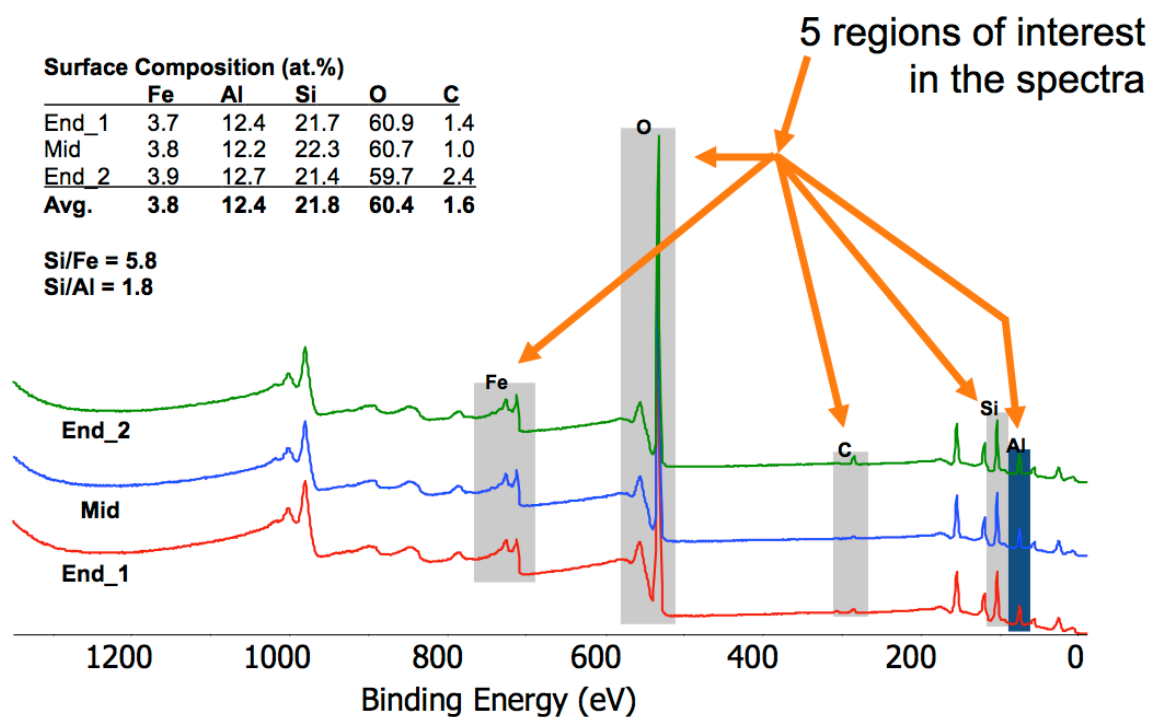


Figure 2. The intensity (arb. units) as a function of binding energy for the as-received AMOx sample.

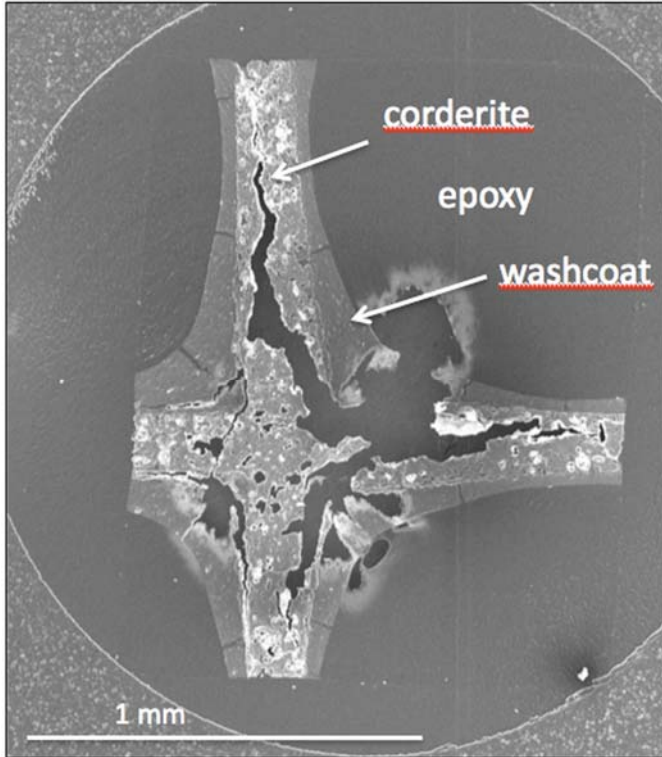


Figure 3. Secondary electron image of a typical TEM thin foil specimen, showing the cordierite “cross” structure embedded in epoxy. Electron transparent edges at the cordierite interface, such as indicated with the inset rectangle, are imaged at higher magnification in the TEM.

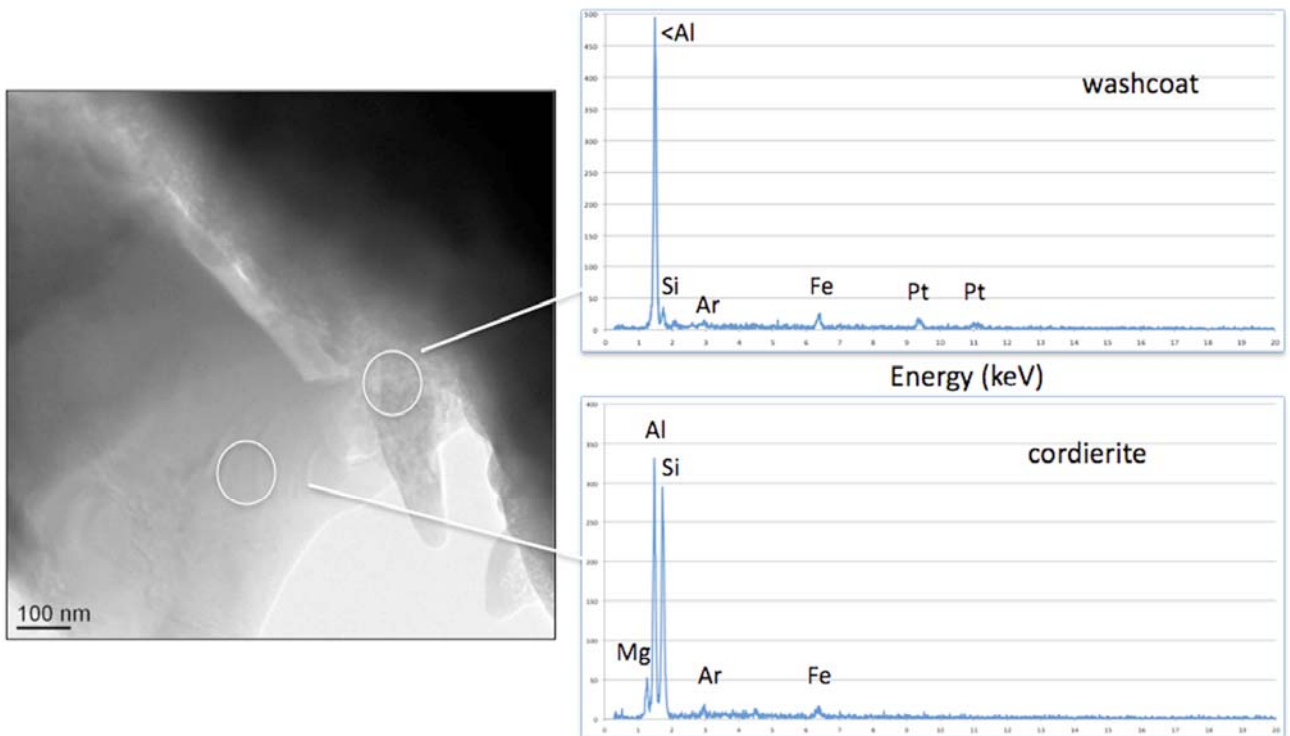


Figure 4. Bright-field TEM image of the interface between cordierite and the washcoat. EDS spectra from the inset regions are shown, confirming Pt in the washcoat.

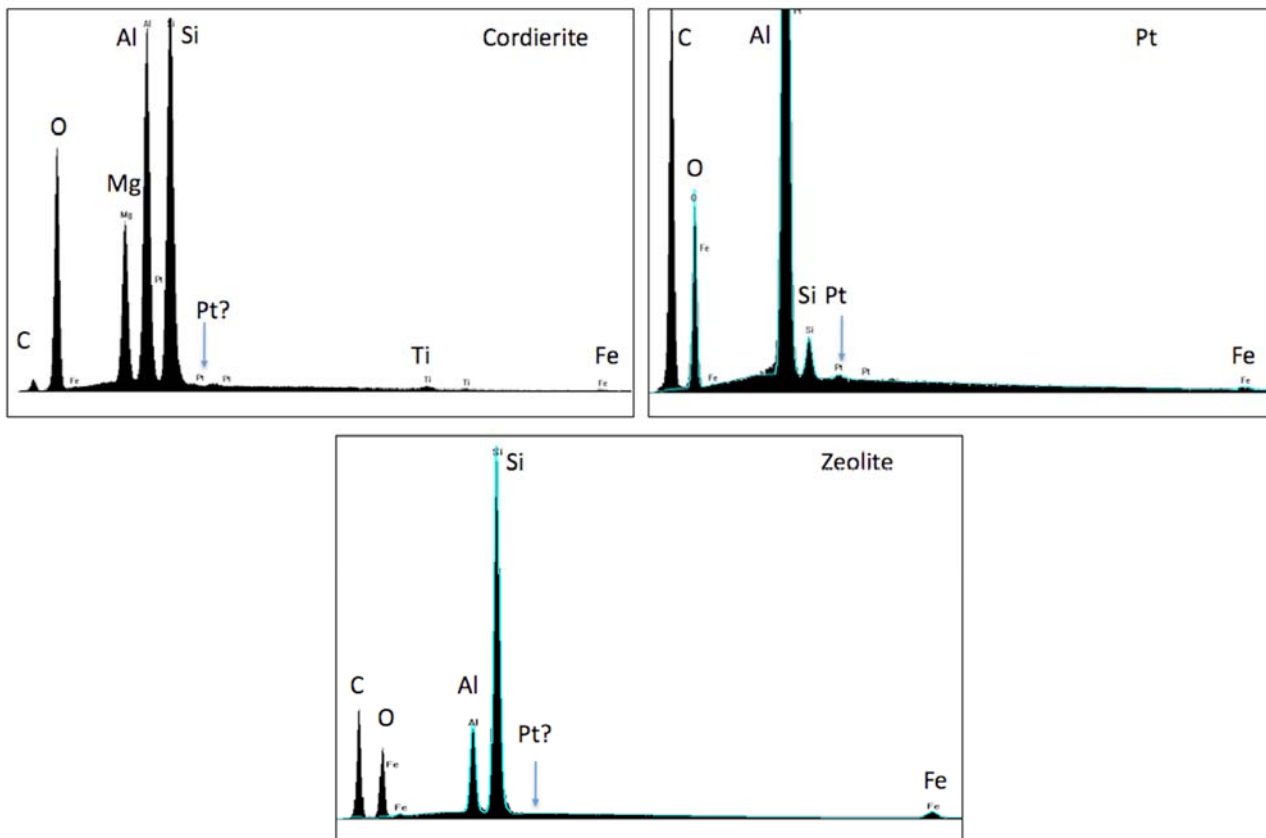


Figure 5. EDS spectra acquired at high count rate from the S-3400 SEM, which show minor Fe peaks in the cordierite and washcoat spectra, with a higher concentration Fe peak from the zeolite phase. These spectra allowed semi quantitative analyses of composition, which showed the Pt loading consistent of about 2 wt.% and 8 wt. % Fe.

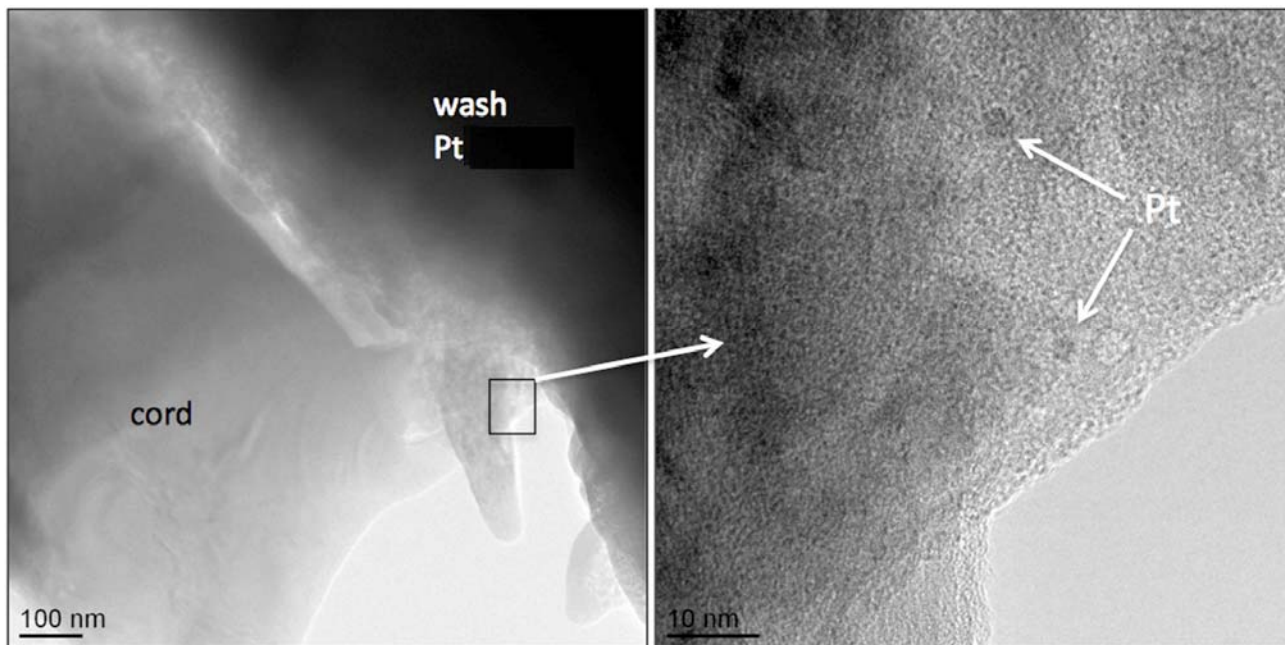


Figure 6. A higher magnification BF image from the area of Figure 4 shows nanoparticles in dark contrast (arrows), presumed to be Pt species.

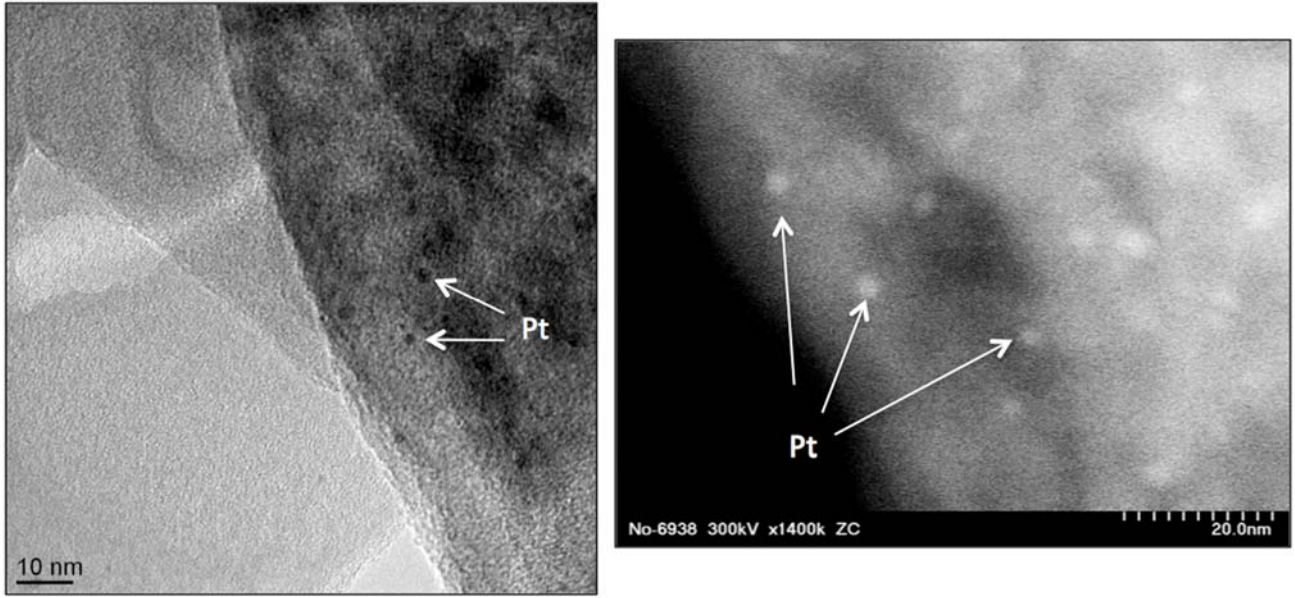


Figure 7. Another BF image from an adjacent area, with an annular dark-field (ADF) image at higher magnification showing the nanoparticles in bright contrast, as expected from the higher atomic number Pt species present.

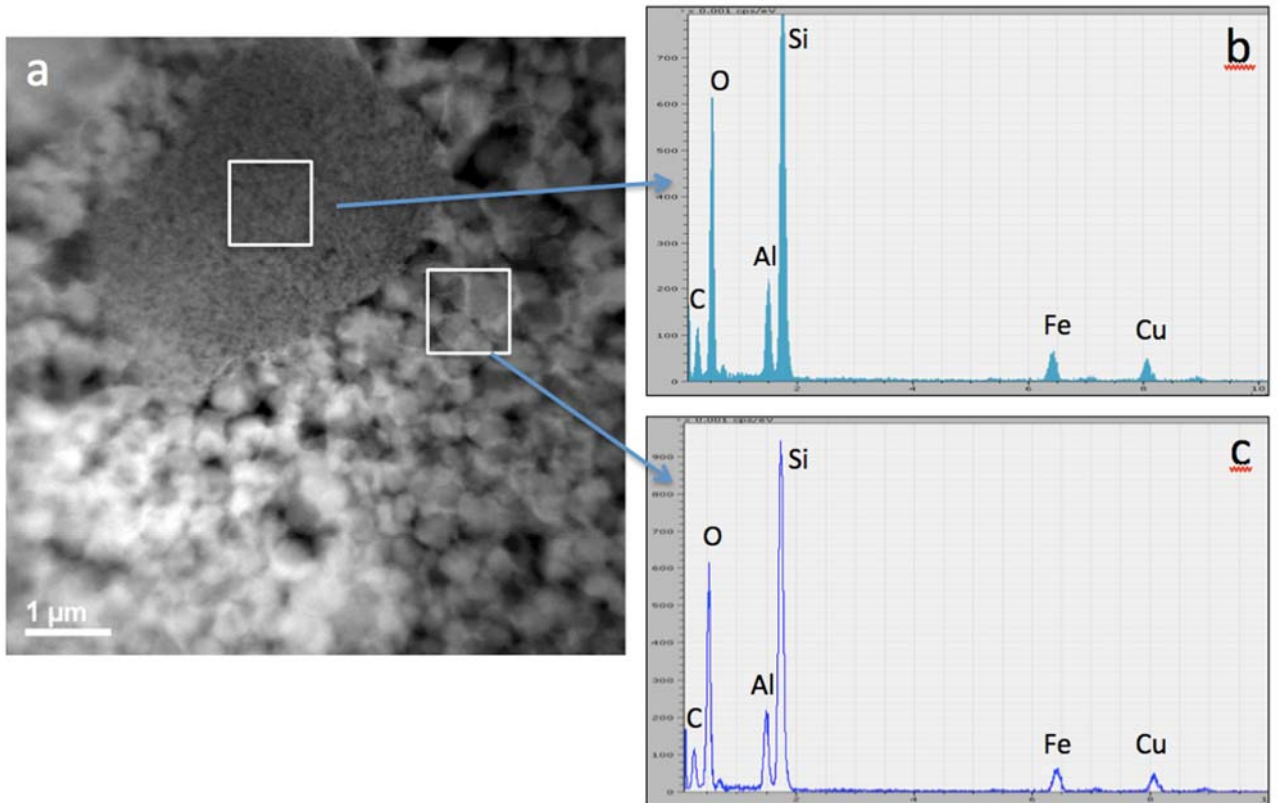


Figure 8. Results from STEM imaging and EDS analysis of the zeolite washcoat using the ACEM shows (a) a typical microstructure, composed of two distinctive structures; a very fine-grained, large aggregate in a matrix of blocky, equiaxed particles in the 0.5mm size range (shown at higher magnification in Figure 9). EDS spectra from the two structures show nearly identical compositions (b) and (c).

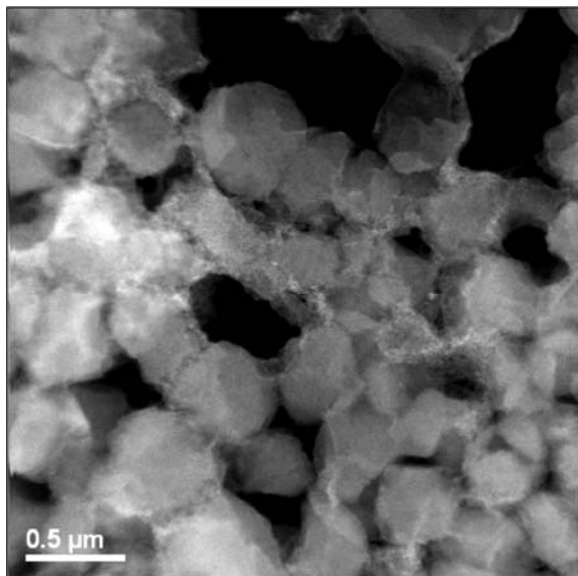


Figure 9. ADF image of the blocky particulate phase, showing a filamentous feature in bright contrast, suggesting higher average atomic number. Elemental mapping (Figure 10) indicates this is a Fe-rich structure.

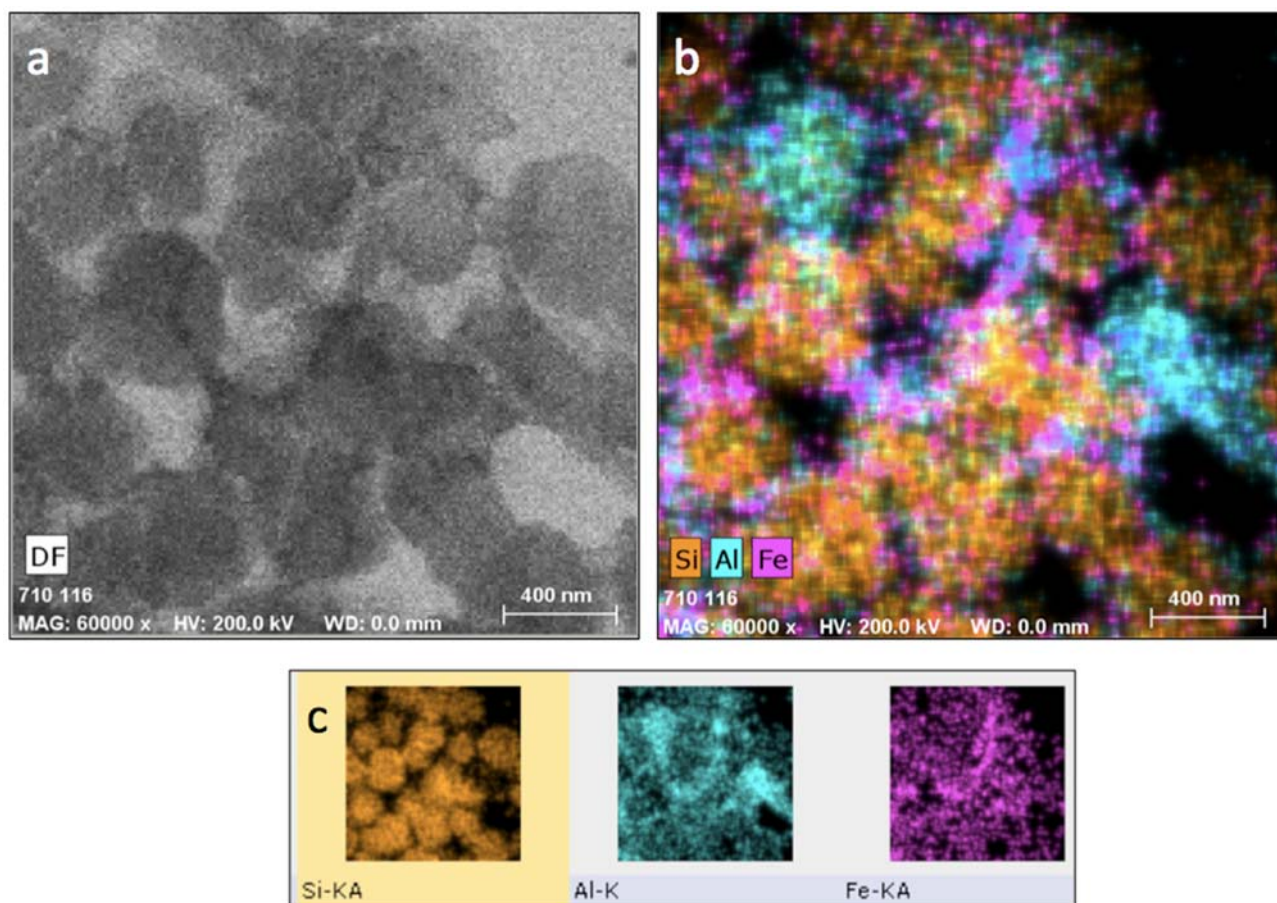


Figure 10. Elemental mapping data acquired using the Bruker-Nano SDD system on the ACEM. (a) the ADF image shown with Si, Al and Fe distributions overlaid in (b). This overlay shows that the blocky particles are either Si-rich or Al-rich, and the Fe distribution correlates primarily to some of the Al-rich areas. Individual maps of the Si, Al and Fe distributions are shown in (c).

Agreement 10461 - Durability of Diesel Particulate Filters (CRADA with Cummins Inc.)

Thomas R. Watkins, Amit Shyam, Hua-Tay Lin and Edgar Lara-Curzio
Oak Ridge National Laboratory
P.O. Box 2008, MS-6064
Oak Ridge, TN 37831-6064
(865) 574-2046; fax: (865) 574-4913; e-mail: watkinstr@ornl.gov

Randall J. Stafford and Tom Yonushonis
Cummins Inc.
1900 McKinley Av., MC 50183
Columbus, IN 47201
(812) 377-3279; fax: (812) 377-7226; e-mail: randy.j.stafford@cummins.com

DOE Materials Engineer: Jerry Lee Gibbs
(202) 586-1182; fax: (202) 586-1600; e-mail: jerry.gibbs@ee.doe.gov
ORNL Technical Advisor: D. Ray Johnson
(865) 576-6832; fax: (865) 574-6098; e-mail: johnsondr@ornl.gov

Contractor: Oak Ridge National Laboratory, Oak Ridge, Tennessee
Contract No.: DE-AC05-00OR22725

Objective

- To identify and implement test techniques to characterize the physical and mechanical properties of ceramic substrates used as diesel particulate filters (DPFs), to identify the mechanisms responsible for the degradation and failure of DPFs and to develop analysis tools for predicting their reliability and durability.

Approach

- Characterize the properties of and rank the thermal shock resistance of candidate DPF substrates.
- Application of probabilistic design tools and non-destructive evaluation (NDE) techniques to DPF ceramic substrates.
- Refinement of DPF service lifetime prediction models based on characterization of field returned filters.

Accomplishments

- Determined the thermal shock resistance of a second alternate substrate (Al_2TiO_5) DPF material.
- Refined the relationship between porosity and the elastic-fracture properties for diesel particulate filter substrates.
- Compared properties of cordierite and Al_2TiO_5 -based DPF materials.

Future Direction

- Continue to investigate the interaction and properties of washcoat, soot and substrate on properties of new and field tested DPFs.
 - Initiate characterization of the dynamic and static fatigue response of SiC DPFs.
-

Introduction

The EPA regulates the emissions of nitrogen oxides (NO_x) and particulate matter (PM) from diesel engines. Stringent regulation on PM went into effect in 2007. There are many technologies designed to reduce emissions from diesel engines; prominent among the technologies for PM control are diesel particulate filters (DPFs). A DPF is often a ceramic device that collects particulate matter in the exhaust stream. The high temperature nature of the ceramic withstands the heat of the exhaust and allows heating to break down (or oxidize) the particles inside. DPFs reduce emissions of PM, hydrocarbons, and CO by 60 to 90%.

Most DPFs consist of a ceramic honeycomb with hundreds of cell passages partitioned by walls (Figure 1). Each cell passage has a square cell opening at one end and is closed at the other end so that the cell passages are alternately closed at each end. The so-called checkerboard plugging structure forces the exhaust gases through the porous, thin ceramic honeycomb walls. When the gases carrying the PM flow through the fine pores of the walls, the PM is filtered out. High porosity values, in the range of 40-70%, heighten filtration efficiency to more than 90% and reduce gas-flow resistance for better engine performance.

The process of diesel PM collection continues while the engine is operating. The particles are collected on the ceramic walls and as a result, the backpressure of the system increases. The back pressure is reduced by oxidizing the trapped PM, aided by a catalytic reaction using exhaust gas heat at 400°C or more, into CO₂ and water vapor. This process, called regeneration, results in a cleaner filter. The regeneration process is dependent upon exhaust temperature, oxygen, NO_x content, time, and PM levels.

The key to the successful application of DPFs is to reliably regenerate the filter (e.g., to clean up the PM that the filter continues to trap or collect). Traditionally, combustion of soot is done in an oxygen atmosphere (air). In air, the soot will oxidize at ~500°C. However, this is not a typical operating temperature for diesel engine exhaust. Therefore, to oxidize soot in air, an active system—i.e., one that increases the temperature of the exhaust using some external heat source—is required. But if an active system is not carefully controlled, or if too much PM collects on the filter walls, the filters can experience

an “uncontrolled regeneration” where the temperature increases to 600°C or more, resulting in damage to the filter element.

A useful conceptual model for the prediction of reliability is the bathtub curve, which describes reliability-related phenomena of a component over its life cycle.¹ A schematic of the reliability bathtub curve is represented in Figure 2. It consists of three stages: the infant mortality phase is characterized by premature failures due to improper manufacturing or assembly, poor workmanship, or defects introduced during processing. The second stage of the curve corresponds to the useful life of the component and is characterized by a constant failure rate. In this regime, failures are typically associated with random, excessive loads. If sufficiently high safety factors are used during the design process, the magnitude of this failure rate should be negligible. The third stage of the bathtub curve is known as the wear-out phase, wherein the failure rate increases with time as a result of aging phenomena. Aging phenomena include thermal and mechanical fatigue, corrosion, creep deformation and environmentally assisted crack growth. The time at the onset of wear-out is often regarded as the useful life of the component.

The reliability bathtub curve can be used as a descriptor of how the failure rate of DPFs evolves over time. Infancy failures of DPFs could be related to manufacturing or process defects (large pores, inclusions, cracking) or defects introduced during assembly. Failures of DPFs during their useful life will be dictated by the intersection between the spectrum of thermomechanical loads and the distribution of DPF strengths. Such failures could result from excessive vibration, for example, or unwanted thermal excursions during transients associated with regeneration. Wear-out and degradation failures of DPFs could also be associated with the growth of microcracks by thermal fatigue, and assisted by the chemistry of the environment, and/or by chemical and microstructural changes in the material due to long-term exposure to elevated temperatures in the exhaust environment.

The objective of this project is to implement test techniques to characterize the physical and mechanical properties of ceramic DPF substrates and to develop analysis and inspection tools for assessing the reliability and durability of DPFs. The

developed tools and methods would allow the design of more durable and reliable DPFs. An important outcome of the development of the test methods is the ability to rank the relative thermal shock resistance of substrates in different conditions (catalyzed, soot loaded, field returned etc.) and of different candidate substrate materials.

Goals, Barriers, Relevance & Integration

In the study area of OVT's Advanced Combustion Engine research, the *goals* are (1) to improve commercial vehicle engine efficiency by at least 20% and (2) to achieve engine system cost, durability and emissions targets. This project addresses the three *barriers* related to the Emission Control System in this study area: Improving durability, numerous components and costly precious metal content. This project is *relevant* to the first goal as the understanding of the relationships of the material properties for the filter (and catalyst) substrates enables optimization of porosity, strength, elastic modulus, thermal conductivity, thermal expansion, etc. leading to thermal management and improved efficiency. This project supports clean diesel, which increases acceptance by the public. Larger acceptance, in turn, results in larger percentages of conversion to diesel, with the resulting reduction in petroleum usage/dependency upon foreign oil. This project is *relevant* to the second goal as the thrust is to characterize and improve the durability, resulting in the lowest overall cost and preventing emission release in service. This project is *integrated* within Vehicle Technologies program as it utilizes characterization tools acquired and maintained by the High Temperature Materials Laboratory (HTML) Program.

Approach

The design process for making DPFs that are durable and reliable includes a complex materials property optimization and selection process.² For example, the porosity of DPFs, which allows them to remove PM from the exhaust gas stream, has a deleterious effect on their mechanical and fracture strength. A higher porosity, though, decreases the engine backpressure and increases efficiency of the diesel engine. Designing mechanically reliable DPFs is important because these components will experience demanding thermo-mechanical

conditions during service. These include, for example, thermal shock resulting from rapid heating/cooling and thermal stresses that arise from temperature gradients.

Techniques to assess the elastic and fracture properties of virgin or unexposed DPF substrates have been identified, implemented and reported earlier.³ The test techniques were applied to rank the suitability of common candidate substrates for application in DPFs. The developed test techniques were applied to characterize field returned DPFs. The material properties responsible for the thermal shock resistance and mechanical property degradation in the various stages of the bathtub curve were determined. These properties include thermal expansion, thermal conductivity, heat capacity, density, porosity, elastic properties, strength, fracture toughness, and environmentally assisted crack growth at ambient and elevated temperatures, in air and in relevant environments.

The information generated will be used in turn to implement probabilistic design tools. Such probabilistic design methodologies are based on a combination of experimentally determined strength data, stress analyses of the component using a finite-element analysis, and selection of appropriate failure criteria. The durability (service life) of the component can also be predicted using this framework by considering the mechanisms that are responsible for the degradation of material strength, such as slow crack growth or creep. In addition, the service life predictions are refined based on the properties of the field returned filters.

Results

New Al_2TiO_5 -based DPFs were sectioned and samples were machined. The cross-section revealed a new honeycomb design with 2 channel sizes (see Figure 3; referred by some as an asymmetric cell size product). The larger channel size is on the inlet side and is designed to allow ash to accumulate in the DPF without plugging the channel. In Figure 4, the microstructure exhibits high porosity, rectangular-shaped grain and numerous microcracks as viewed with a SEM. X-ray diffraction indicates that the Al_2TiO_5 -based DPF material contains 3 phases: Al_2TiO_5 , a feldspar and an unidentified phase which is not mullite (see Figure 5). Figure 6a shows the large thermal expansion hysteresis through two heating and cooling cycles. The

behavior is due the large thermal expansion anisotropy Al_2TiO_5 ; the single crystal coefficients for thermal expansion (CTE, α), the sample contracts are $\alpha_a \approx 20\text{--}22$; $\alpha_b \approx 10\text{--}11$; $\alpha_c \approx -3 \times 10^{-6}/^\circ\text{C}$.¹ The CTE for polycrystalline Al_2TiO_5 without microcracks would be about $9.7 \times 10^{-6}/^\circ\text{C}$.⁴ Initially upon heat up, the expansion along the a and b directions within the grains is directed into the microcracks (closing them) such that only the contraction along the C direction is measured. Around 150°C , these cracks close enough that positive expansion occurs. During heating at the highest temperatures, these microcracks close and sinter together (heal), which is the origin of the different contraction path.^{5,6,7} As stresses build up between the grains on cooling, microcracks form or reform (refracture) noticeably starting at $\sim 700^\circ\text{C}$. At room temperature, there is a noticeable off-set from the initial length. This is due to the fact that the initial sample was sintered at a higher temperature than 1000°C . As such, some microcracks were healed and not refractured because the change in temperature ($1000\text{--}25=975^\circ\text{C}$) of the expansion test was less than that with the initial fabrication sintering temperature ($>975^\circ\text{C}$). Subsequent heating and cooling expansion curves are reproducible. The CTE curves in Figure 6b tell a similar story showing the CTE as negative and gradually increasing to just above $2 \times 10^{-6}/^\circ\text{C}$. The CTEs on cooling are initially due to the reduced number of microcracks. After about 700°C , the CTEs are similar. Reheating shows a near zero CTE until about 400°C . The higher final CTE on reheating is again attributed to the reduced number of microcracks relative to the initial heat. Excluding the initial heat, the average CTEs were 1.07 and $2.17 \times 10^{-6}/^\circ\text{C}$ in the direction parallel and perpendicular to the extrusion direction, respectively. In contrast for cordierite DPF material, the average CTEs were 0.48 and $0.99 \times 10^{-6}/^\circ\text{C}$ in the direction parallel and perpendicular to the extrusion direction, respectively. These low CTE values relative to the polycrystalline average above is due in large part to the large amount of porosity present (bulk density = 1.65 g/cc ; skeletal density (excludes open porosity) = 3.43 g/cc ; relative density = 48.2% or 51.8% porosity).⁸ Figure 7 shows the fracture toughness, K_{IC} , as measured with the double torsion technique, increasing as a function of strength. The strength values were corrected for the moment of inertia of

the honeycomb structure for three DPF materials. Both the fracture toughness and strength increase with decreasing porosity for the cordierite data. The lowest and highest strength samples have relative porosities of 68.1 and 50.2% , respectively. The mullite-based material possessed an unusual microstructure of interpenetrating needles, which results in the high strength and toughness with high porosity (63.1%).

Since fracture toughness measurements are easier to perform and require less material than strength testing, a new thermal shock parameter, $R_K=K_{IC}/\alpha E$, has been adopted as was discussed previously,⁹ where E is the Young's modulus. R_K is calculated from measured parameters and is tabulated for various DPF materials and conditions in Figure 8. This simplified analysis provides a means to compare and suggests the coated samples and samples that have been aged appear to be more thermal shock tolerant. Figure 9 is a Weibull plot for four point bend strengths¹⁰ of the Al_2TiO_5 -based DPF material. The plot suggests two flaw populations are present; a mean strength of 2.98 MPa was determined. Figure 10 shows the dynamic fatigue data. The Al_2TiO_5 -based DPF exhibits a lower strength than cordierite. Although not shown, neither material exhibited a specimen size effect nor a strong response to elevated temperature.

Summary

Mechanical and thermal shock characterization test procedures developed earlier were employed to measure properties in cordierite, aluminum titanate and mullite DPF materials. The aluminum titanate material was the focus here. Its microstructure is porous and microcracked with more "rectangular" grains, while cordierite possessed more plate-like grains (not shown). The Al_2TiO_5 -based DPF material has higher CTE than that of the cordierite DPF. The Al_2TiO_5 -based DPF material has lower strength than that of the cordierite DPF. No strong trends suggesting evidence of slow crack growth at ambient or elevated temperatures. The aluminum titanate material possessed a lot of strength variability requiring more testing before a conclusion can be drawn.

References

1. G. S. Wasserman, *Reliability Verification, Testing and Analysis in Engineering Design*, Marcel Dekker, New York, 2003.
2. J. Adler, "Ceramic Diesel Particulate Filters," *International Journal of Applied Ceramic Technology*, vol. 2, no. 6, pp. 429-439, 2005.
3. Propulsion Materials, 2007 Annual Progress Report, Vehicle Technologies Program, US DOE, Energy Efficiency and Renewable Energy, Office of Vehicle Technologies, Advanced Materials Technologies, E. J. Wall, R. A. Sullivan, J. L. Gibbs, Jan. 2008, www.ornl.gov/sci/propulsionmaterials/Reports.html.
4. Thomas & Stevens, *J. Br. Ceram. Trans.* 1989.
5. Buessem et. al., *Ceram. Age* 1952.
6. Bush & Hummel, *J. Am. Ceram. Soc.* 1958, 1959.
7. Morosin & Lynch, *Acta Cryst.* 1972.
8. Definitions given in ASTM D3766, ASTM International, West Conshohocken, PA.
9. T. R. Watkins, A. Shyam and E. Lara-Curzio, "Durability of Diesel Particulate Filters (CRADA No. ORNL-04-0692 with Cummins Inc.)," FY 2009 Progress Report for the Heavy Vehicle Propulsion Materials Program, December 2009.
10. ASTM C1674-08, Test Method B.

Presentations, etc.

1. T. R. Watkins, A. Shyam, E. Lara-Curzio, R. Stafford, "Microstructure and select mechanical properties of aluminum titanate diesel particulate filter (DPF) substrates," presented at the 34th International Conference on Advanced Ceramics and Composites Meeting held in Daytona Beach, FL, January 27, 2010.
2. T. R. Watkins, A. Shyam, H.T. Lin, E. Lara-Curzio, R. Stafford, T. Yonushonis, "Durability of Diesel Engine Particulate Filters," presented at the DOE 2010 Vehicle Technologies Annual Merit Review and Peer Evaluation Meeting, Washington, D.C., June 10, 2010.

ORNL and Cummins personnel traveled to Daytona Beach, FL for a meeting of the ASTM C28.01 Mechanical Properties and Reliability committee on January 24, 2010 which, in part, provides standards for the DPF community.

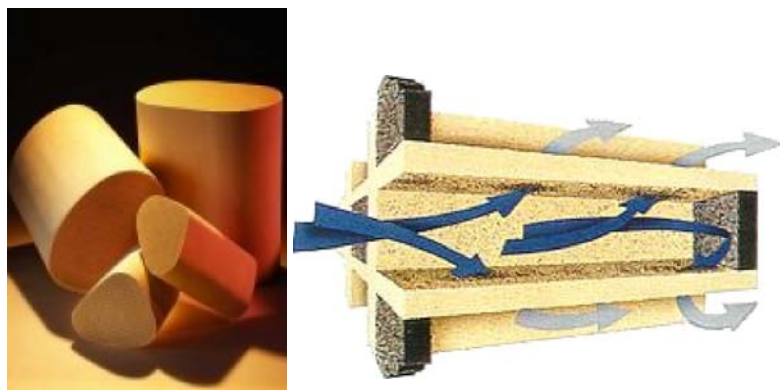


Figure 1. Cordierite-based DPFs.

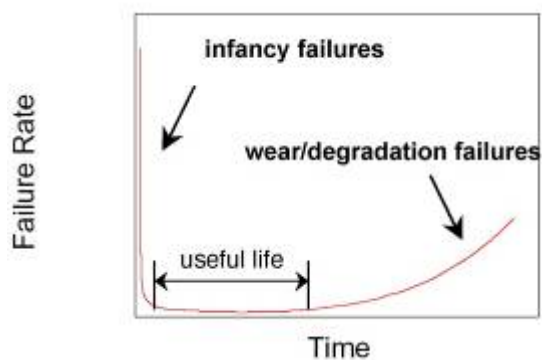


Figure 2. Reliability bathtub curve.

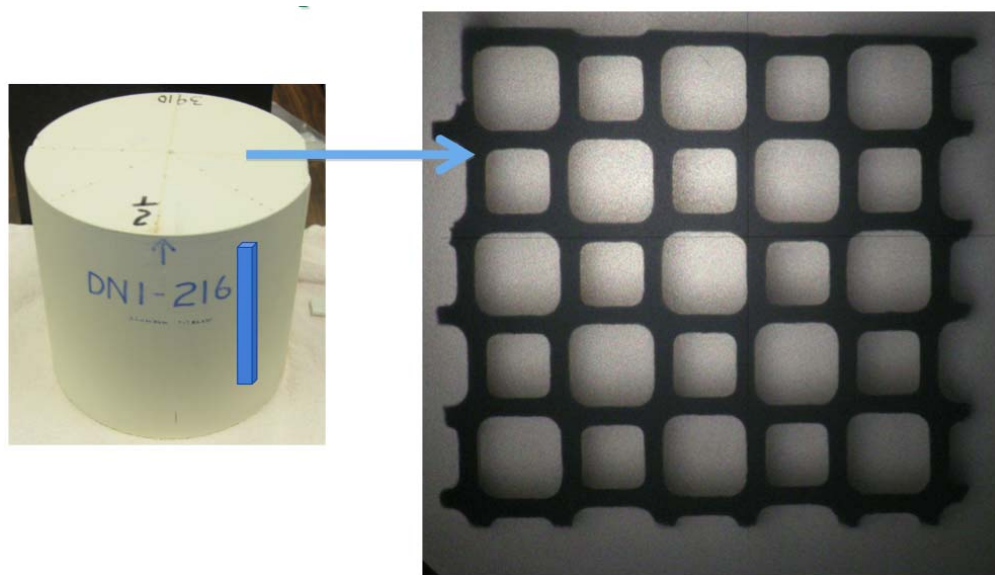


Figure 3. (left) An Al_2TiO_5 -based DPF, nominal dimensions: 26.5 X 25.5 cm (D X H). (right) expanded view of the cross-section showing two channel sizes. The nominal dimensions of the cells are 1.4 x 1.4 and 1 x 1 mm.

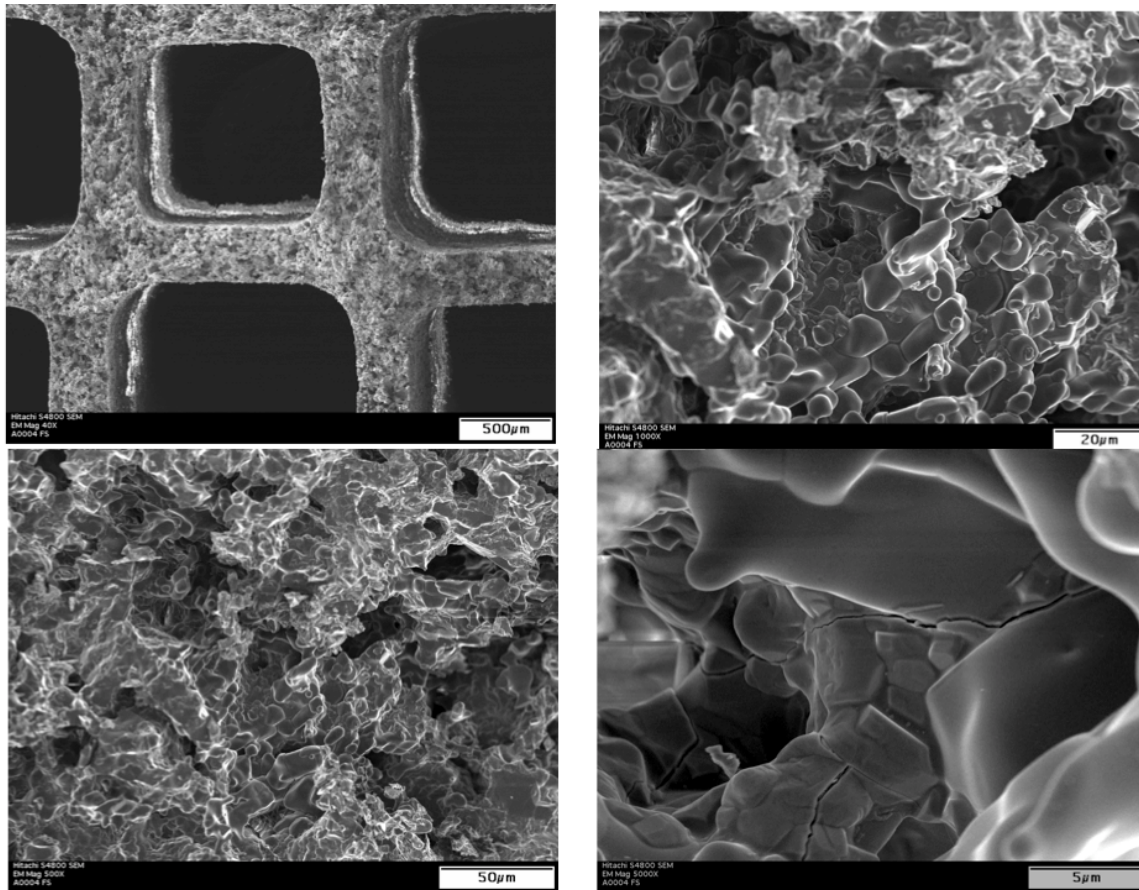


Figure 4. SEM micrographs of the Al_2TiO_5 -based DPF showing rectangular grains in a porous, microcracked microstructure.

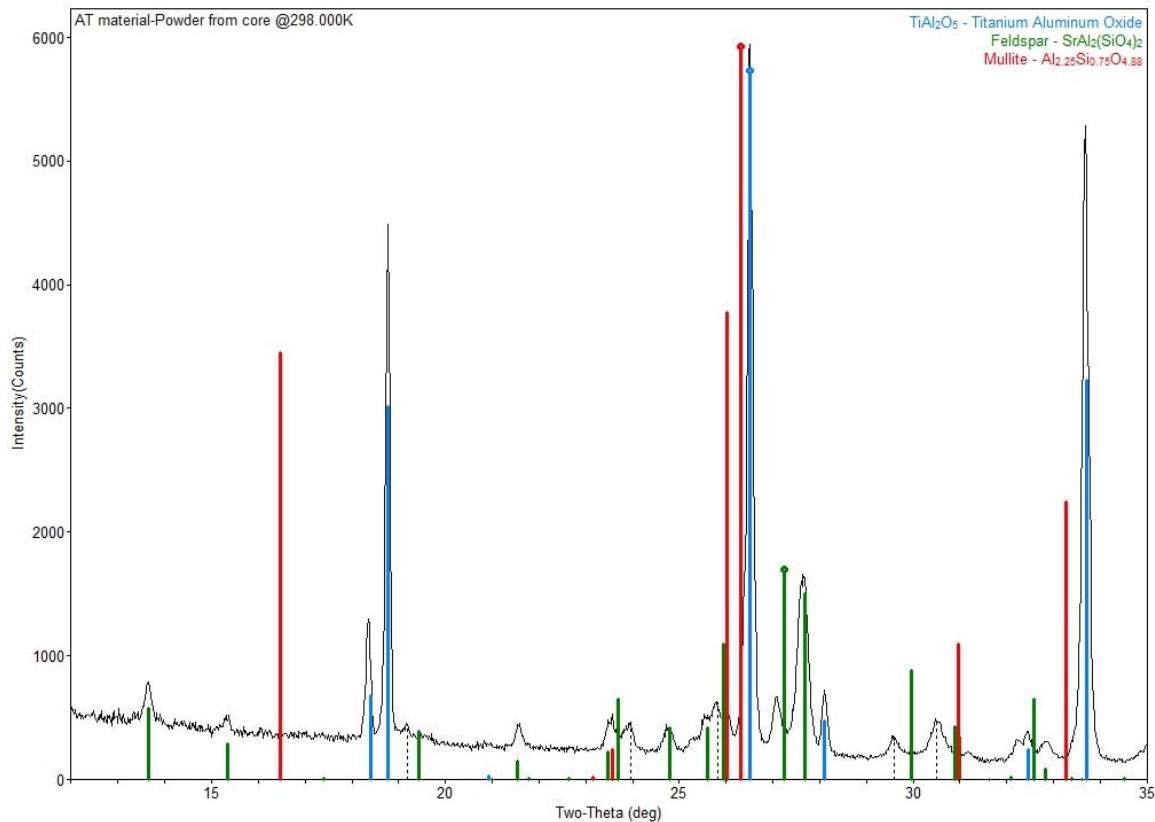


Figure 5. The x-ray diffraction pattern the Al_2TiO_5 -based DPF material.

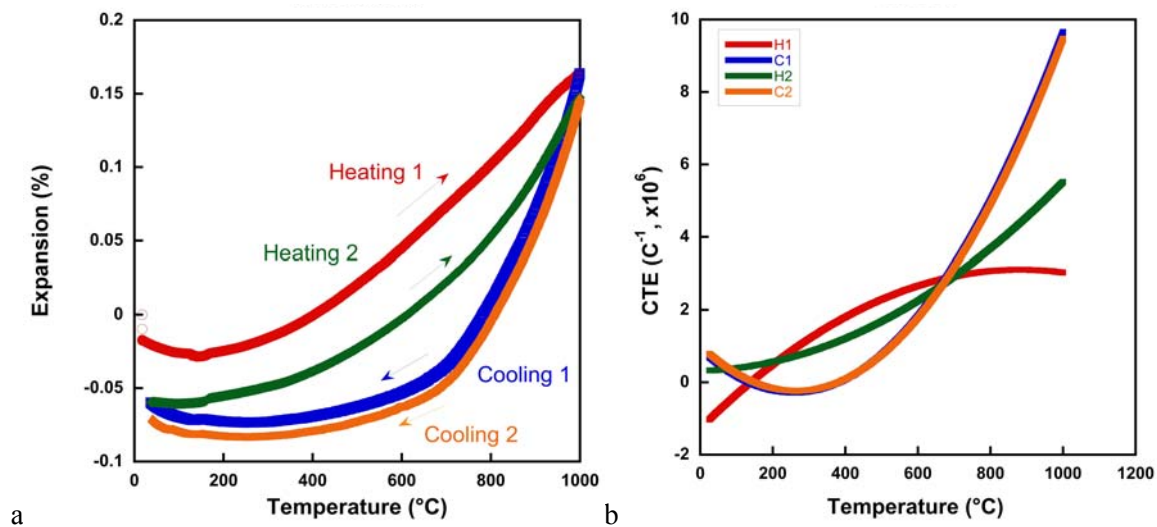


Figure 6. The expansion (left) and thermal expansion coefficient (right) curves as a function of temperature of Al_2TiO_5 -based DPFs.

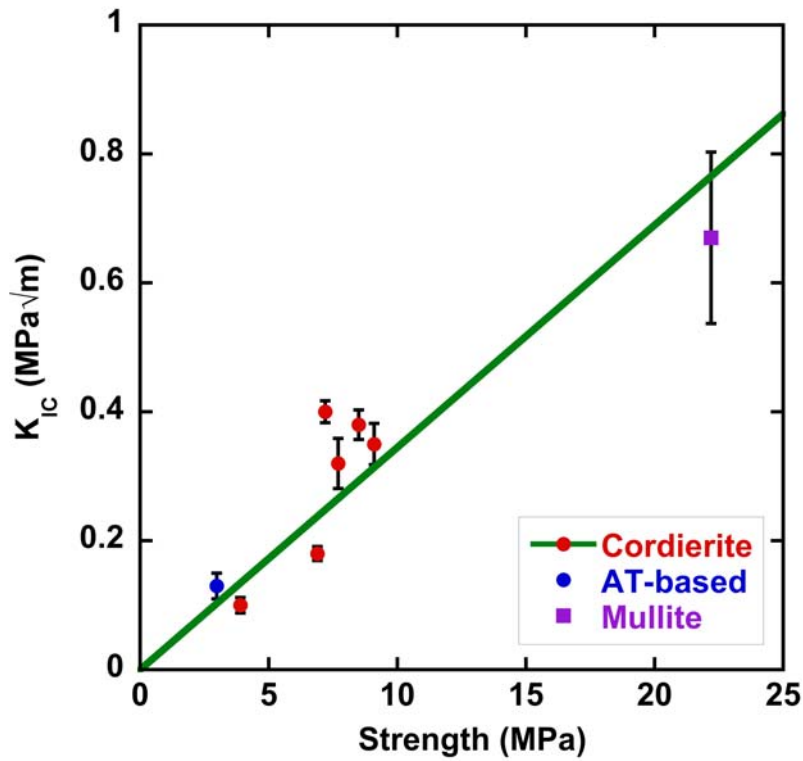


Figure 7. The fracture toughness as a function of strength for three DPF materials.

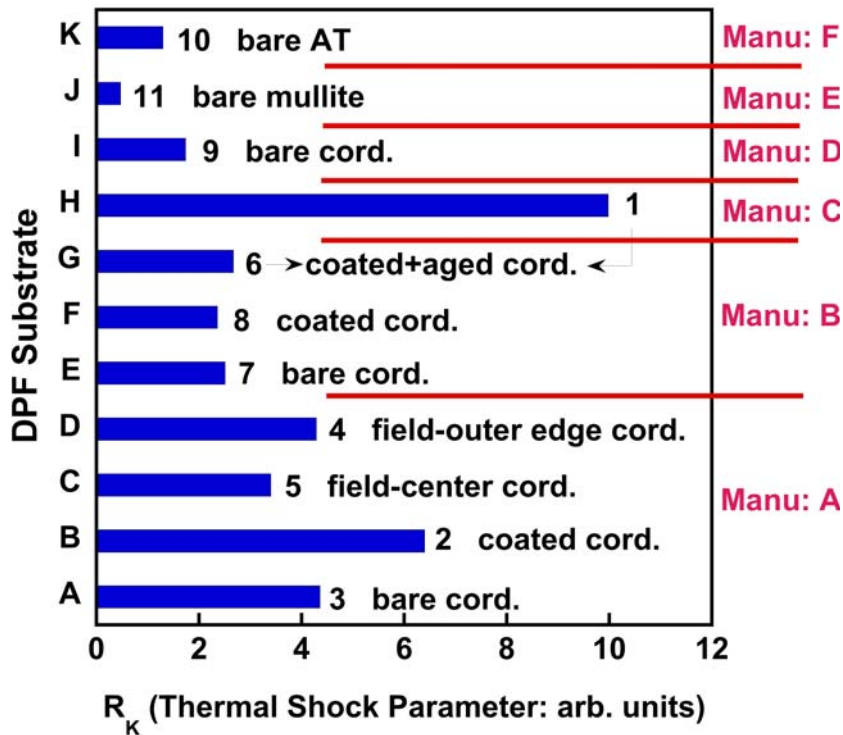


Figure 8. The thermal shock parameter, R_K , for the various DPF examined.

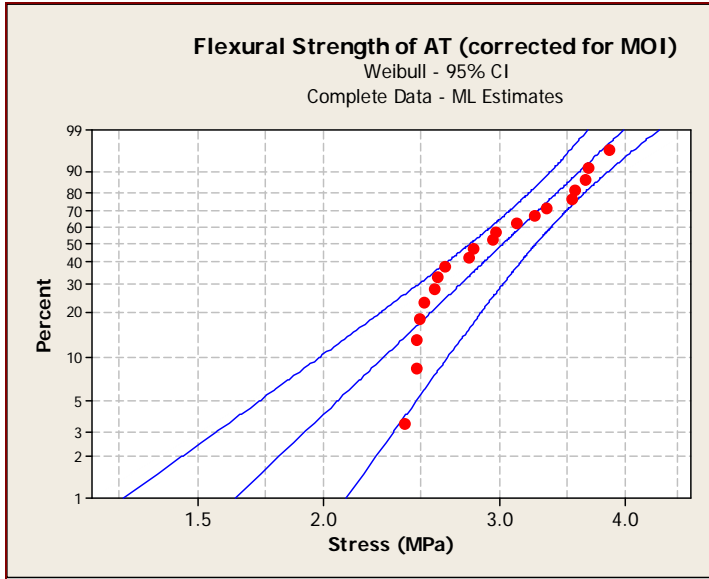


Figure 9. The Weibull plot for the flexural strengths of Al_2TiO_5 -based honeycombs corrected for the moment of inertia.

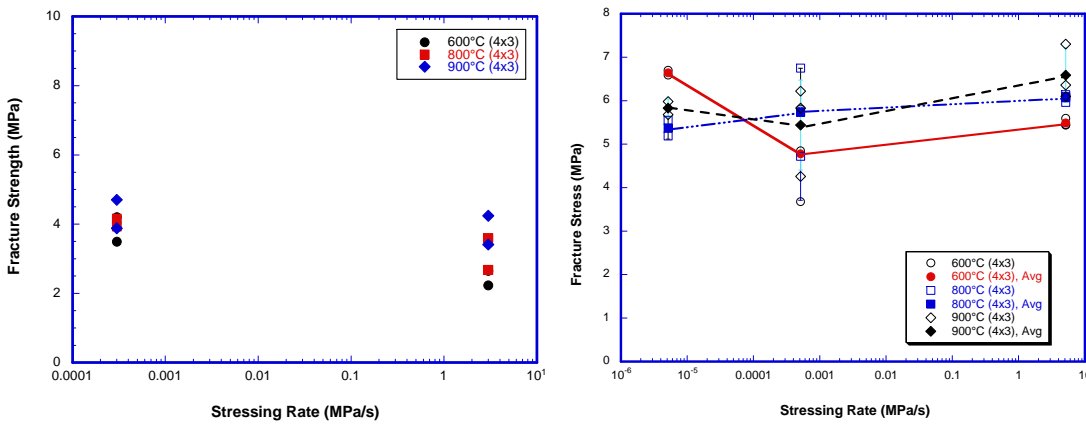


Figure 10. The flexural strength as a function of stressing rate and temperature for the Al_2TiO_5 -based (left)

Agreement 10635 - Catalysis by First Principles

C. K. Narula, L. F. Allard, M. Moses-DeBusk, M. Stocks, X. Yang
 Oak Ridge National Laboratory
 P.O. Box 2008, MS 6116
 (865)574-8445, narulack@ornl.gov

DOE Technology Manager: Jerry L. Gibbs
 (202) 586-1182; fax: (202) 586-1600; e-mail: Jerry.gibbs@ee.doe.gov
 Field Technical Manager: D. Ray Johnson
 (865) 576-6832; fax: (865) 574-6098; e-mail: johnsondr@ornl.gov

Contractor: Oak Ridge National Laboratory, Oak Ridge, Tennessee
 Contract No.: DE-AC05-00OR22725

Objective

The objective of this work is to search for durable emission treatment catalysts (LNT, TWC, OC) from a protocol based on

- an integrated approach between computational modeling and experimental development,
- design and testing of new catalyst materials to rapidly identify the key physiochemical parameters necessary for improving the catalytic efficiency of these materials.

Approach

- Theoretical Modeling
 - Density functional theory-based first-principles calculations
 - Optimization of Pt clusters supported on alumina
 - Interaction of CO, NO_x, and HC with Pt clusters supported on alumina
- Experimental System
 - Synthesize Pt Nanoclusters on morphologically diverse alumina supports
 - Evaluate systems for CO, NO_x, HC oxidation individually and in combination
 - Understand non-structural changes in catalyst under operating conditions and correlating the changes to performance.

Accomplishments

- We have previously shown by theoretical models that nano-particles of Pt are stable as oxides and metallic particles are poorer catalysts than oxides. In this report, we describe theoretical studies of platinum supported on θ -alumina.
 - We optimized a 180 atom charge neutral 010 slab which is 2-cell wide and 4 cell deep and a 420 atom slab made by combining 2 x 3 x 3 cells and found that the preferred position of Pt supported on either of the two slabs is identical. We found that Pt, Pd, Au, and Ag single atom adsorption is in the order of Pt>Pd>Au>Ag.
 - The bonding of platinum with θ -alumina is different from that reported for α - or γ -alumina. Pt is a d9s1 atom and after interaction with θ -alumina, it does not show an unpaired electron suggesting d8 structure with $d\pi - p\pi$ backbonding where 2 electron pairs from two adjacent oxygen atoms is donated to platinum.
 - There is practically no difference in total energy of 2 independent Pt atoms or bonded Pt atoms on alumina 010 slab suggesting that there is no energy barrier to agglomeration and particle growth for sub-nanometer platinum on alumina surface

- There is practically no difference in total energy of independent Pt and Pd atoms or bonded Pt-Pd atoms on alumina 010 slab. Furthermore, there is no difference in Pt atom bonded to Pt-O or Pd-O on alumina 010 slab.
- We have synthesized Pt-Pd nano-particles to experimentally validate our theoretical study on Pt-Pd subnanometer particles.
 - Our results show that hydrothermal aging of samples leads to particle size growth which increases at 900C. In contrast with platinum, the extremely large particles (~300-400 nm) are not observed.
 - This result suggests that palladium prevents extreme sintering of platinum at high temperatures.

Future Direction

- Understanding of the structures of nano-clusters on support.
 - Theoretical models to understand cluster oxidation state (oxidized, reduced, in equilibrium), dependence on cluster size, and the kinetics of oxidation
 - Role of palladium on platinum stabilization
- Reactivity of the clusters
 - Theoretical studies of CO, NO_x, and HC reaction on supported clusters
- Guided by our results, the synthesis and evaluation of new durable supported catalysts for lean NO_x catalysts and other systems such as TWC, OC for diesel etc.

Introduction

This research focuses on an integrated approach between computational modeling and experimental development, design and testing of new catalyst materials, that we believe will rapidly identify the key physiochemical parameters necessary for improving the catalytic efficiency of these materials.

The typical solid catalyst consists of nano-particles on porous supports. The development of new catalytic materials is still dominated by trial and error methods, even though the experimental and theoretical bases for their characterization have improved dramatically in recent years. Although it has been successful, the empirical development of catalytic materials is time consuming and expensive and brings no guarantees of success. Part of the difficulty is that most catalytic materials are highly non-uniform and complex, and most characterization methods provide only average structural data. Now, with improved capabilities for synthesis of nearly uniform catalysts, which offer the prospects of high selectivity as well as susceptibility to incisive characterization combined with state-of-the science characterization methods, including those that

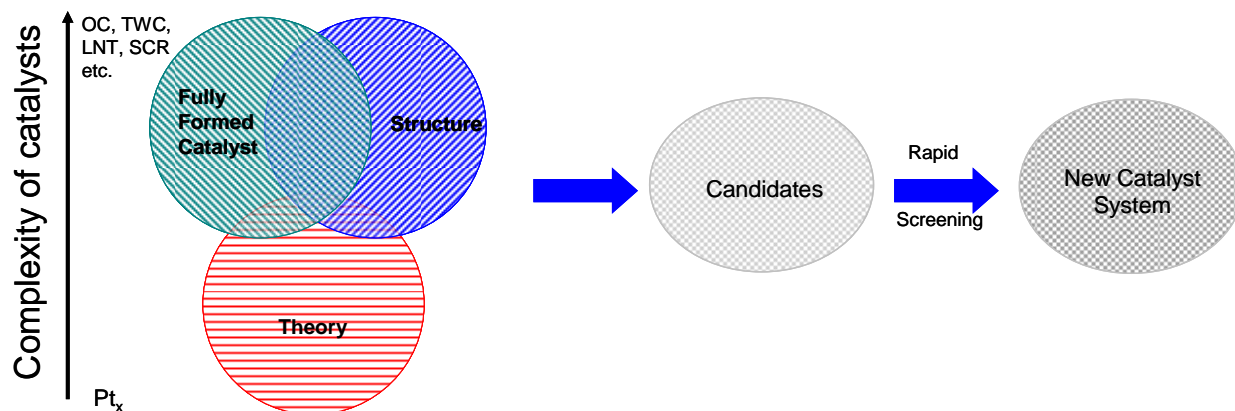
allow imaging of individual catalytic sites, we have compelling opportunity to markedly accelerate the advancement of the science and technology of catalysis.

Computational approaches, on the other hand, have been limited to examining processes and phenomena using models that had been much simplified in comparison to real materials. This limitation was mainly a consequence of limitations in computer hardware and in the development of sophisticated algorithms that are computationally efficient. In particular, experimental catalysis has not benefited from the recent advances in high performance computing that enables more realistic simulations (empirical and first-principles) of large ensemble atoms including the local environment of a catalyst site in heterogeneous catalysis. These types of simulations, when combined with incisive microscopic and spectroscopic characterization of catalysts, can lead to a much deeper understanding of the reaction chemistry that is difficult to decipher from experimental work alone.

Thus, a protocol to systematically find the optimum catalyst can be developed that combines the power of theory and experiments

for the atomistic design of catalytically active sites and can translate the fundamental insights

gained directly to a complete catalyst system that can be technically deployed.



Although it is beyond doubt computationally challenging, the study of surface, nanometer-sized, metal clusters may be accomplished by merging state-of-the-art, density-functional-based, electronic-structure techniques and molecular-dynamic techniques. These techniques provide accurate energetics, force, and electronic information. Theoretical work must be based on electronic-structure methods, as opposed to more empirical-based techniques, so as to provide realistic energetics and direct electronic information.

A computationally complex system, in principle, will be a model of a simple catalyst that can be synthesized and evaluated in the laboratory. It is important to point out that such a system for experimentalist will be an idealized simple model catalyst system that will probably model a “real-world” catalyst.

Thus it is conceivable that “computationally complex but experimentally simple” system can be examined by both theoretical models and experimental work to forecast improvements to obtain optimum catalyst systems.

Approach

The theoretical modeling is based on DFT studies of Pt supported on θ -alumina. We have

completed the study of single atoms of Pt, Pd, Au, and Ag supported on 010 surface of θ -alumina. We have initiated the DFT study of larger clusters of Pt supported on θ -alumina. Our experimental studies suggest that CO oxidation is identical on both Pt supported on γ -alumina and θ -alumina. This suggests that the catalyst site structure is probably identical in both catalysts.

Experimentally, we have synthesized a series of Pt clusters/particles of different sizes supported on γ -alumina and evaluated the catalysts NO oxidation activity. We monitored the microstructural changes throughout the NO oxidation process to correlate microstructure and activity. We have also carried out preliminary study of HC oxidation processes.

Guided by the theoretical models and experimental results of our study, we will anticipate that we will initiate our work on the synthesis of a new set of catalyst materials with higher durability under operating conditions in FY10.

Results

Previously, we have carried out experimental studies on Pt nanoclusters and nanoparticles to correlate their CO, NO and HC oxidation

activity with nanostructural changes. We employed ORNL *ex-situ* reactor¹ and scanning transmission electron microscopy (STEM) using the HD-2000 and HF-3300 to study the nanostructural changes in catalysts upon exposure to CO and NO oxidation condition. It is important to note that the *ex-situ* reactor permits duplication of the oxidation conditions obtained on the bench-top reactor.

Our theoretical studies on single platinum atoms supported on θ -alumina slab shows that the platinum atom is in zero oxidation state. This result is very different from that reported in literature on single platinum atoms supported on α -alumina or simplified models of γ -alumina where a platinum atom generally has an unpaired electron. This also means that mechanism of CO, NO_x, or HC oxidation on Pt(0) will be different from that on Pt(I) or Pt(II). We plan to carry out first principle studies of CO oxidation on Pt atoms supported on θ -alumina slab.

Since our experimental work has already shown that the distribution of platinum on γ -alumina and θ -alumina is almost identical, and the surface properties and CO oxidation of both catalysts are identical, we propose that Pt supported on θ -alumina is a better model for Pt supported on γ -alumina than Pt supported on α -alumina or simplified models of γ -alumina.

Our results on large platinum agglomerates and their activity are described in the following sections so are our preliminary studies to develop hydrothermally stable platinum based catalysts:

THEORETICAL STUDIES OF Pt/ θ -Al₂O₃

We employed Vienna *Ab Initio* Simulation Package (VASP) to carry out first principle total energy calculation within the supercell DFT framework.¹⁻³ Generalized gradient approximation (GGA) in the Perdew-Wang-91 form was employed for electron exchange and correlations.^{4,5} The Kohn-Sham equations were solved using the projector augmented wave (PAW) approach for describing electronic core

states.^{6,7} The plane-wave basis set was truncated at a kinetic energy cut-off of 500eV.

Single Atoms on θ -alumina (010) surface

We have previously summarized the results on DFT calculation of bulk θ -alumina, θ -alumina slab, and a single platinum atom on a θ -alumina slab. We also reported preliminary results on a charge neutral supercell of 420 atoms combining 2 x 3 x 3 cells and found the location of platinum to optimize in an environment identical to the one in 180-atom supercell [Figure 1]. In addition, we optimized the single Ni, Pd, Cu, Ag, or Au atom adsorbed on the [010] surface of θ -alumina and found the adsorption energies for Pt, Pd, Au, and Ag are in the order of Pt>Pd>Au>Ag and are -62.29, -44.84, -20.21, and -13.23 Kcal/mole, respectively suggesting that the absorption of these atoms is exothermic.

The analysis of projected local density of state [LDOS] leads to a different bonding picture than that reported in literature for α -alumina or γ -alumina where platinum has unpaired electrons. The platinum d orbitals and s orbitals are occupied resulting in no unpaired electrons. The interaction of platinum orbitals with O p states results in O p_y orbitals shifting to lower energy. Bonding with two neighboring oxygen atoms and charge transfer to oxygen p_y orbitals result in no unpaired electron on platinum atom. Formally, platinum is in zero oxidation state with d¹⁰ structure and is bonded to two oxygen atoms. The implication of this important result is that the mechanism of CO, NO, or HC oxidation on sub-nanometer particles such as single atoms can be expected to be different from the large particles normally examined by DFT.

The palladium atom on θ -alumina 010 also exhibits bonding picture which is different from that reported for Pd on α -alumina. The configuration of a palladium atom is d¹⁰s⁰, and it has higher energy valence d and s states than those for platinum. For Pd atoms, the Pd-O bond distances are 2.227 Å and 2.201 Å with an O-M-O angle of 134.54°. The distance from sub-surface Al is 2.49 Å and the Pd atom sits 0.86 Å above the cell surface. As expected, these distances are slightly larger than those for

platinum atom but the bonding are identical to Pt atoms. For Au atoms, the Au-O bond distances are 2.45 Å and 2.69 Å with an O-M-O angle of 107.34°. The distance from sub-surface Al is 2.976 Å and nearest surface Al is 2.706 Å. The Au atom sits 1.519 Å above the cell surface. The Ag-O bond distances for Ag/ θ -alumina are 2.483 and 2.549 Å with an O-Ag-O angle of 108.5°. The distance from sub-surface Al is 3.08 Å and from closest surface Al is 3.09 Å.

Both Ag and Au are $d^{10}s^1$ atoms and the energy of their valence d and s orbitals are lower than that of valence orbitals of Pt. For Au atoms, the Au-O bond distances are 2.45 Å and 2.69 Å with an O-M-O angle of 107.34°. The distance from sub-surface Al is 2.976 Å and nearest surface Al is 2.706 Å. The Au atom sits 1.519 Å above the cell surface. The Ag-O bond distances for Ag/ θ -alumina are 2.483 and 2.549 Å with an O-Ag-O angle of 108.5°. The distance from sub-surface Al is 3.08 Å and from closest surface Al is 3.09 Å. Since there is a magnetic moment of 1.0 associated with both atoms, they must be formally in oxidation state 2 (d^9 species). This is supported by the fact that s orbital is empty and d orbitals exhibit polarization and partial occupancy. This bonding picture is also different from Au or Ag on α -alumina where Au is bonded to an oxygen atom and Ag occupies a three-fold hollow site. The bonding picture Au/ α -alumina suggest that Au orbitals are split by interaction with oxygen but remain filled. The s orbital also remains filled. Thus Au-O interaction is proposed to be a weak filled-filled one. The interaction of silver, on the other hand, is proposed to be an ionic one where Ag s states are vacated and do not participate in bonding.

Considering the facts (reported previously) that the Pt supported on γ -alumina and θ -alumina exhibit identical bimodal distribution of platinum (single atoms and 10-20 atom clusters) when examined by ACEM and have identical CO oxidation activity, we suggest that platinum on θ -alumina is a better representative of platinum on γ -alumina than the models reported in literature (platinum on α -alumina or platinum on simplified models of γ -alumina). As described previously, the structure of platinum

on γ -alumina is uncertain due to uncertainty of the structure of γ -alumina.

Multiple Pt atoms and Agglomerates on θ -alumina (010) surface

We also initiated the DFT structural studies of 2-atom and larger clusters of Platinum on a charge neutral supercell of 420 atoms combining 2 x 3 x 3 cells. The single platinum atom prefers the location on both supercells that are identical in local environment and have identical adsorption energies. There are three additional identical locations on 2x3x3 supercell for platinum and we have optimized this supercell with platinum atom at all four positions [Figure 2]. The impetus for this comes from our interest in comparing theoretical model with experimentally observed Pt agglomerates on alumina [Figure 3]. The measurement of Pt-Pt distances in a Pt agglomerate shows that most of the platinum atoms are not bonded to each other since Pt-Pt bonding distance is generally 2.5 Å. Several of Pt atoms are even outside Pt-O-Pt bond distance which is ~3.2 Å (e.g. Pt-O and Pt-Pt distance in a complex 2.1 and 3.227 Å respectively and Pt-O-Pt angle is 100.6; Inorg. Chem. 27 (1988) 956). While some of the atoms are within Pt-O-Pt distance, most of them are too far from each other to have even Pt-O-Pt interaction. Interestingly, the calculated bond distance between Pt1-Pt3 is 5.7 Å showing that the shortest non-bonded Pt-Pt bond distance is 5.7 Å for two platinum atoms on 010 θ -alumina surfaces.

Each of the four platinum atoms is bonded to 2 neighboring oxygen atoms and the bond distances from these oxygen atoms are summarized in Table 1.

Table 1: Platinum-Oxygen bond distances

	Oxygen	Oxygen
Pt1	2.192	2.132
Pt2	2.203	2.129
Pt3	2.135	2.214
Pt4	2.138	2.214

In order to build a large cluster we attempted to optimize platinum 2 bonded to platinum 1. There is no significant difference (1.27kcal/mole) between the energy of configurations where platinum 1 is bonded to platinum 2 or both platinum atoms occupy independent but identical sites. It is important to point out that, experimentally, we do not observe 2-10 atom clusters but 10-20 atom agglomerates are common. Interestingly, a platinum atom bonded to platinum 1 and platinum 3 is not energetically favorable over a platinum atom bonded to platinum 1 and an independent platinum 3 configuration shown in Figure 2 (right). While platinum 1 and 3 are bonded to two neighboring oxygen atoms, the platinum 2 atom is only bonded to platinum 1. The bonding analysis for this configuration is in progress and will be presented in the next quarterly report.

Pt-Pd system on θ -alumina (010) surface

The bonding of platinum on alumina surface is identical to that of single atom and the presence of an independent palladium atom has no impact. [Figure 4, left]. When palladium atom is placed in the vicinity of platinum atom [Figure 4, right] the Pt-Pd bond distance is 2.76 and palladium is not bonded to any other atom. Platinum oxygen bond distances are 2.12 and 2.2 Å. The energy difference between one platinum and one palladium atom on an alumina surface in independent locations vs. Pt-Pd bonded location is 0.6 Kcal/mole.

We also carried out calculations of platinum atom bonded to oxygen atoms which in turn are bonded to two surface platinum or palladium atoms. There was practically no difference in adsorption energy of the platinum atom in both configurations.

This study suggests that alloying of platinum with palladium does not lead to energetically favored structure as compared with platinum subnanometer clusters.

EXPERIMENTAL STUDIES

In order to compare the results of theoretical studies on palladium substituted platinum agglomerates, we have synthesized and characterized platinum-palladium agglomerates supported on γ -alumina substrates.

We followed the procedure described by Toshima *et al.* (J. Chem. Soc. Faraday Trans., 1993, 89, 2537-2543) for the synthesis of homogeneous Pd-Pt nanoclusters with different Pt:Pd ratios, around 1.5 nm, employing poly(N-vinyl-2-pyrrolidone) (PVP, average MW 40,000) to stabilize nanoparticles.

Pd-Pt (1:4) on Al_2O_3 – PVPPdPt14: PdCl_2 (0.0160 g, 0.090 mmol) was dissolved in 170 mL ethanol and filtered after 24h stirring followed and 1.003 g PVP40 was added to the filtrate. A water solution (170 mL) of hexachloroplatinic(IV) acid (0.171 g, 0.368 mmol) and 1.003 g PVP was added to the Pd ethanol solution. The combined yellow ethanol/water solution was refluxed for an hour, resulting in a dark brown transparent solution. 4 g $\gamma\text{-Al}_2\text{O}_3$ was added to the resulting dark brown solution. The slurry was stirred for 48 hours, centrifuged, and washed to obtain grey powder. The grey powder was dried at room temperature (overnight), and calcined at 350°C for 1 hour (1°C/min). Elemental Analysis shows a Pd to Pt ratio of 0.22: Pd 0.06%, Pt 0.52%.

Pd-Pt (1:1) on Al_2O_3 – PVPPdPt11: PdCl_2 (0.0471 g, 0.265 mmol) was dissolved in 200 mL ethanol and filtered after 24 h stirring and 1.180 g PVP40 was added to the filtrate. A water solution (200 mL) of hexachloroplatinic(IV) acid (0.125 g, 0.269 mmol) and 1.180 g PVP was added to the Pd ethanol solution. The combined yellow ethanol/water solution was refluxed for an hour, resulting in a dark brown transparent solution. 4 g $\gamma\text{-Al}_2\text{O}_3$ was added to the resulting dark brown solution. The slurry was stirred for 48 hours, centrifuged, and washed to obtain grey powder. The grey powder was dried at room temperature (overnight), and calcined at 350°C for 1 hour (1°C/min). Elemental Analysis shows a Pd to Pt ratio of 0.86: Pd 0.52%, Pt 0.43%.

Pd-Pt (4:1) on Al₂O₃ – PVPPdPt41: PdCl₂ (0.0914 g, 0.515 mmol) was dissolved in 240 mL ethanol and filtered after 24h stirring 1.432 g PVP40 was added to the filtrate. A water solution (240 mL) of hexa-chloroplatinic(IV) acid (0.060 g, 0.129 mmol) and 1.432 g PVP was added to the Pd ethanol solution. The combined yellow ethanol/water solution was refluxed for an hour, resulting in a dark brown transparent solution. 4 g γ -Al₂O₃ was added to the resulting dark brown solution. The slurry was stirred for 48 hours, centrifuged, and washed to obtain grey powder. The grey powder was dried at room temperature (overnight), and calcined at 350°C for 1 hour (1°C/min). Elemental Analysis shows a Pd to Pt ratio of 3.77: Pd 0.59%, Pt 0.64%.

The TEM images of all three PdPt nanoclusters supported on θ -alumina together with their statistical size distribution curve are shown in Figure 3. The size distributions of all three PdPt nanocluster species exhibit a distribution in 1-6 nm range and are centered at 2.5 nm.

Hydrothermal aging of supported Pt-Pd nanoclusters: All three samples were subjected to hydrothermal aging protocol reported by Graham et al (Catalysis Letters, 2007, 116, 1-8). A 0.7 g of PdPt/alumina sample was treated under a flow (5L/min) of N₂, O₂ (5%) and H₂O (10%) for 3 hours at a series of temperatures (500°C, 600°C, 750°C and 900°C), held for 2.5 hours, and cooled under pure N₂.

The TEM studies of aged PVPPdPt41 (Figure 4) samples show that particle size grows gradually as temperature increases. After aging at 500°C, the particles had grown somewhat with distribution now centered at 3.5 nm. Aging at 600°C and 750°C led to rapid growth in the size of particle and distributions centered at ~7 nm and ~ 14 nm respectively were observed. The increase in aging temperature to at 900°C results in drastic increase in particle size with distribution centered at ~35 nm.

We are synthesizing trans-[(NH₃)₂Pt(C₅H₆N₃O)₂PdCl](NO₃)•H₂O (Lippert et al., J. Am. Chem Soc., 113 (1991) 5129)

which contains a Pt-Pd bond to prepare subnanometer Pt-Pd agglomerates on alumina.

Conclusions

Theoretical studies on single atoms show that the bonding of platinum with θ -alumina is different from that reported for α - or γ -alumina. Pt on θ -alumina is in zero oxidation state while it is d₉s₁ on both α - or γ -alumina. Nickel and palladium atoms also show similar bonding patterns. Interestingly, the agglomeration of single atoms can also be modeled on 010 θ -alumina surface and our studies show that there is no significant barrier that prevents independent platinum atoms to bond and form large particles.

Experimentally, we have found that preformed nanoparticles of platinum-palladium alloys supported on alumina are more stable than pure platinum nano-particles. While both platinum and platinum-palladium alloy particles undergo Oswald ripening, the extremely large particles commonly observed after hydrothermal sintering at 900°C are not seen for platinum-palladium alloys. Theoretical modeling studies are in progress to understand this phenomenon since the experimental observations do not match with our theoretical studies on supported single atoms described in this report.

References

1. Kresse, G.; Hafner, J.; Phys. Rev. B, **1993**, 47, 558.
2. Kresse, G.; Hafner, J.; Phys. Rev. B, **1993**, 48, 13115.
3. Kresse, G.; Hafner, J.; Phys. Rev. B, **1994**, 49, 14251.
4. Perdew, J.P., Chevary, J.A.; Vosko, S.H.; Jackson, K.A.; Pederson, M.R.; Singh, D.J. *Phys. Rev. B*, **1992**, 46, 6671.
5. Perdew, J.P., Chevary, J.A.; Vosko, S.H.; Jackson, K.A.; Pederson, M.R.; Singh, D.J. *Phys. Rev. B*, **1993**, 48, 4978.
6. Bloch, P.E. *Phys. Rev. B*, **1994**, 50, 17953.
7. Kresse, G.; Joubert, D. *Phys. Rev. B*, **1999**, 59, 1758.

Presentations and Publications (FY 10)

1. Narula, C.K.; Chen, X.; Stocks, M.G.; DeBusk, M.M.; Allard, L.F.; Zero oxidation state platinum atom supported on θ -alumina, Physics Review Letters (to be submitted)
2. Narula, C.K.; Chen, X., Stocks, M. G.; First-principles studies of the structure and bonding of metal atoms supported on θ -alumina, American Chemical Society Meeting, San Francisco, March 2010.
3. Narula, C.K.; Chen, X.; Stocks, M.G.; DeBusk, M.M.; Allard, L.F.; First – principles and experimental studies of the sub-nanometer platinum atoms supported on θ -alumina, American Chemical Society Meeting, Boston, August, 2010
4. Narula, C.K.; DeBusk, M.M.; Chen, X.; Stocks, M. G.; Yang, X.; Allard, L.F; Catalyst by Design: theoretical, nanostructural, and experimental studies of emission treatment catalysts, DEER 2010, Detroit, MI Sept. 2010.

Figures

- Figure 1:** Pt location on a 2x4x2 (left) and 2x3x3 (right) supercells of 010 surfaces.
- Figure 2:** Platinum atoms on 2x3x3 supercell.
- Figure 3:** Platinum agglomerates on θ -alumina.
- Figure 4:** Pt and Pd atoms on θ -alumina surface 2 x 3 x 3 slab (left – independent, right – bonded).
- Figure 5:** Pt-O-Pt bonds of platinum atom bonded to oxygen atoms on platinum atoms on 2x3x3 supercells of 010 surfaces.
- Figure 6:** TEM of Pd-Pt (1:4) (left), Pd-Pt (1:1) (middle), and Pd-Pt (4:1) (right) on γ -Al₂O₃.
- Figure 7:** TEM Pd-Pt (4:1) on γ -Al₂O₃ after hydrothermal aging after aging at 500, 600, 750, and 900C

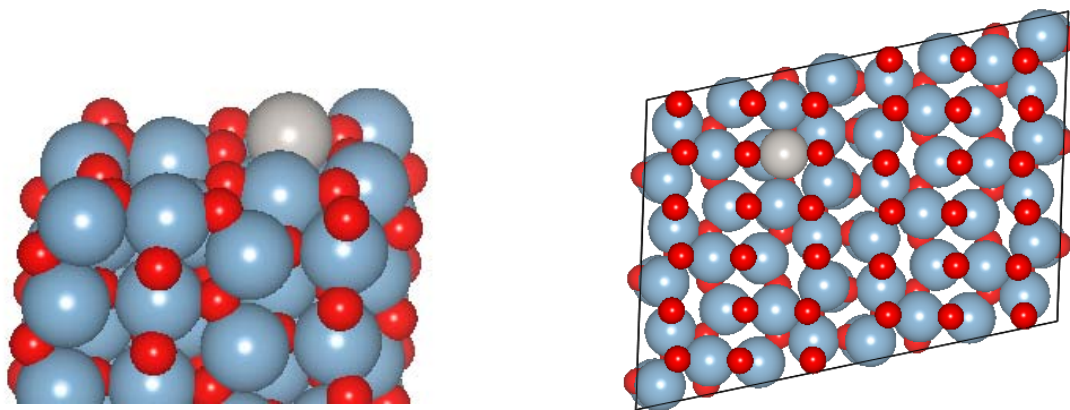


Figure 1: Pt location on a 2x4x2 (left) and 2x3x3 (right) supercells of 010 surfaces.

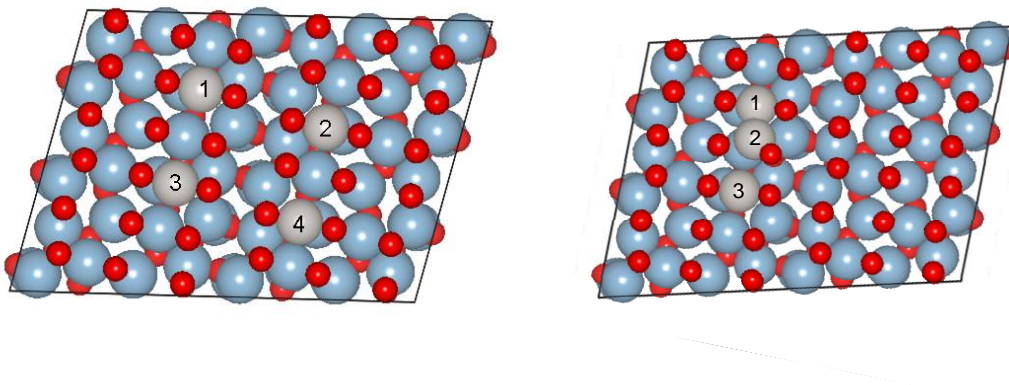
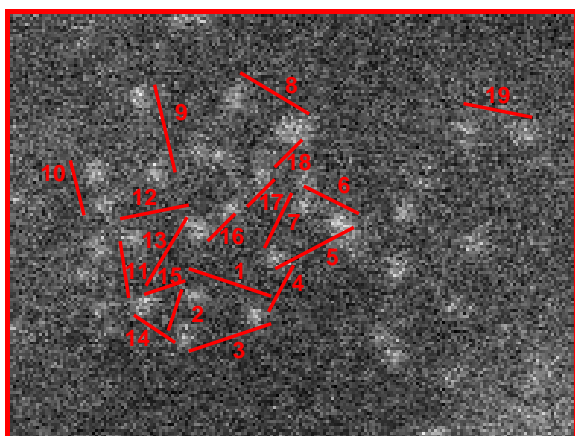


Figure 2: Platinum atoms on 2x3x3 supercell.



1	3.82	6	2.6	11	4.0	16	2.27
2	2.61	7	3.64	12	3.8	17	2.79
3	4.53	8	3.97	13	5.53	18	3.14
4	3.45	9	4.87	14	3.28	19	3.65
5	3.45	10	2.09	15	3.3		

Figure 3: Platinum agglomerates on θ -alumina

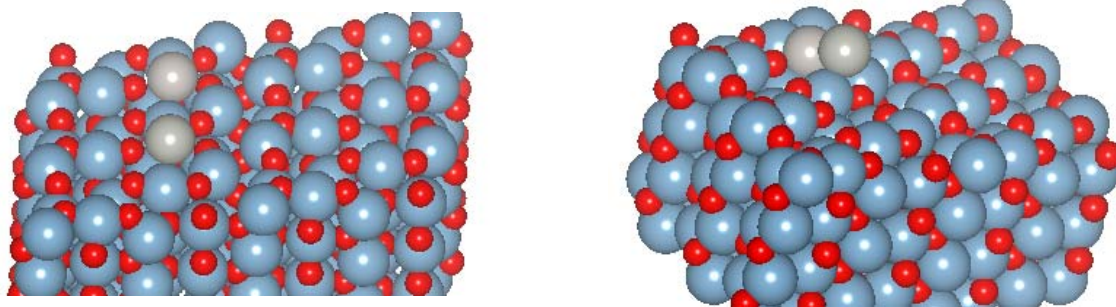


Figure 4: Pt and Pd atoms on θ -alumina surface 2 x 3 x 3 slab (left –independent, right –bonded).

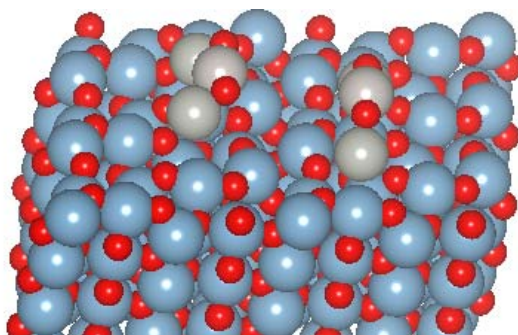


Figure 5: Pt-O-Pt bonds of platinum atom bonded to oxygen atoms on platinum atoms on 2x3x3 supercells of 010 surfaces.

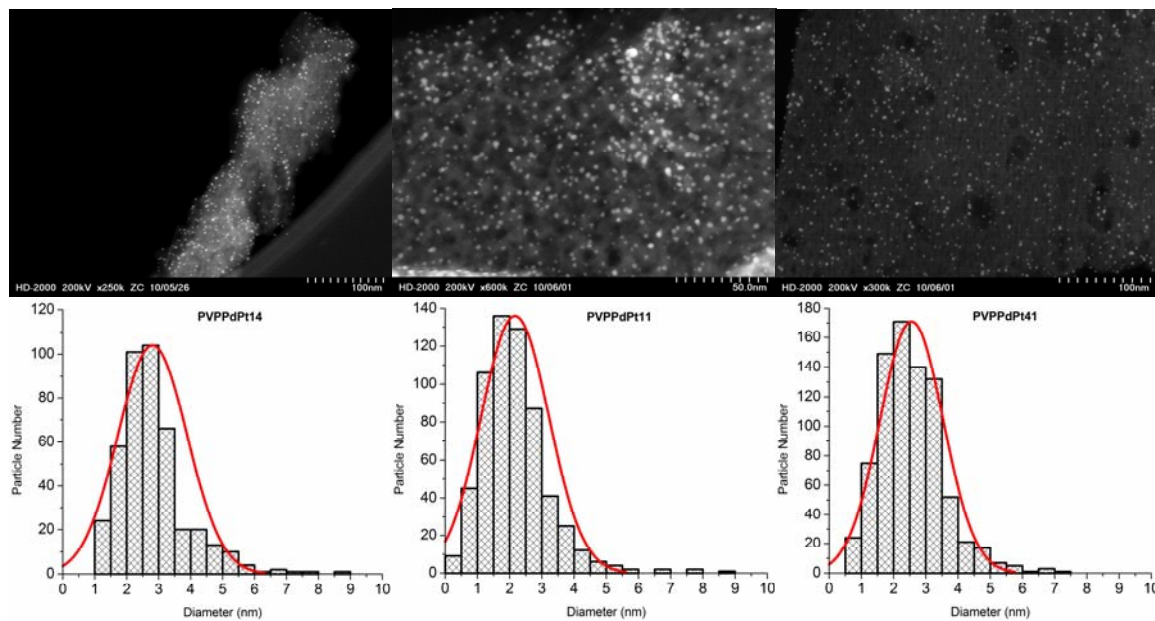


Figure 6: TEM of Pd-Pt (1:4) (left), Pd-Pt (1:1) (middle), and Pd-Pt (4:1) (right) on γ -Al₂O₃.

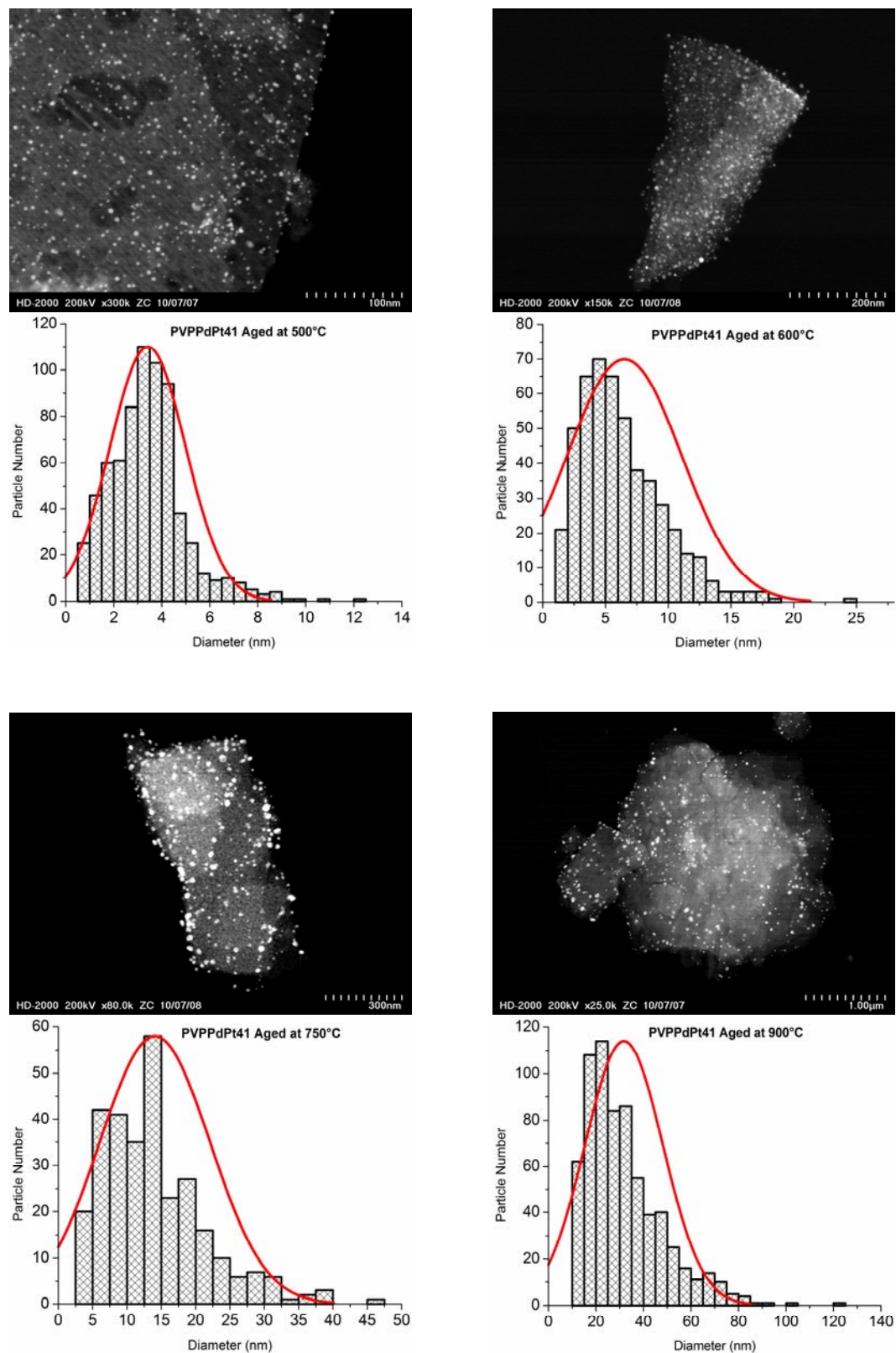


Figure 7: TEM Pd-Pt (4:1) on γ -Al₂O₃ after hydrothermal aging after aging at 500, 600, 750, and 900C.

Agreement 19214 - Effects of Biodiesel Fuel on Diesel Particulate Filter Materials

M.J. Lance, T.J. Toops, S.A. Lewis, Sr. *, J.M.E. Storey*, A.A. Wereszczak, D.F. Wilson and E.E. Fox*

Ceramic Science and Technology Group

Oak Ridge National Laboratory

P.O. Box 2008, MS 6068, Bldg. 4515

Oak Ridge, TN 37831-6068

(865) 241-4536; fax: (865) 574-6098; e-mail: lancem@ornl.gov

** Fuels, Engines and Emissions Research Center, ORNL*

DOE Technology Manager: Jerry L. Gibbs

(202) 586-1182; fax: (202) 586-1600; e-mail: jerry.gibbs@ee.doe.gov

ORNL Technical Advisor: D. Ray Johnson

(865) 576-6832; fax: (865) 574-6098; e-mail: johnsondr@ornl.gov

Contractor: Oak Ridge National Laboratory, Oak Ridge, Tennessee

Prime Contract No.: DE-AC05-00OR22725

Objectives

- To characterize changes in the microstructure and material properties of diesel particulate filters (DPFs) in exhaust gas produced by biodiesel blends.

Approach

- Characterize the residue collected from the original experiment that produced cordierite corrosion with biodiesel operation.
- Repeat the experiment using a different engine and batch of biodiesel fuel to attempt to reproduce the degradation.
- Measure the chemical composition and pH of condensate and PM generated by a diesel engine running with ULSD and biofuel blends under different loads. .
- Use fracture strength as a measurement of corrosion of ceramic DPF materials. Develop a mechanical strength test to separately probe degradation in the skin and the interior of the DPF.

Accomplishments

- Replicated initial engine test that produced DPF degradation.
- Collected solid and semi-volatile particle emissions using ULSD and B20 and measured their chemical composition using GC-MS.
- Developed finite element stress model, using μ -FEA[©], to relate experimental compressive loading of the o-ring test geometry to associated failure stress.

Future Direction

- Expose DPF samples (both cordierite and SiC) to acidic solution comparable to those measured in actual biodiesel condensate.

- Determine relationship between maximum stress of failure and compressive load of failure. Use resulting stress of failure to measure extent of corrosion in DPF samples.

Introduction

In the spring of 2008, soot was collected on uncatalyzed 5.66 X 6 inch cordierite DPFs from a 1.7L Mercedes-Benz engine fueled with biodiesel blends (4 volumetric blends 0 - 100%) for the study of soot oxidation kinetics. The soot was removed by backflushing the filters with pressurized air after which the filters were stored in ambient conditions on a shelf still within the can. Approximately 3 months later, the DPF bricks were removed from the can at which point significant degradation of the DPFs that had seen biodiesel exhaust was observed. No degradation of the brick run with ULSD was found. Figure 1 shows the exterior of the ULSD and B20 bricks. In addition, after burning the collected soot, the biodiesel soot had cordierite and tumescent padding residue in amounts roughly proportional to the biodiesel volume percent in the fuel. This result suggests that biodiesel may cause corrosion of DPF materials under some conditions. This project has the objective to investigate this possibility and potential corrosion mechanisms resulting from biodiesel operation.



Figure 1. The DPF that had seen B20 exhaust showed significant degradation after sitting within the can for 3 months. The ULSD filter appeared undamaged.

Previous measurements of the pH of condensate collected from biodiesels from soy,

rapeseed and palm feedstocks showed no significant difference when compared to the condensate pH from ULSD fuel [1]. However, biodiesel soot may have other properties that accelerate corrosion kinetics under certain conditions.

To investigate this phenomenon, the original cordierite residue collected following soot burn-out from B100 operation was analyzed using an SEM and EDAX in order to determine if any corrosion products were present. Next, the engine test was repeated using a different engine and biodiesel batch in order to try to reproduce the degradation. Third, condensate and soot was collected from a single cylinder engine run with ULSD and B20 at half load and full load and analyzed using polar/non-polar extraction and gas chromatography-mass spectrometry (GC-MS). Finally, mechanical test specimens were designed using finite element analysis in order to isolate the skin and the interior of the DPF as a future method to test corrosion.

Results

Since the damage shown in Fig. 1 seemed to be localized at the outer skin of the brick, electron probe microanalysis (EPMA) was used to measure the chemical composition of the skin relative to the interior. Figure 2 is an SEM image of the region of a fresh filter where the interior meets the skin. The interior (channels) appear more porous than the skin which is required for the filter to allow gas to permeate through the walls of the channels but not out of the brick into the padding. The skin also has a broader particle size distribution than the interior presumably to increase its packing density. Finally, the skin appears to have at least two phases present; a dense cordierite phase and a glassy grain boundary phase. This grain boundary phase may be more susceptible

to corrosive attack than the relatively inert cordierite, which may explain the localization of the degradation shown in Fig. 1. Figure 3 shows a map of silicon collected from the same region in Fig. 2. The glassy grain boundary phase appears to be rich in Si and low in Mg and Al compared to the cordierite grains.

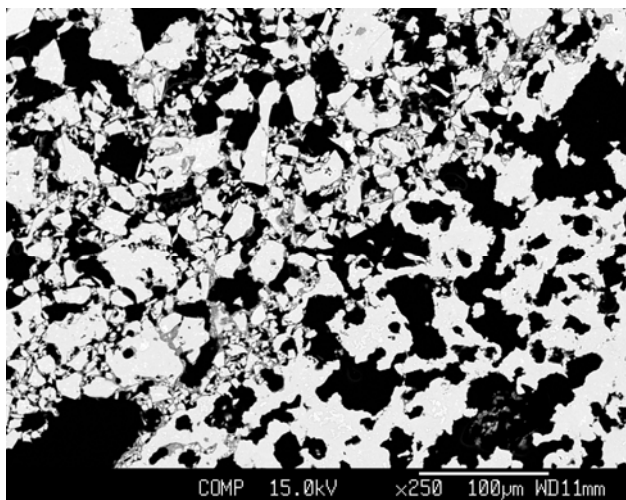


Figure 2. Cross-section of the cordierite filter at the region where the interior channels (lower right) meets the exterior skin (upper left).

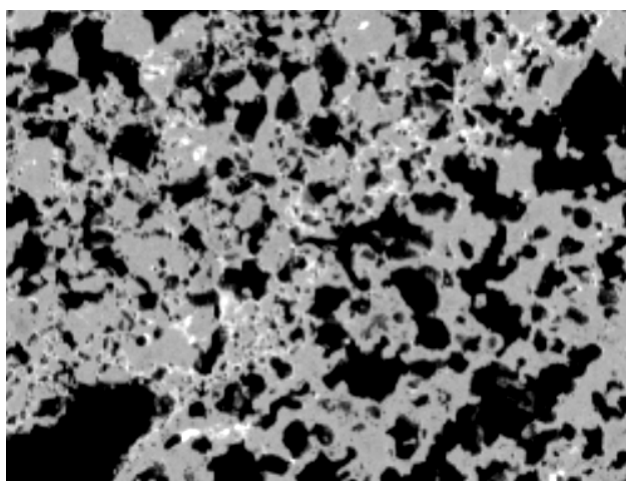


Figure 3. An EPMA map of silicon collected from the same region as Fig. 2.

Energy dispersive spectroscopy (EDS) and SEM were used to characterize the residue collected following burn-out of the B100 soot. (Note: The complete filters shown in Fig. 1 were returned to the DPF supplier which prevented in-depth analysis of these samples).

Figure 4 shows the edge of one flake of cordierite from the B100 residue. EDS spectra were collected from the edge of cordierite particles since this is where corrosion products would be located. The arrows in Fig. 4 indicate regions where high amounts of Cl, Na, K, Ca, and S were detected. Fe, Cr and Cu were also seen in some regions. One region had a Cl and Na content of ~19 and ~23 wt%, respectively. These elements were not observed in significant amounts in either the skin or the interior channels of the as-received DPF.

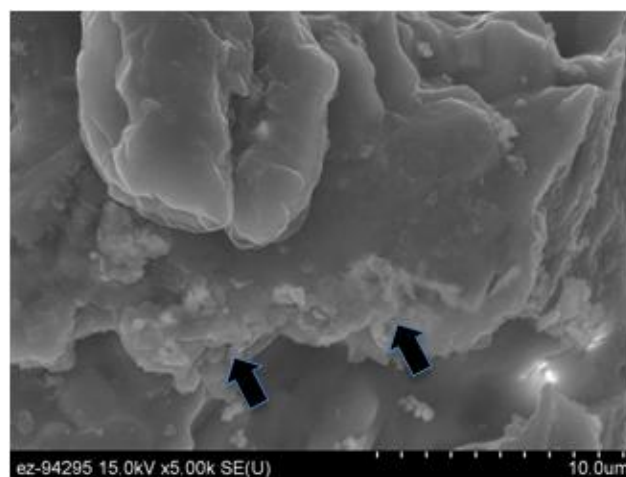


Figure 4. The edge of a flake of cordierite collected from the B100 soot residue following burn-out. Arrows indicate where EDS spectra were collected.

Next, in an attempt to reproduce the degradation observed in the initial engine test, four DPFS were loaded with soot using a different engine and a different biodiesel fuel source. Previously the fuel was purchased from Soy Gold but this test used SME fuel from Renewable Energy Group (REG) which was certified by Southwest Research Institute (SWRI) and GC-MS at Oak Ridge. All DPFS were run for 8 hours. The B100 sample had noticeable oily spots on the back of the filter, a large wet stain in the matting and oily residue dripping from the can/gasket/cone juncture. The higher detectable hydrocarbon content in the DPF is expected due to the lower volatility of B100 compared to ULSD. The samples were

stored for 3 months horizontally at ambient temperature and open to air in the same manner as the original test that produced cordierite degradation. Figure 5 shows the outer surface of the B100 DPF after being removed from the stainless steel pipe that was used to simulate the DPF can. Apart from the discoloration caused by the oily residue, no corrosion of the DPF skin was observed.



Figure 5. Surface of the DPF after being exposed to B100 exhaust and storage for 3 months in order to simulate the original DPF degradation.

A series of engine experiments were implemented to collect solid and semi-volatile particle emissions as a function of fuel type, ULSD or B20, and exhaust temperature, 300°C and 500°C. The exhaust was sampled using three techniques that allow analysis of the following parameters:

- Acidic nature of the condensable species in the exhaust (condensate collection).
- Ratio of organic fraction versus elemental carbon fraction (quartz filters).
- Identification of the species in the organic fraction (Teflon filters).

Additionally, soot was collected using DPF cores to give a representation of the organic and elemental carbon fraction that would be expected in a typical DPF device. Several of the above analysis techniques were employed on these samples, with a focus on the total acid

content of the organic fraction and the specific acidic species that exist. Results showed a higher acid content in the B20 based exhaust at full load (see Table 1) but not enough to explain the significant amount of corrosion observed in the initial test (see Fig. 1). These pH results compare well to those reported in the literature [1].

Table 1: Acid Content of Condensate

	pH Dilute Condensate	Moles H ⁺
ULSD		
half load	3.58	2.70e-5
full load	3.51	3.15e-5
B20		
half load	3.55	2.68e-5
full load	3.39	4.85e-5

Condensates were collected from the exhaust of ULSD (B0) and B20 fuels run on an air-cooled light duty, single cylinder Haatz engine at half and full loads. The condensates were titrated for acid content. Results show (see Table 2) that the nitric and acetic acid levels were comparable for both fuels. However, B20 exhaust has significantly higher concentrations of sulfuric and formic acids as compared to the conventional diesel exhaust at both half and full load. For nitric acid, B20 exhaust had a 29% increase at half load and 119% increase at full load as compared to ULSD fuel. For sulfuric acid, the increase was much more dramatic, 96% and 263% for half and full load respectively.

Table 2: Acid Species in Condensate

	ug in 100 uL of condensate			
	Ni- tric Acid	Sulfu- ric acid	Formic Acid	Ace- tic acid
ULSD				
half load	10.4	28	8.9	3.1
full load	7.4	46.3	18	6.8
B20				
half load	7.7	36.2	17.4	3.9
full load	7.4	101.3	65.3	6.1

Four fuels, ULSD, B5, B20 and B100 were investigated at a single operating point (1500 rpm, 2.6 bar BMEP) on a light duty, late model Mercedes engine. Condensate was collected for each sample from the raw exhaust. These condensates were titrated for acid content, increasing the scope of biofuel blends considered in this study but these results are not ready for this report.

In addition to the condensate, soot collected on DPFs from the Haatz engine was also analyzed using GC-MS. Figure 6 shows the water extract from soot produced with ULSD and B20 at half and full load. The B20 full-load soot appears to be more soluble in water (hence the darker appearance of the extract) than the ULSD. In addition, GC-MS showed more polar species present in the B20 soot than the ULSD, which would explain its hydrophilic behavior. This result may explain the origin of the degradation observed in Fig. 1: the biodiesel soot may be able to retain water better than the ULSD soot thereby allowing aqueous corrosion to occur in the filter.

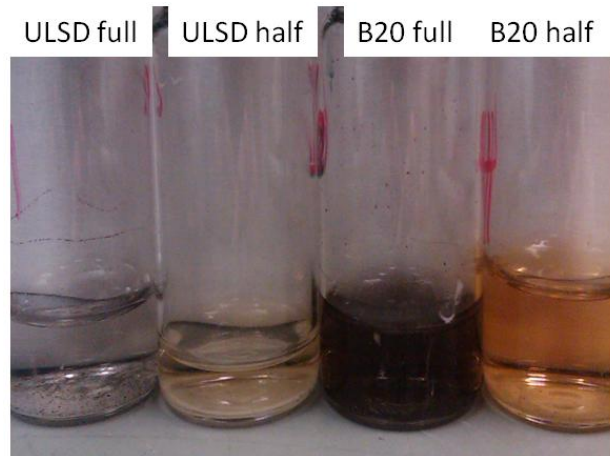


Figure 6. Water extract from the soot collected from the Haatz engine test.

Future corrosion testing will utilize fracture strength as a material property in order to observe the onset of filter degradation. The "o-ring" test coupon is one that often used to measure hoop failure stresses in tubes made from brittle materials. To prepare them, rings are simply cut from a tube. They are then diametrically compressed until fracture occurs, and the failure force is related to a tensile stress failure stress. If diametral compressive loading is vertical (i.e., 12 o'clock toward 6 o'clock), then the maximum tensile stresses occur at the 3 and 9 o'clock positions at the tube's outer diameter (OD) and at the 6 and 12 o'clock positions at the tubes inner diameter (ID). These stresses are related to the failure force. This knowledge of the location of a maximum stress, and an ability to estimate what that stress is, is a tenet of the design of any mechanical test coupon.

Diesel particulate filters (DPFs) may be argued to have a tubular-like geometry. They have an outer skin of material that has a relatively high density and an interior square-arrayed structure whose struts have a relatively high porosity and separated by air.

Given this observation, an initiation of the mechanical evaluation of 25-mm nominal diameter diesel particulate filter was initiated by adapting the "o-ring" test specimen geometry to it. It involves cutting a disk from the DPF and then core-drilling it to make the o-ring

geometry. Examples of this are shown in Figures 7 and 8. It has the prospects of being a simple test geometry whose mechanical loading can allow the DPF community to estimate failure stresses in DPFs that are critical to their design and reliability determination.

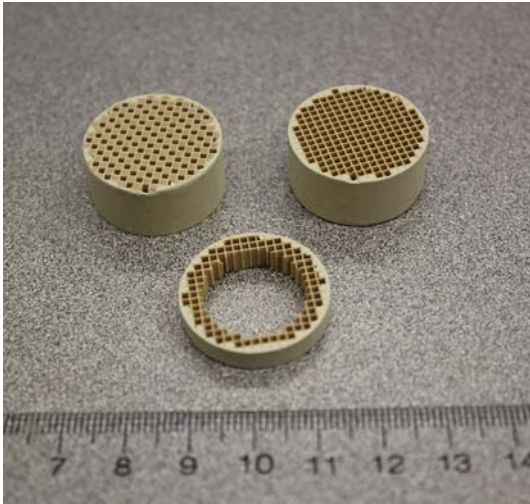


Figure 7. Example of o-ring specimen cut from a cordierite DPF.

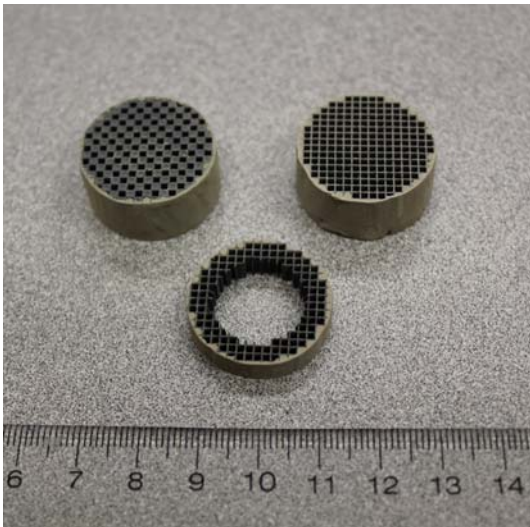


Figure 8. Example of o-ring specimen cut from a silicon carbide DPF.

This task's objective in FY10 was to develop a simple test method (i.e., o-ring test) that can be used to measure tensile stresses associated with crack initiation in these DPFs. Iteratively combining mechanical testing and finite element analysis of the o-ring DPF sample sought this.

Both FEA and mechanical loading are needed for the analysis. A digital picture of the o-ring was taken, preprocessed through the μ -FEA software, and inputted into ANSYS. The recreated structure enabled by the μ -FEA software is shown in Fig. 9.

An example of the produced deformations and stresses from the diametral compression of the geometry shown in Fig. 9 is shown in Figs. 10-13 for a vertically applied load of 20 N to the top an o-ring whose thickness was 10 mm.

The resulting (vertical) displacement field is shown in Fig. 10. Inspection of this field, when correlated to experimental measurement of compressive displacement, enables the back-calculation of apparent elastic modulus of the material constituents shown in Fig. 9. This analysis is underway in Q1 of FY11.

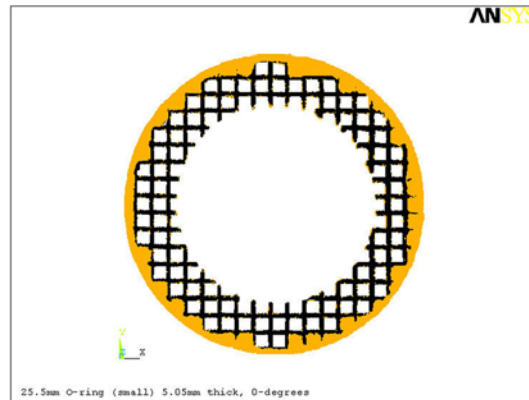


Figure 9. Recreated FEA architecture using the μ -FEA software. Gold represents the outer skin material and the black the inner strut structure.

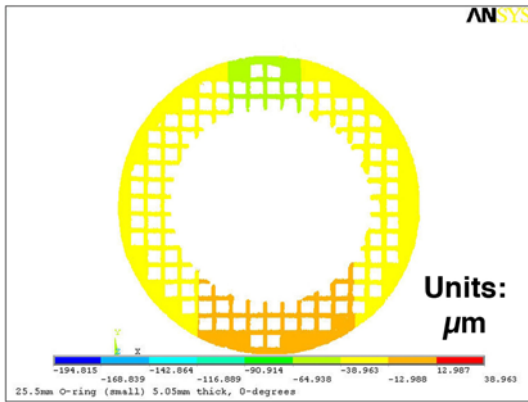


Figure 10. Vertical displacement field for a cordierite DPF vertically loaded to 20 N.

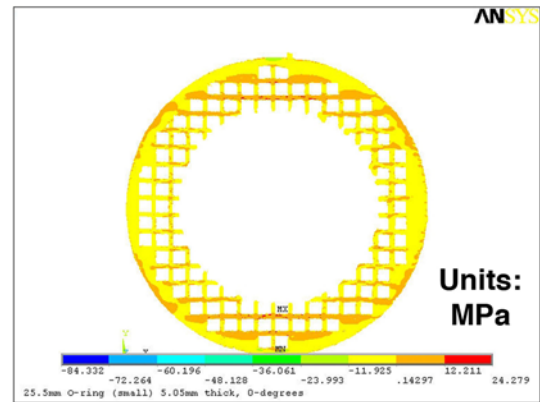


Figure 12. Horizontal component of stress field for a cordierite DPF vertically loaded to 20 N.

The first principal stress field and its horizontal and vertical components are shown in Figs. 11-13. Upon inspection of the horizontal and vertical stress fields, one sees the production of the highest horizontal tensile stresses at the inner diameter of the DPF o-ring at its 6 and 12 o'clock positions and the highest vertical tensile stresses at its 3 and 9 o'clock positions at its outer diameter.

But more iterative FEA modeling needs to be done and is underway in early FY11. In order to get an accurate estimate of the real tensile stresses, one must first have a confident estimate of the elastic properties of the DPF's material constituents. As previously described, the estimation of those properties is being sought by correlating this FEA (i.e., predicted vertical displacements) with experimentally measured vertical displacement. The choice of the correct elastic properties will result in their matching.

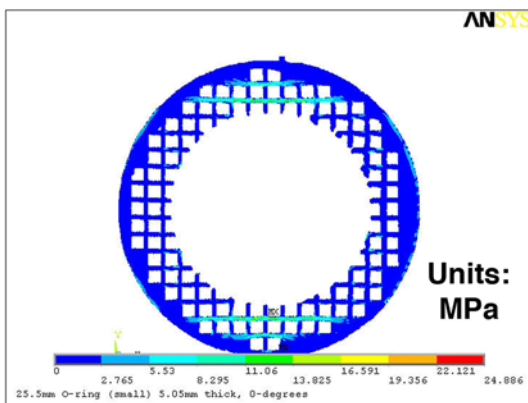


Figure 11. First Principal stress field for a cordierite DPF vertically loaded to 20 N.

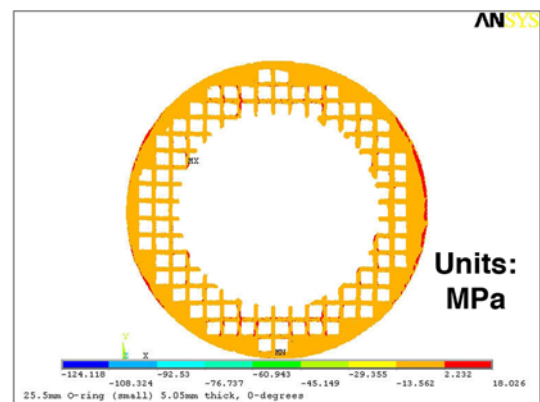


Figure 13. Vertical component of stress field for a cordierite DPF vertically loaded to 20 N.

Examples of the testing of some of the DPF o-rings are shown in Figs. 14-16. The compressive test set-up is shown in Fig. 14. Because of the inherent square array of holes and the circular outer geometry, interest continues to measure failure stress as a function rotational angle. For our FY10 work, we focused on testing on 0-degree (rectangular struts parallel to axis of compressive loading) and 45-degree orientations. The sample shown in Fig. 8 has a 0-degree loading orientation.

Numerous o-rings were machined for mechanical testing and that has started in Q4FY10 but is ongoing in early FY11.

One early observation that is proving consistent is the difference in failure initiation location for the 0-degree and 45-degree orientations. For the 0-degree orientations, crack initiation in each specimen tends to start at the 6 or 12 o'clock positions at the inner diameter and propagate to the outer diameter with additional compressive displacement. This is shown in Fig. 15. This is consistent where the maximum tensile stresses are located in Figure 12. However, for the 45-degree orientation, crack initiation starts at 3 or 9 o'clock but at the o-rings outer diameter and then propagates to the inner diameter. This is shown in Fig. 16. The local strut alignment (e.g., stiffness and stress concentrators) has an influential role in that. Additionally, the maximum compressive force to start crack initiation in the 45-degree orientation is less than that of the 0-degree orientation, so this suggests that the 45-degree orientation is a weaker one. But additional testing and improved statistics will help us conclude that in early FY11.

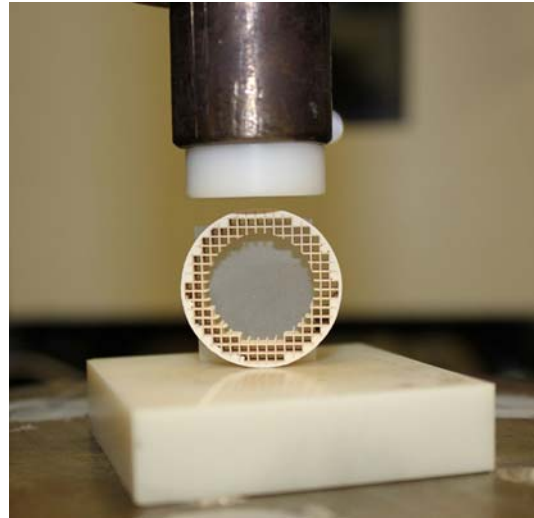


Figure 14. Experimental set-up of the o-ring test. This is designated as the 0-degree orientation with respect to the axis of compressive loading.

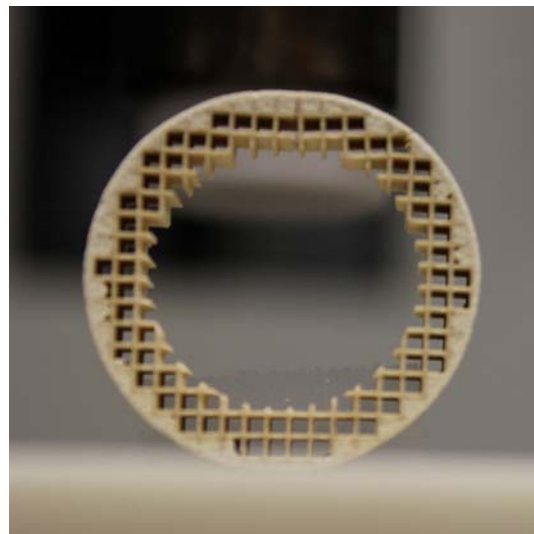


Figure 15. Crack initiation at the o-ring's inner diameter at the 12 o'clock position. This was typical for 0-degree-loaded o-rings.

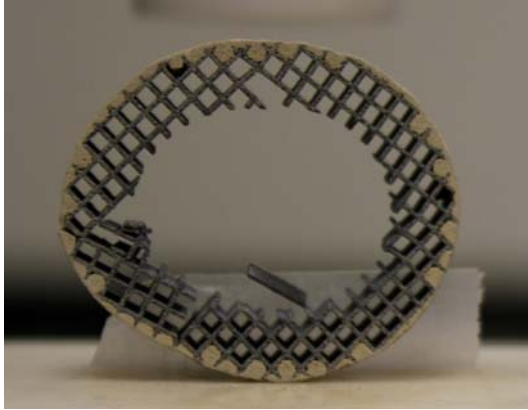


Figure 16. Crack initiation at the o-ring's outer diameter at the 9 o'clock position. This was typical for 45-degree-loaded o-rings.

In FY11, work will continue to generate statistically significant failure stress data for the various orientations and DPF materials, estimate the apparent elastic moduli of the materials comprising each DPF using a combination of mechanical loading and FEA, and determining the relationship between maximum stress of failure and compressive load of failure. The approach above will allow us to isolate corrosion of the skin from the interior of the DPF.

Conclusions

Analysis of the B100 residue from the initial test showed localized increased amounts of Cl, Na, S, K and Ca compared to the as-received filter. These elements maybe associated with corrosion products or merely by-products of biofuel combustion since Na and K are known impurities in biodiesel.

The largest chemical difference between the biodiesel and ULSD soot was the increased hygroscopicity of biodiesel soot. This may explain the corrosion of the B100 sample as the soot could retain water adjacent to the filter better than the ULSD soot.

The mechanical testing of a simple o-ring specimen geometry has potential to be an

effective means to quantify the tensile stress to initiate fracture initiation in DPFs.

The development of a finite element stress model, using μ -FEA, coupled with simple experimental compressive loading of the o-ring test geometry can be a very useful way to back-calculate the elastic properties of the materials comprising the DPF.

Preliminary results show crack initiation appears to occur easier (i.e., at lower tensile stresses) in the 45-degree orientation than in the 0-degree orientation.

References

- [1] S. Moroz, G. Bourgoïn, J.M. Luján and B. Pla, "Acidic Condensation in Low Pressure EGR Systems using Diesel and Biodiesel Fuels," SAE 2009-01-2805.

Agreement 20091 - Electrically-Assisted Diesel Particulate Filter Regeneration

M. J. Lance, J. E. Parks, A. A. Wereszczak, W. P. Partridge,* and E. E. Fox*

Ceramic Science and Technology Group

Oak Ridge National Laboratory

P.O. Box 2008, MS 6068, Bldg. 4515

Oak Ridge, TN 37831-6068

(865) 241-4536; fax: (865) 574-6098; e-mail: lancem@ornl.gov

** Fuels, Engines and Emissions Research Center (FEERC), ORNL*

DOE Technology Manager: Jerry L. Gibbs

(202) 586-1182; fax: (202) 586-1600; e-mail: jerry.gibbs@ee.doe.gov

ORNL Technical Advisor: D. Ray Johnson

(865) 576-6832; fax: (865) 574-6098; e-mail: johnsondr@ornl.gov

Contractor: Oak Ridge National Laboratory, Oak Ridge, Tennessee

Prime Contract No.: DE-AC05-00OR22725

Objectives

Study efficiency benefits and materials issues associated with the electrically-assisted diesel particulate filter (EADPF) device developed by General Motors (GM). This project is divided into three tasks:

Task 1: Fuels, Engines and Emissions Research Center (FEERC)

- Characterize potential fuel savings of the approach and related benefits to other emission control devices.
- Measure gas and substrate temperatures to obtain accurate picture of conditions experienced during regeneration.

Task 2: Ceramic Science and Technology Group (CerSAT)

- Resolve current disconnect between cordierite substrate model predictions and actual substrate durability.
- Use data and results to develop general design rules on heater geometries to optimize substrate durability.

Task 3: Corrosion Sciences Group

- Conduct a high-level discussion on the durability of the heater alloy.
-

TASK 1**Objectives**

- Characterize the potential fuel savings of the electrically-assisted diesel particulate filter (DPF) approach.
- Measure gas and substrate temperatures during DPF regeneration with non-thermally conductive fiber optic based techniques.

Approach

- Measure fuel savings as compared with conventional DPF regeneration techniques with a full-size DPF system on a 1.9-liter GM 4-cylinder diesel engine on an engine dynamometer.
- Measure substrate temperatures with fiber optics via black-body radiation during DPF regeneration.
- Compare temperature measurement history of substrates with materials characterization of substrates (Task 2) to determine failure mechanisms.

Accomplishments

- Installed DPF system and electrical power unit including LabView-based control algorithms to control DPF temperatures during engine operation.
- Developed fiber optic probes with angled tip to enable side view of substrate wall during engine experiments.
- Performed initial black-body radiation experiments with intensified charge coupled device (ICCD) camera spectrometer system.

Future Direction

- Measure fuel savings of technique on engine platform.
- Collect black-body radiation temperature information during DPF

regeneration with side-viewing fiber optic probes.

Introduction

Diesel engines operating at lean air-to-fuel ratios are more efficient than gasoline engines which commonly operate at stoichiometric air-to-fuel ratios. While the diesel engine dominates the heavy-duty truck market, the expansion of diesel engines in light-duty truck and passenger car markets has been limited by various factors. One traditional limitation has been emissions or, specifically as addressed here, particulate matter (PM) emissions which are commonly referred to as “soot”.

In order to reduce PM emissions to meet customer expectations and U.S. EPA emissions regulations, diesel engines use an exhaust emission control technology known as the diesel particulate filter (DPF). The DPF is a ceramic (commonly cordierite or SiC) monolithic filter in the exhaust system that filters PM from the entire exhaust stream during normal operation (Figure 1). Periodically, the DPF is cleaned or “regenerated” to oxidize or “burn” the accumulated PM in the filter. The regeneration procedure occurs by raising the temperature of the DPF to approximately 600°C or higher where the carbon-rich PM readily oxidizes.

Virtually all modern diesel engine vehicles are sold with the DPF technology which is performing well in the field and reducing PM emissions by >95%. However, the current technique for DPF regeneration consumes extra fuel which is oxidized over a diesel oxidation catalyst in the diesel exhaust to heat the DPF to regeneration temperatures. This extra fuel or “fuel penalty” reduces the fuel economy advantage of the diesel engine.

General Motors (GM), the CRADA partner for this project, has developed a DPF technology that utilizes electrical power to heat the DPF for regeneration. This technology called Electrically-Assisted Diesel Particulate Filter (EADPF) may greatly reduce the fuel penalty associated with DPF regeneration. In this project Oak Ridge National Laboratory

(ORNL) is collaborating with GM to better understand material limitations of the EADPF approach so that the technology can be commercialized and realize fuel savings for diesel engine vehicles. Task 1 of the project focuses on measuring the DPF exposure temperatures in exhaust on a full size engine platform. Task 2 focuses on the material failure mechanisms and accuracy of predictive models to develop temperature-specific design rules. Finally, Task 3, while smaller in scope, focuses on material durability of metal alloys used in the EADPF design.

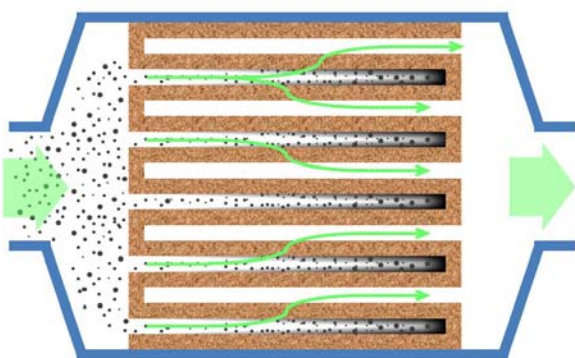


Figure 1. Cross-section schematic of a diesel particulate filter.

Results

The initial work in FY10 for Task 1 has focused on setting up the experimental platforms to conduct the engine-based studies. GM supplied an EADPF unit to ORNL and the unit has been mounted to a 1.9-liter 4-cylinder GM diesel engine previously used for other research projects (Figure 2). An electrical power control system has been developed to operate the EADPF in engine exhaust. The power unit allows precise control of DPF temperature based on multiple thermocouples inserted into the EADPF system. The control algorithm was implemented in LabView (National Instruments) which is the programming language for the engine controller which

operates the engine on the dynamometer system.

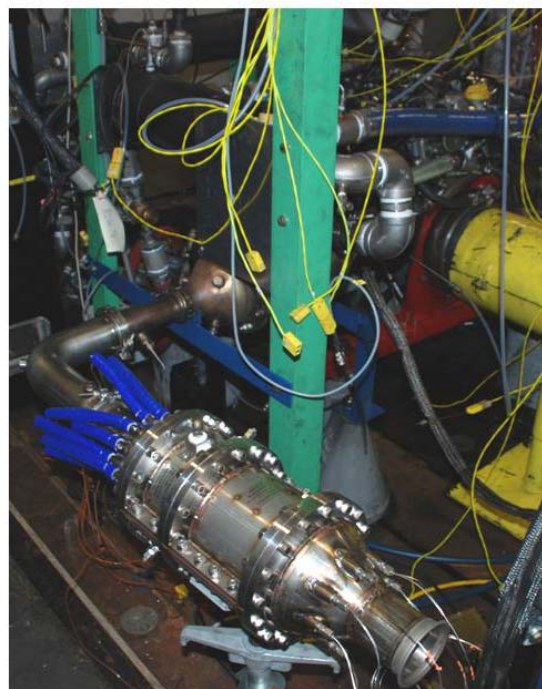


Figure 2. Picture of the GM EADPF installed on a GM 1.9-liter 4-cylinder diesel engine.

In parallel with the engine platform work, progress has been made on the development of the fiber optic temperature measurement technique. Fiber optics have been made with polished tips at a 45° angle which facilitates the collection of light from the side direction of the fiber (Figure 3). This geometry enables a fiber optic inserted into the DPF channels to measure the channel wall temperature which is the critical temperature measurement required to define the material exposure history during regeneration events.

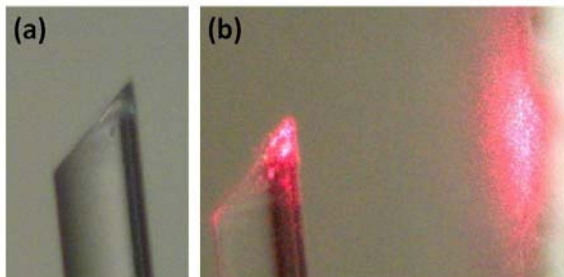


Figure 3. Image of a fiber optic with end polished to a 45° angle (a) and the same fiber optic with light passed through the fiber optic and emitted in the side-viewing direction from the 45° interface (b).

In addition, preliminary black-body radiation measurements have been made with a fiber optic on a bench scale rig to ready the optical system that will collect data with the fiber optic temperature probes. Essentially, the optic system consists of a spectrometer coupled with an intensified charge coupled device (ICCD) imaging detector (Figure 4). Light collected from multiple fibers (up to 32) launches into the entrance slit of the spectrometer and the corresponding spectra can be recorded simultaneously on the ICCD detector for analysis of temperature.

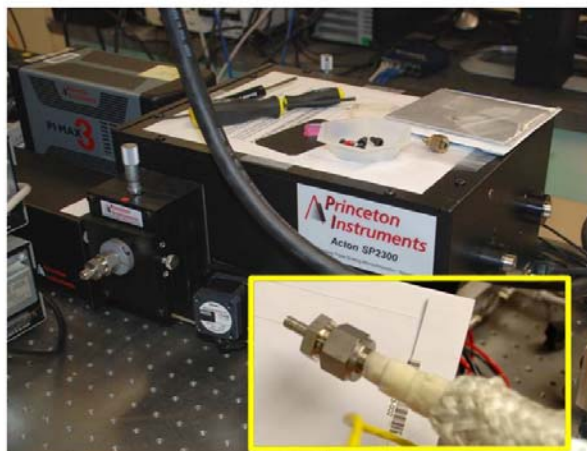


Figure 4. Picture of the ICCD spectrometer apparatus. The inset shows a fiber optic inserted into a heated tube utilized for preliminary black-body radiation experiments.

In FY11, the preparation work in FY10 on the experimental platform will conclude and studies will begin. Initially, the focus will be to study the fuel savings of the EADPF technology as compared with fuel-driven DPF regeneration on the engine dynamometer platform. Then, the fiber optic temperature measurements will be performed in conjunction with EADPF regeneration to accurately measure DPF wall temperatures.

Conclusions

Initial progress has been made on installing an EADPF system on a diesel engine system which includes feedback control algorithms for DPF heating. In parallel, fiber optics with side viewing capability have been made, and an ICCD-based spectrometer system has been setup to collect black-body radiation spectra for temperature measurement. These activities will be combined for future studies in FY11.

TASK 2**Objectives**

- Develop test coupons that enable the determination of failure stresses of diesel particulate filters (DPFs) as a function of DPF orientation and location.

Approach

- Adapt simple and established test methods, used to evaluate ceramic materials, for the testing of a 230-mm diameter DPF.
- Combine mechanical testing and finite element analysis (FEA) to measure and interpret the failure stresses associated with crack initiation.
- Examine orientation effect on the crack initiation failure stress.

Accomplishments

- Designed and harvested test coupons from DPFs.
- Developed finite element stress model, using μ -FEA, to relate experimental compressive loading of the o-ring test geometry to associated failure stress.

Future Direction

- Estimate the apparent elastic modulus of the material comprising the DPF using a combination of mechanical loading and FEA and iterations thereof.
- Complete FEA modeling of all adapted test specimen geometries including the determination of the relationship between maximum stress of failure and compressive load of failure.
- Perform probabilistic design sensitivity (PDS) analysis to better understand which parameters affect maximum tensile stress in a solution.
- Develop general rules of design.

Introduction

Desire exists to develop "rules of design" for diesel particulate filters (DPFs). In principal, such rules would help the DPF manufacturer and its end user design a DPF architecture that would work under a hypothetical service condition or predict what conditions an existing DPF could successfully operate at without mechanically failing.

DPFs do not have an isotropic structure and may not be subjected to symmetric stress fields. Therefore, an ability to achieve "rules of design" is predicated on the understanding of how a DPF mechanically responds to thermal-induced stress of operation and the direction in which that imposed stress field is applied.

The DPFs examined in this study have a 4-fold rotational symmetry so mechanical test coupon geometries were sought whose failure stress testing would portray any failure stress dependence on orientation.

The testings of three specimen geometries are sought: the equibiaxial flexure specimen, the sector flexure specimen, and the o-ring specimen. All are established test specimens used to evaluate failure stress in ceramic materials, and are adapted here to DPFs. All those geometries are easily harvestable from a DPF such as that whose dimensions are shown in Fig. 1.

Equibiaxial flexure testing is an ASTM test method [1]. It is also referred to as the ring-on-ring biaxial flexure test method. Two types of disks were harvested out of cordierite DPF; disks that come from the two ends of a DPF, with 50% of their holes plugged, and those from its interior, no holes plugged. They are shown in Figs. 2-3, respectively. The mechanical testing of this specimen will essentially subject the DPF structure to a biaxial radial tensile stress and induce cracking whose plane will be parallel to the DPFs axis of symmetry. Such a stress state could be produced in service when there is a radial thermal gradient with the outer portion of the DPF hotter than its interior. The modeling and mechanical evaluation of this specimen will commence in early FY11.

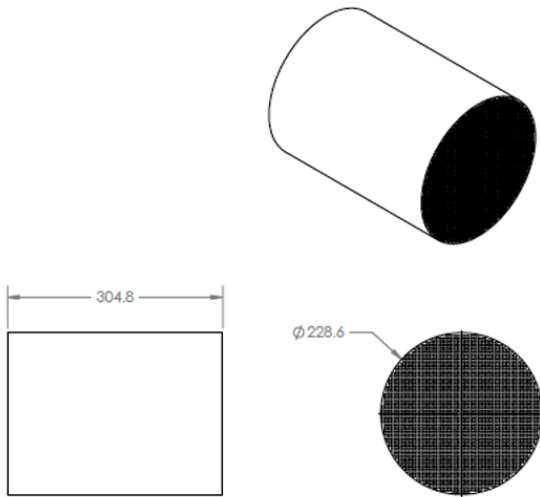


Figure 1. Schematic drawing of the 230-mm diameter x 305-mm long DPF (nominal dimensions).

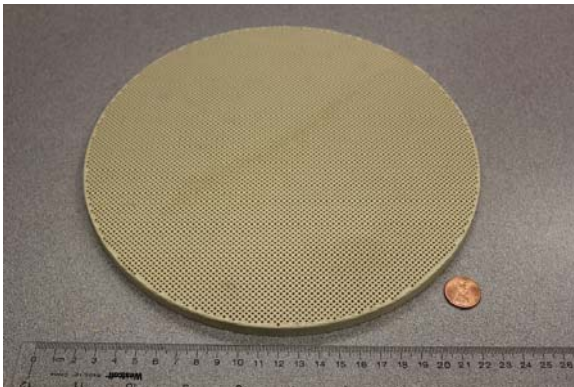


Figure 2. Example of an end-disk harvested from a DPF. Intended for equibiaxial flexure testing. 50% of the holes are plugged.

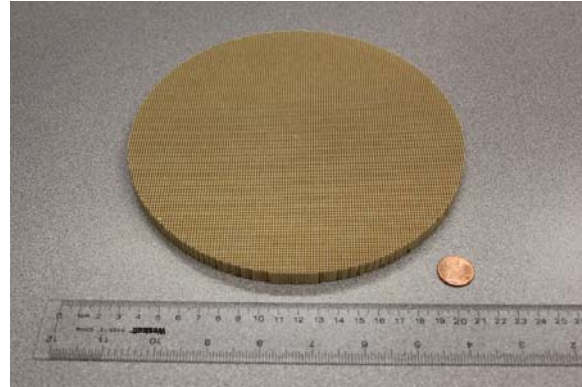


Figure 3. Example of an interior-disk harvested from a DPF. An interior core from a core-drilled o-ring specimen. Intended for equibiaxial flexure testing. None of the holes are plugged.

The sectored flexure specimen is a useful geometry to measure the axial tensile failure stress of a ceramic material in tubular form when the stress is applied to its outer diameter [2]. DPFs may be argued to have a tubular-like geometry. They have an outer skin of material that has a relatively high density and an interior square-arrayed structure whose struts have a relatively high porosity and separated by air. So the sectored flexure specimen was adapted to the DPF to produce a geometry shown in Figs. 4-5. Its testing will involve 4-pt bending.



Figure 4. Example of a sectored flexure bend bar harvested from a DPF. Intended for 4-pt bend testing.

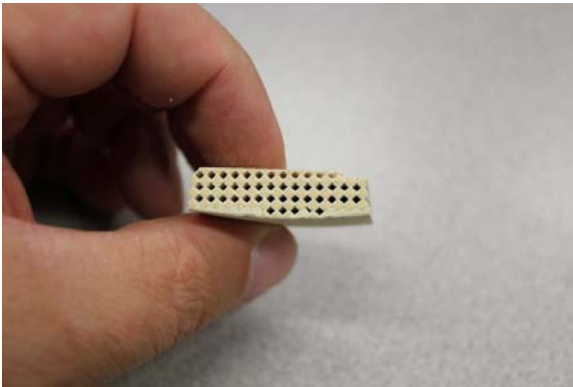


Figure 5. Cross-section of the sectored flexure bend bar. The curved surface will be positioned as the tensile surface in the bend test.

The last considered geometry is the o-ring specimen [3]. It is used to measure hoop failure stresses in tubes made from brittle materials. Rings are simply cut from a tube and then diametrically compressed until fracture occurs. Failure force is directly related to the tensile stress failure stress. If diametral compressive loading is vertical (i.e., 12 o'clock toward 6 o'clock), then the maximum tensile stresses occur at the 3 and 9 o'clock positions at the tube's outer diameter (OD) and at the 6 and 12 o'clock positions at the tubes inner diameter (ID). These stresses are related to the failure force. This knowledge of the location of a maximum stress, and an ability to estimate what that stress is, is a tenet of the design of any mechanical test coupon.

Given this observation, the mechanical evaluation of 230-mm nominal diameter DPF was initiated by adapting the o-ring test specimen geometry to it. It involves cutting a disk from it and then core-drilling it to make the o-ring geometry. An example of it is shown in Fig. 6. It is diametrically compressed until the specimen fractures. Its preliminary analysis of it follows.



Figure 6. Example of an o-ring specimen harvested from a DPF. Its interior provides the interior-disk specimen shown in Fig. 3. Intended for diametral compressive testing.

This task's objective in FY10 was to develop test coupons that enable the determination of failure stresses of diesel particulate filters (DPFs) as a function of DPF orientation and location. The approach to (1) adapt simple and established test methods, used to evaluate ceramic materials, for the testing of a 230-mm diameter DPF, and (2) combine mechanical testing and FEA to measure and interpret the failure stresses associated with crack initiation.

Results

The initial focus in FY10 has been devoted to the testing and analysis of the o-ring. Both FEA and mechanical loading are needed for the analysis. A digital picture of the o-ring was taken, preprocessed through the μ -FEA software, and inputted into ANSYS. The recreated structure enabled by the μ -FEA software is shown in Fig. 7.

An example of the produced deformations and stresses from the diametral compression of the geometry shown in Fig. 6 is shown in Figs. 8-10 for a vertically applied load of 3 N to the top an o-ring whose thickness was 10 mm.

The resulting (vertical) displacement field is shown in Fig. 8. Inspection of this field, when correlated to experimental measurement of

compressive displacement, enables the back-calculation of apparent elastic modulus of the material constituents shown in Fig. 6. This analysis is underway in Q1 of FY11.

The horizontal and vertical stress field components are shown in Figs. 9-10. Upon inspection of the horizontal and vertical stress fields, one sees the production of the highest horizontal tensile stresses at the inner diameter of the DPF o-ring at its 6 and 12 o'clock positions and the highest vertical tensile stresses at its 3 and 9 o'clock positions at its outer diameter.

Examples of the testing of some of the DPF o-rings are shown in Figs. 11-12. The compressive test set-up is shown in Fig. 11. Because of the inherent square array of holes and the circular outer geometry, interest continues to measure failure stress as a function rotational angle. For our FY10 work, we began our focus by testing 0-degree (rectangular struts parallel to axis of compressive loading) and 45-degree orientations. The sample shown in Fig. 12 has a 0-degree loading orientation. Numerous o-rings were machined for mechanical testing and that has started in Q4FY10 but is ongoing in early FY11.

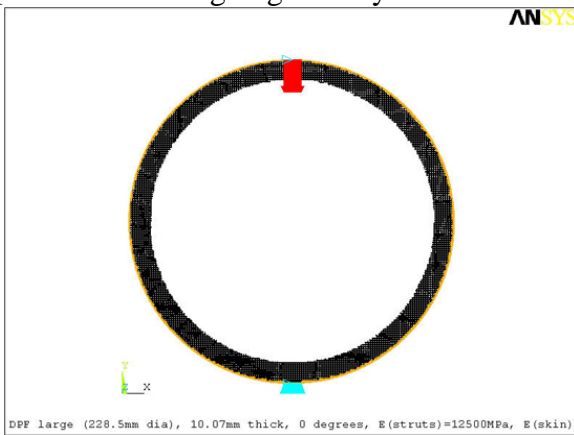


Figure 7. Recreated FEA architecture using the μ -FEA software. Gold represents the outer skin material and the black the inner strut structure. Red and blue arrows represent direction of compressive loading and vertical constraint, respectively.

One early observation that is proving consistent is the difference in failure initiation location for the 0-degree and 45-degree orientations. For the 0-degree orientations, crack initiation in each specimen tends to start at the 6 or 12 o'clock positions at the inner diameter and propagate to the outer diameter with additional compressive displacement. This is shown in Fig. 12. This is consistent with where the maximum tensile stresses are located in Fig. 9. Additional testing and improved statistics will help us more confidently assess differences between those two orientations in early FY11.

More iterative FEA modeling needs to be done and is underway in early FY11. In order to get an accurate estimate of the real tensile stresses, one must first have a confident estimate of the elastic properties of the DPF's material constituents. As previously described, the estimation of those properties is being sought by correlating this FEA (i.e., predicted vertical displacements) with experimentally measured vertical displacement. The choice of the correct elastic properties will result in their matching.

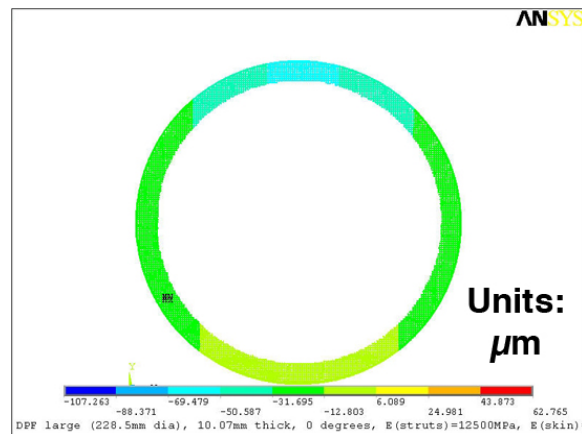


Figure 8. Vertical displacement field for a cordierite DPF vertically loaded to 3 N.

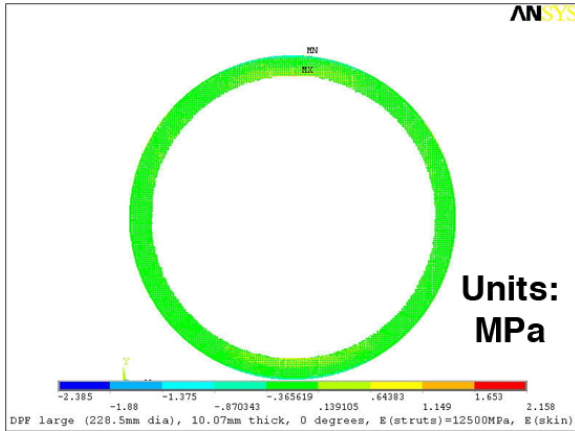


Figure 9. Horizontal component of stress field for a cordierite DPF vertically loaded to 3 N.

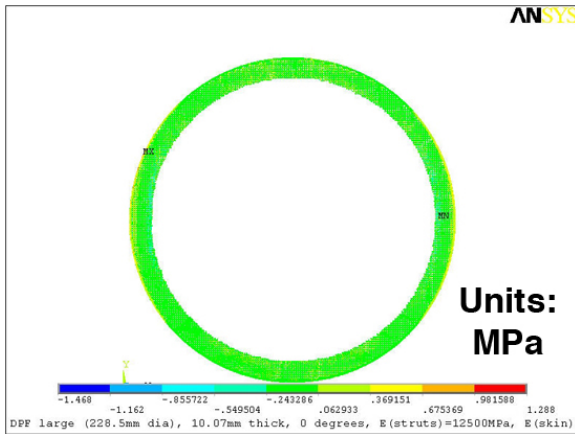


Figure 10. Vertical component of stress field for a cordierite DPF vertically loaded to 3 N.

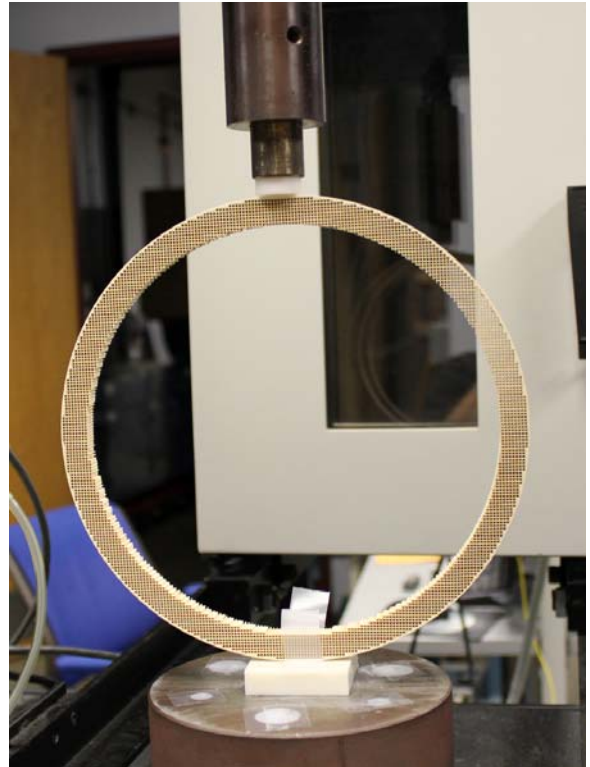


Figure 11. Experimental set-up of the o-ring test. This is designated as the 0-degree orientation with respect to the axis of compressive loading.

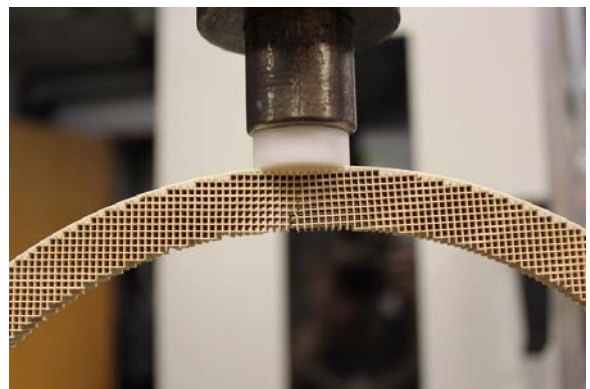


Figure 12. Crack initiation at the o-ring's inner diameter at the 12 o'clock position.

In FY11, work will continue to generate statistically significant failure stress data for the various orientations and DPF materials, estimate the apparent elastic moduli of the materials comprising each DPF using a combination of mechanical loading and FEA, and determining the relationship between maximum stress of failure and compressive load of failure for all of the specimen geometries discussed here. Lastly, probabilistic design sensitivity (PDS) analysis will be pursued to better understand which parameters affect maximum tensile stress in a solution and to aid the development of the "rules of design."

Conclusions

The mechanical testing of equibiaxial flexure, sector flexure, and o-ring specimens have the potential to be an effective means to quantify the tensile stress to initiate fracture initiation in DPFs.

The development of a finite element stress model, using μ -FEA, coupled with simple experimental compressive loading of the o-ring test geometry can be a very useful way to back-calculate the elastic properties of the materials comprising the DPF.

References

- [1] "Standard Test Method for Monotonic Equibiaxial Flexure Strength of Advanced Ceramics at Ambient Temperature," ASTM C1499, Vol. 15.01, ASTM International, West Conshohocken, PA, 2009.
- [2] A. A. Wereszczak, S. F. Duffy, E. H. Baker, J. J. Swab, and G. J. Champoux, "Strength of a Ceramic Sector Flexural Test Specimen," *J. Test. Eval.*, 36:17-23 (2008).
- [3] O. M. Jadaan, D. L. Shelleman, J. C. Conway, Jr., J. J. Mecholsky, Jr., and R. E. Tressler, "Prediction of the Strength of Ceramic Tubular Components: Part 1 - Analysis," *J. Test. Eval.*, 19:181-191 (1991).

TASK 3

Objectives

- We will conduct a high-level discussion on the durability of the heater alloy with experts in the Materials Science and Technology Division.

Approach

- Discuss heater element property requirements with ORNL corrosion scientists and metallurgists.

Accomplishments

- Three potential alloys were suggested as candidate materials.

Future Direction

- Conduct a meeting with GM and the company that will supply the heating elements.

Agreement 13723 - Residual Stresses in Thin Films*

*(This project is jointly funded by Propulsion Materials and Heavy Vehicle Systems Optimization)

Principal Investigators: D. Singh and J. L. Routbort; coworker: Kristen Pappacena

Argonne National Laboratory

9700 S. Cass Avenue, Argonne, IL 60439-4838

630-252-5009 dsingh@anl.gov

DOE Technology Manager: Jerry L. Gibbs

(202) 586-1182; fax: (202) 586-1600; e-mail: jerry.gibbs@ee.doe.gov

Contractor: UChicago Argonne LLC

Contract No.: DE AC03 06CH11357

Objective

- Measure residual stresses in thin films and coatings as a function of film thickness and relate stresses to film properties such as hardness, fracture toughness, and adhesion energy to relate to film processing variables and to predict durability
- Use techniques developed for measurements of residual stresses in thin films and coatings to measure residual stresses in layered structures produced by joining by high-temperature deformation and to improve their mechanical properties

Approach

- Develop X-ray technique to measure change of lattice parameter of coating constituents as a function of depth and hence to calculate the lattice strains and stresses
- Develop indentation and/or scratch techniques to measure hardness, fracture toughness, and adhesion energy of films and coatings
- Relate stresses, properties, and processing conditions to film durability

Accomplishments

- Adhesion energies for MoN/Cu coatings with various processing conditions measured using a scratch technique
- Adhesion energies (and residual stresses) of the MoN/Cu coatings correlated to coating processing; coating adhesion energy dropped with increased copper content
- Wear performance of the various MoN/Cu coatings were evaluated. Direct correlation between wear and adhesion energy observed

Future Directions

- Apply the test protocol developed to measure adhesion energies and performance of ZrN and TiC coatings
 - Develop correlations between processing, residual stresses, adhesion energy for the coating systems studied: MoNCu, ZrN, and TiC. These correlations will help develop processing approaches for the development of coating systems with enhanced durability for applications on heavy vehicle engine components.
-

Introduction

Because of their unusual structural, mechanical, and tribological properties, superhard, nanocrystalline coatings can have an immediate and far-reaching impact on numerous advanced transportation applications including the 21st Century Truck Programs of DOE by reducing parasitic friction losses (hence increasing fuel economy) and wear (hence increasing durability/reliability). They can also be used to overcome toxic emission problems associated with exhaust gas recirculation in diesel engines. Durability of hard coatings is a critical property. The durability is determined by the surface adhesion energy, but is the result, in a large part, of the residual stresses that arise as a result of materials, and processing parameters such as deposition bias voltage, ion flux, and temperature.

The approach for this effort is to use the high-brilliance X-rays produced by the Advanced Photon Source (APS) at Argonne National Laboratory, and a microfocus beam, to measure the residual stresses/strains of MoN based thin films and commercial coatings such as ZrN and TiC as a function of depth from the surface through the interface to the substrate. Subsequently, correlate the residual stress profiles with the film processing conditions and the resulting film/substrate adhesion and its tribological properties.

During the past year, focus has been on measurement of adhesion energy (using scratch testing) of the MoN/Cu coatings deposited on steel substrates under various processing conditions. These coatings are identical to the coatings on which residual stress measurements were made using high-energy X-rays and results reported in the FY08 annual report. In addition, to the adhesion energy, various mechanical behaviors of the coatings were evaluated using nano-indentation tests. Finally, preliminary tests were conducted to

establish the tribological behavior of the coatings.

Experimental Procedures

Samples

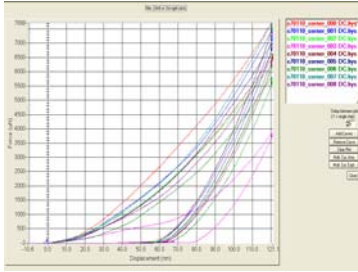
Coatings of MoN with different Cu compositions were deposited onto steel substrates using PVD. As mentioned previous annual reports, the coatings will be referred to as 0 Cu, 5 Cu, and 8 Cu, corresponding to their respective Cu deposition power of 0 W, 5 W, and 8 W, respectively. The respective coating thicknesses for 0 Cu, 5 Cu, and 8 Cu were 2.3 μm , 2.6 μm , and 2.6 μm , respectively. Corresponding measured compressive residual stresses were 3.45 GPa, 3.52 GPa, and 2.7 GPa (as reported earlier).

Nanoindentation

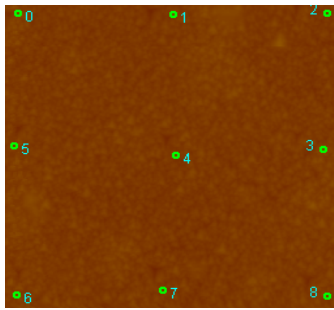
Nanoindentation (Hysitron HI 950) was used to evaluate the mechanical properties of the coatings including elastic modulus and hardness. Nanoindentations were made at several locations on the sample surface as indicated in Figure 1(b) for MoN 5 Cu sample. Corresponding load-displacement curves for the various indentations are shown in Fig. 1 (a). Elastic modulus and hardness are determined from the slope of the load-displacement curves, indenter geometry, and the peak load.

Adhesion Energy Measurement

Scratch tester (Model Romulus) with stylometer attachment, manufactured by the Quad Group (Spokane, WA) was used for the adhesion energy measurements. Figure 2 shows a photograph of the scratch tester. The procedure involves scratching the sample surface using a stylus or indenter at a fixed loading rate that is computer controlled. The system has a built in acoustic transducer that picks up any coating delaminating or fragmentation events. As shown in Figure 3, various parameters such as normal and transverse loads, acoustic signal, and coefficient of friction can be continuously monitored.



(a)



(b)

Figure 1. (a) Load-displacement curves from nanoindentation tests on MoN/0.5 Cu coated sample and (b) location of indentations.

The scratch test system also has a microscope that allows one to examine the scratch path and visually confirm coating delamination. The load at which coating delamination occurs is used to determine the adhesion energy (*W*) of the coating as per the following equations 1 & 2 [1].



Figure 2. Computer controlled scratch tester for coating adhesion energy measurements.

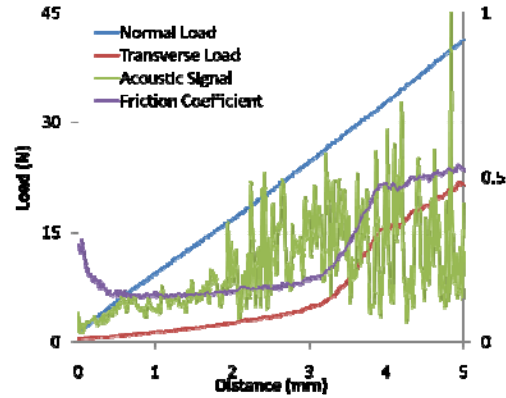


Figure 3. Various signals recorded during the scratch test.

$$\sigma_s = \frac{0.15}{R} \left(\frac{PH_f}{H} \right)^{0.5} E_f^{0.3} E^{0.2} \quad (1)$$

$$W = K_2 (\sigma_s + \sigma_R)^2 t \left(\frac{1 - \nu_f^2}{E_f} \right) \quad (2)$$

where, σ_s is the scratch test stress, *R* is the indenter radius, *P* is the critical load for the coating delamination, *H_f* is the coating hardness, *E_f* and *E* are coating and substrate moduli, respectively, *K₂* is a constant and has a value of 0.343 for spallation failure, σ_R is the residual stress, *t* is the coating thickness, and ν_f is the coating Poisson's ratio.

Wear Testing

Wear testing was performed on a reciprocating rig in the ball on plate configuration. A 3/8" diameter silicon nitride (Si₃N₄) ball was used to achieve sufficient damage on the hard MoN coatings. Tests were done at two loads, 25 and 50 N, for 30 minutes each at a rate of 30 rpm, in a dry environment. The friction was calculated from the as measured normal and transverse forces. The total material removal from each wear test was determined using the micro exam using a histogram to determine the void volume missing using the flat coating surface for a reference. The wear rate (WR) was then calculated as follows:

$$WR = \frac{V}{Fl} \quad (3)$$

where, V is the total wear volume over length l at load F [2].

Results and Discussion

Table 1 lists the hardness and the elastic modulus values for the three MoN/Cu coatings. Hardness values for all three coatings are comparable. However, elastic modulus is highest for the 5Cu coating.

Table 1. Measured Hardness and Elastic Modulus Using Nanoindentation.

Coating	Hardness (GPa)	Modulus (GPa)
0 Cu	22.43 ± 4.32	292.07 ± 28.21
5 Cu	25.93 ± 5.53	317.84 ± 35.33
8 Cu	23.03 ± 3.96	282.59 ± 15.97

Critical load was determined by analyzing the scratch track to see the first instance of exposed substrate, indicating the coating had been removed as a result of the load of the test. An example of a typical critical spallation is shown for the 0Cu sample in Figure 4(a)-(d). Figure 4(a) shows a low mag image of the region of the scratch track containing the critical spall, while Figures 4(b)-(d) show a close up image of the spall, along with Energy Dispersive X-ray Spectroscopy (EDS) mappings of molybdenum and iron. Here it is clear where the Fe is seen in the spallation. This position was measured from the start of the scratch track, and correlated with its respective load value. The acoustic emission of the scratch was also recorded and corroborated with the microscopy results.

Scratch test results indicated that while the mechanical properties such as hardness and modulus of the coatings were similar regardless of coating composition, the adhesion of the coating to the substrate was not. There were significant differences between the critical loads of each of these

three coating compositions (Fig. 5a). Coating 8Cu, with the most copper, began to show spallations at lower peak loads than

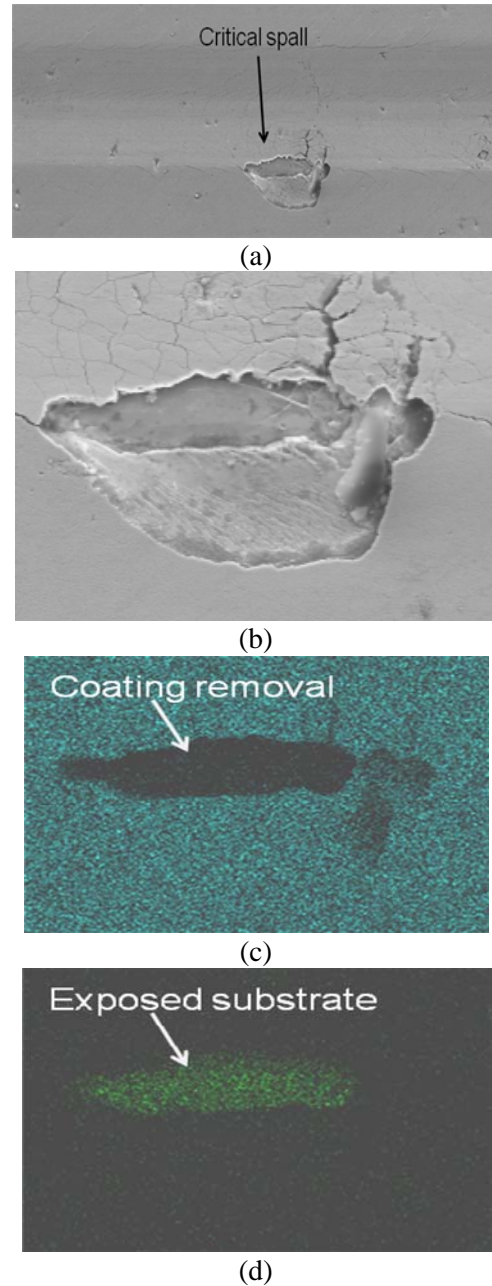


Figure 4. (a) low magnification micrograph of the first coating spall observed along scratch test track, (b) high magnification of the area in (a), (c) EDS mapping for Mo, (d) EDS mapping for Fe.

0 Cu and 5 Cu. The average critical load, from several scratch tests on each coating, increased with decreasing copper content, as

shown in Figure 5. Subsequently, using equations 1 & 2 and the measured residual stresses, adhesion energies were determined and shown in Figure 6. The work of adhesion for coating 8 Cu had the lowest value (67 J/m^2), while 0 Cu and 5 Cu had very similar and much higher adhesion energies (100 J/m^2). This indicates that the addition of 08 Cu copper both decreases the coating adhesion to the substrate, but does not influence the mechanical properties of hardness and elastic modulus.

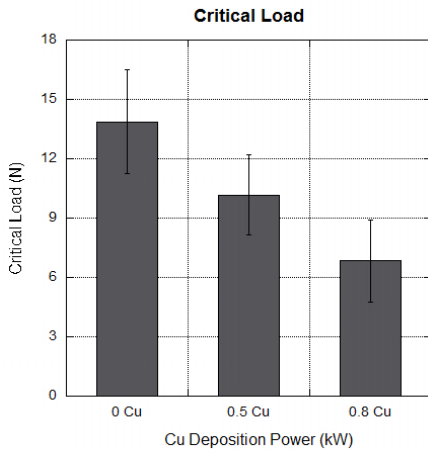


Figure 5. Critical spallation loads for MoN/Cu coatings as a function of Cu deposition power.

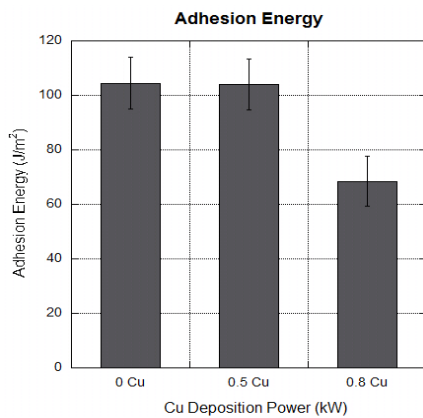


Figure 6. Measured adhesion energies for MoN/Cu coatings as a function of Cu deposition power.

At least two wear tests were done on each coating type at 25N or 50N loads to

correlate the residual stresses and adhesion energies measured to the wear resistance of the coating. The results are shown in figure 7, where the wear rate is shown as a function of adhesion energy. This plot shows a few clear trends. The first is that at 25N, the wear rate decreases with increasing adhesion energy, and consequently, decreasing copper content. This implies that the adhesion energy will play some role in the wear resistance of such materials, and that at some point during the wear test, some of the coating begins to spall off from the substrate. The next trend is that for each coating system, the wear rate is higher at 50N than at 25N. This is expected, as at a higher load, more damage should be occurring throughout the test. It is clear from this plot that the samples with the higher adhesion energy (and lower copper content) show significantly lower wear rates at 25N than the sample with the highest copper content, implying that adhesion energy (and copper processing condition) may play a role in the coating performance.

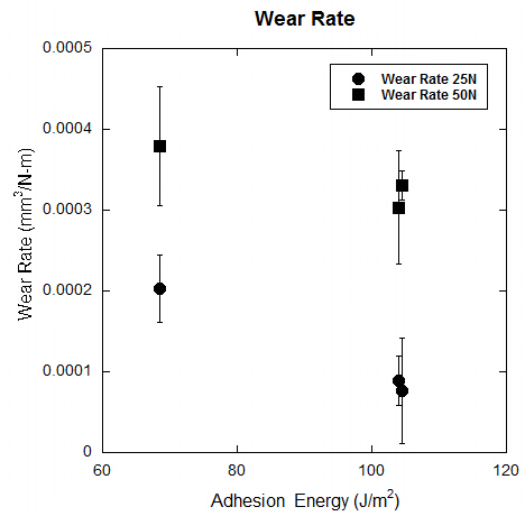


Figure 7. Wear rates as a function of MoN/Cu coating adhesion energies at 25N and 50N test loads.

Conclusions

In conclusion, we have applied scratch test technique to measure adhesion energies of the three differently processed MoN/Cu coatings. Effect of residual stresses in the coating was included in the analysis. Nano-indentation technique was used to determine the coating mechanical properties. Performance of the coatings as per wear test was evaluated. It appears adhesion energy (and possibly residual stresses) plays a significant role in the coating performance.

Future Directions

We will continue to apply the scratch test technique to measure surface adhesion energies for commercial coatings such as nitrides and carbides of Ti and Zr on steel substrates. Further, residual stress measurements will be correlated to processing conditions and the adhesion energy to develop a protocol for fabricating coatings with long-term durability. Finally, collaboration(s) will be established with a coatings manufacturer for heavy vehicle engine OEM and technology will be transferred.

References

1. Xie and Hawthorne, *Surface and Coatings Technology* **141**: 15-25, 2001.
2. Chatterjee, S. and Ganesh, P. and Palai, R. and Wu, J.A. and Kaul, R. and Dutta Majumdar, J. and Roy Choudhury, A. "Effect of h-BN addition on the properties of nanostructured Al₂O₃-TiB₂-TiN based coatings developed by combined SHS and laser surface alloying." *Surface and Coatings Technology* **204**: 1702-1709, 2010.
3. Suszko, T. and Gulbinski, W. and Jagielski, J. "The role of surface oxidation in friction processes on molybdenum nitride thin films." *Surface Coatings and Technology* **194**: 319-324, 2005.

Agreement 9105 - Ultra-High Resolution Electron Microscopy for Characterization of Catalyst Microstructures and Reaction Mechanisms

L. F. Allard, C. K. Narula, F. H. Ribeiro,* S. A. Bradley,** J-H. Kwak,*** C.H.F. Peden,*** and A.K. Datye****

Oak Ridge National Laboratory

P.O. Box 2008, MS-6064

Oak Ridge, TN 37831-6064

(865) 574-4981; e-mail: allardlfjr@ornl.gov

* Purdue University, West Lafayette, IN

** UOP Co., Des Plaines, IL

*** PNNL, Richland, WA

**** Univ. of New Mexico, Albuquerque, NM

DOE Technology Manager: Jerry L. Gibbs

(202) 586-1182; fax: (202) 586-1600; e-mail: jerry.gibbs@ee.doe.gov

ORNL Technical Advisor: D. Ray Johnson

(865) 576-6832; fax: (865) 574-6098; e-mail: johnsondr@ornl.gov

Contractor: Oak Ridge National Laboratory, Oak Ridge, Tennessee

Contract No.: DE-AC05-00OR22725

Objectives

- Develop and utilize new capabilities and techniques for ultra-high resolution transmission electron microscopy (UHR-TEM) to characterize the microstructures of catalytic materials of interest for reduction of NO_x emissions in diesel and automotive exhaust systems.
- Relate the effects of reaction conditions on the changes in morphology of heavy metal species on “real” catalyst support materials (typically oxides), in collaboration with numerous industry, national laboratory and university partners.
- Continue project with Protochips Co. (Raleigh, NC) to demonstrate the utility of a robust MEMS-based heating technology (i.e., "AduroTM" chips) for the ACEM, that allows the behavior of catalytic materials to be studied *in situ* as a function of temperature and time, and under gaseous environments with the development of an environmental cell (E-cell) specimen holder and gas-handling apparatus.
- Design, fabricate and implement a new "double-tilt" specimen holder to allow Protochips Aduro devices to be used in heating experiments while also allowing precise alignment of catalyst samples to crystal zone-axis orientations, thereby improving interpretation of the effects of heating on catalyst behavior.

Approach

- Utilize Oak Ridge National Laboratory ACEM to characterize the atomic morphology and behavior of heavy-metal species such as platinum, gold and rhenium on oxide (and other) support materials (alumina, silica, titania, carbon) as a function of *in situ* heating procedures.

- Improve Aduro heater devices with by MEMS-fabrication of continuous amorphous silicon nitride films on the heater membranes, to allow heating experiments under oxidizing environments both with the standard single-tilt and the E-cell heater holders.
- Demonstrate utility of amorphous silicon nitride films coating Aduro heater devices for support of catalyst materials during oxidation experiments.
- Utilize ACEM high-angle annular dark-field (HAADF) imaging to characterize the structure and chemistry of a series of model bimetallic nanoparticles comprising controlled compositions in the gold/palladium, platinum/zinc, and platinum/rhenium systems, on model oxide and carbon supports such as ZnO "nanobelts" and carbon nanotubes.
- Utilize ACEM for studies of the efficacy of "single-atom" catalysis in systems such as Au/FeO_x, Pt/FeO_x and Pt/alumina, with colleagues at ORNL, UMissouri-St. Louis, and UOP Co. These studies offer evidence for the remarkable potential for ultra-fine dispersions of heavy metals, at the single-atom level, to be stable for reaction processes such as CO oxidation, thereby minimizing by several orders of magnitude the use of precious metals in commercial catalysis processes.
- Utilize ACEM for studies of the fundamental behavior of Au clusters and nanoparticles on model alumina and titania supports, and Pt clusters and nanoparticles on model alumina and silica supports, with colleagues at Purdue University. Couple microscopy with FTIR and DRIFTS studies to develop understanding of principal binding sites for precious metal species on the single-crystal nanoparticle surfaces.

Accomplishments

- Conducted numerous tests of the Gen 2 E-cell holder and determined the need for an improved design to facilitate sample loading and to optimize performance and through-put. A new, more robust "Gen 3" E-cell design was developed and fabrication begun.
- ACEM experiments using Protochips heating showed mechanisms of formation of PdZn bimetallic nanoparticles at elevated temperatures via Pd particle growth and reactions with ZnO surface on novel nanobelt model support. A novel mechanism for anchoring of PdZn nanoparticles was characterized and reported for the first time. This work conducted with Prof. J. Liu and colleagues, University of Missouri-St. Louis.
- Atomic-level imaging of Pt on FeO_x support materials allowed characterization of the efficacy of catalysis processes over single Pt atoms, and showed that dispersions of catalytic species at the single-atom level could be stable in real reaction processes. This work also conducted with Prof. J. Liu and colleagues.
- Coupling spectroscopy results (FTIR and DRIFTS) with aberration-corrected annular dark-field imaging in the ACEM allowed determination that, for example, Au atoms on cube-octahedral nanoparticles at low-coordinated corner and perimeter sites controlled the water-gas shift reaction, whereas all surface Pt atoms on nanoparticles supported on alumina and silica were equally active. This work conducted with Prof. F. Ribiero and colleagues, Purdue University.
- Atomic-level imaging of model Pt/AlO_x catalysts allowed correlation of the behavior of single-atom, dimer, and fine-cluster Pt species with temperature-programmed reduction processes, in a fundamental study to understand how catalyst species behave under reaction conditions. This work conducted with Dr. S. H. Bradley, UOP Co.

Future Directions

- In a cooperative project with Protochips Co., continue to develop techniques for *in situ* heating experiments, especially the development of a reliable environmental cell (E-cell) capability for gas reaction experiments.
- Perform precisely controlled *in situ* thermal experiments using *in situ* heating capabilities to understand the interaction of Pt atoms with catalyst supports, and the development of catalyst nanoparticles and subsequent coarsening kinetics.
- Utilize the Gen 3 E-cell in collaboration with colleagues at Ford Motor Co. and the University of Michigan, to study the behavior in oxidation-reduction cycles of “intelligent” catalyst materials, comprising heavy metal species such as Pd and Rh in perovskite structures like LaFePdO₃ and CaTiRhO₃. This work is aimed at obtaining a fundamental understanding of the mechanisms and kinetics of the cyclic dissolution and subsequent reformation of catalytic nanoparticles on support surfaces during the redox cycles.

Technical Progress

Work this year has progressed on several fronts, including new developments in our *in situ* microscopy thrust area, and in catalysis research with several groups that we are calling “single atom catalysis.” The latter work is leading to the new understanding of the potential for stable, working catalytic systems to be formulated that involve catalytic species such as Pt and Pd to be dispersed at the atomic level on oxide supports, and that give reaction results equivalent or superior to more conventional catalysts. The importance of this development is that it leads to the possibility of dramatically reducing the amount of precious metal species needed for a 'real' catalyst, with a concomitant reduction in cost. We have also made progress in studies of Pt and Au catalyst systems on model alumina, titania and silica supports, in which we have identified the active sites on the surfaces of nanoparticles of these species in the 2-20 nm range, for WGS catalysis. These results were obtained by combining sub-Ångström imaging in the ACEM with spectroscopic methods to elucidate the nature of the active sites. Some of our results in these areas are highlighted in the following sections.

***In Situ* Microscopy Development:**

Our *in situ* microscopy development activities continued this year, with a number of studies that

employed our standard heating holder employing Protochips Co. Aduro™ heating devices. With this holder, we routinely characterize changes in catalysts with heating in the vacuum of the electron microscope. We have also demonstrated the ability to conduct heating experiments in a reducing atmosphere (generally 4% H₂ in Ar) with the heating holder retracted into the specimen airlock, and the reducing gas admitted instead of the usual N₂ atmosphere. This allows samples to be reacted under atmospheric pressure conditions. In order to allow both reduction and oxidation treatments with carefully controlled pressures and (ultimately) gas flow rates, we have devised environmental cell holders that constrain the reaction gas between a heater membrane and a plain SiN "window" device. The early E-cell Gen 1 and Gen 2 designs used Aduro devices with continuous carbon films deposited over holes in the heater membrane, in order to seal the cell, but the carbon film cannot withstand heating in an oxidizing atmosphere. We learned to fabricate continuous amorphous SiN films over the heater membrane, to replace the carbon films on the heater devices. We have demonstrated that the SiN would not only easily withstand oxidizing environments up to 800°C and atmospheric pressure, but also would allow imaging of crystal lattices through the SiN layer (typically ~25 nm

thick) at reasonable *in situ* reaction pressures up to 20 Torr (as tested so far). We reported in the last quarterly that the initial SiN films showed an artifact structure due (it was determined) to a vacuum/furnace system fault during the deposition process, which has been resolved in later depositions. **Figure 1** shows a high-angle annular dark-field and bright-field image pair, recorded on the aberration-corrected JEOL 2200FS ACEM, of a CuAu/TiOx bimetallic catalyst material on the 'defected' SiN film, after a 10min heating in air at 600°C. The SiN film showed no visible effect of this aggressive oxidation treatment; a standard heater membrane with a carbon film supporting the catalyst would show the carbon film totally destroyed by this treatment. **Figure 2** is a high-resolution HAADF image of a CuAu nanoparticle (area outlined in **Fig. 1**) showing atomic resolution and a surface layer determined to be copper oxide, imaged through the ~25nm amorphous SiN film. The ability to fabricate heater devices with SiN films also has made possible an improved design of E-Cell holder, called Gen 3, which will eliminate some operational issues that were identified during experiments with the Gen 2 holder, and simplify (i.e. make more reliable) the process of sample loading. Tests of the Gen 3 holder will begin in Q2, FY 2011. **Figure 3** shows a CAD drawing of the Gen 3 device, positioned inside the objective lens pole piece of the ACEM (shown in green); details of the design will be further revealed in a later report.

We also completed the design, fabrication and testing of a new *in situ* heating holder for the ACEM that permits a second (orthogonal) tilt axis within the specimen goniometer stage, to allow precise orientations of single-crystal catalyst supports to be achieved. This new capability was desired because of the importance of crystal tilt to imaging of crystal lattices in the HAADF mode, which is much more sensitive to sample alignment than conventional bright-field (BF) imaging. A double-tilting capability will significantly facilitate imaging experiments by allowing the catalyst support to be more readily positioned so

the relationship between catalyst nanoparticles and support structure can be analyzed. **Figure 4** shows the new holder and a schematic of the mechanics of control of the second tilt axis. **Figure 5** shows the effects of tilting of a ZnO nanoribbon model support material from a 2° misalignment (**Fig. 5a**) where atomic columns are not clearly distinguished at 15Mx original magnification, to perfect alignment (**Fig. 5b**) in which the atomic columns are fully resolved. **Figure 6** shows the epitactical orientation of a PdZn bimetallic catalyst nanoparticle on a similarly oriented ZnO support. With the new holder, results such as these can be routinely obtained; it is particularly useful during heating cycles, as the support often shows a tendency to slightly shift position as a result of the high temperature treatment, and the holder allows these motions to be effectively tracked.

Single-atom Catalysis:

In conventional catalytic materials for applications such as emission control, CO oxidation, the PROX reaction (preferential oxidation of CO in H₂), the water-gas shift reaction (removal of CO in H₂ for purification of hydrogen), and even in catalysts for use in NOx trap materials such as Pt on g-alumina, the precious metal species are often present in nanoparticle form of sizes in the 1-10nm range. Since catalytic reactions typically only involve surface atoms that are exposed to the reactant species, the atoms in the bulk are not effective for catalysis. It is a grand challenge of catalytic science to develop stable catalyts with high reactivity that reduce the use of expensive, increasingly rare precious metal species. The ultimate catalyst would involve dispersions of the catalytic species at the atomic level, with catalytic reactions occurring at the single-atom level.

We are working with several groups whose studies of precious metal/oxide catalysts have, with the use of various spectroscopy methods correlated to the direct imaging results using our aberration-corrected JEOL 2200FS ACEM, given early

evidence for the ability to formulate stable catalysts with single atoms as the principal catalytic species. For example, fundamental work is ongoing with Dr. S. A. Bradley of UOP Co. (Des Plaines, IL), in which model Pt/alumina catalysts with very low percentage loadings have been shown to maintain stable dispersions as single-atoms or as dimers and trimers during temperature programmed reduction (TPR) experiments. This work, reported in a prior quarterly, utilized our in situ heating and airlock reduction capabilities on the ACEM. Recent work with Prof. J. Liu of the University of Missouri-St. Louis and colleagues at the Chinese Academy of Sciences (Dalian) has shown what we believe is the first practical fabrication of a single-Pt-atom catalyst consisting of only isolated single atoms anchored onto iron oxide (FeO_x) nanocrystallites. This unprecedented single-Pt-atom catalyst exhibits very high activity and stability for both CO oxidation and PROX of CO in H₂, attributed to the partially vacant 5d-orbitals of positively charged, high-valent Pt atoms. Concurrent work with Prof. A. Datye of the University of New Mexico and colleagues at e.g. PNNL (Dr. Y. Wang) on characterization by ACEM HAADF imaging of Pd dispersed on ZnO powders showed that Pd/ZnO catalysts reduced at 500°C exhibited an abundance of bright features whose contrast was consistent with dispersed single atom species of Pd. We have explored the conditions that favor the formation and stabilization of these single atom species on the non-polar ZnO (10-10) surface, which is the dominant facet exposed in ZnO powders. The reactivity of these Pd species for CO oxidation and for the MSR reaction has also been investigated. Brief examples of the microscopy results from the latter two studies highlighted here.

Single-Atom Pt/FeO_x catalysis: This work has resulted in a manuscript presently under review for publication in Nature Chemistry (see Publications section). The single-atom Pt₁/FeO_x catalyst (Sample A) was prepared by a co-precipitation method as previously reported for supported Au

and Pd catalysts [1,2] but with a finely tuned co-precipitation temperature and pH value. Specifically, in order to anchor Pt atoms on the defects of FeO_x surface and to sufficiently isolate the Pt atoms, the Pt loading was controlled to a very low level of 0.17 wt% and a high-surface-area (about 290 m²/g for the as-synthesized samples) FeO_x nanocrystallite support was used. To evaluate the effect of Pt loading on the structure and performance of the final catalysts, a similar catalyst with a Pt loading of 2.5 wt% (Sample B) was also prepared, characterized, and tested.

Sub-Ångström-resolution ACEM HAADF imaging was used to characterize the dispersion and configuration of the Pt clusters in the catalysts. **Figure 7a** clearly shows individual Pt atoms (marked by the white circles), uniformly dispersed over the surfaces of FeO_x nanocrystals in sample A. Examination of different regions revealed that only single Pt atoms were present in sample A. The atomic resolution HAADF image in **Fig. 7b** reveals that individual Pt atoms (indicated by the white circles) occupy exactly the positions of the Fe atoms. As plan-view HAADF images represent the projection of atoms along the incident beam direction, surface atoms cannot be distinguished from the sub-surface atoms in the HAADF images. However, we determined that the Pt atoms were inside the FeO_x nanocrystallites by changing the focus of the electron beam (or “depth sectioning” [3]). By analyzing images obtained sequentially with varying beam focus settings we could conclude that the observed Pt atoms are not located inside the individual FeO_x nanocrystals. In addition, by examining many HAADF images of Sample A, we estimated that the density of Pt single atoms was about 0.07 Pt atoms/nm², which is very close to the actual Pt loading (about 0.09 Pt atoms/nm²) of Sample A. Therefore, all the observed individual Pt atoms were determined to be located either on top of the surfaces or in the near-sub-surfaces of the FeO_x nanocrystallites. These results were correlated to ACEM imaging of Sample B (not shown here) and with methods

such as extended x-ray absorption fine structure (EXAFS) and extended x-ray absorption near-edge structure (EXANES), as well as with probe reactions such as CO oxidation and PROX. EXAFS and EXANES studies were consistent with single-atom dispersions in Sample A, and the presence of larger clusters in Sample B (confirmed by ACEM imaging). In summary, we have synthesized and characterized a novel catalyst consisting of only single Pt atoms uniformly dispersed on high-surface-area FeO_x support. This catalyst shows extremely high activity for both CO oxidation and PROX reactions. The chemical reactivity of our high-valent single Pt atoms is quite different from that of single Au atoms or cations on the same support; the Au/FeO_x catalyst contains polydispersed nano-structures from single atoms to clusters, with single Au atoms inactive for CO oxidation [see e.g. ref. 3]. The more vacant d-orbitals of our single Pt atoms due to the charge transfer from Pt atoms to the FeO_x surface are responsible both for the strong binding and stabilization of single Pt atoms and for providing high-valent Pt atoms, which ultimately account for the excellent catalytic activity of the Pt₁/FeO_x catalyst.

Single-Atom Pd/ZnO Catalysis: This work will be presented at the 22nd Annual Meeting of the North American Catalysis Society in Detroit (June 2011); a full manuscript is under preparation.

The energetics of Pd single atoms on clean and defective ZnO(10-10) surfaces were explored using density-functional-theory (DFT) computations [4]. The surface was modeled as a periodic slab that consisted of eight ZnO layers (**Fig. 8a**), where the bottom three layers were fixed at the DFT-predicted bulk equilibrium positions of ZnO. Periodic images of the slab were separated by a 14Å- thick vacuum region. Dangling bonds at the bottom of the slab were saturated with hydrogen-like atoms in order to mimic the ionic bonding in bulk ZnO. All computations were performed with the Vienna *ab-initio* software package (VASP) [5].

The results of the computations showed that Pd interacts strongly with the ZnO(10-10) surface. Pd bulk interstitials were found to be energetically stable but their stability is significantly lower than Pd binding on the surface. Direct exchange of Pd ⇌ Zn in the surface was found to be unstable. Thus, the computations suggested that the most likely Pd binding sites for clean ZnO(10-10) are on the surface. However, the DFT calculations predict an alternative interaction pathway of Pd with the ZnO(10-10) surface: the formation of ZnO surface vacancies. These defects are predicted to be energetically competitive especially in the presence of H₂. The interactions of Pd with these defects are comparatively strong, the Pd binding energies are predicted to be ~60% higher than those on the surface. The occurrence of these thermally activated defects and their strong stabilizing effect on Pd single atoms is corroborated by our observations that ZnO reconstructs at temperatures above 450°C while these processes are suppressed at lower temperatures. Furthermore HAADF STEM image observations (**Fig. 8b**) show the appearance of isolated Pd atoms in the same temperatures range where the surfaces reconstruct. We conclude that, at least in the case of the ZnO (10-10) surface, elevated temperatures promote ZnO vacancy formation, and these vacancy sites serve as additional strong binding sites for anchoring Pd atoms.

Determination of Active Sites on Catalytic Nanoparticles

Work in collaboration with the Purdue University group of Prof. F. H. Ribeiro has involved high-resolution imaging coupled with FTIR and DRIFT spectroscopies to elucidate the active sites on Au and Pt nanoparticles on oxide supports such as alumina, titania and silica. Au nanoparticles in the 1-7 nm size range were shown to be cubo-octahedral in shape, and the dominant active site was shown to be the low coordinated corner Au atoms, which are ~7 and ~3 times more active than

the perimeter Au atoms for Au/TiO₂ and Au/Al₂O₃ catalysts, respectively. Details of this work will be reported in the next quarterly.

Concluding Remarks:

Our research activities on the forefront studies of the behavior of catalyst clusters and nanoparticles with reaction treatments, imaged at ultra-high resolution with the aberration-corrected electron microscope, are building a foundation towards a better understanding of the phenomena, which control performance in real systems. The implementation of novel methods for conducting these studies on specimens heated inside the electron microscope is the primary thrust of our research. Significant progress has been made in further development of an integrated heating technology for high-resolution electron microscopy, and we are extending these heating capabilities to an environmental cell functionality for studying gas reactions on catalytic materials. We have also introduced a new heating holder with a double-tilt capability, to permit precision alignments of the support crystal that will allow us to elucidate crystallographic relationships between the support structure and catalytic nanoparticles. Our work is in support of a variety of catalyst materials studies supported by DOE and the HTML national user program.

References

1. Qiao, B. & Deng, Y.; "Highly effective ferric hydroxide supported gold catalyst for selective oxidation of CO in the presence of H₂." *Chem. Commun.*, 2192-2193 (2003).
2. Qiao, B., Liu, L., Zhang, J. & Deng, Y. "Preparation of highly effective ferric hydroxide supported noble metal catalysts for CO oxidations: From gold to palladium." *J. Catal.* **261**, 241-244 (2009).
3. L. F. Allard, A. Borisevich, W. Deng, R. Si, M. Flytzani-Stephanopoulos and S. H. Overbury, "Evolution of gold structure during thermal treatment of Au/FeO_x catalysts revealed by aberration-corrected electron microscopy." *J Electron Microsc (Tokyo)* **58**, 199-212 (2009).
4. G. Kresse and D. Joubert, "From ultrasoft pseudopotentials to the projector augmented-wave method." *Physical Review B* 1999, **59** (3), 1758-1775.
5. G. Kresse and J. Furthmuller, "Efficient iterative schemes for *ab initio* total-energy calculations using a plane-wave basis set." *Physical Review B* 1996, **54** (16), 11169-11186.

Publications and Presentations:

"Unique Role of Anchoring Penta-Coordinated Al³⁺ Sites in the Sintering of g-Al₂O₃-Supported Pt Catalysts;" D. Mei, J. H. Kwak, J. Hu, S. J. Cho, J. Szanyi, **L. F. Allard**, and C. H. F. Peden, *J. Phys. Chem. Lett.*, 2010, **1** (18), pp 2688–2691 (August 31, 2010) (Letter) DOI: 10.1021/jz101073p.

"Metallic Corner Atoms in Gold Clusters Supported on Rutile are the Dominant Active Site during Water-Gas Shift Catalysis;" W. D. Williams, M. Shekhar, W.-S. Lee, V. Kispersky, W. N. Delgass, F. H. Ribeiro, S. M. Kim, E. A. Stach, J. T. Miller, and **L. F. Allard**, *J. Amer. Chem. Soc.* (in press 2010).

"Synergy of Combined SEM and TEM Imaging Techniques for the Characterization of Catalyst Behavior During *In Situ* Heating;" J. Y. Howe, **L. F. Allard**, W. C. Bigelow, H. Demers and S. H. Overbury, manuscript submitted to *J. Elect. Micros.* (2010).

"Single-atom catalysis: Remarkable performance of Pt₁/FeO_x for CO oxidation and preferential oxidation of CO in H₂;" B. Qiao, A. Wang, X. Yang, **L. F. Allard**, Z. Jiang, Y. Cui, J. Liu, J. Li and T. Zhang, manuscript in review for *Nature Chemistry* (2010).

"Coalescence and sintering of Pt nanoparticles: *in situ* observation by aberration-corrected HAADF STEM;" M. A. Asoro, D. Kovar, Y. Shao-Horn, **L. F. Allard** and P. J. Ferreira, *Nanotechnology* **21** (2010) 025701 (6pp).

"Characterization of Alumina Supported Pt and Pt-Pd Alloy NO Oxidation Catalysts with Advanced Electron Microscopy;" O. K. Ezekoye, A.R. Drews, H. W. Jen, R.J. Kudla, R.W. McCabe, J.Y. Howe, L.F. Allard, G.W. Graham and X.Q. Pan, manuscript submitted to *Applied Catalysis* (2010).

"Behavior of Au Species in Au/Fe₂O₃ Catalysts Characterized by Novel *In Situ* Heating Techniques and Aberration-Corrected STEM Imaging," L. F. Allard, Maria Flytzani-Stephanopoulos and Steven H. Overbury, *Microsc. Microanal.* **16**, 375–385 (August 2010).

"Surface Channeling in Aberration-Corrected Scanning Transmission Electron Microscopy of Nanostructures," J. Liu and L. F. Allard, *Microscopy and Microanalysis*, Volume 16, Issue 04, pp 425-433 (August 2010).

"New Insights into the Growth Mechanism and Surface Structure of Palladium Nanocrystals;" B. Lim, H. Kobayashi, P. H. C. Camargo, L. F. Allard, J. Liu and Y. Xia, *Nano Res* **3**: pp 180–188 (2010).

"Zero oxidation state platinum atom supported on θ -alumina;" C. K. Narula, X.-Q. Chen, G. M. Stocks, M. Moses-DeBusk and L. F. Allard, in review, *J. Amer. Chem. Soc.* (2010).

"Applications of High-Resolution Aberration-Corrected STEM Imaging to Studies of the Behavior of Catalytic Materials at Elevated Temperatures;" L. F. Allard and K. L. More, ASM Educational Symposium, Oak Ridge, TN (April 2010). **Invited Talk**

***In Situ* Environmental Electron Microscopy, Then and Now;"** L. F. Allard and W. C. Bigelow; EMAL 40th Anniversary Symposium, Dept. of Materials Science & Engineering, University of Michigan
October 2009. **Invited Talk**

"Development of a Novel Environmental Cell for *In Situ* Gas Reaction Experiments via Aberration-Corrected STEM Imaging;" L. F. Allard, W. C. Bigelow, S. H. Overbury, D. P.

Nackashi and J. Damiano, Microscopy Society of America, 2010. **Invited Talk**

"Ultra-high- Resolution STEM and NMR Studies of Poorly Crystalline γ -Al₂O₃ Surfaces: New Insights From Imaging and Spectroscopy," J. H. Kwak, J. Z. Hu, D. Mei, D. H. Kim, J. Szanyi, L. F. Allard and C. H. F. Peden, *Microscopy & Microanalysis* **16** (Suppl. 2) : 310-311, Cambridge University Press (2010). **Invited Talk**

"Morphological and Electronic Structure of Pt-Re Nanoparticles Supported on Carbon under Activation and Reaction Conditions for Aqueous-Phase Reforming of Bioliquid," L. Zhang, G. Xia, Y. Yang, D. Heldebrant, D. King, Y. Wang and L. F. Allard, *Microscopy & Microanalysis* **16** (Suppl. 2): 1428-1429, Cambridge University Press (2010).

"Synergy of Combined (S)TEM Imaging Techniques for the Characterization of Catalyst Behavior During *In Situ* Heating;" J. Y. Howe, L. F. Allard, W.C. Bigelow and S. H. Overbury, *Microscopy & Microanalysis* **16** (Suppl. 2) : 312-313, Cambridge University Press (2010).

"Synthesis and Characterization of ZnO-Supported Noble Metal Nanocatalysts for Energy Applications;" J. Liu and L.F. Allard, Materials Research Society Annual Meeting, Boston (Dec. 2009).

"Strong Interaction of Au with FeOx Surfaces Evidenced in the Water-Gas Shift Reaction, and Probed by Aberration-Corrected Electron Microscopy and Scanning Tunneling Microscopy;" R. Si, L. F. Allard, A. Borisevich, W. Deng, K. T. Rim, Y. Zhai, B. Ricks, A. Frenkel, G. Flynn, M. Flytzani-Stephanopoulos and S. H. Overbury, AIChE Annual Meeting, Nashville (Nov. 2009).

Communications and Visits

University of Michigan, Meeting with Prof. X. Pan, G. Graham, A. Drews and M. Katz; Discussion of new project to study "intelligent catalysts" for NOx reduction applications, (Oct. 2009).

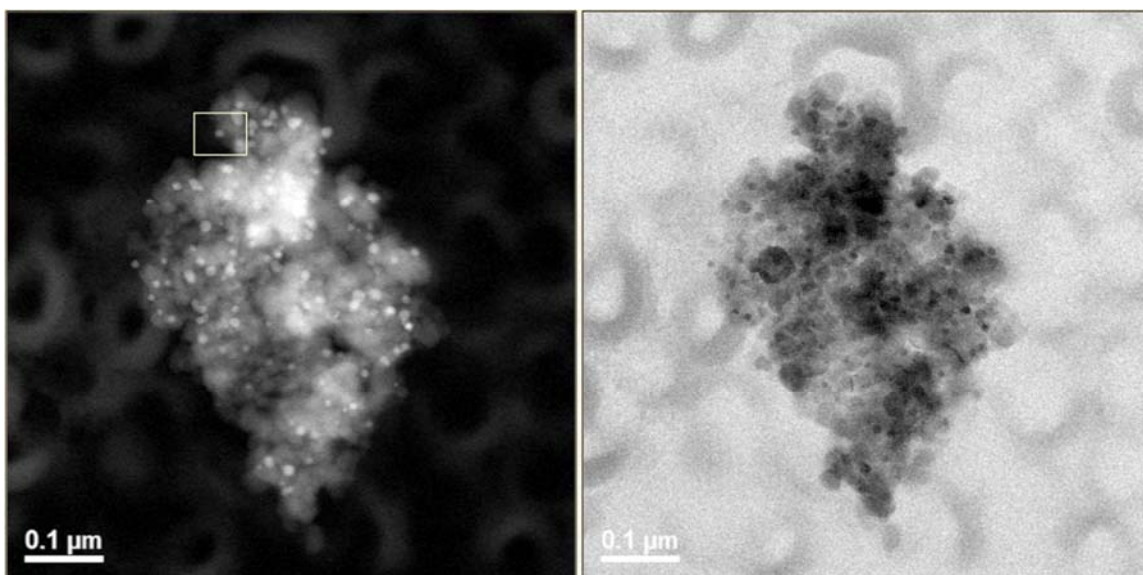


Fig. 1 HAADF (a) and BF (b) images showing a CuAu/FeOx bimetallic catalyst aggregate on the first amorphous SiN continuous film on a Protochips Aduro heater membrane. The sample was heated in air for 10min at 600°C, and the SiN film was not visibly affected by the aggressive oxidation treatment.

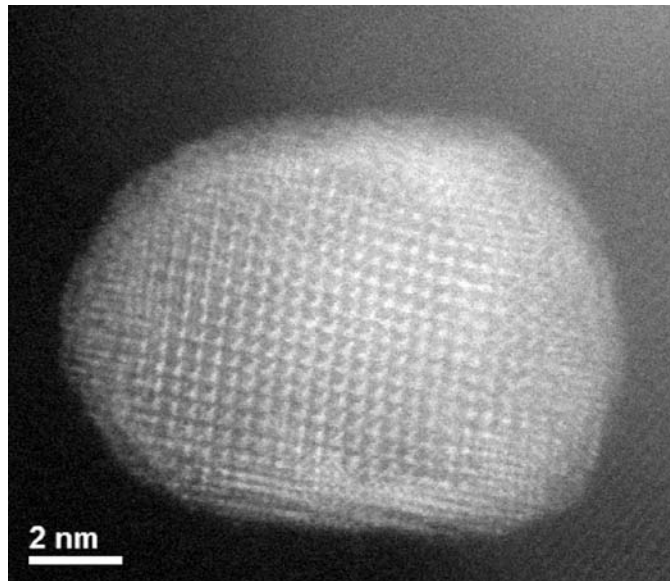


Fig. 2 High-resolution HAADF image of the CuAu particle outlined in Fig. 1, after oxidation. The particle was imaged with the beam passing first through the ~25nm SiN film, the geometry needed for the E-cell holder.

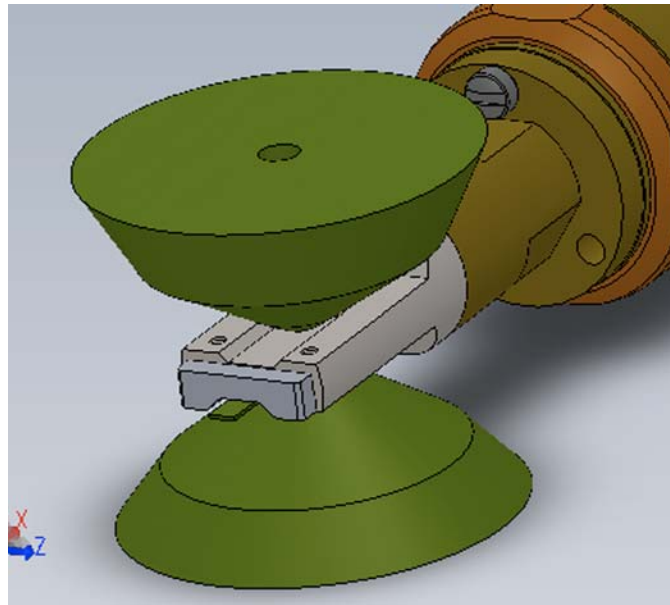


Fig. 3 CAD drawing showing an oblique view of the Gen 3 E-cell, positioned between the upper and lower parts of the objective lens pole piece for the JEOL 2200FS ACEM. The unique thin Aduro device with amorphous SiN overlayer coupled with a thin SiN lower cell window allows the Gen 3 holder to be fabricated with a thickness of only 1.2 mm.

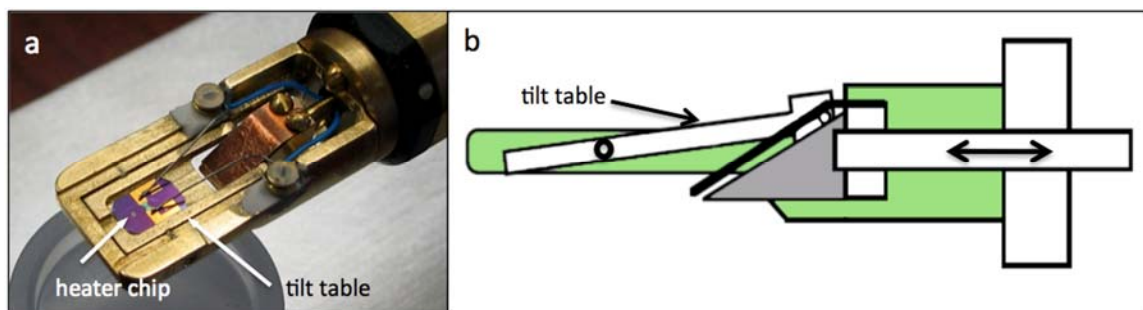


Fig. 4 View of the new double-tilt heating holder (a) with large Aduro heater device installed; (b) schematic showing the mechanics of operation of the tilting table.

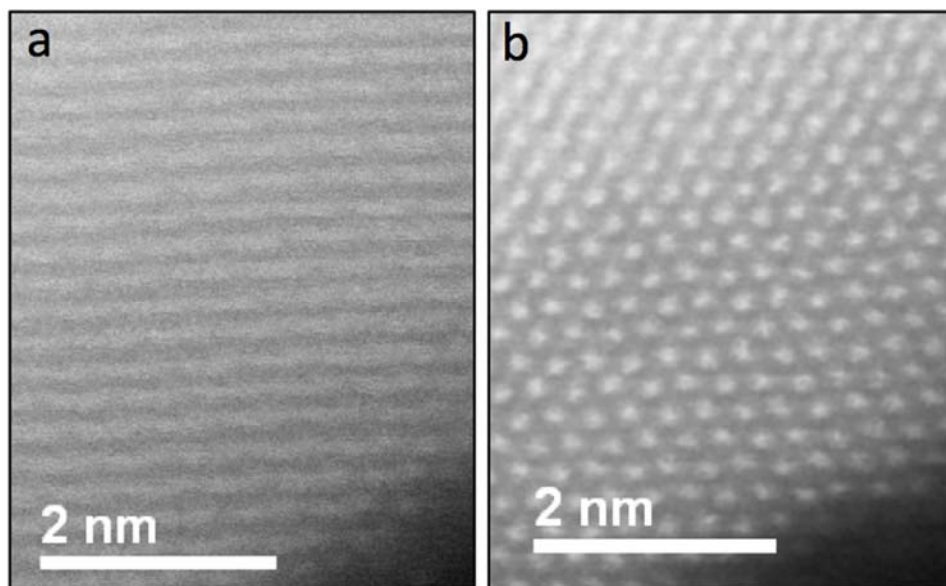


Fig. 5 HAADF images of a ZnO nanoribbon oriented with a 2° mis-tilt (a) and 0° mis-tilt, showing the need for near-perfect orientation for proper imaging of the crystal structure.

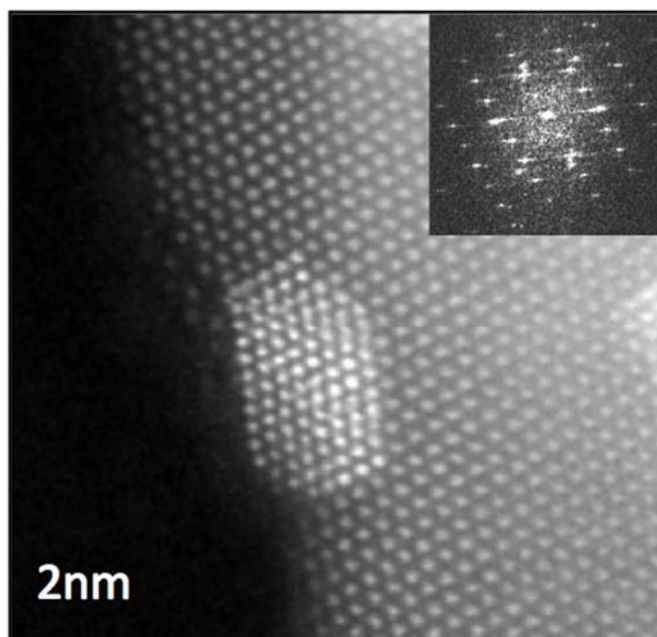


Fig. 6. Model catalyst of Pd on ZnO nanoribbon, showing the epitactical orientation of the catalyst nanoparticle revealed by proper orientation of the support structure as achieved using the double-tilt operation. Pd particle grew during an in situ heating at 700°C for 30 min.

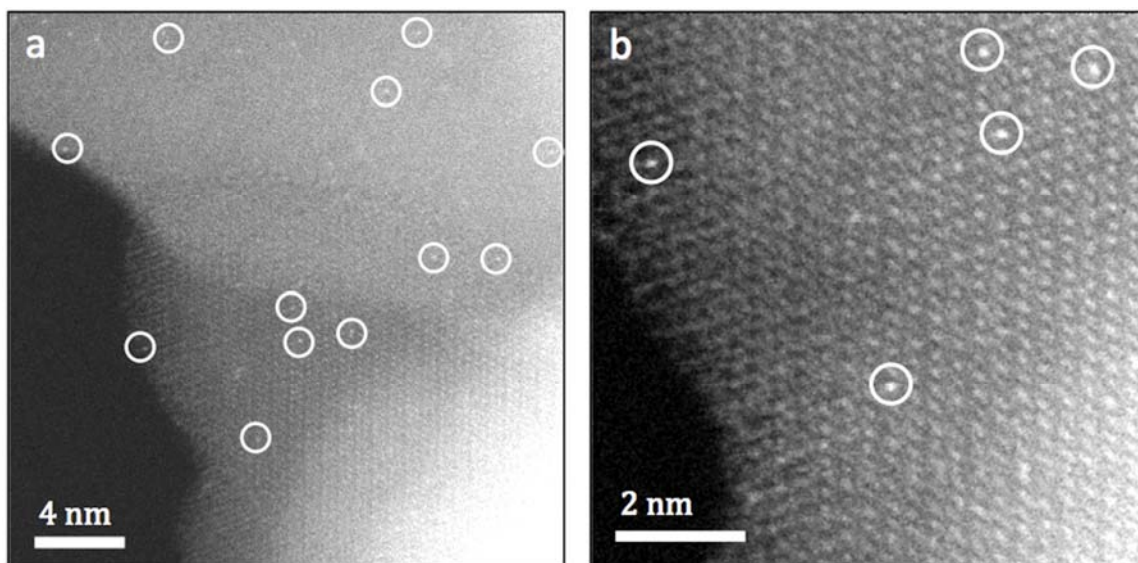


Fig. 7 (a) Medium magnification HAADF image of single-atom dispersion of Pt on FeOx; the oxide support is off-axis for showing the crystal structure, allowing the higher atomic number Pt species to be more easily identified; (b) High-resolution HAADF image of well-oriented FeOx structure, with bright columns associated with Pt atoms located on Fe columns, at the surface of the support (see text for details).

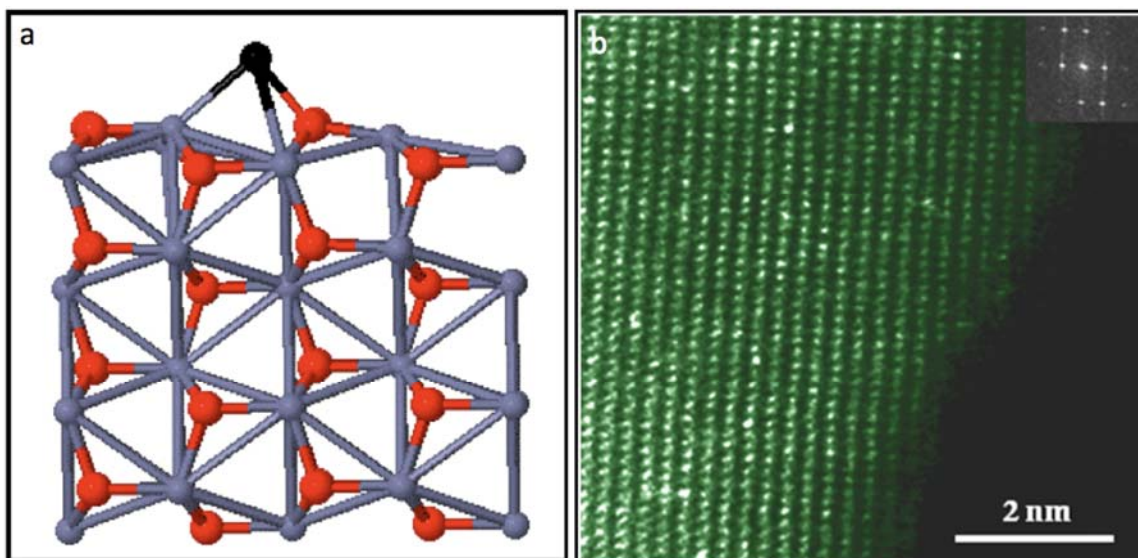


Fig. 8 (a) DFT computation for the energetics of single Pd atoms located on a ZnO (10-10) surface; (b) single Pd atoms are stable on the ZnO surface at temperatures where the ZnO reconstructs with surface vacancies (see text for details).

Agreement 17895 - Durability of ACERT Engine Components

H. T. Lin, B. L. Armstrong, and A. A. Wereszczak

Oak Ridge National Laboratory

P.O. Box 2008, MS-6068

Oak Ridge, TN 37831-6068

(865) 576-8857; fax: (865) 475-6098; e-mail: linh@ornl.gov

Nate Phillips and Jeff Jenson

Caterpillar, Inc.

Peoria, IL 61656-1875

(309) 578-2969; fax: (309) 578-2953; e-mail: Jensen_Jeff_A@cat.com

DOE Technology Manager: Jerry L. Gibbs

(202) 586-1182; fax: (202) 586-1600; e-mail: jerry.gibbs@ee.doe.gov

ORNL Technical Advisor: D. Ray Johnson

(865) 576-6832; fax: (865) 574-6098; e-mail: johnsondr@ornl.gov

Contractor: Oak Ridge National Laboratory, Oak Ridge, Tennessee

Contract No.: DE-AC05-00OR22725

Subcontractor: Caterpillar, Inc., Peoria, Illinois

Objective

- Generate mechanical and physical properties database and characterize damage mechanisms of candidate advanced light-weight high-temperature materials; i.e., ceramics and intermetallic alloys.
- Apply and verify probabilistic life prediction and component design and develop verification methods for reliability assessment of advanced diesel engine components.

Approach

- Evaluate the long-term mechanical performance and reliability of candidate advanced light-weight high-temperature metallic alloys and ceramics at elevated temperatures in air before and after long-term exposure to simulated engine environments, as well as engine field tests.
- Characterize the evolution and role of damage mechanisms, and changes in microstructure and chemistry, linked to the long-term mechanical performance and reliability of ceramics and intermetallic alloys.
- Predict the failure probability and reliability of complex-shaped diesel engine components subjected to application conditions via the use of life prediction codes.

Accomplishments

- Completed development of oxide-based protective coatings for heavy-duty diesel engine components.
- Completed thermal cycle tests for ferritic ductile iron steel substrates with developmental oxide-based coating.
- Completed post characterization of coated ferritic ductile iron steel substrates after thermal cycles to provide insight into the microstructure stability and durability of coating under the simulated engine operation condition.

Future Direction

- Characterize the stainless steel exhaust manifold designed and manufactured for Tier 2 engine before after ACERT engine testing.
 - Characterize and test exhaust valves manufactured using ORNL newly developed alloy after ACERT engine testing.
 - Establish mechanical database for advanced light-weight components designed for Tier 4 engine.
-

Introduction

There has been considerable interest in the potential for extensive use of advanced ceramics and intermetallic alloys in advanced diesel engine systems because of their superior thermomechanical properties at elevated temperatures. The implementation of components fabricated from these advanced materials would lead to significant improvement in engine efficiency and long-term durability and reduced nitrogen oxides (NO_x) and CO exhaust emissions as required in the 21st Century Truck Program. Interest has focused primarily on research into characterization and design methodology development (life prediction) for advanced silicon nitride ceramics and TiAl alloys to enable the manufacture of consistent, reliable complex-shaped components for diesel engine. The valid prediction of mechanical reliability and service life is a prerequisite for successful use of these materials in internal combustion engine components.

This research project has three primary goals: the generation of a mechanical engineering database, from ambient to high temperatures, of candidate advanced materials before and after exposure to simulated engine environments; the microstructural characterization of failure phenomena in these advanced materials and in components fabricated from them; and the application and verification of probabilistic life prediction methods using diesel engine components as test cases. For all three stages, results will be provided to both material suppliers and component end-users for use in refining and optimizing processing parameters to achieve consistent mechanical reliability, and in validating the probabilistic design and life prediction of engine components made from these advanced materials.

Approach

Colloidal processing offers a low cost alternative approach for producing uniform coatings on complex-shaped components via a simple dip coating process (i.e., the ORNL slurry coating process) (1-2). Also, the oxide-based coating could be processed at lower temperature and shorter times, thus preventing the interaction (chemical reaction) between the coating and metallic substrates (e.g., Fe-based alloys). Control of the rheological behavior of the suspension by tailoring interparticle (or surface) forces is paramount to achieve a high quality defect free coating. In aqueous-based suspensions long-range attractive van der Waals forces must be balanced by repulsive forces to tailor the desired degree of suspension stability. Typically, ionizable polymeric dispersants, or polyelectrolytes, are used to modify the surface of particles to impart repulsive electrosteric forces (3-4). Aluminum, (H10, Valimet Inc., Stockton, CA) was used as the metal powder in this study. The aluminum powder had an average particle size of ~ 13.19 μm and surface area of 0.4475 m²/g, determined using dynamic light scattering (Horiba, Inc., Kyoto, Japan) and B.E.T. (Autosorb-1, Quantachrome Instruments, Boynton Beach, FL), respectively. Polyacrylic acid (PAA, 450kg/mol, Aldrich Chemicals, Milwaukee, WI), an anionic polyelectrolyte, was used as the dispersant and PL001 (Polymer Innovations, Inc., Vista, CA) as the rheological modifier for the Al system. Water purity was measured using inductively coupled plasma mass spectroscopy (ICPMS, X Series 2, Thermo Fisher Scientific, Inc., Waltham, MA). The standards (QCS26, High Purity Standards, Charleston, SC) and the nitric acid matrix (Ultrex Pure, J.T. Baker, Phillipsburg, NJ) were used to calibrate the ICPMS. The Al-oxide based coating was employed via a dip or slurry based process. A post heat treatment at 750°C in argon was carried

out to convert the slurry coating into the oxide based coating.

The Si-rich ferritic Fe steel alloy is the current production material used for the exhaust components in the heavy-duty diesel engines. The as-cast Fe steel substrates (6.4 mm thick) extracted from as-cast exhaust component were used for the development of oxide-based coating effort. The thermal cycle tests were carried out between 760°C (1400°F) and 20°C (68°F) in air to simulate the temperature cycling condition encountered during the heavy-duty (HD) diesel engine operation. Detailed optical and scanning electron microscopy analyses were carried out to evaluate the long-term durability and stability of developmental oxide-based coating.

Results

Developmental oxide based coating

Study of Al-oxide based environmental barrier coating (EBC) developed for the ductile ferritic Fe-steel substrate was completed in FY2010. The goal of this EBC developmental study is to provide an alternative approach for an effective protection for the current production ferritic Fe-steel used for exhaust components in heavy-duty diesel (HDD) engine. The application of EBC would allow HDD OEMs to significantly reduce the heat rejection (and thus thermal stress generated) and also prevent the oxidation/corrosion-induced degradation process encountered in the current production materials. Consequently, it would allow the OEMs to avoid the use of the very high-cost stainless steel materials for the exhaust port and manifold components that could potentially lead up to USD \$5M cost saving per year. More importantly this is one of the key enabling materials technologies that would allow end users to achieve 55% HDD engine efficiency and life greater than 1 million miles by 2018 as set under the 21st Century Truck Program.

Figure 1 shows the polished cross section of as-coated Al-oxide based layer on the ferritic Fe steel alloy substrate. The detailed SEM observations show that a dense and coherent Al-oxide layer (~ 20 µm thick) containing also Fe and Si elements, which are presumably from the steel substrate enriched with Si, formed after the heat treatment conversion process (Fig. 1). This Al-Fe-O layer could be FeO-Al₂O₃ (or the solid solution of other complex phases). A dense oxidation reaction layer ~ 10 µm

underneath the Al-oxide layer was also observed. A detailed EDAX mapping for element of Al, Fe, Si, and O was provided in Fig. 2. The element mapping results provide a guideline of the diffusion (and reaction) rate of Al and Fe under the heat-treating condition employed.

A 500h thermal cycle between 300° and 760°C in air was carried out to evaluate the stability and durability of Al-based oxide coating. Figure 3 shows the polished cross section of Al-oxide based layer on the ferritic Fe steel alloy substrate after thermal cycle testing. The detailed SEM observations show that a very thin, but dense and coherent Al-oxide layer (~ 1 µm thick) formed on the surface, as confirmed by the EDAX elements map shown in Fig. 4. It is not clear why the Al-oxide coating became very thin after the thermal cycle testing. There is a very porous Al-oxide layer, which might be the remnants after the coating conversion, above the dense layer. In addition, there is also a dense layer with Al, Fe and Si elements underneath the thin Al-oxide layer, which could be a reaction product from the Fe steel substrate enriched with Si, formed after the heat and thermal cycle process (Fig. 3). Further studies of the heat treatment conditions (i.e., temperature and time) will be needed to determine an optimized window for an effective and durable protective coating layer for hot section components of HDD engines. On the other hand, the dense Al-oxide layer was not always observed in some regions of substrate and only the oxide layer with Fe-Al-Si was detected, as shown in Fig. 5.

Several technical conference call meetings were held among the CRADA participants (Caterpillar, ANL, and ORNL) to discuss the critical materials and components for property evaluation and engine testing using Tier 2 ACERT engine. It was proposed that an exhaust manifold made from ferritic stainless steel and a set of intake and exhaust valves made from advanced alloys developed by ORNL would be installed for current Tier 2 ACERT engine testing. The set of valves have passed the bench rig test at Caterpillar and would be ready for engine evaluation at NTRC ORNL. It will be installed for engine testing in FY2011. On the other hand the exhaust manifold would be casted and fabricated by the material supplier. Thus, engine testing of advanced alloy valves would be initiated

first and then followed by exhaust manifold evaluation in FY2011 as well.

References

1. Armstrong, B., Kirby, G., Cooley, K., *Proceedings of The 29th International Technical Conference on Coal Utilization & Fuel Systems*, Clearwater, FL (2004).
2. Kirby, G., Cooley, K., and Armstrong, B., *Proceedings of GT2005 ASME Turbo Expo 2005: Power for Land, Sea, and Air*, Reno-Tahoe, NV (2005).
3. Cesarano, J. and Aksay, I., *J. Am. Ceram. Soc.*, 71 (4) 250-55 (1988).
4. Cesarano, J. and Aksay, I., *J. Am. Ceram. Soc.*, 71 (12) 1062-67 (1988).

Presentations and Publications

Presentation

1. H. T. Lin, “Durability of ACERT Engine Components,” poster presented at the 2010 DOE Merit Review, June 7-11, Washington D.C.

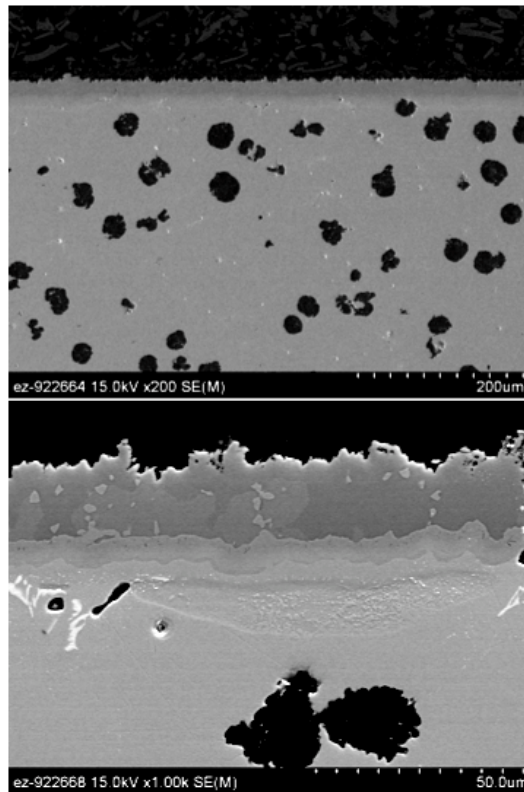


Figure 1. SEM micrographs showed the as-deposited Al-oxide based coating via the low-cost aqueous processing method.

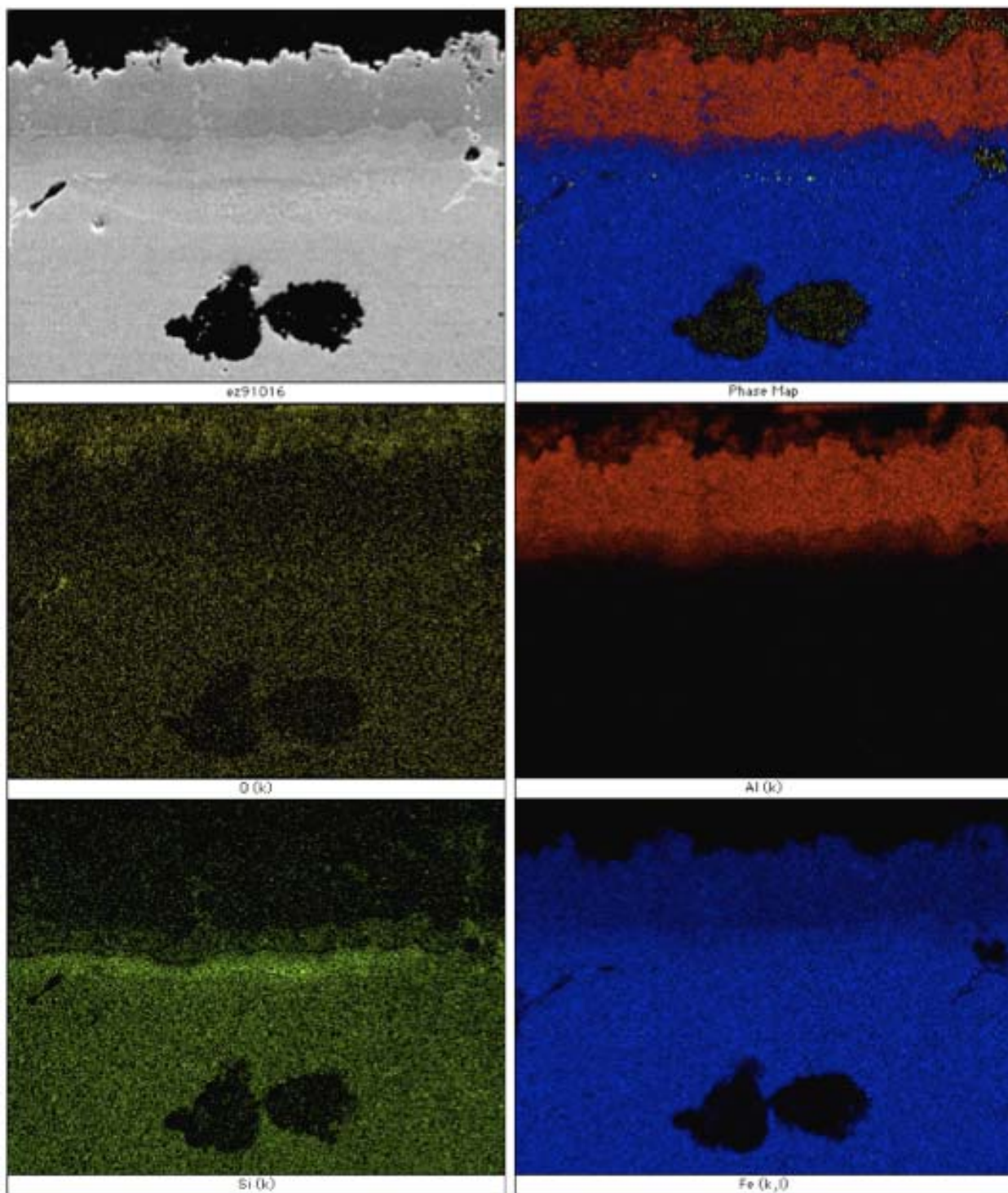


Figure 2. EDAX maps show the details of elements and distribution in the reaction and reaction surface layer on the ferritic Fe-steel substrate.

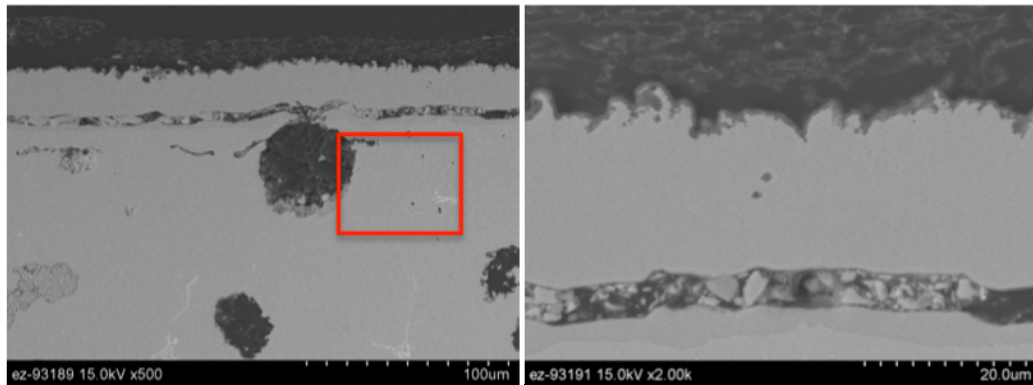


Figure 3. SEM micrographs showed the Al-oxide based coating processed via the low-cost aqueous processing method after the 500h thermal cycles between 300° and 760°C in air.

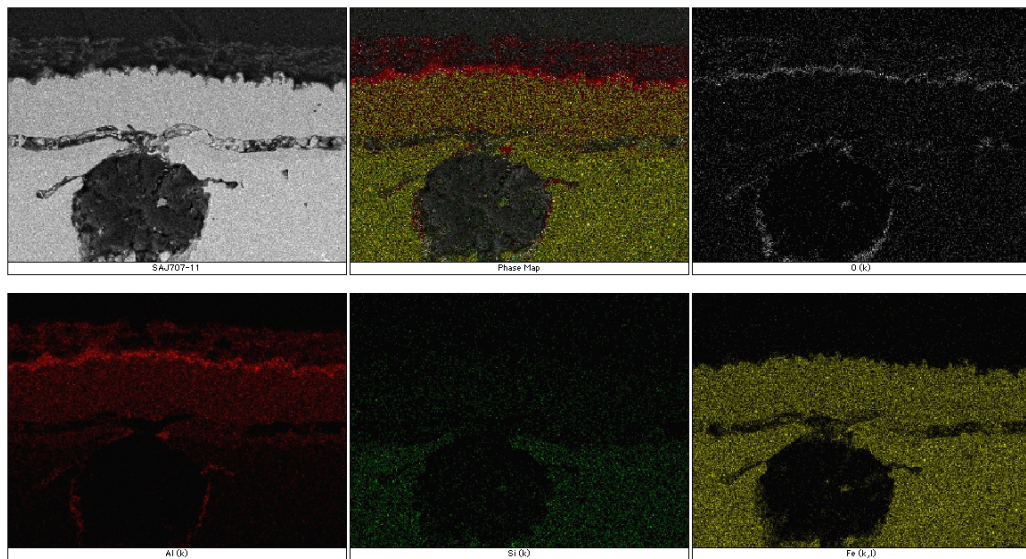


Figure 4. EDAX maps show the details of elements and distribution in the reaction and reaction surface layer of oxide-based coating on the ferritic Fe-steel substrate after thermal cycle test.

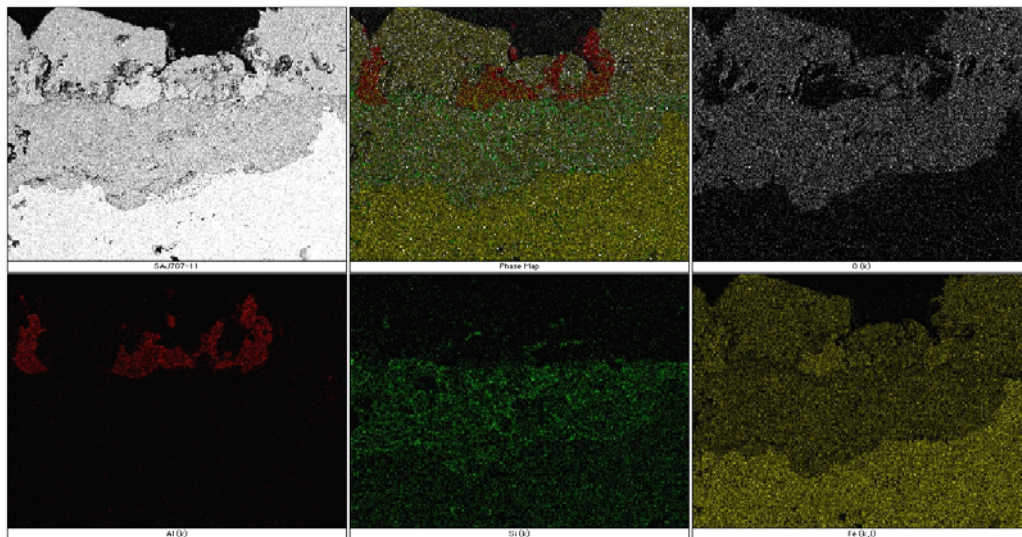


Figure 5. EDAX maps show the details of elements and distribution in the reaction and reaction surface layer on the ferritic Fe-steel substrate. The layer did not exhibit a dense Al-oxide layer.

Agreement 14957 - Modeling of Thermoelectrics

A. A. Wereszczak,* H. Wang,[†] and H. -T. Lin*

* Ceramic Science and Technology Group

[†] Diffraction and Thermophysical Properties Group

Oak Ridge National Laboratory

P.O. Box 2008, MS 6068, Bldg. 4515

Oak Ridge, TN 37831-6068

(865) 576-1169; fax: (865) 574-6098; e-mail: wereszczakaa@ornl.gov

R. McCarty and J. Sharp

Marlow Industries, Inc.

10451 Vista Park Road

Dallas, TX 75238-1645

(214) 342-4287; e-mail: rmccarty@marlow.com

J. Salvador and J. Yang

General Motors R&D Center

30500 Mound Road

Warren, MI 48090

(586) 986-5383; e-mail: james.salvador@gm.com

DOE Technology Manager: Jerry L. Gibbs

(202) 586-1182; fax: (202) 586-1600; e-mail: jerry.gibbs@ee.doe.gov

ORNL Technical Advisor: D. Ray Johnson

(865) 576-6832; fax: (865) 574-6098; e-mail: johnsondr@ornl.gov

Contractor: Oak Ridge National Laboratory, Oak Ridge, Tennessee

Prime Contract No.: DE-AC05-00OR22725

Objectives

- Non-CRADA sub-project: Measure thermomechanical and thermophysical properties of candidate thermoelectric (TE) materials (TEMats) for waste heat recovery to advance TEMats and devices (TEDs).
- CRADA sub-project: Support Marlow with their development of high temperature TEMats and TEDs.

Approach

- Non-CRADA sub-project: Measure elastic modulus, Poisson's ratio, strength, coefficient of thermal expansion, heat capacity, thermal conductivity, electrical resistivity, and Seebeck coefficient of candidate TEMats.
- CRADA sub-project: Measure properties of proprietary Marlow materials and provide development support.

Accomplishments

- Non-CRADA sub-project: Measured thermomechanical and thermophysical properties of skutterudite TEMats.
- CRADA sub-project: Performed testing of Marlow TEMats and supportive evaluation of their TEDs.

Future Direction

- Non-CRADA sub-project: Measure properties of additional high-temperature capable TEMats and provide supportive characterization R&D to support the improvement of TEMats and TED modeling.
 - CRADA sub-project: Perform thermomechanical and thermophysical property measurements of proprietary Marlow TEMats and assist in development of Marlow TEDs.
-

Introduction

Potential next generation thermoelectric devices (TEDs) comprised of p- and n-type materials enjoy strong interest for implementation in high temperature and oxidizing environments in which their waste heat could be used to generate electricity. However, the intended thermoelectric function of these devices will only be enabled if the TED is designed to overcome the thermomechanical limitations (i.e., brittleness) that are usually inherent to these materials. A thermoelectric material (TEMat) with a combination of poor strength and low thermal conductivity can readily fail in the presence of a thermal gradient, thereby preventing the exploitation of the desired thermoelectrical function.

This seemingly insurmountable problem can be overcome with the combined use of established probabilistic design methods developed for brittle structural components, good thermoelastic and thermomechanical databases of the candidate TEMat comprising the TED, and iteratively applied design sensitivity analysis. This project executes this process to involve TEDs.

This project has two parts. The first sub-project focuses on the thermomechanical and thermophysical evaluation of candidate TEMats that are of interest to the entire TE community for high temperature (e.g., 550°C) waste heat recovery. The development of appropriate strength test fixturing and methods are required as there are no widely accepted strength test practices (e.g., ASTM) for thermoelectric materials. The second sub-project involves a CRADA with Marlow Industries and the thermomechanical and thermophysical characterization of their proprietary TEMats.

There will be several outcomes from this work. It will benefit TEMat and TED developers and end-users of these potentially high temperature TEDs. Mechanical reliability of prototypical TEDs will be evaluated from a structural brittle-material perspective, and suggested redesigns will be identified. Thermomechanical reliability of developmental TEMats will be assessed, and minimum required thermomechanical properties of hypothetical TEMats would be identified that produce desired reliability in a TED.

Results

Non-CRADA sub-project

This effort focuses on the thermomechanical and thermophysical evaluation of candidate TEMats that are of interest to the entire TE community for high temperature waste heat recovery. As a reference, mature and lower-temperature-capable TEMats were characterized to facilitate comparison. Additionally, the development of appropriate strength test fixturing and methods are required as there are no widely accepted strength test practices (e.g., ASTM) for thermoelectric materials.

Skutterudites are attractive TEMat candidates for use in TEDs under consideration for power generation associated with intermediate- and high-temperature waste heat recovery. These (any) thermoelectric materials must first possess sufficient thermomechanical robustness to withstand the operational thermal gradients that activate the thermoelectric effect.

Tensile strength (and its scatter) is one indicator of that robustness. To support that assertion, Kingery's [1] thermal resistance parameter, R_{Therm} , is useful to first consider in context with TMs,

$$R_{Therm} = \frac{S_{Tens}(1-\nu)\kappa}{\alpha E} \quad (1)$$

where S_{Tens} is tensile stress or tensile strength, ν is Poisson's ratio, κ is thermal conductivity, α is the coefficient of thermal expansion or CTE, and E is elastic modulus. One desires R_{Therm} to be as large as possible for improved thermomechanical resistance against effects caused by thermal gradients or thermal transients. The parameters ν , κ , α , and E are materials properties and are essentially unchangeable for any given TEMat under consideration. For TEMats, the minimization of κ is purposely and primarily sought because that achievement improves thermoelectric efficiency. Additionally, TEMats typically have a large CTE (> 10 ppm/°C). The ν for most TEMats usually ranges between 0.25-0.30. The E 's for TEMats typically range between 50-140 GPa; however, the E is virtually unchangeable within a given class of TEMats (e.g., skutterudites, TAGS, tellurides, etc.). Therefore, the intent to make the R_{Therm} for TEMats as large as possible is primarily hindered by the inherently low κ and typically high CTE.

The remaining parameter in Eq. 1 is S_{Tens} . Its consideration is complicated by the fact that S_{Tens} for brittle materials, including TEMats, is in general a size- and temperature-dependent value. The S_{Tens} for brittle materials is a function of both intrinsic and extrinsic material parameters. Why consider S_{Tens} and not the material's compressive strength? The S_{Tens} is anticipated to be at least one order of magnitude lower than compressive strength in TEMats for the same amount of stressed material (as is the case for polycrystalline ceramics) because of their brittleness (i.e., low fracture toughness). Therefore, for conservative design, testing should focus on the measurement of a tensile strength in TEMats. Of all the parameters used in the right-hand side of Eq. 1, the manufacturers of TEMats can only tangibly increase R_{Therm} by increasing S_{Tens} . Thus, the valid measurement of strength in TEMats, the identification of those flaws that limit strength, the active reduction of those flaw sizes to increase S_{Tens} , and appropriate strength-size-scaling of TEMats in thermoelectric device design all need to be executed to ultimately achieve the highest probability of survival of a TED in service.

The primary goal of this study was to measure the S_{Tens} (via three-point-bend testing) as a function of temperature of developmental n- and p-type skutterudite materials under consideration for use in devices for power generation via waste heat recovery. Another goal was to measure strength using test coupons whose geometry closely mimics that of thermoelectric legs. Owing to the relatively small size of the test coupons, a third goal was to develop and use a test fixture that: (a) validly tests for failure stress, (b) has high temperature capability, (c) has a means of efficiently and easily promoting alignment, and (d) has a simplicity that enables the testing of large numbers of test coupons in a relatively short period of time.

Material Description

N-type thermoelectric materials ($\text{Yb}_{0.27}\text{Co}_4\text{Sb}_{12.08}$) were prepared on a 60 g scale by combining Co and Sb in approximately a 1:3 ratio and melting them by induction in a boron nitride crucible under an argon atmosphere. The resulting melt was combined with elemental Yb and Sb to a nominal composition of $\text{Yb}_{0.40}\text{Co}_4\text{Sb}_{12}$ in a carbon coated fused silica tube and then flame-sealed under a reduced atmosphere. The excess of Yb above the desired final fraction is required due to the formation

of Yb_2O_3 as a side product. The charge was melted at 1150°C for 5 minutes with subsequent annealing of the melt at 800°C for 1 week. The annealed melt was then milled, cold pressed, and annealed for an additional week at 800°C .

P-type materials were prepared by first alloying Co and Fe in a 1:3 ratio by arc-melting, then combining the alloy with elemental Ce and Sb with a nominal composition of $\text{Ce}_{1.05}\text{CoFe}_3\text{Sb}_{12.10}$ (the excess of Ce and Sb were necessary due to losses by vaporization) with a final mass of 60 g in a boron nitride crucible. The charge was melted by induction under Ar at 1100°C for 1 week.

The synthesis of both n- and p-type materials results in low density sintered powders, which were further milled in preparation for consolidation by spark plasma sintering (SPS). Consolidation of $\text{Yb}_{0.27}\text{Co}_4\text{Sb}_{12.08}$ proceeded by loading 12 g of milled powder into a 12.7-mm boron nitride coated die. The powder was placed under 50 MPa of uniaxial pressure under dynamic vacuum, then heated at a rate of $75^\circ\text{C}/\text{min}$ to 720°C , and then soaked for an additional 2 minutes. The three consolidated pellets from this process were all greater than 98% theoretical density. The p-type material was processed in a similar manner to the n-type samples, but was heated at a rate of $75^\circ\text{C}/\text{min}$ to 675°C with subsequent soaking for 2 minutes.

Prismatic bars of developmental n-type ($\text{Yb}_{0.27}\text{Co}_4\text{Sb}_{12.08}$) and p-type ($\text{Ce}_{0.86}\text{Co}_{1.02}\text{Fe}_{2.98}\text{Sb}_{11.97}$) skutterudite were prepared having nominal dimensions of 1.5 x 1.5 x 12 mm. Samples were cut from the cylindrical SPS consolidated ingots by wafering along the cylinder axis with a low speed diamond saw. Their edges were not chamfered. The electrical resistivity (ρ), Seebeck coefficient (S), and power factor for both materials are shown as a function of temperature in Fig. 1. The transport properties were evaluated using an Ulvac ZEM-3 system. The ρ and S responses for the n-type material are equivalent to responses measured previously on a similar material [2].

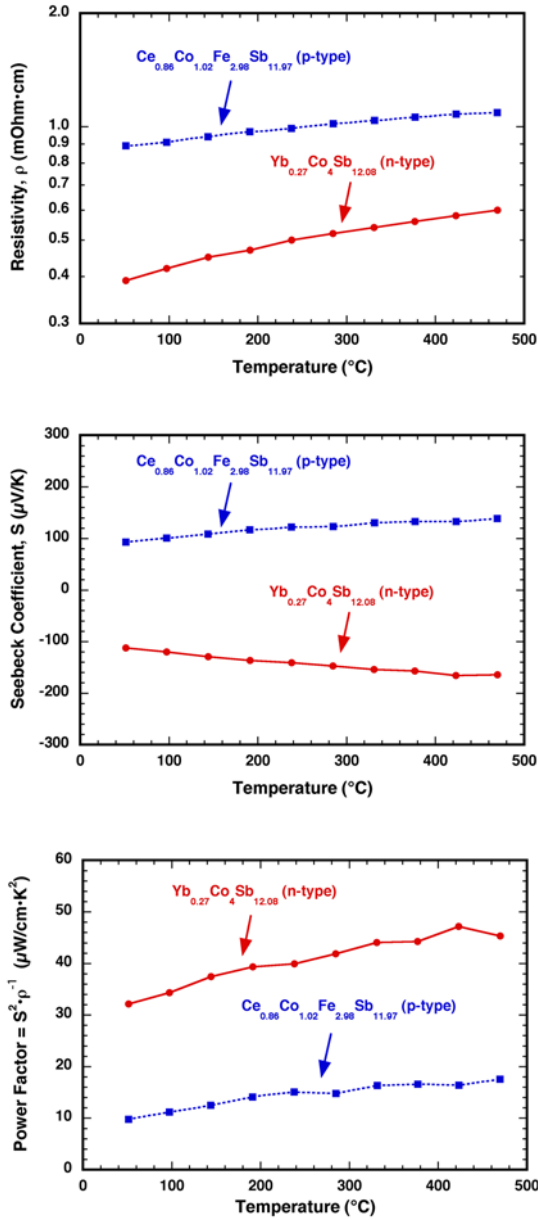


Figure 1. Electrical resistivity (top), Seebeck coefficient (middle), and power factor (bottom) as a function of temperature for the n- and p-type skutterudites.

For the identification of strength-testing temperatures in a material whose general response is an unknown, it is often useful to first perform dilatometry to identify any temperature where a potential change of state could be occurring [3] or where the material goes into a non-equilibrium state. Dilatometry was performed on both the n- and p-type

skutterudite, and the responses are shown in Fig. 2. There was no observable inflection in the elongation as a function of temperature response for the n-type material, but there was one at approximately 425 $^{\circ}$ C for the p-type material. This was observed on two specimens, so its response was consistent. Therefore, strength testing with the n-type was performed through 500 $^{\circ}$ C and that for the p-type to 400 $^{\circ}$ C.

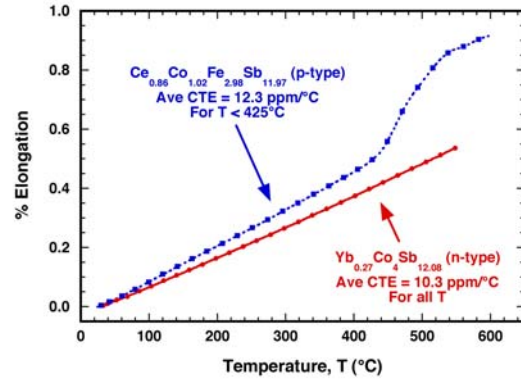


Figure 2. Percent elongation as a function of temperature for the n- and p-type skutterudites. The p-type material underwent a change of state \sim 425 $^{\circ}$ C resulting in an increased rate of elongation.

Strength Testing

The cross-sectional dimensions of thermoelectric legs in TEDs are range in size from 1-4 mm x 1-4 mm, so three-point flexure strength testing was performed on prismatic bars having cross-sectional dimension in that range (1.5 mm x 1.5 mm in this case). This approach was deemed superior to other types of strength tests and geometries (e.g., ring-on-ring biaxial flexure testing of disk specimens) because produced failures can be caused by flaw-types and flaw-locations (e.g., edges, etc.) that are likely to exist in thermoelectric legs.

Owing to the relatively small size of the test coupons, a test fixture was conceived and developed that has high temperature capability, has a means of efficiently and easily promoting alignment, and has a simplicity that enables the testing of large numbers of test coupons in a relatively short period of time. The fixture is shown in Fig. 3. It consists of an alumina tube whose outside diameter closely fits the inside diameter of a larger tube. The inner tube has two grooves cut in one end that retain smaller alumina rollers which serve as the support points for

the test span of the specimen. The specimen is set and centered on the rollers, and then an alumina sphere is set on the specimen, providing the top or third-point loading onto the specimen. The all-alumina fixture construction enables high temperature testing. The diameter of the sphere and the outer diameter of the inner tube are matched, and are kept concentrically aligned by the inner diameter of the outer tube throughout the testing duration. An exploded view of the fixture and specimen is shown on the left of Fig. 3 and its assembly is depicted on the right. The top of the sphere is higher than the outermost tube, and it is compressively loaded by a push rod, thus, loading the top of the specimen. With the specimen inside the fixture, the entire assembly is then placed inside the hot zone of a radiantly heated furnace, which is all within the working zone of an electromechanical test frame. Two complete fixtures were fabricated and the use of both enabled a high throughput rate of testing.

Another attribute of this fixture is its inherent closed assembly restricts the ambient environment from coming into contact with the specimen surface and enables testing to be done in ambient air even if the material is susceptible to oxidation. If oxidation is still operative then, alternatively, there is a “reservoir” formed by the inner tube’s inner diameter that can be filled with metal filings or graphite powder that can serve as an interior oxygen getter. Using metal filings or graphite powder with the fixture was found not to be necessary with the testing of these two skutterudite compositions because the “closed assembly” by itself sufficiently suppressed oxidation of the test specimen surfaces (even to 500°C for the n-type material).

At first glance, the ratio of the test span to specimen height ($8.0/1.5 = 5.33$) used in the present study is much smaller than that used in other flexure tests and fixtures. For example, ASTM C1161B [4] has a span to height ratio of $40/3 = 13.33$ and (the discontinued) ASTM F417 [5] has a ratio of $25.4/1.8 = 14.11$. A ratio that is too small in bend testing can cause high contact stresses to occur between the rollers and specimen if a material’s outer-fiber tensile stress is relatively high, and those high contact stresses can cause premature (and potentially misleading) failure. A contributing reason why the present study’s ratio of $8.0/1.5$ works is the three-point (or outer-fiber) failure force of these test coupons is relatively low because these materials are relatively weak, and is lower than the force necessary to initiate Hertzian cracking at either the

two bottom rollers or in the vicinity of the Hertzian contact circle between the upper side of the bend specimen and the loading sphere. All flexure specimens had failure initiation occur at their tensile surface, which supports the conclusion that a 5.33 ratio is adequate for these materials.



Figure 3. Self-aligning, high-temperature (all-alumina) three-point-bend fixture used to measure flexure strength of 1.5 mm x 1.5 mm x 12 mm prismatic bars. Bend span is 8 mm. Exploded (top) and assembled views (bottom).

Producing failure initiation at the outer fiber surface is itself not a validation of testing because one must be able to accurately estimate the associated failure stress too. The maximum outer-fiber tensile stress of the developed test configuration, as estimated by finite element analysis (FEA), was compared with that calculated from the classical analytic beam bending equation. This comparison is shown in Fig. 4. Two FEA models were constructed: one representing the traditional “roller-on-two-roller” configuration and the other being the “sphere-on-two-roller” configuration used in this study. An elastic modulus of 135 GP and a Poisson’s ratio of 0.20 were used for the thermoelectric materials [2]. The outer-fiber tensile stresses that they produced were identical and were within 3% of that of the classical three-point-bend equation. A 3% difference is small given the potential inaccuracies of any FEA model. Therefore, the analytic classical beam bending equation was used to estimate failure stress for all specimens.

The failure stress (S_{Tens}) was therefore calculated using the analytic three-point bending equation

$$S_{Tens} = \frac{3PS_L}{2bh^2} \quad (2)$$

where P is the failure force, S_L is the test span (8.0 mm), b is the specimen base (1.5 mm nominal), and h is the specimen height (1.5 mm nominal). All testing was done at a crosshead displacement rate of 0.1 mm/min in an electromechanical test frame until fracture was produced and its associated failure load (P) recorded. For high temperature testing, the specimen/fixture assembly was soaked at temperature for approximately 10 minutes prior to the commencement of loading. Testing was performed in ambient air. As indicated earlier, there was no observable evidence of oxidation on the surfaces of the test specimens.

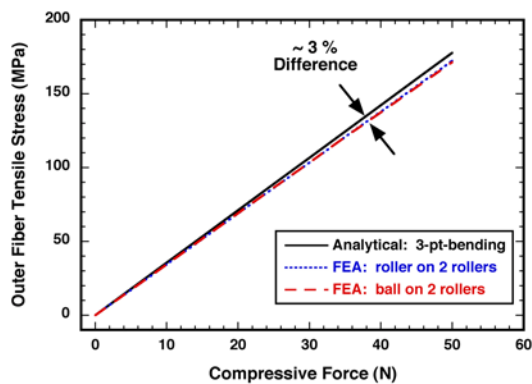


Figure 4. Comparison of the outer fiber tensile stress as a function of 3-point-bend force for the analytical case (black), its finite element analysis (blue), and the case for the bend fixture shown in Fig. 3 (red). Differences were small (~3%), so the analytical expression was used to estimate failure stresses in this study.

Commercial statistical software was used to fit the strengths to an uncensored, unimodal two-parameter Weibull distribution using maximum likelihood estimation. 95% confidence estimates were determined and used to assess any evidence of temperature-dependent changes in strength.

Two vintages of skutterudites were evaluated. The first was processed in early FY10, and the second was processed later in the year. Bend bars from Vintage 2 were cut with traditional, somewhat automated methods used to prepare TEMat legs for TEDs whereas the bend bars from Vintage 1 were cut separately in a laboratory setting.

The strength of the Vintage 1 n-type $\text{Yb}_{0.27}\text{Co}_4\text{Sb}_{12.08}$ and p-type $\text{Ce}_{0.86}\text{Co}_{1.02}\text{Fe}_{2.98}\text{Sb}_{11.97}$ skutterudites as a function of temperature is shown in Fig. 5. The strength of the n-type skutterudite was independent of temperature to 500°C. The strength of the p-type skutterudite was equivalent to that of the n-type material and also was independent of temperature to at least 200°C. The p-type’s strength dropped by ~20% at 400°C. As shown in Fig. 2, both skutterudite materials were believed to be in an equilibrium state at all test temperatures at which they were tested.

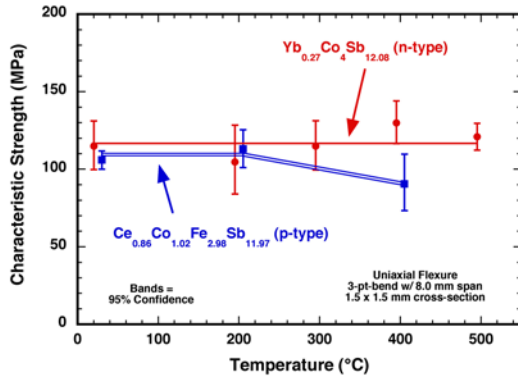


Figure 5. Characteristic strength as a function of temperature for the Vintage 1 n- and p-type skutterudites.

The Vintage 2 sets of skutterudites were stronger than Vintage 1. Much of that is attributable to improved machining that produced less damage. The strengths shown in Fig. 6 are higher than those shown in Fig. 5.

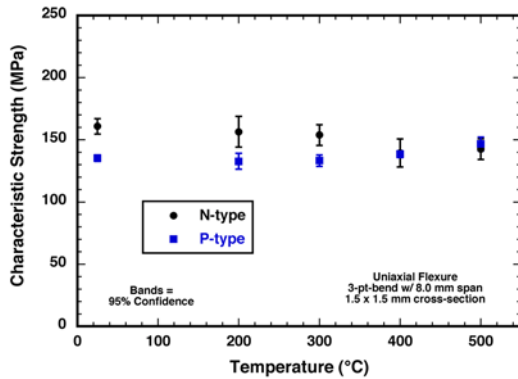


Figure 6. Characteristic strength as a function of temperature for the Vintage 2 n- and p-type skutterudites.

Transport Properties of Thermoelectrics

Understanding the performance of TEDs depends upon accurate knowledge of the transport properties of the TEMats. For the power generation application of automobiles the transport data of candidate materials in the temperature range of 20°C to 500°C are needed. One of the important tasks of this project is to provide experimental data on commonly used materials such as Bi₂Te₃, PbTe and

skutterudite alloys. Materials from Marlow and potential suppliers were tested at ORNL. In order to obtain thermoelectric figure of merit, ZT, three properties must be measured: thermal conductivity, Seebeck coefficient and electrical resistivity.

$$ZT = s^2\sigma T/k \tag{3}$$

where thermal conductivity k is calculated from three measured materials properties:

$$k = \alpha\rho C_p \tag{4}$$

where α is thermal diffusivity, ρ is the density and C_p is the specific heat. Since density is usually known or easy to determine, a complete transport properties data on a given TEMat will require three specimens: a bar for Seebeck coefficient and electrical conductivity, a large disk for thermal diffusivity, and a small disk for specific heat. Specimens for transport measurements were prepared at Marlow. Some selected results are reported here.

Figure 7 shows thermal diffusivity results of n-type PbTe. Four specimens were tested from room temperature to 500°C. Thermal diffusivity values were found to decrease from room temperature and reach minima around 350°C and start to increase up to 500°C. The four specimens showed very good agreement indicating the homogeneity of scale up materials.

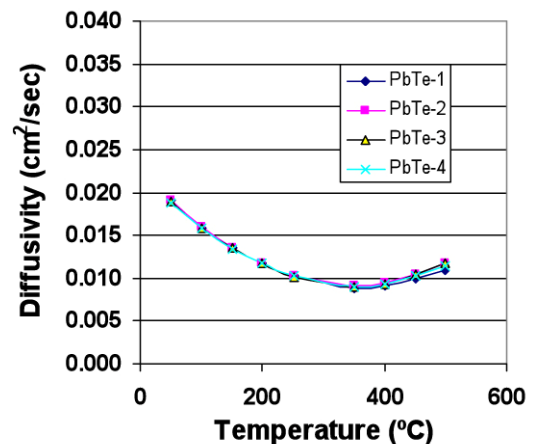


Figure 7. Thermal diffusivity of 4 n-type PbTe.

Figure 8 shows room temperature thermal diffusivity of 12 n-type and 12 p-type Bi₂Te₃ alloy specimens. For the n-type material, the average thermal diffusivity is 0.0111 cm²/sec with a standard deviation of $\pm 2.75\%$. For the p-type material the average thermal diffusivity is 0.0082 cm²/sec with a standard deviation of $\pm 1.54\%$. Both materials showed small variations from specimen to specimen.

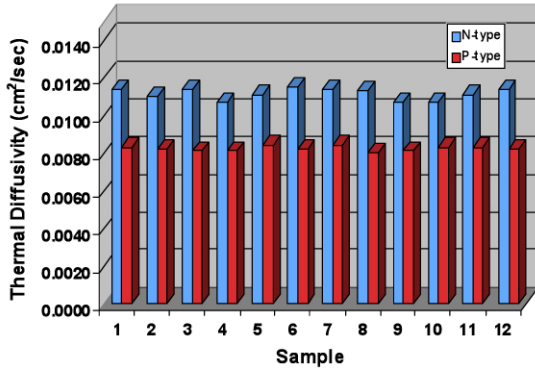


Figure 8. Room temperature thermal diffusivity of 24 n-type and p-type bismuth telluride alloy specimens.

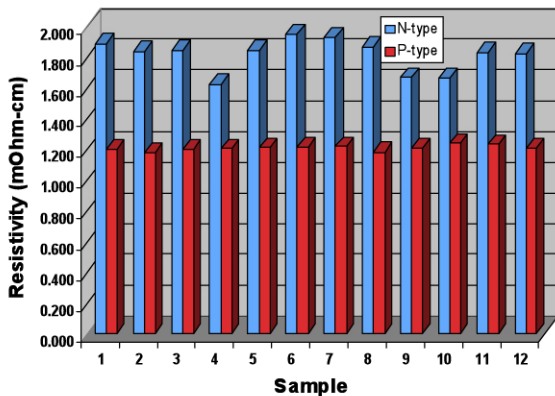


Figure 9. Electrical resistivity of 24 n-type and p-type bismuth telluride alloy specimens.

Figure 9 shows room temperature electrical resistivity of 12 n-type and 12 p-type Bi₂Te₃ alloy specimens. For the n-type material the average electrical resistivity is 1.820 mOhm-cm with a standard deviation of $\pm 6.57\%$. For the p-type material the average electrical resistivity is 1.208 mOhm-cm with a standard deviation of $\pm 1.50\%$.

The p-type material showed small variations from specimen to specimen. However, the n-type material showed much larger variations. These results are consistent with greater sensitivity of the electrical resistivity of the n-type material to variations in the microstructure.

After completing transport property measurements ZT values can be calculated. Due to the lack of standard thermoelectric reference materials and reliable literature data, results from Marlow and ORNL are crosschecked. Figure 10 shows the comparison of measured ZT with that measured by a potential Marlow supplier. The ZT values matched very well in the measured temperature range.

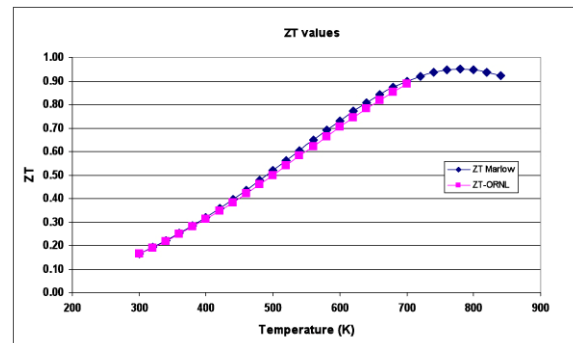


Figure 10. Comparison of Marlow and ORNL ZT results as a function of temperature.

Neutron Strain Mapping of Modules

Thermoelectric modules used for automotive waste heat recovery will experience daily thermal cycling with temperature difference of several hundred degrees. Residual stresses exist after the metallization and bonding to the ceramic substrate. The best tool to study the residual stress is x-ray or neutron diffraction. Since x-ray is a surface technique and could not penetrate deep into/through materials, we conducted preliminary study of residual stress mapping at the High Flux Isotope Reaction (HFIR) using neutron diffraction. On the HFIR beam line HB-2, a prototype PbTe module, shown in Figure 11, was used for strain mapping.

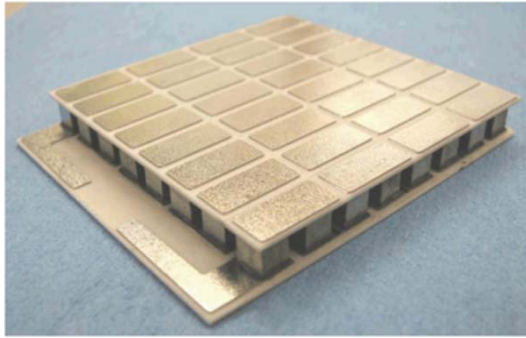


Figure 11. Picture of prototype PbTe module.

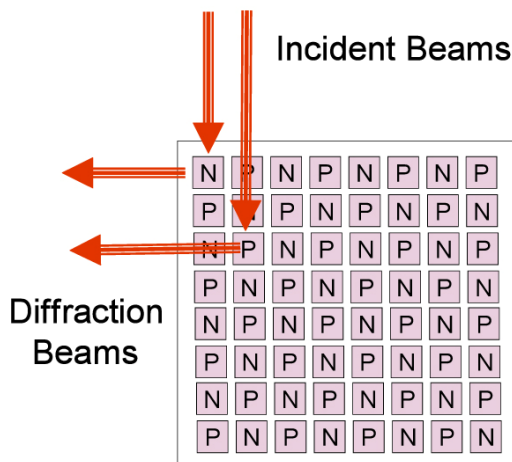


Figure 12. Neutron strain mapping of a PbTe module.

The PbTe module was mounted on a sample stage with precise X-Y-Z movement. Figure 12 shows the experimental set up of neutron strain mapping. The incident beam and diffraction beam are controlled by slits so a pancake shaped gauge volume of 3mm x 3mm x 0.5mm can be defined within the thermoelectric elements. The PbTe elements are 4mm x 4mm x 5mm. The strain mapping in the Z direction (the same as heat and current flow) on 10 points can be carried out.

In order to measure residual stress/strain in a PbTe module by neutron diffraction, a strong diffraction peak must be selected. Figure 13 shows the neutron counts after 10 minutes on the PbTe 422 peak. Neutron count over 500 was achieved indicating a 10-point scan on each element will take less than two hours. The most important feature of neutron scattering is the penetration capability. The

inside elements of the module can be selected and scanned. A slightly longer data collection time is needed to compensate loss of beam intensity through other elements.

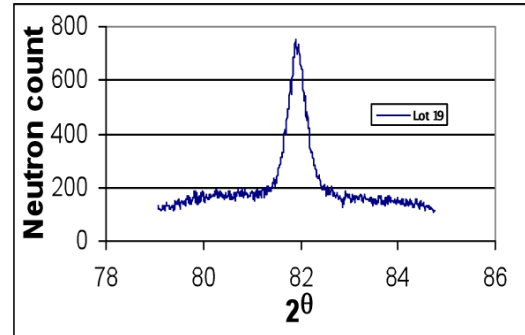


Figure 13. Neutron counts in 10 minutes of 422 peak of PbTe.

Figure 14 is the preliminary results of strain mapping of two legs, one p-type and one n-type. Two stress-free elements broke off the module were used to define the d_0 (d spacing calculated from the Bragg law: $\lambda = 2d\sin\theta$). The d-spacing measured from each location is compared with d_0 . Strain is calculated from $d-d_0/d_0$ and plotted against location. The initial results shown in Fig. 14 indicate tension near the top and bottom of the elements and compression at the center of the elements.

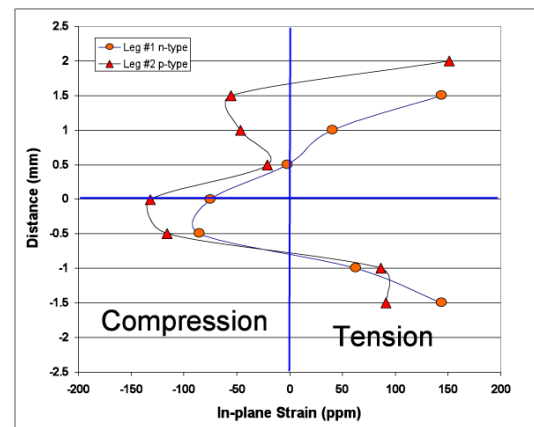


Figure 14. Preliminary neutron strain mapping of a pair of p-type and n-type legs in a PbTe module.

CRADA sub-project

A CRADA with Marlow Industries continued in FY10. The primary intent is to thermomechanically and thermophysically characterize their proprietary TEMats. Testing of their materials continued throughout FY10 and alternative non-destructive test methods to evaluate Marlow TEDs were examined. Transport properties of Marlow production and research thermoelectric materials were evaluated.

Conclusions

The failure stress distributions of $\text{Yb}_{0.27}\text{Co}_4\text{Sb}_{12.08}$ (n-type) and $\text{Ce}_{0.86}\text{Co}_{1.02}\text{Fe}_{2.98}\text{Sb}_{11.97}$ (p-type) skutterudites were measured as a function of temperature. A self-aligning, high-temperature-capable three-point-bend fixture was developed and used to test specimens whose cross-sectional dimensions (1.5 mm x 1.5 mm) are within the range typically used for TED legs. Tests were run at sufficiently rapid loading rates that fast-fracture or inert strengths were measured.

References

- [1] W. D. Kingery, "Factors Affecting Thermal Stress Resistance of Ceramic Materials," *Journal of the American Ceramic Society*, 38:3-15 (1955).
- [2] J. R. Salvador, J. Yang, X. Shi, H. Wang, A. A. Wereszczak, H. Kong, and C. Uher, "Transport and Mechanical Properties of Yb-Filled Skutterudites," *Philosophical Magazine*, No. 19, 89:1517-1534 (2009).
- [3] A. A. Wereszczak, H. -T. Lin, T. P. Kirkland, M. J. Andrews, and S. K. Lee, "Strength and Dynamic Fatigue of Silicon Nitride at Intermediate Temperatures," *Journal of Materials Science*, 37 1-16 (2002).
- [4] "Standard Test Method for Flexural Strength of Advanced Ceramics at Ambient Temperature," ASTM C 1161, Vol. 15.01, ASTM, West Conshohocken, PA, 2008.
- [5] "Test Method for Flexural Strength (Modulus of Rupture) of Electronic-Grade Ceramics (Withdrawn 2001)," ASTM F417, ASTM, West Conshohocken, PA, 1996.

Publications

- A. A. Wereszczak, M. E. Ragan, K. T. Strong, Jr., P. J. Ritt, H. Wang, J. R. Salvador, and J. Yang, "Strength of N- and P-Type Skutterudites," in press, Vol 31, *Ceramic Engineering and Science Proceedings*, 2010.
- P. J. Ritt and H. Wang, "Transport Properties of Thermoelectrics for Waste Heat Recovery," in press, Vol 31, *Ceramic Engineering and Science Proceedings*, 2010.

Agreement 15529 – Utilization of Nanofluid Coolants

Principal Investigators: J. L. Routbort and D. Singh

Co-workers: Elena Timofeeva, Wenhua Yu, David France

Argonne National Laboratory

9700 S. Cass Avenue, Argonne, IL 60439-4838

(630) 252-5065; fax: (630) 252-5568; e-mail: routbort@anl.gov

DOE Technology Manager: Jerry L. Gibbs

(202) 586-1182; fax: (202) 586-1600; e-mail: jerry.gibbs@ee.doe.gov

Contractor: UChicago Argonne LLC

Contract No.: DE AC03 06CH11357

Objective

- Determine if the use of fluids containing a variety of nanoparticles results in erosive damage to radiator materials and coolant pumps.
- Determine figures of merit for use of nanofluids for cooling power electronics
- Measure pumping power of nanofluids in a real system and compare results to theoretical calculations

Approach

- Characterize the thermal conductivity, viscosity, and heat transfer of various nanofluids
- Use surfactants and/or adjustments of pH to lower viscosity of nanofluids
- Conduct experiments to study erosive damage and power to pump various nanofluids in a real system

Accomplishments

- Determined that a 130 nm, 2 vol % SiC/water nanofluid does not degrade aluminum Al3003 in over 700 hours of accelerated testing at 8 m/s for 30° and 90° impacts
- Designed, built, and calibrated a new erosion apparatus to measure wear in an automotive water pump and the torque required to pump nanofluids
- No significant erosive damage has been observed in the cast aluminum pump impeller
- Torque has been measured for both a water-based fluid containing Al₂O₃ and for an ethylene glycol-water fluid containing SiC nanoparticles
- Measured pumping power agrees with power calculated using single phase parameters based on measured values of the nanofluids.

Future Direction

- Erosion of typical radiator materials using fluids containing a variety of well-characterized nanoparticles will be measured, varying the angle, size of the nanoparticles, impact velocity, nanoparticle volume percent, and temperature.
 - If erosion occurs, a predictive model will be developed.
 - Determine wear of nanofluids on automotive pump cast aluminum impeller.
 - Measure the pumping power of nanofluids and compare it to that of the base fluids
 - Test a candidate nanofluid in an instrumented compact heat exchanger
-

Forward

Efforts have shifted away from the in-house production of nanofluids, to development of advanced characterization techniques and establishment of working relationships with industry. Our principal partner on a related project for the Industrial Technology Program is Saint Gobain. They have been supplying SiC/water nanofluids for industrial cooling. ANL has been characterizing the nanoparticles by measuring the particle sizes, adding ethylene glycol to produce a nanofluid suitable for radiator cooling, and reducing the viscosity by changing the pH. Fluids are further characterized by measuring the viscosity, thermal conductivity, and heat transfer coefficients. We have also informal relations with Valvoline (Ashland Oil) because of their interest in lubrication and cooling of transmissions, PACCAR for heavy vehicle radiators, and we have characterized some graphitic based nanofluids for Michelin.

Introduction

Many industrial technologies face the challenge of thermal management. With ever-increasing thermal loads due to trends toward greater power output for engines and exhaust gas recirculation for diesel engines, cooling is a crucial issue in transportation. The conventional approach for increasing cooling rates is use of extended surfaces such as fins and microchannels. Reducing radiator size will reduce the frontal area and hence the aerodynamic drag. However, current radiator designs have already stretched these approaches to their limits. Therefore, an urgent need exists for new and innovative concepts to achieve ultra-high-performance cooling. Nanofluids seem to show enormous potentials as a coolant for radiators. Literature has many examples of increased thermal conductivity of fluids by the addition of nanoparticles (see review by Yu, et al. [1]). Enhanced thermal conductivity could lead to enhanced heat transfer. A CFD calculation of a Cummins 500 hp diesel engine using an ideal

nanofluid as coolant has shown that the radiator size could be reduced by 5% [2], reducing weight and size, and hence aerodynamic drag.

In order for the enhanced thermal conductivity to be utilized it must be shown that liquid erosion of typical radiator materials will be tolerable and that the increased pumping power resulting from higher viscosity will not exceed the gain in parasitic energy losses from enhanced cooling. If nanofluids result in excessive erosive wear or very high increased pumping power, they cannot be used. Hence, the Vehicle Technologies program funds an investigation on liquid erosion of radiator materials using nanofluids.

Experimental data are presented for the thermal conductivity, viscosity, and turbulent flow heat transfer coefficient of nanofluids with SiC particles suspended in ethylene glycol–water (EG/H₂O) mixture with a 50/50 volume ratio. The results are compared to the analogous suspensions in water for four sizes of SiC particles (16–90 nm). It is demonstrated that the heat transfer efficiency is a function of both the average particle size and the system temperature. The results show that adding SiC nanoparticles to an EG/H₂O mixture can significantly improve the cooling efficiency while water-based nanofluids are typically less efficient than the base fluids. This is one of the few times that substantial nanofluid heat transfer enhancement has been reported in the literature based on a realistic comparison basis of constant velocity or pumping power. The trends important for engineering efficient heat transfer nanofluids are summarized.

Results and Discussion

It is clear from Fig. 1 that the thermal conductivity enhancement is better for the larger particles in EG/H₂O and that the enhancement is larger in EG/H₂O than in water. The larger particles for a given volume concentration have less interfacial thermal resistance and hence a larger enhancement [3 and 4].

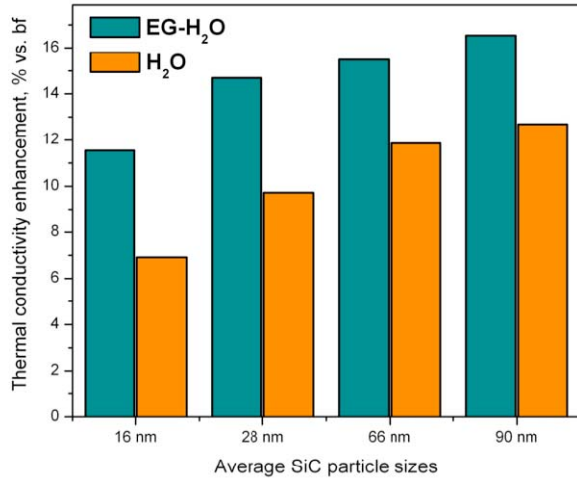


Fig. 1. Comparison of thermal conductivity enhancement in 4 vol % SiC nanofluids with EG/H₂O and H₂O as base fluids at various particle sizes.

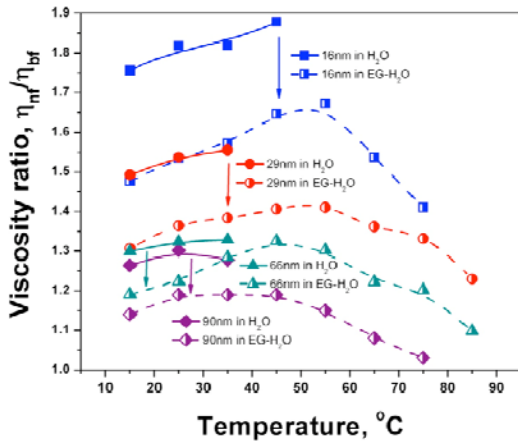


Fig. 2. Temperature dependence of nanofluid-to-base fluid viscosity ratio in 4 vol % SiC suspensions in water and 50/50 EG/H₂O at pH $\sim 9.5 \pm 0.3$. Particle sizes are determined by BET.

The viscosities of the 90-nm SiC nanoparticles in EG/H₂O and the base fluid are equal at 70°C. This is very important as the pumping power depends on the viscosity of the fluid.

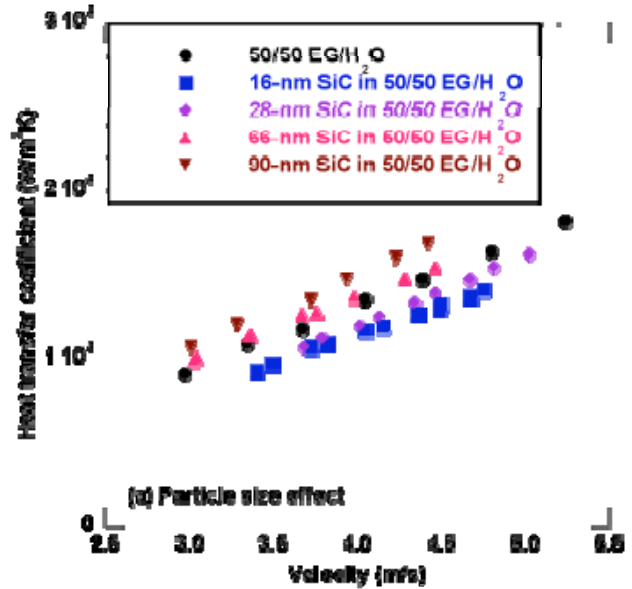


Fig. 3. Heat transfer coefficients of 4 vol % SiC-EG/H₂O nanofluids in turbulent flow at 55°C plotted as a function of flow velocity [5].

The larger SiC nanoparticles have the largest heat transfer coefficient, about 15% enhancement over the base fluid. The results can be combined into a Mouromtseff plot which is a figure of merit for turbulent flow (Fig. 4). There is a large region of positive results ($Mo > 1$, shown in green) especially for the larger particles at the higher temperatures where heat exchangers will operate.

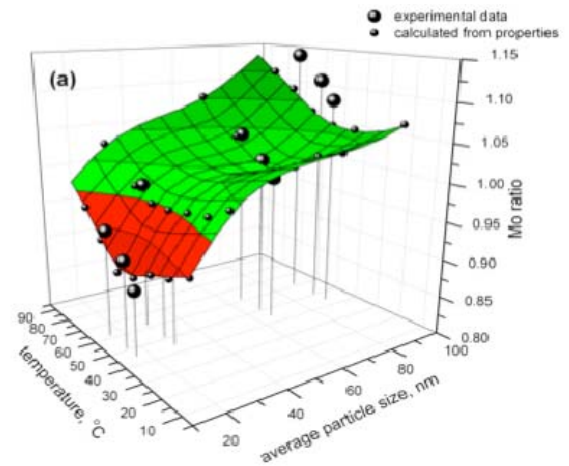


Fig. 4. Property based evaluation of efficiency of 4 vol % SiC fluids in EG/H₂O for fully developed turbulent flow.

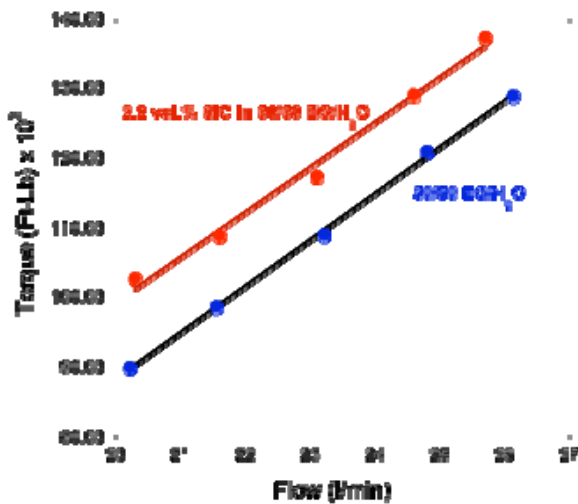


Fig. 5. Measured torque of a 29-nm SiC in EG/H₂O compared to the base fluid at 30°C.

The measured increase in torque was 9.3% while the calculated value considering all of the frictional losses in the system was 8.7%. The agreement is within experimental uncertainties [5]. Furthermore, this shows that the nanofluid can be considered as a single-phase fluid and that the pumping power of the nanofluid can be calculated using the measured property values. Therefore, it can be expected that there will be no additional parasitic energy losses at the higher operating temperatures of the heat exchanger.

Issues & Future Direction

It might be expected that the larger particles will require less pumping power than the small nanoparticles. However, erosion damage to the cast aluminum impeller and radiator materials will be larger because of the higher kinetic energies of the larger nanoparticles. Therefore, we will concentrate of measuring the pumping power and the erosion of the larger nanoparticles. We also hope to work with the power electronics group to utilize our currently best available nanofluid in a commercial heat exchanger. Furthermore, we have proposed a new type of

nanoparticle consisting of a phase change core and a metal shell. Calculations would indicate that this type of particle would have a much higher heat transfer coefficient since the core would absorb heat resulting in a phase change on the “hot” side and give the heat up as it reverts to the original phase on the “cold” side. The metal shell has a higher thermal conductivity than the SiC as well.

Conclusions

We have made considerable progress in advancing the understanding of the particle size dependence of the thermal conductivity and heat transfer coefficient of nanofluids. We also understand the effect of pH on the viscosity of the fluid because the pH changes the Zeta potential. Utilizing this understanding has allowed taking a potentially commercial water-based SiC nanofluid and modifying it to achieve an approximate 15% increase in heat transfer with no increase in viscosity at heat exchanger operating temperatures. However, part of that gain will be lost to increased pumping power because of the higher density of the nanofluid.

References

1. W. Yu, D. M. France, J. Routbort, S.U.S. Choi, “Review and Comparison of Nanofluid thermal Conductivity and Heat Transfer Enhancements, *Heat Transfer Engineering*, **29**, 432-460 (2008).
2. S. K. Saripella, W. Yu, J. L. Routbort, D. M. France, and Rizwan-uddin, “ Effects of Nanofluid Coolant in a Class 8 Truck Engine, SAE Technical Paper 2007-01-21413.
3. E. Timofeeva, J. Routbort, and D. Singh, “Particle shape effects on thermophysical properties of alumina nanofluids”, *JAP* **106**, 014304 (2009)
4. E. Timofeeva, D. Smith, , W. Yu, D. France, D. Singh, and J. Routbort, “Particle Size and Interfacial Effects on Heat Transfer Characteristics of Water-based α -SiC Nanofluids”, *Nanotechnology*, **21**, 215703 (2010)
5. W. Yu, D. France, J. Routbort, “Thermophysical Property-related Comparison Criteria for Nanofluid Heat Transfer Enhancement in Turbulent Flow”, *APL* **96**, 213108 (2010)

6. J. Routbort, S. Singh, E. Timofeeva, W. Yu, and D. France, "Pumping Power of Nanofluids", J. Nanoparticle Research, submitted

Agreement 16308 – Thermoelectrics Theory and Structure

D.J. Singh

Materials Science and Technology Division

Oak Ridge National Laboratory

P.O. Box 2008, MS 6114, Bldg. 4500S

Oak Ridge, TN 37831-6114

(865) 241-1944; fax: (865) 574-7659; e-mail: singhdj@ornl.gov

DOE Technology Manager: Jerry L. Gibbs

(202) 586-1182; fax: (202) 586-1600; e-mail: jerry.gibbs@ee.doe.gov

ORNL Technical Advisor: D. Ray Johnson

(865) 576-6832; fax: (865) 574-6098; e-mail: johnsondr@ornl.gov

Contractor: Oak Ridge National Laboratory, Oak Ridge, Tennessee

Prime Contract No.: DE-AC05-00OR22725

Objectives

- Find ways to optimize existing thermoelectric materials and discover new families of high performance thermoelectrics for waste heat recovery applications using modern science based materials design strategies.
- Find low cost materials that have high thermoelectric figures of merit and are suitable for vehicular applications.

Approach

- First principles calculations based on quantum mechanics are used to calculate electronic structure and thermoelectric properties of materials.
- Boltzmann transport equations are solved to obtain electrical transport properties.
- Vibrational properties are investigated and mechanisms for thermal conductivity reduction are assessed.

Accomplishments

- Performed first principles calculations of transport and other properties of potential thermoelectric materials.
- Discovered that the toxic element Tl is not required to obtain enhanced thermopower in p-type PbTe, and that low cost non-toxic dopants can be used in its place.
- Identified heavily doped p-type PbSe as a high performance lower cost alternative to p-type PbTe.
- Identified potentially high performance skutterudite compositions that do not include rare earth elements and use Fe-Ni alloys instead of Co to lower cost.

Future Direction

- Identify new high performance low cost thermoelectric compositions suitable for vehicular applications.
- Calculate doping level dependence of thermoelectric properties to guide optimization of existing materials.

Introduction

The use of thermoelectric devices to convert waste heat in vehicle exhaust to electricity offers potentially

significant energy savings. Among the requirements for the effective use of such devices is the availability of high performance thermoelectric materials, with low cost and other properties needed for application in vehi-

cles. The dual requirement for both high performance and low cost has constrained thermoelectric applications in the automotive industry, although thermoelectrics have been effectively inserted in the context of seat cooling. In this regard, there is interest in improved thermoelectric materials, not only for waste heat recovery, but also for zonal heating and cooling in automobiles. High performance thermoelectric materials have the potential for improving fuel efficiency and at the same time improving occupant comfort by directing cooling where needed in the cabin.

We are developing improved materials using a science-based approach with a primary focus on materials for waste heat recovery. In particular, we are using materials design strategies based on first principles calculations of electronic, vibrational and transport properties to identify potentially low cost, high performance thermoelectric materials suitable for application in vehicles. We are also calculating properties of existing materials as a function of doping and other parameters to obtain information needed for optimization of these materials. The emphasis is on the thermoelectric figure of merit, ZT at temperatures relevant to waste heat recovery, as well as materials properties of importance in engineering thermoelectric modules, for example anisotropy and mechanical properties. High $ZT = \sigma S^2 T / \kappa$ requires a combination of high thermopower (S), good electrical conductivity (σ), and low thermal conductivity (κ). Finding materials with the needed combination of properties is challenging because, for example, high thermopower and high conductivity most commonly occur in different doping regimes. [1] We use state-of-the-art computational tools such as the linearized augmented planewave method [2] and the BoltzTraP code [3].

Results

(1) Skutterudite and Related Compositions:

Vehicular waste heat recovery requires both high performance and low cost. One class of materials that shows great promise is the filled-skutterudites. The first such material was $\text{La}(\text{Fe},\text{Co})_4\text{Sb}_{12}$. More recently, higher performance was obtained via replacement of La by mixtures of rare earth elements, or rare earth elements plus Ba, particularly in n-type material. These materials derive their performance from the combination of low lattice thermal conductivity due to the rare earth filler [4] and a favorable electronic structure that has multiple heavy conduction bands. We performed electronic structure calculations that indicated that the chemical range where high performance can be achieved is larger than previously thought and identified alkaline earth (Ae)

filled skutterudites containing Ni and Fe instead of Co as promising. We proceeded to transport calculations (Fig. 1) to test whether this is in fact the case and to make quantitative predictions for the thermopower.

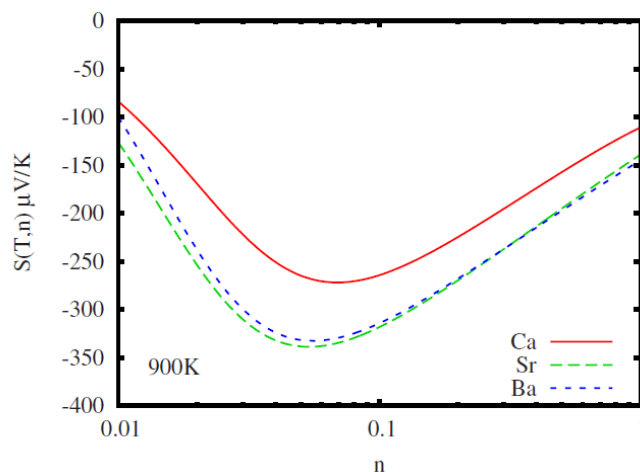


Figure 1: Calculated 900 K thermopower of n-type alkaline earth filled Fe-Ni skutterudites as a function of doping. The p-type (not shown) is similarly favorable.

We also performed first principles calculations of the vibrational densities of states for these materials in order to assess the prospects for obtaining low thermal conductivity. Fig. 2 shows the result for Sr.

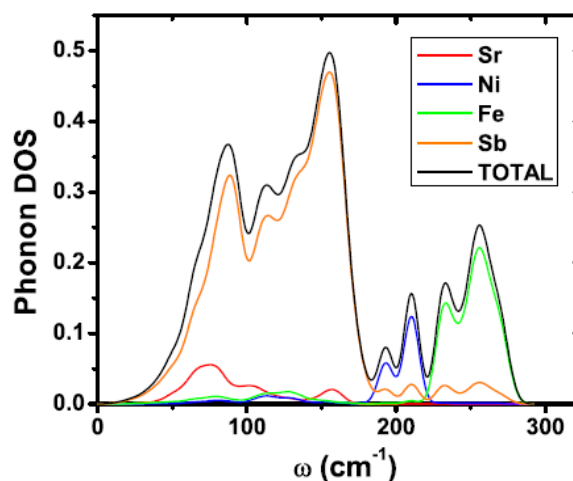


Figure 2: Vibrational density of states for $\text{SrFe}_3\text{NiSb}_{12}$ from first principles calculations.

The results show that these materials can have performance equal to or exceeding that of the best current skutterudite thermoelectrics. The importance of this is (1) alkaline earths are cheap and available as compared to rare earth elements and (2) Ni is substantially cheaper than Co, and furthermore only half as much of this ele-

ment is needed to obtain the optimum electron count. An invention disclosure [6] was prepared based on the promising results obtained. We also examined certain other chemically related Zintl-type compounds based on abundant elements in order to understand the limits on the thermopower in the context of transport theory. These were anionic cluster compounds based on Sn, alkali metals and alkaline earths. We obtained some favorable results for the thermopower. However, based on our other results, these materials are probably inferior to the skutterudites that we identified.

(2) Chalcogenide Thermoelectrics:

PbTe remains one of the most widely applied thermoelectric materials in the intermediate temperature range relevant for waste heat recovery. Furthermore, recent experiments using Tl doping have shown that its performance can be improved so that the peak ZT values are well in excess of unity. This improvement comes about through an enhancement of the thermopower. Unfortunately, Tl is a highly toxic material that is extremely undesirable in vehicular applications. We performed doping dependent transport calculations for PbTe and several potentially lower cost alternatives.

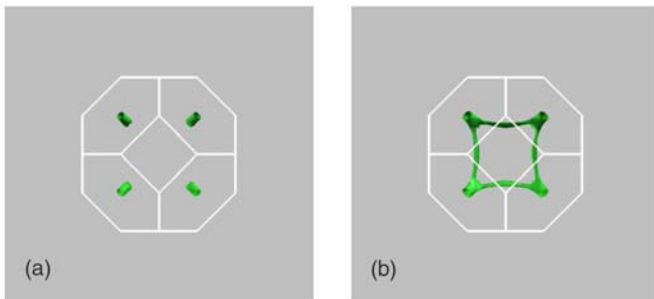


Figure 3. Constant energy cuts of the band structure of p-type PbTe at (a) 0.2 eV and (b) 0.25 eV. Note the connections that develop at low energy. This leads to an enhanced thermopower for suitable doping levels.

We found that the key ingredient in obtaining enhanced thermopowers in PbTe can be traced to a special non-parabolic band structure (see Fig. 3) and that the crucial issue in enhancing the thermopower is obtaining a high well controlled doping level and not the specific chemistry of Tl [8]. This is based on Boltzmann transport calculations. Figure 4 shows the calculated temperature dependent thermopower for heavily p-type PbTe. The implication of our results is that the enhanced thermopowers and high ZT found in Tl doped PbTe can be obtained without the use of Tl. This result was very recently confirmed experimentally. In particular, An-

droulakis and co-workers [11] showed they could obtain similarly enhanced thermopowers using K and Na codoping. In contrast to Tl, K and Na are inexpensive and safe.

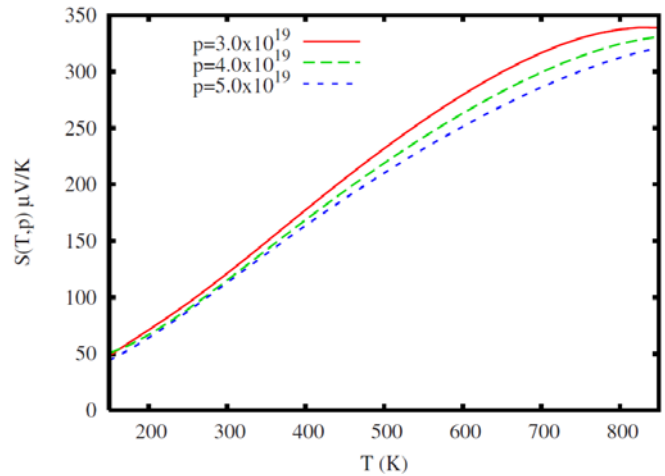


Figure 4. Calculated thermopower of p-type PbTe without a Tl induced resonance but with high doping levels. The results are in excellent agreement with those obtained in Tl-doped samples, showing that Tl does not play an essential role.

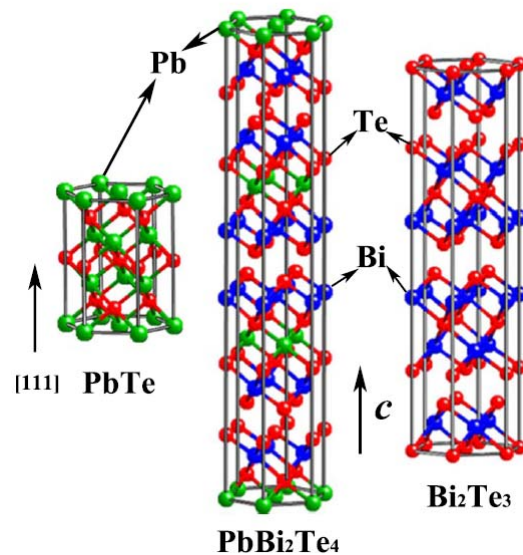


Figure 5. Crystal structure of the intergrowth compound $PbBi_2Te_4$ in relation to Bi_2Te_3 and $PbTe$. We find that this material has thermoelectric behavior similar to Bi_2Te_3 but extending to higher temperature.

While PbTe has a number of desirable characteristics, it has limitations that could prevent widespread use in vehicles. These include the performance, which needs further improvement, and the fact that it contains a large

amount of Te, which is an element with limited supply. We performed studies of PbBi_2Te_4 (Fig. 5) and related intergrowth compounds [10] as well as PbSe [11] in order to identify alternatives. We found that the intergrowth compounds have behavior similar to Bi_2Te_3 but with thermoelectric performance extending to higher temperatures more conducive to waste heat recovery.

PbSe is known to be a thermoelectric composition. However, it has been little studied in comparison to PbTe, and in particular, it is not known what performance it could have if optimized. We used transport calculations in conjunction with mobility data from literature to assess the thermoelectric potential of this material with optimized doping. We found that n-type PbSe is inferior to PbTe. On the other hand, we find that the p-type performance is very good, and likely will exceed that of the best PbTe materials at high temperature. This means that development of optimized p-type PbSe can enable replacement of p-type PbTe.

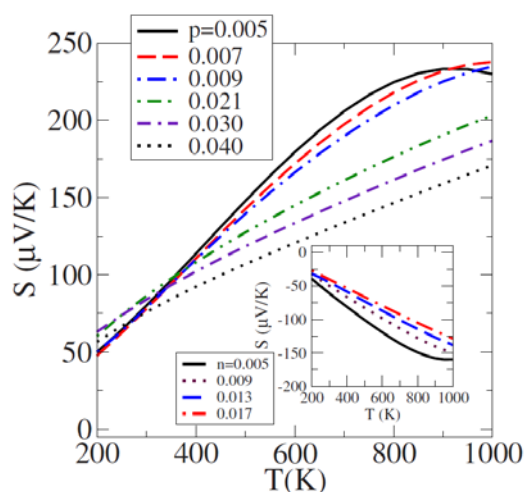


Figure 6. Calculated ZT for p-type doped PbSe. The inset shows results for the thermopower of n-type material, which is inferior.

We used the calculated transport functions of PbSe in conjunction with experimental mobility data to estimate the temperature and doping dependent ZT . As shown in Figure 6, we found that peak p-type ZT values exceeding 1.5 are achievable for doping levels near 0.008 holes per formula unit.

We recently initiated study of several other chalcogenides to determine if there are alternate compositions with reasonable performance that are either lower cost or Pb-free. The materials under investigation include doped SnS, SnTe, and BiCu_2S_2 . These are in progress.

Conclusions

We are obtaining new insights into thermoelectric materials performance using Boltzmann transport theory based on first principles electronic structures. We found that heavily doped PbTe can have enhanced properties even without the toxic element Tl. This prediction was confirmed experimentally. We identified lower cost rare earth free skutterudite thermoelectric compositions. We also found that heavily doped PbSe offers a very high performance alternative to p-type PbTe.

References

- [1] D.J. Singh and I. Terasaki, "Nanostructuring and more", *Nature Materials* **7**, 616 (2008).
- [2] D.J. Singh, "Planewaves, Pseudopotentials and the LAPW Method, 2nd Edition", Springer, Berlin (2006).
- [3] G.K.H. Madsen and D.J. Singh, "BoltzTraP: A code for calculating band-structure dependent quantities", *Computer Physics Communications* **175**, 67 (2006).
- [4] N. Bernstein, J.L. Feldman and D.J. Singh, "Calculations of dynamical properties of skutterudites: Thermal conductivity, thermal expansivity, and atomic mean square displacement", *Physical Review B* **81**, 134301 (2010).
- [5] D.J. Singh and M.H. Du, "Properties of alkaline-earth-filled skutterudites antinodes: $A(\text{Fe},\text{Ni})_4\text{Sb}_{12}$ ($A=\text{Ca}, \text{Sr}, \text{and Ba}$)", *Physical Review B* **82**, 075115 (2010).
- [6] D.J. Singh, Invention Disclosure 20102410, DOE S-115,458, "Alkaline Earth Filled Iron Nickel Skutterudite Antimonide Thermoelectrics"
- [7] L. Zhang, M.H. Du and D.J. Singh, "Zintl-phase compounds with SnSb_4 tetrahedral anions: Electronic structure and thermoelectric properties", *Physical Review B* **81**, 075117 (2010).
- [8] D.J. Singh, "Doping-dependent thermopower of PbTe from Boltzmann transport calculations", *Physical Review B* **81**, 195217 (2010).
- [9] J. Androulakis, I. Todorov, D.Y. Chung, S. Balikaya, G. Wang, C. Uher and M. Kanatzidis, "Thermoelectric enhancement in PbTe with K or Na codoping from tuning the interaction of the light- and heavy-hole bands", *Physical Review B* **82**, 115209 (2010).
- [10] L. Zhang and D.J. Singh, "Electronic structure and thermoelectric properties: PbBi_2Te_4 and related intergrowth compounds", *Physical Review B* **81**, 245119 (2010).
- [11] D. Parker and D.J. Singh, "High-temperature thermoelectric performance of heavily doped PbSe", *Physical Review B* **82**, 035204 (2010).

Agreement 16309 – Carbon Based Thermoelectrics

Principal Investigators: D.M. Gruen, D. Singh, and J.L. Routbort

Co-Workers: P. Bruno, M. Xie, P. Redfren, and L. Curtiss

Argonne National Laboratory

9700 S. Cass Avenue, Argonne, IL 60439-4838

(630) 252-5065; fax: (630) 252-5568; e-mail: dmgruen@anl.gov

DOE Technology Manager: Jerry L. Gibbs

(202) 586-1182; fax: (202) 586-1600; e-mail: jerry.gibbs@ee.doe.gov

Contractor: UChicago Argonne LLC

Contract No.: DE AC02 06CH11357

Objective

- Develop high-temperature, high-ZT thermoelectrics

Approach

- Use nanoensembles to break the interdependence between the thermopower and the electrical and thermal conductivities. Optimize these parameters separately and systematically for high ZT. Enhance the thermopower of the materials by increasing their configurational electronic entropies that enter the expression for the figure of merit in a quadratic fashion thus powerfully affecting conversion efficiencies.

Accomplishments

- In FY10 we have tried to improve our fabrication techniques to introduce boron into our nanocarbon ensembles to improve the thermopower to verify the density functional tight binding calculations reported in the annual report for FY09. During the last year, we refined the synthesis procedure to produce ensembles that are thermally and electrically stable to 2500K. Measurement of their Seebeck coefficients and electrical as well as thermal conductivities were made as a function of temperature.
- A density functional theory calculation has been performed on partial substitution of Al for Si and B for C in SiC.

Future Direction

- The favorable high-temperature thermoelectric properties of the nanocarbon ensembles (NCE) demonstrated by the above “proof of concept” results strongly suggests an extension of this approach for the development of high ZT thermoelectrics
 - The extension involves using silicon carbide as a basic constituent for the next generation of nanoensembles. This material is widely available, is not resource limited and is environmentally benign.
 - Silicon carbide is known to have a large number of coexisting polytypes. By proper doping, we create in each polytype a high density of states near the Fermi level. The usefulness of this idea has been demonstrated in preliminary experiments where much larger thermopowers than in the carbon ensembles have already been measured.
-

Introduction

Boron-doped nanographite ensembles (NGEs) are interesting thermoelectric nanomaterials for high temperature applications. Rapid induction annealing and quenching has been applied to boron-doped NGEs using a relatively low-cost, highly reliable laboratory built furnace to show that substantial improvements by doping with B in thermoelectric power factors can be achieved using this methodology that would confirm the density functional calculations [1]. Details of the design and performance of this compact induction furnace as well as results of the thermoelectric measurements will be reported here.

This project has shown “proof of concept” during the past year. Nanocarbon ensembles that are thermally and electrically stable at temperatures up to 2500K have been synthesized and characterized. They preserve their nanostructures at very high temperatures. Thermoelectric properties are promising but further development work needs to be done to reach the overall objective of the project that is to create materials displaying ZT values in the 4-5 range [2] so as to reach heat to electricity conversion efficiencies of 30-40%.

Measurements of thermal conductivities give low values that are most likely due to the nanostructured nature of the nanoensembles. Support for that conclusion is provided by HRTEM, XRD and Raman characterizations.

In order to gain a better understanding of the effect of thermal treatment on the thermoelectric properties of boron doped NGEs, we have constructed an induction furnace to perform systematic annealing studies over a wide temperature range (1300-2400K) under high vacuum conditions. Additionally and very importantly, induction methodology enables us rapidly to quench samples from temperatures at which diffusional processes would lead to a loss of substitutional boron if cooled slowly because of a steep gradient in boron solubility as a function of temperature. In contradistinction to a

conventional graphite resistance furnace, an induction furnace by restricting heat to a small volume allows temperature reductions to occur at order of magnitude faster rates. Furthermore, induction heating saves up to about 5 hours in heating time for each heat treatment cycle. Induction heating can thus be used for rapid heating and quenching of the NGEs.

Experimental

Nanographite Ensembles



Fig. 1. Photograph of the high temperature induction furnace

Figure 1 is a photograph of the high-temperature, high-vacuum furnace. As a result of the thermal mass, the quench time from 1800°C to 1000°D in helium was \approx 35 seconds. The effect of quenching on the Seebeck coefficient is shown in Fig. 2.

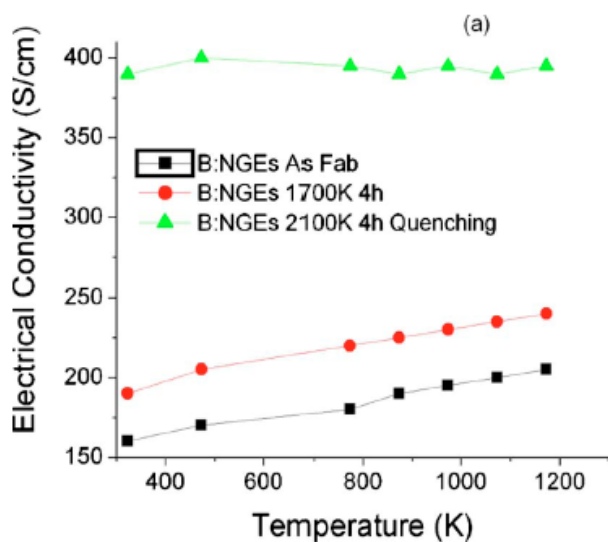


Fig. 2. The effect of quenching on B-doped nanographite ensembles.

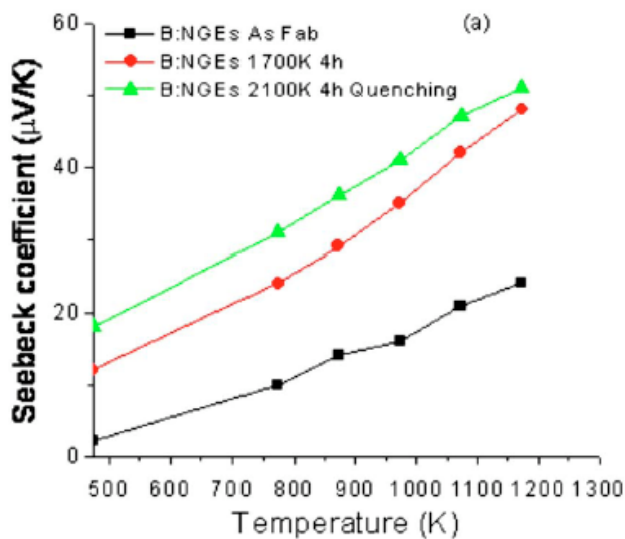


Fig. 3. The effect of quenching on the electrical conductivity of the B-doped nanographite ensembles.

The results of the experiments show that quenching improves both the Seebeck coefficient and the electrical conductivity, hence the power factor, $s^2\sigma/\kappa$, increases. However, the power factor did not increase by a large amount, presumably because in order to increase the solubility of B in the NGE sufficiently, the quench temperature must be higher (the structure has been

shown to be stable to 2700K) and the quench rate faster.

Silicon Carbide

Partial substitution of Al for Si and B for C has enabled us to synthesize, using spark plasma techniques, doped nanoensembles of SiC that have Seebeck coefficients of 330 microV/K at 900K. In attempting to attain an understanding of the Seebeck coefficient, we have extended earlier density functional calculations on stacked graphene sheets to 3C SiC nanoclusters with substitutions of Al in Si sites and B in C sites. The calculations show that both types of doping lead to hole states resulting in pronounced decreases in the HOMO-LUMO gap. As a consequence, some of the Al hole states are located near the Fermi level analogous to the situation encountered in stacked graphene sheets. Each of the large number of discrete electronic states introduced into SiC due to doping are associated with a particular Al and B configuration. We have measured Seebeck coefficient and electrical conductivity and while both increase with temperature, it is difficult to quantitatively correlate the magnitude with the substitutional doping.

We have also synthesized Ni₂Si/6H SiC composites by compressing fine-grained powders into discs in a SPS apparatus. Rapid densification begins at 1400K, at least 200 degrees lower than for pure SiC, presumably because of the presence of Ni₂Si which melts congruently at 1582K. The discs must have considerable porosity since their density is 2.62 g/cm³ which is 72% of theoretical density calculated on the basis of the composition given above. Nevertheless, extensive covalent bonding between Ni₂Si and SiC as a result of SPS processing appears to have taken place as evidenced by the fact that the discs require cutting by a diamond saw for fabrication into shapes appropriate for various measurements. This remarkable material has an electrical conductivity of 100 S/cm that decreases slowly with temperature while the thermopower is essentially temperature invariant at -25 mV/K in the range 500-

1100K. Although not completely homogeneous, one may picture the ensemble as composed principally of particles of SiC surrounded by shells of Ni₂Si.

To gain insight into the origins of the thermoelectric properties (TEP) of the ensembles will require extensive experimental and theoretical work. The TEP of doped SiC and transition metal silicides have been extensively studied individually but, not in combination with each other. Ni₂Si forms ohmic contacts with 6HSiC. However, the degree to which the electronic structures of the two materials are modified by their mutual interactions or by individual dopant and dopant levels is not known. Such knowledge is a prerequisite to obtaining a full understanding of what one might call “quantum proximity effects” that could be crucial to determining the thermoelectric behavior of complex nanomaterials.

Work with Industry

ANL is working with Aegis Technology (San Diego). They are developing fabrication techniques to improve the more “conventional” bulk thermoelectrics. Results are shown in Fig. 4.

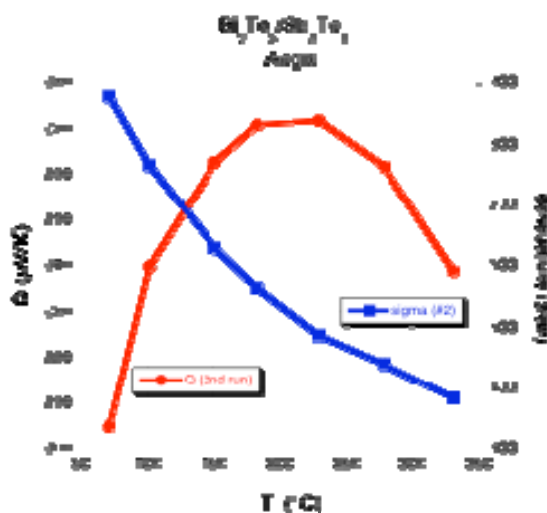


Fig. 4. Plot of Seebeck coefficient and the conductivity measured for a Bi₂Te₃/Sb₂Te₃ sample sent by Aegis Technologies.

Issues & Future Direction

This program will receive no funding from Propulsion Materials in FY11. However, we will continue to work on understanding and improving the thermoelectric properties of the SiC based nanoensembles using some carryover and Office of Basic Energy Sciences funds. Work will concentrate on using the theory to guide experimental work on substitution of dopants in SiC compounds to obtain optimal thermoelectric properties.

Conclusions

Reaching the ultimate objective of a ZT of 4-5 would have a profound impact on energy conversion technology. Single phase materials appear to be limited to ZTs of 1-2. The nanoensemble approach proposed by us may be able to overcome this limitation by independently maximizing the three parameters that determine the figure of merit.

Our work up to now provides some support for the hypothesis that configurational electronic entropy can be very important in determining thermopower. We are further optimizing that quantity by using SiC as a basis for the next step in nanoensemble synthesis. Work in 2011, while limited by funding, will concentrate on developing methodologies that increase electrical while decreasing thermal conductivities of SiC based nanoensembles.

Published Papers

1. P. C. Redfern, D. M. Gruen, L. A. Curtiss, Chem. Phys. Lett., 471, 264 (2009)
2. D. M. Gruen, P. Bruno, M. Xie, Appl. Phys. Lett., 92, 143118 (2008)
3. D. M. Gruen, P. Bruno, R. Arenal, J. Routbort, D. Singh, M. Xie, J. Appl. Phys., 105, 073710 (2009)

Agreement 18340 - Thermoelectric Materials for Advanced Vehicle Energy Recovery

Principal Investigator: Dr. Terry Hendricks

MBI Business Development Manager/Senior Program Manager
MicroProducts Breakthrough Institute
Pacific Northwest National Laboratory
1000 NE Circle Blvd., Suite 11101, Corvallis, Oregon 97330
(541) 713-1353; fax: (541) 758-9320; e-mail: terry.hendricks@pnl.gov

Associate Researchers: Dr. Morris Good and Kamandi Roberts

Chemical, Biological, and Physical Science Division, K5-26
Pacific Northwest National Laboratory
P.O. Box 999, Richland, Washington 99352
Morris Good: (509) 375-2529; fax: (509) 375-6497; e-mail: morris.good@pnl.gov
Kamandi Roberts: (509) 375-3943; fax: (509) 375-6497; kamandi.roberts@pnl.gov

Professor Mas Subramanian and Dr. Krishnendu Biswas

Department of Chemistry
Oregon State University
Corvallis, Oregon 97330
(541)-737-8235; fax (541)-737-2062; e-mail: mas.subramanian@oregonstate.edu

DOE Technology Manager: Jerry L. Gibbs
(202) 586-1182; fax: (202) 586-1600; e-mail: jerry.gibbs@ee.doe.gov
Field Technical Manager: Dean Paxton
(509) 375-2620; fax: (509) 375-2186; e-mail: dean.paxton@pnl.gov

Contractor: Pacific Northwest National Laboratory
Contract No: DE-AC05-76RL01830

Objectives

- Develop new high-performance n-type and p-type thermoelectric (TE) material compositions to enable the DOE Office of Vehicle Technologies (OVT) to achieve or approach 10% fuel efficiency improvements from waste energy recovery in advanced light-duty engines and vehicles.
- Develop new high-performance, n-type and p-type TE material compositions to enable OVT to achieve stretch thermal efficiencies of 55% in advanced heavy-duty engines by 2013.
- Improve cost-effectiveness and performance of exhaust heat recovery in light- and heavy-duty vehicles.
- Design, synthesize, and characterize p-type and n-type skutterudites and metal oxide TE materials for waste-heat-driven power generation in light-duty or heavy-duty vehicle exhaust flows or other comparable exhaust flows. Develop TE materials with operational temperatures as high as 800 K to 900 K.
- Develop advanced n-type and p-type bulk TE materials that have peak ZT (Figure of Merit x Temperature) of approximately 1.6 or higher at 600 K and temperature-dependent properties that provide high performance in the 350 K to 820 K range.

Approach including industrial partner/collaborator and path to technology transfer and commercialization

- Pacific Northwest National Laboratory (PNNL) and Oregon State University (OSU) are systematically investigating multiple-rattler skutterudite materials and metal oxide TE materials that can perform effectively and structurally survive at temperatures from 350 K to 820 K.

- Indium (In)-based cobalt antimony ($\text{In}_x\text{R}_y\text{Co}_4\text{Sb}_{12}$) compounds are one targeted n-type skutterudite material. However, p-type skutterudites also are being investigated and developed.
- PNNL and OSU are simultaneously characterizing the temperature-dependent thermoelectric and structural properties of advanced p-type and n-type TE materials, particularly Seebeck coefficient, electrical conductivity, thermal conductivity, Young's modulus, Poisson's ratio, and the coefficient of thermal expansion (CTE) up to 300°C to 400°C.
- OSU is developing and fabricating the advanced TE material compounds and measuring the TE properties using their TE measurement equipment.
- PNNL is measuring structural properties, Young's modulus, and Poisson's ratio, in resonant ultrasound (RUS) facilities and CTE at PNNL's Physical Sciences Laboratory in Richland, WA.
- PNNL is using its TE system modeling capabilities to characterize system-level benefits of the material compositions in vehicle waste energy recovery applications.

Milestones, Metrics and Accomplishments

- Continued fabricating and characterizing InCe-based n-type dual-rattler skutterudite materials, n-type $\text{In}_{0.15}\text{Ce}_{0.1}\text{Co}_4\text{Sb}_{12}$ and $\text{In}_{0.2}\text{Ce}_{0.15}\text{Co}_4\text{Sb}_{12}$ compounds which showed very good n-type TE behavior.
- n-type $\text{In}_{0.2}\text{Ce}_{0.15}\text{Co}_4\text{Sb}_{12}$ compounds demonstrated ZT values of 1.5 to 1.6 at 450 K to 525 K. **(Milestone)**
- Investigated, fabricated, and characterized $\text{In}_{0.2}\text{Co}_4\text{Sb}_{12}$ compounds, which also showed very good ZT values of 1.2 at 623 K.
- Investigated, fabricated, and characterized n-type $\text{In}_{0.2}\text{Ce}_{0.1}\text{Yb}_{0.05}\text{Co}_4\text{Sb}_{12}$ and $\text{In}_{0.2}\text{Ce}_{0.05}\text{Yb}_{0.1}\text{Co}_4\text{Sb}_{12}$ skutterudite compounds that demonstrated ZT = 1.2 at 620 K. **(Milestone)**
- Investigated, developed, and fabricated promising p-type skutterudite materials based on generic compositions $\text{In}_x\text{Ce}_{0.15-y}\text{Yb}_y\text{FeCo}_3\text{Sb}_{12}$. Characterized the ZT vs. temperature behavior of p-type multiple-rattler compositions $\text{In}_x\text{Ce}_{0.05}\text{Yb}_{0.1}\text{FeCo}_3\text{Sb}_{12}$ and $\text{In}_x\text{Ce}_{0.1}\text{Yb}_{0.05}\text{FeCo}_3\text{Sb}_{12}$. **(Milestone)**
- Measured room-temperature Young's modulus and Poisson's ratios for several n-type InCe-based $\text{Co}_4\text{Sb}_{12}$, skutterudite compounds (exact compositions as above). **(Milestone)**
- Measured coefficients of thermal expansion for several n-type InCe-based $\text{Co}_4\text{Sb}_{12}$ skutterudite compounds (exact compositions as above) at temperatures from 25°C to 400°C. **(Milestone)**.
- Characterized the thermal cycling behavior of several n-type InCe-based skutterudite compounds, and demonstrated their thermal stability after 200 cycles, 50°C to 400°C.
- Completed fabrication of critical high-temperature RUS thermal chamber for high-temperature RUS structural property measurements at PNNL. **(Milestone)**
- Performed x-ray diffraction (XRD) analyses of n-type and p-type InCe-based multiple-rattler skutterudites to verify their pure, single-phase composition.
- Several n-type InCe-based $\text{Co}_4\text{Sb}_{12}$, skutterudite compounds delivered to Oak Ridge National Laboratory (ORNL) for TE property verification measurements; measurements are currently on-going. **(Milestone)**.

Future Direction

- Focus synthesis procedures and fabrication on high-performance n-type $\text{In}_{0.2}\text{Ce}_{0.15}\text{Co}_4\text{Sb}_{12}$ and $\text{In}_{0.2}\text{Co}_4\text{Sb}_{12}$ compositions
 - Good reproducibility
 - Fabricating highly-dense samples
 - Develop hot-pressing techniques
- Complete TE property verification on n-type InCe-based $\text{Co}_4\text{Sb}_{12}$ skutterudite compounds at ORNL
- Perform structural property measurements in n-type and p-type InCe-based $\text{Co}_4\text{Sb}_{12}$ skutterudites at high temperatures (up to 300°C to 400°C).
 - Young's modulus, E(T), and Poisson's ratio, $\nu(T)$
 - CTE (T)
 - Mechanical strength at room temperature
- Integrate n-type $\text{In}_{0.2}\text{Ce}_{0.15}\text{Co}_4\text{Sb}_{12}$ with p-type LASTT (lead antimony silver tin telluride) materials into TE couples
- Measure n-type $\text{In}_{0.2}\text{Ce}_{0.15}\text{Co}_4\text{Sb}_{12}$ / LASTT couple performance for 1-3 couple pairs
- Continue evaluating system-level benefits with the new p-type and n-type TE materials as they are available.

Introduction

Background

DOE's *Transportation Energy Data Book: Edition 24* shows that, in 2002, approximately 130 billion gallons of gasoline were used nationwide by the light-duty passenger car, van, and sport-utility vehicle (SUV) segments. Some current estimates indicate that approximately 4 to 5 Quads (1 Quad = 10^{15} Btu) of the energy in this fuel ends up as waste thermal energy in the vehicle exhaust stream. The same reference also indicates another approximately 30 billion gallons of diesel fuel was used nationwide by heavy-duty vehicles in 2002. Some current estimates indicate that approximately 1.4 Quads of the energy in this fuel ends up as waste thermal energy in the heavy-vehicle exhaust stream. Other estimates indicate that another 5 to 7 Quads of thermal energy originating from the fuel energy ends up in the vehicle coolant systems of light-duty passenger cars, vans, SUVs, and heavy-duty vehicles. DOE's Office of Energy Efficiency and Renewable Energy, Vehicle Technologies Program has initiated a Waste Heat Recovery and Utilization project with the goal of recovering enough of this waste energy to increase the vehicle fuel economy by 10%. Contractor teams are pursuing advanced thermoelectric (TE) systems, leveraging recent advanced TE materials research and development in skutterudites, quantum well, and nanostructured materials to recover and convert this waste thermal energy into high-grade electrical energy onboard the vehicle.

Advanced TE materials are critical to achieving project performance goals and introducing other potential future applications of TE power generation and advanced cooling in vehicle systems. Several researchers have reported advanced TE materials demonstrating ZT values of 1.6 to 2.4, with at least some of this data occurring at high temperatures of 400°C to 700°C. It is possible to expect advanced TE power conversion efficiencies of 12% to 15% with TE materials in this ZT range at high temperatures, which are two to three times the values using older bulk TE materials. Further

advances in TE materials may lead to power conversion efficiencies approaching 20%.

Several technical challenges exist to developing advanced hybrid TE power systems in advanced light-duty and heavy-duty vehicle platforms, including increasing TE device conversion efficiencies through demonstrated high-performance TE materials, transferring hot-side exhaust thermal energy into the TE conversion devices, dissipating cold-side thermal energy to the environment, and optimizing advanced TE systems for a variety of nominal and off-nominal performance conditions. Tasks performed here address these new opportunities by developing the necessary advanced TE materials with a ZT value of ~1.6 at 600 K in bulk form that allows cost-effective engineering transition into high-performance TE power generation devices.

This project leverages recent progress in skutterudite TE materials and metal oxide materials. Skutterudite materials have a cubic crystal structure as shown in Figure 1, which contain "voids" inside the crystal. These "voids" are large enough that various elements can be inserted inside. Any inserted element has a particular resonance frequency associated with it that can be excited by thermal phonons of the proper wavelength traveling through the crystal. The complete wavelength spectrum of thermal phonons is responsible for producing the observed lattice thermal conductivity in any material. The elements inserted into the crystal voids interact with and resonate with particular wavelengths of the spectrum, thereby causing them to resonate or "rattle" at that particular wavelength and, ultimately, scatter the thermal phonon rather than allowing it to transmit through the crystal. This ultimately reduces the lattice thermal conductivity of the skutterudite. The more elements that can be put inside the crystal voids, the more wavelengths or range of wavelengths can be impacted and scattered, further reducing the lattice thermal conductivity. This ultimately increases the ZT (Equation 1) of skutterudite materials, which already have inherently high Seebeck coefficients,

$$ZT = \frac{S^2 \sigma}{K_e + K_L} T \quad (1)$$

where:

S = Seebeck Coefficient [$\mu\text{V/K}$]

σ = Electrical Conductivity [S/cm]

K_e = Electronic Thermal Conductivity [W/m-K]

K_L = Lattice Thermal Conductivity [W/m-K]

T = Temperature [K]

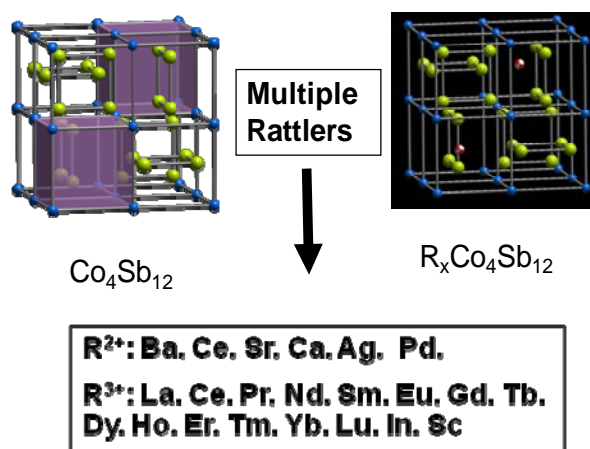


Figure 1. Skutterudite crystal structure and potential rattler elements for thermal conductivity suppression

The box in Figure 1 shows the various elements that potentially can be inserted into the skutterudite crystal voids, which are being investigated in this project. This is the basis for one approach to developing high-performance TE materials.

Project Accomplishments

This year the project has focused on investigating and developing p-type multiple-“rattler” and n-type multiple-“rattler” skutterudites. We have investigated and quantified the thermoelectric properties of various promising compounds, measured room-temperature Young’s modulus and Poisson’s ratio, measured coefficients of thermal expansion, and continued preparing and calibrating systems for high-temperature structural property measurements in PNNL RUS systems. A number of objectives were achieved, namely the microstructural optimization of a series of promising novel thermoelectric materials. Sample density and durability were improved dramatically, thus increasing

reproducibility and reliability of fabricated test samples. In addition, microstructural optimization achieved an overall grain-size reduction with little grain coarsening upon sintering, thereby resulting in a reduction of lattice thermal conductivity, which is a key success in synthesizing efficient thermoelectric materials. This led to fabrication of three different InCe-based compounds discussed below.

Advanced Skutterudite TE Materials Properties

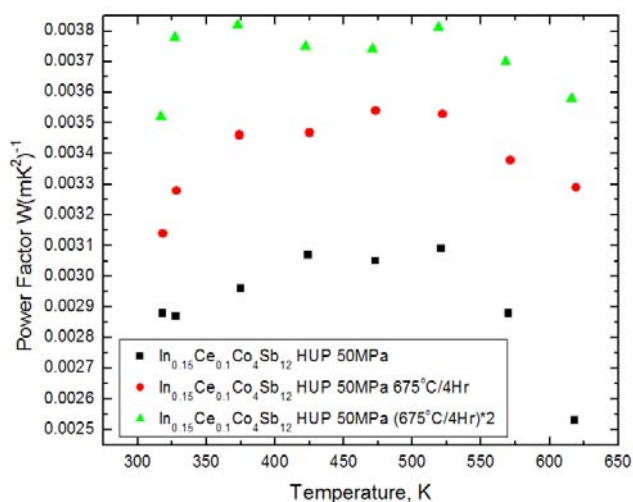
This year the work identified several interesting InCe-based multiple-filled skutterudite TE compounds building on the fundamental $\text{Co}_4\text{Sb}_{12}$ skutterudite composition that could be tailored into n-type TE materials for waste heat recovery applications. This year’s work also investigated Fe-based p-type skutterudites that showed promise, but ultimately showed relatively low ZT values at temperatures of interest to waste heat recovery applications. The focus has been on developing hot-pressing and sintering (HPS) techniques to make bulk TE materials that can easily transition into multiple-couple TE devices. Figure 2 shows the power factor (PF) of the different n-type $\text{In}_{0.15}\text{Ce}_{0.1}\text{Co}_4\text{Sb}_{12}$ and $\text{In}_{0.2}\text{Ce}_{0.15}\text{Co}_4\text{Sb}_{12}$ skutterudite compounds fabricated with these HPS techniques. The power factor is defined as $(\alpha^2\sigma)$, where α = Seebeck coefficient [$\mu\text{V/K}$] and σ = electrical conductivity [$(\Omega\text{-cm})^{-1}$ or (S/cm)].

The n-type $\text{In}_{0.15}\text{Ce}_{0.1}\text{Co}_4\text{Sb}_{12}$ materials in Figure 2a were fabricated with a significant compression pressure of 50 MPa. Their power factor was relatively insensitive to temperature over the range from 350 K to 600 K. The development experience with these materials ultimately led to HPS fabrication of the $\text{In}_{0.2}\text{Ce}_{0.15}\text{Co}_4\text{Sb}_{12}$ materials and their impressive power factors in Figure 2b. The PFs of other $\text{In}_x\text{Ce}_y\text{Co}_4\text{Sb}_{12}$ combinations also are shown in Figure 2b. Figure 3 displays the Seebeck coefficient, α , and electrical resistivity, ρ , as a function of temperature for the $\text{In}_{0.2}\text{Ce}_{0.15}\text{Co}_4\text{Sb}_{12}$ materials in Figure 2b. The Seebeck coefficients are quite comparable for the different $\text{In}_x\text{Ce}_y\text{Co}_4\text{Sb}_{12}$ combinations in Figure 2b, but it is clear in Figure 3 that the driving mechanism for

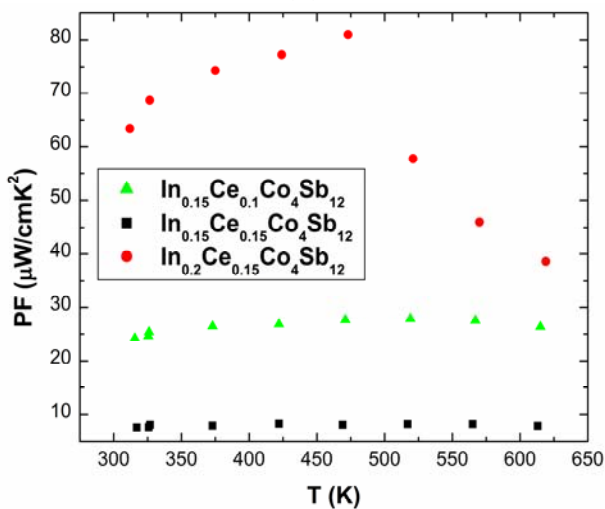
the superior PF of the $\text{In}_{0.2}\text{Ce}_{0.15}\text{Co}_4\text{Sb}_{12}$ materials is their lower electrical resistivity at all temperatures measured.

Figure 4 shows the actual rectangular parallelepiped skutterudite elements whose TE material properties are shown in Figure 2. Their dimensions are also shown in Figure 4. These dimensions are quite similar to what one would expect in a final TE device using these materials and could be tailored to any given final waste heat recovery application.

$\text{In}_{0.15}\text{Ce}_{0.1}\text{Co}_4\text{Sb}_{12}$ HUP 50 MPa "Light" Sample Power Factor

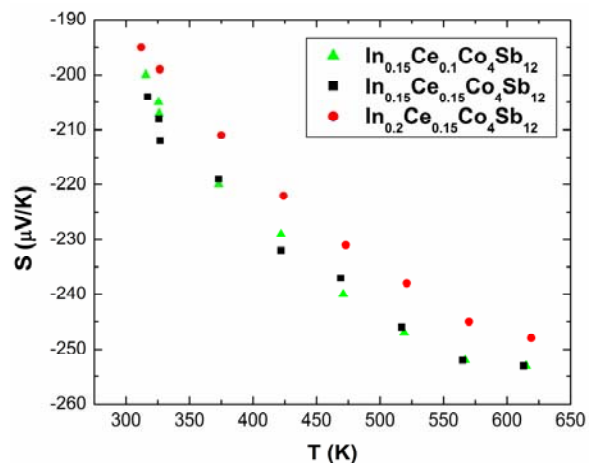


(a)

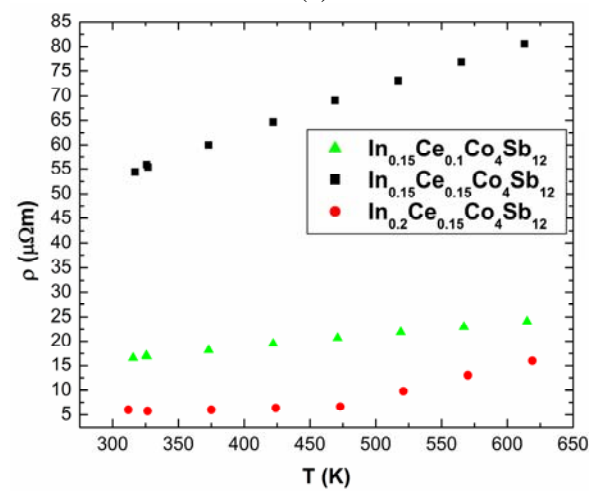


(b)

Figure 2. PFs of various n-type $\text{In}_{0.15}\text{Ce}_{0.1}\text{Co}_4\text{Sb}_{12}$ and $\text{In}_{0.2}\text{Ce}_{0.15}\text{Co}_4\text{Sb}_{12}$ TE materials using sintering and hot-pressing processes



(a)



(b)

Figure 3. Seebeck coefficient (a) and electrical resistivity (b) of various n-Type $\text{In}_{0.15}\text{Ce}_{0.1}\text{Co}_4\text{Sb}_{12}$ and $\text{In}_{0.2}\text{Ce}_{0.15}\text{Co}_4\text{Sb}_{12}$ TE materials in Figure 2

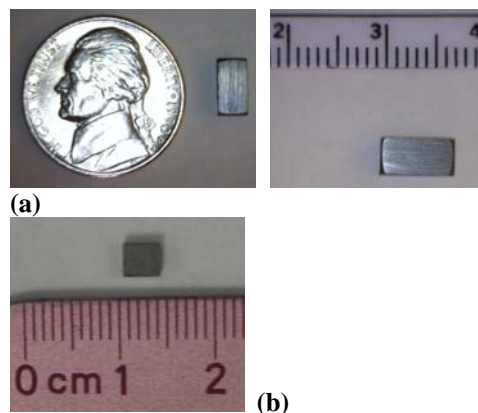


Figure 4. n-type $\text{In}_{0.15}\text{Ce}_{0.1}\text{Co}_4\text{Sb}_{12}$ (a) and $\text{In}_{0.2}\text{Ce}_{0.15}\text{Co}_4\text{Sb}_{12}$ (b) skutterudite TE compounds in Figure 2

The $\text{In}_{0.2}\text{Ce}_{0.15}\text{Co}_4\text{Sb}_{12}$ composition appeared to exhibit optimum TE properties and was therefore investigated further. Figure 5 shows the thermal conductivity (a) and ZT (b) as a function of temperature for $\text{In}_{0.2}\text{Ce}_{0.15}\text{Co}_4\text{Sb}_{12}$ TE materials shown in Figure 2. In these plots and all subsequent thermal conductivity plots $\lambda = K_e + K_L$. The ZT of these early

$\text{In}_{0.2}\text{Ce}_{0.15}\text{Co}_4\text{Sb}_{12}$ compounds in Figure 3b showed ZT values of 1.5 to 1.6 at 425 K to 525 K. We did note that some micro-cracking is sometimes possible in these materials, but it can be monitored and detected through the structural property measurements discussed below. It is a rare occurrence and not a serious problem, but is something that has to be monitored in these materials as in all TE materials.

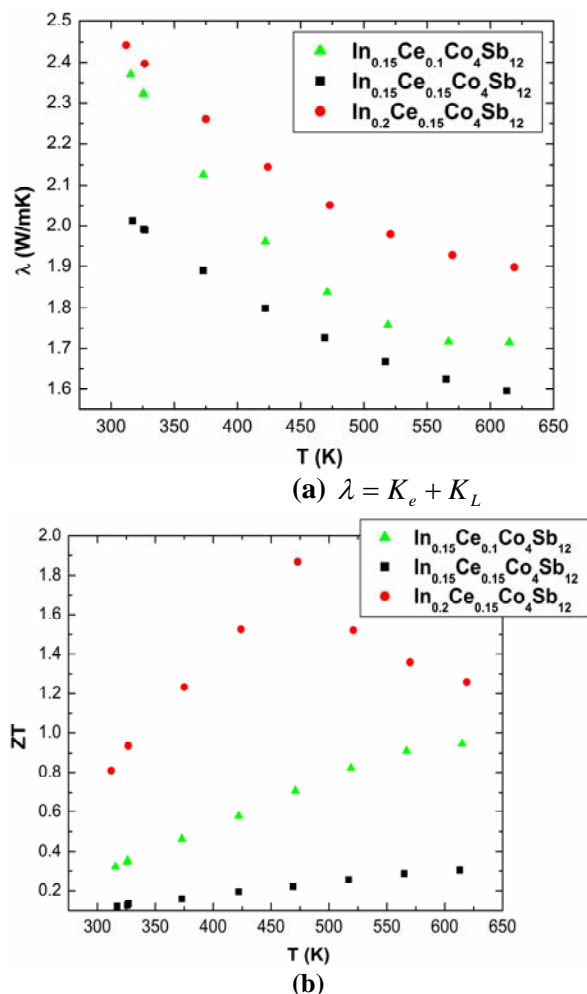


Figure 5. Thermal conductivity (a) and ZT (b) in the $\text{In}_{0.2}\text{Ce}_{0.15}\text{Co}_4\text{Sb}_{12}$ (b) TE skutterudite compounds in Figures 2 and 3

During FY 2010, our project also investigated and developed $\text{In}_{0.2}\text{Co}_4\text{Sb}_{12}$ compounds, which also showed good ZT values. Figure 6 shows the Seebeck coefficient and electrical resistivity of the $\text{In}_{0.2}\text{Co}_4\text{Sb}_{12}$ compounds fabricated in FY 2010. Figure 7 shows the ZT values of these $\text{In}_{0.2}\text{Co}_4\text{Sb}_{12}$ compounds vs. temperature, achieving a ZT of 1.2 at 623 K.

In FY 2009, our project began investigating other heavy-element fillers to the skutterudite crystal structure by using yttrium (Y) in the $\text{Co}_4\text{Sb}_{12}$. The project continued investigating other heavy-element fillers in FY 2010 by using ytterbium (Yb) as a third filler element with

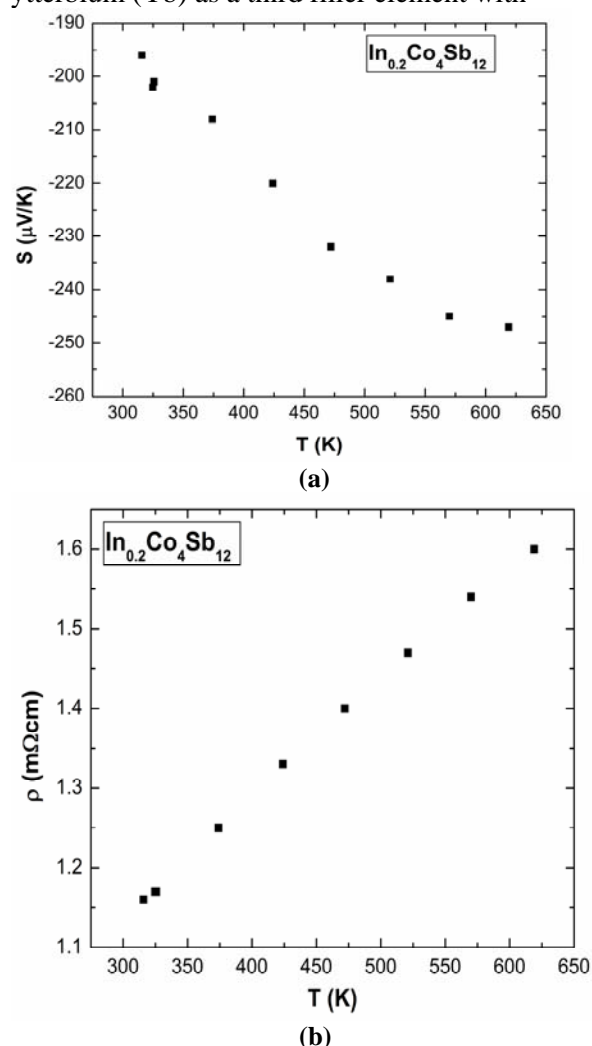


Figure 6. Seebeck coefficient (a) and electrical resistivity (b) of $\text{In}_{0.2}\text{Co}_4\text{Sb}_{12}$ compounds investigated and fabricated in FY 2010

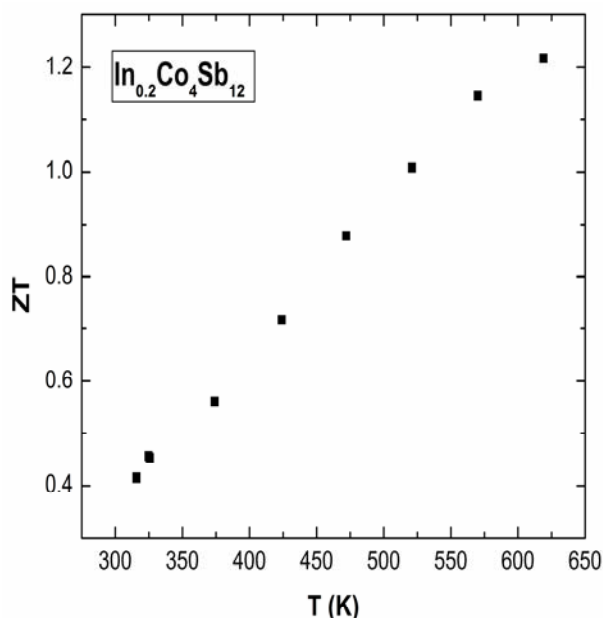


Figure 7. ZT of $\text{In}_{0.2}\text{Co}_4\text{Sb}_{12}$ compound fabricated in FY 2010

In and Ce. The two n-type skutterudite compounds investigated, fabricated, and characterized were n-type $\text{In}_{0.2}\text{Ce}_{0.1}\text{Yb}_{0.05}\text{Co}_4\text{Sb}_{12}$ and $\text{In}_{0.2}\text{Ce}_{0.05}\text{Yb}_{0.1}\text{Co}_4\text{Sb}_{12}$. The HPS process was once again used to essentially produce these triply-filled (i.e., multiple-rattler) skutterudite compound. Figure 8 shows the Seebeck coefficient (a) and electrical resistivity (b) of these two skutterudite compounds. The Seebeck coefficient of these two compounds is very similar in behavior and magnitude, but once again there is a marked difference in the electrical resistivity with the $\text{In}_{0.2}\text{Ce}_{0.05}\text{Yb}_{0.1}\text{Co}_4\text{Sb}_{12}$ compound having a much lower electrical resistivity. Figure 9 displays the thermal conductivity (a) and the resulting ZT value (b) of these two triply-filled skutterudite compounds. Figure 9a demonstrates that the thermal conductivity of the $\text{In}_{0.2}\text{Ce}_{0.05}\text{Yb}_{0.1}\text{Co}_4\text{Sb}_{12}$ compound is also lower than in the $\text{In}_{0.2}\text{Ce}_{0.1}\text{Yb}_{0.05}\text{Co}_4\text{Sb}_{12}$ compound. Both of these effects lead to the significantly higher ZT values for the $\text{In}_{0.2}\text{Ce}_{0.05}\text{Yb}_{0.1}\text{Co}_4\text{Sb}_{12}$ compound in Figure 9b, with the ZT surpassing 1.2 at about 620 K.

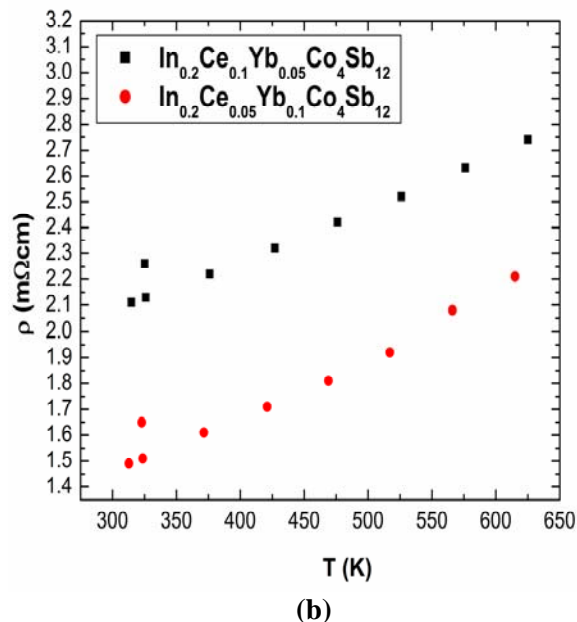
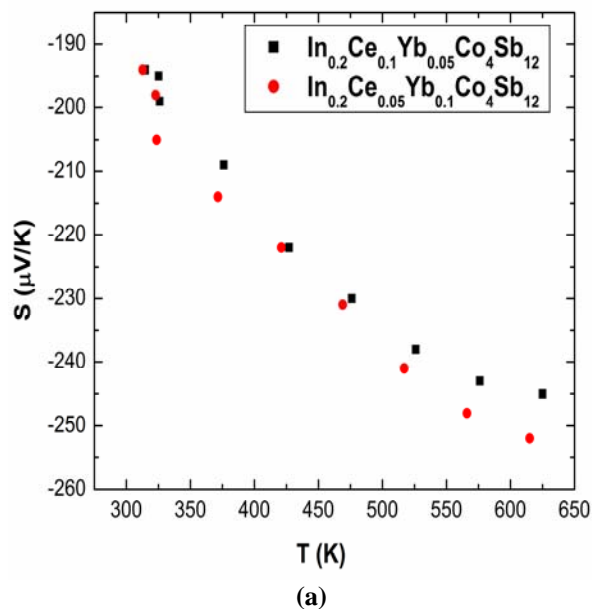


Figure 8. Seebeck coefficient (a) and electrical resistivity (b) of n-type $\text{In}_{0.2}\text{Ce}_{0.1}\text{Yb}_{0.05}\text{Co}_4\text{Sb}_{12}$ and $\text{In}_{0.2}\text{Ce}_{0.05}\text{Yb}_{0.1}\text{Co}_4\text{Sb}_{12}$ TE compounds in FY 2010

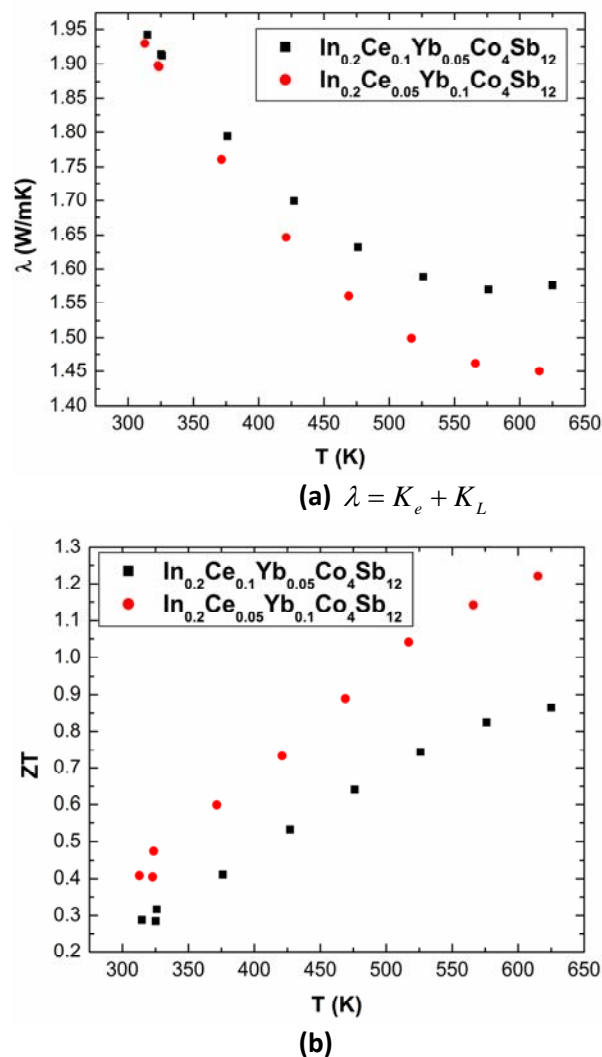


Figure 9. Thermal conductivity (a) and ZT values (b) for n-type $\text{In}_{0.2}\text{Ce}_{0.1}\text{Yb}_{0.05}\text{Co}_4\text{Sb}_{12}$ and $\text{In}_{0.2}\text{Ce}_{0.05}\text{Yb}_{0.1}\text{Co}_4\text{Sb}_{12}$ TE compositions in Figure 8

The method used in fabricating all these n-type materials incorporated ball milling processes into the HPS fabrication process. In, Co, and Sb were mixed together in stoichiometric ratio in a mortar and ground in air. The In-Co-Sb mixture was reacted in a hydrogen and nitrogen gas environment. The sample was calcined in a furnace at temperatures up to 675°C for approximately 40 hours. The In-Co-Sb sample was ground, then ball milled. The ground and dried $\text{In}_{0.15}\text{Co}_4\text{Sb}_{12}$ sample was combined with Ce that was weighed, mixed, and ground to form the proper compound stoichiometry. The In-Ce-Co-Sb sample was reacted in a hydrogen-nitrogen environment at up to 700°C for

24 hours using pre-determined heating and cooling ramp rates. The resulting sample was ground again, ball milled, and dried, the final sample then sintered in a furnace at 675°C. The structure was characterized via powder XRD, and the collected patterns showed evidence of the desired single-phase skutterudite structure. Yb is added along with Ce when fabricating the In-Yb-Ce-Co-Sb samples because these are both rare earth metals. All of these InCe-based skutterudites are bulk materials, making them much easier to integrate into TE devices and, therefore, easier to commercialize in operating devices and systems.

It is informative to see how all these particular n-type InCe-based skutterudite compounds align relative to one another on one temperature-dependent ZT plot. Figure 10 shows this comprehensive ZT plot for the n-type materials investigated in FY 2010, which allows quick comparisons of the n-type ZT values achieved and their different temperature dependencies. The KBMIX26 compound in Figure 10 was determined to have the approximate stoichiometry of $\text{In}_{0.2}\text{Ce}_{0.1}\text{Co}_4\text{Sb}_{12}$ using XRF and solution chemistry techniques. The ZT results shown in Figure 10 are consistent with those reported on these materials at the 2010 International Conference on Thermoelectrics [1,2], except the peak ZT behavior in our materials is at lower temperatures near 623 K.

The temperature dependent behavior of these various n-type materials is critical to:

- 1) determining the average ZT, which is the most important parameter in TE device design, and
- 2) providing important evaluations of material segmenting options and opportunities when designing devices across large temperature differentials associated with waste energy recovery applications. This second point is especially critical in automotive energy recovery systems because temperature dependencies can be so sharp that attempting to design and operate a TE device with just one of these n-type materials in a TE element, even though it has a high peak ZT, may not lead to high device performance because, once again, it is the average ZT across the entire temperature

differential the TE device and elements see that dictates device design optimization and performance. It is therefore often necessary to segment these advanced materials with other lower temperature materials (i.e., bismuth

tellurides) to truly exploit their superior ZT characteristics in particular temperature ranges. The ZT vs. temperature allows one to make the proper TE device design evaluations.

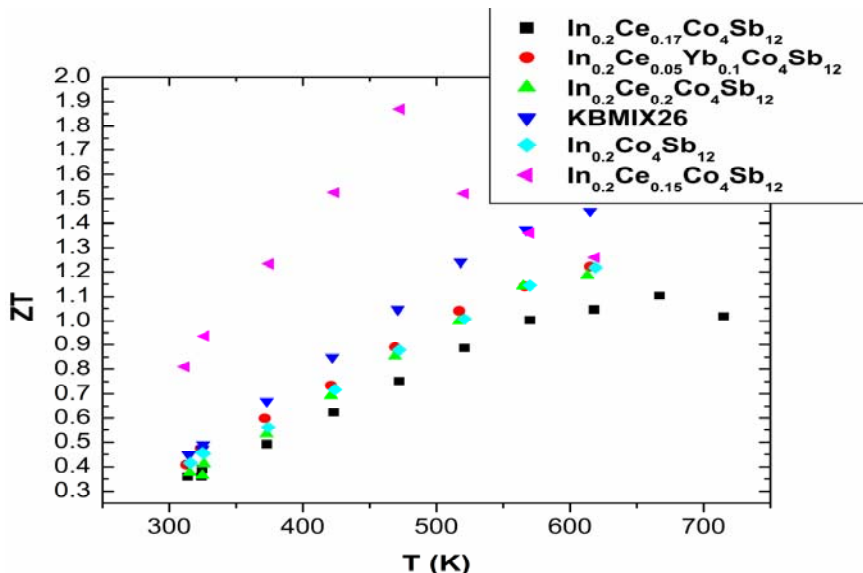


Figure 10. ZT of various n-type InCe-based skutterudite compounds created in FY 2010

In FY 2010, we also investigated and fabricated some promising p-type skutterudite materials based on Fe inclusion into the $\text{Co}_4\text{Sb}_{12}$ crystal structure. The p-type skutterudite materials developed and fabricated this year concentrated on materials with generic compositions $\text{In}_x\text{Ce}_{0.15-y}\text{Yb}_y\text{FeCo}_3\text{Sb}_{12}$. Figure 11 displays the ZT vs. Temperature behavior of these materials, particularly the p-type multiple-rattler compositions $\text{In}_x\text{Ce}_{0.05}\text{Yb}_{0.1}\text{FeCo}_3\text{Sb}_{12}$ and $\text{In}_x\text{Ce}_{0.1}\text{Yb}_{0.05}\text{FeCo}_3\text{Sb}_{12}$. Figure 12 shows the Seebeck coefficient (a), electrical resistivity (b), and thermal conductivity of the p-type $\text{In}_x\text{Ce}_{0.15-y}\text{Yb}_y\text{FeCo}_3\text{Sb}_{12}$ compounds created this year. The thermal conductivity of these $\text{In}_x\text{Ce}_{0.15-y}\text{Yb}_y\text{FeCo}_3\text{Sb}_{12}$ compounds is generally low and the electrical resistivity is generally in line with the n-type InCe-based skutterudite materials discussed above. However, their Seebeck coefficient, only about $100 \mu\text{V/K}$ to $140 \mu\text{V/K}$ at 500 K to 700 K, appears low compared to other n-type skutterudites. Consequently, the ZT of these p-type $\text{In}_x\text{Ce}_{0.15-y}\text{Yb}_y\text{FeCo}_3\text{Sb}_{12}$ compounds is low, with ZT values of only 0.48 at 710 K. This is the best p-type skutterudite

material performance generated in FY 2010. Unfortunately, this value is not high enough to use in high-performance TE devices for automotive energy recovery applications. It is difficult to produce high-performance skutterudite materials because very few dopants act as electron acceptors from the Co-Sb conduction band. Fe appears to be one of the most promising in this regard. Other researchers [3] appear to have overcome this limitation, demonstrating ZT values of 1.2 at 750 K to 800 K can be achieved with $\text{Fe}_3\text{CoSb}_{12}$ compositions. Therefore, our Fe content needs to be higher to achieve better ZT values.

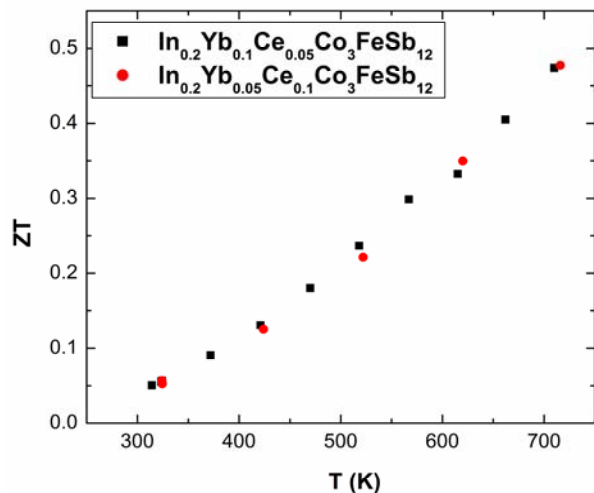


Figure 11. ZT values of p-type $\text{In}_x\text{Ce}_{0.15-y}\text{Yb}_y\text{FeCo}_3\text{Sb}_{12}$ skutterudite compounds

X-Ray Diffraction Patterns of Advanced Skutterudite Materials

XRD analysis was performed on the various n-type skutterudite materials shown in Figure 10 and the p-type skutterudite materials in Figures 11 and 12. Figure 13 displays the XRD patterns obtained for the various n-type and p-type skutterudite materials discussed above. These analyses demonstrate that these materials are pure, single-phase compounds. The XRD patterns allow one to calculate the lattice parameter, a , [units are Angstroms, \AA] that is shown in each XRD pattern for the various material compositions analyzed in Figure 13. The lattice parameter, a , is a measure of the cubic crystal dimension in the basic $\text{Co}_4\text{Sb}_{12}$ cubic structure. Slight (not visible by the naked eye) shifts occur in the resonance angles that allow one to detect the very slight changes in the lattice parameter, a , as more heavy filler atoms are added to the basic $\text{Co}_4\text{Sb}_{12}$ crystal structure. The lattice parameter, a , is clearly increasing in Figure 13 as more heavy filler atoms are added into the skutterudite crystal voids. Clearly, the p-type skutterudites have the larger lattice parameters, a , in this work.

Structural Properties

Additional work has been completed to characterize the room-temperature structural properties; Young’s modulus, E ; and Poisson’s

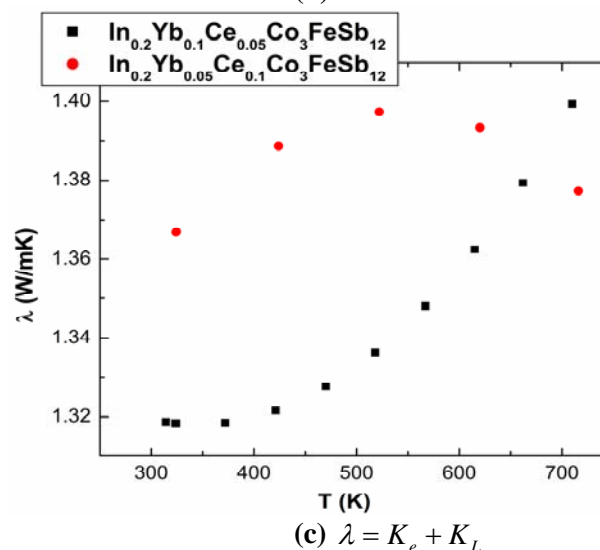
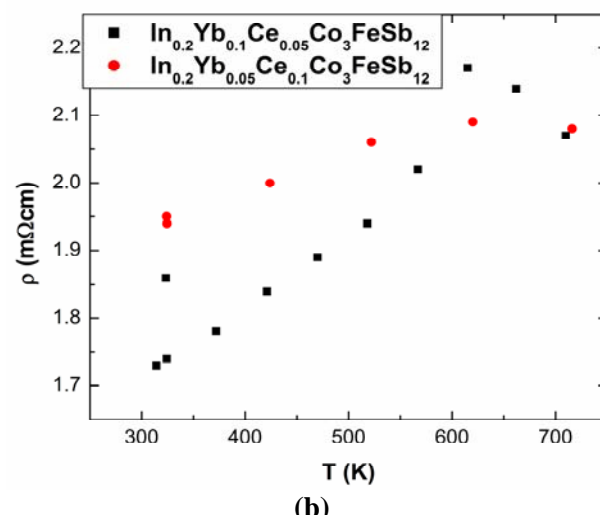
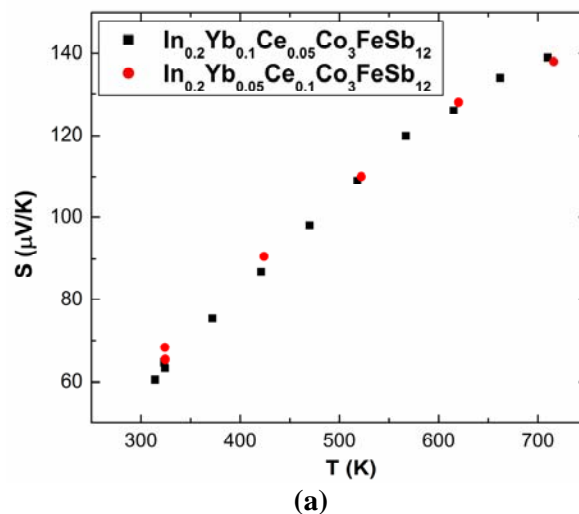
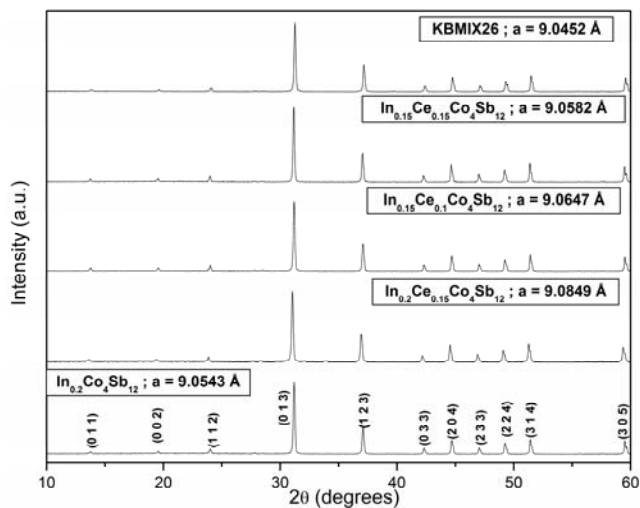


Figure 12. Seebeck coefficient (a), electrical resistivity (b), and thermal conductivity (c) of the p-type $\text{In}_x\text{Ce}_{0.15-y}\text{Yb}_y\text{FeCo}_3\text{Sb}_{12}$ compounds



[KBMIX26 above is a $\text{In}_{0.2}\text{Ce}_{0.1}\text{Co}_4\text{Sb}_{12}$ compound]

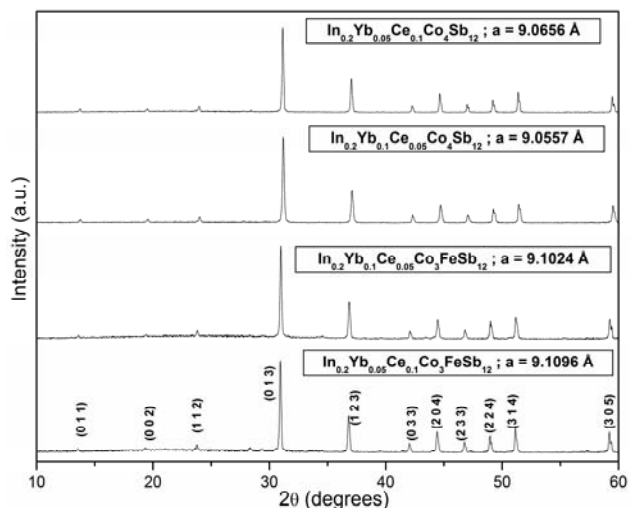


Figure 13. XRD patterns for various n-type and p-type skutterudites

ratio, ν ; and the CTE at high temperature for several n-type $\text{Co}_4\text{Sb}_{12}$, $\text{In}_x\text{Ce}_y\text{Co}_4\text{Sb}_{12}$, and $\text{In}_x\text{Ce}_y\text{Yb}_z\text{Co}_4\text{Sb}_{12}$ compounds and p-type $\text{In}_x\text{Ce}_{0.15-y}\text{Yb}_y\text{FeCo}_3\text{Sb}_{12}$ compounds. The RUS system used for the Young's modulus and Poisson's ratio measurement is shown in Figure 14, along with the typical sample measurement configuration between the input transducers. Generally, a vibrational signal is input to the sample, and the resulting frequency response signal then is generated from the sample, which can be measured and appropriate sample resonant frequencies identified. Then, these resonant frequencies are inversely analyzed



Figure 14. RUS equipment for structural property measurement used at PNNL. The typical sample mount between measurement transducers is shown.

using sophisticated sample structural modeling software to determine Young's modulus and Poisson's ratio of the sample. The sample dimensions, surface planarity, and accuracy of the 90-degree edges and corners are critical to this measurement technique and can greatly impact measurement accuracy. FY 2010 work continued to focus on producing highly accurate sample surfaces, edges, and corners, which requires great attention to detail in sample cutting and preparation. Significant success was demonstrated with sample preparation this year, as evidenced by the extensive structural property data measured and presented below.

Table 1 shows the structural properties, Young's modulus, E , and Poisson's ratio, ν , at room temperature, and CTE for the n-type CoSb_3 , $\text{In}_{0.15}\text{Ce}_{0.1}\text{Co}_4\text{Sb}_{12}$, $\text{In}_{0.1}\text{Y}_{0.1}\text{Co}_4\text{Sb}_{12}$, $\text{In}_{0.2}\text{Ce}_{0.15}\text{Co}_4\text{Sb}_{12}$, $\text{In}_{0.2}\text{Co}_4\text{Sb}_{12}$, and $\text{In}_{0.2}\text{Ce}_{0.05}\text{Yb}_{0.1}\text{Co}_4\text{Sb}_{12}$ compounds investigated during FY 2010. Table 1 also shows the measured ZT of these samples at or near 600 K, as well as some typical data from the literature. The ZT values for the In-Ce and In-Ce-Yb compounds represent a range of "ZT>1" materials with the optimum performance appearing in the

Table 1. Structural and thermoelectric properties for various n-type skutterudites investigated during FY 2010

Specimen Label and Comments	ρ , density (g/cm ³)	ν , Poisson's ratio	CTE (/°C)	E, Elastic Modulus (10 ¹¹ N/m ²)	ZT (@ 600 K)
Bi ₂ Te ₃ Alloys		0.21-0.37	14 x 10 ⁻⁶ 21 x 10 ⁻⁶ (Anisotropic)	0.40-0.47	0.0-0.1
PbTe		0.26	19.8 x 10 ⁻⁶	0.58	0.7
CoSb ₃ (literature)		0.222		1.396	0.6
La _{0.75} CoFe ₃ Sb ₁₂ (literature)		0.228		1.365	
CoSb ₃ (PNNL)		0.225-0.226	12.8x10 ⁻⁶	1.391-1.398	
In _{0.1} Co ₄ Sb ₁₂ (PNNL)		0.227	8.37x10 ⁻⁶	1.396	
In _{0.1} Y _{0.1} Co ₄ Sb ₁₂ (PNNL)		0.247	9.26x10 ⁻⁶	1.413	~0.5
In _{0.15} Ce _{0.1} Co ₄ Sb ₁₂ – Early Sample 11-2009	~7.314		8.30-8.83x10 ⁻⁶		
In _{0.15} Ce _{0.1} Co ₄ Sb ₁₂ – PNNL3 2-5-2010 --- REPEAT of 1-21-2010	~7.314	0.185	8.61x10 ⁻⁶	1.339	0.95
In _{0.15} Ce _{0.1} Co ₄ Sb ₁₂ - LB1 2-5-2010	7.304	0.215	8.56x10 ⁻⁶	1.348	0.95
In _{0.15} Ce _{0.1} Co ₄ Sb ₁₂ - LB2 2-9-2010	7.264	0.204	8.26x10 ⁻⁶	1.326	0.95
In _{0.2} Ce _{0.15} Co ₄ Sb ₁₂ 03161035_3-17-10 6-08-2010 - BNW-60608 – 88(M1-M31)	7.019	0.210-0.214 (2 samples)	8.11-8.44x10 ⁻⁶	1.182-1.185 (2 samples)	1.4 (1.5-1.6 @ 475K)
In _{0.2} Co ₄ Sb ₁₂ – A05061030-A 2010-06-09- BNW-60608 – 90(M1-M29 & M31 – No M30)	7.06-7.10	0.208-.218 (2 samples)	8.27-8.34x10 ⁻⁶	1.178-1.238 (2 samples)	1.2
In _{0.2} Yb _{0.1} Ce _{0.05} Co ₄ Sb ₁₂ - KB0627100_7-23-10 2010-08-16-BNW-60608-123 (M1-M27)	6.421	0.207	7.06–9.7 X 10 ⁻⁶	89.5	1.2

Table 2. Structural property impacts on n-type In_xCe_yCo₄Sb₁₂ and In_{0.2}Ce_{0.05}Yb_{0.1}Co₄Sb₁₂ compounds after thermal cycling (thermal cycling 50 °C to 400 °C, 200 cycles; room temperature structural properties)

	Temperature [°C]	Before Thermal Cycling		After Thermal Cycling	
		Young's Modulus, E X 10 ⁹ [N/m ²]	Poisson's Ratio, ν	Young's Modulus, E X 10 ⁹ [N/m ²]	Poisson's Ratio, ν
In _{0.15} Ce _{0.1} Co ₄ Sb ₁₂ (LBL1) – n-type	20-22	134.8	0.215	134.4	0.204
In _{0.15} Ce _{0.1} Co ₄ Sb ₁₂ (LBL2) – n-type	20-22	132.6	0.204	131.9	0.200
In _{0.15} Ce _{0.1} Co ₄ Sb ₁₂ (PNNL3-G1B) n-type	20-22	133.9	0.185	135.8	0.194
In _{0.2} Ce _{0.15} Co ₄ Sb ₁₂ n-type	20.6	124.5	0.213	125.7	0.214
In _{~0.2} Ce _{~0.1} Co ₄ Sb ₁₂ – n-type (a in Figure 15)	20.5	123.1	0.197	125.1	0.217
In _{0.2} Ce _{0.17} Co ₄ Sb ₁₂ – n-type (b in Figure 15)	19.9	109.5	0.213	108.5	0.210
In _{0.2} Ce _{0.05} Yb _{0.1} Co ₄ Sb ₁₂ n-type (c in Figure 15)	20-22	89.5	0.208	85.9	0.207

Table 3. Structural properties of p-type $\text{In}_{0.2}\text{Ce}_{0.15}\text{Fe}_z\text{Co}_{4-z}\text{Sb}_{12}$ and p-type $\text{In}_{0.2}\text{Ce}_{0.15-y}\text{Yb}_y\text{Fe}_z\text{Co}_{4-z}\text{Sb}_{12}$ compounds

	Temperature [°C]	No Thermal Cycling		ZT
		Young's Modulus, E $\times 10^9$ [N/m ²]	Poisson's Ratio, ν	
$\text{In}_{0.2}\text{Ce}_{0.15}\text{Fe}_{0.5}\text{Co}_{3.5}\text{Sb}_{12}$ p-type	20.3	46.4	0.18	~0.2-0.25 (@ 673 K)
$\text{In}_{0.2}\text{Yb}_{0.05}\text{Ce}_{0.1}\text{Fe}\text{Co}_3\text{Sb}_{12}$ p-type	20.4	99.26	0.210	0.48 (@ 710 K)
$\text{In}_{0.2}\text{Yb}_{0.1}\text{Ce}_{0.05}\text{Fe}\text{Co}_3\text{Sb}_{12}$ p-type	20.8	92.38	0.205	0.48 (@ 710 K)

$\text{In}_{0.2}\text{Ce}_{0.15}\text{Co}_4\text{Sb}_{12}$ -composition achieving our ultimate goal of ZT ~ 1.6, but at temperatures in the 475 K to 525 K range. The CTE measurements in Table 1 are generally taken at 200°C, but show little variation from room temperatures to about 400°C. Table 1 also shows comparisons to the structural and thermoelectric properties of common, more conventional TE materials, such as bismuth telluride (Bi_2Te_3) alloys and lead telluride (PbTe) alloys. The Young's modulus and Poisson's ratio of $\text{In}_{0.2}\text{Ce}_{0.15}\text{Co}_4\text{Sb}_{12}$, $\text{In}_{0.2}\text{Co}_4\text{Sb}_{12}$, and $\text{In}_{0.2}\text{Ce}_{0.05}\text{Yb}_{0.1}\text{Co}_4\text{Sb}_{12}$ compositions (the best performing n-type TE materials) were slightly lower than that for the base $\text{Co}_4\text{Sb}_{12}$ skutterudite material. The CTE of these materials was also lower than the base $\text{Co}_4\text{Sb}_{12}$ skutterudite material.

The project accomplishments in FY 2010 also included performing thermal cycling on several of the n-type InCe-based $\text{Co}_4\text{Sb}_{12}$ materials from 50°C to 400°C (200 cycles), and then re-checking the structural properties for any significant changes that would indicate microcrack initiation or growth [4-6]. Table 2 show the impacts of the thermal cycling on the structural properties (E, ν) of several of the n-type compositions. In general, the thermal cycling impact did not appreciably change either the Young's modulus or the Poisson's ratio in these materials, which indicates that no microcrack initiation or growth is occurring in these advanced n-type skutterudite materials [4-6]. Figure 15 shows three of the InCe-based $\text{Co}_4\text{Sb}_{12}$ materials in Table 2 that went through thermal cycling in FY 2010. Other InCe-based

$\text{Co}_4\text{Sb}_{12}$ materials in Table 2 that went through thermal cycling are shown in Figure 4. Their thermal cycling capabilities show important stability characteristics that are crucial to effectively transitioning these n-type InCe-based skutterudites into TE devices for waste energy recovery applications, as these applications necessarily will require systems to cycle up and down in temperature repeatedly during their intended lifetimes.

Three different p-type skutterudites, $\text{In}_{0.2}\text{Ce}_{0.15}\text{Fe}_{0.5}\text{Co}_{3.5}\text{Sb}_{12}$, $\text{In}_{0.2}\text{Yb}_{0.05}\text{Ce}_{0.1}\text{Fe}\text{Co}_3\text{Sb}_{12}$, and $\text{In}_{0.2}\text{Yb}_{0.1}\text{Ce}_{0.05}\text{Fe}\text{Co}_3\text{Sb}_{12}$ compounds, were fabricated and their properties characterized during FY 2010. Table 3 shows the measured structural properties and ZT values of these p-type compounds. Although their CTE was comparable to the n-type skutterudite compositions discussed herein, their Young's modulus was significantly lower than that for the n-type compositions developed in this work. We have not thermally cycled these p-type materials because their low TE performance did not justify the time and expense.

Additional FY 2010 work focused on constructing the high-temperature thermal chamber and transducers necessary for obtaining the structural properties of TE materials up to 300°C to 400°C. Various components (i.e., transducers, sample holders and gas flow chambers) were fabricated and reported during FY 2009 to prepare for the high-temperature structural property measurements. During FY 2010 the entire thermal chamber was



a.) $In_{0.2}Ce_{\sim 0.1}Co_4Sb_{12}$ – n-type



b.) $In_{0.2}Ce_{0.17}Co_4Sb_{12}$ – n-type



c.) $In_{0.2}Ce_{0.05}Yb_{0.1}Co_4Sb_{12}$ n-type

Figure 15. Actual n-type $In_xCe_yCo_4Sb_{12}$ and $In_{0.2}Ce_{0.05}Yb_{0.1}Co_4Sb_{12}$ TE samples in Table 2. Samples are all about 0.5-cm long.

completed. Figure 16 is a schematic and SolidWorks rendering of the thermal chamber design, and Figure 17 shows the completed thermal chamber. During FY 2010, a new high-temperature transducer design was developed to provide more reliable and consistent RUS signals in the high-temperature structural property measurements planned in FY 2011. This new transducer design shown in Figure 18 will be integrated into the high-temperature thermal chamber system shown in Figures 16 and 17 and the RUS control and analysis software to produce high-temperature structural property measurements, E and ν , in FY 2011.

The high temperature structural measurements are currently planned in FY 2011 for all the n-type materials shown in Table 2 and all the p-type materials shown in Table 3. We plan to report on these results in next year's OVT Merit Review and Annual Report (2011).

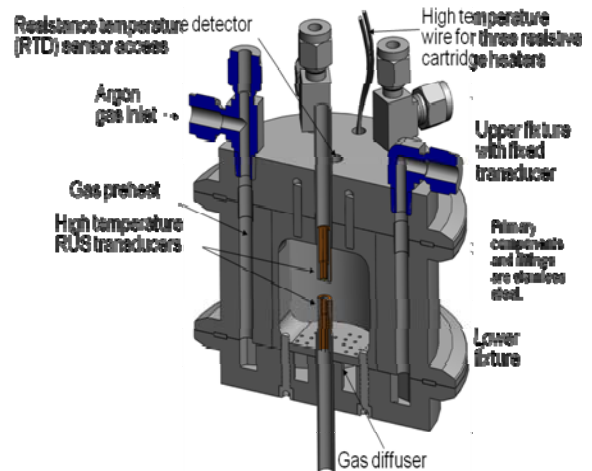


Figure 16. High-temperature thermal chamber design for high-temperature structural measurements

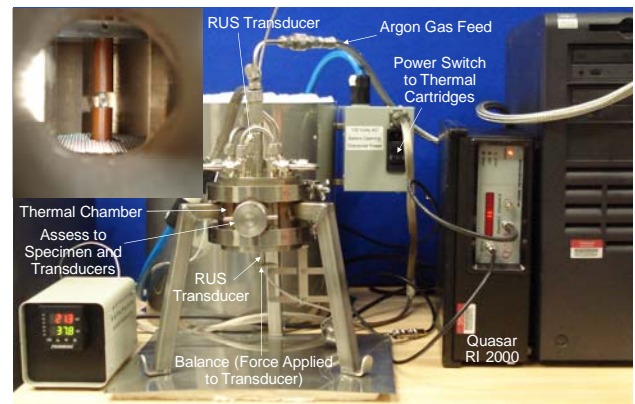


Figure 17. High-Temperature Thermal Chamber Fabricated in FY 2010

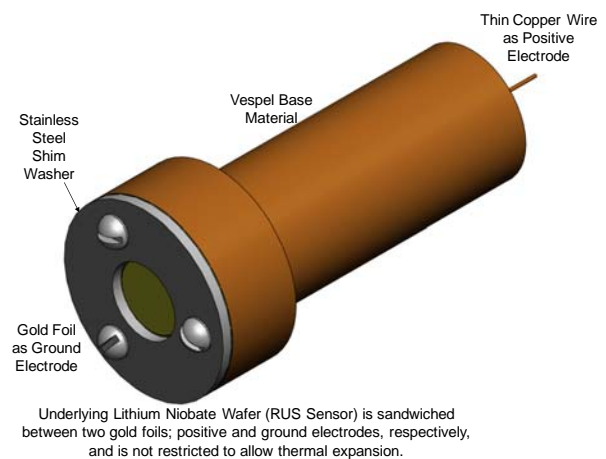


Figure 18. High-Temperature RUS Transducer Design for High-Temperature Structural Measurements

Conclusions

- Several n-type InCe-based $\text{Co}_4\text{Sb}_{12}$ skutterudite compounds were investigated and fabricated this year. The temperature-dependent thermoelectric properties of n-type $\text{In}_{0.15}\text{Ce}_{0.1}\text{Co}_4\text{Sb}_{12}$, $\text{In}_{0.1}\text{Y}_{0.1}\text{Co}_4\text{Sb}_{12}$, $\text{In}_{0.2}\text{Ce}_{0.15}\text{Co}_4\text{Sb}_{12}$, $\text{In}_{0.2}\text{Co}_4\text{Sb}_{12}$, and $\text{In}_{0.2}\text{Ce}_{0.05}\text{Yb}_{0.1}\text{Co}_4\text{Sb}_{12}$ compounds were measured. The room-temperature structural properties of these n-type materials also were measured.
- $\text{In}_{0.2}\text{Ce}_{0.15}\text{Co}_4\text{Sb}_{12}$, $\text{In}_{0.2}\text{Co}_4\text{Sb}_{12}$, and $\text{In}_{0.2}\text{Ce}_{0.05}\text{Yb}_{0.1}\text{Co}_4\text{Sb}_{12}$ compounds showed the best TE property performance, with $\text{In}_{0.2}\text{Co}_4\text{Sb}_{12}$, and $\text{In}_{0.2}\text{Ce}_{0.05}\text{Yb}_{0.1}\text{Co}_4\text{Sb}_{12}$ exhibiting ZT values as high as 1.2 at 620 K and $\text{In}_{0.2}\text{Ce}_{0.15}\text{Co}_4\text{Sb}_{12}$ showing ZT values of 1.5 to 1.6 at 475 K.
- The Young's modulus and Poisson's ratio of $\text{In}_{0.2}\text{Ce}_{0.15}\text{Co}_4\text{Sb}_{12}$, $\text{In}_{0.2}\text{Co}_4\text{Sb}_{12}$, and $\text{In}_{0.2}\text{Ce}_{0.05}\text{Yb}_{0.1}\text{Co}_4\text{Sb}_{12}$ compositions (the best performing n-type TE materials) were slightly lower than that for the base $\text{Co}_4\text{Sb}_{12}$ skutterudite material. The coefficient of thermal expansion of these materials was also lower than the base $\text{Co}_4\text{Sb}_{12}$ skutterudite material. These compounds also have higher Young's modulus, E, and slightly lower Poisson's ratio, ν , than more conventional TE materials, such as Bi_2Te_3 alloys and PbTe alloys.
- The project performed thermal cycling from 50°C to 400°C (200 cycles) on several of the n-type InCe-based $\text{Co}_4\text{Sb}_{12}$ materials and re-checked their structural properties for any significant changes that would indicate microcrack initiation or growth. In general, the thermal cycling impact did not appreciably change either the Young's modulus or the Poisson's ratio in these materials, which indicates that no microcrack initiation or growth is occurring in these advanced n-type skutterudite materials. Their thermal cycling capability shows important stability characteristics that are crucial to effectively transitioning these n-type InCe-based skutterudites into TE devices for waste energy recovery applications.
- Three separate p-type InCe-based $\text{Co}_4\text{Sb}_{12}$ skutterudite compounds, $\text{In}_{0.2}\text{Ce}_{0.15}\text{Fe}_{0.5}\text{Co}_{3.5}\text{Sb}_{12}$, $\text{In}_{0.2}\text{Yb}_{0.05}\text{Ce}_{0.1}\text{Fe}\text{Co}_3\text{Sb}_{12}$, and $\text{In}_{0.2}\text{Yb}_{0.1}\text{Ce}_{0.05}\text{Fe}\text{Co}_3\text{Sb}_{12}$ compounds, were fabricated and their properties characterized during FY 2010. However, their ZT values were generally low, less than 0.5 at 670 K to 710 K. We believe that the Fe content (stoichiometry) must be higher to achieve better ZT values.
- X-ray diffraction analysis has shown that all the n-type skutterudite materials are pure, single-phase compounds whose lattice parameters are 9.0452 Å to 9.0656 Å. The p-type skutterudite compounds also are pure, single-phase compounds whose lattice parameters are 9.1024 Å to 9.1096 Å.
- Sample preparation is critical to making high-quality structural measurements using the RUS technique. It is critical to take the time and effort to make surfaces planar and sharp 90-degree corners and edges. Proper sample preparation requires constant vigilance and attention to detail.
- Our high-temperature equipment is now designed and fabricated to perform high-temperature structural measurements on our n-type and p-type skutterudite TE materials in FY 2011. We plan to measure their structural properties at temperatures up to 300°C.
- We will be selecting the best n-type skutterudite materials to transition into operating TE couples for thermoelectric performance testing during FY 2011. We will likely select our n-type skutterudite from the $\text{In}_{0.2}\text{Ce}_{0.15}\text{Co}_4\text{Sb}_{12}$, $\text{In}_{0.2}\text{Co}_4\text{Sb}_{12}$, and $\text{In}_{0.2}\text{Ce}_{0.05}\text{Yb}_{0.1}\text{Co}_4\text{Sb}_{12}$ compositions discussed in this FY 2010 annual report.

Presentations/Publications/Patents

T.J. Hendricks and M. Subramanian. 2009. *Proactive Strategies for Designing Thermoelectric Materials for Power Generation*. May 22, 2009, Arlington, Virginia. DOE

Vehicle Technologies Program 2009 Annual Merit Review.

T.J. Hendricks and M. Subramanian. 2009. *Proactive Strategies for Designing Thermoelectric Materials for Power Generation*. September 29–October 2, 2009, San Diego, California. DOE 2009 Thermoelectrics Applications Workshop.

T.J. Hendricks and M. Subramanian. 2010. *Proactive Strategies for Designing Thermoelectric Materials for Power Generation*. June 10, 2010, Arlington, Virginia. DOE Vehicle Technologies Program 2010 Annual Merit Review.

T.J. Hendricks, M. Subramanian, K. Biswas, and M. Good, 2010, “*Thermoelectric and Structural Properties of High-Performance In-based Skutterudites for High-Temperature Energy Recovery*”, Materials Research Society Fall 2010 Meeting, Session LL: Thermoelectric Materials for Solid-State Power Generation and Refrigeration, Boston, MA (Paper and Presentation Accepted).

References

1. Li, H., Tang, X.F., Zhang, Q.J., Uher, C., “High Performance $\text{In}_x\text{Ce}_y\text{Co}_4\text{Sb}_{12}$ Thermoelectric Materials with In-Situ Nanostructured InSb Phase”, *Proceedings of the 2010 International Conference on Thermoelectrics*, Shanghai, China, June 2010.
2. Graff, J.W., Peng, J.Y., He, J., Su, Z., Alboni, P.N., Zhu, S., Tritt, T., “High Temperature Thermoelectric Properties of $\text{Co}_4\text{Sb}_{12}$ based Skutterudites with Multiple Filler: $\text{In}_x\text{Ce}_y\text{Yb}_z\text{Co}_4\text{Sb}_{12}$ ”, *Proceedings of the 2010 International Conference on Thermoelectrics*, Shanghai, China, June 2010.
3. Rogl, G., Grytsiv, A., Rogl, P., Bauer, E. Zehetbauer, M., “New Multifilled p-Type Didymium Skutterudites with $\text{ZT} > 1.2$ ”, *Proceedings of the 2010 International Conference on Thermoelectrics*, Shanghai, China, June 2010.

4. Laws, N. and Brockenbrough, J.R., The effect of micro-crack systems on the loss of stiffness of brittle solids, *Int. J. Solids Structures*, **23** (9): 1247-1268, 1987.

5. Budiansky, B. and O’Connell, R.J., Elastic moduli of a cracked solid, *Int. J. Solids Structures*, **12**: 81-97, 1976.

6. E. D. Case, “The Saturation of Thermomechanical Fatigue in Brittle Materials”, 137 – 208 in *Thermo-Mechanical Fatigue and Fracture*, WIT Press, Southampton, UK, 2002.

Acronyms

CTE – Coefficient of Thermal Expansion
 DOE – Department of Energy
 FY - Fiscal Year
 HPS – Hot Pressed and Sintering
 ORNL – Oak Ridge National Laboratory
 OSU – Oregon State University
 OVT – Office of Vehicle Technologies
 PNNL – Pacific Northwest National Laboratory
 RUS – Resonant Ultra-Sound
 SUV – Sport Utility Vehicle
 TE – Thermoelectric
 XRD – X-Ray Diffraction
 XRF – X-Ray Fluorescence

Agreement 13721 – Low-friction Hard Coatings

Principal Investigators: A. Erdemir and O. L. Eryilmaz

Argonne National Laboratory

9700 S. Cass Avenue, Argonne, IL 60439-4838

(630) 252-6571; fax: (630) 252-5568; e-mail: Erdemir@anl.gov; Eryilmaz@anl.gov

DOE Technology Manager: Jerry L. Gibbs

(202) 586-1182; fax: (202) 586-1600; e-mail: jerry.gibbs@ee.doe.gov

Contractor: UChicago Argonne LLC

Contract No.: DE AC03 06CH11357

Objective

- Design, develop, and implement super-hard and low-friction coatings to increase the durability, fuel economy, and environmental compatibility of future engine systems.

Approach

- Optimize deposition parameters that are most effective in the physical, mechanical, and tribological properties of superhard and low-friction coatings.
- Increase bonding and reduce surface roughness, demonstrate large-scale production and cost-competitiveness, and verify durability and performance in actual engine applications.

Accomplishments

- Validated large-scale manufacturability of optimized coatings in commercial-scale deposition systems with our coating partner.
- Further optimized deposition conditions to achieve much stronger bonding and very smooth surface finish on coated parts.
- Developed a very effective polishing and post-deposition conditioning method to further improve the performance and durability of coated parts.
- Filed a new patent application on the method developed for surface conditioning.
- Verified the superior mechanical and tribological properties of optimized coatings by bench-top studies.
- Completed screening tests of optimized coatings with the help of engine company partners.
- Verified significant improvements in efficiency and durability of optimized coatings in actual engine tests.
- Initiated/continued long-duration performance tests of optimized coatings in actual engines.

- Demonstrated batch-to-batch repeatability of optimized coatings in quality control and performance.
- Confirmed cost-competitiveness of optimized coatings.
- Honored with R&D-100 award on November 12, 2009, in Orlando, FL.
- Advanced commercialization efforts. Licensing of technology is in the final stages; term sheet and business plan have been agreed upon.

Future Direction

- Develop faster and more efficient ways to clean, load, unload, and inspect coated engine parts.
 - Develop more effective quality control procedures and deposition protocols for large-scale manufacturing.
 - Explore and adapt the next generation high-power impulse magnetron sputtering (HIPIMS) technique for the production of much harder and more adherent coatings. This technique is a latest development in the coatings field and has proven to result in the most desirable kinds of coatings in terms of their hardness, smoothness, and bonding to substrates at much lower deposition temperatures.
 - Develop new coating procedures to eliminate the need for post-deposition polishing.
 - Control oxygen and copper enrichment in top layer on coating during deposition process.
 - Finalize licensing agreement.
 - Foster technology transfer and commercialization.
-

Introduction

Higher energy efficiency, longer durability, and lower emissions are much desired attributes in future transportation systems; but, without further improvements in the surface mechanical and tribological properties of sliding, rolling, or rotating engine components, these goals will be difficult to realize. In particular, higher loads, speeds, temperatures, and other harsh operating conditions in future engines will render most traditional materials and lubricants useless. Accordingly, in this project, we aim to design, develop, and implement novel superhard and low-friction coatings that can result in much higher energy efficiency, longer durability, and lower emissions in future engines. A nano-structured and composite coating consisting of MoN hard phase and Cu soft phase is a typical example of the superhard coatings that we have developed over the years, while a nearly frictionless diamond-like carbon (DLC) film represents the low-friction coatings that we have been working on at Argonne under this project.

During FY 2010, we made remarkable progress toward large-scale production, field testing, and licensing of our superhard and low-friction coating technology. Specifically, we worked very closely with Hauzer Technocoating (one of the largest company in this field in the world) and Galleon International to produce these coatings on functional surfaces of numerous engine parts by using a production-scale deposition system available at Hauzer. We also worked closely with several engine companies and successfully deposited our superhard and slick coatings on their engine parts and components for

performance and durability tests in simulated and actual engines.

Experimental

During FY 2010, we focused our attention on the deposition and post-process surface conditioning of our superhard coatings using commercial-scale deposition systems with commercial-scale loads. The following needed to be conducted in order to achieve a strongly bonded, dense, hard, and smooth coating:

- Quality control and repeatability studies on the optimized coatings for the same or similar components on full loads.
- Assessment of the dependence of coating property on differently shaped and sized engine parts as well as different substrates (i.e., different grades of steels).
- Determination of the effect of process parameters on the coating's physical, structural, and mechanical properties.
- Development of effective deposition conditions and incorporation of these into computer-based protocols for improved reliability/repeatability.
- Determination of the potential effects of source (target) materials on coating quality and determination of the possible differences between different suppliers.
- Comparison of the mechanical properties and tribological performance of different types of currently used coatings (e.g., CrN and DLC) with those of superhard coatings.

During our engine studies in FY10, the surface roughness was found to be

detrimental to the friction and wear resistance of most coated engine parts. Therefore, we continued our work on post-deposition surface conditioning and polishing to make sure that the parts coated with our coatings had a smooth surface finish in addition to their superhardness. If the surface finish was not smooth enough, then the friction values were not at desirable levels, and the wear on counterface materials was high. The surface smoothening by the running-in process takes a long time due to the hardness of the coatings. For our coatings to function properly in engines (by not only providing high wear resistance but also low friction), they had to be surface conditioned or polished prior to component or engine testing.

Accordingly, during FY10, with our industrial partners, we tried several remedies to control the surface roughness of these coatings, and in the end, we developed an effective method that seems to remove most of the surface asperities and, hence, provides a very desirable surface finish. When these polished parts or test samples were subjected to tribological tests, we attained much lower friction values compared with the current coatings in most engine studies. With our partners, we further optimized our polishing and surface conditioning procedures and filed a patent application. This novel procedure effectively removed the oxygen- and copper-rich top layers; hence, it provided an effective film that was structurally and chemically more homogeneous and representative of the superhard and low friction coatings. Again, without the removal of somewhat rough and chemically different surface layers (which we call “termination layers”), the initial friction and wear coefficients were not at a desired level,

and the run-in process for achieving low friction took very long.

When commercial-scale loads are used in commercial-scale deposition systems, the mechanical and tribological properties of end products might differ from what was achieved in small (experimental) scale loads. Therefore, we carried out a systematic experimental study to optimize the deposition parameters for certain products in large-scale loads. In these studies, we primarily targeted deposition of engine tappets and piston rings, since those components have been successfully tested in the past by the automotive companies with which we have been collaborating. Also, these companies confirmed that those components had the highest priority for the application of superhard coatings, since they were failing prematurely under the much harsher application conditions of new engines. Based on the experimental feedback from them, we optimized the process parameters and achieved much harder (i.e., above 2800 HV) coatings with desired composition and microstructure on tappets and piston rings. These newer coatings met their expectations, and from now on, we will be adopting the same coating protocols to deposit the same quality coatings on tappets and piston rings.

Based on our earlier studies, we determined that having the correct coating chemistry was extremely important for tribological performance and for coating compatibility with lubricants and additives. Accordingly, we spent a significant amount of time and effort this past year to further optimize the coating chemistry and maintain it from batch to batch (which required extensive quality control studies, including chemical

analysis). Without the correct coating chemistry, the tribochemical reactions were not taking place at the desired levels and hence were not leading to the formation of low-shear boundary films on sliding surfaces. In an effort to achieve a consistent and repeatable coating chemistry, we worked closely with a number of sputtering target companies and the expert engineers of our coating partners and reached a consensus on the fabrication of special sputtering targets that would result in the correct coating compositions one run after another.

Results

Based on the knowledge gained from the above studies, we produced a series of smooth and dense MoN-Cu coatings on representative engine parts and steel substrates. We found that larger surface area fixtures increase BIAS current and, hence, result in much denser plasma during deposition. This denser plasma is especially beneficial during low temperature depositions to achieve and maintain denser coating structures.

During FY10, our industrial coating partner prepared and delivered coated tappets, crank shafts (Figure 1), rocker arms, piston rings, and piston pins to several automotive companies for their internal evaluation and engine testing. We also received some of them for our internal evaluation and quality control. Our initial auger analyses showed an oxygen- and copper-rich top layer near the surface of the coatings. This "termination layer" is removed during the post-polishing process, and it might have contributed to higher friction and undesirable counter-face wear in some engine tests. When we inspected some of the parts, we could easily see abrasive

wear marks, suggesting that a rough surface finish was present on the coated parts. The thickness of the structurally and chemically different termination layer depended highly on the thickness of the coating itself, but it was usually around 100 nm. Figure 2 shows an Auger electron spectrum of polished and unpolished coated surfaces. We are currently working on a new experimental procedure to minimize or eliminate the formation of this termination layer during the deposition. If this layer is eliminated, post-polishing may not be necessary. Eliminating this step makes the process much more applicable to many components and, hence, more cost competitive for industrial applications.

During FY10, we continued to closely work with Hauzer Technocoating. Most of the technical interchange included the details of scale-up production of superhard coatings. With our help, they deposited numerous parts for several industrial companies in the transportation field. We held numerous conference calls with their process engineers to teach them how to overcome some of the issues that were related to the processing of full-scale loads. Coatings produced according to our instructions were then sent to us for quality control and tribological evaluation. As part of this close collaboration, we met with Hauzer personnel and discussed the details of the parameters that can play an important role in overall coating quality.

Through our internal studies, we determined that the tribological performance of several industrial coatings was not at the desired or acceptable levels, and the repeatability of test results was not very good. After several rounds of corrective actions and trials, we

succeeded in the production of reliable, high-quality coatings in their production-scale systems with full production loads. We kept performing routine quality control tests on parts and samples for them after each deposition run to make sure that they will provide low friction and wear in actual engine tests. The same coated parts and samples were also subjected to the coating company's tests for hardness, adhesion, thickness, etc. The results from these joint studies were compared and discussed in detail during weekly conference calls.

Figures 3 and 4 compare the results of ball-on-disc tribological tests conducted on CrN and SHNC coatings at 110 °C, respectively. It is clear that the friction and wear performance of the SHNC coating is much better than that of CrN. The CrN coating exhibits a high friction coefficient with a slow decrease and jumps back up to high levels after the run-in period. We believe that the slight reduction in friction with increasing sliding distance is related to the wear of the counterface pin resulting in increasingly lower contact pressures. This effect may push the test condition to a more hydrodynamic regime, and hence may result in a low friction behavior. In contrast, the friction coefficient of SHNC remains stable around 0.06 after a brief high friction regime initially. The wear scar seen in Figure 4 represents the contact area. The line scan image of the counterface clearly shows no measurable wear.

With the installation of a new HIPIMS source, our coating system at Argonne is now one of a kind and is well-suited for the synthesis of much superior coatings for industrial applications. With this new power source, the ionization efficiency of

our deposition system increased by factors of 10 to 15 (this capability will have a positive impact on the structural morphology and adhesion of coatings on the substrate materials). We are in the final stage of starting to adapt the same HIPIMS technique for the production-scale loads with Hauzer Technocoating.

Overall, the recent test results from our industrial partners on coated engine parts were also impressive. The partners have supplied numerous coated engine parts to some of the biggest engine/automotive and racing car engine companies for trial. In most of these, much superior performance and durability were achieved compared to existing materials and coatings. Specifically, our superhard coatings performed extremely well in their friction, wear, and scuffing tests and resulted in huge reductions in friction and wear. Based on these remarkable results, the industrial partners are now preparing to initiate field and fleet studies. They are already working closely with our coating partner for the treatment of numerous engine components, including tappets and piston pins and rings, which will be used in these field studies.

Our licensing discussions are in the final stages with our industrial partners. The contract terms have been agreed to by both the Argonne and partners' legal department. Argonne is preparing the final text of a licensing agreement for approval by the industrial partners that will commercialize the technology.

Conclusions

During FY10, we made remarkable progress in terms of scaling up and

commercializing our superhard and low-friction coatings. Most of the product optimization and quality control studies have now been completed. Our industrial partner in the coating field is able to produce essentially the same quality coatings as the original ones that we had developed at Argonne. During FY10, we also performed extensive tests on numerous coatings provided by our industrial partners and confirmed that the latest coatings were as good as our original coatings in terms of tribological performance. Tests by the engine company partners further confirmed the impressive tribological properties of these coatings in actual engines. The surface analytical studies on coated parts revealed the presence of an undesirable termination layer, which can be removed by post-polishing. Next year we will be focusing on the elimination of this layer during the deposition process. We will also transition to HIPIMS technology, which should provide stronger adhesion, smoother surface finish, and much superior mechanical and tribological properties. All of these attributes are extremely important for achieving further improvements in performance and durability of actual engine parts. We will also continue to test and qualify the coatings produced by our industrial partners and provide our expert opinions on their performance.

During FY11, we hope to finalize technology transfer and licensing, finish cost-benefit analysis, and foster full-scale commercialization of our coating technology.

Patents and Publications

During FY10, a new patent application was filed, and we published and/or presented several new papers on the work that was performed under this project as listed below.

Patent Application

1. A. Erdemir, O. L. Eryilmaz, M. Urgan, F. Sykora, and D. Parsons, "Hard and Low Friction Nitride Coatings," international patent application being filed.

Publications:

1. A. Erdemir and A. Voevodin, "Nanocomposite Coatings for Severe Applications," in *Handbook of Thin Films*, P. Martin, ed., Elsevier, pp. 679-715, 2010.
2. A. Erdemir, O. L. Eryilmaz, M. Urgan, and K. Kazmanli, "Advanced Tribological Coatings for Automotive Applications," in Proc. of the 10th Biennial ASME Conference on Engineering Systems Design and Analysis, Istanbul, Turkey, July 12-14, 2010, pp. 655-659.

Presentations:

1. A. Erdemir, O. L. Eryilmaz, M. Urgan, and K. Kazmanli, "Advances in Superhard and Low-Friction Coatings for Extreme Tribological Applications," invited talk, ASME/STLE International Joint Tribology Conference, Memphis, TN, Oct. 19-21, 2009.
2. A. Erdemir, O. L. Eryilmaz, M. Urgan, and K. Kazmanli, "Novel

- Approaches to the Design of Superhard and Low-Friction Nanocomposite Coatings,” presented at the Theoretical Modeling and Experimental Simulation in Tribology, Cargese, Corsica, France, March 22-26, 2010.
3. A. Erdemir, O. L. Eryilmaz, M. Urgen, and K. Kazmanli, “Development of Multi-functional Nanostructured and Composite Coatings for Tribological Applications,” invited talk, Minerals Metals & Materials Society Meeting & Exhibition, Seattle, WA, February 14, 2010.
 4. K. E. Pappacena, D. Singh, O. Ajayi, J. L. Routbort, and O. L. Eryilmaz, “Processing and Tribological Properties of MoN/Cu Coatings,” to be presented at 35th International Conference and Exposition on Advanced Ceramics and Composites, Daytona Beach, FL, January 23-28, 2011.
 5. D. Singh, J. Routbort, K. Pappacena, O. Eryilmaz, G. Chen, and W. Liu, “Residual Stress Measurements in Thin Coatings,” presented at DOE Hydrogen Program and Vehicle Technologies Program Annual Merit Review and Peer Evaluation Meeting, Washington, DC, June 7-11, 2010.
 6. O. L. Eryilmaz, S. Cakir, K. Kazmanli, A. Erdemir, and M. Urgen, “Characterization of Tribofilms Formed on Mo-N-Cu Coatings under Boundary Lubrication Conditions,” presented at 13th European Conference on Applications of Surface and Interface Analysis, Antalya, Turkey, October 18-23, 2009.
 7. A. Erdemir, O. L. Eryilmaz, M. Urgen, and K. Kazmanli, “Advanced Tribological Coatings for Automotive Applications,” invited talk, 10th Biennial ASME Conference on Engineering Systems Design and Analysis, Istanbul-Turkey, July 12-14, 2010.
 8. A. Erdemir, “Design of Novel Nanocomposite Coatings for Severe Tribological Applications,” invited talk, Gordon Research Conference on Tribology, Waterville, ME, June 27-July 2, 2010.

Agreement 20370 – Life Cycle Modeling of Propulsion Materials

Sujit Das

Energy and Transportation Science Division

Oak Ridge National Laboratory

National Transportation Research Center

Knoxville, TN 37932-6472

(865) 946-1222; fax: (865)946-1314; e-mail: dass@ornl.gov

DOE Technology Manager: Jerry L. Gibbs

(202) 586-1182; fax: (202) 586-1600; e-mail: Jerry.gibbs@ee.doe.gov

ORNL Technical Advisor: D. Ray Johnson

(865) 576-6832; fax: (865) 574-6098; e-mail: johnsondr@ornl.gov

Contractor: Oak Ridge National Laboratory, Oak Ridge, Tennessee

Prime Contract No.: DE-AC05-00OR22725

Objectives

- Develop life cycle technical models that address the viability of existing and new lightweight propulsion materials from economic, energy, and environmental perspectives.
- Use technical modeling to estimate specific technology improvements and major drivers that are detrimental to the viability of advanced propulsion materials technologies.

Approach

- Examine the viability of advanced propulsion materials technologies on a life cycle basis, since the life cycle stages beyond the manufacturing stage form a major share of total life cycle impacts.
- Develop fairly detailed technical models to estimate the impacts of major input parameters at specific processing steps on the overall viability of a propulsion materials part manufacturing technology.

Accomplishments

- Completed a life cycle assessment of alternative lightweight light-duty engine designs for vehicle weight reduction and improved fuel economy.
- Completed a life cycle energy analysis of CF8C+ cast austenitic stainless steel.

Future Direction

- Life cycle cost analysis of an improved efficiency of an internal combustion engine using CF8C+ engine block and head with ceramic exhaust valves and a high temperature compatible piston.

Life Cycle Evaluation of Downsized vs. Lightweight Material Automotive Engines

The study conducts a comparative life cycle evaluation of the energy, environmental, and cost implications of two types of light-duty vehicle engines, downsized and lightweight, with respect to a baseline engine. For this purpose, the downsized engine that utilizes gasoline direct injection (GDI) and turbocharging is a 2.0L, I4, 4-

valve, dual overhead cam (DOHC), dual variable valve timing (d-VVT), turbocharged, GDI engine. The baseline is an equivalent, conventional 3.0L, V6, 4-valve, DOHC, d-VVT, naturally aspirated (NA), port fuel injected (PFI) engine. Both these engine configurations are obtained from Case Study # 0102 of the recent 2010 US Environmental Protection Agency (EPA) Light-Duty Technology Cost Analysis report, conducted by FEV, Inc. Because turbochargers improve both thermal

efficiency and engine specific output, they offer improved performance and improved economy, the latter achieved not only by virtue of better thermal efficiency but also by engine downsizing that reduces vehicle weight. The lightweight option is a variation of the baseline engine that uses magnesium in certain engine components, such as the cylinder block, oil pan, and front cover based on technical feasibility.

Life-Cycle Assessment (LCA) is a tool that allows us to evaluate the energy and environmental consequences of a product or manufacturing process throughout the product’s life, from the extraction of materials, through manufacturing, use, and end-of-life disposition, i.e., reuse, recycling, and/or ultimate disposal. Though only the engines are being compared, the life-cycle impacts of these engines can be assessed by including the amount of fuel consumed during the vehicle operation phase that typically accounts for the major share of energy and environmental impacts during the automobile’s life cycle. For this reason, the functional unit for LCA is taken to be an engine used in a car over its lifetime. The vehicle class defined is a mid- to large-size sedan that seats 4-6 passengers. The performance specifications for all three engine configurations are considered to be equivalent, with a maximum power output of approximately 225 hp and maximum torque of approximately 210 lb-ft. Compared to the baseline engine mass of 360 lbs, downsized and lightweight engine options considered were estimated to provide a mass savings of 19% and 7.2%, respectively. Due to turbocharging and smaller engine mass, the fuel economy improvement for the downsized engine is estimated to be 22%, compared to less than 1% for the lightweight engine material option.

The comparative evaluation of the energy and environmental implications of the downsized and lightweight engine designs was made using the three different impact assessment methodologies available in SimaPro life cycle software, i.e., cumulative energy demand, IPCC 2007 GWP 100a, and the eco-indicator. Using the cumulative energy demand method, it is seen that the vehicle equipped with the baseline engine has the highest lifetime energy consumption of 779 GJ equivalents, whereas the vehicles with the downsized and lightweight engines consume 643 and 744 GJ equivalents, respectively. (Table 1). Fuel use dominates the overall life cycle energy usage; thus, the downsized engine has the most life cycle energy savings potential. In terms of global warming potential, the downsized engine is still the most favorable engine design option, while the lightweight option is unfavorable even compared to the baseline if SF₆, with its higher global warm-

ing potential, continues to be used as the cover gas in magnesium production. From the cost perspective, the incremental costs per engine for the downsized and lightweight material engines are estimated to be \$69 and \$101, respectively.

Table 1: Primary Energy Use per Vehicle by Life Cycle Stages (in GJ Eq.)

Life Cycle Stage	Base-line	Down-sized	Light-weight
Manufacturing	15	10	18
Fuel Use	775	640	739
Recycling	-11	-7	-13
Total Energy	779	643	744

The results of the assessment indicate that engine downsizing through turbocharging and gasoline direct injection leads to significant reductions in energy and environmental impacts, a result of notable improvements in fuel efficiency as well as lesser quantities of materials required for manufacturing. The weight reduction in the downsized engine is estimated to be about 68 lbs, as compared to the baseline engine. The dominance of aluminum use in turbocharged engine will continue, although a different alloy with better mechanical properties to withstand turbocharger’s high temperature and pressure will be used. The downsized turbocharged vehicle fuel efficiency varies widely depending on the engine type and drive cycle, and the literature reports a maximum improvement of 30% to be currently achievable with downsizing. The fuel economy benefits obtained purely by lightweighting the engine are marginal, unless the weight reduction is applied to the other major vehicle components through the use of lightweight metals such as magnesium and glass- and carbon-fiber-reinforced composites. Additional weight savings in the vehicle, estimated at 25-30%, beyond what is possible in the powertrain alone, would be necessary for the lightweight option to achieve improvements comparable to the downsized engine. The downsized engine is also estimated to be the most cost-effective option, since its cost per mpg fuel economy is estimated to be about \$16 compared to \$98 for lightweight material engine. Even if one assumes the significantly higher cost of downsizing that are provided in other published studies, downsizing is still relatively more cost-effective than material lightweighting. A *combined approach* of downsizing the engine and lightweighting the entire vehicle, including

the engine components, wherever feasible, is looked upon as the most preferred path to achieving greater improvements in overall lifetime energy consumption and further reductions in environmental impacts. The overall environmental competitiveness of the lightweight magnesium material option is likely to be superior to the baseline engine, as the use of SF₆ cover gas in magnesium production continues to be phased out in the industry today.

Energy Benefits of CF8C+ Cast Austenitic Stainless Steel

CF8C+ is as a heat resistant, cast, corrosion resistant austenitic stainless steel that is suitable for applications exposed to high temperatures and extreme thermal cycling, such as air/exhaust-handling equipment for diesel and gasoline engines and turbine engine components. A recent cost effectiveness study of CF8C+ indicates CF8C+ offers both mass and cost savings relative to most competing materials, such as Ni-resist, HK30, CN-12, 625, and 617. This study extends the cost-effectiveness study by examining the potential energy benefits of CF8C+ in high temperature applications. Two specific potential market sectors have been considered, i.e., automotive applications and turbines, particularly coal-fired, power-generation, steam and industrial gas turbine market segments. Turbocharger housings and exhaust manifolds are two specific applications considered for the light- and heavy-duty automotive market. The energy-use estimation is made for selected markets on a life cycle basis, compares CF8C+ to the currently used competing material, and considers only three major life cycle stages, i.e., material manufacturing, part manufacturing, and material use. The forecast period is 2010 – 2025, and the projected use of this material is based on the assumed penetration rate and the total market forecasts available from the Energy Information Administration.

Turbocharged gasoline engines will play an increasingly important role in helping OEMs meet future fuel-economy regulations. Market penetration is expected to reach 75% by the end of the forecast period, i.e., 2025. Although not as fuel-efficient as turbo diesel engines, these engines provide both thermal efficiency and improved fuel economy, the latter achieved by virtue of better thermal efficiency but also by engine downsizing, leading to vehicle weight reduction. Research shows that, while maintaining engine power, turbocharging enables gasoline engine downsizing by about 30% and improves fuel economy by 8-10% while improving

torque and acceleration performance. Since the heavy-duty turbocharged automotive market is already saturated, the penetration rate is assumed to be 100% for energy benefit estimates, and the efficiency improvement due to CF8C+ material use is somewhat limited as there exists an upper limit for the turbocharger efficiency. To assess energy benefits, the analysis compares CF8C+ to conventional high-temperature performance HK30.

Figure 1 shows the estimated annual cumulative energy savings from CF8C+ material use and material manufacturing in the specific automotive applications studied here. Energy from part manufacturing is not included since savings are estimated to be significantly less compared to the other two life cycle stages' savings. Energy savings for light-duty vehicles due to material use is estimated to be lower during the early years of the forecast period, but as turbocharging penetrates the market for light-duty gasoline engines, the estimated energy savings achieved by light-duty trucks alone approaches the savings by heavy-duty trucks in 2025. Energy savings by heavy-duty vehicles occurs despite lower annual sales volume because heavy-duty vehicles have lower baseline fuel economy and higher average annual vehicle miles driven. Cumulative energy savings for light- and heavy-duty vehicles during material use are estimated to be around 91 trillion Btus and 40 trillion Btus, respectively, by 2025, compared to corresponding values of 320 billion Btus and 1254 billion Btus, respectively, in 2010. As one would expect, the

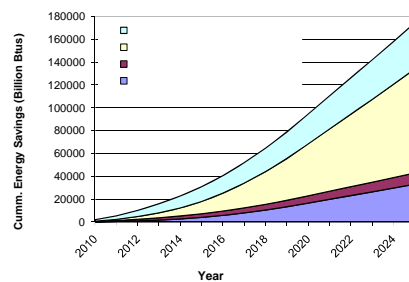


Figure 1. Estimated total cumulative life cycle energy savings of CF8C+ in the automotive market

use phase’s share of total energy savings is significantly higher than manufacturing’s share, increasing to 75% by 2025 in the case of light-duty vehicles. Total cumulative energy savings in the automotive sector is projected to increase from 2 trillions Btus in 2010 to 174 trillion

Btus by 2025. As a comparison, 2006 total manufacturing energy use in transportation equipment was an estimated 477 trillion Btus.

Increased powerplant efficiency will require supercritical and ultra-supercritical technology with continuously higher steam temperatures, conditions in which CF8C+ has potential for application. CF8C+ could be used for casings/shells components such as valves, steam chests, nozzle boxes, and cylinders and would compete with the Ni-base superalloys used today such as Inconel 625. For the industrial gas turbine market, CF8C+ has also been considered for application in combined-cycle plants where it would be used in components such as combustor housings. The potential amounts of CF8C+ used are assumed to be 3200 lbs and 1000 lbs, respectively, for steam turbines and industrial gas turbines sized consistently with those built in the industry today. Energy benefits at the final part use stage have been estimated based on the corresponding electricity generation and fuel use for the annual projected new capacity additions and 5% fuel efficiency improvement due to CF8C+ material use.

As the steam turbine market is projected to remain stagnant beyond 2016, total cumulative energy benefits from material manufacturing alone are projected to reach 115 billion Btus and remain constant throughout the last 10 years of the forecast period. On the other hand, with the comparatively modest growth in the gas/combined cycle turbine market, energy benefits are projected to increase from 38 billion Btus in 2010 to 199 billion Btus by 2025. The combined energy benefits for both turbine markets due to material manufacturing alone is thereby estimated to reach 314 billion Btus by 2025. Energy savings is achieved largely because of the higher nickel and chromium content of the currently used alloys.

Figure 2 shows the projected cumulative energy benefits for turbine use, with the two turbine types showing quite similar trends since both are based on the same projected market growth. Cumulative energy benefits in the gas turbine market are lower than in the steam turbine market during the early forecast period, as the load factor for in the latter case is considerably higher than the other market. Cumulative steam turbine engine use benefits are projected to increase from 17 trillion Btus in 2010 to 30 trillion Btus in 2025. The corresponding estimates for the gas turbine market are 12 trillion Btus and 31 trillion Btus, respectively. The combined energy benefits due to turbine use are thereby estimated to be 62 trillion Btus by 2025. As in the case of automotive market—due to similar values of heat capacity, melting temperature, and latent heat of fusion for

CF8C+ and the competing material superalloy 625—energy benefits due to part manufacturing are estimated to be negligible compared to material manufacturing and use life cycle stages.

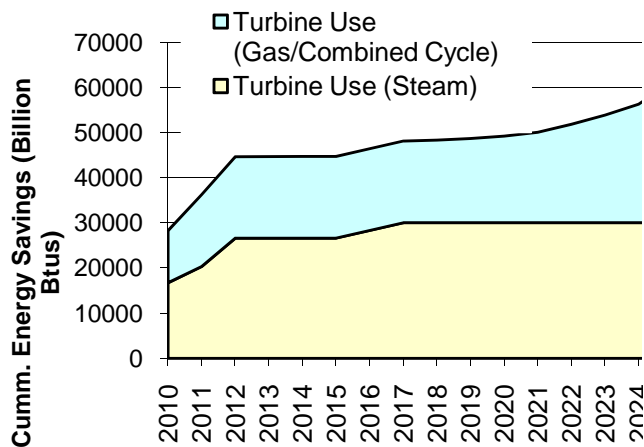


Figure 2. Estimated cumulative material use energy savings due to adoption of CF8C+ in the turbine market

Conclusions

Turbocharging, and the related downsizing of the engine, is estimated to be the more cost-effective, energy-efficient, and environmentally friendly option for light-duty vehicles, compared to the lightweight material use option. Since turbocharging provides the added advantage of fuel efficiency during vehicle use, most energy savings will occur at the main vehicle use life cycle stage. CF8C+ cast austenitic stainless steel has significant energy-savings potential in automotive and turbine markets, the former having almost three times greater potential than the latter market. Although energy benefits at the material use stage dominate life cycle benefits, energy savings per unit mass at the material manufacturing stage are estimated to be also significant also. Total cumulative energy savings for these two markets is estimated to be 236 trillion Btus by 2025, compared to 477 trillion Btus total manufacturing energy use in transportation equipment in 2006.

Publications/Presentations

A draft of an ORNL Report on Potential Energy Benefits of CF8C+ Cast Austenitic Stainless Steel was prepared for DOE/EERE/OVT by Sujit Das in September 2010.

A draft of an ORNL Report on Life Cycle Energy and Environmental Evaluation of Downsized vs. Light-weight Material Automotive Engines was prepared for DOE/EERE/OVT by Rajive Dhingra and Sujit Das in September 2010.

Special Recognitions and Awards/Patents Issued

None

Agreement 16226 – Integrated Surface Engineering Technology Development for Improving Energy Efficiency of Engine Components

S. M. Hsu

George Washington University

Exploration Hall, 20101 Academic Way, Ashburn, VA 20147

(703) 726-8365; fax: (703) 726-3665 ; e-mail: stevehsu@gwu.edu

DOE Technology Manager: Jerry L. Gibbs

(202) 586-1182; fax: (202) 586-1600; e-mail: jerry.gibbs@ee.doe.gov

ORNL Technical Advisor: D. Ray Johnson

(865) 576-6832; fax: (865) 574-6098; e-mail: johnsondr@ornl.gov

Contractor: National Energy Technology Laboratory
Prime Contract No.:

Objectives

- Develop a surface technology that is universal, scalable, low cost, and effective in friction control for engine components under normal operating conditions.
- Develop theory and data sufficient to provide design guidelines for application in engines.

Approach

- Conduct research to understand the effects of surface textures, thin films, and chemical films on friction.
- Develop soft lithographic mask fabrication technique to be used to create textures on surfaces of engine components with curvature.
- Develop test methods in conjunction with OEM partners to simulate engine conditions using actual engine parts for effective screening of textures, films, and surface chemistry.
- Work with OEM partners to validate approach in engines. Work with collaborations around the world to examine new materials, coatings, and fabrication techniques to further improve the fuel economy potentials of such surface technologies.

Accomplishments

- Developed surface texture design guidelines according to operating conditions.
- Developed large area soft lithographic mask fabrication technique capable of fabricating textures on large engine components such as rings, cams, and bearings.
- Developed an apparatus for testing actual engine components for frictional characteristics.

Future Direction

- Using engine parts to conduct simulation tests to examine the combined effect of textures, friction reduction films, bonded chemical films for durability and effectiveness under simulated engine conditions.
- Integrate the various component technologies into an optimized surface technology for each application.

Introduction

This project focuses on surface engineering design and practice to achieve fuel economy improvement in engines. It combines surface textures, topography control, thin solid films, and bonded chemical films to achieve a robust surface technology capable

of friction reduction. There are several technical barriers from concept to practice: (1) surface textures have been shown to be effective under low load, high speed operations of conformal contacts, but many engine contacts are counterformal, we need to extend the texture design to counterformal contact

surfaces; (2) we need to develop a versatile, low cost, easily scalable fabrication process for texture fabrication; (3) contacts in engines undergo variable speeds and loads, the texture design has to be able to function over a range of speed and loads. Current texture patterns are limited to a specific lubrication regime. We need to develop textural design that can function under multiple lubrication regimes.

We aim to overcome these barriers by developing new theory and practice in this important technology. We have generated extensive data base previously using simple laboratory bench tests and we are in the process of translating this knowledge into the real engine environment. The technology, when fully developed, will have universal application in engine technologies.

We are working on the following engine contact interfaces with our OEM partners: piston-ring and liner contact [the piston ring and liner contact accounts for 40-50% of total mechanical friction loss in diesel engines under in-service conditions (1-2)]; cam and the lifter contact (it accounts for 7-15% of the total mechanical energy loss in diesel engines under low speed conditions (including idling condition (1)).

We have previously developed a microlithographic technique coupled with electrochemical etching to fabricate surface textures. This technique is cost effective but is limited in size since the technique is intended for use in MEMS fabrication, and it is also restricted to flat surfaces. Therefore, we need to develop a new soft lithographic mask technique to wrap around piston rings and cam rollers for low cost fabrication.

Development of a soft lithographic mask

Conventional microlithography uses rigid masks (either glass or Mylar) and is not capable of fabricating textures on curved engine parts. Alternative techniques such as embossing, nanomechanical scratching, and laser ablation techniques are: 1) too expensive; 2) potentially cause damage to the surface [3]; 3) not capable of fabricating complex textural features or patterns in one step.

Soft lithography techniques have been developed to pattern organic molecules on surfaces. It uses patterned elastomeric polymer film as a mask to pattern 'soft materials' (polymers, gels and organic

molecules) on surfaces. The process involves the use of PDMS (poly dimethylsiloxane) mask for organic molecule adsorption and attachment (Fig. 2). Soft lithography has been applied in biochemistry, biology, and surface functionalization due to its simplicity, low cost and compatibility with cells (4-5).

Since PDMS mask can conform to irregular surfaces, the technique, in theory, can be applied to curve surfaces. However, soft lithography has not been applied to large area lithography or used in subsequent etching. Engine component requires size of tens of cm size and requires subsequent UV lithography and chemical etching steps. Also PDMS material is transparent to ultraviolet light; therefore, the PDMS mask cannot be used for UV lithography and etching steps. A hybrid lithographic technique has recently been proposed by Kim, et al. (6) to combine soft-lithography and photo-lithography to transfer micro-patterns onto a curved (very slight curvature) surface. The PDMS mask fabricated was still quite small; only about 10 x 10 mm. So far, no report exists on fabricating large size flexible mask for photo lithography.

We combined photo-lithography, thin film deposition technique, and soft- lithography to transfer micro-patterns from Si wafer coated with Ag film onto a soft transparent PDMS film. To separate the PDMS film from the silicon substrate, a self-assembled monolayer (SAM) has to be deposited on the film to ensure that the film can be peeled off easily.

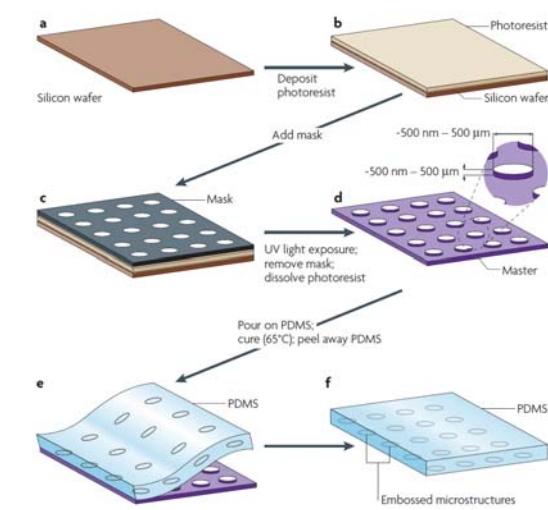


Fig. 2 Schematic illustration of soft lithography [6].

Fig. 3 illustrated the fabrication procedure. A SAM layer was created on the Si wafer. On top of the SAM layer, a 100 nm Ag film was deposited. The silver film covered silicon wafer went through UV lithography and chemical etching to produce the desired dimple pattern. Then another SAM was deposited. A PDMS mixture was then spin coated on the Si surface with Ag pattern and baked at 65°C for 3 hours. Finally, the cured PDMS film was peeled off from the Si surface.

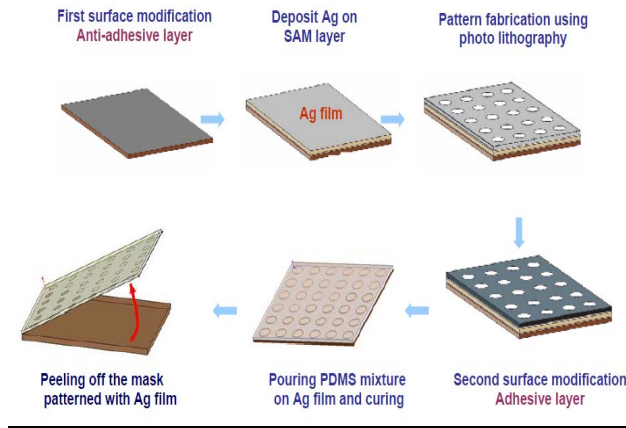


Fig. 3. Soft mask fabrication

The fabricated PDMS soft mask was then used to fabricate texture patterns on the steel surface to see whether the Ag layer could block the UV light or not. As shown in Fig. 4, fabricated PDMS with Ag could act like conventional photo mask, the Ag film blocked UV light; therefore, outside the pattern feature uniform photo resist covered the steel surface. It should be noted that even though the metal mask pattern was wrinkled on the PDMS mask due to the difference in the material property between the PDMS and Ag, the pattern feature fabricated on the steel surface did not show obvious change in pitch distance or shape. It indicates that the wrinkles of the PDMS mask do not influence the photolithography process.

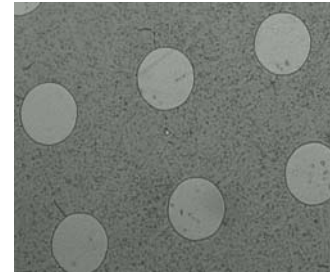


Fig. 4 Optical images showing: the texture on steel surface etched from the soft PDMS mask.

A soft lithography mask was successfully developed. Using this technique, larger size masks can be made limited by the silicon wafer size and the available processing equipment. The fabricated PDMS photo mask when fabricating textures on steel surface was able to maintain the size and shape of the textural pattern. The soft PDMS photo mask was successfully used to fabricate textural pattern on cut engine component surfaces.

Effect of thin films to protect textures

Under high load and slow speed (boundary lubrication conditions), the textures will be worn away unless protective films are used. We evaluated a wide variety of hard films from various sources. These include Chromium nitride, titanium nitride, carbides, and diamond-like carbon films. The film thickness ranges from 90 nm to 2000 nm thick.

Contact mechanics analysis of a dimple suggests that the edges of a dimple under high load low speed conditions induce very high contact stresses, as shown in Fig. 5. Under such stresses, the film covering the dimple will tend to crack under static loading. When shear stresses are added on top of that, the film delaminates, (Fig. 6). Once the film delaminates, the film debris will act as an abrasive in the contact, hence the friction increases.

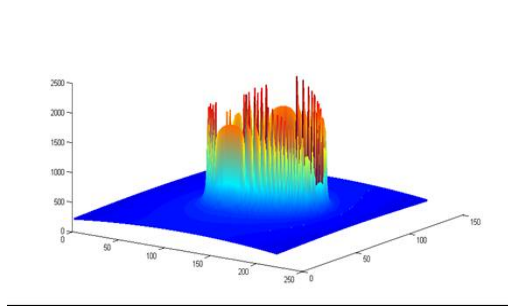


Fig. 5. Contact stress around the dimple edge

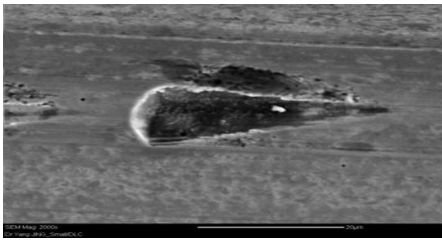


Fig. 6. Delamination of hard film at the edge perpendicular to the direction of sliding

Diamond like carbon film

After many film failures, a diamond-like carbon (DLC) film was selected. The film was deposited using a closed field unbalanced magnetron sputtering ion plating system (Fig. 7).

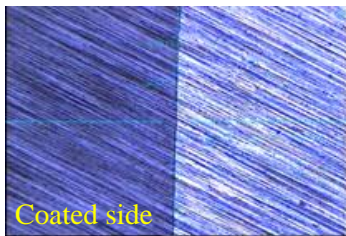


Fig. 7. SEM image of DLC film on steel

The DLC film was deposited on several baseline cases (polished sample, polished sample coated with the DLC film, textures with DLC film). The results are shown in Fig. 8.

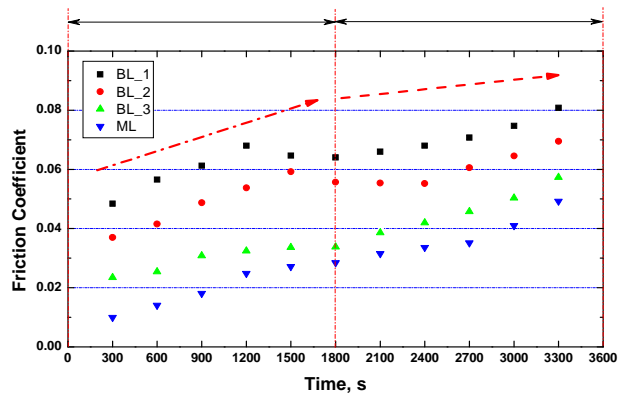


Fig.8. Comparison of friction coefficients of DLC protected textures with baseline cases under 30 kg load with velocity from 1.34m/s to 0.19 m/s.

Combined effect of DLC and chemical film

Since DLC film is not known to react with conventional engine oil additives such as zinc dialkyl dithiophosphate, without protection, a thin DLC film may not be able to provide long term protection for the textures. For this series of experiments, we use Mobil 1 lubricant as a baseline and then add chemicals to the lubricant to measure durability.

A new test procedure was developed to measure durability of the combined effect of DLC and chemistry. The test procedure uses a ball-on-three flats geometry under step loading test sequence. The speed changes from 1.15 m/s, 0.96 m/s, 0.77 m/s, 0.57 m/s, 0.38 m/s, to 0.19 m/s in an increasingly severe test condition.

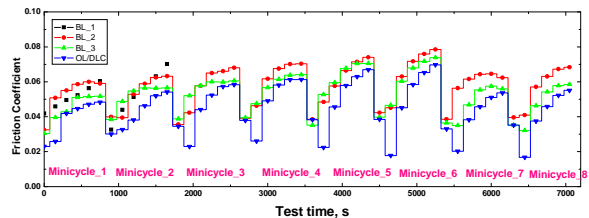


Fig. 9. Friction trace of four kinds of samples tested for durability

As can be seen from Fig.9, BL_1 (polished surface without texture lubricated with mineral oil) failed during the minicycle 2. But the three other

samples continued without failure even though different friction levels were observed.

Through this test procedure, we were able to find the best combination of DLC film and surface chemistry. The best combination increases durability about ten times over the baseline case (without DLC). DLC films by themselves without effective chemistry are not as effective.

Conclusions

We have successfully developed a new soft lithographic mask capable of fabricating textures on large curved surfaces. Surface texture under boundary lubrication conditions requires protection from wear. A DLC film with associated chemistry was able to increase the durability of the textured surface ten times over the base case in a bench test.

References

- [1] A. Comfort, An introduction to heavy- duty diesel engine frictional losses and lubricant properties affecting fuel economy – part I, SAE paper 2003-01-3225, 2003.
- [2] P. Andersson, J. Tamminen, and C.-E. Sandström, Piston ring tribology: A literature survey, VTT Research notes 2178.
- [3] X. Wang a, K. Kato, K. Adachi, K. Aizawa, “The effect of laser texturing of SiC surface on the critical load for the transition of water lubrication mode from hydrodynamic to mixed”, Tribology International 34 (2001) 703–711.
- [4] Douglas B. Weibel, Willow R. DiLuzio, and George M. Whitesides, “Microfabrication meets microbiology”, Nature Reviews | Microbiology, 5 (2007) 209-218.
- [5] Y. Xia, and G. M. Whitesides, “Soft lithography”, Angewandte Chemie, International Edition **37**, 550–575 (1998).
- [6] J. G. Kim, N. Takama, and H. Fujita, “Optical-softlithographic technology for patterning on curved surfaces”, Micromech. Microeng. 19 (2009) 055017.

This document highlights work sponsored by agencies of the U.S. Government. Neither the U.S. Government nor any agency thereof, nor any of their employees, makes any warranty, express or implied, or assumes any legal liability or responsibility for the accuracy, completeness, or usefulness of any information, apparatus, product, or process disclosed, or represents that its use would not infringe privately owned rights. Reference herein to any specific commercial product, process, or service by trade name, trademark, manufacturer, or otherwise does not necessarily constitute or imply its endorsement, recommendation, or favoring by the U.S. Government or any agency thereof. The views and opinions of authors expressed herein do not necessarily state or reflect those of the U.S. Government or any agency thereof.



For more information
1-877-EERE-INFO (1.877.337.3463)
eere.energy.gov

DOE/ORNL-28101

January 2011

Printed with a renewable-source ink on paper containing
at least 50% wastepaper, including 10% post consumer waste.